Topics in Mining, Metallurgy and Materials Engineering
Series Editor: Carlos P. Bergmann

Viswanatha Sharma Korada
Nor Hisham B. Hamid *Editors*

Engineering Applications of Nanotechnology

From Energy to Drug Delivery

Springer

Topics in Mining, Metallurgy and Materials Engineering

Series editor

Carlos P. Bergmann, Porto Alegre, Brazil

"Topics in Mining, Metallurgy and Materials Engineering" welcomes manuscripts in these three main focus areas: Extractive Metallurgy/Mineral Technology; Manufacturing Processes, and Materials Science and Technology. Manuscripts should present scientific solutions for technological problems. The three focus areas have a vertically lined multidisciplinarity, starting from mineral assets, their extraction and processing, their transformation into materials useful for the society, and their interaction with the environment.

More information about this series at http://www.springer.com/series/11054

Viswanatha Sharma Korada
Nor Hisham B. Hamid
Editors

Engineering Applications of Nanotechnology

From Energy to Drug Delivery

Springer

Editors
Viswanatha Sharma Korada
Mechanical Engineering Department
Universiti Teknologi Petronas
Seri Iskandar
Malaysia

Nor Hisham B. Hamid
Electrical Engineering Department
Universiti Teknologi Petronas
Seri Iskandar
Malaysia

ISSN 2364-3293 ISSN 2364-3307 (electronic)
Topics in Mining, Metallurgy and Materials Engineering
ISBN 978-3-319-29759-0 ISBN 978-3-319-29761-3 (eBook)
DOI 10.1007/978-3-319-29761-3

Library of Congress Control Number: 2016949582

Printed on acid-free paper

This Springer imprint is published by Springer Nature
The registered company is Springer International Publishing AG
The registered company address is: Gewerbestrasse 11, 6330 Cham, Switzerland

Contents

Stability of Nanofluids

Suhaib Umer Ilyas, Rajashekhar Pendyala and Narahari Marneni

Abstract Nanofluids are the dilute suspensions of nanomaterials with distinctive and enhanced features. Nanofluids can be used in a variety of industrial applications because of improved thermophysical properties. Stability of nanofluids is the only quandary factor which decreases the efficiency of such smart fluids in engineering applications. The information and studies on interaction of nanomaterials with the liquid have significant importance toward their usage in industrial applications. Agglomeration among particles is a common issue due to interactive forces, which effects the dispersion, rheology, and overall performance of nanosuspensions. Characterization of nanofluids plays an important role to evaluate the stability of nanofluids. The effect of agglomeration on the stability of nanofluids can be reduced by introducing different mechanical and chemical techniques to prolong dispersion of suspended particles in liquids. Complete understanding on the stability of nanofluids can lead to the preparation of different combinations of stable nanofluids with enhanced properties for variety of applications.

Keywords Agglomeration · Dispersion · Nanofluids · Nanoparticles · Stability

Nomenclature

a	Particle radius
a_1	Particle radius of sphere 1
a_2	Particle radius of sphere 2
A	Hamaker constant
A_1	Darcy's permeability constant
A_2	Modified permeability constant
d	Average diameter of particle, nm
d_0	Reference average particle diameter, 100 nm

S.U. Ilyas · R. Pendyala (✉)
Chemical Engineering Department, Universiti Teknologi PETRONAS,
32610 Seri Iskandar, Perak Darul Ridzuan, Malaysia
e-mail: rajashekhar_p@petronas.com.my

N. Marneni
Petroleum Engineering Department, Universiti Teknologi PETRONAS,
32610 Seri Iskandar, Perak Darul Ridzuan, Malaysia

K. Viswanatha Sharma and N. Hisham B Hamid (eds.),
Engineering Applications of Nanotechnology, Topics in Mining, Metallurgy
and Materials Engineering, DOI 10.1007/978-3-319-29761-3_1

D_P Diameter of particle
g Gravitational constant
h Surface-to-surface separation distance
H Height of sediment due to consolidation
H_S Height of sediment/bed height
H_T Total height of sample
H_o Initial height of the sediment due to consolidation
H_∞ Equilibrium height of the sediment due to consolidation
K Thickness of electrical double layer
n Empirical constant
pH_f pH of base fluid
pH_{nf} pH of nanofluids
P_L Hydraulic excess pressure
T Absolute temperature, K
T_0 Reference temperature, 273 K
T_C Consolidation time factor
u Relative velocity of liquid to solids
U_C Average consolidation ratio
v Terminal settling velocity
v_R Potential energy per unit area between two spheres or plates
V_A Energy due to attractive forces
V_B Born interaction potential energy
V_R Electrical double-layer interaction potential energy
V_T Total interaction potential
x Distance
z_{1-8} Regression constants

Greek letters

σ_c Collision diameter
ρ_P Density of particles
ρ_f Density of fluid
μ Viscosity of liquid
ε Porosity
ω Volume of solids per unit cross-sectional area
φ Volumetric concentration of particles
ψ_o Particle surface potential

1 Introduction

Nanoscience and nanotechnology deal with the studies of atoms and molecules at nanoscale and controlling them for the development of efficient materials. The superlative explanation of nanotechnology in a single sentence by Pietsch (2005) states that '*Nanotechnologies deal with the border between the realm of individual atoms and molecules, where quantum mechanics rule, and the macroworld, where bulk properties of materials emerge from the collective behavior of a large number of atoms and molecules.'* In general, nanomaterials with size less than 100 nm are considered to be in the region of nanotechnology. However, micron-sized particles are considered to be bulk materials. A comparison of different materials and substances with respect to size is shown in Fig. 1.

Nanofluid is a subclass of nanotechnology which involves two-phase system, i.e., solids (nanomaterials) in liquids (base fluid). The nanomaterials are termed as engineered materials with nanoscale size. Nanomaterials can be in the form of particles, rods, tubes, sheets, and fibers. Some of the nanomaterials are shown in Fig. 2. Base fluid is termed as the solvent or liquid in which the nanomaterials are suspended to form a nanofluid.

The addition of engineered nanoparticles in liquids alters the overall thermophysical properties of liquids such as thermal diffusivity, thermal conductivity, density, viscosity, and specific heat capacity. Nanomaterials are usually dispersed in dilute concentrations (up to 9 %) in liquids to produce nanofluids. Higher concentrations of nanoparticles in liquid can lead to sedimentation due to poor stability. The notion of using tiny particles (up to micron level) in liquids to improve liquid properties was first experimentally studied by Maxwell in 1873 (Maxwell 1873). The concept was then followed by Ahuja in the 1970s (Ahuja 1975a, b) and later on by Choi and Eastman in the 1990s (Choi et al. 1992; Choi 1995; Eastman et al. 1999, 2001). The former studies include dispersion of 50–100 μm polystyrene spheres in glycerin to increase effective thermal conductivity for biomedical applications. The latter studies include experimental investigations on metallic and

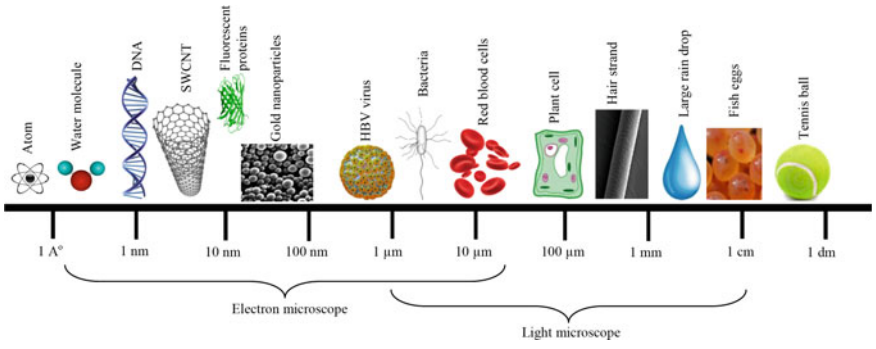

Fig. 1 Comparison of different materials with respect to size

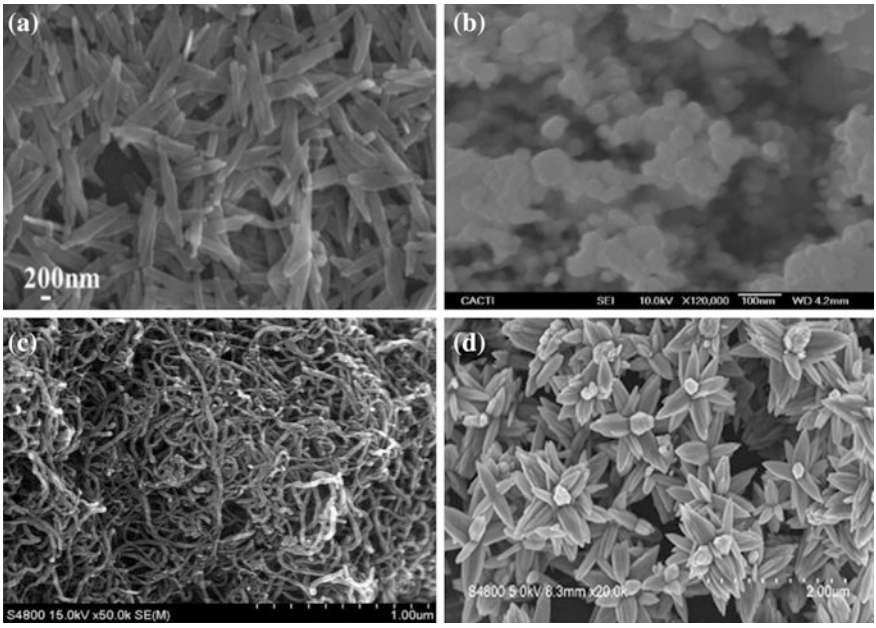

Fig. 2 SEM image of **a** CuO nanorods (Farbod et al. 2015) *adapted with permission*, **b** CuO nanopowder (Pastoriza-Gallego et al. 2011) *adapted with permission*, **c** multi-wall carbon nanotubes (MWCNTs) (Teng et al. 2015) *adapted with permission* and **d** ZnO nanoflower (Fang et al. 2009) *adapted with permission*

metallic oxide nanoparticles as heat carriers in ethylene glycol–water mixtures. A significant enhancement in effective thermal properties was found by the applications of such nano-sized particles. After successful experimental exploitation of these improved results, many researchers started investigations on the advancement and development in the field of nanofluids. Many articles have been published in the last decade demonstrating the significant potential of such smart fluids in wide range of industrial applications.

Stability of nanofluids is very important toward industrial applications. Many researchers have termed stability as the 'validity of nanofluids.' Dispersion behavior of different nanomaterials in solvent is different and depends on many factors. A complete understanding of interaction between particle–particle and particle–liquid is required to prepare a stable fluid. Over the years, the advancement in the equipment for characterization of nanofluids has helped researchers to synthesis nanomaterials in broad range of sizes and shapes. However, there are still some gaps toward the detailed information on the stability of nanofluids.

Recent progress and advancement in the field of nanofluids are discussed. A complete understanding on the dispersion behavior of colloids, interaction among particles, evaluation techniques to measure stability, and methods to prolong stability of nanomaterials in liquids is explained in detail.

1.1 Industrial Applications

Colloidal dispersions of nanoparticles have wide range of chemical industrial applications. Nanofluids have gained the attention of researchers due to attractive features. One of the main incentives of nanofluids is that it can be replaced with any conventional fluid depending on the application. One of the main applications of nanofluids is heat transfer intensification. There are numerous studies on the improved thermal properties of nanofluids. Nanoparticles with high thermal conductivities, when dispersed in liquid, increase the overall thermal performance of nanofluid (Ilyas et al. 2014c). Researchers have prepared highly effective thermal fluids by dispersing metallic (Au, Ag, Cu, Fe, Al, etc.), metallic oxides (Fe_3O_4, TiO_2, Al_2O_3, ZnO, CuO, MgO, etc.), and non-metallic (BN, SiC, synthetic diamond, etc.) nanoparticles in different base fluids and have found significant improvement in effective thermal conductivity and overall convective heat transfer coefficient.

The application of nanofluids in heat transfer processes has been reviewed and investigated in many studies. Experimental and theoretical studies by Xuan and Li (2000), Yu and Xie (2012), Wang and Majumdar (2007), Nguyen et al. (2008), and many others have opened a new horizon to prepare different combinations of nanofluids for heat transfer enhancement.

Nanofluids can provide much higher convective heat transfer rates than the conventional fluids and hence possess a great potential in automotive industry. The size of the radiator or engine cooling jackets can be reduced by the application of smart fluids in heavy duty engines (Pendyala et al. 2015). The overall efficiency of the automotive vehicles can be improved considerably by dispersing nanoparticles in engine oil and radiator coolant.

In a recent study by Sonage and Mohanan (2015), zinc and zinc oxide-based nanofluids in water were prepared at low concentrations (0.15–0.5 vol%) to study the enhancement in heat transfer coefficient at turbulent conditions (Re: 4000–20,000). It was found that the higher concentrations of nanofluids, i.e., 0.5 vol%, provide better heat transfer performance than lower concentrations. Surface area of the car radiator, fluid inventory, and pumping power can be reduced by 24, 40, and 16 %, respectively, by the usage of 0.5 vol% Zn/water nanofluids. Similar results were reported by Srinivas et al. (2015). They prepared Cu-, CNT-, Ag-, and Al_2O_3-based nanofluids in carboxylates of sebacic acid and water for automotive applications. There are some studies available on the nanoparticles dispersion in car fuel. In a recent investigation (Smirnov et al. 2015), Al (20 nm)/n-decane-based nanofluids were prepared and it was found that fuel with 2.5 % aluminum nanoparticles gives much higher temperature upon burning than the combustion of pure n-decane. The overall performance and fuel economy of automotives can be improved by the substituting nanofluids in car radiator, engine oil, brake oil, or fuel itself. The size of the heat transfer equipment can be reduced with the implementation of nanofluids. These fluids can be used as the future-generation cooling/heating media in

aerospace industries which require lighter weight and decreased size of heat transfer equipment.

Investigations into nanofluids have proved that these fluids possess high boiling point than the base fluid alone. This can broaden the operating temperature range of coolant and dissipate more heat from the system. The efficiency of solar collectors can be improved by the implementation of nanofluids, as it depends on the absorption rate of operational fluid in solar collectors (Otanicar et al. 2010).

The advancement in electronic devices requires high level of heat dissipation systems in confined space due to compact design of systems. Nanofluid is an excellent choice of researchers to optimize thermal management as it can provide much better cooling than ordinary coolants in electronic devices with low surface areas to provide smooth operation. Duangthongsuk and Wongwises (2015) investigated the heat transfer behavior of SiO_2/water nanofluids at different concentrations (0.2–0.6 vol%) and found a significant enhancement (4–14 %) in thermal performance in heat sinks. In another study (Sohel et al. 2015), Al_2O_3/water-based nanofluids were used to dissipate heat from a mini-channel heat sink. It was reported that the thermal entropy generation rate reduced around 11.50 % as compared to water.

Nanofluids can be applied in building heating systems especially in the regions with cold environment. Ethylene glycol (EG) or propylene glycol (PG) mixtures with water (60:40) are usually used as heat transfer media. There are many studies available in literature on EG/water- or PG/water-based nanofluids. Experimental investigations by Eastman et al. (2001), Witherana et al. (2013), and Pastoriza-Gallego et al. (2014) have proven the applicability of such fluids in many engineering applications.

Applications of smart fluids in brake oil system are gaining attention of researchers. Brake systems require more improvement as drag force of the vehicle is reduced because of the improvement in aerodynamics of the vehicle. The efficiency of the brake systems depends on the mechanism of heat dissipation. Kao et al. (2007a, b) prepared CuO- and Al_2O_3-based nanofluids in brake oil using arc-submerged and plasma charging arc nanoparticle synthesis system, respectively. The increase in boiling point and thermal conductivity suggests that nanofluids can revolutionize lubrication and heat transmission industry.

Nanofluids play an important role in the field of drug delivery. Polymeric nanoparticle suspension is one of the important examples for efficient drug deliveries. A typical example of drug delivery is the control release of doxorubicin, for cancer treatment, entrapped in polyalkylcyanoacrylate polymeric systems. The particles contain an active component entrapped in polymeric core. Generally, a layer of surfactant surrounds the core to stabilize the system. Drug delivery systems can be improved by using nanofluids in pharmaceuticals and food industry (especially in delivery of bioactive components). The application of nanofluid technology can provide many advantages such as enhanced activity, control release, drug protection, and reduced side effects (Astete 2015).

Nanopaint is one of the recent advancements of nanotechnology in paints and pigment industry. There are many studies available on the insulating properties of

nanopaints for interior and exteriors walls to act as a barrier for heat transmission. MgO-based nanofluids are also used as an additive to enhance bactericidal efficacy for interior wall paints (Huang et al. 2005).

Utilization of nanofluids in fuel cell industry is significant accomplishment in the field of nanotechnology. Nanofluid-based microbial fuel cells (MFCs) can be used to high energies from bacteria by improving MFCs efficiency (Sharma et al. 2008). In an investigation, zinc oxide nanofluids were used as anti-bacterial agent against *E. coli* bacteria, presumably due to interaction (electrostatic forces) between ZnO particles and bacteria cells (Zhang et al. 2008).

Researchers have used nanofluids with high thermal potential in three types of nuclear cooling applications, i.e., main reactor coolant, emergency core cooling systems, and in-vessel retention coolant. Recently, Nematolahi et al. (2015) investigated Cu-, CuO-, Al_2O_3-, Gd_2O_3-, HfO_2-, TiO_2-, and CdO-based nanofluids at different concentrations from 0.001 to 10 vol% as an efficient cooling media to control the temperature of hot core.

2 Agglomeration in Nanofluids

Stability of nanofluids is the main challenge toward their usage in applications and there are some important issues to be faced in two-phase system. The interactions among particles become dominant due to smaller size of particles and high surface area. Each particle in nanofluid system experiences different kinds of interactions. These interactions can be generated between particle–particle system and particle–liquid system (Ilyas et al. 2014a). These interactions are due to attractive and repulsive forces which generate or act on the particle surface. In general, attractive molecular forces are more dominant than other kind of interactions, which causes the particles to come closer. A lump of particles is formed because of attractive forces, which is termed as agglomeration. In general, the transformation of particulate material into larger entities due to interactions is known as aggregation effect. The agglomeration in nanofluids reduces the stability and uniformity of the nanosuspensions. Different scenarios of stable and unstable nanofluids are shown in Fig. 3.

Aggregation among particles is attributed to the following principles (Elimelech et al. 2013):

- Suspended particles in a fluid media must be in motion in such a way that particles remain in contact with each other. These collision phenomena can take place because of fluid motion, Brownian diffusion, or sedimentation.
- Interactions among particles must be in such a way that colloidal particles should remain intact. Particles that dominant repulsive interactions are known to be stable as they do not form aggregates.

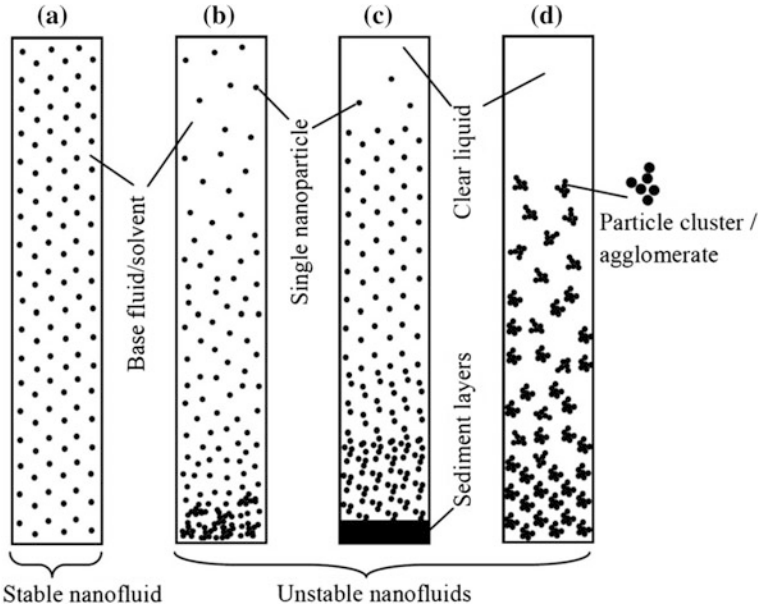

Fig. 3 Different scenarios of stable and unstable nanofluids

The types of interactions among particles during agglomeration process are explained by Pietsch (2005). There are three types of interactions between two moving particles in any suspension, i.e., molecular forces, electrical forces, and magnetic forces (Fig. 4). Molecular forces consist of van der Waals forces, valence forces (Free chemical bonds), and non-valance forces (hydrogen bonding). Interactions due to electrical forces can be due to electrical double layer, electrostatic or excess charge present on the particle surface.

Dispersion of particles in a suspension is also named as colloidal dispersions. Colloid can be liquid–liquid mixture or solid–liquid mixture. In the case of nanofluids, a colloid is termed as two-component system with particles of range from 1 nm to 1 μm, and the motion of the particles is highly affected by thermal forces. Examples of colloidal suspensions are found in multitude of industrial, biological, and natural processes. The information and understating of interactions and rheological flow behavior and the factors affecting rheology of such suspensions have significant importance toward preparation of desired product. By manipulating interactions among particles, nanosuspensions can become ultra-efficient for advanced applications such as heat transfer processes, pharmaceuticals, food, polymers, paints, and pigments.

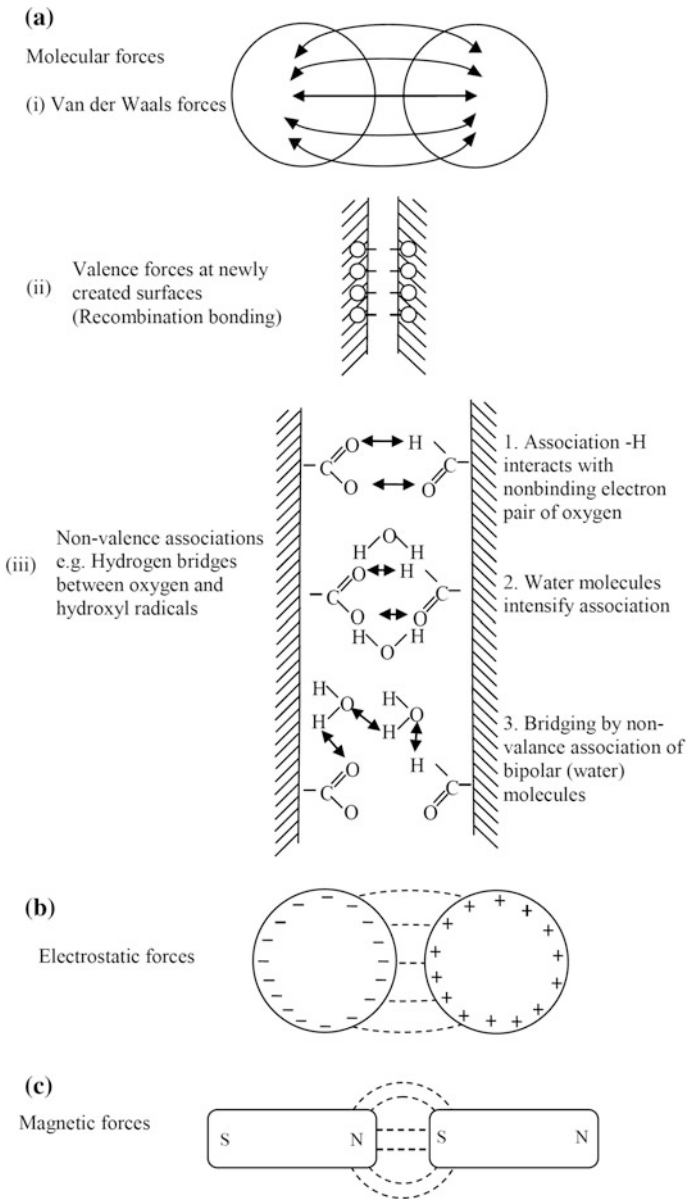

Fig. 4 Different types of interaction forces among particles and solid surfaces (Pietsch 2005) *adapted with permission*

2.1 DLVO Theory

Stability of nanofluids strongly depends on the interaction between particles and suspension. DLVO theory was proposed by B. Derjaguin, L. Landau, E. Verwey, and J. Overbeek in 1940s (Verwey and Overbeek 1948). This theory is a quantitative explanation of such forces which affects the stability of colloids in suspension. The theory is quintessential for explanation about the interactions and separations of colloids caused by the balancing of two adverse forces, i.e., electrostatic repulsion forces and van der Waals attraction forces. The total interactions between two particles are associated with both electrostatic double-layer forces and van der Waals forces. The double-layer repulsive forces are stronger at larger separations of particle surfaces while the attractive forces are dominant when the distance between the two particle surfaces is less. The total interaction energy is the sum of all repulsive, and attractive forces are given as (Eq. 1)

$$V_T(h) = V_A(h) + V_R(h) \tag{1}$$

where $V_T\,(h)$, $V_A\,(h)$, and $V_R\,(h)$ are the total interaction potential, van der Waals attractive energy, and electrostatic repulsive energy as a function of h, which represents minimum separation distance between two surfaces. The theory proves that the electrostatic double-layer forces prevent the particles to approach one another due to an energy barrier between them. In such scenario, a stable dispersion can be obtained which can resist agglomeration due to the repelling forces among particles. Formation of aggregates will be highly likely if the repulsion is not enough. If the particle surfaces collide with adequate energy, the van der Waals forces can attract the particles toward each other to overcome the barrier to form agglomerate.

The van der Waals attractive interaction and electrostatic repulsion are given in Eqs. (2) and (3), respectively (Zhu et al. 2009).

$$V_R(h) = 2\pi\varepsilon\psi_o^2 \ln\left[1 + e^{-kh}\right] \tag{2}$$

$$V_A(h) = -\frac{A}{6}\left[\left(\frac{2a^2}{h^2 + 4ah}\right) + \left(\frac{2a^2}{h^2 + 4ah + 4a^2}\right) + \ln\left(\frac{h^2 + 4ah}{h^2 + 4ah + 4a^2}\right)\right] \tag{3}$$

where ε, ψ_o, and k represent permittivity of the medium, particle surface potential, and thickness of electrical double layer surrounding the particle, respectively. The double-layer interaction energy between spherical particles can also be given by integral equation (Eq. 4) by Derjaguin (1934)

$$V_R = \frac{2\pi a_1 a_2}{a_1 + a_2} \int_h^\infty v_R \mathrm{d}x \tag{4}$$

2.2 Non-DLVO Forces

The importance of two principal interactive forces has been well demonstrated by classical DLVO theory. However, there are more forces which should be taken into account because combinations of two principal forces alone are not in agreement with experimental results by many researchers (Elimelech et al. 2013). The major non-DLVO forces are Born repulsion, hydration forces, and hydrophobic interactions.

The Born repulsion forces are originated when the electron shells are interpenetrated with each other because of strong repulsive forces between atoms. The Ruckenstein and Prieve (1976) equation (Eq. 5) explains the phenomenon of Born repulsion in sphere plate

$$V_B = \frac{A\sigma_c^6}{7560}\left[\frac{8a+h}{(2a+7)^7} + \frac{6a-h}{h^7}\right] \tag{5}$$

where σ_c represents collision diameter of the order 0.5 nm.

The hydration force is a repulsive interaction which takes place due to adsorption of water molecules at each interface. There is a possibility of hydration of particles with ions present in solution because most of the nanoparticles carry a surface charge or ionic groups (Elimelech et al. 2013). The effect of hydration forces on the overall interaction becomes stronger below 5 nm. The particle surface is termed as hydrophobic when there is no hydrogen bond or ionic group attached and there is no room for water molecules. The attractive interactions take place because of the strong interaction between water molecules and weak interaction between water and organic groups. The effect of these forces can be significant below 8 nm.

2.3 Effect of Stability on Thermal Properties

Thermal properties of nanofluids such as thermal conductivity, specific heat capacity, density, and viscosity depend on the stability of nanofluids. Most of the suspended particles in unstable nanofluids are in the form of large agglomerates. The average agglomerate diameter of the particles can reach up to micron sizes from few nanometers of primary size of nanoparticles. The size of particles is a main factor for the estimation of thermophysical parameters of nanofluids. There are questions raised by many researchers on the validity of reported thermophysical data of nanofluids. To ensure the accuracy of data, characterization analysis on each stage of preparation must be done to ensure proper stability of nanofluids.

3 Nanofluids Preparation Methods

Nanofluid stability is highly dependent on the method of preparation. In order to fully understand the phenomenon of stable nanofluid preparation, the information on the production and properties of primary nanomaterials and base fluids is very important. Nanomaterials production involves two different approaches, i.e., top-down methodology and bottom-up methodology. In the former method, a bulk material is modified into desired shape and size with the help of different machining techniques in such a way that the original integrity of the material remains constant. Milling and grinding of bulk materials is one of the important synthesis techniques of top-down method. The bulk material with micro-sized crystals is broken down into nano-sized crystal structures. This method is mostly used to produce metallic or metallic oxide nanomaterials. During this process, crystallites react with each other in the presence of kinetic energy to get desired shape and size of the product. Another example of the top-down methodology is the production of integrated circuits which includes crystal growth, lithography, etching, and ion implementation. The latter technique of producing nanomaterials involves the assembly of complex nanomaterials from simple atoms or molecules. This technique is not as extensively used in industrial scale as compared to top-down approach but extensive research is being carried out as an alternative method to lithographic approach. Examples of bottom-up methodology include laser ablation and sol–gel technology.

Nanofluids can be produced by two methods: single-step method and two-step method. In the single-step method, nanomaterials are prepared and dispersed in the liquid simultaneously. In two-step method, nanoparticles are produced separately and then dispersed in the base fluid using different mixing techniques to form a nanosuspension.

3.1 Single Step

In this method, nanoparticles are produced and dispersed in the primary liquid simultaneously. Generally, a chemical reaction is involved to carry out nanofluids preparation. The different techniques include microwave irradiation technique, vapor deposition (VP) methods, thermal decomposition, grafting, submerged arc nanoparticle synthesis system (SANSS), and phase transfer techniques. Some of the nanofluids can only be prepared by single-step method which depends on the properties of particles, properties of base fluid, interactions, and product application requirement. The advantage of this nanofluid preparation approach over two-step method is that a highly stable nanoparticle dispersion can be obtained. Agglomeration effect in these types of nanofluids is not significant. A better stability is obtained with longer dispersion periods of nanoparticles in liquids.

Despite of better stability, there are many disadvantages of single-step approach. The applications of such nanofluids, prepared from single-step method, are limited

to process with low vapor pressure. The other predicament in this method is the challenging issue of controlling the size and structures of nanoparticles. The reactants are not completely converted into products and the possibility of presence of different impurities is very high. One more quandary factor in this process is the high cost of preparation as compared to two-step approach (Yu and Xie 2012).

Studies are available on the preparation of nanofluids with highly stable dispersion characteristics using single-step approach. In an investigation (Zhu et al. 2007), copper nanofluids were synthesized using transformation method aided with microwave irradiation of copper hydroxide. To achieve good stability, ammonium citrate was used to stop aggregation process of nanoparticles. Yu et al. (2010) prepared Fe_3O_4/kerosene oil-based nanofluids using phase transfer method. Feng et al. (2006) synthesized Au-, Ag-, and Pt-based nanofluids using phase transfer method in oil–water systems. In investigations by Singh and Raykar (2008) and Kumar et al. (2003), silver-based nanofluids were prepared in ethanol and hexane using microwave-assisted synthesis and phase transfer method, respectively. In another study, zinc-based nanofluids were prepared in aqueous media using vapor condensation process. First, the bulk zinc material was heated up to 907 °C (boiling point) and then vapors were condensed into water. The estimated size of the zinc nanoparticles was reported to be 41 nm with high dispersion behavior in water (Sonage and Mohanan 2015).

3.2 Two Step

Two-step method is the most widely used preparation technique for nanofluids. In this method, dry nanopowder is obtained from physical or chemical synthesis and then dispersed in the liquid media to prepare nanofluids. A growing number of industrial-scale nanoparticles with high purity and variety of controlled sizes are commercially available. Generally, a shear mixing is required to disperse nanoparticles in base fluid. Nanofluids dispersed using two-step method show higher agglomeration rates than nanofluids prepared from single-step method.

Nanofluids can be prepared in different concentrations while in single-step method the nanofluid concentration is not uniform. In single-step method, the concentration of nanoparticles in host fluid is mostly altered by dilution or evaporation. Characterization analysis is carried out before and after preparation process to evaluate the stability of nanosuspensions. There are many ways to enhance the stability of nanofluids, mentioned in next sections. A generalized methodology to prepare stable nanofluids using two-step approach is shown in Fig. 5.

During storage, transportation, and handling of dry nanoparticles, the primary size of nanoparticles can change up to micron level due to dominant particle–particle attractive interactions. There are several investigations on the preparation of different nanofluids using two-step method. Preparing nanofluids using two-step method is the most economical method. Nanofluids can be prepared in bulk quantity using this approach. Some of the studies are tabulated in Table 1.

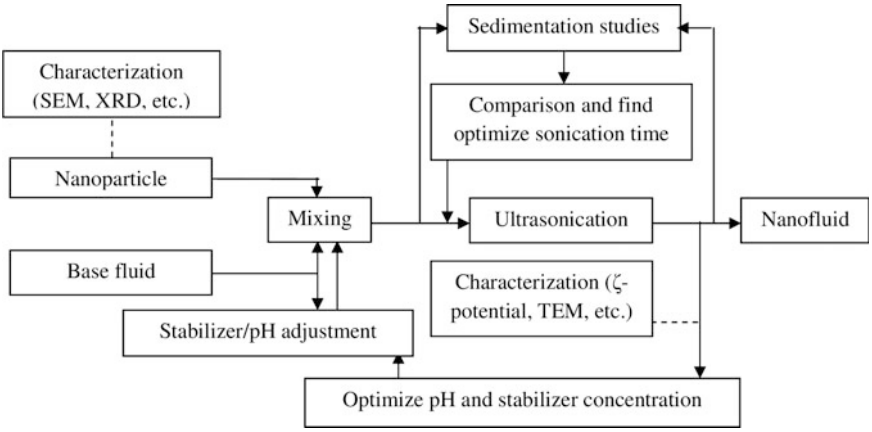

Fig. 5 Methodology for preparing stable nanofluids using two-step method (Ilyas et al. 2014a) *adapted with permission*

Table 1 Investigations using two-step method

Investigator	Nanofluids system	Remarks
Nayak et al. (2009)	Alumina/water	Nanofluids were prepared after ultrasonication (ultrasonic bath) for 4 h. Settling velocities and thermal hydraulic characteristics of nanofluids at different concentrations were estimated
Mahbubul et al. (2014)	Alumina/water	Increase in ultrasonication time decrease average agglomerate size
Sunder et al. (2012)	Fe_3O_4/water	Heat transfer coefficient increases from 21 to 31 % by the addition of 0.6 vol% nanoparticles at different Reynolds number
Farbod et al. (2015)	CuO/engine oil	8.3 % increase in effective thermal conductivity with 6 wt% of nanorods dispersions
Sekhar et al. (2013)	Al_2O_3/water	8–12 % increase in heat transfer coefficient using nanofluids in plain tube as compared to water
Alberola et al. (2014)	Halloysite/water	8 % increase in thermal conductivity with 5 vol% of Hal nanotubes in water at 80 °C as compared to water
Suresh et al. (2012)	Al_2O_3–Cu (hybrid) /water	10.94 % increase in average Nusselt number using hybrid nanofluid system as compared to pure water
Zhang et al. (2013)	Al_2O_3/R141b	Heat transfer effectiveness increases by 110 % by using 0.01 vol% alumina/R141b as compared to R141b as a working fluid

4 Stability Evaluation Methods

Stability of nanofluids can be determined by performing characterization analysis. The recent development in the field of material science especially nanotechnology could not be possible without the innovation and development of characterization equipment.

4.1 Electron Microscopy

The essential characterization technique involved to evaluate stability of nanofluids is the use of electron microscopy. Electron microscopy focuses on the illumination of electrons to generate an image of the material. This technique is useful to display the nanoscale materials with much detail because of high magnification. Electron microscope can determine the particles with lower wavelengths than ordinary. Optical microscopes are the most commonly used technique to examine the quality of dispersion. However, it is not possible to examine nano-sized particles. The function of electron microscopy is similar with the optical microscopy; however, the former analysis uses a focus beam of electrons while the latter analysis uses electromagnetic radiation to generate the image of the material. Generally, particles with average diameter less than 0.5 μm are not visible in optical microscopes. Electron microscopy generates the image of the material through electromagnetic and electrostatic lenses. The advancement in electron microscopy makes it very useful to get the material properties such as morphology, crystalline structure, composition, and topography of the specimen. Information on morphology of the nanomaterials helps to determine the shape, size, strength, and ductility of the particles. The recent progress in this field helps the researchers to identify the arrangement of atoms and molecules in the crystalline structure as well as the composition of compounds and elements present in the specimen using energy dispersive X-ray (EDX) analysis. Two of the major types of electron microscopic analysis used in nanotechnology are scanning electron microscopy (SEM) and transmission electron microscopy (TEM).

4.1.1 SEM

The scanning electron microscope (SEM) is a proficient type of electron microscopy which can produce high-resolution images of the nanomaterial surface to characterize surface structure of the nanomaterial by three-dimensional appearance. The structure, texture, and the agglomerate size can be determined using SEM analysis.

4.1.2 TEM

Transmission electron microscopy (TEM) is another type of electron microscopy which comprises an electron gun. This gun emits electron beam of high energy to transmit through the nanomaterial sample and creates an image of the inner structure of the material. Two major modes of TEM are dark-field imaging and bright-field imaging. The development of high-resolution transmission electron microscopy (HRTEM) can indicate the crystallographic structure of specimen even at atomic level. Currently, the accessible highest resolution of TEM is equivalent to 0.5 A^{o}. Some of the examples of TEM analysis of different nanofluids are shown in Fig. 6.

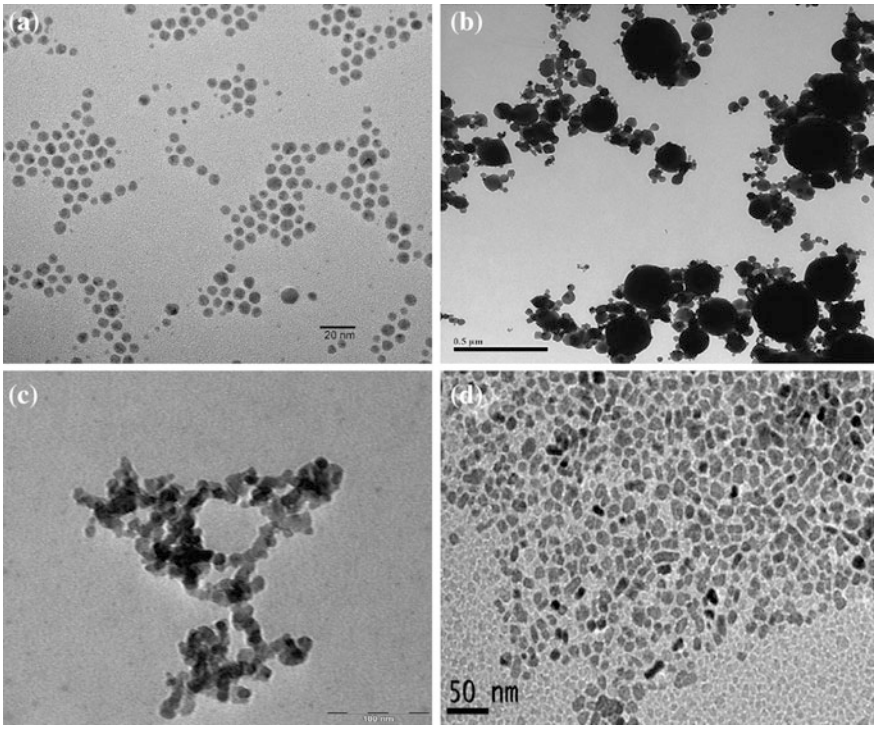

Fig. 6 TEM image of **a** silver nanoparticles in basic media (Li et al. 2010) *adapted with permission*, **b** TiO_2/water nanofluid (Allouni et al. 2009) *adapted with permission*, **c** Al_2O_3/water nanofluid (Said et al. 2013) *adapted with permission* and **d** CuO/water nanofluid (Pastoriza-Gallego et al. 2011) *adapted with permission*

4.2 Sedimentation Techniques

Sedimentation of nanoparticles in nanosuspensions is a natural phenomenon due to gravity which is aided by aggregation among particles. Sedimentation analysis is a simple technique to evaluate the stability of nanofluids. Due to the smaller size of dispersed nanoparticles in liquid, the particle motion behaves as fluid motion. Theoretically, gravity forces on particles with diameter less than 1 μm are not effective. However, agglomeration among particles increase the average diameter of the particle cluster and particle tends to settle down much faster due to dominant gravity forces acting on the agglomerate. There are three types of sedimentation in nanosuspensions, i.e., dispersed-type settling, flocculated-type settling, and mixed-type settling (Ilyas et al. 2013).

Dispersed-type settling behavior can be seen in nanosuspensions with low particle loading where the sediment height increases from bottom to top. The nanoparticle concentration more than critical concentration (equivalent to 1 %) exhibits flocculated-type settling behavior. In this case, the sediment height decreases from top to bottom and the solution becomes clearer from the top. In mixed-type settling, multilayer separations of the particles can be seen. This appearance of multilayers is due to the different agglomerate sizes which settle down at different terminal velocities and hence creating multi-phase separations. Dispersed-type sedimentation process of particles follows Stokes law and is highly dependent on the square of particle/agglomerate size, given as (Eq. 6)

$$v = \frac{gD_P^2(\rho_P - \rho_f)}{18\,\mu} \tag{6}$$

The sediment heights can be recorded over time using visualization technique. Generally, a high-speed camera is used to determine settling velocities of nanosuspensions. Sediment ratios (SR) can be obtained in terms of sediment height (H_S) and total height of the sample (H_T) using Eq. 7

$$\mathrm{SR} = \frac{H_S}{H_T} \tag{7}$$

The settling of particles exhibiting flocculated-type sedimentation is due to consolidation process. In this process, the liquid move upwards through different pores of solid particle clusters. These particle clusters form a bed of different sediment layers and settle down with the passage of time. The sediment bed further consolidates under its own weight, when the upper layers of the sediment exert pressure on the lower sediment layers. The consolidation effect was extensively explained by Shirato et al. (1970). A correlation of relative liquid velocity was proposed using Darcy's law in terms of porosity, differential volume, and hydraulic excess pressure, given in Eq. 8. To determine the average consolidation ratio (U_C), the simple analytical solution was derived by Iritani et al. (2009), given as (Eq. 9)

$$u = -\left(A_1 \frac{(1-\varepsilon)}{\mu}\right) \frac{\partial P_L}{\partial \omega} = -A_2 \frac{\partial P_L}{\partial \omega} \tag{8}$$

$$\begin{aligned} U_C &= \frac{H_o - H}{H_o - H_\infty} \\ &= 1 - \frac{32}{\pi^3} \sum_{n-1}^{\infty} \frac{(-1)^{n-1}}{(2n-1)^3} e^{\left(-\frac{\pi^2 (2n-1)^2}{4} T_C\right)} \end{aligned} \tag{9}$$

4.3 Spectral Analysis

Spectral analysis is one of the important techniques to analyze stability of nanofluids. This type of analysis is carried out on the basis of degree of absorption to examine different properties of nanofluids. Ultraviolet (UV)-visible (Vis) spectroscopy is the most widely used method for spectral analysis of nanofluids. It operates on the principal of absorption spectroscopy in UV visible spectral region. This analysis is only limited to UV-active nanomaterials. Quantitative results are obtained through UV–Vis spectroscopy analysis on the basis of concentration of nanofluids.

LotfizadehDehKordi et al. (2013) investigated the stability of TiO_2/water nanofluids using UV–Vis spectrophotometer at different concentrations and sonication time and power. The optimum conditions were found using Box–Behnken method to achieve high stability after 1 week and 1 month of study on the basis of quantitative analysis of absorption values.

4.4 Zeta Potential

Zeta potential is the measure of interfacial potential between the attached thin layer on the surface of the particle and the dispersion medium. This quantitative analysis determines the repulsive interactions between the particle and the dispersant. Zeta potential is denoted by ζ with the units of mV. Higher zeta potential values indicate high stability of nanosuspensions. Colloidal suspension with ζ-potential 0 to ± 5 mV exhibits poor stability with high agglomeration rates. Nanosuspensions with ζ-potential values more than ± 30 mV are considered to be stable for longer time. Zeta potential values can be altered by changing the pH of the suspension, surface coatings, and functionalization of nanomaterials or by adding surfactants.

Allouni et al. (2009) studied the aggregation affects of titanium dioxide particles in cell culture medium using zeta potential analysis. The effect on ionic strength and electrokinetic properties of titania nanofluids by the addition of human serum albumin (HSA) and fetal bovine serum (FBS) was investigated.

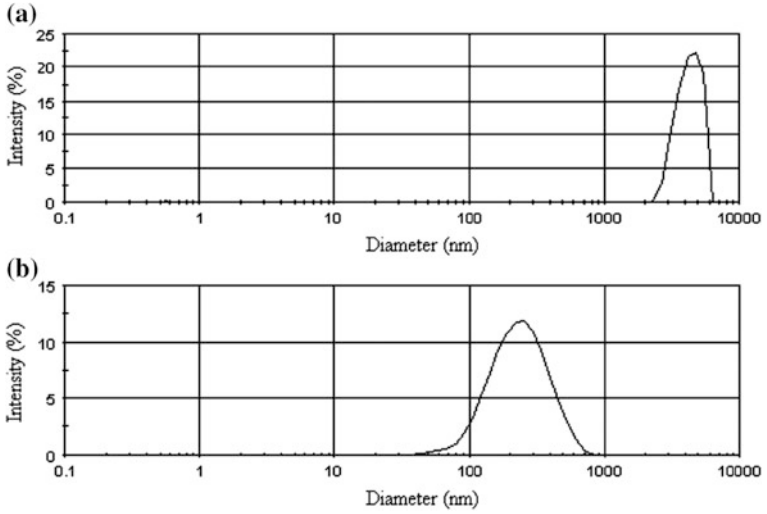

Fig. 7 Particle size distributions of alumina/water nanofluids (0.05 wt%) **a** without and **b** with surfactant (SDBS) (Zhu et al. 2009) *adapted with permission*

4.5 Dynamic Light Scattering

Dynamic light scattering (DLS) technique is used to quantify particle size in nanosuspensions. This analysis identifies the average agglomerate size in liquid. The average particle size is analyzed when the specimen is illuminated using a laser beam and then the fluctuations of scattered light is detected by photon detector. Particle size distribution curves are obtained on the basis of intensity or volume. This method can obtain particle size distribution curves for particles of size as low as 1 nm. Li et al. (2012) investigated the dispersion behaviors of natural- and surface-modified Fe_3O_4/oil nanofluids using particle size distribution curves. In another study, Zhu et al. (2009) studied the effect of surfactant (Sodium dodecyl benzene sulfonate, SDBS) on the stability of alumina nanofluids using particle size distribution curves, as shown in Fig. 7.

5 Ways to Improve Stability

With the help of modern advancement in characterization techniques, it is possible to alter the interactions in nanosuspensions. A uniform and highly stable nanofluid can be obtained by the application of certain mechanical and chemical methods.

5.1 Mechanical Mixing Techniques

Nanofluid preparation includes different mechanical mixing techniques to attain high stability. Mechanical mixing has significant importance toward de-agglomeration of nanoparticles without changing the original particle size. Major examples of this technique include ultrasonication, high-pressure homogenizer, and wet milling. These types of methods are more suitable for nanofluids with low particle concentrations.

5.1.1 Ultrasonication

Ultrasonic agitation is a type of mechanical mixing technique in which the ultrasonic waves are passed through the nanosuspension causing distortion among different layers of sediment. This distortion breaks big agglomerates into smaller agglomerates and a uniform nanosuspension is achieved. Stability of nanofluids is influenced by sonication frequency and sonication time. Both parameters are directly proportional to the better stability of nanosuspension. However, few studies illustrate that excess sonication has negative impact on the stability of nanofluids. Studies by Kole and Dey (2012) indicated that average agglomerate size increases after excess sonication (i.e., 60 h) of ZnO/ethylene glycol nanofluids. Lee et al. (2008) reported the decline in stability of alumina/water nanofluids after 5 h of sonication. In another study (Kwak and Kim 2005), average particle size of CuO/ethylene glycol nanofluids was observed to be increasing after continuous sonication of 9 h.

Different types of commercial ultra-sonication agitators are commercially available such as bath-type sonicators and probe-type sonicators. Probe-type sonicators are found to be effective than all other types of sonicators. The probe-type sonicator or ultrasonic rupture operates in such a way that all waves generated from the probe pass through the suspension. This causes deterioration of sediment folds and a uniform suspension is obtained. Some of the energy from ultrasonic waves is absorbed by the nanosuspension which increases the kinetic energy of molecules. The transport of ultrasonic waves increases the temperature of the specimen. A cooling jacket with continuous flow of cooling media is required to dissipate the excess heat from the sample as agglomeration effects are aided by the increase in temperature. Bath-type sonicators are less effective than probe-type sonicators. In this case, the nanosuspension is immersed in a water bath and the sonication waves pass through the water toward the specimen. Most of the sonication waves do not pass through the sample due to the resistance of glass wall of the sample container. This resistance decreases the effectiveness of this process. Generally, bath-type sonicators take more time and power to de-agglomerate nanosuspension as compared to probe-type sonication.

Rehman et al. (2012) studied sedimentation rates of alumina/water suspensions at different concentrations (1–5 wt%) and ultrasonication times. It was found that

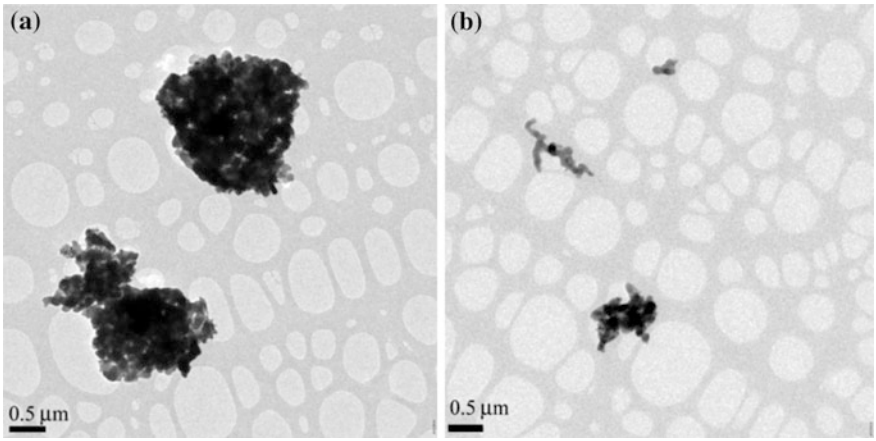

Fig. 8 TEM images of alumina/water nanofluids (1 vol%) after **a** 1 h and **b** 5 h of ultrasonication (Barrett et al. 2013) *adapted with permission*

nanosuspensions with high particle loading showed high agglomerate sizes. In another study (Ilyas et al. 2014b), the settling rates of zinc oxide nanoparticles in ethanol–water mixtures were reduced by the application of ultrasonic bath. Ultrasonication of nanofluids was found to be an effective method to reduce average particle size. The size of agglomerate was decreased by the increase in ultrasonication time. Similar results were found in the studies by Barrett et al. (2013). A stable nanosuspension of alumina/water (1 vol%) was obtained after 5 h of ultrasonication. The TEM images of alumina/water nanofluids are shown in Fig. 8. The effect of ultrasonication on the settling behavior of ZnO nanoparticles in the ethanol–water mixtures is illustrated in Fig. 9 (Ilyas et al. 2014b).

5.1.2 High-Pressure Homogenizer

The most effective de-agglomeration method is the high-pressure homogenization, which is purely a mechanical process. The nanofluids are stabilized by passing through with force in a narrow gap at high-pressure conditions. The subjected shear stress on the nanofluid ruptures big agglomerates into smaller agglomerates. The process is repeated many times until a stable and well-dispersed nanofluid is obtained. Ultra-high-pressure homogenizers operate at very high-pressure and micro-sized agglomerates are converted into primary nano-size.

Hwang et al. (2008) used high-pressure homogenizer to stabilize carbon black (CB) nanoparticles in water and silver nanoparticles in silicon oil. Different mixing techniques were used and comparative studies showed that high-pressure homogenizer is the most effective method to attain uniform nanosuspension. The comparative studies of different mixing techniques by Hwang et al. (2008) are shown in Fig. 10. The quality of CB/water dispersion (0.5 wt%) with normal mixing

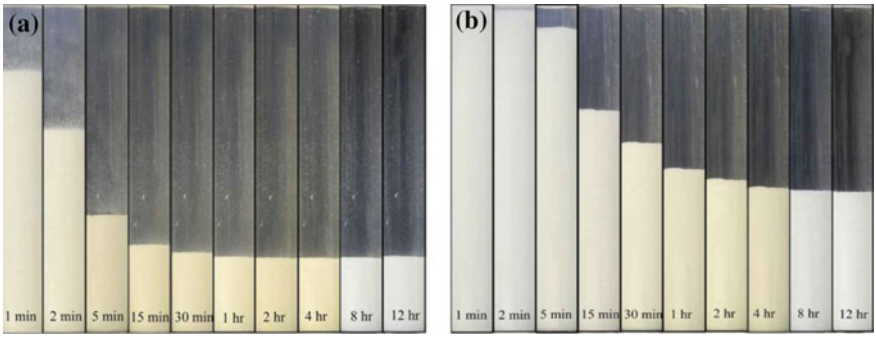

Fig. 9 Settling rates of nanoparticles in base fluid with and without sonication (Ilyas et al. 2014b) *adapted with permission*

(stirring), ultrasonication (bath type and probe type), and high-pressure homogenization is described.

In a recent investigation by Fontes et al. (2015), high-pressure homogenizer was used to disperse multi-wall carbon nanotubes (MWCNTs) and synthetic diamond in mineral oil. The nanosuspensions with different particle loadings exhibit better stability over 24 h. This technique can be applied in many industries to produce nano-emulsions, especially in foods, pharmaceuticals, cosmetics, and paint and pigment industries. The heat of compression causes a sudden increase in temperature of nanofluid. In general, 17–21 °C of rise in temperature takes place per 100 MPa of homogenization. This predicament in this process can affect the production and quality of sensitive food components. The temperature-controlling mechanism or heat dissipation systems are required to achieve better quality of nanosuspension.

5.1.3 Wet Milling

Milling process is used in size reduction of materials. Dispersion characteristics of nanoparticles in liquid can be improved by the use of wet milling process. Wet ball/bead milling of nanofluids can enhance the stability of nanoparticles as the agglomerates are broken into smaller ones. The stability of nanofluids using this method is highly dependent on the sizes of different grinding media, operational time, and rotational speed of the mill. In an investigation by Munkhbayar et al. (2013), influence of milling on the stability of carbon nanotubes in aqueous solutions was investigated. It was reported that milling has significant impact on the dispersion characteristics of nanosuspensions. This process is highly effective when combined with chemical technique (surface modification). The surface area of the nanomaterial increases with the operational time and helps the chemical agent to retain and make bonds on the surface of nanomaterial. Joni et al. (2009) prepared TiO_2/diglyme nanosuspensions using bead milling process. Silane coupling agents

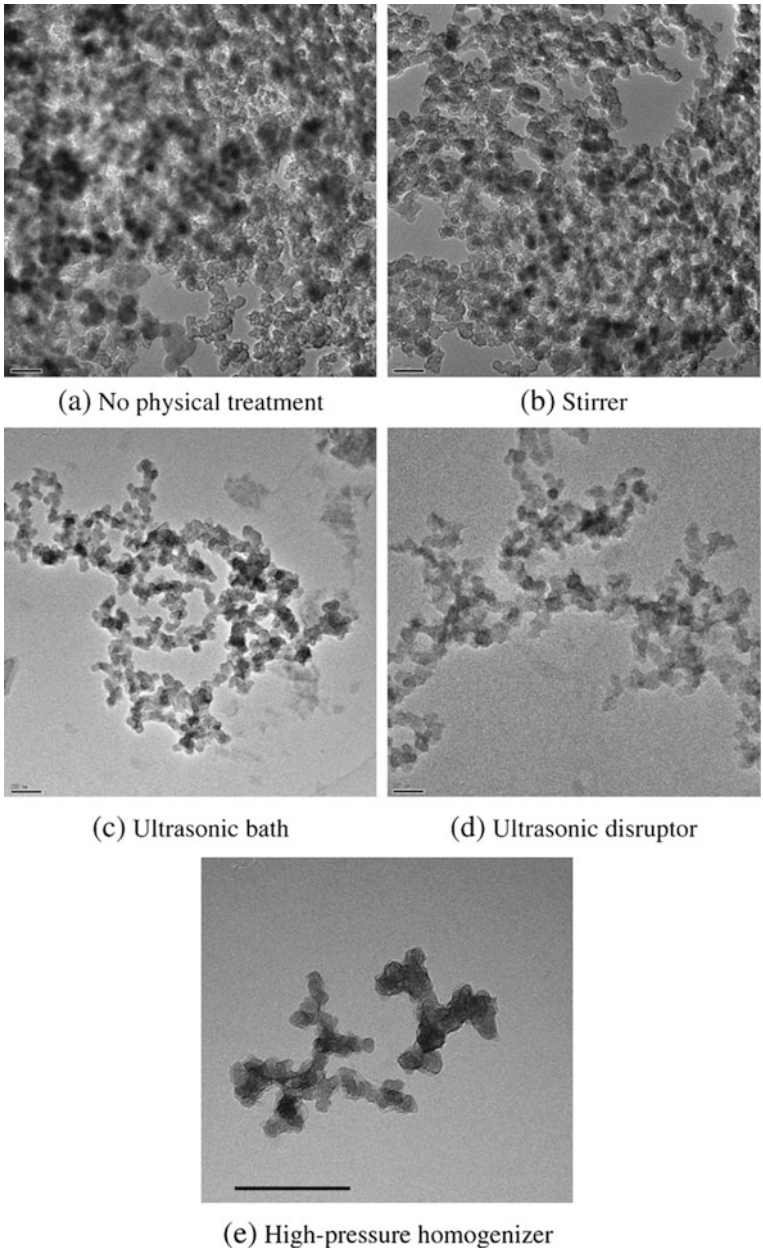

Fig. 10 TEM images of carbon black nanoparticles in water using different mechanical mixing techniques (Scale bar: 200 nm) (Hwang et al. 2008) *adapted with permission*

were introduced to modify the surface of titania during milling process to enhance dispersion stability. A uniform nanosuspension was obtained with 80 mV of zeta potential and particle size was reported to be very close to primary particle size, i.e., 15 nm. In a recent investigation by Farbod et al. (2015), a better stability of copper oxide was found in engine oil by the application of milling process for 3 h at 300 rpm.

Nanomaterials in low quantity can be lost during operation and cleaning of milling process. Furthermore, this method is not effective as compared to other methods because of the possibility of change in the primary shape and size of the nanomaterials. The particle size distribution of the original nanomaterial particularly nanotubes, 2D nanofillers, nanowires, and other structural nanomaterials can be altered during wet milling of nanofluids.

5.2 Chemical Techniques

Chemical techniques have peculiar advantages over mechanical mixing techniques. Mechanical mixing techniques can separate nanoparticles from particles cluster but they are likely to agglomerate again over time during operation. The stability of nanofluids can be prolonged by the use of chemical techniques such as addition of surfactants, pH adjustment, and surface modification of nanoparticles. Investigations till date report that the combination of mechanical and chemical techniques is the most effective way of preparing stable nanofluids for their application at industrial level. There are two types of stability mechanisms, i.e., steric repulsion and electrostatic repulsion. Steric stabilization mechanism involves the use of polymeric compounds which are adsorbed on the particle surface and provides extra repulsive forces on the surface of particles. These surface modifications weaken the attractive forces between particles, and a better stability is achieved. Electrostatic stabilization is a kinetic stability method that involves surface charges which are developed on the surface of nanoparticles creating a barrier between particles. Existences of these charges on the particle surface are due to the depletion or accumulation of electrons on the surface of the particle. Steric stabilization is insensitive to the electrolytes or pH. A large quantity of surfactant is required to functionalize or coat the particle surface as compared to electrostatic stabilization. Electrostatic stabilization is highly sensitive to pH or presence of electrolyte in the nanosuspension. Both colloidal stabilization mechanisms are well demonstrated by Yu and Xie (2012), as shown in Fig. 11.

5.2.1 Surfactant Addition

Surfactants are used to alter the surface properties of nanoparticles in nanofluids. Surfactants are also termed as dispersants or stabilizers. Addition of surfactants in nanofluids, exclusively in two-step preparation method, is the most simple and

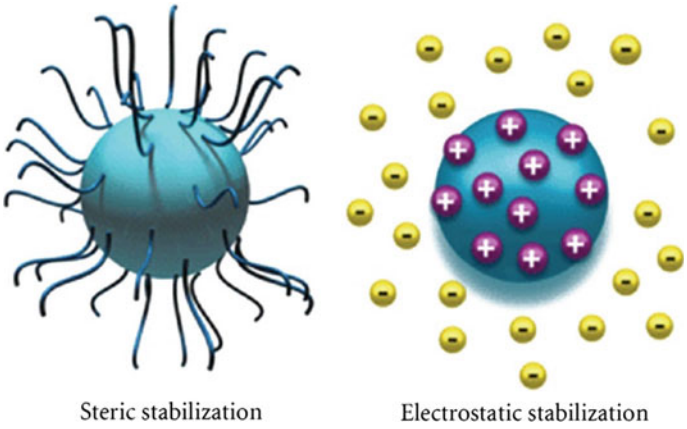

Fig. 11 Difference between steric and electrostatic stabilization (Yu and Xie 2012) *adapted by permission*

economical method of preparing stable nanofluids. The surface tension of the liquid is abated and the particle engagement is escalated in the host fluid by the introduction of surfactants. A rise in zeta potential is obtained due to increase in repulsive force generating from the particle surface. The hydrophobic surfaces of the nanomaterials in aqueous-based nanosuspensions are modified into hydrophilic surface. Similarly, the hydrophilic surfaces of the nanomaterials are modified into hydrophobic for non-aqueous nanofluids. Most of the surfactants consist of long-chain hydrocarbons with hydrophobic component in one corner and hydrophilic component on the other. The presence of these two components provides a strong linkage on the interface between particle and liquid. Sodium dodecyl sulfate (SDS), sodium dodecyl benzene sulfonate (SDBS), cetrimonium bromide (CTAB), and gum Arabic are the most widely used surfactants used to disperse nanoparticles in many commercial fluids.

Selection of suitable surfactant has significant importance toward dispersion characteristics of nanofluids. Yu and Xie (2012) stated that there are four types of surfactants, i.e., cationic, anionic, nonionic, and amphoteric surfactants.

- Cationic: long-chain quaternary ammonium compounds and long-chain amines
- Anionic: sulfonates, sulfosuccinates, long-chain fatty acids, phosphates, and alkyl sulfates
- Nonionic: alcohols, polyethylene oxide, and other polar groups
- Amphoteric: betaines and lecithins

The concentration of surfactant can influence the surface properties. Inadequate concentrations of surfactants in the suspension can dissuade repulsive forces and persuade attractive forces due to improper surface coating. High concentrations of surfactants can alter thermophysical properties of the nanofluid system. The risk of failure of surfactants in high-temperature applications is very likely. Another

quandary factor in the use of surfactant is the production of foam during operation of nanofluids with surfactants.

Kole and Dey (2010) stabilized alumina/EG:water-based nanofluids by using oleic acid as surfactant. Nanosuspensions with surfactants exhibit no sediment even after 80 days of preparation while nanofluids without surfactants exhibited sediments after two hours of preparation. Iyahraja and Rajadurai (2015) used polyvinylpyrrolidone (PVP) and SDS to stabilize silver nanoparticles in water. SDS-based nanofluids exhibit better stability than PVP-based nanofluids. However, PVP-based nanofluids demonstrated higher thermal conductivity values than SDS-based nanofluids.

5.2.2 Surface Modification

Surface modification of nanoparticles is a surfactant-free method and a long-term solution of attaining high dispersion characteristics of nanofluids. This method includes grafting, chemisorptions, plasma treatment, and many other techniques. The surface of the nanoparticle can be linked or modified with hydrophobic or hydrophilic component, depending on the application, to perform better stability in the nanosuspensions. The advantages of this method of stabilizing nanomaterials over other methods are that the modified particles tend to remain suspended for longer time. The effect on thermophysical properties of the nanofluids is negligible; however, effective thermal conductivity and specific heat capacity can be elevated depending on the properties of functionalizing agents. The toxicity and the polarity of some nanoparticles can be altered using this surface modification process.

Yu-zhen et al. (2010) dispersed three types of TiO_2 nanoparticles in transformer oil. Nanoparticles without surface modification, surface modification with stearic acid, and surface modification by silicon oil were used to study the effect of different types of particles on the breakdown strength of transformer oil. It was found that alternating current (AC) and impulse breakdown strength of transformer oil can be improved by dispersing TiO_2 nanoparticles modified with stearic acid as it exhibits less agglomeration. In another study by Li et al. (2010), silver-based nanofluids were prepared in oil. Silver nanoparticles of 5 nm average sizes were prepared by reducing Ag^+ with ascorbic acid. Oleic acid and n-butylamine were used to coat particle surface and stabilizer, respectively. Nanofluids were observed to be highly stable using this process. Surface-modified Fe_3O_4-based uniform nanofluid was prepared in vegetable insulation oil to study the dielectric properties of nanofluids (Li et al. 2012). Oleic acid was coated on the particle surface in ethanol solution before dispersing it into the vegetable oil. A uniform nanosuspension was achieved and nanoparticles remain suspended for 30 days after preparation.

5.2.3 pH Adjustment

pH of the nanofluids is strongly related to the rheological behavior of the suspensions. The adhesive forces present in the nanosuspensions depend on pH of the system. Degree of ionization has significant effect on the electrostatic interactions among charged particles. Changing the degree of ionization in the nanofluid system can improve the stability of suspended nanoparticles.

In a recent study by Konakanchi et al. (2014), Al_2O_3/PG:Water-, SiO_2/PG:Water- and ZnO/PG:Water-based nanofluids were prepared to study the relation of pH with temperature (T), concentration (φ), and size of nanoparticles (d). It was found that the pH values of nanofluids were directly proportional to the temperature and particle diameter. It was reported that the addition of SiO_2 nanoparticles (30 nm) in EG/water turned initially acidic nature of the host fluid to alkaline nature. Similarly, alumina and zinc oxide nanofluids exhibit less acidic behavior. A generalized correlation (Eq. 10) for pH was given as:

$$\frac{\mathrm{pH}_{nf}}{\mathrm{pH}_{f}} = \left(z_1\varphi^2 + z_2\varphi + z_3\right)\left\{z_4\left(\frac{T}{T_0}\right)^2 + z_5\left(\frac{T}{T_0}\right) + z_6\right\}\left\{z_7\left(\frac{d}{d_0}\right)^2 + z_8\right\} \quad (10)$$

Ho et al. (2010) prepared alumina–water nanofluids with average particle size of 33 nm to study the natural convection of nanofluids in squared enclosures. The pH of nanofluids was adjusted to 3 for different concentrations and stable nanofluids were obtained for at least two weeks.

6 Conclusions

Stability of nanofluids is the important characteristic toward their usage in industrial applications. The knowledge of interactions (DLVO and non-DLVO forces) among nanoparticles and particle–liquid has significant role to prepare stable nanofluids. Different techniques can be used during preparation of nanofluids to obtain uniform stable nanosuspension. Aggregation among particles is a natural phenomenon; however, the agglomeration process can be delayed by mechanical and chemical techniques. Mechanical mixing technique is more suitable for low particle concentrations. Appropriate surfactant concentration should be used to prolong the dispersion of nanoparticles in liquid. The application and advancement of characterization equipment is necessary to evaluate the stability of nanofluids. Different combinations of highly stable nanofluids can be prepared with enhanced properties such as improved reactivity, intensified thermal properties, and light weight for different applications.

References

Ahuja, A. S. (1975a). Augmentation of heat transport in laminar flow of polystyrene suspensions. I. Experiments and results. *Journal of Applied Physics, 46*(8), 3408–3416.

Ahuja, A. S. (1975b). Measurement of thermal conductivity of (neutrally and nonneutrally buoyant) stationary suspensions by the unsteady-state method. *Journal of Applied Physics, 46* (2), 747–755.

Alberola, J. A., Mondragón, R., Juliá, J. E., Hernández, L., & Cabedo, L. (2014). Characterization of halloysite-water nanofluid for heat transfer applications. *Applied Clay Science, 99*, 54–61. doi:10.1016/j.clay.2014.06.012.

Allouni, Z. E., Cimpan, M. R., Høl, P. J., Skodvin, T., & Gjerdet, N. R. (2009). Agglomeration and sedimentation of TiO_2 nanoparticles in cell culture medium. *Colloids and Surfaces B: Biointerfaces, 68*(1), 83–87. doi:10.1016/j.colsurfb.2008.09.014.

Barrett, T. R., Robinson, S., Flinders, K., Sergis, A., & Hardalupas, Y. (2013). Investigating the use of nanofluids to improve high heat flux cooling systems. *Fusion Engineering and Design, 88*(9–10), 2594–2597. doi:10.1016/j.fusengdes.2013.03.058.

Choi, S. U. S. (1995). Enhancement thermal conductivity of fluids with nanoparticles. FED 231.

Choi, U. S., France, D. M., & Knodel, B. D. (1992). Impact of advanced fluids on costs of district cooling systems. In *Proceedings of 83rd Annual International District Heating and Cooling Association Conference*. Danvers, MA.

Derjaguin, B. (1934). Friction and adhesion. IV. The theory of adhesion of small particles. *Kolloid Zeits, 69*, 155–164.

Duangthongsuk, W., & Wongwises, S. (2015). A comparison of the heat transfer performance and pressure drop of nanofluid-cooled heat sinks with different miniature pin fin configurations. *Experimental Thermal and Fluid Science, 69*, 111–118. doi:10.1016/j.expthermflusci.2015.07.019.

Eastman, J. A., Choi, U. S., Li, S., Soyez, G., Thompson, L. J., & DiMelfi, R. J. (1999). Novel thermal properties of nanostructured materials. *Materials Science Forum, 312*, 629–634.

Eastman, J. A., Choi, S. U. S., Li, S., Yu, W., & Thompson, L. J. (2001). Anomalously increased effective thermal conductivities of ethylene glycol-based nanofluids containing copper nanoparticles. *Applied Physics Letters, 78*(6), 718–720.

Elimelech, M., Gregory, J., Jia, X. (2013). *Particle deposition and aggregation: Measurement, modelling and simulation*. Butterworth-Heinemann,

Fang, B., Zhang, C., Zhang, W., & Wang, G. (2009). A novel hydrazine electrochemical sensor based on a carbon nanotube-wired ZnO nanoflower-modified electrode. *Electrochimica Acta, 55*(1), 178–182. doi:10.1016/j.electacta.2009.08.036.

Farbod, M., Kouhpeymani asl, R., & Noghreh abadi, A. R. (2015). Morphology dependence of thermal and rheological properties of oil-based nanofluids of CuO nanostructures. *Colloids and Surfaces A: Physicochemical and Engineering Aspects, 474*, 71–75. doi:10.1016/j.colsurfa.2015.02.049.

Feng, X., Ma, H., Huang, S., Pan, W., Zhang, X., Tian, F., et al. (2006). Aqueous-organic phase-transfer of highly stable gold, silver, and platinum nanoparticles and new route for fabrication of gold nanofilms at the oil/water interface and on solid supports. *The Journal of Physical Chemistry B, 110*(25), 12311–12317.

Fontes, D. H., Ribatski, G., & Bandarra Filho, E. P. (2015). Experimental evaluation of thermal conductivity, viscosity and breakdown voltage AC of nanofluids of carbon nanotubes and diamond in transformer oil. *Diamond and Related Materials, 58*, 115–121. doi:10.1016/j.diamond.2015.07.007.

Ho, C. J., Liu, W. K., Chang, Y. S., & Lin, C. C. (2010). Natural convection heat transfer of alumina-water nanofluid in vertical square enclosures: An experimental study. *International Journal of Thermal Sciences, 49*(8), 1345–1353. doi:10.1016/j.ijthermalsci.2010.02.013.

Huang, L., Li, D.-Q., Lin, Y.-J., Wei, M., Evans, D. G., & Duan, X. (2005). Controllable preparation of Nano-MgO and investigation of its bactericidal properties. *Journal of Inorganic Biochemistry, 99*(5), 986–993. doi:10.1016/j.jinorgbio.2004.12.022.

Hwang, Y., Lee, J.-K., Lee, J.-K., Jeong, Y.-M., S-i, Cheong, Ahn, Y.-C., et al. (2008). Production and dispersion stability of nanoparticles in nanofluids. *Powder Technology, 186*(2), 145–153. doi:10.1016/j.powtec.2007.11.020.

Ilyas, S. U., Pendyala, R., & Marneni, N. (2013). Settling characteristics of alumina nanoparticles in ethanol-water mixtures. *Applied Mechanics and Materials, 372*, 143–148.

Ilyas, S. U., Pendyala, R., & Marneni, N. (2014a). Preparation, sedimentation, and agglomeration of nanofluids. *Chemical Engineering and Technology, 37*(12), 2011–2021.

Ilyas, S., Pendyala, R., & Marneni, N. (2014b). Dispersion behaviour and agglomeration effects of zinc oxide nanoparticles in ethanol–water mixtures. *Materials Research Innovations, 18*(S6), S6-179–S176-183.

Ilyas, S. U., Pendyala, R., Shuib, A., & Marneni, N. (2014c). A review on the viscous and thermal transport properties of nanofluids. *Advanced Materials Research, 917*, 18–27.

Iritani, E., Hashimoto, T., & Katagiri, N. (2009). Gravity consolidation–sedimentation behaviors of concentrated TiO2 suspension. *Chemical Engineering Science, 64*(21), 4414–4423. doi:10.1016/j.ces.2009.07.013.

Iyahraja S, Rajadurai JS (2015) Stability of Aqueous Nanofluids Containing PVP-Coated Silver Nanoparticles. Arabian *Journal for Science and Engineering*, 1–8. doi:10.1007/s13369-015-1707-9.

Joni, I. M., Purwanto, A., Iskandar, F., & Okuyama, K. (2009). Dispersion stability enhancement of titania nanoparticles in organic solvent using a bead mill process. *Industrial and Engineering Chemistry Research, 48*(15), 6916–6922.

Kao, M.-J., Chang, H., Wu, Y.-Y., Tsung, T.-T., & Lin, H.-M. (2007a). Producing aluminum-oxide brake nanofluids using plasma charging system. *Journal of the Chinese Society of Mechanical Engineers, 28*(2), 123–131.

Kao, M. J., Lo, C. H., Tsung, T. T., Wu, Y. Y., Jwo, C. S., & Lin, H. M. (2007b). Copper-oxide brake nanofluid manufactured using arc-submerged nanoparticle synthesis system. *Journal of Alloys and Compounds, 434–435*, 672–674. doi:10.1016/j.jallcom.2006.08.305.

Kole, M., & Dey, T. K. (2010). Viscosity of alumina nanoparticles dispersed in car engine coolant. *Experimental Thermal and Fluid Science, 34*(6), 677–683. doi:10.1016/j.expthermflusci.2009.12.009.

Kole, M., & Dey, T. K. (2012). Effect of prolonged ultrasonication on the thermal conductivity of ZnO–ethylene glycol nanofluids. *Thermochimica Acta, 535*, 58–65. doi:10.1016/j.tca.2012.02.016.

Konakanchi, H., Vajjha, R. S., Chukwu, G. A., & Das, D. K. (2014). Measurements of pH of three nanofluids and development of new correlations. *Heat Transfer Engineering, 36*(1), 81–90. doi:10.1080/01457632.2014.906286.

Kumar, A., Joshi, H., Pasricha, R., Mandale, A. B., & Sastry, M. (2003). Phase transfer of silver nanoparticles from aqueous to organic solutions using fatty amine molecules. *Journal of Colloid and Interface Science, 264*(2), 396–401. doi:10.1016/S0021-9797(03)00567-8.

Kwak, K., & Kim, C. (2005). Viscosity and thermal conductivity of copper oxide nanofluid dispersed in ethylene glycol. *Korea-Australia Rheology Journal, 17*(2), 35–40.

Lee, J.-H., Hwang, K. S., Jang, S. P., Lee, B. H., Kim, J. H., Choi, S. U. S., et al. (2008). Effective viscosities and thermal conductivities of aqueous nanofluids containing low volume concentrations of Al_2O_3 nanoparticles. *International Journal of Heat and Mass Transfer, 51*(11–12), 2651–2656.

Li, D., Hong, B., Fang, W., Guo, Y., & Lin, R. (2010). Preparation of well-dispersed silver nanoparticles for oil-based nanofluids. *Industrial and Engineering Chemistry Research, 49*(4), 1697–1702. doi:10.1021/ie901173h.

Li, J., Zhang, Z., Zou, P., Grzybowski, S., & Zahn, M. (2012). Preparation of a vegetable oil-based nanofluid and investigation of its breakdown and dielectric properties. *Electrical Insulation Magazine, IEEE, 28*(5), 43–50. doi:10.1109/MEI.2012.6268441.

LotfizadehDehkordi, B., Ghadimi, A., & Metselaar, H. S. (2013). Box-Behnken experimental design for investigation of stability and thermal conductivity of TiO_2 nanofluids. *Journal of Nanoparticle Research, 15*(1), 1–9.

Mahbubul, I. M., Chong, T. H., Khaleduzzaman, S. S., Shahrul, I. M., Saidur, R., Long, B. D., et al. (2014). Effect of ultrasonication duration on colloidal structure and viscosity of alumina-water nanofluid. *Industrial and Engineering Chemistry Research, 53*(16), 6677–6684. doi:10.1021/ie500705j.

Maxwell, J. C. (1873). Art. 314. Medium in which small spheres are uniformly disseminated, Chapter IX. Conduction through heterogeneous media. *A treatise on electricity and magnetism, 1*, 365–366.

Munkhbayar, B., Nine, M. J., Jeoun, J., Bat-Erdene, M., Chung, H., & Jeong, H. (2013). Influence of dry and wet ball milling on dispersion characteristics of the multi-walled carbon nanotubes in aqueous solution with and without surfactant. *Powder Technology, 234*, 132–140. doi:10.1016/j.powtec.2012.09.045.

Nayak, A. K., Gartia, M. R., & Vijayan, P. K. (2009). Thermal–hydraulic characteristics of a single-phase natural circulation loop with water and Al_2O_3 nanofluids. *Nuclear Engineering and Design, 239*(3), 526–540. doi:10.1016/j.nucengdes.2008.11.014.

Nematolahi, M., Behzadinejad, B., & Golestani, (2015). A feasibility study of using nanofluids as a neutron absorber in reactor emergency core cooling system. *International Journal of Hydrogen Energy,*. doi:10.1016/j.ijhydene.2015.03.159.

Nguyen, C. T., Desgranges, F., Galanis, N., Roy, G., Maré, T., Boucher, S., et al. (2008). Viscosity data for Al2O3–water nanofluid—hysteresis: Is heat transfer enhancement using nanofluids reliable? *International Journal of Thermal Sciences, 47*(2), 103–111. doi:10.1016/j.ijthermalsci.2007.01.033.

Otanicar, T. P., Phelan, P. E., Prasher, R. S., Rosengarten, G., & Taylor, R. A. (2010). Nanofluid-based direct absorption solar collector. *Journal of renewable and sustainable energy, 2*(3), 033102.

Pastoriza-Gallego, M. J., Casanova, C., Legido, J. L., & Piñeiro, M. M. (2011). CuO in water nanofluid: Influence of particle size and polydispersity on volumetric behaviour and viscosity. *Fluid Phase Equilibria, 300*(1–2), 188–196. doi:10.1016/j.fluid.2010.10.015.

Pastoriza-Gallego, M. J., Lugo, L., Cabaleiro, D., Legido, J. L., & Piñeiro, M. M. (2014). Thermophysical profile of ethylene glycol-based ZnO nanofluids. *The Journal of Chemical Thermodynamics, 73*, 23–30. doi:10.1016/j.jct.2013.07.002.

Pendyala, R., Chong, J. L., & Ilyas, S. U. (2015). CFD analysis of heat transfer performance in a car radiator with nanofluids as coolants. *Chemical Engineering Transactions, 45*, 1261–1266. doi:10.3303/CET1545211.

Pietsch, W. (2005). *Agglomeration in industry*. Wiley-VCH-Verlag.

Rehman, H., Batmunkh, M., Jeong, H., & Chung, H. (2012). Sedimentation study and dispersion behavior of Al_2O_3–H_2O nanofluids with dependence of time. *Advanced Science Letters, 6*(1), 96–100. doi:10.1166/asl.2012.2135.

Ruckenstein, E., & Prieve, D. C. (1976). Adsorption and desorption of particles and their chromatographic separation. *AIChE Journal, 22*(2), 276–283.

Said, Z., Sajid, M. H., Alim, M. A., Saidur, R., & Rahim, N. A. (2013). Experimental investigation of the thermophysical properties of AL_2O_3-nanofluid and its effect on a flat plate solar collector. *International Communications in Heat and Mass Transfer, 48*, 99–107. doi:10.1016/j.icheatmasstransfer.2013.09.005.

Sabliov. C. M., & Astete, C. E. (2015). 17 Polymeric nanoparticles for food applications. *Nanotechnology and Functional Foods: Effective Delivery of Bioactive Ingredients* 272.

Sekhar, R. Y., Sharma, K. V., Karupparaj, T. R., & Chiranjeevi, C. (2013). Heat transfer enhancement with Al_2O_3 nanofluids and twisted tapes in a pipe for solar thermal applications. *Procedia Engineering, 64*, 1474–1484. doi:10.1016/j.proeng.2013.09.229.

Sharma, T., Mohana Reddy, A. L., Chandra, T. S., & Ramaprabhu, S. (2008). Development of carbon nanotubes and nanofluids based microbial fuel cell. *International Journal of Hydrogen Energy, 33*(22), 6749–6754. doi:10.1016/j.ijhydene.2008.05.112.

Shirato, M., Kato, H., Kobayashi, K., & Sakazaki, H. (1970). Analysis of settling of thick slurries fue to consolidation. *Journal of Chemical Engineering of Japan, 3*(1), 98–104.

Singh, A., & Raykar, V. (2008). Microwave synthesis of silver nanofluids with polyvinylpyrrolidone (PVP) and their transport properties. *Colloid and Polymer Science, 286*(14–15), 1667–1673. doi:10.1007/s00396-008-1932-9.

Smirnov, V. V., Kostritsa, S. A., Kobtsev, V. D., Titova, N. S., & Starik, A. M. (2015). Experimental study of combustion of composite fuel comprising n-decane and aluminum nanoparticles. *Combustion and Flame,*. doi:10.1016/j.combustflame.2015.06.011.

Sohel, M. R., Saidur, R., Khaleduzzaman, S. S., & Ibrahim, T. A. (2015). Cooling performance investigation of electronics cooling system using Al_2O_3–H_2O nanofluid. *International Communications in Heat and Mass Transfer, 65*, 89–93. doi:10.1016/j.icheatmasstransfer.2015.04.015.

Sonage, B., & Mohanan, P. (2015). Miniaturization of automobile radiator by using zinc-water and zinc oxide-water nanofluids. *Journal of Mechanical Science and Technology, 29*(5), 2177–2185.

Srinivas, V., Moorthy, C. V., Dedeepya, V., Manikanta, P., Satish, V. (2015). Nanofluids with CNTs for automotive applications. *Heat and Mass Transfer* 1–12.

Sundar, L. S., Naik, M. T., Sharma, K. V., Singh, M. K., & Siva, R. T. C. (2012). Experimental investigation of forced convection heat transfer and friction factor in a tube with Fe_3O_4 magnetic nanofluid. *Experimental Thermal and Fluid Science, 37*, 65–71. doi:10.1016/j.expthermflusci.2011.10.004.

Suresh, S., Venkitaraj, K. P., Selvakumar, P., & Chandrasekar, M. (2012). Effect of Al_2O_3–Cu/water hybrid nanofluid in heat transfer. *Experimental Thermal and Fluid Science, 38*, 54–60. doi:10.1016/j.expthermflusci.2011.11.007.

Teng, T.-P., Hsu, Y.-C., Wang, W.-P., & Fang, Y.-B. (2015). Performance assessment of an air-cooled heat exchanger for multiwalled carbon nanotubes-water nanofluids. *Applied Thermal Engineering, 89*, 346–355. doi:10.1016/j.applthermaleng.2015.06.042.

Verwey, E. J. W., Overbeek, J. T. G., & Ness K. V. (1948). *Theory of the stability of lyophobic colloids—The interaction of soil particles having an electrical double layer*. Elsevier.

Wang, X.-Q., & Mujumdar, A. S. (2007). Heat transfer characteristics of nanofluids: a review. *International Journal of Thermal Sciences, 46*(1), 1–19. doi:10.1016/j.ijthermalsci.2006.06.010.

Witharana, S., Palabiyik, I., Musina, Z., & Ding, Y. (2013). Stability of glycol nanofluids—The theory and experiment. *Powder Technology, 239*, 72–77. doi:10.1016/j.powtec.2013.01.039.

Xuan, Y., & Li, Q. (2000). Heat transfer enhancement of nanofluids. *International Journal of Heat and Fluid Flow, 21*(1), 58–64. doi:10.1016/S0142-727X(99)00067-3.

Yu, W., Xie, H. (2012). A Review on Nanofluids: Preparation, Stability Mechanisms, and Applications. Journal of Nanomaterials 2012. doi:10.1155/2012/435873.

Yu, W., Xie, H., Chen, L., & Li, Y. (2010). Enhancement of thermal conductivity of kerosene-based Fe_3O_4 nanofluids prepared via phase-transfer method. *Colloids and surfaces A: Physicochemical and engineering aspects, 355*(1–3), 109–113. doi:10.1016/j.colsurfa.2009.11.044.

Yu-zhen, L., Xiao-xin, L., Yue-fan, D., Fo-chi, W., Cheng-rong, L. (2010). Preparation and breakdown strength of TiO_2 fluids based on transformer oil. In *Proceedings of 2010 Annual Report Conference on Electrical Insulation and Dielectric Phenomena (CEIDP)* (pp. 1–3), 17–20 Oct 2010. doi:10.1109/CEIDP.2010.5723974.

Zhang, J., Diao, Y. H., Zhao, Y. H., Tang, X., Yu, W. J., & Wang, S. (2013). Experimental study on the heat recovery characteristics of a new-type flat micro-heat pipe array heat exchanger using nanofluid. *Energy Conversion and Management, 75*, 609–616. doi:10.1016/j.enconman.2013.08.003.

Zhang, L., Ding, Y., Povey, M., & York, D. (2008). ZnO nanofluids—A potential antibacterial agent. *Progress in Natural Science, 18*(8), 939–944. doi:10.1016/j.pnsc.2008.01.026.

Zhu, D., Li, X., Wang, N., Wang, X., Gao, J., & Li, H. (2009). Dispersion behavior and thermal conductivity characteristics of Al_2O_3–H_2O nanofluids. *Current Applied Physics, 9*(1), 131–139. doi:10.1016/j.cap.2007.12.008.

Zhu, H. T., Zhang, C. Y., Tang, Y. M., & Wang, J. X. (2007). Novel synthesis and thermal conductivity of CuO nanofluid. *The Journal of Physical Chemistry C, 111*(4), 1646–1650. doi:10.1021/jp065926t.

Considerations on the Thermophysical Properties of Nanofluids

K.V. Sharma, Akilu Suleiman, Hj. Suhaimi B. Hassan and Gurumurthy Hegde

Abstract The properties such as viscosity, thermal conductivity, specific heat, and density of nanofluids have been determined by various investigators through experiments. An equation developed for specific heat and density employing the law of mixtures is observed to be valid when compared with the experimental data. However, the experimental data of viscosity and thermal conductivity reported by investigators are observed to vary by more than 25 % for certain nanofluids. Theoretical models for the estimation of properties are yet to be developed. The nanofluid properties are essential for the comparison of heat transfer enhancement capabilities. Equations are developed for the estimation of viscosity and thermal conductivity by Corcione and Sharma et al. These equations are flexible to determine the nanofluid properties for a wide range of operating parameters which can predict the experimental data of water-based nanofluids with a maximum deviation of 12 %.

Keywords Water-based nanofluids · Nanofluid properties · Regression equations · Estimation of thermal conductivity and viscosity

Nomenclature

C	Specific heat at constant pressure, J/(K kg)
C_{RM}	Random motion velocity of nanoparticles, m/s
D	Diameter, nm
HR	Non-dimensional heat capacity ratio $[(\rho C)_p/(\rho C)_{nf}]$
H	Interparticle spacing
K	Thermal conductivity, J/(K m)

K.V. Sharma (✉) · A. Suleiman · Hj.S.B. Hassan
Mechanical Engineering Department, Universiti Teknologi PETRONAS, 32610 Bandar Seri Iskandar, Perak Darul Ridzuan, Malaysia
e-mail: kvsharmajntu@gmail.com

G. Hegde
BMS R&D Centre, BMS College of Engineering, Basavanagudi, Bangalore 560019, India

K. Viswanatha Sharma and N. Hisham B Hamid (eds.),
Engineering Applications of Nanotechnology, Topics in Mining, Metallurgy and Materials Engineering, DOI 10.1007/978-3-319-29761-3_2

k_B Boltzmann constant, 1.3807×10^{-23} J/K
k_{pe} Equivalent thermal conductivity
L Molecular weight of the base fluid
N Avogadro's number
N Empirical shape factor 'n' is equal to $3/\psi$
Pr Prandtl number
R Thermal resistance (K m^2)/W
R_b Interfacial thermal resistance between nanoparticle and the fluid
Re Reynolds number
r_m Radius of the liquid species
r_p Radius of the suspended particles
T Thickness, m
T Temperature, K or °C

Greek symbols

α Thermal diffusivity, $[k/\rho C]$ (m^2/s)
β Ratio of nanolayer thickness to the particle radius
ω $= \left[\frac{d_p}{(d_p+2t)}\right]^3$
$\varnothing$ Volume fraction of nanoparticles in per cent
ϕ_m Maximum packing fraction
γ Ratio of thermal conductivity of the layer to that of the particle
μ Absolute viscosity, kg/(m s)
μ_r Relative viscosity of the suspension
ϑ Kinematic viscosity (m^2/s)
ρ Density (kg/m^3)
ρ_{bf0} Mass density of the base fluid calculated at 20 °C
fr Freezing point of the base liquid
η Intrinsic viscosity
ψ Sphericity

Subscripts

bf Base fluid
eff Effective
i Interface
nf Nanofluid
neff Net effective
w Water
p Nanoparticle

1 Introduction

Nanofluids are particle suspensions of metals, metal oxides, carbides, nitrides, carbon nanotubes, etc., dispersed in a continuous medium such as water, ethylene glycol, refrigerants, and engine oil of size less than 100 nm. The thermophysical properties of nanofluids are observed to be greater than those of the base liquids. Their use in industrial applications require the development of stable nanofluids with their properties determined.

The properties of stable nanofluids with metals such as copper, silver, gold, and oxides, namely Al_2O_3, CuO, TiO_2, SiO_2, ZnO, and ZrO_2, in water and ethylene glycol are widely investigated because of their potential as heat transfer fluid with applications for thermal energy transfer in automotive, solar, and cooling electronic appliances. Studies are undertaken to determine ways to stabilize nanofluids from agglomeration for long term applications. The thermophysical properties of nanofluids which are important for applications involving single phase convective heat transfer are viscosity, thermal conductivity, specific heat and density.

2 Viscosity Models

The earliest studies for the determination of viscosity of suspended particles in liquids were undertaken by Einstein. An equation has been proposed based on the liquid particle interaction, which can predict the effective viscosity of liquid for volume concentrations lower than 1.0 %. The Einstein's equation is given by Eq. (1):

$$\mu_r = \mu_{nf}/\mu_w = (1.0 + 2.5\varnothing) \tag{1}$$

Brinkman (1952) extended the validity of Einstein's equation up to 4.0 % volume concentration given by Eq. (2) as:

$$\mu_r = \mu_{nf}/\mu_w = 1/(1 - \varnothing)^{2.5} \tag{2}$$

Krieger and Dougherty (1959) presented a semiempirical equation expressed as in Eq. (3):

$$\mu_r = \mu_{nf}/\mu_w = (1 - \varnothing/\varnothing_m)^{-[\eta]\varnothing_m} \tag{3}$$

where η is the intrinsic viscosity (2.5 for solid spheres) and $\varnothing_m$ is the maximum packing fraction. The maximum close-packing fraction is approximately 0.64 for randomly monodispersed spheres. Frankel and Acrivos (1967) proposed an equation for viscosity given by:

$$\mu_r = \frac{\mu_{nf}}{\mu_w} = \frac{9}{8}\left[\frac{(\varnothing/\varnothing_m)^{1/3}}{1-(\varnothing/\varnothing_m)^{1/3}}\right] \tag{4}$$

where $\varnothing_m$ is the maximum particle volume fraction determined from experiments. Nielsen (1970) proposed a different model for a low concentration of particles. Nielsen's equation is given by:

$$\mu_r = \mu_{nf}/\mu_w = (1+1.5\varnothing)\exp[\varnothing/(1-\varnothing_m)] \tag{5}$$

where $\varnothing$ and $\varnothing_m$ are the volume fraction of particles and the maximum packing fraction, respectively. Lundgren (1972) proposed an equation developed in the form of Taylor series given by:

$$\mu_r = \mu_{nf}/\mu_w = 1+2.5\varnothing+\frac{25}{4}\varnothing^2+O(\varnothing^3) \tag{6}$$

With increasing particle volume concentration, the flow around a particle is influenced by the neighbouring particles. Batchelor (1977) studied the effect of these hydrodynamic interactions or the Brownian motion on viscosity of suspensions and developed a relation valid for particle volume concentrations up to 10.0 % as:

$$\mu_r = \mu_{nf}/\mu_w = (1+2.5\varnothing+6.2\varnothing^2) \tag{7}$$

where μ_r is the relative viscosity of the suspension and $\varnothing$ is the volume fraction. Graham (1981) proposed a generalized form of Frankel and Acrivos (1967) formula that agrees well with Einstein's equation for small values of volume concentration. The equation developed is:

$$\mu_r = \mu_{nf}/\mu_w = 1+2.5\varnothing+4.5/\left(\frac{h}{d_p}\right)\left(2+\frac{h}{d_p}\right)\left(1+\frac{h}{d_p}\right)^2 \tag{8}$$

where d_p is the particle diameter and h is the interparticle spacing. A simple expression was proposed by Kitano et al. (1981) by involving maximum particle volume concentration term $\varnothing_m$ to predict the viscosity of nanofluids:

$$\mu_r = \mu_{nf}/\mu_w = (1-\varnothing/\varnothing_m)^{-2} \tag{9}$$

The White (1991) formula estimates the viscosity of water considering the effect of temperature given by:

$$\ln\left(\frac{\mu_{bf}}{\mu_o}\right) \approx a+b\left(\frac{T_o}{T}\right)+c\left(\frac{T_o}{T}\right)^2 \tag{10}$$

where μ_o, T_o are the reference values and a = 2.10, b = 4.45, and c = 6.55. The most referred equation on dynamic viscosity of water with the influence of temperature is given by Hagen (1999) as follows:

$$\mu_{\mathrm{bf}} \times 10^4 = \exp[(1.12646 - 0.039638T)/(1 - 0.00729769T)] \tag{11}$$

The data of Wang et al. (1999) have been regressed by Duangthongsuk and Wongwises (2009) with less than 1 % deviation for the determination of Al_2O_3/water nanofluid viscosity given by:

$$\mu_{\mathrm{r}} = \mu_{\mathrm{nf}}/\mu_{\mathrm{w}} = (1 + 7.3\varnothing + 123\varnothing^2) \tag{12}$$

Depending on the physical state of the phases, e.g. solid–solid or solid–liquid, different forms of representing concentration are convenient. In a solid–liquid system, the volume fraction of a phase is usual. In a solid–solid system, the Fullman model for the mean free path λ shown in Fig. 1 can be used to indicate the average distance between two particles of phase ph. Based on the mean free path λ of the nanoparticles in the base fluid, Noni et al. (2002) proposed a correlation which is given as:

$$\mu_{\mathrm{nf}}/\mu_{\mathrm{w}} = 1 + c\frac{1}{\lambda^n} \tag{13}$$

where an average distance between two particles of phase ph having an average size d_{ph} in a matrix of phase α and $\lambda = \frac{2}{3}d_{\mathrm{ph}}\left(\frac{1-\varnothing_{\mathrm{ph}}}{\varnothing_{\mathrm{ph}}}\right)$ given by Fullman (1953),

$\varnothing_{\mathrm{ph}}$ is the volume fraction of phase in the system,
$d_{\mathrm{ph}}$is the average diameter of phase,
'c' and 'n' are constants.

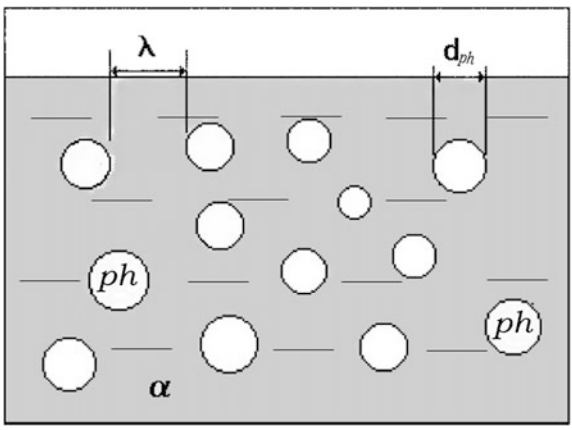

Fig. 1 A typical two-phase system

Tseng and Lin (2003) developed viscosity correlation for TiO_2 nanoparticles (7–20 nm) suspended in distilled water in the particle concentration from 0.05 to 0.12 % with a correlation factor $R^2 = 0.98$ which is given as:

$$\mu_{nf}/\mu_w = 13.45 \exp(35.98\varnothing) \tag{14}$$

Chen et al. (2007) modified the Krieger–Dougherty (1959) equation by considering $\varnothing = (a_a/a)^{3-D}$

$$\mu_r = \mu_{nf}/\mu_w = \left(1 - \frac{\varnothing}{\varnothing_m}\left(\frac{a_a}{a}\right)^{1.2}\right)^{-[\eta]\varnothing_m} \tag{15}$$

where a_a and a are the radii of aggregates and primary nanoparticles, respectively. The term D is defined as the fractal index, which for nanoparticles has a typical value of 1.8 given by Chen et al. (2007). Review articles are presented by Ghadimi et al. (2011), Mahbubul et al. (2012), Sundar et al. (2013), Mishra et al. (2014), and Sharma et al. (2016) covering theoretical and experimental works.

2.1 Experimental Determination of Viscosity

The experimental determination of nanofluid viscosity was undertaken by Pak and Cho (1998) who observed Newtonian behaviour with Al_2O_3 of size 13 nm and TiO_2 of size 27 nm for particle volume concentration lower than 3 and 10 %, respectively. The fluids showed shear thinning behaviour (i.e. decrease in viscosity with shear rate) indicating non-Newtonian behaviour at higher volume concentrations. They showed that the Bachelor's model failed to predict the viscosity of the nanofluids, although the volume fraction of the particles is within the range of applicability.

Junming et al. (2002) have measured the viscosity of CuO nanoparticles dispersed in water with the particle concentration range of 2–10 % and in the temperature range of 30–80 °C. The viscosity of the suspensions was reported to be higher than that of water by 15–30 %.

Prasher et al. (2006) have performed experiments to determine the viscosity of Al_2O_3-based nanofluids and pure propylene glycol at various temperatures (30–60 °C), nanoparticle diameter (27, 40, and 50 nm), and nanoparticle volume fraction (0.5–3 %). The viscosities of pure propylene glycol (PG) at 20 and 40 °C were found to be 0.0629 and 0.02 Pa s, respectively.

Kulkarni et al. (2006) conducted experiments to determine the rheological behaviour of copper oxide (CuO) nanoparticles having an average diameter of 29 nm, dispersed in deionized (DI) water, over a range of volume concentrations between 5 and 15 % and temperatures varying between 278 and 323 K. Their work

yielded a well-developed generalized correlation for liquid viscosity given by Eq. (16):

$$\ln \mu_s = A(1/T) - B \tag{16}$$

where μ_s is the suspension viscosity and A and B are polynomials which are functions of particle volumetric concentrations. These factors are given as:

$$A = 20587\varnothing^2 + 15857\varnothing + 1078.3\varnothing^3 \quad \text{with } R^2 = 0.99$$
$$B = -107.12\varnothing^2 + 53.548\varnothing + 2.8715 \quad \text{with } R^2 = 0.97$$

where $\varnothing$ is the volume fraction ranging from 0.05 to 0.15.

Calculated values from the above equation and the experimental values were compared, and these values are within ±10 %, except for two data points at temperatures 278 and 283 K, for a 15 % CuO suspension.

Kulkarni et al. (2007) have studied the rheological properties of CuO nanoparticles dispersed in PG and water in the ratio of 60:40 by weight in the temperature range of −35 to 50 °C in particle concentration range of 0–5.9 %. The experimental data of base fluid without any particle suspension and nanofluid were compared with ASHRAE data (2005) and Batchelor's equation (1977), respectively, and it was observed to show good agreement with ASHRAE data for the former, whereas the latter shows substantial deviation from the equation. A correlation has been developed for the nanofluid given by:

$$\mu_s = Ae^{B\varnothing} \tag{17}$$

where the factors A and B are correlated as:

$$\ln(A) = 736.9 \exp(-0.0199T) \text{ with } R^2 = 0.99$$
$$B = 44.794 - 0.0765T \text{ with } R^2 = 0.99$$

The deviation between experimental data and values given by this correlation is reported to be within ±10 %. Nguyen et al. (2007) conducted experiments for the determination of viscosity of Al_2O_3 and CuO nanofluids in water at different concentrations, particle sizes, and a temperature range of 22–75 °C. Experiments with Al_2O_3 having particle sizes of 36 and 47 nm and CuO with 29 nm size revealed a strong dependence of viscosity on volume concentration of the nanofluid. The viscosity is not significantly influenced by the particle size for concentration less than 4.0 %. They presented equations for the determination of dynamic viscosity of Al_2O_3 and CuO nanofluid based on concentration for 1.0 and 4.0 %, respectively, as:

$$\mu_r = \mu_{nf}/\mu_w = (1.1250 - 0.0007T) \tag{18}$$

$$\mu_r = \mu_{nf}/\mu_w = (2.1275 - 0.0215T + 0.0002T^2) \tag{19}$$

Lee et al. (2008) conducted experiments for a maximum volume concentration of 0.3 % with 30 nm Al_2O_3 particles dispersed in deionized water in the temperature range of 21–39 °C. Duangthongsuk and Wongwises (2009) conducted experiments with TiO_2 (21 nm) nanoparticles dispersed in water in the volume concentration of 0.2–2.0 % for temperatures varying between 15 and 35 °C. They developed Eq. (12) using the experimental data of Wang et al. (1999).

Turgut et al. (2009) undertook experiments to determine the viscosity of TiO_2 (21 nm) nanoparticles in deionized water for volume concentration up to 3 % and in the temperature range of 13–55 °C. It is reported that the increase in viscosity is greater than the values predicted with Einstein model.

Namburu et al. (2007) conducted experiments to compare the viscosity of SiO_2 (20, 50, and 100 nm) nanoparticles suspended in ethylene glycol (EG) and water mixture in the ratio of 60:40 by weight in the concentration range of 0–10 % and temperature of −35 to +50 °C. It is observed that SiO_2 nanofluid dispersed with 100-nm-sized particles at 8 % concentration has the lowest viscosity. Godson et al. (2010) in their article detailed their experiments to determine the viscosity of silver (Ag) nanofluid in DI water in the range of 0.3–0.9 % volume concentration and temperature of 50–90 °C. The effect of Brownian motion and thermophoresis on the thermophysical properties is discussed. An experimental correlation for viscosity relating the volume concentration and temperature is developed. The correlation between Eqs. (20) and (21) is reported to be in good agreement with the experimental data.

$$k_{nf}/k_w = (0.9692\varnothing + 0.9508) \tag{20}$$

$$\mu_{nf}/\mu_w = (1.005 + 0.497\varnothing - 0.1149\varnothing^2) \tag{21}$$

Experiments are conducted for the determination of nanofluid viscosity prepared by dispersing Al_2O_3 nanoparticles of size <50 nm for application as a coolant in a commercial vehicle by Kole and Dey (2010). The experiments are conducted in the temperature range of 10–80 °C. Newtonian behaviour is observed for nanofluid at volume concentrations lower than 4 % and non-Newtonian behaviour at higher concentrations in the range of temperature measured. An empirical correlation has been proposed by Kole and Dey (2010) given by:

$$\log(\mu_{nf}) = A\exp(-BT) \tag{22}$$

where

$$A = -225.245\varnothing^2 + 18.404\varnothing + 1.749 \text{ and}$$
$$B = 575.835\varnothing^3 - 32.101\varnothing^2 + 0.149\varnothing + 0.011$$

Corcione (2011) proposed an empirical correlation for the nanofluid effective dynamic viscosity. It was derived from a wide selection of experimental data available in the literature consisting of Al_2O_3, TiO_2, SiO_2, and Cu nanoparticles with diameters in the range of 25–200 nm, suspended in water, ethylene glycol, propylene glycol, and ethanol. The best fit of regression analysis with 1.84 % deviation as:

$$\mu_{nf}/\mu_w = 1/\left[1 - 34.87(d_p/d_{bf})^{-0.3}\varnothing^{1.03}\right] \tag{23}$$

where $d_{bf} = 0.1\left(\frac{6M}{N\pi\rho_{bfo}}\right)^{1/3}$ is the equivalent diameter of a base fluid molecule, in which M is the molecular weight of the base fluid, N is the Avogadro's number, and ρ_{bfo} is the mass density of the base fluid calculated at 293 K. The equation is applicable for volume concentration up to 7.1 % in the temperature range of 293–333 K.

Sundar et al. (2014) undertook experimental investigation to determine the influence of EG/water-based liquid mixture ratios of 20:80, 40:60, and 60:40 % by weight, with Al_2O_3 nanoparticles, on viscosity in the temperature range of 20–60 °C. It is reported that a maximum enhancement ratio of 2.58 is obtained with nanofluid of 1.5 % concentration at a temperature of 0 °C with 60:40 % EG/water ratio as compared to base liquid.

Based on the studies undertaken by various investigators, the following observations can be deduced for nanofluids in base liquid water, EG, and EG/water mixtures.

- Newtonian behaviour is observed for volume concentration lower than 4 % in the temperature range of 20–70 °C.
- Viscosity increases with the increase in concentration of the nanofluid.
- Viscosity of the nanofluid decreases with the increase in temperature.
- Viscosity increases with the decrease in particle size which is observed by most of the investigators.
- Viscosity enhancement in base liquid EG is reported by many investigators to be higher than that with water.
- The nature of material may not have significant influence on nanofluid viscosity.

Based on the observations, an empirical equation has been presented by Sharma et al. (2010) as:

$$\mu_r = \frac{\mu_{nf}}{\mu_w} = C_1\left(1 + \frac{\varnothing}{100}\right)^{11.3}\left(1 + \frac{T_{nf}}{70}\right)^{-0.038}\left(1 + \frac{d_p}{70}\right)^{-0.061} \tag{24}$$

The value of C_1 is 1.0 for metal and metal oxide nanofluids. The value is 1.4 for SiC nanofluid. The data could be correlated with an average deviation of 3.18 %, standard deviation of 3.8 %, and a maximum deviation of 13 %.

3 Nanofluid Thermal Conductivity

Early studies devoted for the determination of effective thermal conductivity of nanofluid are based on the classical analysis of Maxwell (1881) for two-phase solid–liquid mixtures given by:

$$k_{\text{eff}} = k_{\text{bf}} \left[\frac{k_{\text{p}} + 2k_{\text{bf}} + 2\varnothing(k_{\text{p}} - k_{\text{bf}})}{k_{\text{p}} + 2k_{\text{bf}} - \varnothing(k_{\text{p}} - k_{\text{bf}})} \right] \tag{25}$$

The model makes satisfactory predictions for spherical shaped particles at low volume concentration $\varnothing$ and at ambient conditions. The limitation on the particle volume concentration proposed by Maxwell has been relaxed by Bruggemen (1935). The interactions among the randomly distributed particles is taken into consideration, and an equation has been proposed in implicit form given by:

$$\varnothing \left[\frac{k_{\text{p}} - k_{\text{eff}}}{k_{\text{p}} + 2k_{\text{eff}}} \right] + (1 - \varnothing) \left[\frac{k_{\text{p}} - k_{\text{eff}}}{k_{\text{p}} + 2k_{\text{neff}}} \right] = 0 \tag{26}$$

where k_{eff} is estimated using Eq. (25) and the net effective thermal conductivity k_{neff} of the two-phase fluid is determined.

Even though nanoparticles are many orders smaller than micron sized solid suspensions, modifications and addition of suitable terms and/or consideration of dynamic factors associated with nanofluids are made to Maxwell's model by the investigators. Various models are developed to predict the thermal conductivity of nanofluids as they exhibit higher thermal conductivity even at low concentrations of the suspended nanoparticles. Further information can be had from review articles of Das et al. (2006), Wang and Mujumdar (2007), Buongiorno et al. (2009), Kakaç and Pramuanjaroenkij (2009), Özerinç et al. (2010), Lee et al. (2010), Khanafer and Vafai (2011), Ghadimi et al. (2011), Sridhara and Satapathy (2011), Xie et al. (2011), and Kleinstreuer and Feng (2011).

3.1 Nanofluid Thermal Conductivity, k_{nf} Models

The equation of Hamilton and Crosser (1962) is widely used for comparison of the experimental data by various investigators. The equation for determining the nanofluid thermal conductivity is given by:

$$k_{nf} = k_{bf}\left[\frac{k_p + (n-1)k_{bf} - \varnothing(n-1)(k_{bf} - k_p)}{k_p + (n-1)k_{bf} + \varnothing(k_{bf} - k_p)}\right] \tag{27}$$

where the empirical shape factor 'n' is equal to $3/\psi$ and ψ the sphericity. Sphericity is defined as the ratio of the surface area of a sphere with the volume equal to that of the average particle, to the surface area of the particle. The sphericity is 1.0 and 0.5 for spherical and cylindrical shapes. The model is valid as long as the conductivity of the particle is larger by a factor of 100 compared to that of the continuous phase. The Hamilton and Crosser model reduces to Maxwell's model when $\psi = 1$ and is found to be in agreement with experimental data for $\varnothing < 30\,\%$. Equation (27) does not include the effect of particle size on thermal conductivity. The value of thermal conductivity predicted by this model is observed to be lower than the experimental values obtained from nanosized particles.

Wasp (1977) has given a correlation for determining the nanofluid k_{nf}

$$k_{nf} = k_{bf}\left[\frac{k_p + 2k_{bf} + 2(k_{bf} - k_p)\varnothing}{k_p + 2k_{bf} - (k_{bf} - k_p)\varnothing}\right] \tag{28}$$

A modification to the Maxwell model is proposed by Keblinski et al. (2002). According to Keblinski et al. (2002), it be due to (i) particle collisions occurring during Brownian motion, (ii) ordered atomic structure of liquid layer at the solid–liquid interface, (iii) propagation of heat due to lattice vibrations by phonons in random directions and (iv) rapid movement of heat in clusters formed by particles, contributing for the overall enhancement of nanofluid thermal conductivity.

Yu and Choi (2003) renovated the Maxwell model by considering the base fluid molecules close to the surface of the nanoparticles to form a solid-like nanolayered structure with thermal conductivity greater than the bulk fluid. The thermal conductivity of the solid particles and the nanolayer is combined to arrive at equivalent thermal conductivity k_{pe} of particle given by:

$$k_{pe} = k_p\left\{\frac{\gamma\left[2(1-\gamma) + (1+\beta)^3(1+2\gamma)\right]}{-(1-\gamma) + (1+\beta)^3(1+2\gamma)}\right\} \tag{29}$$

where γ is the ratio of thermal conductivity of the layer to that of particle and β is the ratio of nanolayer thickness to the particle radius. The nanofluid thermal conductivity is estimated with the relation given by:

$$k_{nf} = k_{bf}\left[\frac{k_{pe} + 2k_{bf} + 2(k_{pe} - k_{bf})(1+\beta)^3\varnothing}{k_{pe} + 2k_{bf} - (k_{pe} - k_{bf})(1+\beta)^3\varnothing}\right] \tag{30}$$

The layer thermal conductivity is varied in the range of 10–100 k_{bf}, and layer thickness is in the range of 1–2 nm. The experimental thermal conductivity ratio of CuO nanofluid in base liquid ethylene glycol (EG) is observed to be in good

agreement with the values estimated with Eq. (30) in the concentration range of $0 < \varnothing < 5\,\%$ for a particle diameter of 30 nm. A maximum enhancement of 20 % is shown along with the experimental data of CuO nanofluid. Thermal conductivity enhancement of up to 90 % is predicted by Yu and Choi (2003) for 6-nm Cu nanoparticles dispersed in EG for an assumed layer thickness of 2 nm.

Xue (2003) developed a model based on Maxwell employing average polarization theory. The particle with its liquid interface termed 'complex nanoparticle' is considered to be dispersed in a base liquid. The predicted values of thermal conductivity ratio for Al_2O_3/water are shown to vary linearly for 'interfacial shell thickness' in the range of 3–5 nm for nanofluid concentration of $0 < \varnothing < 5\,\%$.

$$9\left(1-\frac{\varnothing}{\omega}\right)\frac{k_{\text{eff}}-k_{\text{bf}}}{2k_{\text{eff}}+k_{\text{bf}}}+\frac{\varnothing}{\omega}\left[\frac{k_{\text{eff}}-k_{c,x}}{k_{\text{eff}}+B_{2,x}\left(k_{c,x}-k_{\text{eff}}\right)}+4\frac{k_{\text{eff}}-k_{c,y}}{2k_{\text{nf}}+\left(1-B_{2,x}\right)\left(k_{c,y}-k_{\text{eff}}\right)}\right]=0 \tag{31}$$

In another paper, Yu and Choi (2004) modelled the thermal conductivity enhancement as due to liquid layering around a nanoparticle considering Hamilton–Crosser model. It is observed that the thermal conductivity of the interfacial layer k_{i} should be at least 100 times the value of k_{p} or k_{bf} in order to obtain an increase in the effective thermal conductivity for non-spherical particles. The authors compared the experimental values of CNT in oil to substantiate their observations. For spherical particles, the predicted value of k_{nf} is observed to increase with thickness or thermal conductivity of the interfacial layer.

Xie et al. (2005) solved the heat conduction equation in spherical coordinates with the consideration of interfacial liquid layer on nanoparticle. They related the nanofluid thermal conductivity to system parameters, viz. k_{p}, k_{pe}, k_{i}—volume fraction, size of nanoparticle, and thickness of the nanolayer. They compared the experimental data of Al_2O_3/water, CuO/EG, and Cu/EG nanofluid for concentrations up to 5.0 % with the results from their model. They assumed the nanolayer thermal conductivity to be 5 times that of the base liquid and reported good agreement with experimental data for 2 nm layer thickness.

A theoretical model having shells on the surface of the solid nanoparticles is proposed by Xue and Xu (2005). Based on the model, an implicit relation for the determination of nanofluid thermal conductivity is developed as:

$$\left(1-\frac{\varnothing}{\omega}\right)\left[\frac{k_{\text{nf}}-k_{\text{bf}}}{2k_{\text{nf}}+k_{\text{bf}}}+\frac{\varnothing}{\omega}\frac{\left(k_{\text{nf}}-k_{\text{i}}\right)\left(2k_{\text{i}}+k_{\text{p}}\right)-\omega\left(k_{\text{p}}-k_{\text{i}}\right)\left(2k_{\text{i}}+k_{\text{nf}}\right)}{\left(2k_{\text{nf}}-k_{\text{i}}\right)\left(2k_{\text{i}}+k_{\text{p}}\right)+2\omega\left(k_{\text{p}}-k_{\text{i}}\right)\left(2k_{\text{i}}-k_{\text{nf}}\right)}\right]=0 \tag{32}$$

where $\omega = \left[\frac{d_{\text{p}}}{\left(d_{\text{p}}+2t\right)}\right]^3$ and k_{i} is the thermal conductivity of the interfacial shell and 't' represents the thickness of the shell which is different for different nanofluids.

The thickness of the shell is considered as 3 nm to obtain a value of $k_i = 5.0\ \mathrm{W/mK}$.

The enhancement in nanofluid thermal conductivity is due to Brownian motion according to Jang and Choi (2004). They showed a good agreement of the experimental data of Al_2O_3/water, CuO/water, CuO/EG, and Cu/EG nanofluids with the results from their model.

A semiempirical correlation considering Brownian motion proposed by Chon et al. (2005) is given by Eq. (33). The authors showed a good agreement of the experimental data of Al_2O_3 nanofluid for different parameters with values estimated by using Eq. (33).

$$\frac{k_{nf}}{k_{bf}} = 1 + 64.7\varnothing^{0.7460}\left(\frac{d_{bf}}{d_p}\right)^{0.3690}\left(\frac{k_p}{k_{bf}}\right)^{0.7476} Pr_{bf}^{0.9955} Re^{1.2321} \tag{33}$$

where d_{bf} is the molecular diameter of the base fluid, $\mathrm{Re} = \frac{\rho_{bf} K_B T}{3\pi\mu_{bf}^2 l_{bf}}$ where $l_{bf} = 0.17\,\mathrm{nm}$ the mean free path for water and Boltzmann constant $k_B = 1.3807e^{-23}\ \mathrm{J/K}$ used in their analysis.

Koo and Kleinstreuer (2004) proposed an equation for the determination of effective thermal conductivity of nanofluid which is modelled for combined influence of Maxwell and Brownian motion. It takes into account the effect of particle size, volume concentration, temperature, and properties of base fluid as well as nanoparticle subject to Brownian motion given by:

$$k_{nf} = k_{bf}\left[\frac{k_p + 2k_{bf} - 2(k_{bf} - k_p)\varnothing}{k_p + 2k_{bf} - (k_{bf} - k_p)\varnothing}\right] + 5 \times 10^4 \beta_1 \rho_{bf} c_{bf} f(T, \varnothing)\sqrt{\frac{K_B T}{\rho_{bf} d_p}} \tag{34}$$

where β_1 is the fraction of the liquid volume which travels with a particle and decreases with particle volumetric concentration because of the viscous effect of the moving particles. The values of β_1 for certain particles are given in Table 1. They introduced an empirical equation for $f(T, \varnothing)$ using the experimental data of Das et al. (2003) for CuO nanofluids valid in the range of $1 < \varnothing < 4\ \%$ and $300 < T < 325$ K given by:

$$f(T, \varnothing) = (-6.04\varnothing + 0.4705)T + (1722.3\varnothing - 134.63)$$

In another paper, Koo and Kleinstreuer (2005) studied the influence of different motion mechanisms such as Brownian, thermophoresis, and osmophoresis on thermal conductivity of nanofluids. They reported the influence of Brownian motion to be significant on thermal conductivity ratio compared to thermophoresis and osmophoresis. The Brownian motion is influenced by particle size, whereas motion due to thermophoretic and osmophoretic effects is observed to be independent of particle size.

Table 1 Value of β_1 to be used with Eq. (34) of Koo and Kleinstreuer (2005)

Sl. No.	Type of particles	β_1	% Concentration/temperature range	Authors
1	Au citrate, Ag citrate, and CuO	$0.0137(100\varnothing)^{-0.8229}$	$\varnothing < 1$	Koo and Kleinstreuer (2005)
2	CuO	$0.0011(100\varnothing)^{-0.7272}$	$\varnothing > 1$	Koo and Kleinstreuer (2005)
3	Al_2O_3	$0.0017(100\varnothing)^{-0.0841}$	$\varnothing > 1$	Koo and Kleinstreuer (2005)
4	Al_2O_3	$8.4407(100\varnothing)^{-1.07304}$	$1 < \varnothing < 10\,\%,\ 298 < T_{nf} < 363$ K	Vajjha and Das (2009)
5	ZnO	$8.4407(100\varnothing)^{-1.07304}$	$1 < \varnothing < 7\%$, $298 < T_{nf} < 363$ K	Vajjha and Das (2009)
6	CuO	$9.8810(100\varnothing)^{-0.9446}$	$1 < \varnothing < 6\%$, $298 < T_{nf} < 363$ K	Vajjha and Das (2009)

The combined Maxwell–Garnett conduction and convection caused by the Brownian motion of the suspended particles are the basis for thermal conductivity enhancement, according to Prasher et al. (2006). They proposed an equation for the estimation of thermal conductivity ratio based on the model given by:

$$\frac{k_{nf}}{k_{bf}} = \left(1 + 4 \times 10^4 Re_B^m Pr_{bf}^{0.33} \varnothing\right) \left[\frac{\{k_p(1+2\alpha) + 2k_m\} + 2\varnothing\{k_p(1-\alpha) - k_m\}}{\{k_p(1+2\alpha) + 2k_m\} - \varnothing\{k_p(1-\alpha) - k_m\}}\right] \tag{35}$$

where $m = 2.5$

$k_m = k_{bf}(1 + 0.25 \mathrm{Re_B}\ \mathrm{Pr})$ is the matrix conductivity

$Re_B = \frac{1}{\vartheta}\sqrt{\frac{18K_B T}{\pi \rho_p d_p}}$ is the Brownian–Reynolds number

$\alpha = \left(\frac{2R_b k_m}{d_p}\right)$ nanoparticle Biot number

R_b interfacial thermal resistance between nanoparticle and the surrounding fluid.

The authors ignored the interfacial resistance in their analysis and stated that it could be considered in the calculations using the model of Every et al. (1992). Leong et al. (2006) developed a model to determine the effective thermal conductivity of nanofluids taking into account the effect of interfacial layer at the particle/liquid interface.

$$k_{\mathrm{nf}} = k_{\mathrm{bf}} \frac{\left(K_{\mathrm{p}} - k_{\mathrm{i}}\right)\varnothing k_{\mathrm{i}}\left[2\beta_{2\_}^{3}\beta^{3} + 1\right] + \left(K_{\mathrm{p}} + 2k_{\mathrm{i}}\right)\beta_{2}^{3}\left[\varnothing\beta^{3}\left(k_{\mathrm{i}} - K_{\mathrm{bf}}\right) + K_{\mathrm{i}}\right]}{\beta_{2}^{3}\left(K_{\mathrm{p}} + k_{\mathrm{i}}\right) - \left(K_{\mathrm{p}} - k_{\mathrm{i}}\right)\varnothing\left[\beta_{2}^{3} - \beta^{2} - 1\right]} \quad (36)$$

where

$$\beta_2 = \left(1 + \frac{t}{a_{\mathrm{p}}}\right)$$

According to Jang and Choi (2007), there are four mechanisms contributing to the energy transfer responsible for the enhancement of thermal conductivity of nanofluids. The first mode is collision between the base fluid molecules, the second is the thermal diffusion of nanoparticles, the third is the collision of nanoparticles with each other due to Brownian motion, and the fourth is collision between the base fluid molecules and nanoparticles due to thermally induced fluctuations. They developed an equation for the evaluation of the effective thermal conductivity of nanofluid given by:

$$k_{\mathrm{nf}} = k_{\mathrm{bf}}(1 + \varnothing) + \beta_3 k_{\mathrm{p}}\varnothing + C_1 \frac{d_{\mathrm{bf}}}{d_{\mathrm{p}}} k_{\mathrm{bf}} Re_{\mathrm{d}}^{2} Pr_{\mathrm{bf}}\varnothing \quad (37)$$

where $\beta_3 = 0.01$, $C_1 = 18 \times 10^6$, $Re_{\mathrm{d}} = \frac{C_{\mathrm{RM}} d_{\mathrm{p}}}{\vartheta}$, $C_{\mathrm{RM}} = \frac{K_{\mathrm{B}} T}{3\pi\mu_{\mathrm{bf}} d_{\mathrm{p}} l_{\mathrm{bf}}}$ and is a constant considering the Kapitza resistance per unit area. The equivalent diameter $d_{\mathrm{bf}} = 0.384,\ 0.561$ and mean free path, $l_{\mathrm{bf}} = 738,\ 0.875$ nm, at 300 K are the values considered for water and EG-based nanofluids, respectively. The experimental data of Al_2O_3 and CuO in water and EG, Cu/EG are observed to be in good agreement with the values estimated with Eq. (37).

Murshed et al. (2008) solved the steady-state heat conduction equation considering interfacial layer with appropriate boundary conditions for cylindrical and spherical coordinate system. The numerical values are compared with the experimental data for spherical particles of Al_2O_3 (80 nm), TiO_2 (15 nm) in ethylene glycol, Al_2O_3 (38.4, 47, and 150 nm) in water, and CNT in engine oil. In another paper, Murshed et al. (2009) included the dynamic Brownian motion to the static conduction model in deriving an equation for effective thermal conductivity of nanofluid, which has the flexibility to be reduced to Maxwell's equation in the absence of interaction between the nanoparticle and interfacial layer. The authors showed good agreement of theory with the experimental data of various investigators.

Khanafer and Vafai (2011) have given a few general correlations for the effective thermal conductivity of Al_2O_3/water and CuO/water nanofluids at ambient temperatures accounting for various volume fractions and nanoparticle diameters. Equation (38) proposed using the experimental data of Al_2O_3/water and CuO/water nanofluids, respectively, is given by:

$$k_{\mathrm{nf}} = \left[1.0 + 1.0112\varnothing + 2.4375\varnothing\left(\frac{47}{d_{\mathrm{p}}}\right) - 0.0248\varnothing_{\mathrm{p}}\left(\frac{k_{\mathrm{p}}}{0.613}\right)\right]k_{\mathrm{bf}} \tag{38}$$

Equation (38) is applicable for ambient range of temperature.

$$k_{\mathrm{nf}} = \left[0.9843 + 0.398\varnothing^{0.7383}\left(\frac{1}{d_{\mathrm{p}}}\right)^{0.2246}\left(\frac{\mu_{\mathrm{nf}}(T)}{\mu_{\mathrm{f}}(T)}\right)^{0.0235} - 3.9517\frac{\varnothing}{T} + 34.0.341\frac{\varnothing}{T^2}\right]k_{\mathrm{bf}} \tag{39}$$

where $\mu_{\mathrm{f}}(T) = 2.414 \times 10^{-5} \times 10^{-247.8(T-140)}$ and valid for $11 \leq d_{\mathrm{p}} \leq 150$ nm; $20\ ^{\circ}\mathrm{C} \leq T \leq 70\ ^{\circ}\mathrm{C}$.

Thus, the theoretical models developed till now are improvement of Maxwell's equation with the consideration of (i) shells/interface on the surface of the particle (ii) Brownian motion (iii) interaction between base liquid molecules or nanoparticles and (iv) base liquid molecules and nanoparticles. Certain models include parameters such as mean free path of water used in the process of obtaining dimensionless terms.

3.2 *Experimental Thermal Conductivity,* $\mathbf{k}_{nf}$

It can be observed that most of the investigators who improved Maxwell's models used certain empiricism in their equations. Early determination of nanofluid thermal conductivity through experiments was undertaken using base liquid as water.

Pak and Cho (1998) determined the thermal conductivity of Al_2O_3 and TiO_2 nanofluids at 27 °C which can be presented as:

$$k_{\mathrm{nf}} = (1 + 7.47\varnothing)k_{\mathrm{bf}} \tag{40}$$

The determination of nanofluid thermal conductivity based on experiments has grown rapidly since the work of Lee et al. (1999) who conducted experiments with Al_2O_3 and CuO nanoparticles of sizes 38 and 24 nm, respectively, in water and EG using transient hot-wire method. The experimental data with Al_2O_3/water and Al_2O_3/EG are observed to be in close agreement, whereas CuO/water and CuO/EG nanofluids showed higher values when compared with Hamilton–Crosser model. They reasoned that the obtained lower values of thermal conductivity with Al_2O_3/water were due to larger particle size of 38 nm used when compared with the values of Masuda et al. (1993) who used 13-nm-sized particles. They opined that the equation of Hamilton–Crosser is capable of predicting thermal conductivity of large agglomerated clusters but inadequate for nanosized particles. Xuan and Li (2000) reported the thermal conductivity ratio of Cu/water to increase between 1.24 and

1.78 for corresponding volume concentration of 2.5–7.5 %. The particle size is reported to be lower than 100 nm; the average size was not disclosed.

Yu et al. (2000) reported the observation of molecular layering at the solid–liquid interface from X-ray reflectivity data. Spherical Tetrakis (2-ethylhexoxy) silane (TEHOS) liquid molecules of size 10 Å diameter are used in the experiment. Silicon substrates of 45–90 Å thick are prepared, and reflectively measurements were undertaken. They reported the measurement of oscillations near the solid–liquid interface with a period of about 10 Å, common to all samples and independent of the film thickness.

Xie et al. (2002) obtained a maximum enhancement of 15.8 % in thermal conductivity with 26-nm spherical SiC/water nanoparticles at a volume concentration of 4.2 %. The thermal conductivity is reported to increase linearly with concentration in the lower range.

Das et al. (2003) determined the thermal conductivity of 29 nm CuO/water and 38 nm Al_2O_3/water. They reasoned the deviation of 24 nm CuO/EG and CuO/water experimental data of Lee et al. (1999) to the 'insensitive' nature of Hamilton and Crosser Eq. (27) for temperature.

Murshed et al. (2005) reported 30 % enhancement in thermal conductivity of water-based TiO_2 nanofluid with particle size of 15 nm at 5 % vol concentration. Zhu et al. (2006) measured the thermal conductivity of Fe_3O_4 nanofluid in base liquid water. They observed a nonlinear variation of thermal conductivity ratio with volume fraction from their experimental data and reported relatively higher enhancement rate at lower volume fractions.

Li and Peterson (2006) undertook experimental investigations to determine the influence of thermal conductivity on volume concentration and temperature. The experiments are conducted with sizes of 29 nm of CuO/water and 36 nm of Al_2O_3/water, temperatures ranging from 27.5 to 34.7 °C for 2–10 % volume fractions. A linear regression equation for the estimation of thermal conductivity ratio based on temperature and volume fraction is presented for Al_2O_3 and CuO nanofluids, respectively, as:

$$k_{nf}/k_w = (0.69266 + 3.761088\varnothing + 0.4705T) \tag{41}$$

$$k_{nf}/k_w = (0.53785 + 0.7644815\varnothing + 0.018689) \tag{42}$$

The values of thermal conductivity obtained by Li and Peterson (2006) reported monotonic decrease in thermal conductivity with increasing particle size. The results indicate the dependence of effective thermal conductivity on material suspensions, particle size, concentration/volume fraction, and the bulk temperature.

Yoo et al. (2007) measured the thermal conductivities of TiO_2 (25 nm) and Al_2O_3 (48 nm) dispersed in deionized water and Fe (10 nm) and tungsten trioxide WO_3 (38 nm) dispersed in EG and reported high enhancements with Fe and WO_3 nanofluids. Hwang et al. (2007) determined the thermal conductivity of MWCNT, fullerene, CuO, and SiO_2 in deionized water, EG, and oil. The thermal conductivity

of nanofluid increased with concentration except for water-based fullerene ($k_p = 0.4$ W/mK) which is lower than water.

Experiments have been conducted by Mintsa et al. (2009) to estimate the thermal conductivity of aluminium oxide (36 and 47 nm) and copper oxide (29 nm) nanofluids in water in the temperature range of 20–50 °C and up to 18 % volume concentration. Linear equations with volume concentration applicable at ambient temperature for these nanofluids are given, respectively, as:

$$k_{nf}/k_w = 1.0 + 1.72\phi \tag{43}$$

$$k_{nf}/k_w = 0.99 + 1.74\phi \tag{44}$$

It can be observed that the values of the oxide nanofluids estimated with Eqs. (43) and (44) at different volume concentrations do not vary significantly for the two materials. The thermal conductivity data obtained at higher temperatures and volume concentration are observed to be in good agreement with the Eq. (33) of Chon et al. (2005).

Garg et al. (2008) have investigated the thermal conductivity of Cu (200 nm) nanoparticles in ethylene glycol in the concentration range of 0.5–2.5 %. Based on their experimental thermal conductivity data, a linear equation is presented as:

$$k_{nf} = (1 + 6\varnothing)k_{bf} \tag{45}$$

Mintsa et al. (2009) observed that Eq. (33) given by Chon et al. (2005) is in good agreement with the experimental data of both Al_2O_3/water and CuO/water nanofluids. Sundar et al. (2013) determined the effective thermal conductivity of magnetic Fe_3O_4/water nanofluid experimentally in the volume concentration range of 0–2.0 % in the temperature range of 20–60 °C. Thermal conductivity enhancement at the temperatures of 20 and 60 °C is reported to be, respectively, 8.4 and 17 % at $\varnothing = 0.2\,\%$ and 25 and 48 % at $\varnothing = 2.0\,\%$ concentration.

3.3 k_{nf} *in Base Liquid Ethylene Glycol*

Lee et al. (1999) investigated oxide nanofluids by suspending CuO 35-nm particles in ethylene glycol. A 20 % increase in thermal conductivity at 4 % volume is reported by them. Eastman et al. (2001) determined the thermal conductivity of Cu/EG nanofluid. They observed a maximum enhancement of 40 % in thermal conductivity at 0.3 % volume concentration with 10-nm-sized particles dispersed in ethylene glycol. The enhancement with CuO/EG and Al_2O_3/EG of 35-nm-sized particles at a volume concentration of 4 % is approximately 20 %.

Wang et al. (2002) determined the thermal conductivity of Al_2O_3, ZnO, TiO_2, CuO, Fe_2O_3, Cerium oxide (CeO_2) nanoparticles in base liquid ethylene glycol for 0.5, 1.5, 3.0 and 4.0 % concentration at an ambient temperature of 25 °C. The

maximum thermal conductivity enhancement was observed at 4 % volume concentration varied between 13 and 21 % for the nanofluids considered.

Xie et al. (2010) undertook thermal conductivity determination with MgO, TiO_2, ZnO, Al_2O_3, and SiO_2 nanoparticles dispersed in base liquid EG. They observed MgO/EG nanofluid to have superior features of the highest thermal conductivity and the lowest viscosity when compared with other nanofluids. The enhancement of 40.6 % is reported with MgO nanofluid at 30 °C for a volume concentration of 5 %.

Murshed (2011) determined the thermal conductivity of nanofluids which are prepared by suspending TiO_2 (15 nm), Al_2O_3 (80 nm), and Al (80 nm) nanoparticles in ethylene glycol for a maximum concentration of 5 %. The TiO_2 nanofluid at 5 % concentration, a maximum enhancement of thermal conductivity is reported to be 17 %. However, the enhancement in thermal conductivity at the same concentration of 5 % with Al and Al_2O_3 is observed to be 45 and 14 %, respectively.

3.4 k_{nf} in Ethylene Glycol Water Mixtures

Sun and Teja (2004) determined the thermal conductivity, viscosity, and density for different ratios of EG/water mixture and presented linear equations for their estimation. Kim et al. (2007) estimated the thermal conductivity of Al_2O_3, ZnO, and TiO_2 nanofluids in water and ethylene glycol. They reported linear increase in thermal conductivity with nanofluid concentration. The enhancement is observed to increase with the decrease in particle size for the two base fluids undertaken.

Karthikeyan et al. (2008) determined the thermal conductivity of CuO (8 mm) nanofluid in base liquid water and ethylene glycol for 1.0 % volume concentration. They observed enhancements of 31 and 54 % with CuO/water and CuO/EG, respectively, and the temperature of the nanofluid was not specified. Patel et al. (2010) observed enhancement of 11.5 and 14 % with CuO/water and CuO/EG at 50 °C with a particle size of 31 nm. The significant enhancement in thermal conductivity is attributed to the finer particle size and monodispersion of nanoparticles in the base liquid. It has been observed that the thermal conductivity of nanofluid increases nonlinearly with the volume fraction of nanoparticles.

Vajjha and Das (2009) measured the thermal conductivities of Al_2O_3, CuO, and ZnO nanofluids with particles dispersed in EG/water mixture in the ratio of 60:40 by mass. They conducted experiments in the temperature range of 25–90 °C for volume concentration up to 10 % and observed the data to fit in Eq. (34) of Koo and Kleinstreuer (2005) resulting in obtaining new relations for $f(T, \phi)$ and β_1 given by:

$$f(T,\phi) = \left(2.8217 \times 10^{-2}\phi + 3.917 \times 10^{-3}\right)\left(\frac{T}{T_o}\right) + \left(-3.0669 \times 10^{-2}\phi - 3.91123 \times 10^{-3}\right) \quad (46)$$

The relations for β_1 are listed in Table 1 for different nanofluids.

Beck et al. (2010) determined the thermal conductivity of Al_2O_3 nanofluids in water, EG, and 50:50 ratio of EG/water mixture. They undertook experiments with Al_2O_3 of 10 and 50 nm particle sizes in EG/water mixture and 12 nm in both water and EG base liquids to determine the thermal conductivity at different temperatures and concentrations up to a maximum of 4.93 % by volume. They attributed a decrease in nanofluid thermal conductivity due to changes in phonon transport as the particle size increases from 10 to 50 nm.

Yu et al. (2012) investigated the heat transfer properties of Al_2O_3 experimentally using a mixture of ethylene glycol and water in the ratio of 45:55 by volume and observed thermal conductivity enhancement of 3.8 and 11.8 % for volume concentrations of 1 and 3 %, respectively. They observed Al_2O_3 nanofluid to exhibit Newtonian and non-Newtonian behaviour for temperatures greater than 45 °C and below 45 °C, respectively, at 2.0 % volume concentration.

Sahoo et al. (2012) conducted experimental investigations for the determination of thermal conductivity of SiO_2 (20 nm) nanoparticles dispersed in 60:40 EG/water by mass, in the temperature range of 20–90 °C for a maximum concentration of 10 vol%. An enhancement of 20 % in thermal conductivity was reported at $\varnothing =$ 10 % and 87 °C. An equation for the estimation of thermal conductivity at 6 % concentration of nanofluid valid in the temperature range of 290–365 K is given by:

$$k_{\mathrm{nf}} = \left[-0.45577\left(\frac{T}{T_o}\right)^2 + 1.72837\left(\frac{T}{T_o}\right) - 0.18589\right]k_{\mathrm{bf}}; \quad T_o = 293\,\mathrm{K} \tag{47}$$

Branson et al. (2013) prepared nanofluid by deaggregation of diamond oxide in dimethyl sulphoxide followed by reaction with glycidol monomer, purification via aqueous dialysis, and dispersion in EG base fluid. It is observed that diamond (11 nm) nanofluid exhibited 12 % enhancement in thermal conductivity at 0.9 % vol concentration. In a similar manner when diamond oxide is deaggregated in the presence of oleic acid followed by dispersion in a light mineral oil, the oil-based dispersions of nanodiamond (ND) exhibited 11 % enhancement in thermal conductivity with a particle size of 18 nm at 1.9 % vol concentration. From the experimental values, equations for the estimation of thermal conductivity are presented which are given by:

$$k_{\mathrm{nf}} = (1 + 14\varnothing)k_{\mathrm{bf}};\ \mathrm{ND} - \mathrm{EG} \tag{48}$$

$$k_{\mathrm{nf}} = (1 + 6\varnothing)k_{\mathrm{bf}};\ \mathrm{ND} - \mathrm{MO} \tag{49}$$

Sundar et al. (2014) prepared nanofluids by dispersing Al_2O_3 particles in EG–water mixture ratio of 20:80, 40:60, and 60:40 by weight. The thermal conductivity and viscosity are determined between 20 and 60 °C in the volume concentration range of 0.3–1.5 %. A maximum thermal conductivity enhancement of 32.26 %

was reported with 20:80 % EG/water nanofluid at 1.5 % volume concentration at a temperature of 60 °C.

3.5 Effect of PH on Nanofluid Thermal Conductivity

Murshed et al. (2005) conducted experiments with TiO_2 (15 nm) nanofluid with cetyltrimethylammonium bromide (CTAB) surfactant to ensure uniform dispersion of spherical particles in base liquid water. The pH of the nanofluid is maintained between 6.8 and 6.2 for particle volume concentrations between 0.1 and 2.0 %. The enhancement is 17 % greater than the values predicted by Hamilton–Crosser and Bruggeman models at 5 % nanofluid concentration, while the temperature of the nanofluid is not disclosed.

Yurong He et al. (2007) maintained a pH value of 11 in the absence of stabilizer by dispersing TiO_2 (20 nm) nanoparticles in water. The values of thermal conductivity from their experiments are reported to be lower than those obtained by Murshed et al. (2005). The difference in the thermal conductivity value is attributed to a large difference in pH value employed in addition to larger particle size used by Yurong He et al. (2007). This is in conformity with the observations of Xie et al. (2002) who observed thermal conductivity to increase with the decrease in pH (from basic to acidic range).

Li et al. (2008) optimized the use of sodium dodecylbenzene sulphonate (SDBS) surfactant for Cu/water (25 nm) suspensions to maintain pH in the range of 8.5–9.5 for enhanced thermal conductivity. The maximum thermal conductivity enhancement of 10.7 % is observed with 0.10 wt% suspension. Wang et al. (2009) conducted experiments to determine the thermal conductivity of Al_2O_3/water and Cu/water-based nanofluids for 0.02, 0.05, 0.1, and 0.15 % weight concentrations at different pH values by adding different quantities of SDBS. They observed a maximum thermal conductivity enhancement of 7, 8, 8.5, and 10 % for Al_2O_3/water and 8, 9, 11, and 12 % for Cu/water when the pH is maintained at 7.5 and 9.0 for Al_2O_3/water and Cu/water, respectively.

3.6 Effect of Particle Size on k_{nf}

Xie et al. (2001) prepared non-oxide ceramic (SiC) nanofluid with particle size varying between 26 and 600 nm. Xie et al. (2002) produced Al_2O_3 nanofluid with particle size ranging from 1.2 to 302 nm to determine the influence of particle size on thermal conductivity.

Kim et al. (2007) measured thermal conductivity of alumina, ZnO (10, 30, and 60 nm), and TiO_2 (10, 35, and 70 nm) particle suspensions in water and ethylene glycol up to 3.0 % volume concentration. They determined a maximum thermal conductivity enhancement with ZnO/water nanofluid of 14.2, 11.5, and 7.3 % with

10-, 30-, and 60-nm-sized particles, respectively, at 3 % concentration. At the same concentration, the value of maximum thermal conductivity enhancement for ZnO/EG is reported to be 21 and 10.7 % with 30- and 60-nm-sized particles, respectively. The maximum enhancement values for TiO_2 (10, 35, and 70 nm)/water are 11.4, 8.7, and 6.4 %, and for TiO_2 (10, 35, and 70 nm)/EG, the values are 15.4, 12.3, and 7.5 %, respectively.

Chon et al. (2005) observed 4.8–15.8 % enhancement in nanofluid thermal conductivity k_{nf} when the size of Al_2O_3 nanoparticles in water decreased from 150 to 11 nm. Similar observations have been reported by other researchers like Mintsa et al. (2009), He et al. (2007) including the recent study of Kazemi-Beydokhti et al. (2014) who has determined thermal conductivity with Al (25 nm), Al_2O_3 (30 nm), CuO (18 nm), SnO_2 (20 nm), SiO_2 (12 nm) and TiO_2 (35 nm) water-based nanofluids in the temperature range of 20–60 °C.

An increase in thermal conductivity of magnetite (Fe_3O_4) nanoparticles with particle size of less than 10 nm has been observed by Shima et al. (2009). The Fe_3O_4 nanoparticles have been prepared in the range of 2.8–9.5 nm by precipitating iron salts with sodium hydroxide using an established procedure and stabilized with a protective surfactant layer. Nanofluid thermal conductivity at 1.0 and 5.5 % volume concentrations, at 25 °C, in an oil-based carrier fluid has been estimated. They observed an increase in nanofluid thermal conductivity with particle size and attributed the thermal conductivity enhancement to the agglomeration of nanoparticles. The observation of Shima et al. (2009) for particle size lower than 10 nm is contrary to the observed phenomenon with particle size larger than 10 nm by Jang and Choi (2004) and Feng et al. (2008).

Beck et al. (2010) conducted experiments with Al_2O_3 nanoparticles in water and ethylene glycol at five different sizes in the range of 8–282 nm. They concluded from their experimental analysis that the rate of thermal conductivity enhancement is significant for particle size below 50 nm with no significant change thereafter.

Teng et al. (2010) studied the effect of particle size, temperature, and concentration on the thermal conductivity ratio of Al_2O_3 (20, 50, and 100 nm) nanofluid dispersed in water in the concentration range of 0.5–2.0 % and temperature range of 10–50 °C. The enhancement in thermal conductivity is reported to be 6.5, 6.0, and 5.6 % measured at 10 °C and 14.7, 7.3, and 5.6 % at 50 °C for the particle sizes of 20, 50, and 100 nm, respectively. They observed a decrease in thermal conductivity of Al_2O_3 with the increase in particle size measured at temperatures of 10 and 50 °C.

Patel et al. (2010) have presented thermal conductivity experimental data for oxide and metal nanofluids for different particle–base fluid combinations, particle size, volume fraction and temperature using transient hot wire and temperature oscillation equipment. The experiments are undertaken with Cu (80 nm), CuO (31 nm), and Al_2O_3 (11, 45, and 150 nm) nanofluids in the concentration range of $0 < \varnothing < 3\,\%$ and temperature between 20 and 50 °C. The maximum enhancement in thermal conductivity was observed to be 38 and 26 % with Cu and CuO nanofluids, respectively, in transformer oil at 9.27 and 9.11 % volume concentration at 50 °C, respectively. The maximum enhancement reported is 32 and 18 % with Al_2O_3 (11 nm) suspended in EG and water, respectively, at 50 °C with 3 %

volume concentration. A nonlinear regression analysis is undertaken for the thermal conductivity estimation of spherical shaped oxide and metal nanofluids given by:

$$k_{\mathrm{nf}} = \left[1.0 + 0.135\left(\frac{k_{\mathrm{b}}}{k_{\mathrm{p}}}\right)^{0.273} \varnothing^{0.467}\left(\frac{T}{20}\right)^{0.547}\left(\frac{100}{d_{\mathrm{p}}}\right)^{0.234}\right] k_{\mathrm{bf}} \tag{50}$$

An empirical correlation is proposed by Corcione (2011) for the determination of nanofluid thermal conductivity. The experimental data of alumina, copper oxide, titania, and copper nanoparticles determined by various investigators with particle diameters in the range of 10–150 nm and suspended in water and EG are used in their analysis. An Eq. (51) with a mean deviation of 1.86 % is presented.

$$\frac{k_{\mathrm{nf}}}{k_{\mathrm{bf}}} = 1 + 4.4Re^{0.4}Pr_{\mathrm{bf}}^{0.66}\left[\frac{T}{T_{\mathrm{fr}}}\right]^{10}\left[\frac{k_{\mathrm{p}}}{k_{\mathrm{bf}}}\right]^{0.03}\varnothing^{0.66} \tag{51}$$

where $Re = \frac{2\rho_{\mathrm{bf}}k_{\mathrm{bf}}T}{\pi\mu_{\mathrm{bf}}^2 d_{\mathrm{p}}}$ is the nanoparticle Reynolds number, Pr_{bf} is the Prandtl number of the base liquid, T is the nanofluid temperature, T_{fr} is the freezing point of the base liquid, and k_{p} is the nanoparticle thermal conductivity. The equation is applicable for volume concentrations up to 9 % in the temperature range of 294–324 K.

The investigators observed the thermal conductivity ratio to depend on the material, particle size, volume concentration, and nanofluid temperature in their study. It can be concluded that nanofluid thermal conductivity increases with a decrease in particle size. A few other studies suggest the dependence of particle size on thermophysical properties which can influence the thermal conductivity of nanofluids.

3.7 *Effect of Size on Particle Specific Heat*

The influence of particle size on thermal conductivity is supported with the theoretical and experimental observations by Wang et al. (2006) who studied the effect of particle size on specific heat capacity. The values of bulk specific heat obtained with CuO nanoparticles from experiments are found to be in close agreement with the theoretical predictions for temperatures lower than 225 K for particles up to 50 nm. However, for temperatures above 225 K, the theoretical values of specific heat capacity decrease as the particle size is reduced from 50 to 10 nm. For particles below 10 nm, the specific heat capacity increases with particle size.

Wang et al. (2006) reasoned that for particles larger than 10 nm, the quantum effect can be neglected and the specific heat will decrease monotonically as the particle size is reduced from 50 to 10 nm. For particles that are smaller than 10 nm, the quantum effect will increase the specific heat capacity of the nanoparticles

uniformly and thus create an irregular behaviour for particles of different sizes. This observation is also stated to be in conformity with the monotonic decreasing relation proposed by Prasher et al. (2006).

The experimental observations indicate the dependence of material, concentration, particle size, temperature, and the influence of pH value on nanofluid thermal conductivity. The following observations can be made from the investigations undertaken:

- The thermal conductivity of metal and oxide nanofluids is observed to be greater than that of equivalent macroparticle suspensions.
- Experiments for the determination of nanofluid thermal conductivity are undertaken mostly with spherical particles having diameters in the range of 20–300 nm and temperature between 20 and 70 °C having Newtonian properties for a maximum volume concentration of 4.0 % in base liquid water, EG, and EG/water mixtures.
- Experimental data have confirmed higher thermal conductivities than the base liquid which increases with concentration and temperature.
- The conductivity ratios of ethylene glycol-based nanofluids are reported to be higher than those of water-based nanofluids.
- Metal nanofluids have higher enhancements than those of oxide nanofluids.
- Nanofluid thermal conductivity is relatively higher at lower volume fractions, thereby giving a nonlinear dependence on particle volume fraction.
- The experimental results indicate the thermal conductivity ratio to increase linearly with volume fraction, but with different rates of increase for each nanofluid.
- Nanofluid thermal conductivity is observed to depend on particle size and suspension temperature.
- Material properties influence the thermal conductivity of nanofluids leading to higher enhancements compared to viscosity. This observation may vary with temperature, nanofluid concentration, and particle size.

It can be observed from Eqs. (25)–(50) that particle thermal conductivity k_p is considered in the development of equations for the estimation of nanofluid thermal conductivity k_{nf}. The equations developed do not consider the impact of material density and specific heat on nanofluid thermal conductivity. Since the properties are different, their influence on nanofluid thermal conductivity k_{nf} can be included with thermal diffusivity term α_p. Hence, the experimental data of water-based nanofluids are used in the development of a regression equation by Sharma et al. (2010) as:

$$k_r = \frac{k_{nf}}{k_w} = \left[0.8938\left(1+\frac{\phi}{100}\right)^{1.37}\left(1+\frac{T_{nf}}{70}\right)^{0.2777}\left(1+\frac{d_p}{150}\right)^{-0.0336}\left(\frac{\alpha_p}{\alpha_w}\right)^{0.01737}\right] \tag{52}$$

The correlation equation is validated with 252 data values with a maximum deviation of 11 % for a few points. The experiments are conducted mostly with spherical shaped particles having diameters in the range of 20–150 nm, temperatures between 20 and 70 °C, and a volume concentration of less than 4.0 %.

4 Nanofluid Specific Heat

According to Wang et al. (2006), specific heat capacity of a particle varies with particle size. Since smaller particles have larger specific surface areas, the influence of surface energy on the effective specific heat capacity increases with a reduction in particle size. Ping Zhou et al. (2010) showed the deviation of specific heat capacity of CuO/EG nanofluid at different volume concentrations evaluated using equations given by Eqs. (53) and (54) with their experimental data.

$$C_{\text{pnf}} = \frac{(1-\phi)\left(\rho C_{\text{p}}\right)_{\text{bf}} + \phi(\rho C_{\text{p}})_{\text{p}}}{(1-\phi)\rho_{\text{bf}} + \phi\rho_{\text{p}}} \tag{53}$$

$$C_{\text{pnf}} = \phi C_{\text{p}} + (1-\phi)C_{\text{bf}} \tag{54}$$

It can be observed from their results that experimental values of specific heat capacity decreased from 2550 to 2450 kJ/(kg K) with the increase in volume concentration between 0.1 and 0.6 %. The experimental values are higher than the values calculated with Eqs. (53) and (54) which are based on the law of mixtures. However, the variation of heat capacities with volume concentration is observed to be constant. Ping Zhou et al. (2010) state that the deviation in the values of heat capacity of nanofluids for different sizes of nanoparticles is not significant with increasing volume concentration, due to the large specific heat capacity of the base fluid. Based on the observations of Wang et al. (2006) and Zhou et al. (2010), it can be concluded that the heat capacity of particle varies, while that of nanofluid remains constant with the size of the nanoparticle.

Zhou and Ni (2008) measured the specific heat of Al_2O_3/water nanofluids using a differential scanning calorimeter, with Al_2O_3 particle size of 45 nm at a temperature of 33 °C in the concentration range of 00–21.7 vol%. The specific heat of Al_2O_3, ZnO_2, and SiO_2 nanoparticles has been determined by Vajjha and Das (2009). The first two nanoparticles are dispersed in the base fluid mixture of ethylene glycol and water (60:40 EG/W) and the third silicon dioxide in deionized water. The samples of Al_2O_3, ZnO, and SiO_2 nanofluids tested had average particle sizes of 44, 77, and 20 nm, respectively. Measurements were undertaken over a temperature range of 315–363 K. The nanoparticle volumetric concentrations tested were up to 10 %. The equation that best fits the experimental data of all three nanofluids prepared from two kinds of base fluids is given as:

$$C_{\mathrm{p,eff}} = \left[\frac{(A \times T) + \left(\frac{C_{\mathrm{p,p}}}{C_{\mathrm{p,bf}}}\right)}{C + \varnothing}\right] C_{\mathrm{p,bf}} \tag{55}$$

$$\mathrm{Al_2O_3}: A = 0.0008911;\ B = 0.5719;\ C = 0.4250$$
$$\mathrm{SiO_2}: A = 0.001769;\ B = 1.1937;\ C = 0.8021$$
$$\mathrm{ZnO}: A = 0.0004604;\ B = 0.9855;\ C = 0.2990$$

Murshed et al. (2011) observed that nanofluids at low concentrations have lower values of effective specific heat than their base fluids. Barbés et al. (2013) have measured the thermal conductivities and specific heat capacities of Al_2O_3 (40–50 nm) dispersed in water and ethylene glycol for a particle volume concentration of 1.0–10.0 % in the temperature range of 298 and 338 K. Yiamsawasd et al. (2012) determined the specific heat of TiO_2 and Al_2O_3 nanofluids in water and a mixture of EG/water (20/80 wt%). The measurement is based on a differential thermal analysis technique for a maximum concentration of 8.0 vol% and temperatures between 15 and 65 °C. The authors presented a correlation equation to predict the specific heat of Al_2O_3 and TiO_2 nanofluids in a form of specific heat ratio between nanofluids and base fluid given by:

$$C_{\mathrm{p,eff}} = \left[A \varnothing_{\mathrm{P}}^{B} T^{C} \left(\frac{C_{\mathrm{p,p}}}{C_{\mathrm{p,bf}}}\right)\right]^{\mathrm{D}} C_{\mathrm{p,bf}} \tag{56}$$

$$\mathrm{Al_2O_3}: A = 1.249458;\ B = -0.05846;\ C = 0.006467;\ D = -0.17236$$
$$\mathrm{Al_2O_3}: A = 1.387402;\ B = -0.06425;\ C = 0.001124;\ D = -0.21159$$

Sekhar and Sharma (2015) have conducted experiments to determine the specific heat of water-based nanofluids containing Al_2O_3 (47 nm) nanoparticles for 0.01–1.0 % concentration in the temperature range of 25–45 °C. They presented an equation for the determination of specific heat applicable for water-based nanofluids given by:

$$C_{\mathrm{p,eff}} = \left[0.8429\left(1 + \frac{T_{\mathrm{nf}}}{50}\right)^{-0.3037}\left(1 + \frac{d_{\mathrm{p}}}{50}\right)^{0.4167}\left(1 + \frac{\varnothing}{100}\right)^{2.272}\right] \tag{57}$$

The following observations can be made from the investigations undertaken on nanofluid specific heat:

- The nanofluid specific heat is lower than the values of base liquid.
- The specific heat of nanofluid decreases with the increase in concentration.
- The specific heat of nanofluid does not vary significantly with temperature.
- The deviation in the values of heat capacity of nanofluids for different sizes of nanoparticles is insignificant with increasing volume concentration, due to the

large heat capacity of the base fluid. Hence, the variation of heat capacity with volume concentration is a constant.

5 Density

The experimental determination of nanofluid density reported in the literature is limited compared to thermal conductivity and viscosity. Density measurements were performed by Vajjha et al. (2009) on three different nanofluids containing Al_2O_3 (44 nm), antimony tin oxide, Sb_2O_5:SnO_2 (22–44 nm), and ZnO (70 nm) nanoparticles in a base fluid of 60:40 EG/water by mass over a temperature range of 0–50 °C for concentration range of 1–10 %. A good agreement is observed between the measured values with Eq. (58) of Pak and Cho 1998 (1998) at all temperatures and concentrations for Al_2O_3 and Sb_2O_5:SnO_2 with maximum deviation of 1.2 %. However, a maximum deviation of 8.0 % is observed with ZnO nanofluid.

$$\rho_{nf} = \varnothing_p \rho_p + (1 - \varnothing)\rho_{bf} \tag{58}$$

Teng and Hung (2014) in their study analysed the density of Al_2O_3/water nanofluid in the concentration range of 0–1.5 %. It is observed that by comparing the calculated values of density based on Eq. (58) with the experimental data, the deviation of density is observed to be in the range of −1.50 to 0.06 %. The calculated results of density show a trend of greater deviation as the concentration of nanofluid increases.

Mahian et al. (2013) have conducted experiments with ZnO (20 nm) nanoparticles suspended in EG/water mixture of weight ratio 40:60 in the temperature range of 25–40 °C for a maximum concentration of 4.0 %. The deviation in the values of nanofluid density with the values estimated with Eq. (58) is approximately 7.0 % at all volume fractions. The maximum density is observed to be 1328.72 kg/m^3 at 25 °C for 4.0 vol%. Mariano et al. (2013) conducted experiments with SnO_2($\approx$17 nm) dispersed in EG in the temperature range of 10–50 °C and between 1 and 5 % volume concentration. The maximum density was observed at 10.5 °C for 5.0 vol%. The following observations can be made from the investigations undertaken on nanofluid density:

- The nanofluid density is higher than that of the base liquid.
- The nanofluid density increases with concentration.
- The density of nanofluid decreases with the increase in temperature.

6 Results and Discussion

The variation of experimental data of viscosity with temperature reported by various investigators for TiO_2/water nanofluid is shown in Fig. 2 for particle diameter of 21 nm in the concentration range of 1.0–3.0 % volume. The variation of viscosity of SiO_2/EG water mixture with temperature is shown in Fig. 3 for different concentrations and particle size by Namburu et al. (2007) and Kulkarni et al. (2008). It can be observed from Figs. 2 and 3 that the viscosity increases with concentration and decreases with temperature for any base liquid. Further, from Fig. 2, the values of SiO_2/EG water mixture at 4.0 % concentration between researchers differ for the same particle size. However, the deviation of experimental

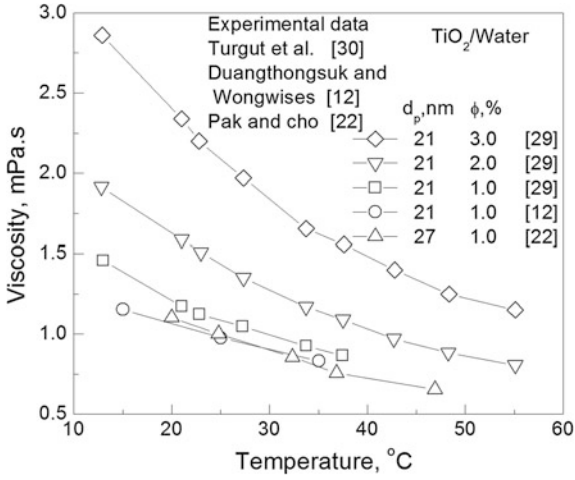

Fig. 2 Variation in experimental values of viscosity with temperature for TiO_2 nanofluid

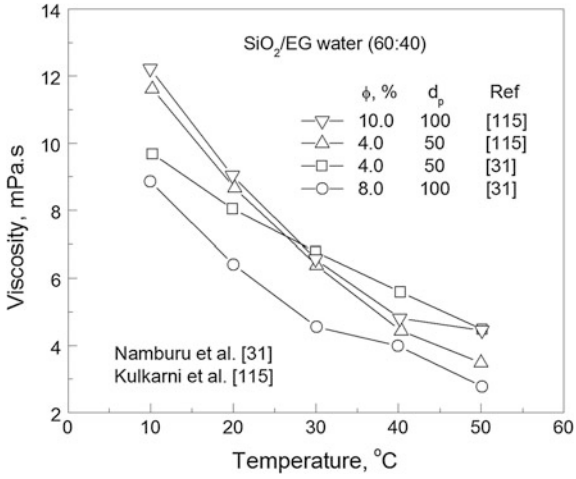

Fig. 3 Variation in experimental values of viscosity with temperature for different nanofluid concentrations and particle sizes

data for TiO_2/water at 1.0 % concentration between the authors is about 30 % at lower temperature and decreases to about 20 % as the temperature increases. Consequently, the data of Duangthongsuk and Wongwises (2009) for viscosity of TiO_2 (21 nm)/water with concentration deviate from the lines drawn with Eqs. (53) and (54) shown in Fig. 4 by a maximum of 7.0 % due to different values reported by various researchers. This may be due to different methods of preparation employed, particle size dispersion, and pH among other factors resulting in the variation of viscosity.

The variation of thermal conductivity with concentration is shown in Figs. 5 and 6 for various nanofluids and particle size. It can be observed that the thermal conductivity increases with concentration. Metals show higher enhancements in comparison with oxide nanofluids. From the experimental data reported by various

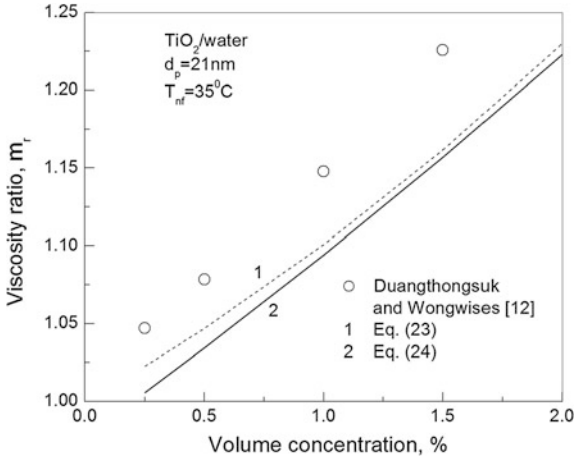

Fig. 4 Comparison of experimental values of viscosity with equations for TiO_2 nanofluid

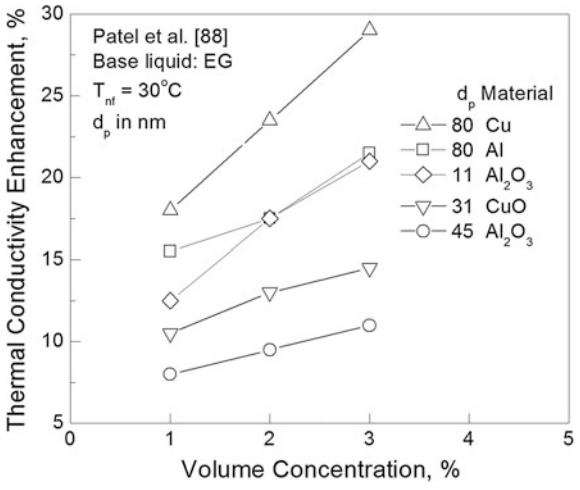

Fig. 5 Influence of nanofluid on thermal conductivity enhancement

investigators, it is possible that the thermal conductivity might reflect nonlinearity for concentrations lower than 1.0 % volume.

It can be observed from Fig. 6 that the enhancement with Al metal is greater with a particle size of 80 nm in comparison with its oxide having smaller particle size. The influence of particle size on thermal conductivity is shown in Fig. 7 with the experimental data of Beck et al. (2009), Kim et al. (2007). Most of the investigators observed a decrease in thermal conductivity with the increase in particle size. This is in agreement with the data of Kim et al. (2007) with TiO_2 and ZnO which reflect a decrease in thermal conductivity in contrast to the data of Beck et al. (2009).

The experimental data of nanofluid specific heat in different base liquids are shown in Fig. 8. The specific heat increases with temperature, and the enhancement

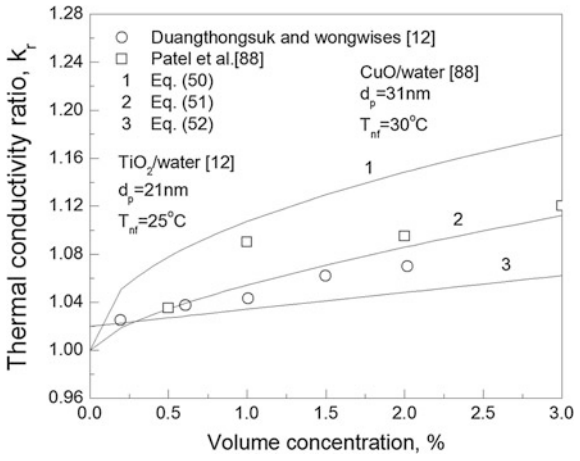

Fig. 6 Comparison of experimental data with various equations for thermal conductivity ratio

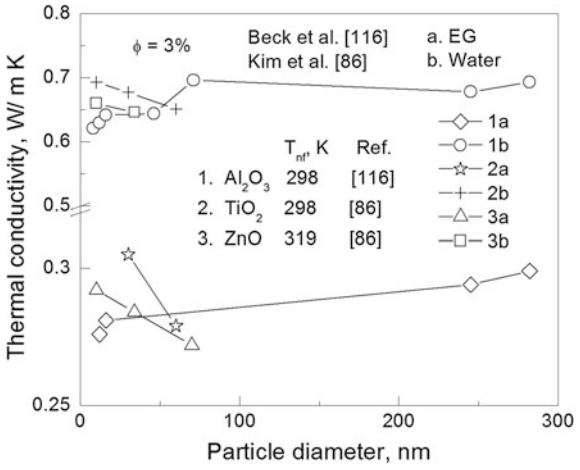

Fig. 7 Variation in experimental values of thermal conductivity with particle diameter for various metal oxides at 3 % volume concentration

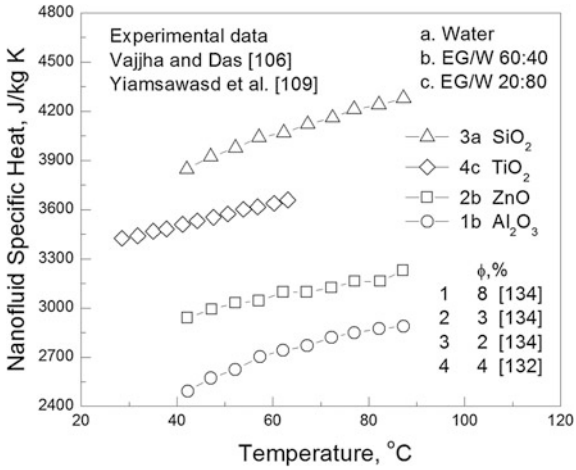

Fig. 8 Variation in experimental values of specific heat with temperature for different nanofluids in base liquid EG/water

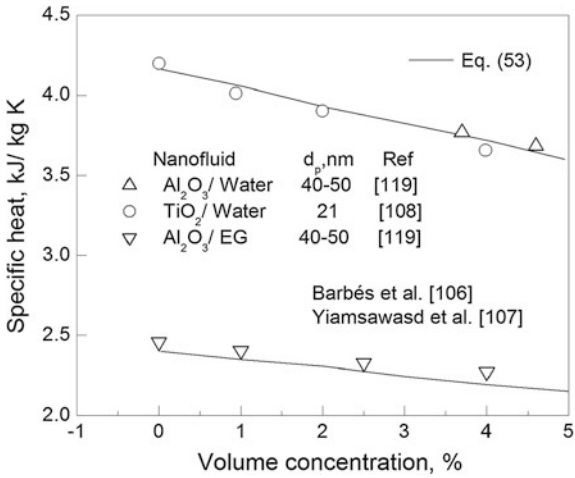

Fig. 9 Comparison of experimental data with mixture equation of specific

is pronounced for higher concentrations of nanofluid. The effect of concentration on nanofluid specific heat is shown in Fig. 9. The values of nanofluid specific heat can be observed to decrease with the increase in concentration. The observation is in agreement with the data shown in Fig. 9 along with the values drawn with Eq. (53) which is based on the law of mixtures.

The variation of density with temperature for different concentrations of Al_2O_3 (44 nm)/EG–water nanofluid is shown in Fig. 10. The density of nanofluid increases with concentration. However, the decrease in density with nanofluid temperature is not significant.

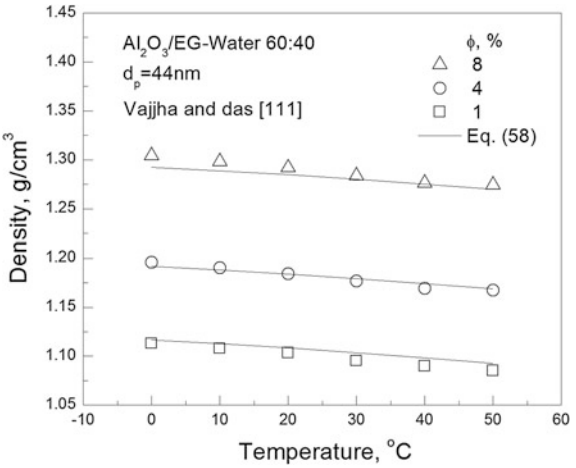

Fig. 10 Comparison of experimental values of density with mixture equation for different concentrations

7 Conclusions

The following conclusions are drawn from the present study:

(a) The nanofluid viscosity is significantly influenced by concentration, temperature, and particle size.
(b) The experimental data of viscosity reported by different authors deviate by more than 30 % for certain nanofluids.
(c) The Eqs. (23) and (24) developed with the aid of experimental data can be used to determine the viscosity of metal and oxide nanofluids.
(d) The thermal conductivity of nanofluid is dependent on volume fraction, particle diameter, and temperature of the nanofluid. The nanofluid thermal conductivity increases with volume fraction or concentration and temperature.
(e) Most of the authors reported an increase in thermal conductivity with the decrease in particle size
(f) The Eqs. (51) and (52) can be used to determine the thermal conductivity of metal and oxide nanofluids.
(g) The thermal diffusivity term in Eq. (52) distinguishes the material effects on nanofluid thermal conductivity. The equation can predict the thermal conductivity with a maximum deviation of 10 % for most metal and oxide nanofluids.
(h) The Eqs. (53) and (58) can be used to determine the specific heat and density of nanofluids, respectively.

Acknowledgments The authors acknowledge the financial assistance from the Ministry of Higher Education, Malaysia under FRGS grant vide Reference No. FRGS/1/2014/TK01/UTP/01/1 with cost centre 0153AB-K01.

References

ASHRAE, A. (2005). *Handbook of fundamentals*. Atlanta, GA: American Society of Heating Refrigerating and Air Conditioning Engineers.

Barbés, B., Páramo, R., Blanco, E., Pastoriza-Gallego, M. J., Piñeiro, M. M., Legido, J. L., et al. (2013). Thermal conductivity and specific heat capacity measurements of Al_2O_3 nanofluids. *Journal of Thermal Analysis and Calorimetry, 111*(2), 1615–1625.

Batchelor, G. K. (1977). Effect of Brownian-motion on bulk stress in a suspension of spherical-particles. *Journal of Fluid Mechanics, 83*(1), 97–117.

Beck, M. P., Yuan, Y., Warrier, P., & Teja, A. S. (2009). The effect of particle size on the thermal conductivity of alumina nanofluids. *Journal of Nanoparticle Research, 11*(5), 1129–1136.

Beck, M. P., Yuan, Y., Warrier, P., & Teja, A. S. (2010). The thermal conductivity of alumina nanofluids in water, ethylene glycol, and ethylene glycol + water mixtures. *Journal of Nanoparticle Research, 12*(4), 1469–1477.

Branson, B. T., Beauchamp, P. S., Beam, J. C., Lukehart, C. M., & Davidson, J. L. (2013). Nanodiamond nanofluids for enhanced thermal conductivity. *ACS Nano, 7*(4), 3183–3189.

Brinkman, H. C. (1952). The viscosity of concentrated suspensions and solutions. *Journal of Chemical Physics, 20*(4), 571–581.

Bruggeman, D. A. G. (1935). Berechnung verschiedener physikalischer konstanten von heterogenen substanzen. I. Dielektrizitätskonstanten und Leitfähigkeiten der mischkörper aus isotropen substanzen. *Annalen der Physik, 24*, 636–679.

Buongiorno, J., Venerus, D. C., Prabhat, N., McKrell, T., Townsend, J., Christianson, R., et al. (2009). A benchmark study on the thermal conductivity of nanofluids. *Journal of Applied Physics, 106*(9), 094312.

Chen, H., Ding, Y., He, Y., & Tan, C. (2007). Rheological behaviour of ethylene glycol based titania nanofluids. *Chemical Physics Letters, 444*(4–6), 333–337.

Chon, C. H., Kihm, K. D., Lee, S. P., & Choi, S. U. (2005) Empirical correlation finding the role of temperature and particle size for nanofluid (Al2O3) thermal conductivity enhancement. *Applied Physics Letters*, *87*(15), 153107–153107–3.

Corcione, M. (2011). Empirical correlating equations for predicting the effective thermal conductivity and dynamic viscosity of nanofluids. *Energy Conversion and Management, 52*(1), 789–793.

Das, S. K., Choi, S. U., & Patel, H. E. (2006). Heat transfer in nanofluids—A review. *Heat Transfer Engineering, 27*(10), 3–19.

Das, S. K., Putra, N., Thiesen, P., & Roetzel, W. (2003). Temperature dependence of thermal conductivity enhancement for nanofluids. *Journal of Heat Transfer, 125*(4), 567–574.

De Noni Jr, A., Garcia, D. E., & Hotza, D. (2002). A modified model for the viscosity of ceramic suspensions. *Ceramics International, 28*(7), 731–735.

Duangthongsuk, W., & Wongwises, S. (2009). Measurement of temperature-dependent thermal conductivity and viscosity of TiO_2–water nanofluids. *Experimental Thermal and Fluid Science, 33*(4), 706–714.

Eastman, J., Choi, S., Li, S., Yu, W., & Thompson, L. (2001). Anomalously increased effective thermal conductivities of ethylene glycol-based nanofluids containing copper nanoparticles. *Applied Physics Letters, 78*(6), 718–720.

Every, A., Tzou, Y., Hasselman, D., & Raj, R. (1992). The effect of particle size on the thermal conductivity of ZnS/diamond composites. *Acta Metallurgica et Materialia, 40*(1), 123–129.

Feng, Y., Yu, B., Feng, K., Xu, P., & Zou, M. (2008). Thermal conductivity of nanofluids and size distribution of nanoparticles by Monte Carlo simulations. *Journal of Nanoparticle Research, 10*(8), 1319–1328.

Frankel, N. A., & Acrivos, A. (1967). On the viscosity of a concentrated suspension of solid spheres. *Chemical Engineering Science, 22*(6), 847–853.

Fullman, R. (1953). *Measurement of particle sizes in opaque bodies*. General Electric Research Laboratory.

Garg, J., Poudel, B., Chiesa, M., Gordon, J., Ma, J., Wang, J., et al. (2008). Enhanced thermal conductivity and viscosity of copper nanoparticles in ethylene glycol nanofluid. *Journal of Applied Physics, 103*(7), 074301.

Ghadimi, A., Saidur, R., & Metselaar, H. (2011). A review of nanofluid stability properties and characterization in stationary conditions. *International Journal of Heat and Mass Transfer, 54* (17), 4051–4068.

Godson, L., Raja, B., Lal, D. M., & Wongwises, S. (2010). Experimental investigation on the thermal conductivity and viscosity of silver-deionized water nanofluid. *Experimental Heat Transfer, 23*(4), 317–332.

Graham, A. L. (1981). On the viscosity of suspensions of solid spheres. *Applied Scientific Research, 37*(3), 275–286.

Hagen, K. D. (1999). *Heat transfer with applications*. : Prentice Hall.

Hamilton, R. L., & Crosser, O. K. (1962). Thermal conductivity of heterogeneous two-component systems. *Industrial and Engineering Chemistry Fundamentals, 1*(3), 182–191.

He, Y., Jin, Y., Chen, H., Ding, Y., Cang, D., & Lu, H. (2007). Heat transfer and flow behaviour of aqueous suspensions of TiO_2 nanoparticles (nanofluids) flowing upward through a vertical pipe. *International Journal of Heat and Mass Transfer, 50*(11), 2272–2281.

Hwang, Y., Lee, J. K., Lee, C. H., Jung, Y. M., Cheong, S. I., Lee, C. G., et al. (2007). Stability and thermal conductivity characteristics of nanofluids. *Thermochimica Acta, 455*(1–2), 70–74.

Jang, S. P., & Choi, S. U. (2004). Role of Brownian motion in the enhanced thermal conductivity of nanofluids. *Applied Physics Letters, 84*(21), 4316–4318.

Jang, S. P., & Choi, S. U. (2007). Effects of various parameters on nanofluid thermal conductivity. *Journal of Heat Transfer, 129*(5), 617–623.

Kakaç, S., & Pramuanjaroenkij, A. (2009). Review of convective heat transfer enhancement with nanofluids. *International Journal of Heat and Mass Transfer, 52*(13–14), 3187–3196.

Karthikeyan, N. R., Philip, J., & Raj, B. (2008). Effect of clustering on the thermal conductivity of nanofluids. *Materials Chemistry and Physics, 109*(1), 50–55.

Kazemi-Beydokhti, A., Heris, S. Z., Moghadam, N., Shariati-Niasar, M., & Hamidi, A. A. (2014). Experimental investigation of parameters affecting nanofluid effective thermal conductivity. *Chemical Engineering Communications, 201*(5), 593–611.

Keblinski, P., Phillpot, S. R., Choi, S. U. S., & Eastman, J. A. (2002). Mechanisms of heat flow in suspensions of nano-sized particles (nanofluids). *International Journal of Heat and Mass Transfer, 45*(4), 855–863.

Khanafer, K., & Vafai, K. (2011). A critical synthesis of thermophysical characteristics of nanofluids. *International Journal of Heat and Mass Transfer, 54*(19), 4410–4428.

Kim, S. H., Choi, S. R., & Kim, D. (2007). Thermal conductivity of metal-oxide nanofluids: Particle size dependence and effect of laser irradiation. *Journal of Heat Transfer, 129*(3), 298–307.

Kitano, T., Kataoka, T., & Shirota, T. (1981). An empirical equation of the relative viscosity of polymer melts filled with various inorganic fillers. *Rheologica Acta, 20*(2), 207–209.

Kleinstreuer, C., & Feng, Y. (2011). Experimental and theoretical studies of nanofluid thermal conductivity enhancement: A review. *Nanoscale Research Letters, 6*(1), 439.

Kole, M., & Dey, T. K. (2010). Thermal conductivity and viscosity of Al_2O_3 nanofluid based on car engine coolant. *Journal of Physics. D. Applied Physics, 43*, 315501.

Koo, J., & Kleinstreuer, C. (2004). A new thermal conductivity model for nanofluids. *Journal of Nanoparticle Research, 6*(6), 577–588.

Koo, J., & Kleinstreuer, C. (2005). Impact analysis of nanoparticle motion mechanisms on the thermal conductivity of nanofluids. *International Communications in Heat and Mass Transfer, 32*(9), 1111–1118.

Krieger, I. M., & Dougherty, T. J. (1959). A mechanism for non-newtonian flow in suspensions of rigid spheres. *Transactions of The Society of Rheology, 3*(1), 137–152.

Kulkarni, D. P., Das, D. K., & Chukwu, G. A. (2006). Temperature dependent rheological property of copper oxide nanoparticles suspension (nanofluid). *Journal of Nanoscience and Nanotechnology, 6*(4), 1150–1154.

Kulkarni, D. P., Das, D. K., & Patil, S. L. (2007). Effect of temperature on rheological properties of copper oxide nanoparticles dispersed in propylene glycol and water mixture. *Journal of Nanoscience and Nanotechnology, 7*(7), 2318–2322.

Kulkarni, D. P., Namburu, P. K., Ed Bargar, H., & Das, D. K. (2008). Convective heat transfer and fluid dynamic characteristics of SiO_2 ethylene glycol/water nanofluid. *Heat Transfer Engineering, 29*(12), 1027–1035.

Lee, J.-H., Hwang, K. S., Jang, S. P., Lee, B. H., Kim, J. H., Choi, S. U. S., et al. (2008). Effective viscosities and thermal conductivities of aqueous nanofluids containing low volume concentrations of Al_2O_3 nanoparticles. *International Journal of Heat and Mass Transfer, 51* (11–12), 2651–2656.

Lee, J.-H., Lee, S.-H., Choi, C. J., Jang, S. P., & Choi, S. U. (2010). A review of thermal conductivity data, mechanisms and models for nanofluids. *International Journal of Micro-Nano Scale Transport, 1*(4), 269–322.

Lee, S., Choi, S.-S., Li, S., & Eastman, J. (1999). Measuring thermal conductivity of fluids containing oxide nanoparticles. *Journal of Heat Transfer, 121*(2), 280–289.

Leong, K. C., Yang, C., & Murshed, S. M. S. (2006). A model for the thermal conductivity of nanofluids—The effect of interfacial layer. *Journal of Nanoparticle Research, 8*(2), 245–254.

Li, C. H., & Peterson, G. (2006). Experimental investigation of temperature and volume fraction variations on the effective thermal conductivity of nanoparticle suspensions (nanofluids). *Journal of Applied Physics, 99*(8), 084314.

Li, J., Li, Z., & Wang, B. (2002). Experimental viscosity measurements for copper oxide nanoparticle suspensions. *Tsinghua Science and Technology, 7*(2), 198–201.

Li, X. F., Zhu, D. S., Wang, X. J., Wang, N., Gao, J. W., & Li, H. (2008). Thermal conductivity enhancement dependent pH and chemical surfactant for Cu–H_2O nanofluids. *Thermochimica Acta, 469*(1–2), 98–103.

Lundgren, T. S. (1972). Slow flow through stationary random beds and suspensions of spheres. *Journal of Fluid Mechanics, 51*(02), 273–299.

Mahbubul, I., Saidur, R., & Amalina, M. (2012). Latest developments on the viscosity of nanofluids. *International Journal of Heat and Mass Transfer, 55*(4), 874–885.

Mahian, O., Kianifar, A., & Wongwises, S. (2013). Dispersion of ZnO nanoparticles in a mixture of ethylene glycol–water, exploration of temperature-dependent density, and sensitivity analysis. *Journal of Cluster Science, 24*(4), 1103–1114.

Mariano, A., Pastoriza-Gallego, M. J., Lugo, L., Camacho, A., Canzonieri, S., & Piñeiro, M. M. (2013). Thermal conductivity, rheological behaviour and density of non-Newtonian ethylene glycol-based SnO_2 nanofluids. *Fluid Phase Equilibria, 337*, 119–124.

Masuda, H., Ebata, A., Teramae, K., & Hishinuma, N. (1993). Alteration of thermal conductivity and viscosity of liquid by dispersing ultra-fine particles. *Netsu Bussei, 7*(4), 227–233.

Maxwell, J.C. (1881). *Treatise on electricity and magnetism* (2nd ed.). Oxford, UK: Clarendon Press.

Mintsa, H. A., Roy, G., Nguyen, C. T., & Doucet, D. (2009). New temperature dependent thermal conductivity data for water-based nanofluids. *International Journal of Thermal Sciences, 48* (2), 363–371.

Mishra, P. C., Mukherjee, S., Nayak, S. K., & Panda, A. (2014). A brief review on viscosity of nanofluids. *International Nano Letters, 4*(4), 109–120.

Murshed, S. M. S. (2011a). Simultaneous measurement of thermal conductivity, thermal diffusivity, and specific heat of nanofluids. *Heat Transfer Engineering, 33*(8), 722–731.

Murshed, S. M. S., Leong, K. C., & Yang, C. (2005). Enhanced thermal conductivity of TiO2–water based nanofluids. *International Journal of Thermal Sciences, 44*(4), 367–373.

Murshed, S. M. S., Leong, K. C., & Yang, C. (2008). Investigations of thermal conductivity and viscosity of nanofluids. *International Journal of Thermal Sciences, 47*(5), 560–568.

Murshed, S. M. S., Leong, K. C., & Yang, C. (2009). A combined model for the effective thermal conductivity of nanofluids. *Applied Thermal Engineering, 29*(11–12), 2477–2483.

Murshed, S. S. (2011b). Determination of effective specific heat of nanofluids. *Journal of Experimental Nanoscience, 6*(5), 539–546.

Namburu, P., Kulkarni, D., Dandekar, A., & Das, D. (2007). Experimental investigation of viscosity and specific heat of silicon dioxide nanofluids. *Micro and Nano Letters, IET, 2*(3), 67–71.

Nguyen, C. T., Desgranges, F., Roy, G., Galanis, N., Maré, T., Boucher, S., et al. (2007). Mintsa, temperature and particle-size dependent viscosity data for water-based nanofluids—Hysteresis phenomenon. *International Journal of Heat and Fluid Flow, 28*(6), 1492–1506.

Nielsen, L. E. (1970). Generalized equation for the elastic moduli of composite materials. *Journal of Applied Physics, 41*(11), 4626–4627.

Özerinç, S., Kakaç, S., & Yazıcıoğlu, A. G. (2010). Enhanced thermal conductivity of nanofluids: A state-of-the-art review. *Microfluidics and Nanofluidics, 8*(2), 145–170.

Pak, B. C., & Cho, Y. I. (1998). Hydrodynamic and heat transfer study of dispersed fluids with submicron metallic oxide particles. *Experimental Heat Transfer an International Journal, 11*(2), 151–170.

Patel, H. E., Sundararajan, T., & Das, S. K. (2010). An experimental investigation into the thermal conductivity enhancement in oxide and metallic nanofluids. *Journal of Nanoparticle Research, 12*(3), 1015–1031.

Prasher, R., Phelan, P. E., & Bhattacharya, P. (2006a). Effect of aggregation kinetics on the thermal conductivity of nanoscale colloidal solutions (nanofluid). *Nano Letters, 6*(7), 1529–1534.

Prasher, R., Song, D., Wang, J., & Phelan, P. (2006b). Measurements of nanofluid viscosity and its implications for thermal applications. *Applied Physics Letters, 89*(13), 133108.

Sahoo, B. C., Das, D. K., Vajjha, R. S., & Satti, J. R. (2012). Measurement of the thermal conductivity of silicon dioxide nanofluid and development of correlations. *Journal of Nanotechnology in Engineering and Medicine, 3*(4), 041006.

Sekhar, Y. R., & Sharma, K. (2015). Study of viscosity and specific heat capacity characteristics of water-based Al_2O_3 nanofluids at low particle concentrations. *Journal of Experimental Nanoscience, 10*(2), 86–102.

Sharma, A. K., Tiwari, A. K., & Dixit, A. R. (2016). Rheological behaviour of nanofluids: A review. *Renewable and Sustainable Energy Reviews, 53*, 779–791.

Sharma, K., Sarma, P., Azmi, W., Mamat, R., & Kadirgama, K. (2010). Correlations to predict friction and forced convection heat transfer coefficients of water based nanofluids for turbulent flow in a tube. *International Journal of Microscale and Nanoscale Thermal and Fluid Transport Phenomena, 3*, 283–308.

Shima, P., Philip, J., & Raj, B. (2009). Role of microconvection induced by Brownian motion of nanoparticles in the enhanced thermal conductivity of stable nanofluids. *Applied Physics Letters, 94*(22), 223101.

Sridhara, V., & Satapathy, L. N. (2011). Al_2O_3-based nanofluids: A review. *Nanoscale Research Letters, 6*(1), 1–16.

Sun, T., & Teja, A. S. (2004). Density, viscosity and thermal conductivity of aqueous solutions of propylene glycol, dipropylene glycol, and tripropylene glycol between 290 K and 460 K. *Journal of Chemical and Engineering Data, 49*(5), 1311–1317.

Sundar, L. S., Ramana, E. V., Singh, M. K., & Sousa, A. C. (2014). Thermal conductivity and viscosity of stabilized ethylene glycol and water mixture Al_2O_3 nanofluids for heat transfer applications: an experimental study. *International Communications in Heat and Mass Transfer, 56*, 86–95.

Sundar, L. S., Sharma, K., Naik, M., & Singh, M. K. (2013a). Empirical and theoretical correlations on viscosity of nanofluids: A review. *Renewable and Sustainable Energy Reviews, 25*, 670–686.

Sundar, L. S., Singh, M. K., & Sousa, A. C. (2013b). Thermal conductivity of ethylene glycol and water mixture based Fe_3O_4 nanofluid. *International Communications in Heat and Mass Transfer, 49*, 17–24.

Teng, T.-P., & Hung, Y.-H. (2014). Estimation and experimental study of the density and specific heat for alumina nanofluid. *Journal of Experimental Nanoscience, 9*(7), 707–718.

Teng, T.-P., Hung, Y.-H., Teng, T.-C., Mo, H.-E., & Hsu, H.-G. (2010). The effect of alumina/water nanofluid particle size on thermal conductivity. *Applied Thermal Engineering, 30*(14), 2213–2218.

Tseng, W. J., & Lin, K.-C. (2003). Rheology and colloidal structure of aqueous TiO_2 nanoparticle suspensions. *Materials Science and Engineering A, 355*(1–2), 186–192.

Turgut, A., Tavman, I., Chirtoc, M., Schuchmann, H. P., Sauter, C., & Tavman, S. (2009). Thermal conductivity and viscosity measurements of water-based TiO_2 nanofluids. *International Journal of Thermophysics, 30*, 1213–1226.

Vajjha, R., Das, D., & Mahagaonkar, B. (2009). Density measurement of different nanofluids and their comparison with theory. *Petroleum Science and Technology, 27*(6), 612–624.

Vajjha, R. S., & Das, D. K. (2009a). Experimental determination of thermal conductivity of three nanofluids and development of new correlations. *International Journal of Heat and Mass Transfer, 52*(21), 4675–4682.

Vajjha, R. S., & Das, D. K. (2009b). Specific heat measurement of three nanofluids and development of new correlations. *Journal of Heat Transfer, 131*(7), 071601.

Wang, B.-X., Zhou, L.-P., & Peng, X.-F. (2006). Surface and size effects on the specific heat capacity of nanoparticles. *International Journal of Thermophysics, 27*(1), 139–151.

Wang, X., Xu, X., & Choi, S. U. S. (1999). Thermal conductivity of nanoparticle–fluid mixture. *Journal of Thermophysics and Heat Transfer, 13*(4), 474–480.

Wang, X.-J., Zhu, D.-S., & Yang, S. (2009). Investigation of pH and SDBS on enhancement of thermal conductivity in nanofluids. *Chemical Physics Letters, 470*(1–3), 107–111.

Wang, X.-Q., & Mujumdar, A. S. (2007). Heat transfer characteristics of nanofluids: A review. *International Journal of Thermal Sciences, 46*(1), 1–19.

Wang, Y., Fisher, T. S., Davidson, J., & Jiang, L. (2002). Thermal conductivity of nanoparticle suspensions. In *8th AIAA and ASME Joint Thermophysics and Heat Transfer Conference*.

Wasp, F. J. (1977). *Solid-liquid slurry pipeline transportation*. Berlin: Trans. Tech.

White, F. M. (1991). *Viscous fluid flow*.

Xie, H., Fujii, M., & Zhang, X. (2005). Effect of interfacial nanolayer on the effective thermal conductivity of nanoparticle-fluid mixture. *International Journal of Heat and Mass Transfer, 48*(14), 2926–2932.

Xie, H., Wang, J., Xi, T., & Liu, Y. (2001). Study on the thermal conductivity of SiC nanofluids. *Journal-Chinese Ceramic Society, 29*(4), 361–364.

Xie, H., Wang, J., Xi, T., Liu, Y., Ai, F., & Wu, Q. (2002a). Thermal conductivity enhancement of suspensions containing nanosized alumina particles. *Journal of Applied Physics, 91*(7), 4568–4572.

Xie, H., Yu, W., & Chen, W. (2010). MgO nanofluids: Higher thermal conductivity and lower viscosity among ethylene glycol-based nanofluids containing oxide nanoparticles. *Journal of Experimental Nanoscience, 5*(5), 463–472.

Xie, H., Yu, W., Li, Y., & Chen, L. (2011). Discussion on the thermal conductivity enhancement of nanofluids. *Nanoscale Research Letters, 6*(1), 124.

Xie, H.-Q., Wang, J.-C., Xi, T.-G., & Liu, Y. (2002b). Thermal conductivity of suspensions containing nanosized SiC particles. *International Journal of Thermophysics, 23*(2), 571–580.

Xuan, Y., & Li, Q. (2000). Heat transfer enhancement of nanofluids. *International Journal of Heat and Fluid Flow, 21*(1), 58–64.

Xue, Q., & Xu, W.-M. (2005). A model of thermal conductivity of nanofluids with interfacial shells. *Materials Chemistry and Physics, 90*(2), 298–301.

Xue, Q.-Z. (2003). Model for effective thermal conductivity of nanofluids. *Physics Letters A, 307*(5), 313–317.

Yiamsawasd, T., Dalkilic, A. S., & Wongwises, S. (2012). Measurement of specific heat of nanofluids. *Current Nanoscience, 8*(6), 939–944.

Yoo, D.-H., Hong, K., & Yang, H.-S. (2007). Study of thermal conductivity of nanofluids for the application of heat transfer fluids. *Thermochimica Acta, 455*(1), 66–69.

Yu, C. J., Richter, A., Datta, A., Durbin, M., & Dutta, P. (2000). Molecular layering in a liquid on a solid substrate: an X-ray reflectivity study. *Physica B: Condensed Matter, 283*(1), 27–31.

Yu, W., & Choi, S. (2004). The role of interfacial layers in the enhanced thermal conductivity of nanofluids: a renovated Hamilton-Crosser model. *Journal of Nanoparticle Research, 6*(4), 355–361.

Yu, W., & Choi, S. U. S. (2003). The role of interfacial layers in the enhanced thermal conductivity of nanofluids: A renovated Maxwell model. *Journal of Nanoparticle Research, 5* (1–2), 16–171.

Yu, W., Xie, H., Li, Y., Chen, L., & Wang, Q. (2012). Experimental investigation on the heat transfer properties of Al_2O_3 nanofluids using the mixture of ethylene glycol and water as base fluid. *Powder Technology, 230*, 14–19.

Zhou, L.-P., Wang, B.-X., Peng, X.-F., Du, X.-Z., & Yang, Y.-P. (2010) On the specific heat capacity of CuO nanofluid. *Advances in Mechanical Engineering*.

Zhou, S.-Q., & Ni, R. (2008). Measurement of the specific heat capacity of water–based Al2O3 nanofluid. *Applied Physics Letters*, *92*(9), 093123–093123–3.

Zhu, H., Zhang, C., Liu, S., Tang, Y., & Yin, Y. (2006). Effects of nanoparticle clustering and alignment on thermal conductivities of Fe3O4 aqueous nanofluids. *Applied Physics Letters, 89* (2), 3123.

Heat Transfer Enhancement with Nanofluids for Automotive Cooling

Adnan M. Hussein, K. Kadirgama, K.V. Sharma, D. Ramasamy and R.A. Bakar

Abstract The increasing demand of nanofluids for the industrial applications has led to focus on it from many researchers in the last decade. This thesis includes both experimental study and numerical study to improve heat transfer with slightly pressure drop in the automotive cooling system. The friction factor and heat transfer enhancement using different types of nanofluids are studied. The TiO_2 and SiO_2 nanopowders suspended to four different base fluids (pure water, EG, 10 % EG + 90 %W, and 20 %EG + 80 %W) are prepared experimentally. The thermophysical properties of both nanofluids and base fluids are measured and validated with the standard and the experimental data available. The test section is setup including car radiator and the effects under the operating conditions on the heat transfer enhancement analyzed under laminar flow condition. The volume flowrate, inlet temperature, and nanofluid volume concentrations are in the range of (1-5LPM) for pure water and (3-12LPM) for other base fluids, (60–80 °C) and (1–4 %), respectively. On the other side, the CFD analysis for the nanofluid flow inside the flat tube of a car radiator under laminar flow is carried out. A simulation study is conducted by using the finite volume technical to solve the continuity, momentum, and energy equations. The processes of the geometry meshing of problem and describing the boundary conditions are performed in the GAMBIT then achieving of FLUENT software to find the friction factor and heat transfer coefficient. The experimental results show the friction factor decreases with the increase of the volume flowrate and increases with the nanofluid volume fraction but slightly decreases with the increase of the inlet temperature. Furthermore, the simulation results show good agreement with the experimental data with deviation, not more than 4 %. The experimental results show that the heat transfer coefficient increases with the increase in the volume flowrate, the nanofluid volume fraction,

K.V. Sharma
Department of Mechanical Engineering, Universiti Teknologi PETRONAS, 32610 Bandar Seri Iskandar, Perak Darul Ridzuan, Malaysia
e-mail: sharma.korada@petronas.com.my

A.M. Hussein · K. Kadirgama (✉) · D. Ramasamy · R.A. Bakar
Department of Mechanical Engineering, Universiti Malaysia Pahang, 26600 Pekan, Malaysia
e-mail: kumaran@ump.edu.my

K. Viswanatha Sharma and N. Hisham B Hamid (eds.),
Engineering Applications of Nanotechnology, Topics in Mining, Metallurgy and Materials Engineering, DOI 10.1007/978-3-319-29761-3_3

and the inlet temperature. Likewise, the simulation results show good agreement with the experimental data with deviation not more than 6 %. In addition, the SiO_2 nanofluid appears high values of the friction factor and heat transfer coefficient than TiO_2 nanofluid. Also, the base fluid (20 %EG + 80 %W) gives high values of the heat transfer coefficient and proper values of friction factor than other base fluids. It seems that the SiO_2 nanoparticles dispersed to (20 %EG + 80 %W) base fluid are a significant enhancement of the thermal properties than others. It is observed that the SiO_2 nanoparticles dispersed to (20 %EG + 80 %W) base fluid are a significant augmentation of heat transfer in the automobile radiator. The regression equations among input (Reynolds number, Prandtl number, and nanofluid volume concentration) and response (friction factor and Nusselt number) are found. The results of the analysis indicated a significant input parameters to enhance heat transfer with the automotive cooling system. The comparison between experimental results and other researchers' data is conducted, and there is a good agreement with a maximum deviation approximately 10 %.

Keywords Automotive · Cooling system · Nanofluid · Heat transfer

1 Introduction

The general definition of convection is the energy transfer between the surface and fluid due to temperature difference, and this energy transfer by either forced (external and internal flow) or natural convection. Forced convection is a mechanism or type of transport in which fluid motion is generated by an external source such as a fan, a pump, and a suction device. It should be considered as one of the main methods of useful heat transfer as significant amounts of heat energy can be transported very efficiently, and this mechanism is found very commonly in everyday life, including air-conditioning, central heating, steam turbines, and in many other machines. Forced convection is often encountered by engineers designing or analyzing heat exchangers, flow over a flat plate and pipe flow at a different temperature than the stream. The increasing demand for more efficient heat transfer fluids in many applications has led to enhance heat transfer to meet the cooling challenge necessary such as the photonics, transportation, electronics, and energy supply industries (Das et al. 2007). Conventional fluids nowadays are inherently poor heat transfer fluids and with the increasing demand of industries, micro-sized heat-generating systems are unable to provide adequate heat transfer. One of the possible solutions to this limited capability can be achieved by integrating the high heat transfer capability of solid metals into a flowing heat transfer fluid. In the past, attempts have been conducted to add micro-sized metal particles into conventional liquids, which ended with significant results as well as large disadvantages. Flow characteristics such as viscosity will change which led to the need to higher pumping power due to the addition of micro-particles. There is also a concern of agglomeration over time as well as corrosively of the system which can both result in high maintenance demands. The concept of nanofluids refers to a new

kind of heat transfer fluid formed by dispersing nano-scaled metallic or nonmetallic particles in base fluids (water, ethylene glycol, and oil). Energy transport of the nanofluid is affected by the properties and dimension of nanoparticles as well as a solid volume fraction. Some experimental investigations have revealed that the nanofluids have remarkably higher thermal conductivities than those of conventional pure fluids and have great potential for heat transfer enhancement. The addition of nano-sized particles is very proper to augment heat transfer as compared to the adding millimeter or micrometer sized to liquids with little penalty in pressure drop. A possible effective method for heat enhancement is to include high thermal conductivity particles in the liquid. Some general examples of applications that can benefit from this technology include home heating and cooling appliances, automotive radiator systems, power plant cooling systems, and computer processing cooling equipment, and more examples including heat are transferred from one medium to another. The use of high conductivity heat transfer materials will lead to benefit fully the available energy of a system which will reduce the environmental footprint of companies as well as their operating costs. It is believed that the most important reasons to enhance heat transfer of the nanofluids may be from the intensification of a turbulence eddy, repression, or interruption of the boundary layer as well as nanoparticles suspension. Therefore, the convective heat transfer coefficient of nanofluids is a function of properties, volume fraction of suspended nanoparticles, and dimension as well as the flow velocity. Taking advantage of the nanoparticles in the liquid causes the particles to stay in the solution for a long time. Another feature is that these particles have large surface area for thermal conductivity than ordinary liquids. From an engineering point of view, forced convection utilizing liquid coolants in laminar or turbulent flow regimes is always a key heat transfer solution. The better convective heat transfer performance means higher values of heat transfer coefficient. There are a number of techniques to enhance heat transfers such as modified heat transfer surface roughness, fins (extended surfaces), and injection. However, these techniques have led to higher pressure drop and hence lift pumping power requirement. Also, with low thermal conductivity and high viscosity of conventional heat transfer fluids such as water, ethylene glycol, oil, and ammonia, the convective thermal performance created barriers in designing small heat-rejecting devices. Therefore, an innovative coolant with improving heat transfer properties is required. The solid particles usually exhibit high thermal conductivity than liquids, and one approach to enhance thermal conductivity of liquids is by using suspensions, which contain dispersed particles into base fluids. One of the pioneering researchers of stationary, dilute dispersions of solid spheres has been studied by Ahuja (1975) performed number of tests on thermal conductivity and heat transfer coefficients of 40–100 μm-sized polystyrene–water-based solutions with 1-mm inside tube. Furthermore, the effective thermal conductivity of the suspension increases with the increasing of Reynolds number and nanofluid volume fraction. Because of shortage of available technology in those years, the particles size was large (in micro-scale). So this size has led to two penalties: The first on are not stable enough, and other are the larger particles can easily cause erosion to flow loop components.

1.1 Automotive Cooling System

Most internal combustion engines have used fluid coolant run through a heat exchanger (radiator) cooled by air. The water often used directly for the engine cooling, but there were obstacles as sedimentation may clog coolant passages, or salt may chemically damage the engine. Most engines' liquid for cooling has been used a mixture of water and chemicals such as antifreeze and rust inhibitors. The industrial term for the antifreeze mixture is engine coolant. Some antifreezes use no water at all, instead using a liquid with different properties, such as propylene glycol or ethylene glycol. Main requirement is that an engine fails if just one part overheats. Therefore, it is essential that the cooling system keeps all parts at properly low temperatures. Engine cooling systems are able to vary the size of their passageways through the engine block so that coolant flow may be adapted to the needs of each part. A typical four cylinder engine cruising along the highway at around 50 miles per hour will produce 4000 controlled explosions per minute inside the engine as the spark plugs ignite the fuel in each cylinder to propel the vehicle down the road. Clearly, these explosions produce an enormous amount of heat and, if not controlled, will destroy an engine in a matter of minutes. Controlling these high temperatures is the job of the cooling system. The radiator has been usually made of flattened aluminum or brass tubes with many fins on the external surface of tubes. These fins are capable of transferring heat from tubes into the airstream to be carried away from the vehicle. At the two ends of the radiator, there is a tank covers the ends of the radiator; in most of the cars, the tubes have run vertically with the tank on the top and bottom. On the back of the radiator on the side closest to the engine, there are one or two electrical fans inside a housing that is designed to direct the airflow. This fan is there to keep the airflow going through the radiator while the vehicle is going slow or is stopped while the engine is running. The engine temperature has been increased if this fan stops working, every time. The electrical fan is controlled by the vehicle's computer. A temperature sensor monitors engine temperature and sends this information to the computer. The computer determines whether the fan should be turned on and actuates the fan relay if additional airflow through the radiator is necessary. Another important device is the radiator pressure cap which will keep pressure in cooling system up to set point. The spring loaded valve when the pressure builds up higher than the set pressure point, calibrated to the correct Pascal (N/m^2), to release the pressure. Also, a small amount of fluid will bleed off if the cooling system pressure reaches the point to the cap needs till release this excess pressure. Since there is now less fluid in the system, as the engine cools down a partial vacuum has been formed. There is a secondary valve relates to the radiator cap to complete closed systems which allowed the vacuum in the cooling system to draw the fluid back into the radiator from the tank. Another simple device also keeps the fluid moving as long as the engine is running and this device is defined as a water pump. It is usually setup on the front of the engine and operates whenever the engine is working. The thermostat is a valve that controls the temperature of a fluid whenever hot weather enough, opens to allow the fluid to flow

through the radiator. And if the fluid is not hot enough, the flow to the radiator is blocked, and fluid is directed to bypass system that allows the coolant to return directly back to the engine. The bypass system allows the coolant to keep moving through the engine to balance the temperature and avoid hot spots. Because the flow to the radiator is blocked, the engine will reach operating temperature sooner and, on a cold day, will allow the heater to begin supplying hot air to the interior more quickly (Andrew 2008).

1.2 Nanofluid Synthesis Methods

A nanofluid may be synthesized by simply mixing nanoparticles dispersed to a liquid. In fact, the processes of synthesis are more involved. Metal oxide, carbon nanotube, nitride, carbide, and others nanoparticles may be readily purchased from the market. The reason to their side effective, these nanoparticles can normally be handled outside the boxes and other sealed containers during the preparation of the nanofluid. In order to break up the agglomerated particles and form a well-dispersed nanoparticle suspension, a stabilizing agent should add to avoid reagglomeration of the nanoparticles. In addition, the stabilizing agent affected the thermal properties, for instance, with altering the optical properties or viscosity of the nanoparticle solutions. Furthermore, the applicability of the nanofluid to the systems hinges on ability and real-life products to retain the small-sized character, and thus, for dispersing. Due to the high surface reactivity of the metal, it is reacting with the environment so nanofluids cannot be synthesized from pure solid metal nanoparticles. The single-step methods for the nanofluid synthesized with a limit agglomeration as reported by Das et al. (2007). Over the years, a few processes have been developed for the direct nanofluid synthesis. The metal salt solutions are reduced to a stabilizing agent, and the small particles form sediment. There are also a number of plasma synthesis approaches: Metal oxide, nitride, or carbide nanoparticles may be synthesized by condensation/evaporation with the nitrogen, oxygen, or a light hydrocarbon. The main advantages of the plasma synthesis processes are the possibility to synthesize complex chemical compositions and structures, in situ stabilization, and scalability. The nanoparticles in a host fluid interact strongly with van der Waals interactions because of the large surface area of the nanofluid and incessant solid–solid collisions due to Brownian effect. Undesirably, particle collision can lead the agglomeration process whereby large, sometimes up to micron-sized, particles are produced. Due to the weight, such particles cannot be maintained in suspension by Brownian moving and settle out of dispersions. In applications where the fluid is pumped through conduits, this process also leads to abrasion of conduit walls. In the agglomeration process, soft and hard agglomerates may form. Soft agglomerates may be broken up by sonication which means of fluid agitation. Hard agglomerates, however, which are associated with nanoparticle sintering, cannot be broken up by simple means. In the last years, many attempts have been made to make stable nanofluids with partial success.

Various methods have been used to stabilize the nanoparticle suspension. Some rely on electrostatic repulsion where the nanoparticles acquire surface charges once in solution forming an electrical double layer. The hydrophilic end of the compound ensures compatibility with a polar solvent. Chemical functionalization of the nanoparticle surface can also be used to cause particles to favor interactions with the host liquid. Using surfactants has been wide-spread across the nanofluid applications though their usefulness is somewhat overshadowed by its limitations. One well-known issue is the irreversible deterioration of the surfactant at rather modest temperatures. Typically, surfactants degrade significantly above 60 °C.

1.3 Nanofluid Applications

One of the major advantages of going to a system that uses nanoparticle suspensions is the operating mode of the system. Small changes of these fields can change scattering and absorption. The first one using particles in the solar collector was who mixed particles in a gas-working fluid. In years following, gas particle receivers have been extensively modeled, and several prototype collectors have been built and tested. The researchers experimentally illustrate the absorption of radiation using nanoparticles and have been done by the following: (Abdelrahman et al. 1979). Although the researchers used particles mixed with a gas (not liquids), there are a few recent studies that have been used the concept of liquid-based nanofluid experimentally in the solar collectors. Their experimental results showed that the volume fraction of nanoparticles can achieve the incoming light to be absorbed in a thin surface layer where the thermal energy was easily lost to the environment. The regime map of the solar absorbing nanofluids in comparison with other common particulate mediums has been reported.

1.3.1 The Big Impact of Nanoparticles

What does the future hold for nanofluids? Although there still exist a growing number of publications in the field of nanofluids, one has to be concerned with the funding trends going forward, particularly in the thermal transport community. After detection of the last ten years, the nanofluid researches peaked in 2007 and have been increasing since. On the other hand, with so many emerging, exciting applications (i.e., excluding conductive/convective studies), we believe nanofluids will have a big impact for some time to come.

2 Forced Convection in a Car Radiator

There are many different applications of thermal fluid systems, including automotive cooling systems. Base fluids, such as water, ethylene glycol, and glycerol, have been used as conventional coolants in automobile radiators for many years; however, these fluids have low thermal conductivities. The low thermal conductivities have thus prompted researchers to search for fluids with high thermal conductivities than that of conventional coolants. Therefore, nanofluids have been used instead of the commonly used base fluids.

(i) ***Experimental studies***

Investigated forced convection heat transfer to reduce circulating water in an automobile radiator.

The effects of different amounts of Al_2O_3 nanoparticles on the heat transfer performance of an automobile radiator were determined experimentally as shown in Fig. 1. The range of flowrates was varied between 2 and 6 LPM with a changing fluid inlet temperature for all experiments. The results showed that the enhancement of heat transfer using nanofluids is 40 % compared with using water.

Forced convection heat transfer of both CuO and Fe_2O_3 nanofluids flow through the car radiator has presented by Peyghambarzadeh et al. (2013). The overall heat transfer coefficient (U) according to the conventional 3-NTU technique has been evaluated to find the performance of heat transfer as shown in Fig. 2. Three volume fractions 0.15, 0.4, and 0.65 % have been added to water to prepare nanofluids. The range of Reynolds number is 50–1000, and the inlet liquid temperature is changed

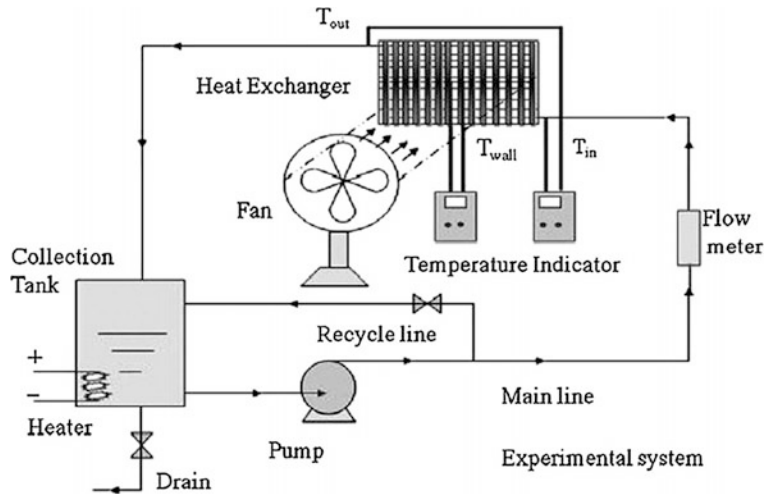

Fig. 1 Test rig in the experimental work. *Source* Peyghambarzadeh et al. (2011)

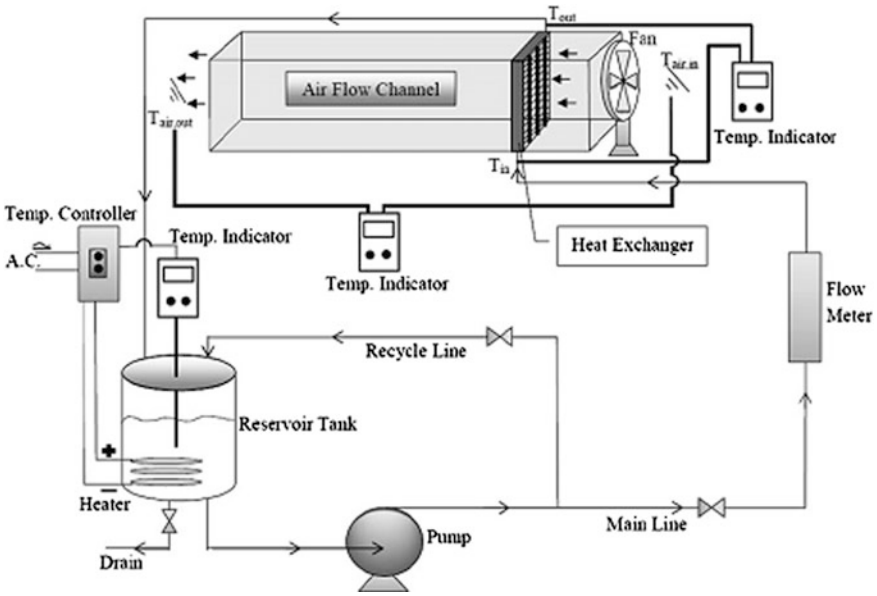

Fig. 2 Cooling loop setup of automobile cooling system. *Source* Peyghambarzadeh et al. (2013)

to 50, 65 and 80 °C. Results showed that both nanofluids appear greater overall heat transfer coefficient as compared to water up to 9 %. Furthermore, increasing the nanoparticle concentration, air velocity, and nanofluid velocity enhances the heat transfer coefficient.

(ii) ***Numerical studies***

A numerical study analyzed mixed convective flows through a U-shaped grooved tube in a radiator has been conducted. The enhanced heat transfer of an automobile radiator was investigated with properties of the nanofluid as input data. It appeared that the heat transfer coefficient and heat transfer rate in the engine cooling system increased using copper–ethylene glycol nanofluids compared with using pure ethylene glycol. The results showed that the addition of 2 % copper particles in ethylene glycol achieved a result of 3.8 % better compared with using pure ethylene glycol at air and coolant Reynolds number of 6000 and 5000, respectively. The influence of the working conditions on both fluids (mass flow and inlet temperature) and the impact of the selected coolant fluid in a car radiator were investigated numerically by Oliet et al. (2007). The application of a copper–ethylene glycol nanofluid in a car cooling system was studied. Several geometrical parameters (fin pitch and louver angle) and the importance of the coolant flow layout on the radiator global performance were analyzed. The results showed that the use of this numerical model as a rating and design tool for car radiator manufacturers is a reasonable compromise between the NTU and the CFD methods. A numerical study on laminar heat transfer using CuO and Al_2O_3-ethylene glycol

and water inside a flat tube of a car radiator was performed. A modified SIMPLE algorithm for the irregular geometry was developed to determine the flow and temperature field. The results have been used as a fundamental data for the tube design by suggesting optimal specifications for radiator tubes. Two liquids, water and ethylene glycol/water mixture, used as the coolant fluid in a meso-channel heat exchanger were studied numerically. The predicted results (heat transfer rate, pressure, and temperature drops in the coolants) from the numerical simulation were compared with the experimental data for the same geometrical and operating conditions and showed good agreement. Additionally, the results showed the heat exchanger was enhanced, with heat transfer rate approximately 20 % greater than that of a straight slab of the same length; the enhanced heat exchanger has a good potential to be used as a car radiator with reasonably enhanced heat transfer characteristics using an ethylene glycol/water mixture as the coolant. Different types of nanoparticles (copper, diamond, and silicon dioxide) in ethylene glycol in automotive flat tube plate-fin cross-flow compact heat exchangers (CHEs) were investigated numerically. The volume concentration for all nanofluid types used was 2 %. The three-dimensional governing equations were solved with the finite volume method using the k-• turbulence model with Reynolds numbers ranging from 4000 to 7000. The nanofluids used in the compact heat exchangers results in more energy transfer and are more cost-effective than conventional coolants. A CFD model of the mass flowrate of air passing across the tubes of a car radiator was introduced. The airflow was simulated using the commercial software ANSYS 12.1, where the geometry was created in the software SOLIDWORKS, followed by creating both the surface mesh and the volume mesh accordingly. The results were compared and verified according to the known physical situation and existing experimental data. The results serve as a good database for future investigations.

2.1 Outlook

Regarding all these experimental studies of the heat transfer fluid flow may be enhanced when suspended small solid particles less than 100 nm diameter of a metal or non-metallic on fluids with a little percentage of volume fraction. On the other side, noted from all these investigations of numerical studies is to enhance heat transfer in fluid through circular tube and heat exchanger using simulation commercial software. The studies of heat transfer nanofluids in a car radiator are limited. The experimental researches of heat transfer nanofluid in an automotive radiator have been conducted with CuO, Al_2O_3, and Fe_2O_3 with volume concentration not more than 1 % and Reynolds number in the range less than 1000. Likewise, the numerical studies of nanofluid heat transfer in a car radiator were in the laminar flow condition, and volume fractions were less than 2 %.

3 Experimental Work

The heat transfer performance of liquids is limited by their poor thermophysical properties compared with that of solids, which is the primary reason behind adding solid particles less than 100 nm in diameter to a fluid, i.e., to improve the thermal properties of the fluid; this new type of fluid is called a nanofluid. Dispersing solidly metallic or non-metallic materials in a base fluid (liquid), such as water, ethylene glycol, and glycerol, has become an interesting topic in recent years (Buongiorno 2006; Abbasian and Amani 2012; Bozorgan et al. 2012). There are many different applications of thermal fluid systems, including automotive cooling systems. Base fluids, such as water, ethylene glycol, and glycerol, have been used as traditional coolants in automobile radiators for many years; however, these fluids have low thermal conductivities. The low thermal conductivities have thus prompted researchers to search for fluids with higher thermal conductivities than that of conventional coolants. Therefore, nanofluids have been used instead of the commonly used base fluids.

In this chapter, the first part of methodology is the experimental work which contained the preparation of nanofluids and thermal properties measurement, the experimental test rig setup with all devices and also, the data analysis and uncertainty calculations are conducted. Another part is the CFD analysis which included the grid independent test and the simulation results of the heat transfer nanofluid through the flat tube of the radiator.

3.1 Nanofluid Preparation

The VEROS method (Akoh et al. 1978) to prepare nanofluid has been conducted which contained dispersing nanoparticles into base fluids (pure water, EG, and Water/EG). Nanofluids are prepared in the thermal laboratory of mechanical engineering faculty University Malaysia Pahang. Deionized water was prepared in the laboratory by double distillation before using it for the experiments as shown in Fig. 3a. The nanopowders as shown in Fig. 3b have been purchased from the US Research Nanomaterial's, Inc. (NovaScientific Resources (M) Sdn. Bhd). On the other side, the ethylene glycol was already purchased with nanoparticles.

Mechanical stirrers have been applied to be a homogeneous mixture for at least one hour as shown in Fig. 4a. An ultrasonic process has been done for two hours approximately to break up any residual agglomerations as shown in Fig. 4b.

The volumetric ratio of 10 % and 20 % of EG is added to the deionized water to prepare other base fluids (10 %EG-90 %water) and (20 %EG-80 %water). The reason to make these types of base fluids is to find the optimum base fluid has the highest ability of heat transfer enhancement.

(a) Distillation of water (b) the nanopowders

Fig. 3 Base fluid and nanopowders used in the experiment

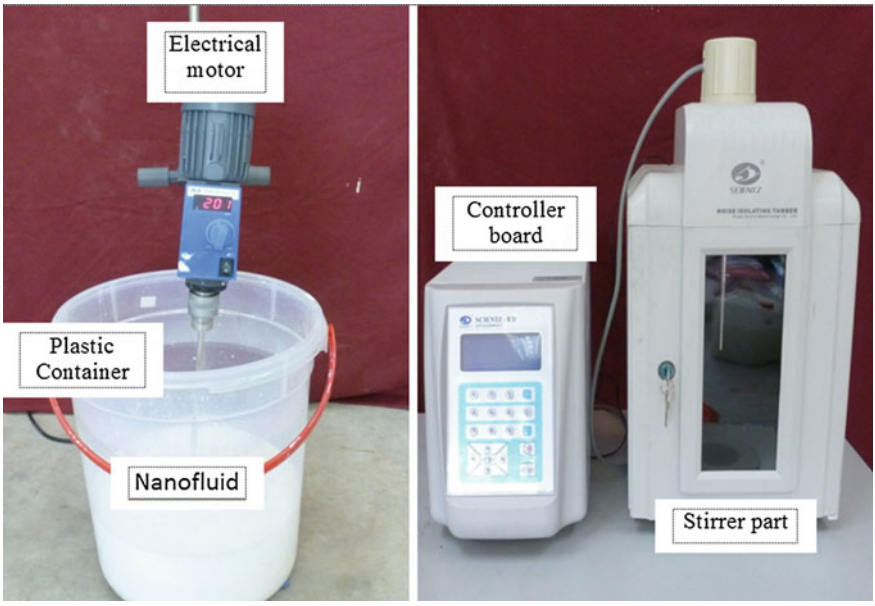

(a) Mechanical stirrer (b) Ultrasonic stirrer

Fig. 4 Stirrers' apparatus

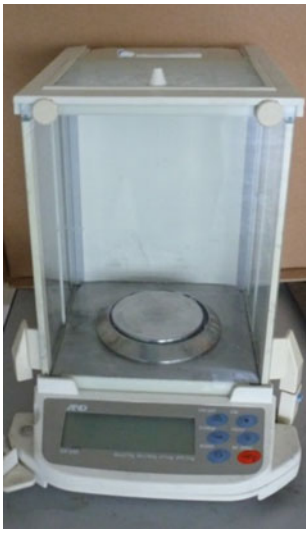

Fig. 5 Laboratory balance

Measured quantities of TiO_2 and SiO_2 nanoparticles were suspended a base fluid (pure water, pure EG, 10 %EG-90 %water, and 20 %EG-80 %water) to obtain mass concentration φ. The mass of nanoparticles (m_p) and base fluid (m_f) has been measured by weighing measurement with accuracy ($\pm 0.0001g$) as shown in Fig. 5.

To find the weight percentage (φ), Eq. (3.1) has been used as:

$$\varphi = \left(\frac{m_p}{m_p + m_f}\right) \times 100 \tag{3.1}$$

To estimate the volume concentration of nanofluid $\emptyset$ depending on nanoparticles density $\left(\rho_p = \frac{m_p}{\rho_p}\right)$ and base fluid density $\left(\rho_f = \frac{m_f}{\rho_f}\right)$ at 25 °C, Eq. (3.2) was used as:

$$\emptyset = \frac{\rho_p}{\rho_p + \rho_f} \tag{3.2}$$

The nanofluid volume concentrations desired in the study undertaken are (1–4) % Table 1.

3.1.1 Experimental Test Rig Setup

The test rig shown in Fig. 6 has been used to measure the friction factor and heat transfer coefficient in the automotive engine radiator. This experimental test rig setup has included:

Table 1 Thermal properties of nanoparticle and base fluids at 25 °C

Materials	Density (Kg/m^3)	Specific heat (J/Kg. °C)	Thermal conductivity (W/m. °C)	Viscosity (Pa. s)
SiO_2	2220	703	1.2	–
TiO_2	4175	692	8.4	–
Pure water	992	4174	0.633	0.00065
EG	1101	2382	0.256	0.0095
10 % EG-90 % Water	1002	4090	0.59	0.00165
20 % EG-80 % water	1006	4024	0.57	0.00188

Source, ASHRAE (2005)

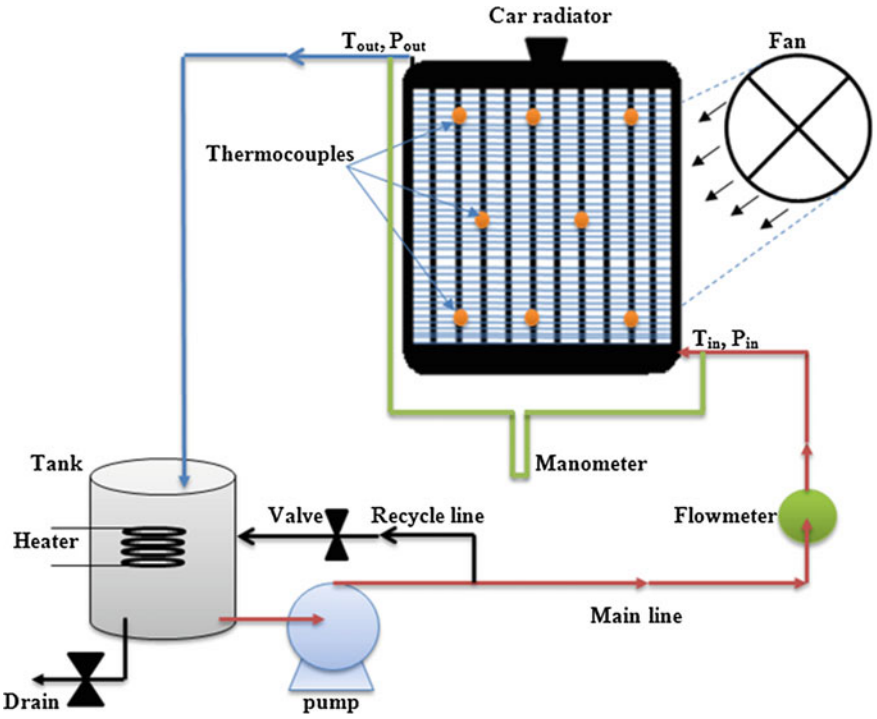

Fig. 6 Experimental test rig setup

The car radiator is shown in Fig. 7 which contained inlet and outlet gap with 0.75*in* and 32 flat tubes with major and minor dimensions as ($D = 9\ mm$) and ($d = 3\ mm$), respectively. Fins plates with 1 mm thickness and brass material have been inherent with the tubes. The equally spaced 1 mm among the fins has been

Fig. 7 Car radiator

fabricated to flow air inside it. The coolant fluid flows through the inlet gap to the 32 flat tubes from the bottom to the top and then exits from the outlet gap of radiator. The air-side fins are flowing horizontally to cool the surface wall.

3.1.2 Experimental Procedure

The nanofluid is directly pumped through the test section of the apparatus. At the first, there was a high vibration in the system till steady state at that time no vibration and flow with keeping quite. To ensure the radiator filling with the fluid, the outlet point should be up to level than radiator level as shown in Fig. 6. The valves have been opened to allow the nanofluid flowing through the pipes and control the velocity of flow. The two-pass flow had been found to allow the pump in the rest and did not press. The apparatus tubing was a major factor in the reliability of the results of the experiments. The first factor that was supposed when looking at the tubing selection was the material of which they were made. Ideally, the material would be chosen to have as little heat transfer resistance as possible. This would help to reduce error as it would help raise the overall heat transfer, and, therefore, that heat transfer would be measured with far higher accuracy. However, in this real-world experimental apparatus, other factors affected the selection. Considering the nanofluids contained solid particles, these particles have a tendency to agglomerate and sediment that would lead to clog in the tubes. This makes it difficult to use metallic tubes, perfect for high heat transfer rates, and suggests that perhaps a rubber or soft plastic tube for more perfect in order to break these clogs loose without affecting the experiment. The abrasiveness of the flowing nanofluid was also considered. This could cause erosion damage to a softer material and would most likely mean that the testing section would regularly have to be replaced if one of these softer materials has been used. Also, a factor that likely has a minimal effect on the convection coefficient but still may need to be considered is a

contact resistance. This is because the solid particles in the nanofluid may experience a resistance due to imperfect contact as occurs in nearly all solid-to-solid heat transfer, and this resistance could vary based on the material that of which the tubing is made. The second factor for tubing has been considered is the tube diameter. This factor had to differ as it helped change flowrate and velocity. Also, the diameter has been employed by the definition of Nusselt number. The difference did not have to be extremely large, but some variation was needed. The final decision on the using tube was based on all of these factors. The tubing used was all plastic at different sizes. The sizes were based on traditional inner diameter standards of a $1/2in$ and $3/4in$. The material was chosen as to resist as much abrasion from the nanoparticles as possible. The sizes were selected to balance the necessary variation with the need to be able to alter the Reynolds Number as many as possible with the pump flowrate restrictions.

The following parameters should measure to determine the heat transfer coefficient at various flow conditions: flowrate, pressure drop, and fluid temperature in and out of the car radiator, the wall temperature of the car radiator, and the heater voltage and current. All data collected have been first handwritten and then copied into Excel so that a hard copy of the data was kept for record. This reduced the risk of errors associated with simply typing raw data into Excel and provided a hard copy of the data to be preserved. Depending on the status of the loop, any number of procedures may be required before collecting data. If starting with a new fluid and cleaning apparatus, the filling procedure must be run to charge the system. If the system were already charged at the start of the test, then only the start-up procedure was run. Once these preliminary steps had been accomplished, the pump and heaters were started to begin collecting data. Each run consisted of the temperature, flowrate, pressure, and heat input data for a minimum of 5 individual process flowrates. It was decided early on that at least five flowrates were necessary for each fluid in order to determine any trends. For all tests, the heating power was held constant, and the process flowrate has been varied. The volumetric flowrate range of 1-5 LPM for water and 3-12 LPM for other base fluids has been tested. Given its poor heat transfer properties, EG could not be run at flowrates below 2 LPM due to overheating and the flow keep it slowly and laminar along experiments. The steady-state operation should be conducted for convective heat transfer coefficient calculations. The system has been taken approximately 20 min to reach steady operating conditions. At the beginning with the lowest flowrate, data were obtained at steady-state conditions. The flowrate was then increased by a small amount, and the system was allowed to return to steady state. For keeping the constant inlet temperature, the voltage regulator should provide the heater with proper voltage and keeping at this point. Then, changing of the voltage will lead to change the inlet temperature. Typically, the system took 15–20 min to return to steady state after the increasing flowrate manner. Once the inlet temperature set point was reached, the data were once again obtained. This procedure was repeated up to the maximum flowrate. The nanofluid volume concentration has been changed then repeating all these procedures.

3.1.3 Experimental Data Analysis

According to Newton's cooling law, the following procedure followed to obtain heat transfer coefficient and corresponding Nusselt number as (Bejan 2004) is as follows:

$$Q_c = hA\Delta T = hA_s(T_b - T_s) \tag{3.7}$$

A_s is the surface area of the tube, and T_b is the bulk temperature

$$T_b = \frac{T_{\text{in}} + T_{\text{out}}}{2} \tag{3.8}$$

(T_{in}, T_{out}) are the inlet and outlet temperatures and T_s is the tube wall temperature which is the mean value of two surface thermocouples as:

$$T_s = \frac{1}{a}\sum_{i=1}^{a} T_i \tag{3.9}$$

And heat transfer rate calculated by:

$$Q_c = \dot{m}C\Delta T = \dot{m}C(T_{\text{in}} - T_{\text{out}}) \tag{3.10}$$

$\dot{m}$ is the mass flowrate which is determined as:

$$\dot{m} = \rho \times \dot{V} \tag{3.11}$$

The electrical power supplied to provide the system with heat by electrical heater has been calculated as:

$$\not{P} = I \times E \tag{3.12}$$

where I and E are the current and the voltages, respectively, have been measured directly from the voltage regular.

The heat rejected (Q_{rej}) outside the system has been calculated as follows:

$$Q_{\text{rej}} = \not{P} - Q_c \tag{3.13}$$

The heat transfer coefficient can be evaluated by collecting Eq. (3.7) and Eq. (3.10):

$$h = \frac{\dot{m}C(T_{in} - T_{out})}{nA_s(T_b - T_s)} \tag{3.14}$$

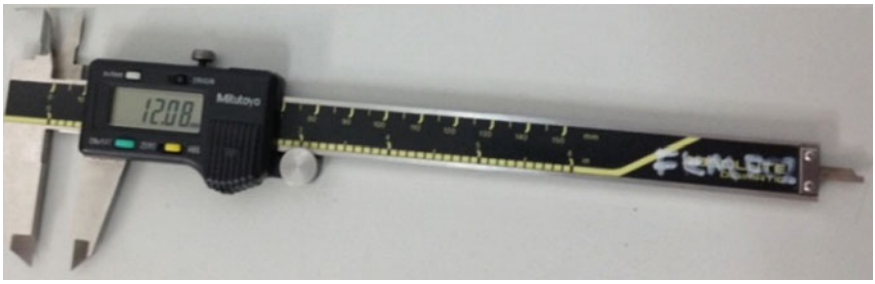

Fig. 8 Digital clipper

where n is the tubes number of the radiator. Then Nusselt number can be also calculated as:

$$Nu = \frac{h \times D_h}{k} \tag{3.15}$$

D_h is the hydraulic diameter of the tube which is estimated by describing the problem undertaken as cylindrical geometry coordinates. Dimensions of the flat tube are major and minor diameters ($D = 9\ mm$, $d = 3\ mm$) have been measured by using digital clipper as shown in Fig. 8. The length (L) and hydraulic diameter (D_h) of the flat tube are 345 and 4.68 mm, respectively. The Reynolds number calculated regarding hydraulic diameter (D_h) is as follows:

$$D_h = \frac{4 \times \left[\frac{\pi}{4} d^2 + (D - d) \times d\right]}{\pi \times d + 2 \times (D - d)} \tag{3.16}$$

Assume all thermal properties have estimated at the bulk temperature of the fluid.

Reynolds number (Re) is determined as:

$$Re = \frac{4\dot{m}}{\pi D_h \mu} \tag{3.17}$$

u is the velocity at inlet radiator which is evaluated from volumetric flowrate $(\dot{V})$ and the cross-sectional area of tube (A_{cross}) as:

$$u = \frac{\dot{V}}{nA_{cross}} \tag{3.18}$$

The friction factor (f) can be calculated depending pressure drop $(\cdot P)$ reading from manometer as:

Table 2 Uncertainty analysis for data measured

Quantity	Uncertainty	Unit
Tube length	±1.5712	mm
Hydraulic diameter	±0.0072	mm
Surface area	±0.7669	mm^2
Cross-sectional area	±0.055	mm^2
Temperature	±0.1	°C
Pressure	±0.133416	N/m^2
Density	±2.0	kg/m^3
Specific heat capacity	±4.0	J/kg.°C
Thermal conductivity	±0.05	W/m.°C
Viscosity	±0.0004	N. s/m^2
Velocity	±0.0087	m/s
Flowrate	±0.5	m^3/s
Power	±0.51	W
Coolant heat transfer	±1.3323	W
Heat transfer rejected	±1.3433	W
Heat transfer coefficient	±5.4225	W/m^2. °C
Nusselt number	±0.22	_
Reynolds number	±3.456	_

$$\Delta P = S \times g \times H \tag{3.19}$$

$$f = \frac{2 \times \Delta P}{\frac{L}{D} \times \rho \times u^2} \tag{3.20}$$

3.1.4 Uncertainty Analysis

The uncertainty analysis has been performed by calculating the measurement error as shown in detail in Appendix B. According to uncertainty analysis described, the error measurement of the parameters is summarized in Table 2. Furthermore, to check the reproducibility of the experiments, some runs were repeated later which proved to be excellent.

4 Result and Discussion

4.1 Outlet Temperature

The outlet temperature after the heat transfer across the radiator has been measured by connecting a thermocouple sensor at the exit point of the test rig as outlined in Chapter 3. In order to consider the influence of the temperature on heat transfer of

the car radiator, different inlet temperatures of the nanofluids have been applied. It is important to mention that from a practical viewpoint for every cooling system, at equal mass flowrate the more reduction in working fluid temperature indicates a better thermal performance of the cooling system Peyghambarzadeh et al. (2011). Figure 9 shows the outlet temperature at the volume flowrate range (1–5) LPM with the range of the inlet temperature (60, 70, and 80 °C). It seems the outlet temperature increases with the increasing of the volume flowrate. Figure 9a indicates the outlet temperature increases by 17 % for TiO_2 suspended to water with increase of volume flowrate at different inlet temperatures. On the other side, at fixed flowrate the outlet temperature decreases by 8 % when the volume fraction increases from 1 to 4 %. Likewise, the pure water appears high outlet temperature as compared to the nanofluid. This behavior refers to the increase of heat transfer across the system when adding solid nanoparticles to the liquid. Figure 9b shows also the outlet temperature increases by 17 % for SiO_2 dispersed to water with increase of volume flowrate at different inlet temperature. It seems the outlet temperature values of SiO_2 nanofluid are lower than the values of TiO_2 nanofluid.

It should be said the SiO_2 nanofluid is better than TiO_2 nanofluid for heat transfer enhancement. Figure 10a illustrates the outlet temperature increases by 11 % for TiO_2 suspended to EG with increase of the volume flowrate from 2 LPM to 12 LPM at different inlet temperatures. Furthermore, at fixed flowrate the outlet temperature decreases by 6 % when the volume fraction increases from 1 % to 4 %. Likewise, the pure EG gives high outlet temperature as compared to the nanofluid. Figure 10b indicates also the outlet temperature increases by 11 % for SiO_2 dispersed to EG with increase of volume flowrate at different inlet temperatures. It observes the outlet temperature values of SiO_2 nanofluid are lower than the values of TiO_2 nanofluid. In the same manner should be said the SiO_2 nanofluid is better than TiO_2 nanofluid for heat transfer enhancement. Figure 11a demonstrates the

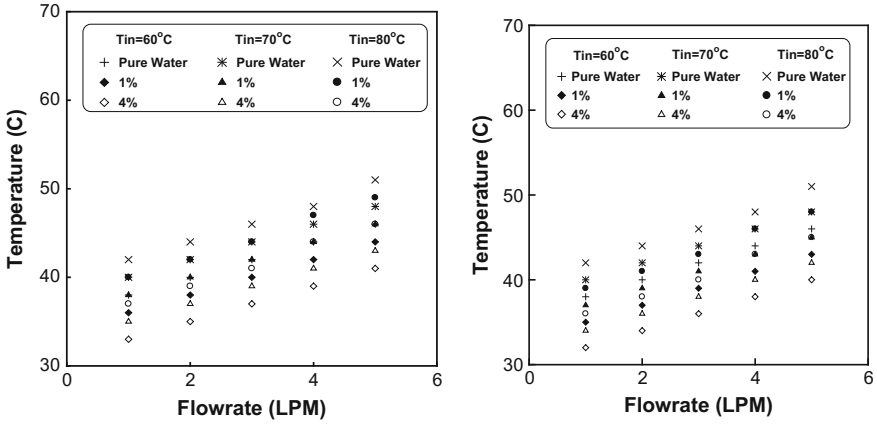

(a) TiO_2-Water (b) SiO_2-Water

Fig. 9 Outlet temperature at different flowrate for nanoparticles suspended to water as a base fluid

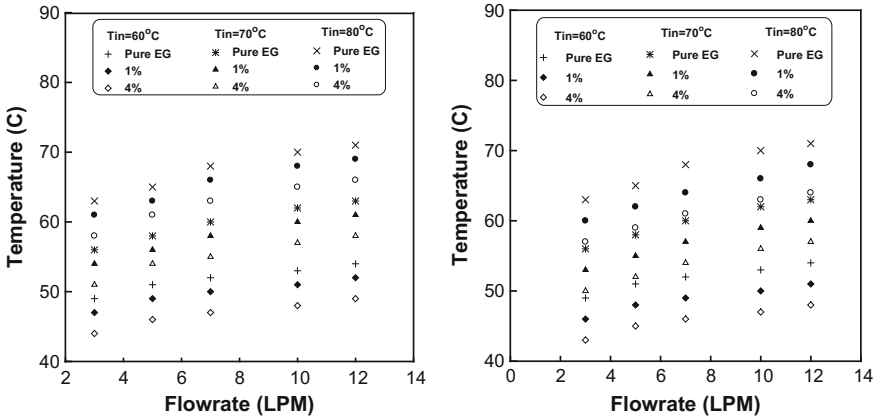

Fig. 10 Outlet temperature at different flowrate for nanoparticles suspended to EG as a base fluid

outlet temperature increases by 10 % for TiO_2 suspended to 10 %EG + 90 %W with increase of the volume flowrate at different inlet temperature. Furthermore, at fixed flowrate the outlet temperature decreases by 6 % when the volume fraction increases from 1 to 4 %. Likewise, the pure 10 %EG + 90 %W gives high outlet temperature as compared to the nanofluid. Figure 11b indicates also the outlet temperature increases by 11 % for SiO_2 dispersed to 10 %EG + 90 %W with increase of volume flowrate at different inlet temperatures. It observes the outlet temperature values of SiO_2 nanofluid are lower than the values of TiO_2 nanofluid. In the same manner should be said the SiO_2 nanofluid is better than TiO_2 nanofluid for heat transfer enhancement.

Figure 12a illustrates the outlet temperature increases by 7 % for TiO_2 suspended to 20 %EG + 80 %W with increase of the volume flowrate at different inlet temperatures. Furthermore, at fixed flowrate the outlet temperature decreases by 7 % when the volume fraction increases from 1 to 4 %. Likewise, the pure 20 % EG + 80 %W gives high outlet temperature as compared to the nanofluid. Figure 12b indicates also the outlet temperature increases by 11 % for SiO_2 dispersed to 20 %EG + 80 %W with increase of volume flowrate at different inlet temperatures. It observes the outlet temperature values of SiO_2 nanofluid are lower than the values of TiO_2 nanofluid. In the same manner should be said the SiO_2 nanofluid is better than TiO_2 nanofluid for heat transfer enhancement.

4.2 Heat Transfer

The heat transfer inside the flat tube of the radiator is represented the coolant heat transfer which is plotted in Fig. 13.

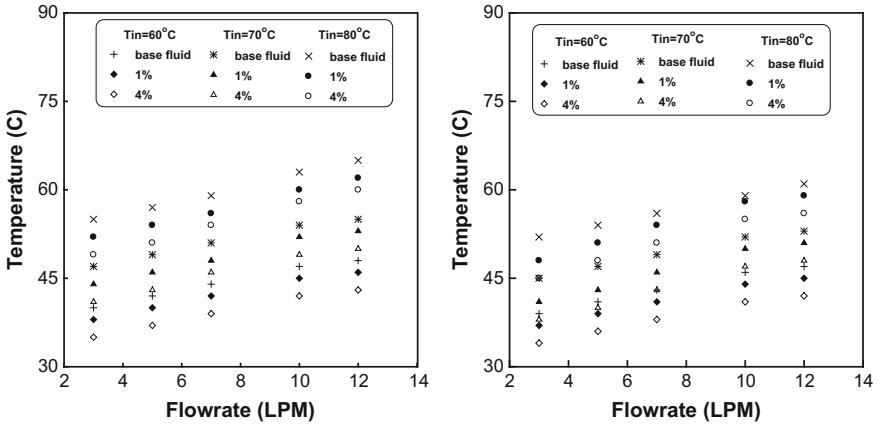

(a) TiO_2-10%EG+90%W (b) SiO_2-10%EG+90%W

Fig. 11 Outlet temperature at different flowrate for nanoparticles suspended to 10 %EG + 90 % W as a base fluid

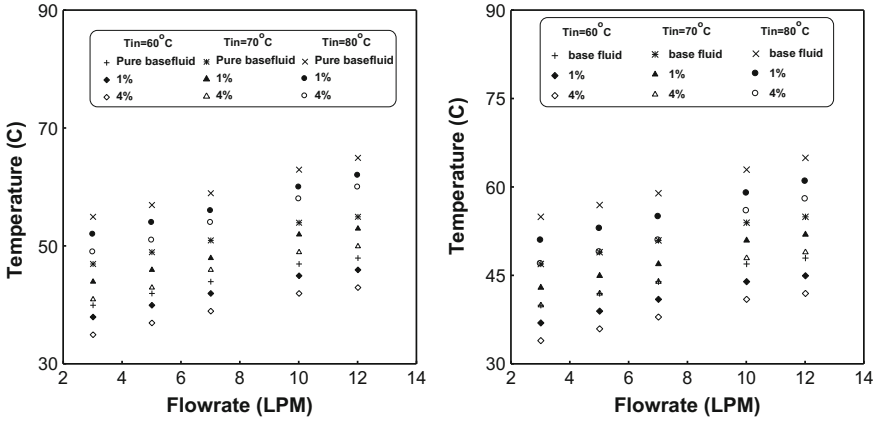

(a) TiO_2-20%EG+80%W (b) SiO_2-20%EG+80%W

Fig. 12 Outlet temperature at different flowrate for nanoparticles suspended to 20 %EG + 80 % W as a base fluid

The coolant heat transfer at the range of the volume flowrate from 1 LPM to 5 LPM for TiO_2 suspended to water is indicated in Fig. 13a. It can be observed the coolant heat transfer increases from 53 to 178 W and 62 to 218 W for 1 and 4 % of TiO_2-water at 60 °C. It can be seen, at 1 LPM volume flowrate the coolant heat transfer increases from 53 W at 60 °C to 89 W at 80 °C. On the other hand, at 5 LPM volume flowrate the coolant heat transfer increases from 178 W at 60 °C to 384 W at 80 °C for 1 % TiO_2-water. This means the increasing percentage of the

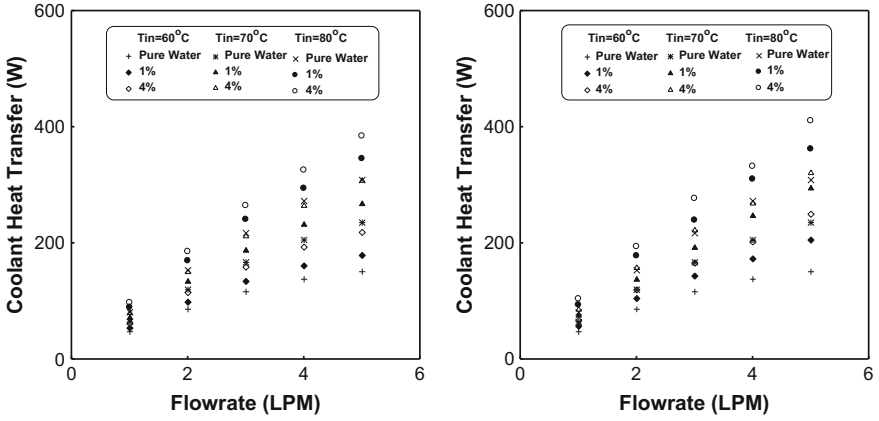

Fig. 13 Coolant heat transfer at different flowrate for nanoparticles suspended to water as a base fluid

coolant heat transfer is 13 % and 75 % at the volume flowrate from 1 LPM to 5 LPM, respectively. Figure 13b shows the coolant heat transfer increases from 56 to 205 W for 1 % SiO_2 suspended in water at 60 °C. However, the increasing of the cooling heat transfer is from 66 to 249 W for 4 % volume fraction of SiO_2-water. Likewise, at 80 °C the coolant heat transfer increases from 93 to 361 W. Figure 14a shows the coolant heat transfer at the range of the volume flowrate from 3 LPM to 12 LPM for TiO_2 suspended to EG. It can be seen the coolant heat transfer increases from 52 to 128 W and 70 to 160 W for 1 % and 4 % of TiO_2-water at 60 °C. It can be noted at 3 LPM volume flowrate the coolant heat transfer increases from 52 W at 60 °C to 75 W at 80 °C.

On the other hand, at 12 LPM volume flowrate the coolant heat transfer increases from 128 W at 60 °C to 175 W at 80 °C for 1 % TiO_2-water. This means the increasing percentage of the coolant heat transfer is 13 and 75 % at the volume flowrate from 1 LPM to 5 LPM, respectively. Figure 14b shows the coolant heat transfer increases from 62 to 159 W for 1 % SiO_2 suspended in water at 60 °C. However, the increasing of the cooling heat transfer is from 75 to 214 W for 4 % volume fraction of SiO_2-water. Likewise, at 80 °C the coolant heat transfer increases from 88 to 211 W. Figure 15a shows the coolant heat transfer at the range of the volume flowrate from 3 LPM to 12 LPM for TiO_2 suspended 10 % EG + 90 %W. It can be seen the coolant heat transfer increases from 143 to 366 W and 165 to 450 W for 1 % and 4 % of TiO_2-10 %EG + 90 %W at 60 °C.

It can be noted at 3 LPM volume flowrate the coolant heat transfer increases from 143 W at 60 °C to 194 W at 80 °C. On the other hand, at 12 LPM volume flowrate the coolant heat transfer increases from 366 W at 60 °C to 518 W at 80 °C for 1 % TiO_2-10 %EG + 90 %W. This means the increasing percentage of the coolant heat transfer is 25 and 40 % at the volume flowrate from 3 LPM to 12 LPM,

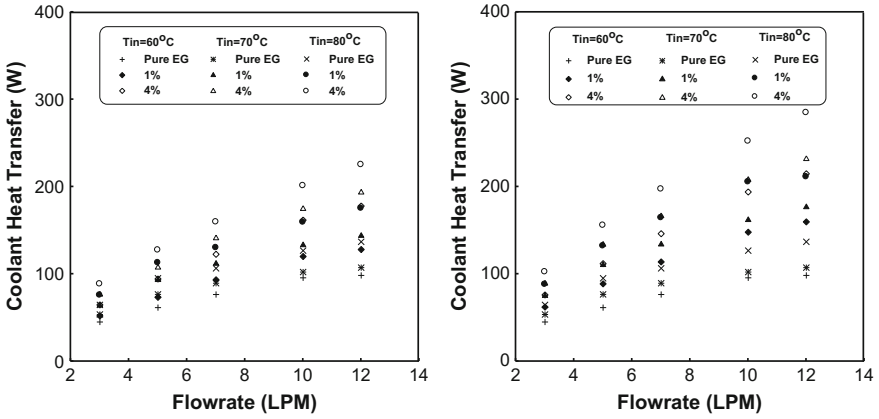

(a) TiO_2-EG (b) SiO_2-EG

Fig. 14 Coolant heat transfer at different flowrate for nanoparticles suspended to water as a base fluid

respectively. Figure 15b shows the coolant heat transfer increases from 158 to 413 W for 1 % SiO_2 suspended in 10 %EG + 90 %W at 60 °C. However, the increasing of the cooling heat transfer is from 183 to 507 W for 4 % volume fraction of SiO_2-10 %EG + 90 %W. Likewise, at 80 °C the coolant heat transfer increases from 218 to 574 W.

Figure 16a indicates the coolant heat transfer at the range of the volume flowrate from 3 LPM to 12 LPM for TiO_2 suspended to 20 %EG + 80 %W. It can be seen the coolant heat transfer increases from 143 to 365 W and 167 to 455 W for 1 %

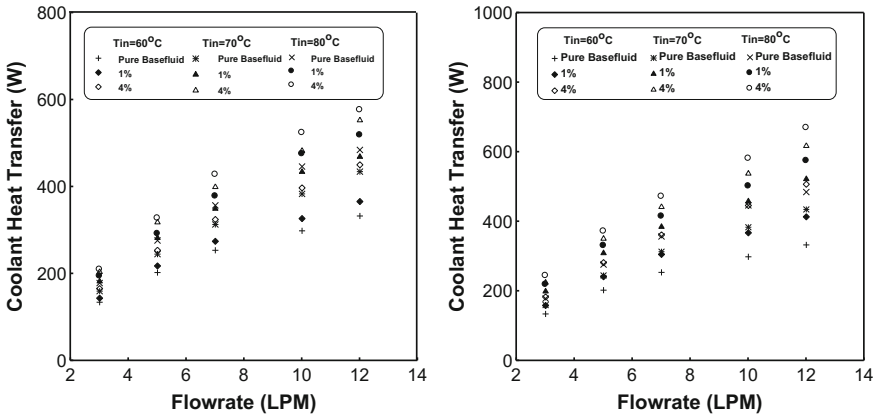

(a) TiO_2-10%EG+90%W (b) SiO_2-10%EG+90%W

Fig. 15 Coolant heat transfer at different flowrate for nanoparticles suspended to 10 % EG + 90 %W as a base fluid

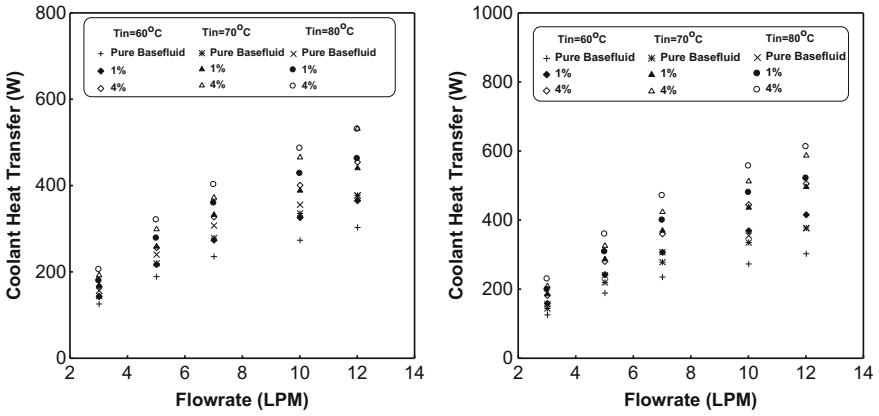

Fig. 16 Coolant heat transfer at different flowrate for nanoparticles suspended to 20 % EG + 80 %W as a base fluid

and 4 % of TiO_2-20 %EG + 80 %W at 60 °C. It can be noted at 3 LPM volume flowrate the coolant heat transfer increases from 143 W at 60 °C to 179 W at 80 °C. On the other hand, at 12 LPM volume flowrate the coolant heat transfer increases from 365 W at 60 °C to 462 W at 80 °C for 1 % TiO_2-20 %EG + 80 % W. This means the increasing percentage of the coolant heat transfer is 51 and 57 % at the volume flowrate from 3 LPM to 12 LPM, respectively.

Figure 16b shows the coolant heat transfer increases from 159 to 416 W for 1 % SiO_2 suspended in 20 %EG + 80 %W at 60 °C. However, the increasing of the cooling heat transfer is from 182 to 506 W for 4 % volume fraction of SiO_2-20 % EG + 80 %W. Likewise, at 80 °C the coolant heat transfer increases from 199 to 521 W.

4.3 Heat Rejected

The heat leaved the radiator from the air side is now the heat rejected. Figures 17, 18, 19, and 20 show the heat rejected from the system at different volume flowrate. It can be seen the effect of the volume concentration and the inlet temperature on the heat rejected. Figure 17a indicates the heat rejected decreases from 646 W and 637 W to 521 W and 480 w for both 1 % and 4 % TiO_2-water from 1 LPM to 5 LPM at 60 °C. It seems the increasing in the inlet temperature caused to decrease in the heat rejected by 32 %. However, the increase in the volume fraction is due to decrease in the heat rejected by 4 %. Figure 17b shows the heat rejected decreases from 620 W and 598 W to 493 W and 450 W for both 1 and 4 % SiO_2-water from 1 LPM to 5 LPM at 60 °C. It seems the increasing in the inlet temperature caused to

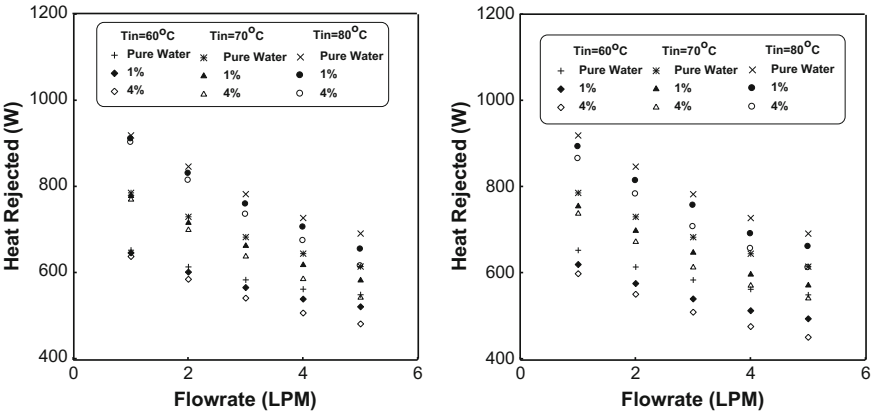

(a) TiO_2-Water (b) SiO_2-Water

Fig. 17 Heat rejected at different flowrate for the nanoparticles suspended to water

decrease in the heat rejected by 31 %. However, the increase in the volume fraction is due to decrease in the heat rejected by 3 %.

Figure 18a illustrates the heat rejected decreases from 647 W and 35 W to 571 W and 522 W for both 1 and 4 % TiO_2-EG from 3 LPM to 12 LPM at 60 °C. It seems the increasing in the inlet temperature caused to decrease in the heat rejected by 31 %. However, the increase in the volume fraction is due to decrease in the heat rejected by 3 %. Figure 18b shows the heat rejected decreases from 612 W and 598 W to 518 W and 465 w for both 1 and 4 % SiO_2-EG from 3 LPM to 12 LPM at 60 °C. It seems the increasing in the inlet temperature due to decrease in the heat rejected by 32 %. However, the increase in the volume fraction is due to decrease in the heat rejected by 4 %. Figure 19a indicates the heat rejected decreases from 556 W and 534 W to 333 W and 249 w for both 1 and 4 % TiO_2 suspended to 10 %EG + 90 %W from 3 LPM to 12 LPM at 60 °C. It seems the increasing in the inlet temperature caused to decrease in the heat rejected by 32.5 %. However, the increase in the volume fraction is due to decrease in the heat rejected by 4 %.

Figure 19b indicates the heat rejected decreases from 538 W and 508 W to 300 W and 209 w for both 1 and 4 % SiO_2 suspended to 10 %EG + 90 %W from 3 LPM to 12 LPM at 60 °C. It seems the increasing in the inlet temperature caused to decrease in the heat rejected by 33.5 %. However, the increase in the volume fraction is due to decrease in the heat rejected by 5 %.

Figure 20a indicates the heat rejected decreases from 556 W and 532 W to 334 W and 244 w for both 1 and 4 % TiO_2 dispersed to 20 %EG + 80 %W from 3 LPM to 12 LPM at 60 °C. It appears the increasing in the inlet temperature caused

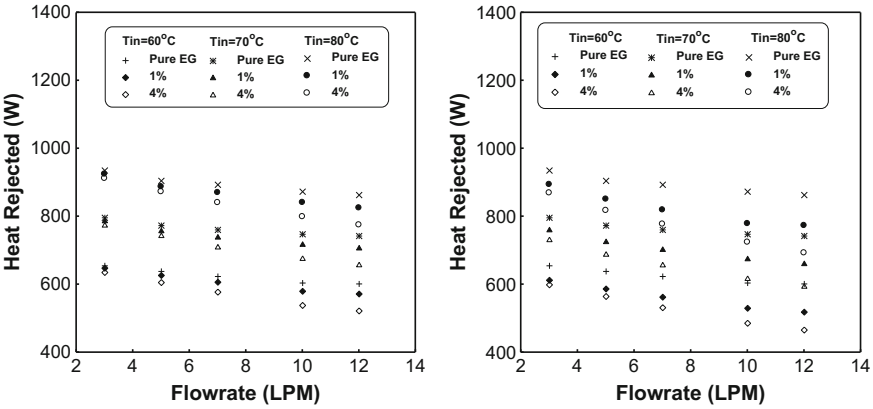

(a) TiO_2-EG (b) SiO_2-EG

Fig. 18 Heat rejected at different flowrate for the nanoparticles suspended to EG

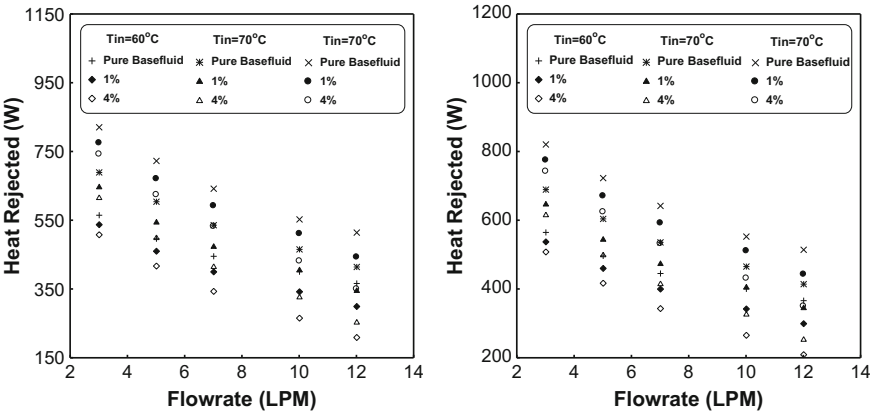

(a) TiO_2-10%EG+90%W (b) SiO_2-10%EG+90%W

Fig. 19 Heat rejected at different flowrate for the nanoparticles suspended to 10 %EG + 90 %W

to decrease in the heat rejected by 35 %. However, the increase in the volume fraction is due to decrease in the heat rejected by 5 %. Figure 20b indicates the heat rejected decreases from 537 and 509 W to 297 and 220 W for both 1 and 4 % SiO_2 dispersed to 20 %EG + 80 %W from 3 LPM to 12 LPM at 60 °C. It appears the increasing in the inlet temperature caused to decrease in the heat rejected by 33 %. However, the increase in the volume fraction is due to decrease in the heat rejected by 4 %.

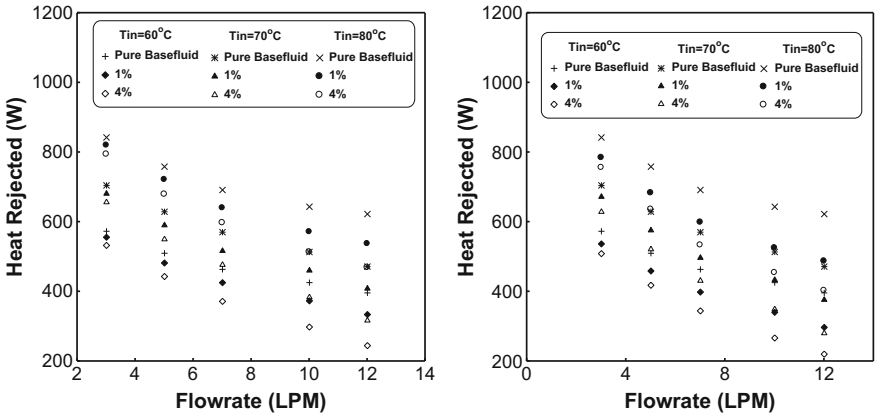

(a) TiO_2-20%EG+80%W (b) SiO_2-20%EG+80%W

Fig. 20 Heat rejected at different flowrate for the nanoparticles suspended to 20 %EG + 80 %W

4.4 Heat Transfer Enhancement

The percentage of heat transfer enhancement depending on nanofluid volume concentration and inlet temperature to the radiator has been calculated by Eq (4.10). Figures 21 and 22 show the heat transfer enhancement depending on the nanofluid volume fraction and the inlet temperature, respectively.

It seems that the heat transfer enhancement increases with increasing of nanofluid volume concentration and inlet temperature, respectively. The values of heat transfer enhancement are from 12 to 31 % for TiO_2 nanofluid volume concentration from 1 to 4 % while the values of heat transfer enhancement are from 18 to 42 % for SiO_2 nanofluid volume concentration from 1 to 4 %. Likewise, the values of heat transfer enhancement are from 8 to 20 % for TiO_2 nanofluid at the inlet temperature from 60 to 80 °C, whereas the values of heat transfer enhancement are from 12 to 22 % for TiO_2 nanofluid at the inlet temperature from 60 °C to 80 °C. This refers to the nanofluid volume concentration affected more than the inlet temperature on the heat transfer enhancement, but significantly of using all of them. It can be seen the comparison of Nusselt number among nanofluids and base fluids at laminar flow. It appears that the nanofluid has higher values of the heat transfer enhancement than base fluid. It seems that the heat transfer enhancement for SiO_2 nanofluid is better than TiO_2 nanofluid by 80 %. In addition, the base fluid (20 % EG + 80 %W) has given higher values of the heat transfer than water by 60 %. On the other hand, the nanoparticles suspended to the base fluid (20 %EG + 80 %W) is the best type of the nanofluids due to the highest values of the heat transfer enhancement followed by 10 %EG + 90 %W then EG and finally water.

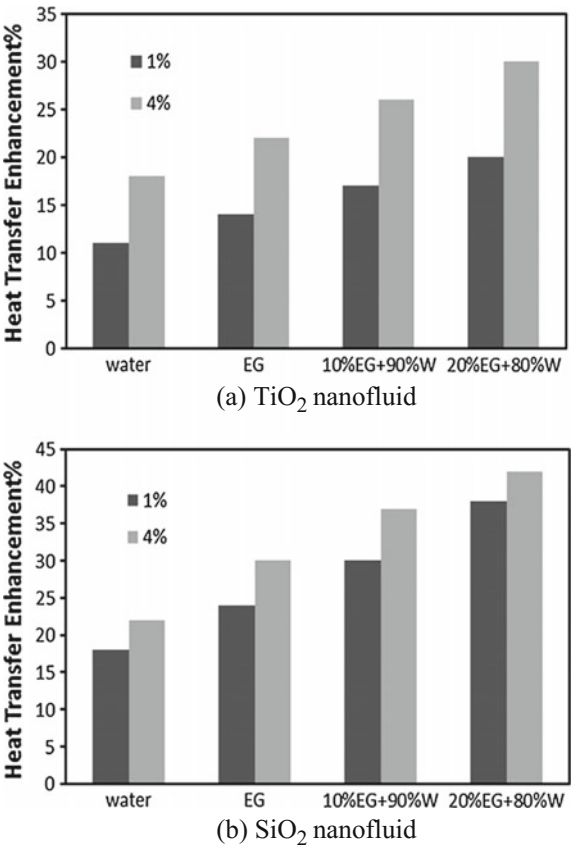

Fig. 21 Effect of nanofluid volume fraction on the heat transfer enhancement

5 Conclusions and Recommendations

This chapter focuses on the conclusions derived from the results of the experiment and recommends further procedure and experiments which could have been done if limitations in experimental instruments and time were not a factor to conduct this research. In addition, CFD simulations have been successfully applied to solve the steady, laminar flow of a Newtonian fluid in the automotive cooling system. The results of this study have led to draw the following conclusions.

1. The density and specific heat capacity of the nanofluids and base fluids are studied. It seems significant increasing of the density with the increasing of volume fraction and decreasing of the temperature. On the other hand, there are significant decreasing of the specific heat capacity with the increasing of volume fraction and decreasing of the temperature.
2. There is a significant enhancement of the thermal conductivity measurement data with increase of both the volume fraction and the temperature.

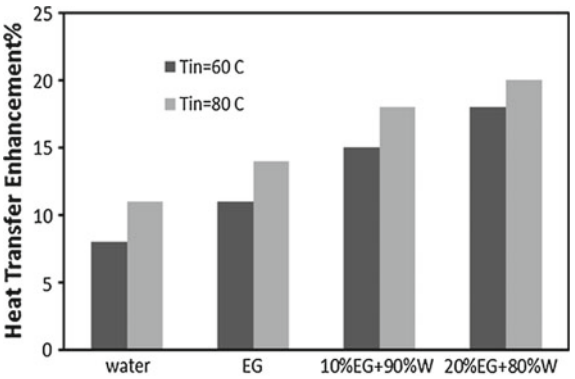

(a) TiO_2 nanofluid

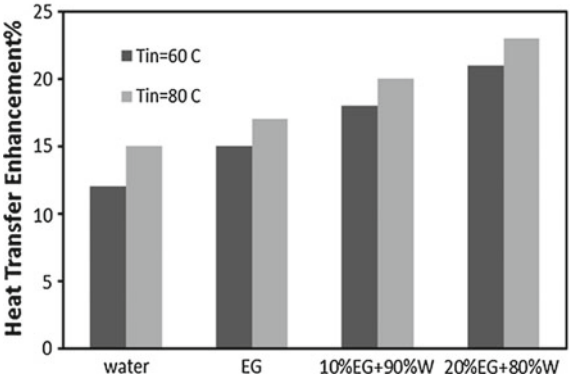

(b) SiO_2 nanofluid

Fig. 22 Effect of the inlet temperature on the heat transfer enhancement

3. The viscosity data measured decrease with the increasing of both the volume fraction and the temperature.
4. The friction factor decreases with the increase of Reynolds number and increases with the increase of the inlet temperature.
5. The heat transfer coefficient increases with the increase of both the volume fraction and the inlet temperature.
6. The outlet temperature increases with the increasing of the volume flowrate and the inlet temperature but decreases with the increase of the volume fraction.
7. The coolant heat transfer inside the flat tube increases with the increasing of the volume flowrate, the volume fraction, and the inlet temperature.
8. The heat rejected outside the cooling system decreases with the increasing of the volume flowrate and the volume fraction but increases with the increase of the inlet temperature.
9. Empirical correlations of the friction factor as a function of Reynolds number, Prandtl number, and the volume fraction for the nanofluids under the laminar

flow have been developed based on the experimental data. The deviations between correlations and the experimental data are not more than 3 %.

10. Empirical correlations of the Nusselt number as a function of Reynolds number, Prandtl number, and the volume fraction for the nanofluids under the laminar flow have been developed based on the experimental data. The deviations between correlations and the experimental data are not more than 6 %.
11. The aim of this thesis has been met to fabricate and build equipment that could be used to the nanoparticles suspended to base fluid replacement heat transfer water for automotive cooling system.

References

Abbasian, A. A., & Amani, J. (2012). Experimental study on the effect of TiO_2/water nanofluid on heat transfer and pressure drop. *Experimental Thermal and Fluid Science, 44*, 520–533.

Abdelrahman, M., Fumeaux, P., & Suter, P. (1979). Study of solid-gas-suspensions used for direct absorption of concentrated solar radiation. *Solar Energy, 22*(1), 45–48.

Ahuja, A. S. (1975). Augmentation of heat transport in laminar flow of polystyrene suspensions. *Journal of Applied Physics, 46*(8), 3408–3416.

Akoh, H., Tsukasaki, Y., Yaysuya, S., & Tasaki, A. (1978). Magnetic properties of ferromagnetic ultrafine particles prepared by vacuum evaporation on running oil substrate. *Journal of Crystal Growth, 45*, 495–500.

Andrew, L. T. (2008). Cooling system analysis, University of New South Wales at the Australian Defence Force Academy, Final Thesis Report.

ASHRAE. (2005). ASHRAE handbook: Fundamentals. *American Society of Heating, Refrigerating, and Air Conditioning Engineers*.

Bejan, A. (2004). *Convection heat transfer*. New York: John Wiley and Sons Inc.

Bozorgan, N., Krishnakumar, K., & Bozorgan, N. (2012). Numerical study on application of CuO-water nanofluid in automotive diesel engine radiator. *Modern Mechanical Engineering., 2*, 130–136.

Buongiorno, J. (2006). Convective transport in nanofluids. *Journal of Heat Transfer, 128*, 240–250.

Das, S. K., Choi, S. U. S., & Yu, W. (2007). *Nanofluids Science and Technology*. John Wiley and Sons, Inc.

Transparent Carbon Nanotubes (CNTs) as Antireflection and Self-cleaning Solar Cell Coating

Morteza Khalaji Assadi and Hengameh Hanaei

Abstract Carbon nanotubes have fascinating chemical and physical properties as indicated by graphite and diamond characteristics, and the reason is their individual atomic structure. They have acquired critical achievements in various fields such as materials, electronic devices, energy storage, separation, and sensors. Recently, antireflective coatings with self-cleaning properties attract critical consideration for their theoretical characteristics and their wide-ranging applications. In this chapter, the benefits of using CNTs as an antireflection and self-cleaning thin coating layer have been discussed to improve mechanical and electrical behavior of solar cells. Transfer-matrix method (TMM) and finite-difference time-domain (FDTD) method were studied as most suitable technique for thin films.

Keywords Solar cells · Carbon nanotube · Antireflection

1 Introduction

Solar energy plays an important role as a vital type of renewable energy, owing to its inexhaustible nature, environmental friendliness, and the potential for power conversion efficiency of solar energy harvesting devices (Hyo Jin Gwon et al. 2014; Dincer 2000). Enhancing the power conversion efficiency is an essential research subject in the manufacture of photovoltaic (PV) advances, as it makes them more cost-competitive compare to traditional sources of energy (Hyo Jin Gwon et al. 2014; Ye et al. 2013; Raut et al. 2011).

Solar cells with heterojunction arrangements incorporating carbon materials have generated a lot of enthusiasm in experimental essentials and great applications in different innovative optoelectronic devices, e.g., photovoltaic solar cells (Zhu et al. 2009).

M.K. Assadi · H. Hanaei (✉)
Mechanical Engineering Department, Universiti Teknologi PETRONAS, 32610 Bandar Seri Iskandar, Perak Darul Ridzuan, Malaysia
e-mail: Hengameh_Hanaei@yahoo.com

K. Viswanatha Sharma and N. Hisham B Hamid (eds.),
Engineering Applications of Nanotechnology, Topics in Mining, Metallurgy and Materials Engineering, DOI 10.1007/978-3-319-29761-3_4

There are many reports that have investigated to improve efficiency of solar cells with different contents, especially transparent conductive films (TCFs) such as CNTs, graphene, and semiconducting polymers that can be conveniently deposited on commercial Si wafers (Shi et al. 2012). Numerous experiments predicted to new advances were related to photovoltaic cells with the intention of expanding the enthusiastic yields of such environmentally friendly energy generation tools.

However, there is a need to produce economical optical coatings to permit the maximum solar emission to achieve semiconductor intersection. Applying an antireflective layer, with an advanced refractive index and thickness to cover device, can mostly eliminate this issue (Mathew et al. 2014; Benzekkour et al. 2009). Mostly, the current coatings have problem for stability in water, and they have higher adsorption of contaminants from the outdoor environment; therefore, problem in light trapping will be created by decreasing of efficiency in solar cells (Faustini et al. 2010).

To solve the issues and increase efficiency, thin-film coating should be used with wide spectrum of light trapping ranging from visible to near-infrared wavelengths; the existence of reachable pores in the nanometer range helped for the adsorption of contaminations from the environment. This is one of the important issues, and it leads to higher antireflection layer refractive index. Water uptake can be significantly decreased by making the thin film's pores, hydrophobic (Faustini et al. 2010; Garnett and Yang 2010).

Because of the incredible mechanical, electrical, and thermal properties and substance steadiness of CNTs, they have been involved in much research through the previous decades (Li et al. 2013a). In the solar energy area, it is conceivable to utilize CNT films as transparent electronic materials and to utilize nanotube composites for solar cell applications. In addition, carbon nanomaterials could be used to deliver conductive ink for printed solar cells. As a rule, an alternate application in the energy division is coatings for wind turbine razor sharp edges (Ralph Seitz et al. 2012). CNTs are a promising novel of innovative materials. Carbon is known as the most fascinating element that exists in nature as it has a wide range of properties due to how its particles are organized (Wei et al. 2008).

Figure 1 shows a macrograph of CNTs in the laboratory. The structure of CNTs is different with graphite or diamond, and CNTs have metallic or semiconductor arrangement (Kamat 2006). CNTs are an allotrope of carbon with appearance in the form of hollow cylinders composed of rolled-up sheets of graphene. The strong interatomic bonds will increase the mechanical properties of a solid. The covalent bonding of carbon–carbon sp^2 is an exceptionally solid bonding. As an aftereffect of this bond, carbon nanotubes grow high stiffness. Similarly, carbon nanotubes have the most astounding Young's modulus, tensile strength, and axial strength (Donaldson et al. 2006; Chee Howe See 2007; Chee Howe See et al. 2008; Seung Yong Son et al. 2008; Belin and Epron 2005).

Researcher's reports showed that mechanical properties of CNTs are divided into two groups, and this is related to the diameter of carbon nanotubes. CNTs can be single-walled nanotubes (SWNTs) or multiwalled nanotubes (MWNTs) Fig. 2. In SWNTs, it is anticipated that the Young's modulus is free of tube chirality.

Fig. 1 Macrograph of CNTs (Hengameh Hanaei et al. 2013)

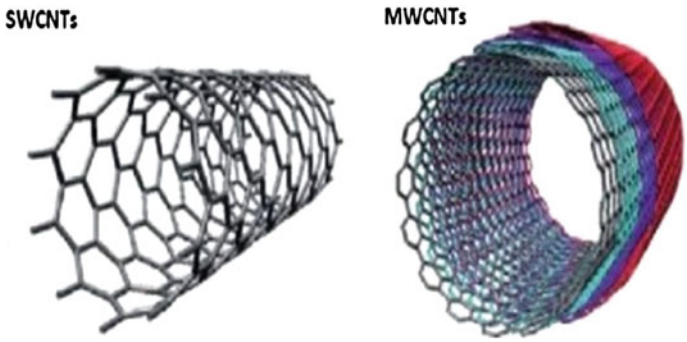

Fig. 2 Example of schematic micrographs for SWNT (*left*) and MWNT (*right*)

A smaller diameter brings a smaller Young's modulus. A few studies reported that the Young's modulus of MWNTs is higher than SWNTs (Danafar et al. 2009, 2011). Electrical properties of carbon nanotubes have been fascinating researchers for many years. Theoretical and experimental results show that carbon nanotubes can create an electric current maximum 1000 times higher than that of copper wires. Contingent upon diameter and chirality of CNTs, nanotubes have conducting or semiconducting behavior (Philip and Collins 2000; Avouris 2002). The high aspect ratio and small dimension of CNTs make them suitable for electronic properties. The armchair structure of CNTs is metallic, but the other two configurations, chiral and zigzag CNTs, can be either metallic or semiconducting (Popov 2004).

2 Photovoltaic Properties of Carbon Nanotubes

The CNTs' extraordinary properties, such as its lightweight, excellent mechanical strength, three-dimensional flexibility, and outstanding electrocatalytic property, can improve the performance of solar cells (Yan et al. 2013; Angmo et al. 2012). One of the recent photovoltaic solar cells that have been introduced to use carbon nanotubes in photocurrent generation is nanotube–silicon heterojunction (NSH). It is similar to a single intersection crystalline silicon solar cell, but the emitter layer is replaced by a thin film of SWNTs or MWNT. This is especially demanding for SWNT as opposed to MWNT, meanwhile SWCNTs are significantly more sensitive to catalyst structure and carbon loading than the MWCNTs. Sometimes, compound adjustment of the nanotube surface has been discovered to be essential to achieve a surface with stable superhydrophobicity. Therefore, many researchers have emphasized that MWNT appoints to the fascinating possibility of hydrophobicity when fluctuating parameters such as ionic strength, nature of the electrolyte, or pH of the water droplet. Additionally, it was observed that the droplet's behavior can be changed from superhydrophobic to hydrophilic by utilization of an electric field. It will show significant changes in the hydrophobicity of SWCNT microstructures of various structures (Kamat 2006).

The unprecedented inherent properties of a SWNT have been the subject of broad considerations. SWCNTs possess excellent electrical properties (SWCNTs are naturally p-type), and we mix it with n-type semiconductor like silicon, and then, we can create a P-N junction solar cells. SWCNT is suitable for solar application due to its chemical stability, hydrophobicity and strongly absorption (visible and near-infrared) spectrum of sunlight. In numerous applications, the organization of SWCNT at the microscale is the variable that decides the execution of the nanotube-based devices, such as nanosensors, nanocontrol, and microfluidic gadgets. Extensive efforts have been devoted to creating synthesized routines for developing SWCNT specifically on substrates with particular arrangements, such as vertically oriented forests (Li et al. 2013a, b; Cui et al. 2014).

3 Antireflection and Self-cleaning Coatings

Transparent surface coatings with suitable optical properties can suppress the reflection of substrates. Such coatings are typically called antireflective coatings (ARCs). There exist numerous antireflective surfaces in nature. Antireflection innovation has been generally utilized as a part of high-accuracy optical segments, solar cells, flat-panel displays, and light radiating diode lighting to expand the transmittance of incident light (Verma et al. 2011; Wan et al. 2010; Zhang and Yang 2010). For solar cells, because of the reflection at the air/glass interface of the bundling glass and dissipation due to accumulated dust on outdoor panels, some pieces of episode vitality on solar-powered modules are lost. On the one hand, ARC

on the glass can help ease reflection in systems; on the other hand, the self-cleaning properties can, to some extent, solve the dust accumulation problem (Verma et al. 2011). Roughness is important to minimize reflection on surfaces.

Nowadays, it is demonstrated that the efficiency of silicon wafers can be increased with high-power conversion efficiency using CNTs, graphene, or conducting polymers (Shi et al. 2012). Besides these excellent optical properties, the ARC arrays also exhibit self-cleaning capability because of the high fraction of air trapped between arrays (Sun et al. 2005; Li and Yang 2010). It is a common knowledge that smooth surfaces shine more than rough ones. It contains the very basic idea of antireflection that roughness is necessary to reduce reflection of surfaces. Therefore, many materials with micro-/nanostructure are perspective to fabricate ARC, including silicon, silica, titania, zirconia, zinc oxide, cobalt oxide, tin oxide, carbon, and polyethylene terephthalate (PET), polystyrene (PS), and gallium nitride (Xiong et al. 2010; Yongjin Wang et al. 2010; Liu et al. 2008; Zhu et al. 2006; Li et al. 2009; Yao and He 2014).

Wettability is an important property of a solid surface, and contact angle (θ) has been commonly used to characterize the surface wettability. Young's equation has predicted the suitable contact angle of solution for optimizing the smooth and homogeneous surface. Theoretical works for contact angle of a realistic solid surface were done by Wenzel and Cassie–Baxter (Yao and He 2014; Cai and Qi 2015), in addition Wenzel's equation (Cai and Qi 2015) developed by Wenzel. The next equation is Cassie–Baxter equation (Yao and He 2014; Cai and Qi 2015). The Cassie–Baxter state considers that under some roughness conditions, air bubbles may be trapped when $\theta > 90$. In this case, the liquid–surface interface actually consists of two phases, i.e., the liquid–solid interface and the liquid–vapor interface, respectively. Therefore, the apparent contact angle can be calculated by total amount of all the elements in various phases.

4 Modeling and Simulation Approach for Nanolayer

In this paper, the modeling of antireflective coating using nanomaterial will be reviewed. For the modeling of antireflective nanostructure, researchers have reported several methods; however, the most attractive and common methods which are suitable for thin films are transfer-matrix method (TMM) and finite-difference time-domain (FDTD) method. Each of these methods has their own advantages and drawbacks. Maxwell's equation and its mathematical explanation have so many advantages; for instance, time-based solution such as FDTD computes reflectance for numerous wavelengths of incident light. Diagnostic methodology answers for Maxwell's equation such as TMM are suitable for extremely basic thin films. One approach to make a cost-effective solar cell is diminishing light reflection at surface

and interfaces. It is reported that TMM is fitted out for representing the geometry of subwavelength structures.

In solar cells, optimizing and improving optical properties of material can be achieved with the optimum thickness of thin film.

4.1 Finite-Difference Time-Domain (FDTD) Method

Finite-difference time-domain (FDTD) method solves Maxwell's equations in the time domain using finite-difference approximations. Being a time-domain method, FDTD is more intuitive than other techniques and works by creating a "movie" of the fields flowing through a device. The benefits of FDTD method (such as its excellent large-scale simulations, easily parallelized, excellent broadband and transient simulations, accurate, robust, and its maturity) make it an incredible method.

In addition, sources of error are well understood and it is a proven method in many fields. The Faraday's and Ampere's laws are used for FDTD method, and also, electric field (E), the electric displacement field (D), the magnetic field (B), and the auxiliary magnetic field (H) are used. These four equations are used to derive Maxwell's curl equations as shown in Fig. 3a the position of each field H and E. Figure 3b also shows the arrangement to approximate Maxwell's curl equations.

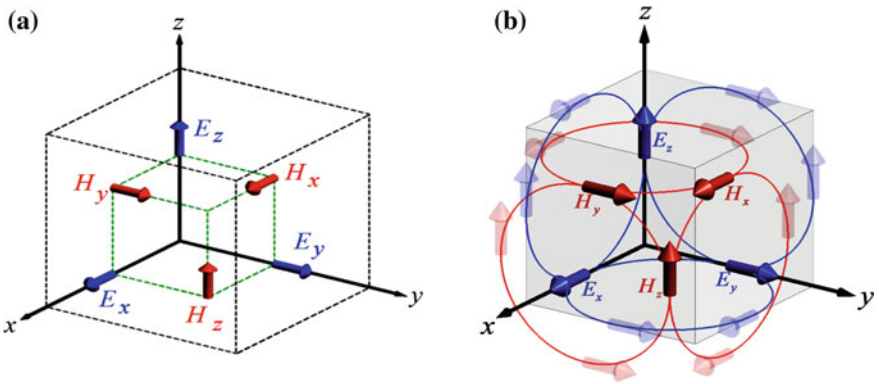

Fig. 3 **a** The position of each field component within the grid cells and **b** elegant arrangement to approximate Maxwell's curl equations

4.1.1 Theory of FDTD

The FDTD is common solution which has been used for electromagnetic problems. The FDTD method discretizes Maxwell's equations by replacing derivatives with their finite-difference approximations, directly in the time domain (Gizem Toroğlu 2014). In this chapter, we are talking about simple one-dimensional method. Maxwell's equations in such an environment are characterized with three parameters [the permittivity (ε), permeability (μ), and conductivity (σ)]. Maxwell's equations can be written as follows:

$$\nabla \times \vec{E} = -\mu \frac{\partial \vec{H}}{\partial t} \rightarrow \frac{\partial \vec{H}}{\partial t} = -\frac{1}{\mu} \nabla \times \vec{E} \tag{1}$$

$$\nabla \times \vec{H} = \varepsilon \frac{\partial \vec{E}}{\partial t} \rightarrow \frac{\partial \vec{E}}{\partial t} = \frac{1}{\varepsilon} \nabla \times \vec{H} \tag{2}$$

The FDTD equations can be derived from (1) and (2) which is obtained from finite-difference approximations:

$$\frac{\vec{H}\left(t + \frac{\Delta t}{2}\right)}{\Delta t} = -\frac{1}{\mu} \nabla \times \vec{E}(t) \tag{3}$$

$$\frac{\vec{E}\left(t + \frac{\Delta t}{2}\right) - \vec{E}(t)}{\Delta t} = \frac{1}{\varepsilon} \nabla \times \vec{H}\left(t + \frac{\Delta t}{2}\right) \tag{4}$$

Update equations which derived from (3) and (4):

$$\vec{H}\left(t + \frac{\Delta t}{2}\right) = \vec{H}\left(t - \frac{\Delta t}{2}\right) - \frac{\Delta t}{\mu} \vec{E}(t) \tag{5}$$

$$\vec{E}(t + \Delta t) = \vec{E}(t) + \frac{\Delta t}{\varepsilon} \nabla \times \vec{H}\left(t + \frac{\Delta t}{2}\right) \tag{6}$$

These equations can be directly implemented in a computer code.

These are the final form of Maxwell's equations from which we will formulate the FDTD method.

$$\frac{\partial E_z}{\partial y} - \frac{\partial E_y}{\partial z} = -\frac{\mu_{xx}}{C_0} \frac{\partial H_x}{\partial t} \tag{7}$$

$$\frac{\partial E_x}{\partial z} - \frac{\partial E_z}{\partial x} = -\frac{\mu_{yy}}{C_0} \frac{\partial H_y}{\partial t} \tag{8}$$

$$\frac{\partial E_y}{\partial x} - \frac{\partial E_x}{\partial y} = -\frac{\mu_{zz}}{C_0}\frac{\partial H_z}{\partial t} \tag{9}$$

$$\frac{\partial H_z}{\partial y} - \frac{\partial H_y}{\partial z} = \frac{\varepsilon_{xx}}{C_0}\frac{\partial E_x}{\partial t} \tag{10}$$

$$\frac{\partial H_x}{\partial z} - \frac{\partial H_z}{\partial x} = \frac{\varepsilon_{yy}}{C_0}\frac{\partial E_y}{\partial t} \tag{11}$$

$$\frac{\partial H_y}{\partial x} - \frac{\partial H_x}{\partial y} = \frac{\varepsilon_{zz}}{C_0}\frac{\partial E_z}{\partial t} \tag{12}$$

For the basic example of FDTD code in MATLAB, you can refer to our references (The Finite-Difference Time-Domain Method (FDTD) 2012; Lesina et al. 2015; Ta 2014; Vaccari et al. 2014; Lesina et al. 2015; Saravanan et al. 2015; Duche et al. 2009; Deinega et al. 2013). The FDTD technique has much attention due to its accuracy and simplicity for modeling of antireflection coating layer. In spite of the fact that it is computationally serious, the FDTD technique handles any arbitrarily shaped model structure actually utilizing an unequivocal numerical solution for Maxwell's curl equations. In 2004, Yang et al. (2004) initially utilized the FDTD technique to model a 3D nanoporous structure. The presentation of exponentially expanding processing assets in the 2000s invested the EM modeling group to use FDTD to its most prominent point of preference; analysts were at long last ready to demonstrate the conduct of light at an interface of any composition, size, or shape, regardless of its regularity, with just the information of mass material properties. Computations in the time area maintain problem of the single wavelength restriction of other methods. However, structured grid does not efficiently represent curved surfaces during this method, and it is slow for small devices and very inefficient for highly resonant devices.

4.2 Transfer-Matrix Method (TMM)

One of the most attractive models for thin film is TMM method, and it is a simple way to deal with modeling sunlight going through layered media. This method utilizes coherence border situations through different interfaces of material and wavelength comparisons to depict the transmittance, absorbance, and reflectance for each layer. Congruity obliges that the electric and magnetic fields (EMFs) at the border between two materials are same in every substantial. At that point, if the electric field is known at the beginning of the layer, a transfer matrix based on the wave equation can be utilized to focus the electric field at the flip side of the layer. Both reflected and transmitted waves are considered to compute the general electric fields. As shown in Fig. 4 a beam of light with its associated EMFs undergoes an external reflection at (R) and transmitted portion at (T).

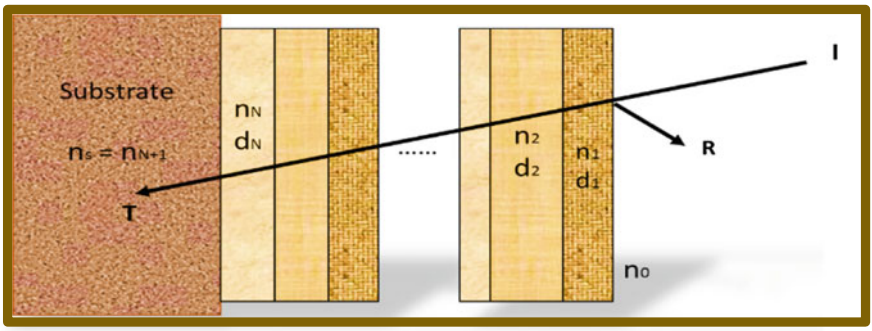

Fig. 4 Schematic diagram of TMM model

The mathematical derivation of TMM is summarized as below, and we consider an external environment refractive index n_0 and N thin layers C_n. The refractive indexes of these layers are as follows: n_i, $n_i + 1$,…,$n_i + n$. The refractive index of a substrate S is n_s. Here, we demonstrate the characteristic matrix of one layer. As mentioned earlier, the matrix relates tangential components of the electric $E(z)$ and magnetic $H(z)$ fields at the layer boundaries $z = 0$ and $z = s$. The TMM method is shortly presented below (Sahouane and Zerga 2014).

$$\left(\frac{E(0)}{H(0)}\right) = M\left(\frac{E(s)}{H(s)}\right) \tag{13}$$

The matrix itself is obtained which relates the fields at two adjacent boundaries (González-Ramírez et al. 2009)

$$M = \begin{bmatrix} \cos\emptyset & j\sin\emptyset/n_c \\ jn_c\sin\emptyset & \sin\emptyset \end{bmatrix} \tag{14}$$

The characteristic matrix of a multilayer is a product of corresponding single-layer matrix. If i is the number of layers, then the field at the first ($z = z0$) and the last ($z = z_i$) boundaries are related as follows:

$$M_i = \prod_{i=1}^{N} \begin{bmatrix} \cos\emptyset_i & j\sin\emptyset_i/n_i \\ jn_i\sin\emptyset_i & \cos\emptyset_i \end{bmatrix} \tag{15}$$

With $j_2 = -1$, n_i, the refractive index of the its layer, Φ_i is dephasing between the reflected waves of layers i and $i + 1$

$$\emptyset_i = \frac{2\pi}{\lambda} n_i d_i \cos\theta \tag{16}$$

ϕ θ is the angle of wave propagation in the layer. The detailed derivation of amplitude reflection (r) and transmission (t) coefficients is given and the resulting expressions are shown in Eqs. 6 and 7.

$$r = \frac{n_0 M_{11} + n_0 n_s M_{12} + M_{21} - n_s M_{22}}{n_0 M_{11} + n_0 n_s M_{12} + M_{21} + n_s M_{22}} \tag{17}$$

$$t = \frac{2n_0}{n_0 M_{11} + n_0 n_s M_{12} + M_{21} + n_s M_{22}} \tag{18}$$

M_{ij} are the elements of the characteristic matrix of the multilayer. The energy coefficients (reflectivity, transmissivity, and absorptance) are given by

$$R = |r|^2 \tag{19}$$

$$T = \frac{n_s}{n_0}|t|^2 \tag{20}$$

$$A = (1 - R)\left[1 - \frac{R_e(n_s)}{R_e[(M_{11} + n_s M_{12})(M_{21} + n_s M_{22})]}\right] \tag{21}$$

With R_e the real part, n_s and n_0 are refractive index of the silicon and vacuum, respectively.

$$R + T + A = 1 \tag{22}$$

Note that this technique talks about the solution of mathematical equations in a manner that predict back wavelength also; one wavelength starts with the sunlight transmitted through every one of the layers and afterward back-computes to get the data light power. This is obliged to represent the combined impacts of light reflected at every interface. In the utilization of measuring reflectivity for thin-film ARCs, the TMM strategy is a quick and straightforward demonstrating modeling technique. TMM has an ability to compute reflectance and transmittance and can deal with numerous wavelengths, scattering, and different angles of incidence. This strategy can likewise handle retention by means of complex refractive records (Sahouane and Zerga 2014; Zhan et al. 2014; Kosarian and Jelodarian 2011; Katsidis and Siapkas 2002).

However, the TMM-based optical modeling of solar cells is still lacking in some points. The matrix method for the analysis of the optical response of coherent multilayers has been generalized to take into account partially coherent and incoherent reflected or transmitted light. This approach is also integrated to include models for refractive index depth profiling. Its applicability was demonstrated concerning the optical characterization of ion-implanted materials as well as multilayers with a thick substrate in an arbitrary position within their structure and multilayers of conducting or insulating layers with rough surface and interfaces.

Generalized transfer-matrix method (GTMM) has been suggested to examine the reflection and transmission of optical multilayers with rational. The GTMM has been utilized to compute the efficiency of absorption inside an indistinct silicon flimsy film solar cell with reasonable and incomprehensible multilayers. In any case, optical modeling of the GTMM has not yet been connected to the solar cells. Moreover, the itemized detail of optical absorption structure of the solar cells together with the unintelligible glass substrate has not been analyzed as far as the interior optical power (Katsidis and Siapkas 2002; Jung et al. 2011).

5 Conclusions

Several conclusions can be drawn from this research:

1. The large carrier density and high mobility of CNTs ensure much enhanced current density and power efficiency of solar cells compared with extensively studied polymer composite structures.
2. There are still a few difficulties in the manufacture of the AR coatings. First and foremost, the improvement of the cost-effective and substantial scale creation techniques for the perfect AR structures. Second, the antireflection coatings must have special properties such as thermal and mechanical steadiness for long-term use in different situations. Based on this chapter and our research, CNTs improved multifunctional materials which helped to increase antireflection and self-cleaning performance, and they involved into the component of cells to provide high-power conversion and reduce the cost as well.
3. Its high strength and tough surface made CNTs a suitable materials for antireflection and self-cleaning which in the future will encouraged industries to use them to improve the mechanical strength.
4. The present modeling approaches are capable of predicting antireflection properties of thin films such as CNT film for different thicknesses in all wavelength. Finally, for predicting the solar properties of our model, we can use solar simulator such as Atlas software and Silvaco.

In conclusion, the findings of application of CNTs in solar cells in the future research are crucial factor to improve a simple, cost-effective solar cell with high efficiency and it might provide new concepts and ideas for the development of high-performance antireflective and self-cleaning surface.

Acknowledgments The authors wish to acknowledge the financial supports given by the Universiti Teknologi PETRONAS under a YAYASAN Universiti Teknologi PETRONAS (YUTP) grant No. 0153AA-A96.

References

Angmo, D., Hösel, M., & Krebs, F. C. (2012). All solution processing of ITO free organic solar cell modules directly on barrier foil. *Solar Energy Materials and Solar Cells, 107*, 329–336.

Avouris, P. (2002). Carbon nanotube electronics. *Chemical Physics Letters, 281*, 429–445.

Belin, T., & Epron, F. (2005). Characterization methods of carbon nanotubes: A review. *Materials Science and Engineering B, 119*(2), 105–118. doi:10.1016/j.mseb.2005.02.046

Benzekkour, N., Ghomrani, F. Z., Gabouze, N., Kermadi, S., Boumaour, M., & Ferdjani, K. (2009) Formation of rough TiO2 thin films on glass and porous silicon by sol-gel method. *Materials Science Forum, 609*, 139–143. doi:10.4028/www.scientific.net/MSF.609.139

Cai, J., & Qi, L. (2015). Recent advances in antireflective surfaces based on nanostructure arrays. *Materials Horizons, 2*(1), 37–53. doi:10.1039/c4mh00140k

Chee Howe See, A. T. H. (2007). A Review of carbon nanotube synthesis via fluidized-bed chemical vapor deposition. *Industrial and Engineering Chemistry Research, 46*(4).

Chee Howe See, O. M. D., MacKenzie, Kieran J., & Harris, Andrew T. (2008). Process parameter interaction effects during carbon nanotube synthesis in fluidized beds. *Industrial and Engineering Chemistry, 47*, 7686–7692.

Cui, K., Anisimov, A. S., Chiba, T., Fujii, S., Kataura, H., Nasibulin, A. G., et al. (2014). Air-stable high-efficiency solar cells with dry-transferred single-walled carbon nanotube films. *Journal of Materials Chemistry A, 2*(29), 11311–11318. doi:10.1039/c4ta01353k

Danafar, F., Fakhru'l-Razi, A., Mohd Salleh, M. A., & Awang Biak, D. R. (2011). Influence of catalytic particle size on the performance of fluidized-bed chemical vapor deposition synthesis of carbon nanotubes. *Chemical Engineering Research and Design, 89*(2), 214–223. doi:10.1016/j.cherd.2010.05.004

Danafar, F., Fakhru'l-Razi, A., Salleh, M. A. M., & Biak, D. R. A. (2009). Fluidized bed catalytic chemical vapor deposition synthesis of carbon nanotubes—A review. *Chemical Engineering Journal, 155*(1–2), 37–48. doi:10.1016/j.cej.2009.07.052

Deinega, A., Belousov, S., Valuev, I. (2013) Transfer-matrix approach for finite-difference time-domain simulation of periodic structures. *Physical Review E*, *88*(5). doi:10.1103/PhysRevE.88.053305

Dincer, I. (2000). Renewable energy and sustainable development: A crucial review. *Renewable and Sustainable Energy Reviews, 4*, 157–175.

Donaldson, K., Aitken, R., Tran, L., Stone, V., Duffin, R., Forrest, G., et al. (2006). Carbon nanotubes: a review of their properties in relation to pulmonary toxicology and workplace safety. *Toxicological Sciences, 92*(1), 5–22. doi:10.1093/toxsci/kfj130

Duche, D., Torchio, P., Escoubas, L., Monestier, F., Simon, J.-J., Flory, F., et al. (2009). Improving light absorption in organic solar cells by plasmonic contribution. *Solar Energy Materials and Solar Cells, 93*(8), 1377–1382. doi:10.1016/j.solmat.2009.02.028

Faustini, M., Nicole, L., Boissière, Cd, Innocenzi, P., Cm, Sanchez, & Grosso, D. (2010). Hydrophobic, antireflective, self-cleaning, and antifogging sol–gel coatings: An example of multifunctional nanostructured materials for photovoltaic cells. *Chemistry of Materials, 22*(15), 4406–4413. doi:10.1021/cm100937e

Garnett, E., & Yang, P. (2010). Light trapping in silicon nanowire solar cells. *Nano Letters, 10*(3), 1082–1087. doi:10.1021/nl100161z

Gizem Toroğlu LS (2014) Finite-Difference Time-Domain (FDTD) MATLAB Codes for First- and Second-Order EM Differential Equations. IEEE Antennas and Propagation Magazine, 56 (2).

González-Ramírez, J. E., Fuentes, J., Hernández, L. C., & Hernández, L. (2009). Evaluation of the thickness in nanolayers using the transfer matrix method for modeling the spectral reflectivity. *Physics Research International*

Hengameh Hanaei, F. R. B. A., Mohammadpour, E., & Kakooei, S. (2013). Optimization of carbon nano tubes synthesis using fluidized bed chemical vapor deposition: A statistical approach. *Caspian Journal of Applied Sciences, 2*(3), 46–55.

Hyo Jin Gwon, Y. P., Moon, Cheon Woo, Nahm, Sahn, Yoon, Seok-Jin, Kim, Soo Young, & Jang, Ho Won. (2014). Superhydrophobic and antireflective nanograss-coated glass for high performance solar cells. *Nano Research, 7*(5), 670–678. doi:10.1007/s12274-014-0427-x

Jung, S., Kim, K.-Y., Lee, Y.-I., Youn, J.-H., Moon, H.-T., Jang, J., et al. (2011). Optical modeling and analysis of organic solar cells with coherent multilayers and Incoherent glass substrate using generalized transfer matrix method. *Japanese Journal of Applied Physics, 50*(12R), 122301.

Kamat, P. (2006). Carbon nanomaterials: Building blocks in energy conversion devices. *The Electrochemical Society Interface*

Katsidis, C. C., & Siapkas, D. I. (2002). General transfer-matrix method for optical multilayer systems with coherent, partially coherent, and incoherent interference. *Applied Optics, 41*(19), 3978–3987.

Kosarian, A., & Jelodarian, P. (2011). Numerical evaluation and characterization of single junction solar cell based on thin-film a-Si: H/a-SiGe: H hetero-structure. In: *Electrical Engineering (ICEE), 2011 19th Iranian Conference on*, 2011. IEEE, pp 1–6.

Lesina, A. C., Paternoster, G., Mattedi, F., Ferrario, L., Berini, P., Ramunno, L., et al. (2015a). Modeling and characterization of antireflection coatings with embedded silver nanoparticles for silicon solar cells. *Plasmonics,*. doi:10.1007/s11468-015-9957-7

Lesina, A. C., Vaccari, A., Berini, P., & Ramunno, L. (2015b). On the convergence and accuracy of the FDTD method for nanoplasmonics. *Optics Express, 23*(8), 10481–10497. doi:10.1364/OE.23.010481

Li, X., He, J., & Liu, W. (2013a). Broadband anti-reflective and water-repellent coatings on glass substrates for self-cleaning photovoltaic cells. *Materials Research Bulletin, 48*(7), 2522–2528. doi:10.1016/j.materresbull.2013.03.017

Li, F., Li, Q., & Kim, H. (2013b). Spray deposition of electrospun TiO2 nanoparticles with self-cleaning and transparent properties onto glass. *Applied Surface Science, 276*, 390–396. doi:10.1016/j.apsusc.2013.03.103

Li, L., Li, Y., Gao, S., & Koshizaki, N. (2009). Ordered Co3O4 hierarchical nanorod arrays: Tunable superhydrophilicity without UV irradiation and transition to superhydrophobicity. *Journal of Materials Chemistry, 19*(44), 8366. doi:10.1039/b914462e

Li, Y. Z. J., & Yang, B. (2010). Antireflective surfaces based on biomimetic nanopillared arrays. *Nano Today, 5*, 117–127.

Liu, Z., Zhang, X., Murakami, T., & Fujishima, A. (2008). Sol–gel SiO2/TiO2 bilayer films with self-cleaning and antireflection properties. *Solar Energy Materials and Solar Cells, 92*(11), 1434–1438. doi:10.1016/j.solmat.2008.06.005

Mathew, S., Yella, A., Gao, P., Humphry-Baker, R., Curchod, B. F., Ashari-Astani, N., et al. (2014). Dye-sensitized solar cells with 13 % efficiency achieved through the molecular engineering of porphyrin sensitizers. *Nature Chemistry, 6*(3), 242–247. doi:10.1038/nchem.1861

Philip, G., & Collins, P. A. (2000). *Nanotubes FOR electronics*. Scientific American, Inc.

Popov, V. (2004). Carbon nanotubes: Properties and application. *Materials Science and Engineering: R: Reports, 43*(3), 61–102. doi:10.1016/j.mser.2003.10.001

Ralph Seitz, B. P. M., Axel, T., Andreas, S., Michael, M., Mickael P., Oliver, K., et al. (2012). Nanotechnology in the sectors of solar energy and energy storage.

Raut, H. K., Ganesh, V. A., Nair, A. S., & Ramakrishna, S. (2011). Anti-reflective coatings: A critical, in-depth review. *Energy and Environmental Science, 4*(10), 3779. doi:10.1039/c1ee01297e

Sahouane, N., & Zerga, A. (2014). Optimization of antireflection multilayer for industrial crystalline silicon solar cells. *Energy Procedia, 44*, 118–125.

Saravanan, S., Dubey, R. S., & Kalainathan, S. (2015). Design and analysis of thin film based silicon solar cells for efficient light trapping. *Advances in Optical Science and Engineering, 166*, 129–134. doi:10.1007/978-81-322-2367-2_17

Seung Yong Son, Y. L., Won, Sungho, & Lee, Dong Hyun. (2008). High-quality multiwalled carbon nanotubes from catalytic decomposition of carboneous materials in gas-solid fluidized beds. *Industrial and Engineering Chemistry, 47*, 2166–2175.

Shi, E., Zhang, L., Li, Z., Li, P., Shang, Y., Jia, Y., et al. (2012). TiO(2)-coated carbon nanotube-silicon solar cells with efficiency of 15 %. *Scientific reports, 2*, 884. doi:10.1038/srep00884

Sun, T. F. L., Gao, X., & Jiang, L. (2005). Bioinspired surfaces with special wettability. *Accounts of Chemical Research, 38*, 644–652.

The Finite-Difference Time-Domain Method (FDTD). (2012).

Vaccari, A., Lesina, A. C., Cristoforetti, L., Chiappini, A., Crema, L., Calliari, L., et al. (2014). Light-opals interaction modeling by direct numerical solution of Maxwell's equations. *Optics Express, 22*(22), 27739–27749. doi:10.1364/OE.22.027739

Verma, L. K., Sakhuja, M., Son, J., Danner, A. J., Yang, H., Zeng, H. C., et al. (2011). Self-cleaning and antireflective packaging glass for solar modules. *Renewable Energy, 36*(9), 2489–2493. doi:10.1016/j.renene.2011.02.017

Wan, D., Chen, H.-L., Tseng, T.-C., Fang, C.-Y., Lai, Y.-S., & Yeh, F.-Y. (2010). Antireflective nanoparticle arrays enhance the efficiency of silicon solar cells. *Advanced Functional Materials, 20*(18), 3064–3075. doi:10.1002/adfm.201000678

Wei, F., Zhang, Q., Qian, W.-Z., Yu, H., Wang, Y., Luo, G.-H., et al. (2008). The mass production of carbon nanotubes using a nano-agglomerate fluidized bed reactor: A multiscale space–time analysis. *Powder Technology, 183*(1), 10–20. doi:10.1016/j.powtec.2007.11.025

Xiong, J., Das, S. N., Shin, B., Kar, J. P., Choi, J. H., & Myoung, J. M. (2010). Biomimetic hierarchical ZnO structure with superhydrophobic and antireflective properties. *Journal of Colloid and Interface Science, 350*(1), 344–347. doi:10.1016/j.jcis.2010.06.053

Yan, J., Uddin, M. J., Dickens, T. J., & Okoli, O. I. (2013). Carbon nanotubes (CNTs) enrich the solar cells. *Solar Energy, 96*, 239–252. doi:10.1016/j.solener.2013.07.027

Yang, Z., Zhu, D., Zhao, M., & Cao, M. (2004). The study of a nano-porous optical film with the finite difference time domain method. *Journal of Optics A: Pure and Applied Optics, 6*(6), 564.

Yao, L., & He, J. (2014). Recent progress in antireflection and self-cleaning technology—From surface engineering to functional surfaces. *Progress in Materials Science, 61*, 94–143. doi:10.1016/j.pmatsci.2013.12.003

Ye, L., Zhang, Y., Zhang, X., Hu, T., Ji, R., Ding, B., et al. (2013). Sol–gel preparation of SiO2/TiO2/SiO2–TiO2 broadband antireflective coating for solar cell cover glass. *Solar Energy Materials and Solar Cells, 111*, 160–164. doi:10.1016/j.solmat.2012.12.037

Yongjin Wang, F. H., Kanamori, Y., Wu, T., & Hane, K. (2010) Large area, freestanding GaN nanocolumn membrane with bottom subwavelength nanostructure. *Optic Express, 18*(6).

Zhan, F., Li, Z., Shen, X., He, H., & Zeng, J. (2014) Design multilayer antireflection coatings for terrestrial solar cells. *The Scientific World Journal*

Zhang, J., & Yang, B. (2010). Patterning colloidal crystals and nanostructure arrays by soft lithography. *Advanced Functional Materials, 20*(20), 3411–3424. doi:10.1002/adfm.201000795

Zhu, W., Feng, X., Feng, L., & Jiang, L. (2006). UV-manipulated wettability between superhydrophobicity and superhydrophilicity on a transparent and conductive SnO2 nanorod film. *Chemical Communications, 26*, 2753. doi:10.1039/b603634a

Zhu, H., Wei, J., Wang, K., & Wu, D. (2009). Applications of carbon materials in photovoltaic solar cells. *Solar Energy Materials and Solar Cells, 93*(9), 1461–1470. doi:10.1016/j.solmat.2009.04.006

Zou C. S., & Ta, M. (2014). Investigation of moth-eye antireflection coatings for photovoltaic cover glass using FDTD modeling method. *IEEE, 1*(4).

Nanofluids for Enhanced Solar Thermal Energy Conversion

Vivek Sreenivasan, Y. Raja Sekhar and K.V. Sharma

Abstract Over the recent years, addressing solar energy utilization for different applications has grabbed attention of many research groups around the world. From the past few decades, scientists had made progress in innovating new devices and methods for harnessing solar energy. In this respect, they developed new materials to improve energy efficiency as one of the major focal domain. During twentieth century, scientists engineered the application of nanotechnology in various domains including solar thermal conversion devices. Nanofluids, a homogeneous dispersion and stable suspension of nanoparticles in the base fluids, have made possible progress to achieve higher thermal properties at the smallest possible concentrations. This chapter intends to summarize the research done on the nanofluid applications in different solar thermal conversion systems. This chapter includes comprehensive information about thermophysical properties of nanofluids, the design of solar thermal system at optimum conditions, and the applications of solar collector with nanofluid. Also, challenges and opportunities for future research are identified and reported as well.

Keywords Solar energy · Heat transfer enhancement · Thermal conductivity · Nanofluid and nanoparticle

V. Sreenivasan
School of Civil and Chemical Engineering, VIT University, Vellore, Tamil Nadu, India

Y. Raja Sekhar (✉)
School of Mechanical Engineering, VIT University, Vellore, Tamil Nadu, India
e-mail: sekhar.rajay@gmail.com

K.V. Sharma
Department of Mechanical Engineering, Universiti Teknologi PETRONAS, 31750 Tronoh, Malaysia
e-mail: kvsharmajntu@gmail.com

K. Viswanatha Sharma and N. Hisham B Hamid (eds.),
Engineering Applications of Nanotechnology, Topics in Mining, Metallurgy and Materials Engineering, DOI 10.1007/978-3-319-29761-3_5

1 Introduction

Utilization of different energy resources is done in a poor manner, i.e., to satisfy critical domestic and industrial needs, and harnessing energy in a clean and efficient way is still a continuing quest. In more practical terms, sustainable energy is the need for the day, especially for the industrial sector. Rapid industrialization led to a tremendous impact on the environment that resulted in the rise of global surface temperatures. Energy generation through fossil fuels has been identified as one of the primary reasons for environmental pollution. Since the production of electrical power form fossil fuel resources is in the verge of extinct and the global population growth rate is exponential, the solar thermal conversion is acquiring worldwide attention and undoubtedly an alternative source which is entirely eco-friendly. Hence, to combat climate change, clean and sustainable energy resources need to be developed to meet the current and future energy demands. In this aspect, solar thermal energy is a better alternative in spite of its higher capital cost.

At early twentieth century, the first installation of solar thermal energy conversion devices happened in the Sahara desert where sunlight operated a steam engine. Solar thermal conversion system suffers from low efficiency; hence, harvesting solar energy with high efficiency is primary conquering quest. In this paper, applications of nanotechnology in terms of nanofluid (nanoparticle) analysis in solar thermal conversion and devices have been carried both experimentally and numerically.

Nanotechnology in the broad term is used to describe materials and phenomenon at the nanoscale, i.e., 1×10^{-9} m. The benefits of exploiting nanotechnology are going into depth of theoretical understanding of storage and conversion phenomena at the nanoscale. Improvements in the nanoscale characterization of electronic properties and developments enable economical nanomanufacturing of robust devices. Nanotechnology leads to the application of nanofluid and nanomaterial in an innovative form of heat transfer in solar thermal conversion devices. Nanotechnology finds its applications in various fields of solar energy such as in direct solar absorber systems—flat plate collectors, concentrating collectors—solar cells, photovoltaic thermal devices, and desalination. It has the potential to reduce the impact of energy usage during production, storage, and other processes significantly. The applications of nanotechnology aim for improvement in power, efficiency, and reduction of costs and are found in process industries with the aim of both increasing and decreasing the temperature working fluid (Norton and Brian 2013). Most of the conventional fluid such as water, ethylene glycol, or oil has lower thermal conductivity, and alternate methods to improve the properties for effective utilization in thermal conversion devices are necessary. Many experimental investigations in the field of solar energy using nanofluids have were performed (Mahian et al. 2013). Theoretical and experimental studies lead to enhanced solar energy generation, high performance in terms of improved lifetime, power, and large storage capacity, respectively, using nanotechnology.

1.1 Nanofluids

Nanofluid is a fluid containing a particle of nanometer- sized, called nanoparticles with various volume concentrations and size used in heat transfer applications. They provide better efficiency compared to the conventional fluid employed in the present scenario and are also environmentally friendly. These fluids are colloidal suspensions of nanoparticles in a base fluid. The various nanoparticles used in nanofluids are typically made up of metals, oxides, carbides, or carbon nanotubes (CNTs), graphene nanoflakes, and ceramic particles that combined with base fluids such as water, ethylene glycol, and oil (Dharmalingama et al. 2014). The enhanced thermal conductivity and the convective heat transfer coefficient were first investigated by Choi et al. in (1995) using nanofluid. Their rheological behavior of nanofluids is found to be very critical in deciding their suitability for convective heat transfer applications. It led to enormous potential in heat transfer rate in various domains of the area such as in industry, thermal generation, transportation, and microelectronics.

Nanofluids are synthesized by two methods, i.e., one-step and two-step methods. The most extensively used method for mass production of nanofluid is two-step technique. Nanoparticles, nanofibers, nanotubes, or other nanomaterials were utilized in this process. Initial method for preparation was dry powders by chemical or physical methods. One-step method is used to minimize the agglomeration of nanoparticles, and the stability of fluid is increased (Li et al. 2009). The nanoparticles prepared by this method exhibit morphological shapes such as a needle, polygonal, square, and circular. This method avoids the undesired particle aggregation; in addition, they cannot manufacture nanofluids in large scale, and the cost is also high.

Many researchers, for the past two decades, have investigated the heat transfer enhancement using nanofluids both experimentally and theoretically. Wong and De Leon (2009) carried out a review of research detailing the current and future applications of nanofluids. Lee et al. (1999) reported that the addition of nanoparticles such as Cu, Al_2O_3, and CuO to base fluids of water and ethylene glycol resulted in an increase of thermal conductivity. The thermal conductivity of CNT–water nanofluid was higher than conventional liquid studied by Choi and Eastman in (2004). Due to the properties of the base fluid, the geometry of CNT, and volume fraction, a wide range of enhancement has been reported in the literature. For example, with 1 % volumetric fraction of multi-walled carbon nanotubes (MWCNTs) into the base fluid, the thermal conductivity of the medium was enhanced by $\sim$40 %. Keblinski et al. (2002) observed an enhancement of thermal conductivity of about 60 % for water-based nanofluid. Many experimental observations on the characteristics of nanofluids such as nucleate pool boiling and critical heat flux (CHF) have been carried out. Das et al. (2003) presented the pool boiling characteristics of Al_2O_3–water nanofluid on smooth and roughened heating surface for different particle concentrations. It showed that nanoparticle degraded the boiling performance with an increase in particle concentration. Wen and Ding (2005) demonstrated that alumina nanofluids of particle size 10–15 nm can significantly enhance boiling heat transfer. Their studies have shown an enhancement in boiling

heat transfer coefficient with increasing particle concentrations by 40 %, at a loading rate of 1.25 % by weight.

The effect of nanoparticle size and volume fraction also plays a role in the enhancement of the heat transfer characteristics (Xuan et al. 2000). Arun et al. (2015) conducted study upon nanofluids such as CeO_2/water, Al_2O_3/water, TiO_2/water, and SiO_2/water with volume concentrations of 0.75, 1, 0.75, and 1.25 % for a flow rate of 3 L/min. It was reported that a maximum heat transfer enhancement of about 35.9, 26.3, 24.1, and 13.9 % was observed, respectively. Wongcharee et al. (2011) studied about CuO–water nanofluid with volume fractions of 0.3, 0.5, and 0.7 % for a laminar regime. They reported an improvement in Nusselt number as nanofluid concentration rose. Kulkarni et al. (2008) investigated heat transfer and fluid dynamic performance of nanofluids. Silicon dioxide (SiO_2) nanoparticles suspended in ethylene glycol and water (EG/water) mixture in 60:40 % by weight were used. They observed an enhancement in heat transfer coefficient due to nanofluids for different volume concentrations and pressure drop obtained with increasing nanoparticle volume concentration in the base fluid. Sharma et al. (2009) experimentally studied the heat transfer coefficient and friction factor for transitional flow in a tube with twisted tape inserts using Al_2O_3 nanofluid. They reported that by using twisted tape in the flow path gives higher heat transfer rates compared to flow in a plain tube, and the heat transfer coefficient with 0.1 % volume concentration was 23.7 % higher compared with water.

Nanofluid is used as a coolant in many conversion devices. Jang and Choi (2006) designed a new cooler, combined microchannel heat sink with nanofluid. They obtained higher cooling performance when compared to the instrument using pure water as working medium. It reduces both the thermal resistance and the temperature difference between the heated microchannel wall and the coolant. In another experiment (Selvakumar and Suresh 2012) on CuO–water nanofluid in an electronic heat sink, the result exhibited an improvement in thermal conductivity compared to base fluid.

2 Solar Collector

Solar collectors are devices that convert the absorbed incident solar radiation to heat. The working fluid converts the generated heat for different applications. Solar collectors were classified into two types, non-concentrating and concentrating collectors (Kalogirou 2004). Non-concentrating solar collectors are usually used for low- and medium-temperature applications such as space heating/cooling, water heating, and desalination, whereas concentrating solar collectors are exploited in high-temperature applications such as electricity generation. Therefore, these systems are acquiring more and more attention, prevailing to low efficiency which is still a major concern. These nanofluids have the ability for enhancing the efficiency of solar systems. In this paper, the research over employing nanofluid in solar collectors is reported.

2.1 Flat Plate Solar Collector

Yousefi et al. (2012) experimentally investigated the efficiency of a flat plate solar collector with Al_2O_3/water nanofluid used as working fluid as shown in Fig. 1. The effectiveness of Al_2O_3 nanofluid used as working fluid with and without surfactant on the solar collector has studied. They considered nanoparticles of diameter 15 nm having two different weight fractions of 0.2 and 0.4 % for preparation of the nanofluid. The effect of mass flow rate 1, 2, 3 L/min on efficiency is also considered for experimentation. With 0.2 % weight fraction of Al_2O_3 nanofluid, the efficiency of the solar collector was 28.3 % higher compared with the water. Efficiency of collector was observed to change with surfactant Triton X-100. The ASHRAE standard was used to calculate the efficiency. They reported enhancement in efficiency of collector with nanofluids as a working fluid, compared to water as the absorption medium. Also, addition of surfactant has shown increase in heat transfer. The maximum enhanced efficiency was 15.63 % in the presence of the surfactant.

Yousefi et al. (2012) also demonstrated experimentally the effect of efficiency of the flat plate collector when water–MWCNT nanofluid was used as working fluid. In this study also, they used Triton X-100 as surfactant and prepared working fluid samples with and without surfactant. The effect of different weight fractions of nanoparticles in the nanofluid having particle diameter range from 10 to 30 nm, and

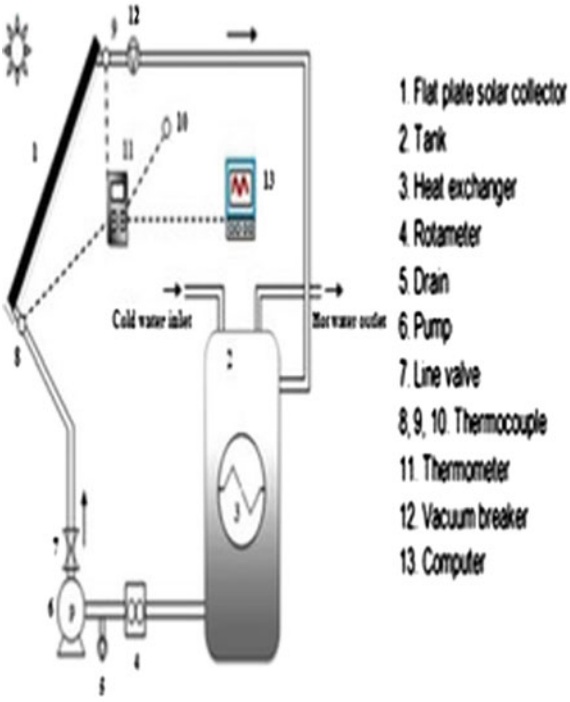

Fig. 1 Experimental setup (Yousefi et al. 2012)

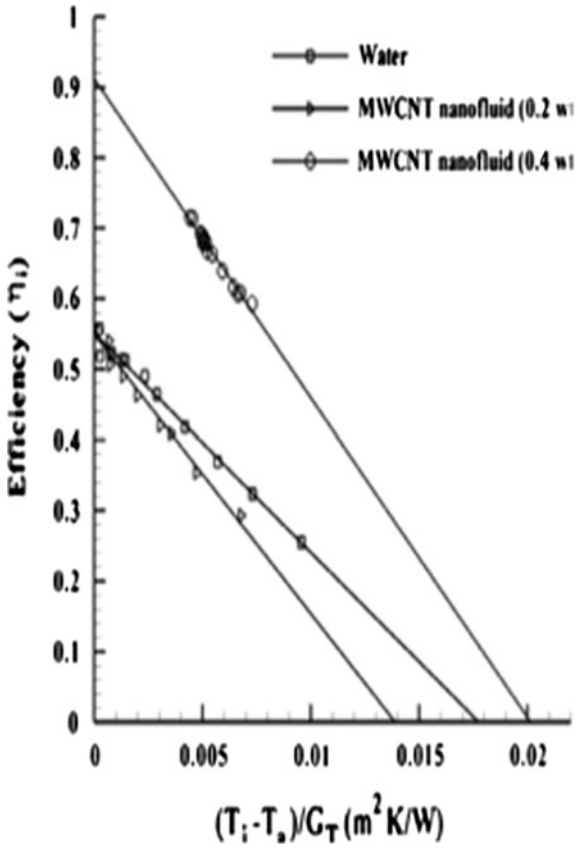

Fig. 2 Efficiency of solar collector for MWCNT nanofluid without surfactant and for water in the same mass flow rate (Yousefi et al. 2012)

the impact of mass flow rate was also taken into consideration. An increase in the efficiency was observed by increasing the weight fraction from 0.2 to 0.4 % and also by the addition of surfactants. The rise in the efficiency of collector depends on the ratio of temperature difference between inlet and ambient to the input solar flux. However, the collector efficiency when 0.4 wt% MWCNT nanofluid without addition of surfactant is used as working fluid is higher as shown in Fig. 2. It was reported that the efficiency can be also increased by increasing the mass flow rate for subtle values of reduced temperature difference parameter, and beyond these small values, the efficiency exhibits a reversed trend.

In another similar kind experiment conducted by Yousefi et al. (2012), they verified the effect of pH for MWCNT–H_2O nanofluid on the efficiency of a flat plate solar collector. The experimental work was carried out by 0.2 % weight fraction under different pH values from acidic to base range, i.e., 3.5, 6.5, and 9.5. They again considered Triton X-100 as surfactant and undertaken the study at a mass flow rate of 0.0333 kg/s. They observed that the efficiency for pH = 3.5 was greater than that for pH = 9.5, if the temperature differences were higher than the mean

temperature difference. Larger differences between the pH of nanofluids to that of isoelectric point (pH = 7.5) increase the efficiency of the collector as shown in Fig. 3. Therefore, the positive effect of nanofluids on the efficiency of flat plate solar collector becomes higher as the nanofluids become more acidic than basic.

Chougule et al. (2012) fabricated the experimental set up of flat plate collectors using heat pipes. The effects of nanofluids as working fluid using the solar tracker on solar heat pipe collector were analyzed. In this three identical wickless copper, heat pipes with a length of 620 mm and an outer diameter of 18 mm were fabricated. The nanoparticles used were CNTs 10–12 nm in diameter, and the concentration of nanoparticles used in the preparation of nanofluid was 0.15 % by volume. Nanofluids increase the average efficiency of the solar heat pipe collector irrespective of change in tilt angle. Nanofluids with solar heat pipe collector gives better performance at a higher tilt angle. This solar tracking system provides an add-on advantage to improve the efficiency in both water and nanoworking fluid solar heat pipe collector at each tilt angles for the solar heat pipe collector. They

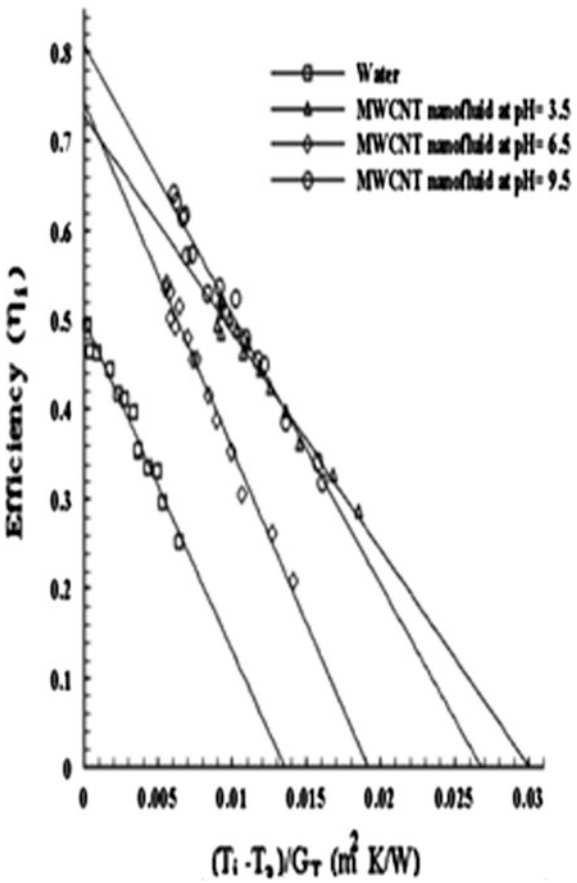

Fig. 3 Efficiency of the flat plate solar collector with MWCNT nanofluid as base fluid at three pH values

show better performance during winter; that is, solar heat pipe collector should be used in cold climatic conditions. They concluded that at 50° tilt angle working fluid gave better performance as compared to standard average angle in both conditions, i.e., fixed and tracking. Nasrin et al. (2013) numerically studied the influence of Prandtl (Pr) number on free convection in a solar collector filled with nanofluid. Here, the working fluid used is water–Al_2O_3 nanofluid. By using finite element method, the governing differential equations are solved numerically. The influence of Pr number was taken into consideration for the temperature and flow fields as well as the radiative and convective heat transfer rates, while Rayleigh number (*Ra*), volume fraction (*Ø*), and emissivity (ε) are fixed at 104, 5 %, and 0.9, respectively. They observed that the structure of the fluid streamlines and isotherms within the solar collector is found to dependent upon the Pr number. They found that the Al_2O_3 nanoparticles with the highest Pr were found to be most effective in increasing the performance of heat transfer rate than base fluid. Average heat transfer is obtained higher for convection than radiation. Mean temperature diminishes for both fluids with rising mentioned parameter. Average velocity field increases due to falling Pr. They concluded that analysis highlighted the operating range in which water–Al_2O_3 nanofluid can effectively utilized for high level of heat transfer augmentation. Faizal et al. (2013) presented a comprehensive overview of the energy and economic and environmental analysis of metal oxides nanofluid for a flat plate solar collector. For a solar thermal conversion system, increasing the heat transfer area can lead to increasing the output temperature of the system. So this study is focussed on potential size reduction and its associated energy saving of flat plate solar collectors when applying Al_2O_3, SiO_2, TiO_2, and CuO nanofluid that can produce the same desired output temperature. They found out that the higher density and lower specific heat of nanoparticles lead to greater thermal efficiency and CuO nanofluids have the highest value compared to other three nanofluids. 25.6, 21.6, 22.1, and 21.5 % solar collector area reduction has been achieved using CuO, SiO_2, TiO_2, and Al_2O_3, respectively. It is estimated that 10,239, 8625, 8857, and 8618 kg total weight for 1000 units of solar collector can be saved using CuO, SiO_2, TiO_2, and Al_2O_3 nanofluid. The payback period and emissions of the nanofluid-based solar collector is 2.4 years and 170 kg less CO_2 emissions compared to the conventional solar collector. Environmental damage cost is lower with the nanofluid-based solar collector.

Said et al. (2013) experimentally investigated the effect of density, thermal conductivity, and viscosity of alumina nanofluid ($0.05\ \% < \phi < 0.1\ \%$) using water and EG/water mixture (60:40 by mass). They studied the effect of pressure drop and pumping power for a flat plate solar collector at a temperature ranging from 25 to 80 °C. It was observed that nanofluid containing nanoparticles had enhanced thermal conductivity compared to that of base fluid. Here, the viscosity of nanofluids increases with increase in nanoparticle volume concentration. Also, the viscosity of alumina nanofluids decreases exponentially with a rise in temperature. Water-based alumina nanofluid of 0.05 % volume concentration exhibits Newtonian behavior at below 40 °C temperature, whereas it behaves as non-Newtonian fluid for all other higher concentration at any temperature. The

effect of pumping power and pressure drop noticed for low concentration nanofluids is found to have negligible effect. Raja Sekhar et al. (2013) conducted an experimental simulation of convective heat transfer analysis for a horizontal circular pipe with fluid in mixed laminar flow range under constant heat flux. Here, the variation of heat transfer coefficient and pressure drop in the pipe flow for water and water-based Al_2O_3 nanofluids at a different volume concentration and twisted tapes was studied and compared. They found that with the increase in heat transfer coefficient in a plain tube with the use of nanofluids is 8–12 % greater compared to the flow of water in the plain tube. The nanofluid of 0.5 % particle concentration has higher friction factor compared to water. Friction factor and Nusselt number increase with the rise of particle concentration. They reported that the use of twisted tape in heat flow of pipes and the energy gained in the heat exchanger was more than energy spent on pumping power. From the results, it was concluded that the heat transfer enhancement in a horizontal tube increases with Reynolds number of flow and nanoparticle concentration. Tiwari et al. (2013) presented a comprehensive overview of the thermal performance of solar flat plate collector for water heating using different nanofluids. The effect of using the Al_2O_3 nanofluid as an absorbing medium in a flat plate solar collector was investigated. The impact of mass flow rate and particle volume fraction on the efficiency of the collector was studied. They reported that by using an optimum particle volume fraction of 1.5 % Al_2O_3 nanoparticles, increase in thermal efficiency was 31.64 % as well as saving in kg of CO_2 emissions per unit kWh energy generated by solar collector. Chaji et al. (2013) experimentally investigated the thermal efficiency of flat plate solar collector (FPSC) using TiO_2/water nanofluid. They evaluated the effect of nanofluid on solar collector efficiency for different mass flow rates and with three levels of nanoparticles concentrations without using a surfactant. They observed an increase of mass flow rates of base fluid inside the solar collector that enhanced the index of total collector efficiency area curve up to 15.7 %. Also, adding the nanoparticles to water improved the ratio of collector efficiency area under the curve between 2.6 and 7 % about base fluid at the same flow rate. Amirhossein et al. (2014) experimental investigated the performance effect of Cu nanoparticle on the efficiency of a flat plate solar collector. The nanoparticles having an average diameter of 10 nm, with a weight fraction of 0.2 and 0.3 % of the nanofluid, were used. A one-step method was used to prepare copper nanofluid with ethylene glycol as the base fluid. The experiments were performed at different volume flow rates of the nanofluid from 0.016 to 0.050 kg/s, and the ASHRAE 93 standard was used to test the solar collector's performance. From experiment, solar collector efficiency decreased with decreasing the volume flow rate, and the highest $F_R(\overline{\tau\alpha})n$ value was obtained for 1 L/min. They found that by increasing the nanoparticle weight fraction, the improved efficiency of the collector had observed. Optimum point for solar collector efficiency is observed for 0.3 wt% Cu/EG nanofluid at 1.5 L/min. Said et al. (2014) theoretically examined the entropy generated, heat transfer enhancement capabilities, and pressure drop for a flat plate solar collector operated with single-walled carbon nanotube (SWCNT)-based nanofluids as an absorbing medium. Specific heat (Cp) and density of nanofluid were measured using a

PerkinElmer DSC 4000 and density meter. They found out that SWCNT-based nanofluids have better thermal properties, and this consequently leads to better thermal and exegetic efficiencies compared to the metal oxide nanofluids. Analytical outcomes also revealed that SWCNT nanofluid could reduce the entropy generation and enhance heat transfer coefficient by 4.34 and 15.33 % theoretically compared to water as an absorbing fluid. Moghadam et al. (2014) experimentally investigated the efficiency of a flat plate solar collector using CuO–H_2O nanofluid as a working fluid. The efficiency of two working fluids was compared. The volume fraction of nanoparticle was taken as 0.4 %, the mean particle dimension is kept constant at 40 nm, and the mass flow rate is varied from 1 to 3 kg/min. They found out that under optimum mass flow rate, solar collector efficiency increases by 16.7 % with that of water. They also observed that highest heat absorption by collector occurred at a different mass flow rate for water and nanofluid, and optimum mass flow rate depends on the working fluid thermal characteristics. Omid et al. (2014) have done a comprehensive investigation on heat transfer and entropy generation of Al_2O_3/water nanofluids in a flat plate solar collector. They considered the effects of tube roughness and nanoparticle size where the mass flow rather is deemed to be constant ranging from 0.1 to 0.8 kg/s. The impact of different thermophysical models, solar radiation, and ambient temperature on entropy generation was evaluated for the turbulent flow regime. There finding shows that with an increase in the volume fraction of nanofluid, the outlet temperature increases, while with increasing in nanoparticle size, very insignificant decrease had observed in the outlet temperature. They found that change in the outlet temperature was exactly opposite to Nusselt number trend. The effect is more visible at high mass flow rates, and the impact of uncertainties in thermophysical models on entropy generation is not significant in any of volume fraction and mass flow rate. They observed the effect of roughness on entropy generation was more important when the solar radiation and ambient temperature decrease.

Rehena et al. (2014) numerically investigated the impact of forced convection flow by four different nanofluids inside a flat plate solar collector. They examined the temperature, heat function, the rate of heat transfer, mean temperature, the percentage of collector efficiency, and temperature of fluid along the mid-height of the rise pipe. They found out that equation of the temperature and heat function through the riser is found to be significantly dependent upon the performance of nanofluid. The Ag nanoparticle with 5 % solid volume fraction has the highest rate of heat transfer. They found that collector efficiency improved from 65 to 85 % using Cu–water nanofluid. It was reported that as the volume fraction increased from 0 to 5 %, the temperature of water–Cu nanofluid increases steadily while passing through the pipe. Omid et al. (2014) experimentally and numerically evaluate the first- and second-law analyses of a flat plate mini channel-based solar collector. The effect of nanoparticle shape, the impact of tube material on the heat transfer, and entropy generated are evaluated using boehmite alumina nanoparticles in a mixture of water and ethylene glycol. Volume concentrations up to 4 % in turbulent flow conditions are utilized in this study. Four different shapes of

nanoparticles included are platelets, blades, cylinders, and brick, and tube and absorber plate are made up of copper and steel. They found that the platelet-shaped nanoparticles showed the lowest heat transfer coefficient and the brick displayed the highest heat transfer coefficient at the maximum volume fraction, i.e., 4 %. They concluded that the entropy generation rate of copper was minimized by using brick-shaped particles with the volume fraction of 2 %, while using steel tubes, minimum entropy generation is achieved by using blade-shaped particles. And also reported that when the mass flow rate is 0.5 kg, the entropy generation rate for steel tubes is found to be 11 % higher than that of copper tubes. Omid et al. (2014) analytically analyzed the performance of four different nanofluids including Cu/water, Al_2O_3/water, TiO_2/water, and SiO_2/water in a mini channel flat plate solar collector. Pressure drop was also taken into account for the entropy generation analysis. The analysis of the first law of thermodynamics shows that Al_2O_3/water nanofluids have the highest heat transfer coefficient, while the lowest value belongs to SiO_2/water nanofluids. The higher outlet temperature was provided by Cu/water nanofluids followed by TiO_2/water, Al_2O_3/water, and SiO_2/water nanofluids. The results of second-law analysis determine that Cu/water nanofluid produces the lowest entropy generated among the nanofluids. The Nusselt number is also lowest for Cu/water nanofluid, while SiO_2/water nanofluid provides the highest value of Nusselt number. They reported that the pressure drop of nanofluids decreases with volume fraction, expect for SiO_2/water nanofluids in low mass flow rate. For SiO_2/water nanofluids, it was found that when the mass flow rate is 0.1 kg/s, the entropy generation increases because SiO_2 nanoparticles have the lowest density of nanoparticles. Goudarzi et al. (2014) experimentally investigated the effect of the pH variation on the efficiency of a new cylindrical solar collector using two different nanofluids, Al_2O_3–H_2O and CuO–H_2O. The experimental setup consists of a cylindrical glass tube with the helical pipe as the receiver of the solar energy. The experiments were performed using 0.1 wt% CuO and 0.2 wt% Al_2O_3 nanofluid with different pH values and tested based on ASHRAE standard. They found that the differences between the pH of nanofluid and the pH of isoelectric point (IEP) caused an increase in the thermal efficiency of the solar collector. It was also observed that for the acidic condition (pH = 3), of CuO nanofluid (pH_{IEP} = 9.5), the efficiency increased by 52 % compared to nanofluid at pH 10.5. For Al_2O_3 nanofluid (pH_{IEP} = 7.4) at basic condition (pH = 10.5), the efficiency of the collector is obtained to be 64.5 % greater than that of the nanofluid at pH = 9.2. They concluded that the effectiveness of the solar collector with Al_2O_3 nanofluid at the primary condition and far from the isoelectric point was higher than that with CuO nanofluid. Saleh et al. (2015) experimentally investigated the thermal efficiency and performance characteristics of a flat plate solar collector using SiO_2/ethylene glycol (EG)–water nanofluids. Volume fractions up to 1 % and mass flow rate between 0.0018 and 0.0045 kg/s were considered for the study. They reported that when there is an increase in nanofluid concentration from 0 to 1 %, then it results in an efficiency enhancement approximately between 4 and 8 %. It was observed that the thermal efficiencies associated with concentrations of 0.75 and 1 % were very close. The experimental data demonstrated that energy parameter decreases with an

increase in the mass flow rate of nanofluid. Said et al. (2015) executed the energy and exergy efficiency analysis of a flat plate solar collector using controlled pH for Al_2O_3–H_2O nanofluid both theoretically and experimentally. The effect of mass flow rate, nanoparticle volume fraction, and the effect pH on the exergy and energy efficiency of the collector were examined. Stability of nanofluid was obtained by controlling the pH of the solution over a period of 30 days. It shows that in contrast with water as the working medium, nanofluid efficiency was enhanced up to 83.5 % for the first law for 0.3 % v/v and 1.5 kg/min. The second-law efficiency had enhanced up to 20.3 % for 0.1 % v/v and 1 kg/min. They noted that the increased volume flow rate can strengthen the effectiveness of the system, but the exergy efficiency decreases. The thermal efficiency of the system was found to be more than 50 % compared to the existing system. Eshan et al. (2015) experimentally and numerically investigated the optimization of exergy efficiency of a nanofluid-based solar collector using Al_2O_3 nanoparticles in water as a base fluid. Collector area and tilt angle are assumed to be constant. The effect of different parameters such as mass flow rate of liquid, collector inlet fluid temperature, solar radiation, ambient temperature, and nanoparticle volume concentration on the collector exergy was investigated. The procedure to determine the optimum value of nanoparticle volume concentration, mass flow rate of fluid, and collector inlet fluid temperature for maximum exergy delivery had been developed by applying the interior-point method for constrained optimization under a given condition. It shows that each of the parameters can differently affect the collector exergy. Optimization result indicates that under actual constraints, in both pure water and nanofluid cases of working fluids on solar collector, efficiency had increased about 0.72 %. The corresponding optimized values of mass flow rate and collector inlet fluid temperature are decreased about 67.8 and 1.9 %, respectively. Said et al. (2015) analyzed numerically and experimentally the use of TiO_2–water nanofluid as a working fluid for enhancing the performance of flat plate solar collector. The volume fraction of nanoparticles of 0.3 and 0.1 % and mass flow rate of nanofluid varied from 0.5 to 1.5 kg/min were studied. They found that thermal conductivity is enhanced up to 6 % with 0.3 vol% of TiO_2. They reported that the viscosity increases with particle loading and reduces with rising temperature. Energy efficiency and exergy efficiency were observed to be 76.6 and 16.9 % for 0.1 vol and 0.5 kg/min, respectively, with respect to water. Using TiO_2 nanofluid in the solar collector, it was found to have higher energy and exergy efficiencies than water.

2.2 Direct Absorption Solar Collector

Otanicar and Golden (2009) determined the environmental and economic effects of using nanofluids to enhance solar collector efficiency as compared with conventional solar collectors for domestic hot water systems. For the current cost of nanoparticles, the nanofluid-based solar collector was found out to have slightly

higher payback period but has the same economic savings as compared to the conventional solar collector. A nanofluid-based collector has a lower embodied energy 9 % and approximately 3 % higher levels of pollution offsets than a typical collector. The solar-weighted absorption coefficient for fluid's baseline capacity for absorbing solar energy had investigated. Results showed that water is the best absorber among the four tested liquids, namely water, EG, propylene glycol, and therminol VP-1. Tyagi et al. (2009) theoretically studied the capability of using a non-concentrating direct absorption solar collector (DASC) and investigated its performance with that of a conventional flat plate collector. In this research, a nanofluid mixture of water and aluminum nanoparticles was used as the absorbing medium. According to the results, the efficiency of a DASC using nanofluids as the working fluid is up to 10 % higher than that of pure water in a flat plate collector. Otanicar et al. (2010) investigated the use of nanofluid-based in direct absorption solar collectors. They found that mixing nanoparticles in a liquid dramatically affects the liquid thermophysical properties, such as thermal conductivity. Nanoparticles can improve the radiative properties of fluids and increase the efficiency of DASC. The experimental results were obtained from solar collectors based on the nanofluids from various nanoparticles such as carbon nanotubes, graphite, and silver. They demonstrate efficiency improvements of up to 5 % in solar thermal collectors by utilizing nanofluids as the absorption mechanism. The experimental and numerical evaluation shows that the efficiency increases rapidly initially with volume fraction and then gets stabilized as the volume fraction continues to grow. The addition of small amounts of nanoparticles results in a rapid enhancement in the efficiency from the pure fluid case until a volume fraction of approximately 0.5 %. With 20-nm silver particles, an efficiency improvement of 5 % can be achieved as shown in Fig. 4. As shown in figure, reducing the particle size further leads to an even greater enhancement in efficiency through the dependence of the optical properties on particle size.

Taylor et al. (2011) theoretically and experimentally investigated the optical property characterization of different nanoparticles such as silver, copper, graphite, aluminum, and gold suspended in water and therminol VP-1 as the base fluids in DASC. To determine the optical property of nanofluids, modeling and measurement techniques was used. For different concentrations of aqueous graphite nanofluids, extinction coefficients were studied by using experimental and modeling methods. They obtained a nanofluid that could absorb approximately 95 % sunlight with very low nanoparticle volume fractions of 10 ppm. So nanofluid could be used to absorb sunlight with a small amount of viscosity and density. They concluded that energy absorption for nanoparticles was at shorter wavelengths and for the base fluids at longer wavelengths. Taylor et al. (2011) reported that power tower solar collectors could benefit from the potential efficiency improvements that arise from using a nanofluid as a working fluid. A notional design of this type of nanofluids receiver was presented. Using their design model, they had shown a 10 % increase in theoretical nanofluid efficiency compared to that of surface-based collectors when solar concentration ratios range from 100 to 1000. Experiments on laboratory-scale nanofluid dish receiver suggest that up to 10 % increase in efficiency is possible

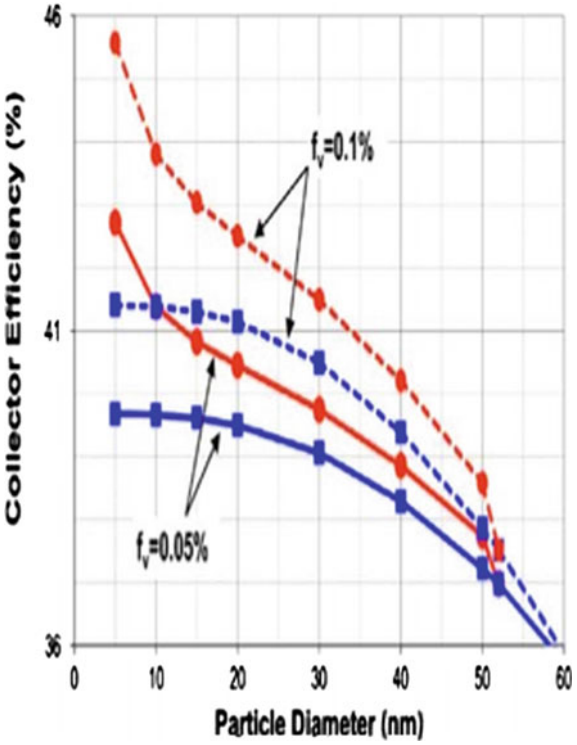

Fig. 4 Collector efficiency as a function of silver nanoparticle diameter—*squares* bulk properties; *circles* size-dependent properties—and volume fraction (Otanicar et al. 2010)

under optimal operating conditions. Khullar and Tyagi (2012) examined the potential of the nanofluid-based concentrating solar water heating system to the existing systems based on fossil fuels. The paper presented a quantitative assessment to assess the potential environmental benefits that could be obtained from the nanofluid-based concentrating solar water heating system to that obtained using fossil fuels. Their analysis revealed that considerable emission reductions by approximately 2.2103 kg of CO_2/household/year and fuel savings can be obtained by using nanofluid-based concentrating solar water heating system. Saidur et al. (2012) analyzed the effect of using nanofluids as working fluid on the DASC. The extinction coefficients of water-based aluminum nanofluids were evaluated under different nanoparticle sizes and volume fractions. Aluminum nanoparticles showed the highest extinction coefficient at a short wavelength and a peak of 0.3 mm, and at the visible and shorter wavelength region, these nanoparticles can be used to increase the light absorption ability of water. Particle size shows minimal influence on the optical properties of nanofluids, whereas extinction coefficient is linearly proportionate to volume fraction. Although the extinction coefficient of nanofluids was independent of the nanoparticle size, they should be controlled to below 20 nm. The transmissivity of light is valued between nanofluids and pure water-based fluid. The improvement was promising only with 1.0 % volume

fraction; the nanofluids were almost opaque to a light wave to the rest of volume fraction. A volume fraction of 1.0 % shows satisfactory improvement to solar absorption; therefore, they concluded that the aluminum nanofluids were meant to be a real solution for direct solar collector compared with the others.

Kundan and Sharma (2013) performed experimental work on performance evaluation of a DASC using CuO–H_2O nanofluid. They found that by using CuO nanofluids in DASC efficiency enhancement was of the order of 4–6 %. With 0.005 % volume fraction possess 2–2.5 % of efficiency improvement than 0.05 % volume fraction, when compared to water. Enhancement of effectiveness is due to a subtle particle size that enhances the absorption capacity of nanofluids. He et al. (2013) prepared Cu–H_2O nanofluids through a two-step method. The transmittance of nanofluids is over the solar spectrum (250–2500 nm). Factors—such as particle size, mass fraction, and optical path—influencing transmittance of nanofluids were investigated. The extinction coefficients were measured experimentally compared with that of theoretically calculated value. The photothermal properties of nanofluids were studied. The transmittance of Cu–H_2O nanofluids is considerably less than that of deionized water. Also, it decreases with increasing nanoparticle size, mass fraction, and optical depth. The highest temperature of Cu–H_2O nanofluids (0.1 wt%) can be up to 25.3 % compared with deionized water. The good absorption ability of Cu–H_2O nanofluids for solar energy indicates that it is suitable for direct absorption solar thermal energy systems. Ladjevardi et al. (2013) experimentally and numerically studied the performance of DASC by using different diameter and volume fraction of graphite nanoparticles. Here for every case, the efficiency of solar receivers in the absorption of solar energy, irradiation spectrum distribution, impacts on the harvested solar energy, and irradiation energy level versus the depth of flow have been studied and compared. They used numerical code to solve radiative transfer equation along with momentum, and mass and energy equations are solved together for simulating the operating characteristics of direct absorption solar collector. It is seen that increase in graphite nanoparticle diameters from 50 to 300 nm enhances the extinction coefficient from around 0.4–10 in UV and visible ranges. It states that increase in nanoparticle concentrations increases collector output temperature and volume fraction around 0.00025 %. The rises in the outlet temperature from 0.27 to 0.915 was compared to pure water that lead to an increase in cost around 0.045$/L. Verma and Kundan (2013) investigated the effect of Al_2O_3–H_2O-based nanofluids experimentally as an absorbing medium in DASC as shown in Fig. 5. The volume fractions of Al_2O_3 nanoparticles used were 0.005 and 0.05 %, respectively. They calculated the efficiency of the collector for different mass flow rates (60, 80, and 100 ml/h) of the nanofluid. They found that the collector efficiency increased by 3–5 % when the nanofluid used was compared to mere water. They also concluded that the collector efficiency depended on the size, shape, and the volume fraction of nanoparticles.

Parvin et al. (2013) numerically investigated the heat transfer performance and entropy generation of forced convection through a DASC using Cu–water nanofluid as working fluid. Various Reynolds number (*Re*) and solid volume fraction (*Ø*) was considered for the temperature and heat flux fields as well as heat transfer rate. The

Fig. 5 Direct absorption solar collector (Verma and Kundan (2013)

percentage of collector efficiency, mean entropy generation, and Bejan number of the fluids through the collector was analyzed. It had found that the structure of isotherms and heatlines through the solar collector depends upon *Re* and *Ø*. The Cu nanoparticle with highest *Re* and *Ø* = 3 % is established to be most effective in enhancing the performance of heat transfer rate, and it enhances with a variation of *Re* and *Ø*. Collector efficiency increases more than two times with two times for increasing Reynolds number and volume fraction. Bejan number approaches to 1 for Reynolds number variation. Hordy et al. (2014) quantitatively examined both the long-term and high-temperature stability of plasma-functionalized MWCNT nanofluids for wide concentration dispersed in water, ethylene glycol, propylene glycol, and therminol VP-1 for use in direct solar absorption. They reported long-term room temperature stability currently tested up to 8 months had been demonstrated for glycol-based nanofluids, while gradual MWCNT agglomeration had observed with water-based nanofluid because of polar nature of oxygen functionalities. It was reported from the high-temperature test that no agglomeration was found to occur at a temperature range from 85 to 170 °C for both the nanofluids. MWCNTs show 100 % solar energy absorption even at low concentrations and small collection volume for various optical characterization of nanofluid.

Bandarra Filho et al. (2014) experimentally investigated the potential of silver nanoparticles as direct sunlight absorbers for solar thermal applications under direct sunlight without focusing, for 10 h. The result showed that thermal energy is increased by 52, 93, and 144 % for silver particle concentrations of 1.62, 3.25, and 6.5 ppm, respectively, at peak temperature. They reported that nearly constant specific absorption rate (SAR) ~0.6 KW/g was obtained for the initial heating period for nanofluid up to 6.5 ppm, but significantly decreases at higher concentrations. Luo et al. (2014) numerically investigated the performance improvement of a DASC with nanofluids. A simulation model was designed by combining the radiative heat transfer in particulate media with conduction and convection heat transfer in the DASC collector to predict the photothermal efficiency. TiO_2, AL_2O_3, Ag, Cu, SiO_2, graphite nanoparticles, and carbon nanotubes were dispersed into base medium and used as nanofluids. It shows that nanofluid improved outlet temperature and effectiveness by 30–100 K and by 2–25 % than the base fluid. The photothermal efficiency of nanofluid with 0.01 % graphite and 0.5 % Al_2O_3 is found to be 122.7 and 117.5 % to that of the coating absorbing collector. The low loading can efficiently enhance the absorption of radiation from 200 to 2000 nm. Zhang et al. (2014) studied the radiation properties of nanofluids systematically for the first time by experimental and theoretical methods by varying particle material, volume fraction, and optical path length. The extinction coefficients of the nanofluids have been obtained based on theoretical predictions and experimental investigations. They found that at the volume fraction of 10 ppm, the extinction coefficient of the nanofluid containing the Ni nanoparticles with an average size of 40 nm is higher than that containing the Cu nanoparticles. Nanofluid containing the carbon-coated Ni (Ni/C) nanoparticles exhibits lower transmittance and higher extinction coefficient, compared with the one containing the Ni nanoparticles with the similar average size. The radiative properties of this Ni/C nanofluids increase with the volume fraction of the nanoparticles. As the volume fraction rises to 40 ppm, the absorbed energy fraction by the Ni/C nanofluid reaches up to almost 100 % after that incident light only penetrates 1 cm.

Sadique and Verma (2014) performed an experimental study on the effect of the nanofluid on the performance of a direct solar thermal collector. Three different groups of nanofluids with water were considered—graphite sphere of 30 nm diameter, carbon nanotube of 6–20 nm diameter, and silver sphere of 20 and 40 nm diameters. They concluded that nanofluids could be used to absorb sunlight with a negligible amount of viscosity and density increase. Liu et al. (2015) experimentally and numerically studied high-temperature direct solar thermal collector using graphene/ionic liquid, i.e., 1-hexyl-3-methylimidazolium tetrafluoroborate ($[HMIM]BF_4$) nanofluids as the absorbers. A model was used to predict the temperature of graphene/ionic liquid with various geometrical parameters and operating conditions such as graphene concentration, heat transfer fluid (HTF) height, and solar concentration. Based on the model, it was shown that the receiver efficiency increases with receiver height and solar concentration but decreases with the graphene concentration. An experimental setup was used to measure temperature profiles of 0.0005 and 0.001 wt% of graphene in 1-hexyl-3-methylimidazolium

tetrafluoroborate ([HMIM]BF_4). For corresponding fluid height 7.5 cm and 3.8 cm, the experimental results show good agreement with the numerical results. Gupta et al. (2015) experimentally studied the effect of Al_2O_3–H_2O nanofluid on the efficiency of a DASC flowing as a thin film over the glass absorber plate as a direct absorbing medium under outdoor condition. Three different nanofluid flow rates, i.e., 1.5, 2, and 2.5 L/min at a volume fraction of 0.005 %, were considered. The DASC efficiency and performance were compared with base fluid distilled water. They found that collector efficiency enhancement of 8.1 and 4.2 % increased with nanofluid at a mass flow rate of 1.5 and 2 L/min. In this study, optimum mass flow rate of 2.5 L/min for water and 2 L/min for nanofluid leads to maximum collector efficiency. Chen et al. (2015) performed experimental simulation of photothermal conversion efficiency and specific absorption rate using ZnO, TiO_2, and Ag nanofluid at different concentrations. Under simulated sunlight, the efficiency of silver nanofluid is 84.61 % after 5-min irradiation with a mass level of 80.94 ppm that was twice than water and much higher than the rest of nanofluid. They found that after 5 min of irradiance time, both temperature and specific absorption rate (SAR) decreased which show the effect of nanofluid as working fluid was excellent from the start. The highest value of SAR reached is 827 W/g at 20.24 ppm of concentration during increasing period of irradiance time. Moradi et al. (2015) investigated the utilization of carbon nanohorn-based nanofluids for a DASC used in the civil applications numerically. In their work, a three-dimensional model of the absorption phenomena in nanofluids within a cylindrical tube was coupled with a CFD analysis of the flow and temperature fields were studied. They also computed the heat losses due to the conduction, convection, and radiation at the boundaries.

Cregan and Myers (2015) presented an approximate analytical solution to the steady-state two-dimensional model for the efficiency of an inclined nanofluid-based DASC. The model consists of a system of two differential equations. A radiative transport equation is describing the propagation of solar radiation through the nanofluid and an energy equation for analytical progress. They introduced an approximate power law function for the radiative flux. By using the method of separation of variables, the resulting solution is used to investigate the efficiency of the collector subject to variation in model parameters. In their study, they included the wavelength-dependent absorption parameter and scattering due to both the base fluid and nanoparticles. An approximation for reflectance and absorptance due to the collector and its associated surfaces are computed. Gorji et al. (2015) characterized optical properties of chemically functionalized SWCNT aqueous suspensions in the application of DASC. Dispersion of functionalized CNT nanofluids in deionized water was prepared by two methods, by treating it with nitric and hydrochloric acid in the first method and nitric and sulfuric acid in the second method. Their optical properties at room and elevated temperature were measured and compared with the pristine carbon nanotube. Due to their increased polarity, carboxyl-functionalized SWCNTs show better solubility than pristine SWCNTs in water. They can bind hydrogen bonding with a polar solvent, and this effect is more evident in the second method compared to the first method of treated

SWCNTs. Optical characterization shows that functionalized carbon nanotube nanofluids show remarkable stability for being left at room temperature for three months and after undergoing thermal cycling. They concluded that compared with pristine SWCNT nanofluids, functionalized SWCNT aqueous suspensions can remarkably enhance radiation absorption of the spectrum without causing significant agglomeration and particle settling.

2.3 Evacuated Tube Solar Collector

Lu et al. (2011) designed a unique open thermosyphon device utilized in high-temperature evacuated tubular solar collectors. They investigated the thermal performance of the open thermosyphon using water-based CuO nanofluids and deionized water as working liquid using an indoor experimental setup. The effects of base fluid type, mass flow rate, nanoparticle concentration, and temperature on the effect of evaporating heat transfer characteristics in the open thermosyphon are investigated and discussed. Substituting water-based CuO nanofluids for water as the working fluid can significantly increase the thermal performance of the evaporator. Approximately 30 % increase in the evaporating heat transfer coefficients compared with those of deionized water was observed. The mass concentration of CuO nanoparticles has made a remarkable influence on the heat transfer coefficient in the evaporation section. Also, the mass concentration of 1.2 % corresponds to the optimal heat transfer enhancement shown in Fig. 6.

Liu et al. (2013) designed a novel evacuated tubular solar air collector integrated with a simplified compound parabolic concentrator (CPC) and special open thermosyphon using water-based CuO nanofluid as working fluid to provide air at different temperature range. The maximum value and the mean value of the collector efficiency with open thermosyphon by adopting nanofluids can increase by 6.6 and 12.4 %, respectively, as shown in Fig. 7. The maximum temperature of air at outlet is about 170 °C for a volume flow rate of 7.6 m^3/h in winter as shown in Fig. 8. They concluded that solar collector integrated with open thermosyphon had greater collecting performance than that incorporated with the conventional concentric tube.

Tong et al. (2015) analytically and experimentally evaluated the thermal performance of the enclosed-type evacuated U-tube solar collector (EEUSC) with a broad range of operating conditions. A MWCNT nanofluid was used as a working fluid to increase the heat transfer efficiency in U-tube over the thermal resistance offered by the air gap. The influence of the thickness of the air gap between the copper fin and the absorber filled with filling liquid on the heat transfer efficiency was also evaluated. They reported a 4 % increase in the ability of the EEUSC with the use of the MWCNT nanofluid with 0.24 vol% concentration. Heat transfer coefficient was about 8 % higher than that of water, mainly influenced by the air gap. The conductance of filing material was found to be larger than 0.17 W/(m K). They neither corrode the copper tube nor increase the cost. From the environmental

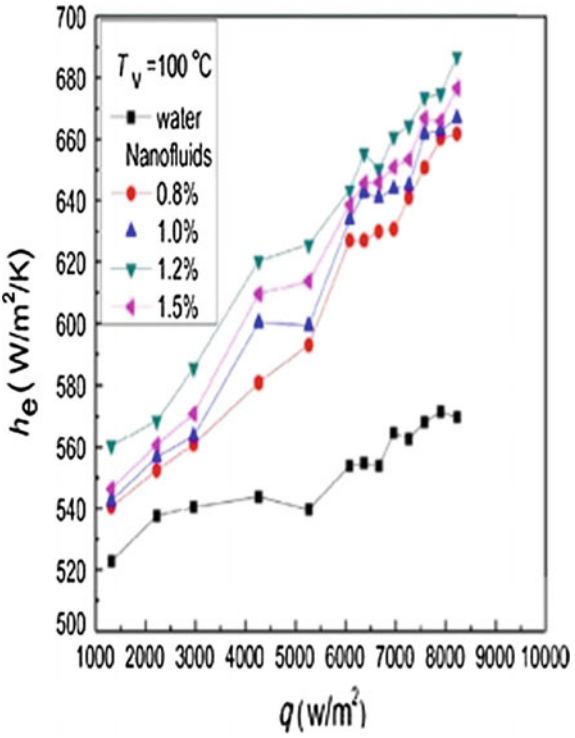

Fig. 6 Effect of filling ratio on evaporating high-temperature collector (Lu et al. 2011)

and economic point of concern, they concluded that the performance of collector can significantly contribute to the mitigation of greenhouse effects. Thus, enabling significant cost saving of 615 kg of coal yearly contributes to 1600 kg of CO_2 and 5.3 kg of SO_2, i.e., equivalent to the use of 50 solar collectors.

2.4 Parabolic Trough Collector

Risi et al. (2013) mathematically optimized and modeled the transparent parabolic trough collector (TPTC) based on gas-phase nanofluids. A new method of solar transparent parabolic trough collector (TPTC) which directly absorbs solar energy using gas-based nanofluid as heat transfer medium was suggested and examined. Also, a current composition of CuO and Ni (0.25 % CuO and 0.05 % Ni) nanoparticles has been designed for complete absorption of the solar energy within the receiver tube. Figure 9 shows the solar-to-thermal efficiency as a function of nanofluid mass flow rate. Result shows that the maximum solar-to-thermal efficiency increases up to a maximum value (62.5 %) with the rise in mass flow rate and gradually decreases up to a value of 2.5 kg/s. Simulation showed that TPTC

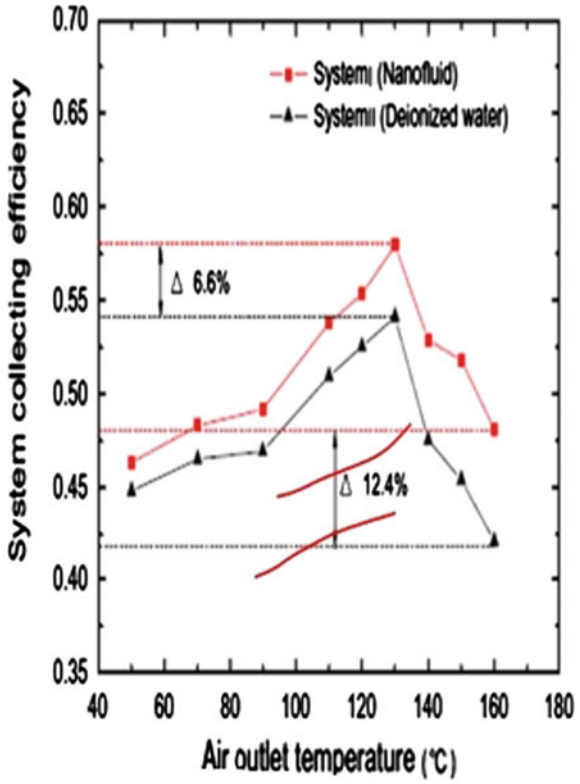

Fig. 7 Solar collecting efficiency under different operating temperatures (Liu et al. 2013)

solar-to-thermal efficiency is 62.5 % at 650 °C outlet temperature and 0.3 % nanoparticle volume concentration.

Sokhansefat et al. (2014) investigated the effect of Al_2O_3 nanoparticle concentration in the synthetic oil on the rate of heat transfer from the absorber tube in parabolic trough collector (PTC) under turbulent-mixed convection flow. Here, numerical study is validated with standard experimental cases. Studies were performed to determine the heat transfer coefficient for various nanoparticle concentrations (<5 % in volume) at the operational temperatures of 300 and 400 K presented along axial and circumferential directions. They found out that the presence of nanoparticle enhanced their heat transfer coefficient, and it increases with increases in the concentration of nanoparticles in base fluid. For a given Reynolds number, heat transfer coefficient decreased as the operational temperature of the absorber tube is increased. The maximum heat transfer coefficients obtained at the left and right sides of the tube, i.e., $\theta = 310$ and 210. They concluded that the use of a nanofluid in PTC could minimize the environment impact and improve heat transfer, which directly reduces the need for the heat exchanger and heat transfer area of tubes.

Kasaeian et al. (2014) experimentally designed and manufactured solar trough collector for global collector efficiency, using multi-walled carbon nanotube

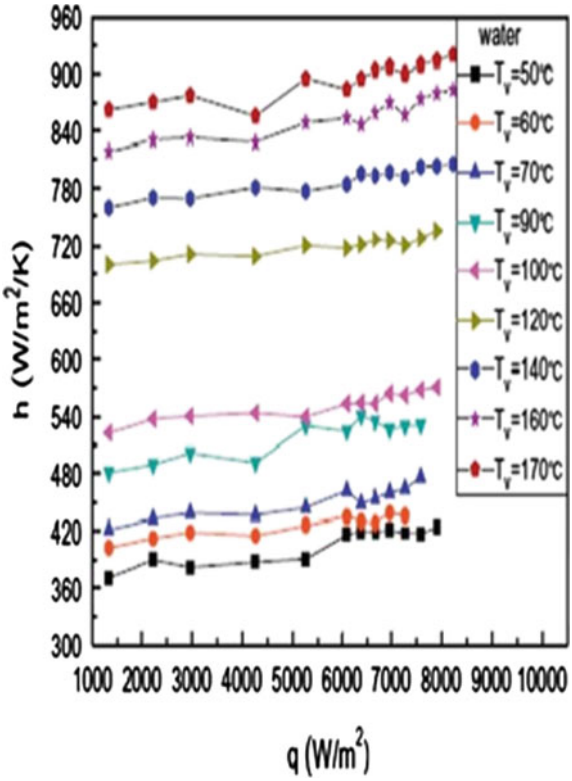

Fig. 8 Evaporating HTC of water in thermosyphon under different operating temperatures (Liu et al. 2013)

oil-based nanofluid as a working medium. Here, the time constant and optical and thermal efficiency of four different kinds of receiver tubes with different coating are used. They are black painted vacuumed steel tube, copper tube with black chrome coating, a vacuumed copper tube with black chrome coating, and a glass encircled non-evacuated copper tube with black chrome coating has been analysed and compared. All the operating conditions were tested according to ASHRAE standard. Results showed that the copper absorber tube coated with black chrome has the highest absorptivity 0.98 and thermal conductivity, and their global efficiency is 11 % greater than standard absorber tube. Their optical and thermal efficiencies are 0.61 and 0.68, respectively, for vacuumed copper absorber tube. With 0.2 and 0.3 %, MWCNT/mineral oil nanofluid efficiency was enhanced by 4–5 and 5–7 %. They concluded that using MWCNT/mineral oil nanofluid effectively increased the performance of high flux solar collector.

Sunil et al. (2014) experimentally studied the performance of a parabolic solar collector using SiO_2–H_2O-based nanofluid. Experiments were conducted for nanofluid concentration of 0.01 and 0.05 %, and at different volume flow rates of 20, 40, and 60 L/h. Here, the surfactants are not used; here, they use an ultrabath sonicator to enhance the stability and dispersion of nanoparticles in water. They found at a

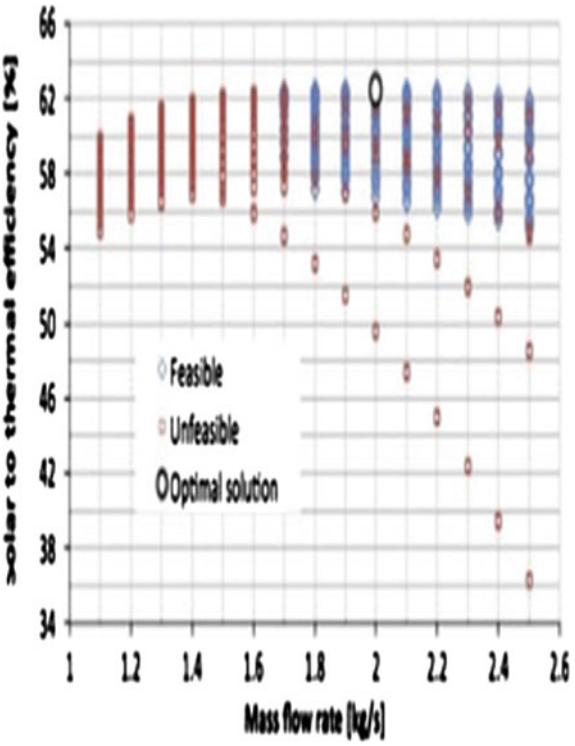

Fig. 9 Solar-to-thermal efficiency as a function of nanofluid mass flow rate (Risi et al. 2013)

particular volume concentration of 0.05 % and volume flow rate of 20, 40, and 60 L/h the performance was high. The maximum temperature rises, and maximum overall thermal efficiency is found to be 63.9, 63.2, and 65.4 °C and 7.4, 7.73, and 7.83 %, respectively at volume concentration of 0.05 %.

Jafar and Sivaraman (2014) experimentally studied the heat transfer, friction factor, and pressure drop characteristics of Al_2O_3/water nanofluids. Nanofluid passed through the receiver with nail twisted tape of two different twist ratios of $y = 2.0$ and 3.0, at a particle volume concentration of 0.1 and 0.3 % under laminar flow condition. The use of nanofluid enhances the heat transfer coefficient with no significant pressure drop compared to water. Twisted tape inserts result in pressure drop due to the increase of the disturbance in the laminar layer of the boundary layer. They found that the maximum Nusselt number was observed to be around 16 % when nanofluid is 0.3 % of volume concentration in a plain tube. The highest enhancement in Nusselt number is about 20 % when nanofluid with 0.3 % volume concentration is used with nail twisted tape tube.

Mwesigye et al. (2015) numerically investigated the thermal and thermodynamic performance of a parabolic trough receiver with a rim angle of 80° and concentration ratio of 86 using synthetic oil–Al_2O_3 nanofluid with the entropy generation minimization method. Here, nanoparticle volume fractions vary from 0 to 8 %, and Reynolds number varies from 3,560 to 1,151,000. They reported that using

nanofluid improves the thermal efficiency of the receiver by up to 7.6 % at lowest temperature and flow rate considered. Use of nanofluid enhanced the heat transfer by up to 76, 54, and 35 % as volume fraction increases from 0 to 8 %, 0 to 6 %, and 0 to 4 %, respectively. From the analysis, it is concluded that optimal Reynolds number was obtained for which entropy generation at receiver is minimum, and it decreases as volume fraction increases. From observations, there is Reynolds number beyond which the use of nanofluids makes no thermodynamic sense.

2.5 Concentrated–Parabolic Solar Collector

Khullar et al. (2010) performed theoretical and numerical investigation on the application of nanofluids as the working fluid in concentrating parabolic solar collectors using Al–water-based nanofluid as the working medium. The study was conducted to solve the equations numerically using finite difference method technique. To achieve the desired output temperature, the effect of various operating criteria such as receiver length, fluid velocity, concentration ratio, and the volume fraction of nanoparticles is taken into consideration. It showed that in terms of higher outlet temperatures, optical and thermal efficiency under similar working conditions, using nanofluid as a working fluid, showed better performance as compared to the conventional collector. They concluded that the inclusion of aluminum nanoparticles into the base fluid (water) significantly improves its absorption characteristics.

Vishwakarma et al. (2012) modeled the novel vapor absorption air-conditioning system (VACS). They studied the concept of nanofluid-based DASC for space cooling application for approximately 100 tons of refrigeration for both hourly variation in sunlight and seasonal changes for temperate climate conditions. Five types of nanoparticle volume fractions were used, i.e., 0.04, 0.03, 0.01, 0.005, and 0.001 %, respectively, and three nanoparticle sizes are 5, 15, and 40 nm. They found that nanofluids-based concentrated parabolic solar collector (NCPSC) was having higher efficiency compared to conventional parabolic trough solar collector. They concluded that the COP of the VACS kept on increasing with increase in collector outlet temperature as shown in Fig. 10. The NCPSC had the potential to offer high temperature, while maintaining greater efficiency, and hence, potentially can provide a sustainable and alternative way of providing air-conditioning.

Lenert et al. (2012) integrated a model and experimentally studied to optimize the efficiency of liquid-based solar receivers seeded with carbon-coated absorbing nanoparticles. They experimentally investigated a cylindrical nanofluid volumetric receiver. The efficiency was observed to be increasing with increase in solar concentration and nanofluid height and was a good agreement with varying optical thickness of the nanofluids with the model. Receiver-side efficiencies were predicted to exceed 35 % when nanofluid volumetric receivers are attached to their power cycle. These side efficiencies were optimized with respect to their solar

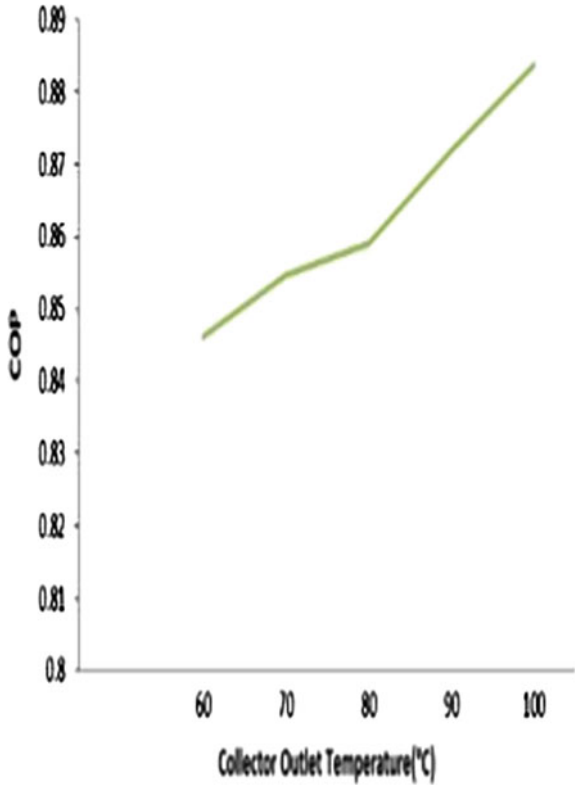

Fig. 10 Graph between COP and collector outlet temperature (Vishwakarma et al. 2012)

exposure time and optical thickness. Their study provides an important aspect of using nanofluids as volumetric receivers in concentrated solar applications.

Khullar et al. (2013) examined the nanofluid-based concentrating parabolic solar collector (NSPSC). The results of the model obtained were compared to that of experimental results of conventional parabolic solar collectors operating under same operating conditions. Aluminum nanoparticle with 0.05 volume fraction suspended in therminol VP-1 as a base fluid was used for analysis. While maintaining same external conditions, the thermal efficiency of NCPSC compared to a conventional collector is about 5–10 % higher under the same weather conditions. It indicated that the nanofluid-based concentrating parabolic solar collector has the potential to utilize solar radiant energy in a more efficient manner to that of the conventional parabolic trough. They observed that for getting the desired output in terms of thermal efficiency and maximum outlet fluid temperatures, shape, size, and material need to be optimized. They concluded that harvesting solar radiant energy into a commercial reality mathematical analysis needs to be validated by experimentation.

2.6 PV/T Collectors

Kabeel and Said (2013) modeled an integrated system using flashing desalination technique coupled with nanofluid-based collector as a heat source to investigate the effect of different operating modes. They also studied the variation of functioning parameter and weather condition on freshwater production. Thermal properties of the collector are improved by using different concentrated nanoparticles, and economic analysis is also conducted to determine the final cost of water production. Schematic setup of the commercial multi-stage flashing (MSF) shown in Fig. 11 can be applicable for daily freshwater productivity up to 7.7 L/m^2/day. They analyzed the cost of potable water to be about 11.68US \$/m^3. Freshwater production cost decreases with increase in solar collecting area and optimum solar water heater collecting area that gives higher productivity and low cost equal about 3.54 m^2. They concluded that increase in collecting the area of solar water heater could reduce the water production cost by 63.3 % with an increase in the fixed capital cost of 87 %.

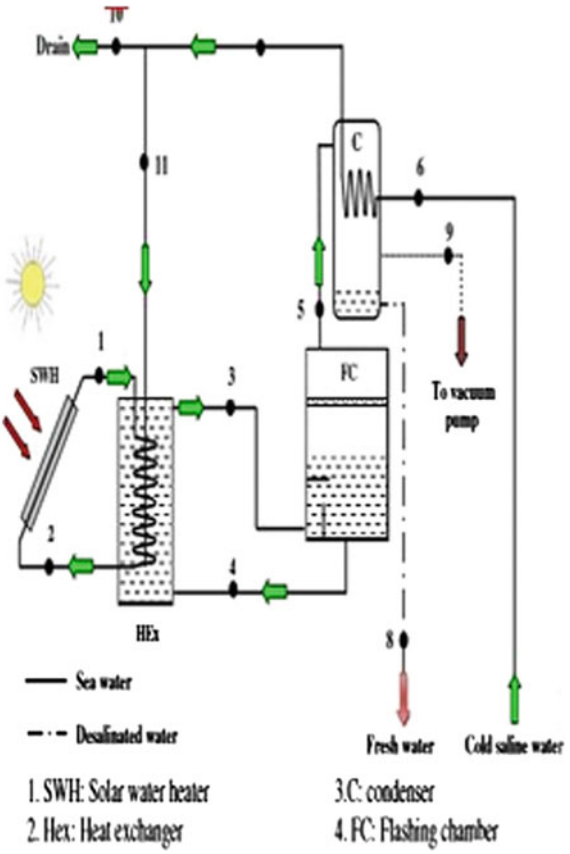

Fig. 11 Schematic diagram of small-scale single-stage flash (SSF) system (Kabeel and Said 2013)

Michael and Iniyan (2015) experimentally studied the performance of novel photovoltaic–thermal (PV\T) collector, constructed by laminating copper sheet directly to silicon cell. By this process, they reduce the heat resistance and its performance was further improved by using copper oxide–water nanofluid. Various characterizations were performed using CuO/water nanofluid at a small concentration of 0.05 % compared to that of water at a fixed mass flow rate of 0.01 kg/s. The analysis shows the effect of higher thermal conductivity of nanofluid on the electrical performance and thermal performance of the PV/T collector. The lower electrical performance was observed in the PV/T collector using nanofluid when compared to water due to higher temperature of the PV/T collector as shown in Figs. 12 and 13. They attributed the reason as higher thermal conductivity of nanofluid and higher outlet temperature of CuO/water nanofluid are partly attributable to the slightly lower Reynolds number and higher viscosity compared to water. They found that nanofluid had enhanced the thermal efficiency up to 45.76 % to that of pure water. They concluded that PV/T collector can improve if the heat exchanger is redesigned for the new nanofluid.

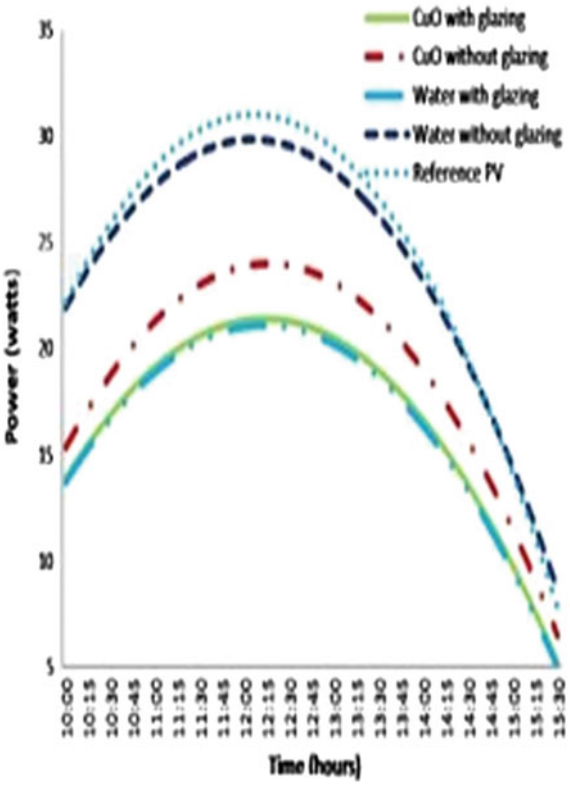

Fig. 12 Electrical power output of the PV/T collector (Michael and Iniyan 2015)

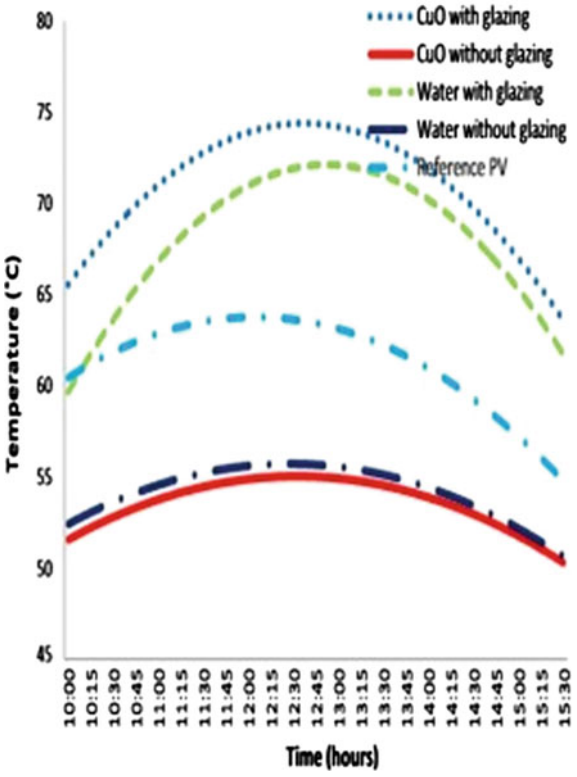

Fig. 13 Top glass layer temperature of the PV/T collector (Michael and Iniyan 2015)

3 Challenges of Utilizing Nanofluids

There are many challenges that engineers and researchers currently encounter in terms of increasing overall performance of systems including sustainable increase in efficiency, reliability, durability, safety for different operating parameters, and decrease in the overall costs, size, and weight. From the hypothetical perspective, using nanofluid is definitely beneficial with respect to improvement in rate of heat transfer of the system. However, on the contrary, it has some disadvantages when compared to base fluid as reported in the literature on nanofluids. The problems include increased pressure drop and pumping power due to viscosity factor, lower specific heat (Said et al. 2015), and decreased stability of nanoparticles suspension with time (Saidur et al. 2011). Also, the method and cost involved in the preparation of nanofluids is an area of concern where advanced and sophisticated equipment is required for characterization.

4 Future Directions

To account for the use of nanotechnology to overcome future energy challenges, there are several practical issues that need to be solved such as particle migration, Brownian motion of particle, varied thermophysical properties with temperature, particle agglomeration, and change of nanofluid properties with the addition of surfactants (Saidur et al. 2011). Studies on the physical and chemical surface interactions between the nanoparticles and base fluid molecules to understand the mechanisms of enhanced flow and thermal behavior of nanofluids are incomplete. Development of new experimental methods for characterizing and understanding nanofluid behavior in the laboratory scale is scarce. Development of collector with different fluid flow geometries utilizing nanofluid as a working fluid was not yet reported. Lack of studies on optical properties of nanofluid in the solar collector to use a direct absorber and other features needs attention expect that much information is available only on the determination of thermal conductivity. Improving the theoretical understanding of the behavior of complex nanofluids has even broader impact in this field of research.

5 Conclusions

Application of nanotechnology has a high potential for solar energy conversion and highly suitable for domestic hot water and process heating systems. Because properties of nanofluids are unique, due to a smaller size and larger surface area, they make a massive evolution in different thermochemical and photocatalytic applications. Therefore, nanotechnology shows higher potential for engineering applications related to heat transfer by increasing the energy performance and decreasing energy losses. In specific to solar thermal conversion devices, nanotechnology can be used in coatings, fluid dispersions, and storage media. They provide alternative ways for engineers to develop highly efficient green devices. Despite the fact that optical properties of nanofluid change with an increase in concentration, these fluids had a considerable impact on the performance of non-direct collector. Indirect absorber solar collector due to change in optical properties of base fluid such as transmittance and extinction coefficient leads to a significant improvement in the energy collection per unit area. The critical challenges for the use of nanofluids in solar systems comprise high cost of production, agglomeration problems, instability, increased pumping power, and erosion that had reported in the literature. Such type of issues would eventually be overcome shortly with the development of nanotechnology. Optimization and modeling of nanotechnology-based thermochemical and photocatalytic applications with different materials are still scared.

References

Amirhossein, Z., Mansoor, K. R., Maryam, K. N., & Milad, T. J.-A. (2014). An experimental study on the effect of Cu-synthesized/EG nanofluid on the efficiency of flat-plate solar collectors. *Renew Energy, 71*, 658–664.

Arun, K. T., Vikas, K., & Subrata, K. G. (2015). Implementation of nanofluids in plate heat exchanger. *International Journal of Advanced Research in Science, Engineering and Technology, 4*, 2319–8354.

Bandarra Filho, E. P., Hernandez Mendoza, O. S., Lins Beicker, C. L., Menezes, A., & Wen, D. (2014). Experimental investigation of a silver nanoparticle-based direct absorption solar thermal system. *Energy Conversion and Management, 84*, 261–267.

Chaji, H., Ajabshirchi, Y., Esmaeilzadeh, E., Heris Saeid, Z., Hedayatizadeh, M., & Kahani, M. (2013). Experimental study on the thermal efficiency of flat plate solar collector using TiO_2/water nanofluid. *Modern Applied Science, 7*, 60–69.

Chen, M., He, Y., Zhu, J., Shuai, Y., Jiang, B., & Huang, Y. (2015). An experimental investigation on sunlight absorption characteristics of silver nanofluids. *Solar Energy, 115*, 85–94.

Choi, S. (1995). Enhancing thermal conductivity of fluids with nanoparticles. In D. A. Siginer & H. P. Wang (Eds.), *Development and applications of non-newtonian flows* (Vol. 66, pp. 99–105). New York: ASME.

Chougule, S. S., Pise, A. T., & Madane, P. A. (2012). Performance of nanofluid-charged solar water heater by the solar tracking system. In *Proceedings of IEEE International Conference on Advances in Engineering, Science and Management.* EGS Pillay Engineering College Nagapattinam, Tamil Nadu, India, March 30–31, 2012.

Cregan, V., & Myers, T. G. (2015). Modelling the efficiency of a nanofluid direct absorption solar collector. *International Journal of Heat and Mass Transfer, 90*, 505–514.

Das, S. K., Putra, N., & Roetzel, W. (2003). Pool boiling characteristics of nano–fluids. *International Journal of Heat and Mass Transfer, 46*, 851–862.

De Risi, A., Milanese, M., & Laforgia, D. (2013). Modelling and optimization of transparent parabolic trough collector based on gas-phase nanofluids. *Renew Energy, 58*, 134–139.

Dharmalingama, R., Sivagnanaprabhub, K. K., Senthil Kumar, B., & Thirumalaid, R. (2014). Nanomaterials and nanofluids: An innovative technology study for new paradigms for technology enhancement. *Procedia Engineering, 97*, 1434–1441.

Eastman, J. A., Phillpot, S., Choi, S., & Keblinski, K. (2004). Thermal transport in nanofluids. *Annual Review of Materials Research, 34*, 219–246.

Eshan, S., Farzad, V., & Ahmad, K. (2015). Exergy efficiency investigation and optimization of an Al_2O_3-water nanofluid based flat-plate solar collector.

Faizal, M., Saidur, R., Mekhilef, S., & Alim, M. A. (2013). Energy, economic and environmental analysis of metal oxides nanofluid for the flat-plate solar collector. *Energy Conversion and Management, 76*, 162–168.

Gorji, T. B., Ranjbar, A. A., & Mirzababaei, S. N. (2015). Optical properties of carboxyl functionalized carbon nanotube aqueous nanofluids as direct solar thermal energy absorbers. *Solar Energy, 119*, 332–342.

Goudarzi, K., Nejati, F., Shojaeizadeh, E., & Asadi, Y.-A. (2014). Experimental study on the effect of pH variation of nanofluids on the thermal efficiency of a solar collector with the helical tube. *Experimental Thermal Fluid Science, 60*, 20–27.

Gupta, H. K., Agrawal, G. D., & Mathur, J. (2015). Investigations of the effect of Al_2O_3–H_2O nanofluid flow rate on the efficiency of direct absorption solar collector. *Case Studies in Thermal Engineering, 5*, 70–78.

He, Q., Wang, S., Zeng, S., & Zheng, Z. (2013). Experimental investigation on photothermal properties of nanofluids for direct absorption solar thermal energy systems. *Energy Conversion and Management, 73*, 150–157.

Hordy, N., Rabilloud, D., Meunier, J.-L., & Coulombe, S. (2014). High temperature and long-term stability of carbon nanotube nanofluids for direct absorption solar thermal collectors. *Solar Energy, 105*, 82–90.

Jafar, K. S., & Sivaraman, B. (2014). Thermal performance of solar parabolic trough collector using nanofluids and the absorber with nail twisted tapes inserts. *International Energy Journal, 14*, 189–198.

Jang, S. P., & Choi, S. (2006). Cooling performance of a microchannel heat sink with nanofluids. *Applied Thermal Engineering, 26*, 2457–2463.

Kabeel, A. E., & El-Said, E. M. S. (2013). Applicability of flashing desalination technique for small-scale needs using a novel integrated system coupled with the nanofluid-based solar collector. *Desalination, 333*, 10–22.

Kalogirou, S. A. (2004). Solar thermal collectors and applications. *Progress in Energy and Combustion Science, 30*, 231–295.

Kasaeian, A., Daviran, S., Azarian, R. D., & Rashidi, A. (2014). Performance evaluation and nanofluid using capability study of a solar parabolic trough collector. *Energy Conversion and Management, 89*, 368–375.

Keblinski, P., Phillpot, S., Choi, S., & Eastman, J. (2002). Mechanisms of heat flow in suspensions of nano-sized particles (nanofluids). *International Journal of Heat and Mass Transfer*, *9*, 855–863. doi:10.1016/S0017-9310(01)00175-2

Khullar, V., & Tyagi, H. (2010). *Application of nanofluids as the working fluid in concentrating parabolic solar collectors*. Paper presented at the 37th National & 4th International Conference on Fluid Mechanics & Fluid Power, IIT Madras, Chennai, India, December 16–18, 2010.

Khullar, V., Tyagi, H., Phelan, P. E., Otanicar, T. P., Singh, H., & Taylor, R. A. (2013). Solar energy harvesting using nanofluids-based concentrating solar collector. *Journal of Nanotechnology in Engineering and Medicine, 3*, 1003–1012.

Khullara, V., & Tyagia, H. (2012). A study on environmental impact of nanofluid-based concentrating solar water heating system. *International Journal of Environmental Studies, 69*, 220–232.

Kulkarni, D. P., Namburu, P. K., Bargar, H. E., & Das, D. K. (2008). Convective heat transfer and fluid dynamic characteristics of SiO_2-ethylene glycol/water nanofluid. *Heat Transfer Engineering, 29*, 1027–1035.

Kundan, L., & Sharma, P. (2013). Performance evaluation of a nanofluid ($CuO–H_2O$) based low flux solar collector. *International Journal of Engineering Research, 2*, 108–112.

Ladejevardi, S. M., Asnaghi, A., Izadkhast, P. S., & Kashano, A. H. (2013). Applicability of graphic nanofluids in direct solar energy absorption. *Solar Energy, 94*, 327–334.

Lee, S., Choi, S., & Li, Eastman J. A. (1999). Measuring thermal conductivity of fluids containing oxide nanoparticles. *ASME Journal of Heat Transfer, 121*, 280–289.

Lenert, A., & Wang, E. N. (2012). Optimization of nanofluid volumetric receivers for solar thermal energy conversion. *Solar Energy, 86*, 253–265.

Li, Y., Zhou, J., Tung, S., Schneider, E., & Xi, S. (2009). A review on development of nanofluid preparation and characterization. *Powder Technology, 196*, 89–101.

Liu, Z.-H., Hu, R.-L., Lu, L., Zhao, F., & Xiao, H.-S. (2013). Thermal performance of an open thermosyphon using nanofluid for evacuated tubular high-temperature air solar collector. *Energy Conversion and Management, 73*, 135–143.

Liu, J., Ye, Z., Zhang, L., Fang, X., & Zhang, Z. (2015). A combined numerical and experimental study on graphene/ionic liquid nanofluid-based direct absorption, solar collector. *Solar Energy Materials and Solar Cells, 136*, 177–186.

Lu, L., Liu, Z.-H., & Xiao, H.-S. (2011). Thermal performance of an open thermosyphon using nanofluids for high-temperature evacuated tubular solar collectors. *Solar Energy, 85*, 379–387.

Luo, Z., Wang, C., Wei, W., Xiao, G., & Ni, M. (2014). Performance improvement of a nanofluid solar collector based on direct absorption collection (DAC) concepts. *International Journal of Heat and Mass Transfer, 75*, 262–271.

Mahian, O., kianifar, A., Kalogirou, S. A., Pop, I., & Wongwises, S. (2013). A review of the applications of nanofluids in solar energy. *International Journal of Heat and Mass Transfer, 57*, 582–594.

Michael, J. J., & Iniyan, S. (2015). Performance analysis of a copper sheet laminated photovoltaic-thermal collector using copper oxide—water nanofluid. *Solar Energy, 119*, 439–451.

Moghadam, A. J., Mahmood, F.-G., Sajadi, M., & Monireh, H.-Z. (2014). Effects of CuO/water nanofluid on the efficiency of a flat-plate solar collector. *Experimental Thermal and Fluid Science, 58*, 9–14.

Moradi, A., Sani, E., Simonetti, M., Francini, F., Chiavazzo, E., & Asinari, P. (2015). Carbon–nano horn based nanofluids for a direct absorption solar collector for the civil application. *Journal of Nanoscience and Nanotechnology, 15*, 3488–3495.

Mwesigye, A., Huan, Z., & Meyer, J. P. (2015). Thermodynamic optimisation of the performance of a parabolic trough receiver using synthetic oil–Al_2O_3 nanofluid. *Applied Energy, 156*, 398–412.

Nasrin, R., Parvin, S., & Alim, M. A. (2013). Effect of Prandtl number on free convection in a solar collector filled with nanofluid. *Procedia Engineering, 56*, 54–62.

Norton, B. (2013). *Harnessing solar heat*. Northern Ireland.

Omid, M., Ali, K., Ahmet, Z. S., & Somchai, W. (2014a). Entropy generation during Al_2O_3/water nanofluid flow in a solar collector: Effect of tube roughness, nanoparticle size, and different thermophysical model. *International Journal of Heat and Mass Transfer, 78*, 64–75.

Omid, M., Ali, K., Ahmet, Z. S., & Somchai, W. (2014b). Performance analysis of a mini channel-based solar collector using different nanofluids. *Energy Conversion and Management, 88*, 129–138.

Omid, M., Ali, K., Saeed, Z. H., & Somchai, W. (2014c). First and Second law analysis of a mini channel-based solar collector using boehmite alumina nanofluids: effects of nanoparticle shape and tube materials. *International Journal of Heat and Mass Transfer, 78*, 1166–1176.

Otanicar, T. P., & Golden, J. S. (2009). Comparative environmental and economic analysis of conventional and nanofluid solar hot water technologies. *Environmental Science and Technology, 43*, 6082–6087.

Otanicar, T. P., Phelan, P. E., Prasher, R. S., Rosengarten, G., & Taylor, R. A. (2010). Nanofluidbased direct absorption solar collector. *Journal of Renewable and Sustainable Energy, 2*, 33–102.

Parvin, S., Nasrin, R., & Alim, M. A. (2013). Heat transfer and entropy generation through nanofluid filled direct absorption, solar collector. *International Journal of Heat and Mass Transfer, 71*, 386–395.

Raja Sekhar, Y., Sharma, K. V., Thundil Karupparaja, R., & Chiranjeevi, C. (2013). Heat transfer enhancement with Al_2O_3-nanofluids and twisted tapes in a pipe for solar thermal applications. *Procedia Engineering, 64*, 1474–1500.

Rehena, N., Salma, P., & Alim, M. A. (2014). Heat transfer by nanofluids through a flat plate solar collector. *Procedia Engineering, 90*, 364–370.

Sadique, M., & Verma, A. (2014). Nano fluid-based receivers for increasing efficiency of solar panels. *International Journal of Advanced Structural Engineering, 4*, 77–82.

Said, Z., Sabiha, M. A., Saidur, R., Hepbasli, A., Rahim, N. A., Mekhilef, S., et al. (2015a). Performance enhancement of a flat plate solar collector using Titanium dioxide nanofluid and polyethylene glycol dispersant. *Journal of Cleaner Production, 92*, 343–353.

Said, Z., Saidur, R., Rahim, N. A., & Alim, M. A. (2014). Analyzes of energy efficiency and pumping power for a conventional flat plate solar collector using SWCNTs based nanofluid. *Energy Buildings, 78*, 1–9.

Said, Z., Saidur, R., Sabiha, M. A., Hepbasli, A., & Rahim, N. A. (2015b). Energy and exergy efficiency of a flat plate solar collector using pH for Al_2O_3–H_2O nanofluid. *Journal of Cleaner Production*, 1–12.

Said, Z., Saidur, R., Sabiha, M. A., & Rahim, A. M. R. (2015c). Thermophysical properties of single wall carbon Nanotubes and its effect on exergy of a flat plate solar collector.

Said, Z., Sajid, M. H., Alim, M. A., Saidur, R., & Rahim, N. A. (2013). Experimental on a flat plate solar collector. *International Communications in Heat and Mass Transfer, 48*, 99–107.

Saidur, R., Leong, K. Y., & Mohammad, H. A. (2011). A review on applications and challenges of nanofluids. *Renewable and Sustainable Energy Reviews*, *15*,1646–1668.

Saidur, R., Meng, T. C., Said, Z., Hasanuzzaman, M., & Kamyar, A. (2012). Evaluation of the effect of nanofluid-based absorbers on the direct solar collector. *International Journal of Heat and Mass Transfer, 55*, 5899–5907.

Saleh, S., Ali, K., Hamid, N., Omid, M., & Somachi, W. (2015). Experimental investigation on the thermal efficiency and performance characteristics of a flat plate solar collector using SiO_2/ethylene glycol (EG)-water nanofluids. *International Communications in Heat and Mass Transfer*. doi:10.1016/j.icheatmasstransfer.2015.02.011

Selvakumar, P., & Suresh, S. (2012). Convective performance of CuO/water nanofluid in an electronic heat sink. *Experimental Thermal and Fluid Science, 40*, 57–63.

Sharma, K. V., Sunder, L., & Shyam, Sharma P. K. (2009). Estimation of heat transfer coefficient and friction factor in transition flow with low volume concentration of Al_2O_3 nanofluid flowing in a circular tube and with twisted tape. *International Communications in Heat and Mass Transfer, 36*, 503–507.

Sokhansefat, T., Kasaeian, A. B., & Kowsary, F. (2014). Heat transfer enhancement in parabolic trough collector tube using Al_2O_3/synthetic oil nanofluid. *Renewable and Sustainable Energy Reviews, 33*, 636–644.

Sunil, K., Kundan, L., & Sumeet, S. (2014). Performance evaluation of a nanofluid based parabolic solar collector—An experimental study. *International Journal of Mechanical and Production Engineering Research and Development (IJMPERD), 10*, 2320–2400.

Taylor, R. A., Phelan, P. E., Otanicar, T. P., Adrian, R., & Prasher, R. P. (2011a). Nanofluid optical property characterization towards efficient direct absorption solar collectors. *Nanoscale Research Letters, 6*(1), 225.

Taylor, R. A., Phelan, P. E., Otanicar, T. P., Walker, C. A., Nguyen, M., & Trimble, S. (2011b). Applicability of nanofluids in high flux solar collectors. *Journal of Renewable and Sustainable Energy, 3*, 023104.

Tiwari, A. K., Ghosh, P., & Sarkar, J. (2013). Solar water heating using nanofluids—a comprehensive overview and environmental impact analysis. *International Journal of Emerging Technology and Advanced Engineering, 3*, 221–224.

Tong, Y., Kim, J., & Cho, H. (2015). Effects of thermal performance of enclosed-type evacuated U-tube solar collector with multi-walled carbon nanotube/water nanofluid. *Renew Energy, 83*, 463–473.

Tyagi, H., Phelan, P., & Prasher, R. (2009). Predicted efficiency of a low-temperature nanofluid-based direct absorption solar collector. *Journal of Solar Energy Engineering, 131*, 1–7.

Verma, V., & Kundan, L. (2013). Thermal performance evaluation of a direct absorption flat plate solar collector (DASC) using Al_2O3–H_2O based nanofluids. *ISOR Journal of Mechanical and Civil Engineering, 6*, 2320–3344.

Vishwakarma, V., Singhal, N., Khullar, V., & Tyagi, H. (2012). Space cooling using the concept of nanofluids-based direct absorption solar collectors. In R. A. Taylor, T. P. Otanicar & A. Jain (Eds.), *Proceedings of the ASME 2012 international mechanical engineering congress & exposition*. Houston, Texas, USA, November 9–15, 2012.

Wen, D., & Ding, Y. (2005). Experimental investigation into the pool boiling heat transfer of aqueous based-alumina nanofluids. *Journal of Nanoparticle Research, 7*, 265–274.

Wong, K. V., & De Leon, O. (2009). Applications of nanofluids: Current and future. *Add in Mechanical Engineering*. doi:10.1155/s11519659

Wongcharee, K., & Smith, E.-A. (2011). Enhancement of heat transfer using CuO/water nanofluid and twisted tape with the alternate axis. *International Communications in Heat and Mass Transfer, 38*, 742–748.

Xuan, Y., & Li, Q. (2000). Heat transfer enhancement of nanofluids. *International Journal of Heat and Fluid Flow, 21*, 58–64.

Yousefi, T., Shojaeizadeh, E., Veysi, F., & Zinadini, S. (2012a). An experimental investigation on the effect of pH variation of MWCNT–H_2O nanofluid on the efficiency of a flat-plate solar collector. *Solar Energy, 86*, 771–779.

Yousefi, T., Veisy, F., Shojaeizadeh, E., & Zinadini, S. (2012b). An experimental investigation on the effect of MWCNT-H_2O nanofluid on the efficiency of flat-plate solar collectors. *Experimental Thermal Fluid Science, 39*, 207–212.

Yousefi, T., Veysi, F., Shojaeizadeh, E., & Zinadini, S. (2012c). An experimental investigation on the effect of Al_2O_3–H_2O nanofluid on the efficiency of flat-plate solar collectors. *Renew Energy, 39*, 293–298.

Zhang, L., Liu, J., He, G., Ye, Z., Fang, X., & Zhang, Z. (2014). Radiative properties of ionic liquid-based nanofluids for medium-to-high-temperature direct absorption solar collectors. *Solar Energy Materials and Solar Cells, 130*, 521–528.

Thin Film Hydrodynamic Bearing Analysis Using Nanoparticle Additive Lubricants

T.V.V.L.N. Rao, A.M.A. Rani, S. Sufian and N.M. Mohamed

Abstract Analysis of thin film lubrication of (i) nanoparticle additive three-layered journal bearing lubricated with Newtonian fluid, (ii) nanoparticle additive three-layered journal bearing lubricated with couple stress fluid, (iii) Newtonian fluid lubricated partial slip slider bearing with electric double layer, and (iv) porous-layered carbon nanotubes (CNTs) additive Newtonian fluid lubricated slider bearing with electric double layer are presented. The analysis of three-layered journal bearing with nanoparticle additives incorporates Reynolds boundary conditions to predict load capacity parameter and coefficient of friction. The load capacity parameter increases for thick, high-viscosity fluid film layers and nanoparticle additive fluid film. Coefficient of friction is reduced for high viscosity surface adjoining layer. Stokes microcontinuum theory is used in the analysis of couple stress fluids in a three-layered journal bearing lubricated with nanoparticle additives. A three-layered journal bearing using couple stresses fluids with nanoparticle additives increases nondimensional load capacity and decreases coefficient of friction. A slider bearing with partial boundary slip and electric double layer leads to an increase in apparent viscosity of lubricant and hence load carrying capacity in thin film lubrication. A parallel slider bearing with partial slip on bearing and electric double layer increases the bearing load capacity. The flow of lubricant with CNT additives in a slider bearing in thin film and porous layers with electric double layer is governed by Stokes and Brinkman equations, respectively, including electrokinetic force. The nondimensional load capacity of slider bearing increases with decrease in permeability and increase in thickness of porous layer as

T.V.V.L.N.Rao (✉) · A.M.A. Rani
Department of Mechanical Engineering, Universiti Teknologi PETRONAS,
32610 Bandar Seri Iskandar, Perak Darul Ridzuan, Malaysia
e-mail: tadimalla_v@petronas.com.my

S. Sufian
Department of Chemical Engineering, Universiti Teknologi PETRONAS,
32610 Bandar Seri Iskandar, Perak Darul Ridzuan, Malaysia

N.M. Mohamed
Department of Fundamental and Applied Sciences, Universiti Teknologi PETRONAS,
32610 Bandar Seri Iskandar, Perak Darul Ridzuan, Malaysia

K. Viswanatha Sharma and N. Hisham B Hamid (eds.),
Engineering Applications of Nanotechnology, Topics in Mining, Metallurgy
and Materials Engineering, DOI 10.1007/978-3-319-29761-3_6

well as increase in both electro-viscosity and CNT additives volume fraction. A thin film slider bearing using CNT additive lubricants with porous and electric double layer provides higher load capacity.

Keywords Slider and journal bearing · Load capacity · Coefficient of friction · Couple stress fluids · Porouslayer · Electric double layer · CNT additive lubricants

Nomenclature

a_a, a	Radii of aggregate and primary CNT
a_h	Nondimensional slider bearing slope parameter; $a_h = 1 - h_2$
A	Nondimensional slip coefficient
c_{wf}	Load capacity parameter, friction coefficient parameter
C_f	Friction coefficient
C	Journal bearing radial clearance, m
D	Fractal index of nanoparticles
f	Friction force in journal bearing, N; $F = fC/\mu_f u_j RL$
h	Film thickness, m; $H = h/h_1$ for slider bearing, $H = h/C$ for journal bearing
h_1, h_2, h_0	Film thickness at inlet and outlet of slider bearing and reference film thickness, m
k	Permeability of the porous layer, m^2; $K = k/h_1^2$
L_s	Slider bearing length, m
L	Slider bearing width, journal bearing length, m
p	Pressure distribution, N/m^2; $P = ph_1^2/\mu_f u_j L$ for slider bearing, $P = pC^2/\mu_f u_j R$ for journal bearing
r	Aspect ratio of CNT
R	Journal radius, m
u_j	Shaft speed, m/s; $u_j = \omega R$
w	Static load, N; $W = wh_1^2/\mu_f u_j L^2 L_s$ for slider bearing, $W = wC^2/\mu_f u_j R^2 L$ for journal bearing
W_ε, W_ϕ	Nondimensional load capacity for journal bearing in radial and tangential directions
x	Coordinate along sliding (x) direction, m; $X = x/L$ for slider bearing, $\theta = x/R$ for journal bearing
X_s	Nondimensional slip length in slider bearing
y	Coordinate along radial direction, m; $Y = y/h$ for slider bearing, $Y = y/C$ for journal bearing

Greek letters

α	Slip coefficient; $A = \alpha\mu_f/h_1$
$\beta_a, \beta_{e0}, \beta_e$	Nondimensional apparent viscosity, electro-viscosity, and reference electro-viscosity, respectively; $\beta_a = \mu_a/\mu_f$, $\beta_{e0} = \frac{\zeta^2\varepsilon_d^2\varepsilon_0^2}{\mu_f\lambda_i h_0^2}$, $\beta_e = \beta_{e0}\left(\frac{h_a}{h_1}\right)^2$

B_{nf}, β_{sc}	Nano to base fluid and surface to core layer dynamic viscosity ratios, respectively; $\beta_n = \mu_n/\mu_f$, $\beta_{sc} = \mu_s/\mu_c$
β_d	Nondimensional constant charge density; $\beta_d = \rho_d h_1^2/\zeta\varepsilon_d\varepsilon_o$
γ	Journal/bearing surface fluid film layer thickness ratio; $\gamma = \frac{h_s}{h}$
Δ	Journal/bearing surface adsorbent fluid film layer thickness; $\Delta = \frac{\delta}{C}$
δ	Porous layer thickness, m; $\Delta = \delta$/C
ε	Eccentricity ratio of journal bearing
ε_d	Dielectric permittivity
ε_0	Vacuum permittivity, F/m
ζ	Zeta potential on the surface, V
μ_a, μ_e	Apparent viscosity and electro-viscosity, respectively, Ns/m^2
μ_n, μ_f	Nano and base fluid viscosity, Ns/m^2
μ_s, μ_c	Surface and core layer viscosity, Ns/m^2
η	Couple stress material constant, kg m/s
κ_i	Inverse Debye length, 1/m; $K_i = \kappa_i h_1$
ρ_d	Constant charge density, C/m^3
λ	Couple stress parameter; $\lambda = \left(\sqrt{\eta/\mu}\right)/C$
λ_i	Specific conductance, S/m
ϕ	Nanoparticles volume fraction
ϕ_a, ϕ_m	Aggregate and maximum volume fraction of nanoparticles
θ	Coordinate in angular direction measured from maximum film thickness in journal bearing
θ_r	Extent of film rupture measured in angular direction for journal bearing
τ	Shear stress in journal bearing, N/m^2; $\Pi = \tau C/\mu_f U$
ω	Journal bearing angular velocity, rad/s

1 Three-Layered Journal Bearing Analysis Using Nanoparticle Additive Lubricants

Analysis of journal bearing with three-layered film using nanoparticle additive lubricants is presented. The three fluid film layers in journal bearing are assumed to be Newtonian. The analysis of three-layered journal bearing is presented based on the theory of composite-film bearings and takes into account of fluid film layer's thickness and viscosity of nanoparticle additive fluid. Nondimensional pressure distribution is obtained from integration of modified Reynolds equation using Reynolds boundary conditions. Load capacity parameter and coefficient of friction are analyzed with surface absorbent layer's thickness ratio (γ), dynamic viscosity ratio of surface layer to core layer (β_{sc}), and volume fraction of nanoparticles (ϕ).

1.1 Thin Film Lubrication

Fluid film properties and structure significantly influence thin film hydrodynamic lubrication. In thin film lubrication (TFL), effective viscosity of adsorbed layer at the surfaces under relative motion is much greater than the bulk Newtonian viscosity. The adsorbed molecular layer thickness and viscosity are the most critical factors in thin film lubrication. Tichy (1995) and Qingwen et al. (1998) studied the effect of lubricant molecular structure and developed thin film model of solid surfaces adhered high viscosity layer. Based on thin film lubrication analysis, as viscosity and thickness of adsorbed layer at solid surfaces increases, results indicate increase in load capacity and decrease in coefficient of friction. Meurisse and Espejel (2008) also presented a generalized Reynolds equation for a three-layered film model.

Analysis of journal bearing load capacity and friction coefficient in three-layered film is influenced by dynamic viscosity of fluid film. Szeri (2010) investigated composite film configuration for increase in load capacity (high viscosity lubricant) and decrease in friction (low viscosity lubricant). The composite film journal bearing consists of higher and lower viscosity fluid layers adjacent to bearing surface and journal surface, respectively. Nabhan et al. (1997) also investigated binary fluid film (oil-in-water) lubricated hydrodynamic journal bearing.

1.2 Nanoparticle Additive Lubricants

Nanoparticle additive lubricants increase the load capacity of fluid film bearings due to increase in lubricant viscosity. Shenoy et al. (2012) presented the influence of API-SF engine oil with nanoparticle additives on the characteristics of an externally adjustable statically loaded fluid film bearing. Nair et al. (2009) presented characteristics of statically loaded journal bearing operating lubricants with nanoparticle additives. Babu et al. (2012) presented the effect lubricants with nanoparticle additives on static and dynamic characteristics of journal bearing. The commercial lubricant with copper oxide, cerium oxide, and aluminum oxide nanoparticles is used in the analysis. Viscosity models for nanoparticle additive lubricants were developed using the available experimental data.

Theory on viscosity of nanofluids suggested by Einstein (1906) based on dilute suspended spherical particles in viscous fluids. Einstein's pioneering formula is valid for spherical particles with low nanoparticle volume fraction. Brinkman (1952) contributed to extend the Einstein equation considering the effect of moderate spherical nanoparticle suspensions in viscous fluids. Batchelor (1977) proposed second order formula for the viscosity of nanofluids considering Brownian motion effect of spherical nanoparticle additives and their interactions. Both these models (Brinkman 1952; Batchelor 1977) predict viscosity of nanoparticle suspensions from the base fluid viscosity and volume fraction of nanoparticles. Krieger

and Dougherty (1959) derived the shear viscosity equation considering particle concentrations. Chen et al. (2007) derived Modified Krieger and Dougherty equation to predict high shear viscosity of nanofluids based on aggregate nanoparticle structure considering the effects of variable packing fraction. Chen et al. (2007) presented classification of nanofluids into (i) dilute ($0 < \phi \leq 0.001$), (ii) semi-dilute ($0.001 < \phi \leq 0.05$), (iii) semi-concentrated ($0.05 < \phi \leq 0.1$), and (iv) concentrated ($\phi \geq 0.1$) depending on nanoparticle concentration and structure. Duangthongsuk and Wongwises (2009) proposed correlations for thermal conductivity and viscosity of nanofluids based on experimental results. The viscosity of nanofluids (i) decreases significantly with increasing temperature and (ii) increases with increasing particle volume concentration. Hosseini et al. (2010) presented an empirical model of viscosity of nanoparticle suspensions based on dimensionless groups. The empirical model of viscosity of nanofluid was derived from viscosity of the base liquid, particle volume fraction, particle size, properties of the surfactant layer, and temperature. Hosseini et al. (2011) reviewed formulae and correlations about thermal conductivity, viscosity, density, and specific heat of nanofluids. Mahbubul et al. (2012) presented review of theoretical models of viscosity for suspensions and described viscosity correlations for volume concentrations, temperature, and particle diameter of nanofluids.

1.3 *Nondimensional Pressure in Three-Layered Journal Bearing*

The journal bearing with three-layered configuration is shown in Fig. 1. The adsorbent layer viscosity at surfaces in three-layered journal bearing is higher than core layer. The bearing surface, core, and journal surface layers are modeled using Newtonian fluids. A nanoparticle additive three-layered journal bearing one-dimensional analysis is reported.

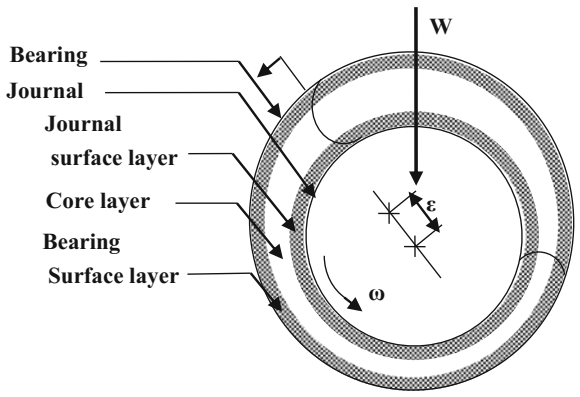

Fig. 1 Three-layered journal bearing

The fluid dynamic viscosity of nanoparticle additives increases with increase in volume fraction of nanoparticles. The dynamic viscosity ratio of spherical-shaped nanoparticle additive lubricant based on Batchelor (1977) model is

$$\beta_{nf} = \frac{\mu_n}{\mu_f} = \left(1 + 2.5\phi + 6.5\phi^2\right) \tag{1}$$

The nondimensional pressure in nanoparticle additive three-layered journal bearing for surface layer of higher dynamic viscosity than the core layer ($\beta_{sc} = \frac{\mu_s}{\mu_c}$ and $\mu_c = \mu_n$) is

$$P(0 \le \theta \le \theta_r) = \frac{\beta_{nf}}{\Delta_p}\left(6\int_0^{\theta}\frac{1}{H^2}\mathrm{d}\theta - 12c_0\int_0^{\theta}\frac{1}{H^3}\mathrm{d}\theta\right) \tag{2}$$

where

$$\Delta_p = \frac{\left[2\gamma^3 + \beta_{sc}(1-2\gamma)^3 + 6\gamma(1-\gamma)^2\right]}{\beta_{sc}} \tag{3}$$

1.4 Three-Layered Journal Bearing Analysis

The parameters used in the analysis of three-layered journal bearing with nanoparticle additive lubricant are as follows: eccentricity ratio (ε) = 0.2; surface to core layer dynamic viscosity ratio (β_{sc} = 2, 5, 10); journal or bearing surface adjoining fluid layer thickness ratio (γ = 0.0001–0.4999); and volume fraction of nanoparticles (ϕ = 0.0, 0.04). Results of load capacity parameter (c_{wf}) and coefficient of friction (C_f) are computed for different values of surface to core layer dynamic viscosity ratio (β_{sc} = 10, 100) and volume fraction of nanoparticles (ϕ = 0.0, 0.04).

1.4.1 Load Capacity Parameter

The nondimensional load capacity is

$$W = \sqrt{W_\varepsilon^2 + W_\phi^2} \tag{4}$$

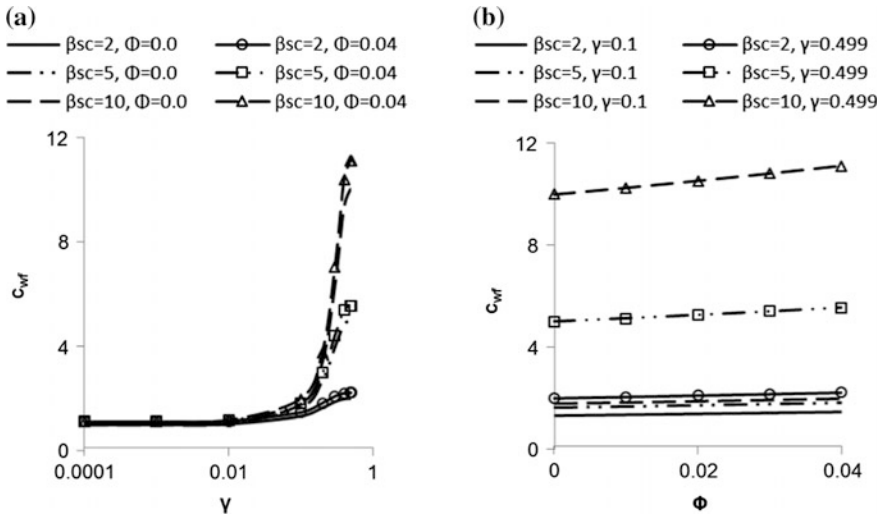

Fig. 2 Load capacity parameter

where

$$W_{\varepsilon} = -\int_0^{\theta_r} P\cos\theta \mathrm{d}\theta \quad \text{and} \quad W_{\phi} = \int_0^{\theta_r} P\sin\theta \mathrm{d}\theta \tag{5}$$

The load capacity parameter ($c_{wf} = \frac{\beta_{nf}}{\Delta_p}$) is expressed as the ratio of the nondimensional load capacity of three-layered nanoparticle additive film to the base fluid (uniform viscosity film without nanoparticle additives).

Figure 2a, b show the effect of journal or bearing surface adjoining fluid film layer thickness ratio (γ = 0.0001–0.4999) on load capacity parameter (c_{wf}) for journal bearing of three-layered film with nanoparticle additive lubricants. The influence of surface layer of higher dynamic viscosity than core layer (β_{sc}) on the load capacity parameter is in the range of γ = 0.01–0.499 as shown in Fig. 2a. The surface film layer thickness ratio (γ) and surface to core fluid film dynamic viscosity ratio (β_{sc}) are significant on the load capacity parameter. The load capacity parameter (c_{wf}) increases with increase in surface to core fluid film (β_{sc} = 10) dynamic viscosity ratio. From Fig. 2b, it is observed that the load capacity parameter increases with nanoparticle additive volume fraction (ϕ) by the magnitude of β_{nf} given in Eq. (1).

1.4.2 Coefficient of Friction

The nondimensional shear stress for surface layer of higher dynamic viscosity than the core layer (β_{sc}) is expressed as follows:

$$\Pi = \frac{\beta_{nf}}{\Delta_p}\left(\frac{3}{H} - \frac{6c_0}{H^2}\right) + \beta_{nf}\frac{\beta_{sc}}{[2\gamma + \beta_{sc}(1-2\gamma)]}\frac{1}{H} \tag{6}$$

The coefficient of friction is calculated as follows:

$$C_f = \left(\frac{R}{C}\right)\frac{f}{w} = \frac{F}{W} \tag{7}$$

where the nondimensional friction force is expressed as follows:

$$F = \int_0^{\theta_r} \Pi \mathrm{d}\theta \tag{8}$$

The variation of friction coefficient (C_f) with fluid surface layer thickness ratio (γ) for a journal bearing of three-layered film with eccentricity ratio (ε) = 0.2 is shown in Fig. 3a, b. The friction coefficient (C_f) is significantly decreased by increase in surface to core fluid film dynamic viscosity ratio (β_{sc}). The coefficient of friction (C_f) decreases for a journal bearing with three-layered film in the range of γ = 0.01–0.3 for journal/bearing surface layer of higher dynamic viscosity than the core layer (β_{sc}) = 10 as shown in Fig. 3a, b for eccentricity ratio ε = 0.2 and ε = 0.4, respectively. Both nondimensional load capacity (W) and nondimensional friction force (F) increase with nanoparticle additive volume fraction (ϕ) by the magnitude of β_{nf} given in Eq. (1). The friction coefficient (C_f) for a journal bearing with three-layered film is not affected by addition of nanoparticles.

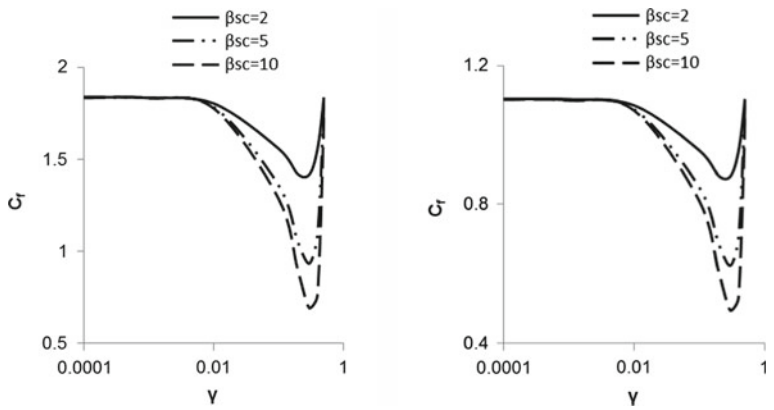

Fig. 3 Coefficient of friction

2 Three-Layered Journal Bearing Analysis Using Nanoparticle Additive Couple Stress Fluids

An analysis of load support and friction coefficient in a couple stress fluid lubricated nanoparticle additive journal bearing with three-layered film is presented. The nondimensional pressure and shear stress are presented. Modified Reynolds equation is solved using Reynolds boundary conditions to determine nondimensional pressure distribution. The nondimensional bearing load capacity and friction coefficient are analyzed for (i) journal/bearing surface adsorbent layer thickness (Δ); (ii) surface to core dynamic viscosity ratio (β_{sc}); (iii) volume fraction of nanoparticles (ϕ); and (iv) couple stress parameter (λ).

2.1 Couple Stress Fluids

Lubricants with additives improve characteristics of hydrodynamic bearing. The couple stress fluid theory is used to analyze the improvement in bearing performance characteristics considering the effect of lubricant additives. Surface adsorbent layer with effective viscosity of adsorbed layer at the surfaces under relative motion much greater than the bulk Newtonian viscosity improves the characteristics of hydrodynamic bearing. Both adsorbent layer at journal/bearing surfaces and lubricant additive effects (based on couple stress fluid model) have significant influence in the analysis of hydrodynamic lubrication. Stokes (1966) derived couple stress theory of fluids based on microcontinuum theory. Lin (1997) analyzed finite journal bearing characteristics considering couple stress fluid theory. Mokhiamer et al. (1999) computed the performance of couple stress fluid-lubricated compliant finite journal bearings considering elastic deformation of liner. Li and Chu (2004) carried out analysis of hydrodynamic journal bearing taking into account porous layer and couple stress fluid models.

2.2 Nondimensional Pressure in Couple Stress Fluid Lubricated Nanoparticle Additive Three-Layered Journal Bearing

Rao et al. (2012) conducted investigations on the role of nanoparticle additive couple stress fluids on the bearing load capacity and friction coefficient of a journal bearing with three-layered film. Stokes microcontinuum theory is used in the analysis of couple stresses effects. The nondimensional pressure profile in couple stress fluid lubricated journal bearing with three-layered film along with nanoparticle additives is given as follows:

$$P = \beta_n \left(\int_0^{\theta} \frac{G_1}{G_2} \mathrm{d}\theta - Q \int_0^{\theta} \frac{1}{G_2} \mathrm{d}\theta \right) \tag{9}$$

where

$$G_1 = \frac{1}{2}\Delta + \frac{1}{2}(F_1 + F_3)(H - \Delta) = \frac{1}{2}H,$$

$$G_2 = \frac{1}{2}(F_2 + F_4)(H - \Delta) + \frac{1}{12\beta_{sc}}\left[2\Delta^3 + \beta_s(H - 2\Delta)^3\right] - \frac{1}{\beta_{sc}}\left[2\lambda_s^2\Delta + \beta_{sc}\lambda_n^2(H - 2\Delta)\right] + \frac{2}{\beta_{sc}}\left[2\lambda_s^3 H_1^* + \beta_{sc}\lambda_n^3 H_2^*\right],$$

$$F_1 = \frac{-E_{12}E_{231}}{E_{11}E_{22} - E_{12}E_{21}}, \quad F_2 = \frac{E_{22}E_{13} - E_{12}E_{232}}{E_{11}E_{22} - E_{12}E_{21}},$$

$$F_3 = \frac{E_{11}E_{231}}{E_{11}E_{22} - E_{12}E_{21}}, \quad F_4 = \frac{-E_{21}E_{13} + E_{11}E_{232}}{E_{11}E_{22} - E_{12}E_{21}},$$

$$E_{11} = E_{22} = \frac{\beta_{sc}}{\Delta} + \frac{1}{(H - 2\Delta)}, \quad E_{12} = E_{21} = -\frac{1}{(H - 2\Delta)},$$

$$E_{13} = -\lambda_s H_1^* - \lambda_n H_2^* + \frac{1}{2}(H - \Delta), \quad E_{231} = \frac{\beta_{sc}}{\Delta}, \quad E_{232} = E_{13},$$

$$H_1^* = \left[\coth\left(\frac{\Delta}{\lambda_s}\right) - \operatorname{csch}\left(\frac{\Delta}{\lambda_s}\right)\right], \quad H_2^* = \left[\coth\left(\frac{H - 2\Delta}{\lambda_n}\right) - \operatorname{csch}\left(\frac{H - 2\Delta}{\lambda_n}\right)\right],$$

$$\lambda_s = \frac{\lambda}{\sqrt{\beta_{sc}\beta_n}}, \quad \lambda_n = \frac{\lambda}{\sqrt{\beta_n}}, \quad H = 1 + \varepsilon\cos\theta \tag{10}$$

2.3 Couple Stress Fluid Lubricated Nanoparticle Additive Three-Layered Journal Bearing Analysis

The parameters used in the analysis of a couple stress fluid lubricated journal bearing with three-layered film and nanoparticle additives are as follows: eccentricity ratio (ε) = 0.2; surface to core layer dynamic viscosity ratio (β_{sc} = 2, 5, 10); journal/bearing adsorbent layer thickness (Δ = 0.001–0.1); couple stress parameter (λ = 0.01, 0.1); and nanoparticles volume fraction (ϕ = 0.0–0.04). The influence of journal/bearing adsorbent layer thickness (Δ) and nanoparticles volume fraction (ϕ) on the nondimensional bearing load capacity and friction coefficient is investigated.

2.3.1 Load Capacity

The nondimensional load capacity is calculated using Eq. (4). The variation of nondimensional load capacity (W) of nanoparticle additive couple stress fluid lubricated three-layered journal bearing is shown in Fig. 4a, b. The nondimensional load capacity (W) is presented with variation in journal and bearing surface adsorbent fluid film layer thickness (Δ) (Fig. 4a) and volume fraction of nanoparticles (ϕ) (Fig. 4b). As shown in Fig. 4a, it is observed that the nondimensional load capacity significantly increases with increase in journal/bearing adsorbent layer thickness (Δ = 0.01–0.1). It is shown that with lower journal/bearing adsorbent layer thickness (Δ < 0.01) configuration, nondimensional load capacity (W) remains constant. The couple stress parameter (λ = 0.1) enhances nondimensional load capacity under the influence of increase in both surface to core layer dynamic viscosity ratio (β_{sc} = 2–10) and volume fraction of nanoparticles (ϕ = 0.0–0.04). The nondimensional bearing load capacity (W) increases with increase in volume fraction of nanoparticles (ϕ = 0.0–0.04) as shown in Fig. 4b. The journal/bearing adsorbent layer (Δ = 0.1) enhances the nondimensional load capacity under the influence of increase in both surface to core layer dynamic viscosity ratio (β_{sc} = 2–10) and couple stress parameter (λ = 0.01–0.1).

2.3.2 Coefficient of Friction

The journal bearing shear stress in nondimensional form is expressed as follows:

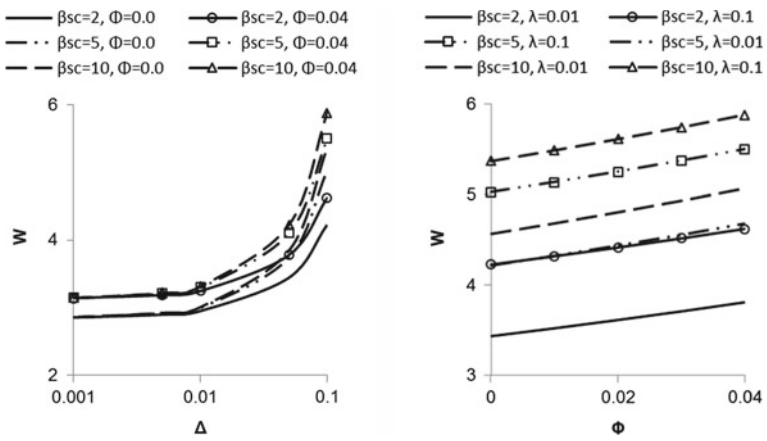

(a) λ=0.1 (b) Δ=0.1

Fig. 4 Load capacity (ε = 0.2)

$$\Pi|_{Y=H} = \beta_s \beta_n \left.\frac{\mathrm{d}U_3}{\mathrm{d}Y}\right|_{Y=H} = \beta_n \left[(1-F_3)\left(\frac{\beta_s}{\Delta}\right) + \left(\frac{G_1 - Q}{G_2}\right)\left(F_4 \frac{\beta_s}{\Delta} + \frac{\Delta}{2} - \lambda_s H_1^*\right)\right] \tag{11}$$

Equation (7) is used in the calculation of friction coefficient. The friction coefficient (C_f) of couple stress fluid lubricated journal bearing with three-layered film and nanoparticle additives is shown in Fig. 5a, b. It is observed from Fig. 5a that friction coefficient (C_f) decreases with increase in both surface adsorbent fluid layer thickness (Δ) and surface to core layer dynamic viscosity ratio (β_s) for the parameters considered in the study. Furthermore, the coefficient of friction (C_f) decreases significantly with increase in journal/bearing adsorbent layer thickness (Δ = 0.01–0.1) as shown in Fig. 5a. For a given couple stress parameter (λ = 0.1), it is observed that coefficient of friction (C_f) reduces with increase in both surface to core layer dynamic viscosity ratio (β_{sc} = 2–10) and volume fraction of nanoparticles (ϕ = 0.0–0.04). However, as shown in Fig. 5b, the coefficient of friction (C_f) remains constant with increase in volume fraction of nanoparticles (ϕ = 0.0–0.04). It is seen that the journal/bearing adsorbent layer (Δ = 0.1) reduces significantly the coefficient of friction (C_f) with increase in both surface to core layer dynamic viscosity ratio (β_{sc} = 2–10) and couple stress parameter (λ = 0.01–0.1).

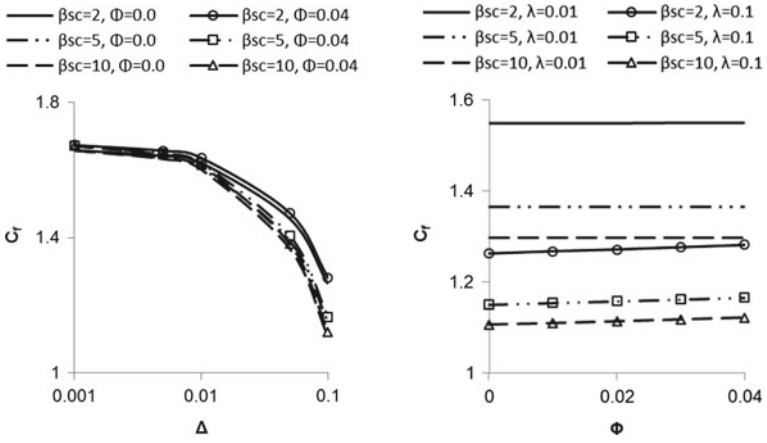

(a) λ=0.1 (b) Δ=0.1

Fig. 5 Coefficient of friction (ε = 0.2). **a** λ = 0.1, **b** Δ = 0.1

3 Partial Slip Thin Film Lubrication with Electric Double Layer

The slider bearing load capacity under the effect of both partial slip and electric double layer (EDL) configuration is investigated. Charge migration at the interface between solid and subsequent liquid within electric double layer induces an electro-viscous force to retard fluid flow which reveals as an enhanced fluid dynamic viscosity. Hydrodynamic lubrication effects are improved with EDL and partial slip on bearing surface. Nondimensional pressure and nondimensional load capacity in one-dimensional slider bearing are presented considering partial slip and EDL on the bearing surface. The parameters considered in the analysis are as follows: slope parameter (a_h), slip region extent on the bearing surface (X_S), nondimensional slip coefficient (A), and nondimensional reference electro-viscosity (β_{e0}).

3.1 Electric Double Layer

The surface phenomenon in solid/lubricant interfaces in a lubrication system is referred as electric double layer (EDL). Both boundary slip and electric double layer (EDL) at the bearing surface enhance thin film hydrodynamic lubrication conditions. Bike and Prieve (1990) studied the effect of electric double layer (EDL) in lubrication under thin film conditions. Zhang and Umehara (1998) derived modified Reynolds equation for hydrodynamic lubrication of ceramics considering the influence of zeta potential in EDL. Li (2005) presented flow factors considering coupled effects of EDL and surface roughness in slider bearing analysis. The load capacity of slider bearing was determined based on the flow factors derived using apparent viscosity with EDL effects. The bearing load capacity increases with EDL and surface roughness effects. Bai et al. (2006) developed mathematical model of electro-viscosity and carried out numerical analysis of thin film lubrication considering EDL effects. Electric double layer induces electro-viscosity for thin films with thickness below 100 nm. The electro-viscosity in the thin film regime leads to a significant increase in the apparent viscosity of lubricant and film thickness. The influence of boundary slip and EDL on the apparent viscosity was analyzed by Li and Jin (2008) for load capacity evaluation of slider bearing. Zuo et al. (2012) presented a mathematical model of asymmetrical EDL effects on thin film lubrication. The analyses of variation in apparent viscosity were conducted to examine the combined influence of asymmetrical EDLs on the elastohydrodynamic and hydrodynamic lubrication properties.

3.2 Slip in Fluid Film Bearing

Boundary conditions of fluid flow largely govern the hydrodynamic behavior of lubricated contacts. Recently slip surfaces have received great deal of attention and can occur with specially engineered surfaces such as molecularly smooth surfaces and surfaces with few microscale patterns. The fluid flow in the hydrodynamic bearing can be altered by heterogeneous surface enhancement (in which slip occurs in certain regions and is absent in others) to improve load support and reduce friction. Craig et al. (2001), Zhu and Granick (2001, 2002), and Spikes (2003) have experimentally observed slip using engineered surfaces and presented critical shear stress model for surface slip. Spikes (2003a, b) investigated half-wetted bearing hydrodynamic properties based on critical shear stress model and investigated potential of slip surfaces with application to hydrodynamic lubrication. Salant and Fortier (2004) and Fortier and Salant (2005) introduced artificial slip/no-slip concept and conducted numerical analysis of both slider and journal bearings that gives high load support and low friction. Wu et al. (2006) studied the hydrodynamic load support of slider bearing with artificial slip surface using different (convergent, parallel, and divergent) configurations. Ma et al. (2007) investigated journal bearing for high load support and low friction under the influence of surface slip. Wang et al. (2012) derived a generalized Reynolds equation based on modified slip length model for a journal bearing. Tauviqirrahman et al. (2013) analyzed slip in texture region of slider bearing for increased load capacity and decreased friction. Rao et al. (2014) examined the effects of load capacity and friction coefficient in journal bearing considering partial slip on bearing surface with two-layered film configuration. The two-layered film consists of different Newtonian viscosities, and the partial slip configuration on bearing surface is analyzed using Navier slip boundary conditions.

3.3 Nondimensional Pressure for Partial Slip Slider Bearing with Electric Double Layer

Rao et al. (2013) presented slider bearing one-dimensional analysis with effects of slip on partial bearing surface and electric double layer (EDL) on thin film lubrication. The apparent viscosity of thin fluid film in slider bearing with partial slip and EDL is derived. The derived apparent viscosity is a combination of the electro-viscosity, the bulk fluid viscosity, and slip length. Partial slip surface with EDL guides to an increase in thin film apparent viscosity and consequently load bearing capacity of slider. The configuration of slider bearing with EDL and partial slip on pad surface is shown in Fig. 6.

The slip on partial pad surface and no-slip exit region nondimensional pressure profile is

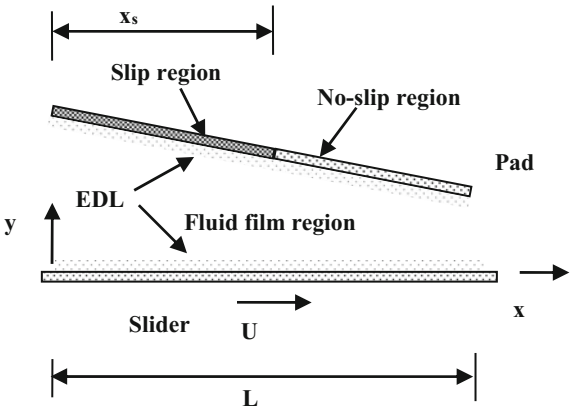

Fig. 6 Partial slip slider bearing with electric double layer (EDL)

$$P(0 \le X \le X_s) = \int_0^X \frac{G_1}{G_2} \mathrm{d}X - Q \int_0^X \frac{1}{G_2} \mathrm{d}X. \tag{12}$$

$$P(X_s \le X \le 1) = P|_{X=X_s} + \int_{X_s}^X \frac{G_{1r}}{G_{2r}} \mathrm{d}X - Q \int_{X_s}^X \frac{1}{G_{2r}} \mathrm{d}X. \tag{13}$$

where

$$H = 1 - a_h X, \quad a_h = 1 - H_2,$$

$$G_1 = \frac{H}{2}\left(\frac{H+2A}{H+A}\right), \quad G_2 = \frac{H^3}{12\beta_a}, \quad \beta_e = \beta_{e0}\left(\frac{h_0}{h_1}\right)^2 \text{ and}$$

$$\beta_a = \left(\frac{H+A}{H+4A}\right)\left[1 + \frac{12\beta_e}{H^2}\left(1 + \frac{2}{K_i H}\frac{(1-\cosh K_i H)}{\sinh K_i H} + \frac{K_i H A}{2(H+A)}\frac{(\cosh K_i H - 1)}{\sinh K_i H}\right)\right]$$

$$G_{1r} = \frac{H}{2}, \quad G_{2r} = \frac{H^3}{12} \quad \text{and} \quad \beta_{ar} = 1 + \frac{12\beta_e}{H^2}\left(1 + \frac{2}{K_i H}\frac{(1-\cosh K_i H)}{\sinh K_i H}\right) \tag{14}$$

3.4 Partial Slip Slider Bearing Nondimensional Load Capacity with Electric Double Layer

The parameters used in the investigation of slider bearing with partial slip surface and EDL are as follows: slider bearing slope parameter (a_h) = 0.0–0.3; nondimensional surface slip coefficient (A) = 0.01, 0.1, 1, 10; slip region extent on the

bearing surface (X_S) = 0.1–0.5; nondimensional reference electro-viscosity (β_{e0}) = 0.00001–0.01; nondimensional inverse reference Debye length ($\kappa_i h_0$) = 10; and nondimensional inverse Debye length (K_i) = 10.

The nondimensional slider bearing load capacity is expressed as follows:

$$W = \int_0^1 P \mathrm{d}X \tag{15}$$

Figure 7a shows the effect of nondimensional surface slip coefficient (A) on the nondimensional bearing load capacity (W). The nondimensional bearing load capacity (W) increases as both nondimensional slip coefficient (A = 0.01–10) and nondimensional reference electro-viscosity (β_{e0} = 0.001–0.01) increase for bearing slope parameters (a_h) of 0.0, 0.1, and 0.2. It can be noticed that nondimensional bearing load capacity (W) is significantly increased at higher values of both nondimensional values of slip coefficient (A = 10) and nondimensional values of reference electro-viscosity (β_{e0} = 0.01). Figure 7b shows the effect of angular extent of slip on the partial bearing surface (X_S) on the nondimensional bearing load capacity (W). Nondimensional bearing load capacity (W) is enhanced in the case of partial bearing surface slip (A = 0.1, 1.0, 10) with EDL effects (β_{e0} = 0.001, 0.01). The nondimensional bearing load capacity (W) is enhanced for increase in angular extent of slip region on the bearing surface (X_S = 0.1–0.5). For variation in the bearing slope parameter (a_h) from 0.0 to 0.4 in Fig. 7c, an increase in both nondimensional surface slip coefficient (A = 0.1, 1.0, 10) and nondimensional reference electro-viscosity (β_{e0} = 0.001–0.01) shows an increase in nondimensional load capacity (W). Figure 7d shows the influence of nondimensional reference electro-viscosity (β_{e0}) on the nondimensional bearing load capacity (W). Nondimensional one-dimensional slider bearing load capacity is influenced by EDL effects for values of nondimensional reference electro-viscosity (β_{e0}) greater than 0.001. The nondimensional load capacity (W) is found to increase at higher nondimensional surface slip coefficients (A = 1.0–10) for variation in nondimensional reference electro-viscosity (β_{e0}) from 0.001 to 0.01.

4 Thin Film Lubrication with Porous and Electric Double Layer Using CNT Additives

The investigation of load generation of carbon nanotubes (CNTs) additive lubricant in a porous-layered slider bearing with electric double layer (EDL) is presented. The nondimensional pressure gradient expression presented is based on the effects of EDL, porous layer, and CNT additives.

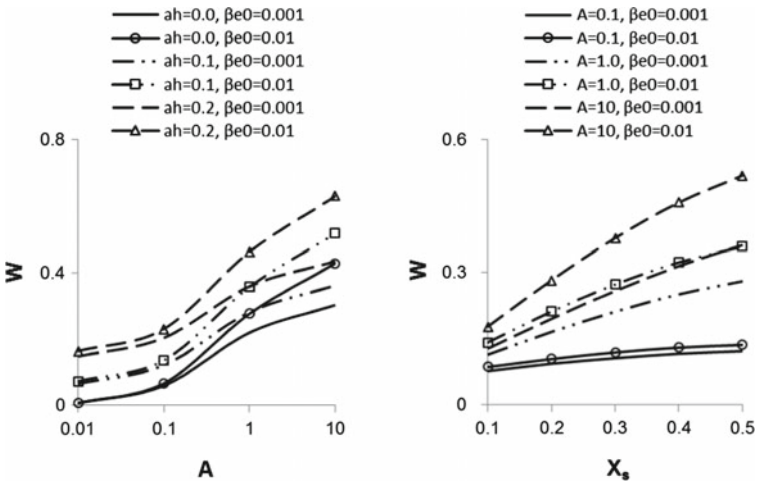

(a) X_s=0.5 (b) a_h=0.1

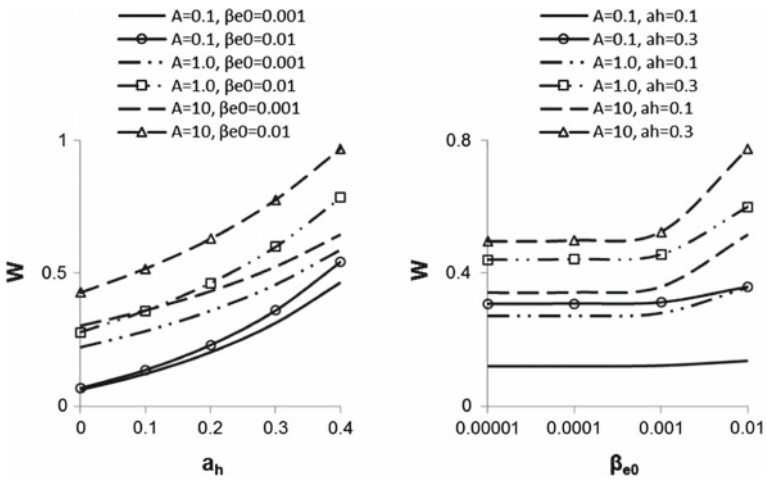

(c) X_s=0.5 (d) X_s=0.5

Fig. 7 Nondimensional load capacity (K = 10, κh_0 = 10). **a** X_s = 0.5, **b** a_h = 0.1, **c** X_s = 0.5, **d** X_s = 0.5

4.1 Porous-Layered Thin Film Lubrication

A porous-layered thin film lubrication steady state performance considering the lubricant additives effects (Li and Chu 2004; Elsharkawy 2005) are presented. A thin porous film attached to bearing surfaces is modeled as microstructure of boundary layer due to additives. Li and Chu (2004) and Elsharkawy (2005)

developed porous layer and couple stress fluid models for porous and fluid film regions, respectively. Li (2009) developed lubrication theory that includes electric double layer (EDL) effects in porous media for modeling the microstructure on lubricating surfaces. The apparent viscosity is determined for EDL effects with porous layer attached to the lubricating surfaces. The apparent viscosity increases as permeability decreases and electro-viscosity increases.

4.2 CNT Additive Fluids

Brenner and Condiff (1974) introduced intrinsic viscosity equation for shape effects of nonspherical nanoparticles. Aladag et al. (2012) have experimentally investigated shearing time and temperature on viscosity of alumina and CNT nanofluids at low temperatures and concentrations. Experiments showed that alumina water-based nanofluids are nonNewtonian while CNT water-based nanofluids are Newtonian at high shear rate. Song (2006) characterized the rheological behavior of polyethylene oxide nanocomposites embedded with CNTs and evaluated shear viscosity under the effect of CNT loading using the Krieger–Dougherty equation. The shear viscosity of nanocomposites increased drastically with an increase in the content of carbon nanotubes (CNTs). Vakili-Nezhaad and Doranyb (2012) experimentally investigated the effect of the temperature and the SWCNT concentration on the viscosity index of nanofluids. Their results indicated the increase in kinematics viscosity of nanofluids with increase in SWCNT concentration and decrease in temperature. Lim and Norani (2012) and Lim et al. (2012) investigated the effects of type of catalyst and pretreatment duration on the diameter of CNTs.

4.3 Nondimensional Pressure for Slider Bearing with Porous and Electric Double Layer

Rao et al. (2015) presented one-dimensional analysis of porous-layered thin film lubrication of slider bearing including the effects of electric double layer (EDL) and carbon nanotubes (CNTs) additive lubricant. Stokes and Brinkman equations including electrokinetic force govern the CNTs additive lubricant flow in porous media and thin film layers, respectively. The apparent viscosity and nondimensional pressure expression are derived considering the effects of EDL, porous layer, and CNT additives. Figure 8 shows slider bearing configuration with EDL and porous layer. The CNTs additive lubricant viscosity in porous layer is assumed to be same as that in film region.

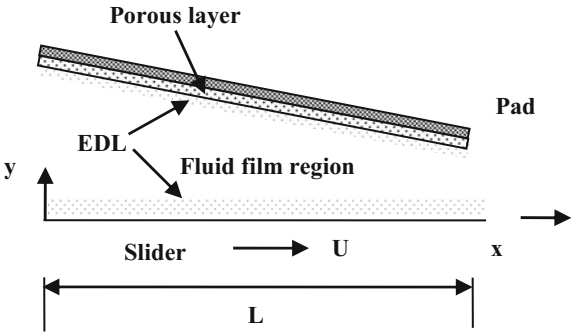

Fig. 8 Slider bearing with porous and electric double layer

The viscosity of fluid with CNT additives increases with aggregate volume fraction and intrinsic viscosity. The ratio of dynamic viscosity of nano to base fluid in Eq. (16) is based on modified Krieger and Dougherty equation.

$$\beta_n = (1 - \phi_a/\phi_m)^{-\eta\phi_m} \tag{16}$$

where

$$\phi_a = \phi(a_a/a)^{3-D} \tag{17}$$

The aggregate volume fraction increases with CNTs particle volume fraction and ratio of aggregate to particle radius.

The intrinsic viscosity increases with aspect ratio of CNT. The intrinsic viscosity for nonspherical nanoparticles (Brenner and Condiff 1974; Aladag et al. 2012) is expressed as follows:

$$\eta = \frac{0.312r}{\ln 2r - 1.5} + 2 - \frac{0.5}{\ln 2r - 1.5} - \frac{1.872}{r} \tag{18}$$

The nondimensional pressure for slider bearing with porous and electric double layer profile is obtained as follows:

$$P(0 \le X \le X_s) = \int_0^1 \frac{G_1}{G_2} \mathrm{d}X - Q \int_0^1 \frac{1}{G_2} \mathrm{d}X \tag{19}$$

where

$$G_1 = F_1 H_2^* + \frac{1}{2}(F_1 + 1)(H - \Delta), \quad G_2 = \frac{(H - \Delta)^3}{12\beta_a}, \quad \beta_a = \frac{(H - \Delta)^3 \beta_n}{12G_{31}} + \frac{G_{32}}{G_{31}},$$

$$G_{31} = \frac{(H-\Delta)^3}{12} + K\left(\Delta - 2H_2^*\right) + \frac{1}{E_{11}}\left(\frac{1}{2}(H-\Delta) + H_2^*\right)^2,$$
$$G_{32} = \frac{1}{K_i}\beta_e\left(2H_1^* + K_i(H-\Delta)\right) - \frac{1}{E_{11}}\left(\frac{1}{2}(H-\Delta) + H_2^*\right) \times \left(\beta_e K_i H_1^* + \beta_d \beta_e H_2^*\right) - \beta_d \beta_e K\left(\Delta - 2H_2^*\right) \quad (20)$$

4.4 Nondimensional Load Capacity of Slider Bearing with Porous and Electric Double Layer

Analysis of CNTs additive porous-layered thin film lubrication of slider bearing with EDL is presented. The parameters used in the analysis are as follows: a_h = 0.1–0.4; β_{e0} = 0.00001–0.01; K_i = 10; $\kappa_i h_0$ = 10; β_d = 10; $K = 10^{-2}$, 10^{-3}, 10^{-4}; Δ = 0.05–0.2; a = 15 nm; a_a = 50 nm; D = 1.8; φ_m = 0.6; r = 100; and φ = 0.01–0.04.

Figure 9a–d depict the nondimensional load capacity (W) variation with (i) slope parameter (a_h), (ii) nondimensional thickness of porous layer (Δ), (iii) CNTs volume fraction (φ = 0.01–0.04), and (iv) nondimensional reference electro-viscosity (β_{e0}). Figure 9a shows increase in nondimensional load capacity (W) with decrease in nondimensional permeability of porous layer ($K = 10^{-2}$–10^{-4}). The nondimensional load capacity (W) increases with decrease in nondimensional permeability of porous layer due to increase in resistance to flow in porous layer. Figure 9b shows nondimensional load capacity (W) increases with increase in nondimensional thickness of porous layer (Δ). The increase in nondimensional load capacity (W) is primarily attributed to low nondimensional permeability of surface porous layer ($K = 10^{-4}$) and high nondimensional reference electro-viscosity (β_{e0}). Figure 9c shows that the nondimensional slider bearing load capacity (W) increases significantly with increase in volume fraction of CNTs (φ = 0.01–0.04) as slope parameter (a_h) increases from 0.1 to 0.3. The nondimensional slider bearing load capacity (W) increases significantly with increase in both CNTs volume fraction (φ = 0.01–0.04) and slope parameter (a_h = 0.1–0.3). The nondimensional load capacity (W) is plotted as function of nondimensional reference electro-viscosity (β_{e0} = 0.001–0.01) in Fig. 9d. It is shown that increase in nondimensional reference electro-viscosity (β_{e0} = 0.001–0.01) increases nondimensional load capacity (W). The nondimensional load capacity (W) increases with (i) increase in slope parameter (a_h = 0.1–0.3) and (ii) decrease in nondimensional permeability of porous layer ($K = 10^{-4}$) as well as (iii) increase in nondimensional reference electro-viscosity (β_{e0} = 0.01).

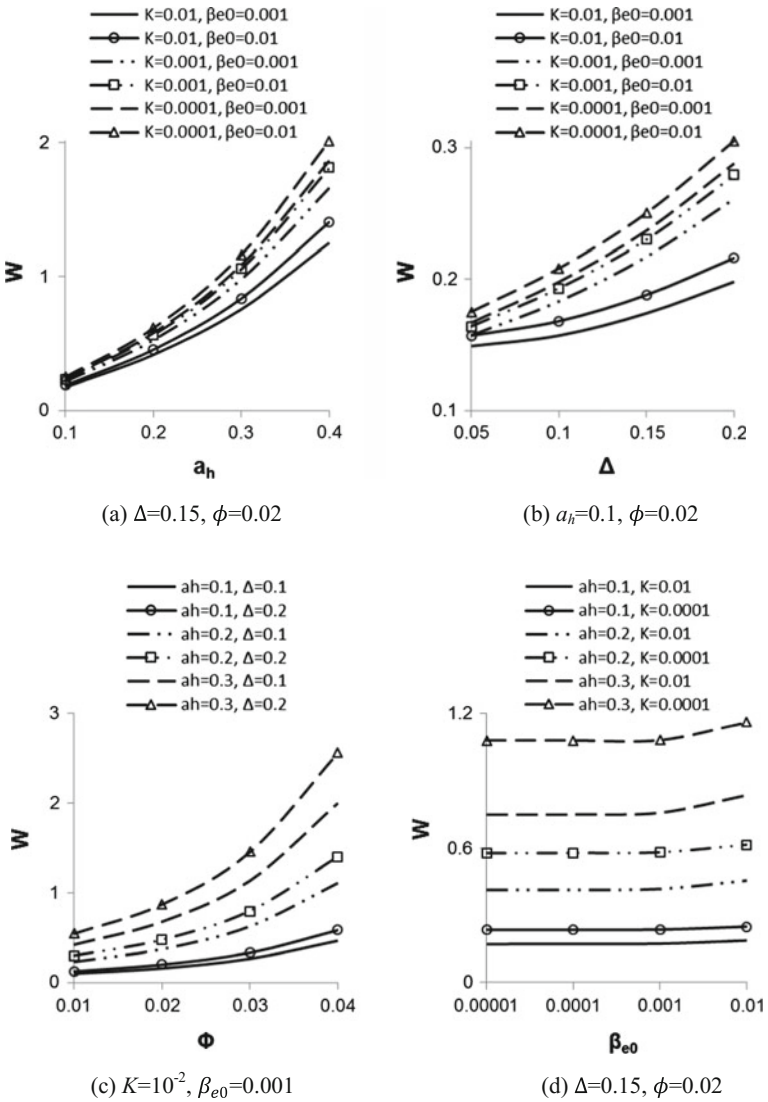

(a) Δ=0.15, ϕ=0.02

(b) a_h=0.1, ϕ=0.02

(c) K=10^{-2}, β_{e0}=0.001

(d) Δ=0.15, ϕ=0.02

Fig. 9 Nondimensional load capacity (β_d = 10, K_i = 10, $\kappa_i h_0$ = 10)

5 Conclusions

A three-layered fluid film journal bearing of different dynamic viscosities at the surface (journal and bearing surface fluid film layers) and core is presented. The nondimensional pressure presented is based on consideration of surface adjacent

and core fluid film layer's viscosity and film thickness. Higher nondimensional bearing load capacity (W) for a journal bearing with three-layered film and nanoparticle additives is obtained with higher dynamic viscosity of fluid film layers. The friction coefficient (C_f) decreases as journal/bearing surface layer dynamic viscosity of fluid film increases.

A three-layered journal bearing lubricated with nanoparticle additive couple stress fluid is presented. Load capacity improvement and in coefficient of friction reduction are investigated. The pressure and shear stress in nondimensional form are derived using Reynolds boundary conditions. Results show that the nondimensional bearing load capacity (W) significantly increases with increase in journal/bearing surface fluid film layer thickness (Δ), ratio of dynamic viscosity of journal/bearing surface to core layer (β_s), and volume fraction of nanoparticles (ϕ). It is also seen that considering the effect of couple stress parameter (λ) with increase in journal/bearing adsorbent fluid film surface layer thickness (Δ) results increase in nondimensional load capacity (W). Results show that the friction coefficient (C_f) significantly decreases with increase in journal/bearing adsorbent fluid film surface layer thickness (Δ) and surface to core layer viscosity ratio (β_s). A journal bearing with three-layered film lubricated with nanoparticle additive couple stress fluid has a prospective to increase the bearing load capacity but has no improvement in the friction coefficient (C_f).

The improvement in load capacity considering EDL effects and partial slip configuration for a slider bearing is presented. The slider bearing pressure expression in nondimensional form is presented and the EDL effects with slip on partial boundary of bearing surface on load capacity are analyzed. The nondimensional slider bearing load capacity (W) (a_h = 0.0–0.3) increases with EDL (β_{e0} = 0.001–0.01) under the influence of slip on partial bearing surface (SA = 0.01–10). The nondimensional slider bearing load capacity (W) increases as the angular extent of slip region on partial bearing surface (X_s = 0.1–0.5) increases.

The influence of EDL effects and porous-layered film on CNTs additive thin film lubricated slider bearing is investigated. The nondimensional pressure gradient expression is presented and the EDL effects with porous layer on load capacity are analyzed. Results show increase in nondimensional slider bearing load capacity (W) under the influence of porous layer configuration ($K = 10^{-2}$, 10^{-3}, 10^{-4} and Δ = 0.05–0.2) on the slider bearing (a_h = 0.0–0.3) with EDL effects (β_{e0} = 0.001–0.01). The nondimensional bearing load capacity (W) increases for values of higher nondimensional reference electro-viscosity (β_{e0} = 0.01) as well as for lower nondimensional porous layer permeability ($K = 10^{-4}$). The nondimensional bearing load capacity (W) significantly increases with increase in both volume fraction of CNTs (ϕ = 0.01–0.04) and bearing slope parameter (a_h = 0.1–0.3).

References

Aladag, B., Halelfadl, S., Doner, N., Maré, T., Duret, S., & Estellé, P. (2012). Experimental investigations of the viscosity of nanofluids at low temperatures. *Applied Energy, 97*, 876–880.

Babu, K. S., Nair, K. P., Rajendrakumar, P. K. (2012). Analysis of static and dynamic performance characteristics of THD journal bearing operating under lubricants containing nanoparticles. *International Journal of Precision Engineering and Manufacturing*, *13*(10), 1869–1876.

Bai, S., Huang, P., Meng, Y., & Wen, S. (2006). Modeling and analysis of interfacial electro-kinetic effects on thin film lubrication. *Tribology International, 39*, 1405–1412.

Batchelor, G. K. (1977). The effect of Brownian motion on the bulk stress in a suspension of spherical particles. *Journal of Fluid Mechanics, 83*, 97–117.

Bike, S. G., & Prieve, D. C. (1990). Electrohydrodynamic lubrication with thin double layers. *Journal of Colloid and Interface Science, 136*, 95–112.

Brenner, H., & Condiff, D. W. (1974). Transport mechanics in systems of orientable particles. IV. Convective transport. *Journal of Colloid and Interface Science, 47*, 199–264.

Brinkman, H. C. (1952). The viscosity of concentrated suspensions and solution. *Journal of Chemical Physics, 20*, 571–581.

Chen, H., Ding, Y., & Tan, C. (2007). Rheological behaviour of nanofluids. *New Journal of Physics, 9*(10), 267.

Craig, V. S. J., Neto, C., & Williams, D. R. M. (2001). Shear-dependent boundary slip in an aqueous Newtonian liquid. *Physical Review Letters, 87*(5), 054504.

Duangthongsuk, W., & Wongwises, S. (2009). Measurement of temperature-dependent thermal conductivity and viscosity of TiO_2-water nanofluids. *Experimental Thermal and Fluid Science, 33*, 706–714.

Einstein, A. (1906). Eine neue bestimmung der moleküldimensionen. *Annalen der Physik, 324*(2), 289–306.

Elsharkawy, A. A. (2005). *Tribology Letters, 18*, 63–73.

Fortier, A. E., & Salant, R. F. (2005). Numerical analysis of a journal bearing with a heterogeneous slip/no-slip surface. *Journal of Tribology, 127*(4), 820–825.

Hosseini, S. M., Moghadassi, A. R., & Henneke, D. E. (2010). A new dimensionless group model for determining the viscosity of nanofluids. *Journal of Thermal Analysis and Calorimetry, 100*, 873–877.

Hosseini, S. S., Shahrjerdi, A., & Vazifeshenas, Y. (2011). A review of relations for physical properties of nanofluids. *Australian Journal of Basic and Applied Sciences, 5*(10), 417–435.

Krieger, I. M., & Dougherty, T. J. (1959). A mechanism for non-newtonian flow in suspensions of rigid spheres. *Transactions of the Society of Rheology, 3*, 137–152.

Li, W.-L. (2005). Effects of electrodouble layer (EDL) and surface roughness on lubrication theory. *Tribology Letters, 20*, 53–61.

Li, W.-L. (2009). Derivation of modified Reynolds equation: A porous media model with effects of electrokinetics. *Journal of Tribology, 131*, 031701-1-10.

Li, W.-L., & Chu, H.-M. (2004a). Modified Reynolds equation for couple stress fluids—A porous media model. *Acta Mechanica, 171*, 189–202.

Li, W.-L., & Chu, H.-M. (2004b). *Acta Mechanica, 171*, 189–202.

Li, W.-L., & Jin, Z. (2008). Effects of electrokinetic slip flow on lubrication theory. *Proceedings of the Institution of Mechanical Engineers, Part J: Journal of Engineering Tribology, 222*, 109–120.

Lim, S. Y., & Norani, M. M. (2012). The effect of catalyst on carbon nanotubes (CNTs) synthesized by catalytic chemical vapor deposition (CVD) technique. *Advanced Materials Research, 364*, 232–237.

Lim, S. Y., Norani, M. M., & Suriati, S. (2012). Effect of parameters on carbon nanotubes grown by floating catalyst chemical vapor deposition. *AIP Conference Proceedings, 1502*, 242–254.

Lin, J.-R. (1997). Effects of couple stresses on the lubrication of finite journal bearings. *Wear, 206*, 171–178.

Ma, G. J., Wu, C. W., & Zhou, P. (2007). Wall slip and hydrodynamics of two-dimensional journal bearing. *Tribology International, 40*, 1056–1066.

Mahbubul, I. M., Saidur, R., & Amalina, M. A. (2012). Latest developments on the viscosity of nanofluids. *International Journal of Heat and Mass Transfer, 55*, 874–885.

Meurisse, M.-H., & Espejel, G. M. (2008). Reynolds equation, apparent slip, and viscous friction in a three-layered fluid film. *Proceedings of IMechE: Journal of Engineering Tribology, 222*, 369–380.

Mokhiamer, U. M., Crosby, W. A., & El-Gamal, H. A. (1999). A study of a journal bearing lubricated by fluids with couple stress considering the elasticity of the liner. *Wear, 224*, 194–201.

Nabhan, M. B. W., Ibrahim, G. A., & Anabtawi, M. Z. (1997). Analysis of hydrodynamic journal bearings lubricated with a binary water-based lubricant. *Wear, 209*, 13–20.

Nair, K. P., Ahmed, M. S., & Al-qahtani, S. T. (2009). Static and dynamic analysis of hydrodynamic journal bearing operating under nano lubricants. *International Journal of Nanoparticles, 2*, 251–262.

Qingwen, Q., Yahong, H., & Jun, Z. (1998). An adsorbent layer model for thin film lubrication. *Wear, 221*, 9–14.

Rao, T. V. V. L. N., Rani, A. M. A., Nagarajan, T., & Hashim, F. M. (2014a). Analysis of two-layered film journal bearing with partial slip surface. *Advanced Materials Research, 903*, 215–220.

Rao, T. V. V. L. N., Rani, A. M. A., Sufian, S., & Mohamed, N. M. (2015). Analysis of CNT additives in porous layered thin film lubrication with electric double layer. *AIP Conference Proceedings, 1669*, 020034.

Rao, T. V. V. L. N., Sufian, S., Mohamed, N. M. (2013). Analysis of nanoparticle additive couple stress fluids in three-layered journal bearing. The 3rd ISESCO international workshop and conference on nanotechnology (IWCN 2012), UKM, Bangi, Malaysia, December 5–7, 2012. *Journal of Physics: Conference Series*, *431*(1), 012023.

Rao, T. V. V. L. N., Sufian, S., Mohamed, N. M. (2014b). Analysis of electric double layer on thin film lubrication with partial slip. BOND21, Joint international conference on nanoscience, engineering, and management, Penang, Malaysia, August 19–21, 2013. *Advanced Materials Research*, *925*, 538–542.

Salant, R. F., & Fortier, A. E. (2004). Numerical analysis of a slider bearing with a heterogeneous slip/no-slip surface. *Tribology Transactions, 47*(3), 328–334.

Shenoy, B. S., Binu, K. G., Pai, R., Rao, D. S., & Pai, R. S. (2012). Effect of nanoparticles additives on the performance of an externally adjustable fluid film bearing. *Tribology International, 45*, 38–42.

Song, Y. S. (2006). Rheological characterization of carbon nanotubes/poly (ethylene oxide) composites. *Rheol Acta*, *46*, 231–238.

Spikes, H. A. (2003a). The half-wetted bearing. Part 1: Extended Reynolds equation. *Proceedings of the Institution of Mechanical Engineers, Part J: Journal of Engineering Tribology, 217*(1), 1–14.

Spikes, H. A. (2003b). The half-wetted bearing. Part 2: Potential applications in low load contacts. *Proceedings of the Institution of Mechanical Engineers, Part J: Journal of Engineering Tribology, 217*(1), 15–26.

Stokes, V. K. (1966). Couple stresses in fluids. *Physics of Fluids, 9*, 1709–1715.

Szeri, A. Z. (2010). Composite-film hydrodynamic bearings. *International Journal of Engineering Science, 48*, 1622–1632.

Tauviqirrahman, M., Ismail, R., Jamari, J., & Schipper, D. J. (2013). Combined effect of texturing and boundary slippage in lubricated sliding contacts. *Tribology International, 66*, 274–281.

Tichy, J. A. (1995). A surface layer model for thin film lubrication. *Tribology Transactions, 38*, 577–582.

Vakili-Nezhaad, G., & Doranyb, A. (2012). Effect of single-walled carbon nanotube on the viscosity of lubricants. *Energy Procedia, 14*, 512–517.

Wang, L.-L., Lu, C.-H., Wang, M., & Fu, W.-X. (2012). The Numerical analysis of radial sleeve bearing with combined surface slip. *Tribology International, 47*, 100–104.

Wu, C. W., Ma, G. J., Zhou, P., & Wu, C. D. (2006). Low friction and high load support capacity of slider bearing with a mixed slip surface. *Journal of Tribology, 128*(4), 904–907.

Zhang, B., & Umehara, N. (1998). Hydrodynamic lubrication theory considering electric double layer for very thin water film lubrication of ceramics. *JSME International Journal Series C Mechanical Systems, Machine Elements and Manufacturing, 41*, 285–290.

Zhu, Y., & Granick, S. (2001). Rate-dependent slip of Newtonian liquid at smooth surfaces. *Physical Review Letters, 87*(9), 096105.

Zhu, Y., & Granick, S. (2002). Limits of hydrodynamic no-slip boundary condition. *Physical Review Letters, 88*(10), 106102.

Zuo, Q., Huang, P., & Su, F. (2012). Theory analysis of asymmetrical electric double layer effects on thin film lubrication. *Tribology International, 49*, 67–74.

Mechanism of Heat Transfer with Nanofluids for the Application in Oil Wells

A.H. Bhat, Imran Khan, Irshad Ul Haq Bhat, H. Soleimani and Mohd Amil Usmani

Abstract Nanofluid plays an important role in a drilling process which includes the removal of cuttings, lubricating, and cooling the drill bits. Nonetheless, production increases from the reservoirs which are non-conventional, and the stability and performance of conventional drilling fluids under high-temperature and high-pressure (HTHP) environment have apprehensiveness. Both water- and oil-based drilling fluids are likely to experience a number of degenerations such as degradation of weighting materials, gelation, and disintegration of polymeric additives under HTHP conditions. Lately, nanotechnology has shown a lot of promise in the oil and gas sectors, including nanoparticle-based drilling fluids. This chapter is focused on to explore the influence of nanoparticles on the heat transfer efficiency of drilling fluids to make the drilling phenomena smooth and cost effective. The chapter begins with explaining the importance of drilling fluid during the drilling process with a historical assessment of drilling fluid industry development. It is followed by definitions, uses, and types of drilling fluid as well as the additives that are appended to enhance drilling fluid performance. Moreover, the progress of the oil production industry from unconventional wells has been discussed after which the limitations and degradation of the traditional drilling fluid have been taken up. Finally, this chapter discusses the great potential of nanotechnology in solving drilling problems in addition to the technical and the economic benefits of using nanomaterials in drilling fluids before offering a brief conclusion.

A.H. Bhat (✉) · H. Soleimani
Department of Fundamental and Applied Sciences, Universiti Teknologi PETRONAS, 32610 Bandar Seri Iskander Perak, Darul Ridzuan, Malaysia
e-mail: aamir.bhat@petronas.com

I. Khan
Department of Chemistry, College of Science, Sultan Qaboos University, P.O. Box 36, P.C. 123 Al-Khod Muscat, Sultanate of Oman

I.U.H. Bhat
Faculty of Earth Science, Universiti Malaysia Kelantan, 17600 Campus Jeli, Kelantan, Malaysia

M.A. Usmani
Department of Chemistry, Eritrea Institute of Technology, P.O. Box 12676, Asmara, Eritrea

K. Viswanatha Sharma and N. Hisham B Hamid (eds.),
Engineering Applications of Nanotechnology, Topics in Mining, Metallurgy and Materials Engineering, DOI 10.1007/978-3-319-29761-3_7

Keywords Nanofluid · Heat Transfer · Drilling

Nomenclature

ODA	Octadecylamine
GONs	Graphene oxide nanosheets
PVP	Polyvinylpyrrolidone
Csf	Empirical coefficient
q''	Heat flux
Pe	Peclet number
Re	Reynolds number
(x/D)	Larger axial distance/pipe diameter
Nu	Nusselt number
HTHP	High temperature and high pressure
OBM	Oil-based mud
WBM	Water-based mud

1 Introduction

The operation of drilling has three operational components that work simultaneously in the boring hole: a rotating system which rotates the drill bit, a lifting system that raises and lowers the drill string into the hole, and a circulating system which performs the function of moving a fluid around from the drill stem, out of the drill bit and up again to the hole at the surface, and this fluid is referred as drilling fluid (Van Dyke 1998). Drilling fluids are important for the success of the process as they enhance oil recovery and decreases the time required to achieve first oil (Nasser et al. 2013). The drilling fluids in the drilling process can be compared with the blood in the human physical body.

The mud pump can be related to the heart; the transfer of the cuttings from the borehole by the drilling fluid represents the unwanted materials that are cleaned from the human body by blood, and the mud cleaning system represents the kidney and lungs. Latest investigations have demonstrated that nanofluids have additional features for applications where heat transfer, drag reduction, binding ability for sand consolidation, gel formation, wettability alteration, and corrosive control are of great interest.

The synthesis of nanofluids is a simple process of addition of nanoparticles in low volumetric quantities to a fluid. The nanoparticles improve the fluid's mechanical, rheological, optical, and thermal characteristics. The nanoparticles may provide the following supports to the fluids: (i) improved stability against sedimentation since surface forces easily balance the gravitational force, (ii) thermal, mechanical, optical, rheological, electrical, and magnetic properties of nanoparticles

depend notably on the size and shape, can be fabricated during the manufacturing, and are often more advanced to the base material.

The important parameters for the drilling fluid to be germane are high-temperature transfer and flow properties. Furthermore, it must be ecofriendly in order to perform the functions in an efficient and responsible manner (Wawrzos and Weintritt 2007). Lately, these specifications have been achieved, with some constraints by water-based and oil-based muds. Both water-based and oil-based muds contain bentonite clay and some of the chemical additives (Shah et al. 2010). These chemical additives may amend density, reduce corrosion rate, change viscosity, and ceases bacterial growth. Nonetheless, for the deep well drilling, the conditions of temperatures and pressures are challenging, and the heat transfer demand on the drilling fluid are nearly impossible to meet (Oakley et al. 2000).

Thus, to design a drilling fluid in this situation which has a potential to work efficiently, it is required to notably improve the fluid's thermal properties.

Nanotechnology presents a light, strong, and corrosion-resistant material required for the stake holders in the drilling fluid (Salem and Noah 2014). The application of nanoparticles in the drilling fluids will facilitate the drilling engineers to maintain the rheology of the drilling fluid by modifying the type, composition, or size distribution of nanoparticles in drilling fluid to conform any special situation (Abdo and Haneef 2013). The materials manufactured from nanoparticles are different from those prepared using their larger equivalents. Nanomaterials are stronger and more interactive than other materials and also conduct heat efficiently (Singh et al. 2010). The reason behind that is the increased surface area. For a given amount of material, there are a larger number of particles on account of their size reduction and there is more aspect ratio to bear the heat (Shah et al. 2010).

The nanotechnology has transformed the field of science and engineering due to its incredible range of applications. The oil industries like many industries can be greatly benefited from nanotechnology (Abdo and Haneef 2013). The most encouraging prospect among them is the use of nanoparticles in drilling muds so as to have a better operational performance, stability, and suitability. These features make drilling fluids adopt comprehensively under operating conditions by slight changes in composition and sizes (Ibid). Amanullah and Al-Tahini (2009) define drilling fluids loaded with nanomaterials as mud containing additives with particle sizes between 1 and 100 nm; nanofluids were also classified into simple and advanced nanofluids based on the concentration of the nanoparticles in drilling fluids. Nanoparticles in drilling fluids can play a distinctive role in fixing the most common issues during drilling like wellbore instability, lost circulation, pipe sticking, toxic gases, high torque, and drag.

This chapter discusses the preparatory methods of nanofluids and also throws light on the type of heat transfer capabilities in nanofluids along with mechanism.

2 Nanofluid Preparation

2.1 Two-Step Method

This method is commonly used method for preparing nanofluids. In the very first step, chemical or physical methods are generally applied to produce dry powders of nanoparticles, nanofibers, nanotubes, or other nanomaterials. Next step involves the nanosized powder being dispersed into a fluid with the aid of intensive ultrasonic agitation, magnetic force agitation, high-shear mixing, ball milling, and homogenizing. The two-step method is the most economic method to develop nanofluids in large scale, because nanopowder synthesis techniques have already been scaled up to industrial production levels. On account of high surface area and surface activity, nanoparticles have the proneness to aggregate. To ameliorate the stability of nanoparticles in fluids, use of surfactants is an important technique. However, for high-temperature applications, the functionality of the surfactants under high temperature is a big concern. The disadvantage of two-step method is the preparation of stable nanofluids, and to overcome this difficulty, many advanced techniques are developed to produce nanofluids, including one-step method which is given in detail below.

2.2 One-Step Method

Eastman et al. (2001) introduced a one-step physical vapor condensation method to prepare Cu/ethylene glycol nanofluids in order to minimize the agglomeration of nanoparticles. In this method, preparing and dispersing the particles in the fluid takes place simultaneously. The processes of drying, storage, transportation, and dispersion of nanoparticles are ignored in this method, so the agglomeration of nanoparticles is reduced and the stability of fluids is increased (Li et al. 2009). The preparation of uniformly dispersed and the stably suspended nanoparticles in the base fluid can be easily achieved by this method. Another efficient method to prepare nanofluids using different dielectric liquids is the vacuum-SANSS (submerged arc nanoparticle synthesis system) (Lo et al. 2005a, b). Various thermal conductivity properties of the dielectric liquids can alter and determine the different morphologies of the liquid. Many morphological shapes such as needle, polygonal, square, and circular are exhibited by the prepared nanoparticles in this method. The method avoids the unwanted particle aggregation adequately well.

The synthesis of large-scale nanofluids is not possible by one-step physical method and also the cost is too high, so the one-step chemical method is developing briskly. Novel one-step chemical method was presented by Zhu et al. for preparing copper nanofluids by reducing $CuSO_4 \cdot 5H_2O$ with $NaH_2PO_2 \cdot H_2O$ in a solvent ethylene glycol under the influence of microwave irradiation (Zhu et al. 2004). The uniformly dispersed and stably suspended copper nanofluids were achieved. The

same method was used to prepare mineral oil-based nanofluids having silver nanoparticles with a narrow-size distribution (Bönnemann et al. 2005). The particles could be stabilized by Korantin, which coordinated to the silver particle surfaces through two oxygen atoms forming a dense layer around the particles. The silver nanoparticle-based nanofluids were stable for about one month. Also, the microwave-assisted one-step method was used to prepare stable ethanol-based nanofluids containing silver nanoparticles (Singh and Raykar 2008). Polyvinylpyrrolidone (PVP) was employed as the stabilizer of colloidal silver and reducing agent for silver in solution in the method. For the synthesis of silver colloids, the cationic surfactant octadecylamine (ODA) is also an efficient phase-transfer agent (Kumar et al. 2003). The phase transfer of the silver nanoparticles emerges on account of coupling of the silver nanoparticles with the ODA molecules contained in organic phase via either weak covalent interaction or coordination bond formation. For the preparation of homogeneous and stable graphene oxide colloids, phase-transfer method has been developed. Graphene oxide nanosheets (GONs) were favorably transferred from water to *n*-octane after treatment by oleylamine (Yu et al. 2011). However, there are some drawbacks for one-step method. The most critical one is that the residual reactants are left in the nanofluids because of incomplete reaction or stabilization. It is difficult to clear up the nanoparticle effect without eliminating this impurity effect.

2.3 Other Novel Methods

The continuous flow microfluidic microreactor to prepare nanofluids of copper was developed by Wei et al. This method can be used to prepare continuously copper nanofluids, and by adjusting certain factors such as concentration of the reactant, flow rate, and additive, the microstructure and properties of the nanofluid can be changed. A unique precursor transformation method with the aid of ultrasonic and microwave irradiation can prepare CuO nanofluids with high solid volumetric percentage ($\sim$10 vol%) (Zhu et al. 2007). The precursor $Cu(OH)_2$ is converted to CuO nanoparticle in water under the influence of microwave irradiation. The addition of ammonium citrate helps in the prevention of agglomeration and nucleation of nanoparticles, thereby stabilizing CuO nanofluid with enhanced thermal conductivity as compared to the other methods of dispersion. In order to prepare monodisperse colloids of noble metal, phase-transfer method is simply an effortless way to prepare (Chen and Wang 2008). The phase-transfer method was adopted by Feng et al. for synthesizing gold, silver, and platinum nanoparticles on account of the decline of the dissolution of polyvinyl pyrrolidone in water with the increase in the temperature (Feng et al. 2006). The kerosene-based Fe_3O_4 nanofluids is withal prepared by phase-transfer method. The grafting of oleic acid on the surface of ferric oxide nanoparticles has been successfully carried out by the process of chemisorption, thereby rendering ferric oxide nanoparticles to have good consonance with the kerosene (Feng et al. 2006). Since, it was reported earlier that

thermal conductivity is a function of time while the same was not found in case of Fe_3O_4 nanofluids synthesized by phase-transfer method. One of the main problem of nanofluids synthesizes is to prepare them with controllable microstructure. The nanofluids characteristics very much depend on the shape and structure of nanoparticles. The latest findings proves that nanofluids prepared by chemical solution method show great deal of enhancement in conductivity and stability as compared to the rest of the methods (Yu et al. 2010). The controllability is the best virtue of this method. Various factors of synthesis such as temperature, acidity, ultrasonic, and microwave irradiation can be controlled.

3 Heat Transfer in Nanofluids

3.1 Thermal and Heat Transfer Characteristics

Thermal conductivity is one of the important characteristic of nanofluids due to its immense theoretical and practical interests to researchers and technical personnel. Various methods has been described by Wu et al. (2009) and Paul et al. (2010) for analyzing the thermal conductivity of nanofluids such as transient hot-wire method (Kostic and Simham 2009; Vadasz 2010; Hong et al. 2011), steady-state parallel plate method (Shalkevich et al. 2010), temperature oscillation method (Das et al. 2003), and 3-u method (Wang et al. 2007). From these methods, the transient hot-wire technique has been largely in use. The mechanism of the hot-wire method relies on the following components: continuous heat generation source, an infinitely long and thin constant line, and blowing the heat into an illimitable test medium. Nanofluids being electrically conductive, it is complex to apply the simple transient hot-wire technique precisely. Nagasaka and Nagashima suggested a modified hot-wire cell and electrical system (Nagasaka and Nagashima 1981) by painting the hot wire with an adhesive made of epoxy resin, which has exceptional properties of electrical insulation and heat conduction. This method is known to be fast and very much precise method (Kostic and Simham 2009).

The most typical and cost-effective nanoparticles frequently used by scientists in their experimental designs include alumina (Al_2O_3) and copper oxide (CuO). These investigations have established that with the increase in the loading percentage of nanoparticles up to a volumetric percentage of 5 %, the thermal conductivity of nanofluids also increases. It is very important to describe here that nanofluids with low loading percentage of nanoparticles are advantageous in order to achieve better dispersion stability which is exclusively necessary for studying the characteristics of nanofluids and their applications (Saidur et al. 2011). In certain cases, the increment in thermal conductivity has been found to be nonlinear with respect to their nanoparticle concentration which shows ambiguity with the classical effective medium theory (EMT) as reported by Singh et al. (2010). The same behavior has also been described by Choi et al. (2001). The nonlinear behavior was first observed

in CNTs-based PAO nanocomposites where thermal conductivity increment was found to be nonlinear with loading percentage of nanoparticles. It was further proved by Xie et al. (2003), Wen and Ding (2004), and Shaikh et al. (2007) that CNTs-based nanofluids showed less increment in thermal conductivity as compared to the data by Choi et al. (2001). Strikingly, the same nonlinear behaviors are observed in the nanofluids with spherical nanoparticles reported by Murshed et al. (2005), Hong et al. (2005), and Chopkar et al. (2006).

The research in the last decade proves that the discernible increment in the thermal conductivity of nanofluids depends on many parameters which include type of material, concentration, particle size and shape, basefluid, temperature, and chemical treatments (Eastman et al. 2001; Xie et al. 2002; Liu et al. 2005; Chon et al. 2005; Ding et al. 2006; Wen and Ding 2006; Yang and Han 2006). Mostly, the enhancement in thermal conductivities of nanofluids is due to increase in the loading percentage of nanoparticles (Eastman et al. 2001; Xie et al. 2002; Liu et al. 2005; Chon et al. 2005; Ding et al. 2006), reduced particle size (Xie et al. 2002), and increased temperature (Wen and Ding 2006). The stability due to the dispersion of nanofluids mainly is enhanced with chemical additives, which basically alters the pH values which in turn affects the thermal conductivity (Wen and Ding 2006; Yang and Han 2006; Wang et al. 2009; Meibodi et al. 2010; Kang et al. 2006; Chiesa and Das 2009).

However, the issue of nonlinearity is still to be addressed and needs further attention from the researchers. How to remove the ambiguity between the linear increment of thermal conductivity and that in nonlinear? How to manage the agglomeration or flocculation of nanoparticles, which has been found to be the main contributor for the increased thermal conductivity by some scientists, and to maintain balance between the thermal conductivity and dispersion stability? How to optimize the experimental process in order to standardize the optimal conditions to achieve enhanced thermal conductivity?

3.2 Convective Heat Transfer

The study on the convective and boiling heat transfer of nanofluids as compared to the thermal conductivity is still limited. The heat transfer coefficient for convective heat transfer process depends on many characteristics other than thermal conductivity which includes density, specific heat capacity, and dynamic viscosity of nanofluids. The properties of density and specific heat capacity at low particle loading are close to those specifying the base fluid, and the following theoretical equations were proposed by Pak and Cho (1998) and Xuan and Roetzel (2000), respectively.

$$\rho nf = \rho p \varnothing + \rho nf(1 - \varnothing) \tag{1}$$

$$C_{p,nf} = \frac{\varnothing \rho_p C_{p,p} + (1 - \varnothing)\rho_{bf} C_{p,bf}}{\rho_{nf}} \tag{2}$$

There is limitation in using Eq. (2) both theoretically and experimentally on nanofluids (Vajjha and Das 2012). Lately, some of the scientists have determined the dynamic viscosity of nanofluids. The viscosity of the TiO_2-based water nanofluids has been determined by Murshed et al. (2008), and the same property has been compared with previous studies, and it was observed that the nanofluids show higher viscosities with the increase in the loading percentage of nanoparticles. Nevertheless, in case of Al_2O_3-based water nanofluids, viscosity was found to decrease with the increase in the particle dispersion (Wang et al. 1999). For such ambiguity, further detailed research is required.

For any fluid, heat transfer coefficient is a function of the Nusselt number. The experimentally derived interrelation for the Nusselt number for nanofluids was first reported by Pak and Cho (1998)

$$Nu_{nf} = 0.021 Re_{nf}^{0.8} Pr_{nf}^{0.5} \tag{3}$$

The Peclet number effect of copper-based water nanofluid was reported by Xuan and Li (2003) and Li and Xuan (2002) through the following equations, and this includes the convective heat transfer interrelations for both laminar and turbulent flow of the nanofluids.

$$Nu_{nf} = 0.4328\left(1.0 + 11.285 \varnothing^{0.754} Pe_d^{0.218}\right) \underbrace{Re_{nf}^{0.333} Pr_{nf}^{0.4}}_{\text{Laminar flow}} \tag{4}$$

$$Nu_{nf} = 0.0059\left(1.0 + 7.6286 \varnothing^{0.6886} Pe_d^{0.001}\right) \underbrace{Re_{nf}^{0.9238} Pr_{nf}^{0.4}}_{\text{Turbulent flow}} \tag{5}$$

Wen and Ding (2004) reported that Reynolds number in the range of 700–2000 shows an increment in the heat transfer coefficient in case of Al_2O_3-based water nanofluids for laminar flow with the increase in the volumetric fraction of particles; likewise, the thermal conductivity was discussed in the previous section. The same researcher reported the increment in heat transfer coefficient in case of MWCNT-based water nanofluid (Ding et al. 2006) for downstream flow with larger ratio of (axial distance, *x,* pipe diameter, *D*). One of the ambiguities with respect to the graphite in transmission fluids or in synthetic oil mixture with *Re* less than 110 for laminar flow is that the heat transfer increment is found to decrease with the increase in the temperature, which is a reverse trend as found in the case of thermal conductivity. However, this observation is weak as the temperature range is too low. Further results are required to establish this trend. The heat transfer increment versus Peclet number in the range of 2000–7000 for laminar flow of Al_2O_3-based

water and CuO-based water nanofluids has been reported by Heris et al. (2006). The Nusselt number ratios increase with the increase in Peclet number in two types of fluids with the identical volumetric concentrations but different particle size. For heat transfer increment, it is concluded that particle types and particle size have little effect it.

However, the available literature in most of the cases reports that the heat transfer enhancement could be ameliorated with the dispersion of nanoparticles in the basefluid. The heat transfer increment versus Reynolds number has tendency to be identical in all three forms of nanofluids. The increment in the heat transfer is observed to increase with the volumetric concentration of particles, however; there is no clear influence of Reynolds number on the heat transfer increase. Many researchers have studied the convective heat transfer in nanofluids under non-laminar and laminar flows like Daungthongsuk and Wongwises (2008), Yu et al. (2009), Williams et al. (2008), Rea et al. (2009), He et al. (2007), Sommers and Yerks (2010), Anoop et al. (2009), Daungthongsuk and Wongwises (2007), Mohammed et al. (2011), and Sarkar (2011).

Typically, heat transfer equations for nanofluids were revised from the common equations such as Dittus-Boelter equation (1930) or the Gnielinski equation (1976) with the added factual parameters.

3.3 *Boiling Heat Transfer*

The process of boiling is basically a change in the phase of liquid to vapor from a heated surface or in a superheated liquid layer near to the hot surface. Normally, pool boiling and forced convective boiling are the two types of boiling process. Generally, very little advancement has been made on flow boiling heat transfer of nanofluids, while pool boiling heat transfer has made substantial progress and will be discussed here in this section. In this kind of process, two main conditions are included: excess temperature (the difference between wall and the liquid saturation temperatures at ambient pressure, $\Delta T = T_w - T_s$) and heat flux (q'') (Murshed et al. 2011). The established research finding reports that the inclusion of solid particles in the conventional base fluid can escalate its boiling heat transfer efficiency (Wen and Ding 2005; Prakash et al. 2007; Soltani et al. 2009; Henderson et al. 2010; Das et al. 2003; Bang and Chang 2005; Rohsenow 1952; Zuber 1959). This is notably due to the difference in the characteristics of nanofluids such as the effect of particle materials, their sizes and concentrations, chemophysical characteristics of basefluid, various types of heaters involved. In the majority of the cases, the inclusion of nanoparticles to the fluid increases the rate of the heat transfer, and the enhancement increases with the increase in the nanoparticle concentration. This result is in complete agreement with the thermal conductivity increment. Further, pool boiling data for heat transfer of alumina particles in water reported by Pioro (1999) and Vassallo et al. (2004) showed that the inclusion of nanoparticles to the base fluid deescalates the rate of heat transfer and the rate decreases further as the particle

volumetric concentration increases. Two important interrelations which determine the boiling heat transfer coefficient and critical heat flux include Das et al. (2006) and Keblinski et al. (2002) correlations:

$$\frac{C_p(T_w - T_s)}{h_{fg}} = C_{sf}\left[\frac{q'}{\mu h_{fg}}\sqrt{\frac{\sigma}{g(\rho - \rho g)}}\right]0.33\left(\frac{C_p\mu}{k}\right)n \tag{6}$$

The C_{sf} and exponent n values for different surface–fluid mix can be obtained somewhere (Lee et al. 2010). The CHF correlation proposed from Keblinski et al. (2002) is shown as:

$$q'_{\mathrm{CHF}} = K\rho g^{1/2}h_{fg}[g\sigma(\rho - \rho g)]^{1/4} \tag{7}$$

K as a constant is fixed from 0.138 to 0.157. These two reported equations do not support experimental data well (Sergis and Hardalupas 2011). So, new correlation is needed in order to replace this classical model.

4 Mechanism of Heat Transfer in Nanofluids

The mechanism of the heat transfer increment has many discrepancies and ambiguities in nanofluids, although the experimental studies showed substantial increase. Hence, it is important to understand various mechanisms which contribute to the increment in the thermal properties of nanofluids, and the prime discrepancy has been discussed in this section.

It has been mentioned by Yu et al. (2008) that the vivid increase of heat transfer in nanofluids could not be clarified clearly by the present theories and it is on account of this study being spread over different disciplines such as heat transfer, material science, physics, chemical engineering, and synthetic chemistry. Chandrasekar and Suresh (2009) presented four different reasons for the divergent behavior in thermal conductivity of nanofluids:

1. The probable collisions between the nanoparticles which accounts to Brownian motion of particles within the fluid thereby ameliorating the thermal conductivity by direct transmission of heat between particles.
2. The layering of the liquid at the molecular level especially at the liquid/particle interface: The liquid at the solid interface is more regular than bulk of the liquid. The crystalline materials are expected to possesses enhanced thermal conductivity.
3. It has been understood that transport of heat in crystalline materials is being taking place by phonons as a result of vibrations in the crystal lattice. The nanoparticle agglomeration has a substantial influence on thermal conductivity. However, large agglomeration will cause sedimentation, which results in the deescalation of thermal conductivity. It has been proposed that thermal diffusion

is much higher than the Brownian. Nonetheless, the researchers have only evaluated the cases of stationary nanofluids.

Mostly, the mechanism of heat transport in nanofluids can be divided into static and dynamic mechanisms (Wang and Fan 2010). In case of static mechanisms, nanoparticles are supposed to be without any motion in nanofluids, which contains nanolayer, clustering and percolation, interface heat resistance, and frontal geometry while mechanism based on motion called as dynamic mechanisms presumed to have irregular movement of particles in nanofluids, such as Brownian motion and convection at nanosize level. The statistical theory has explained the controversial heat transfer modes of nanofluids in order to describe the mechanism of increment in the heat transport (Sergis and Hardalupas 2011; Yu et al. 2008; Wang and Fan 2010). Finally, it is obvious that more theoretical discussions are required to decrease the ambiguities and explain the controversies in the increment of heat transfer in nanofluids.

5 Prospective Performances

5.1 Wellbore Instability

Generally, huge amount of money is being spent on the stability of wellbore which normally exist due to the incessant exposure of shale to drilling fluid. The wellbore instability is reported to decrease with the inclusion of nanoparticles (Shah et al. 2010). It has been established that the size of the nanoparticles must be less than the size of the pore throat. Also, particle size should not be greater than one-third of the pore throat in order to form a bridge and plug the pores (Suri and Sharma 2004).

5.2 Lost Circulation

Loss of circulation has been categorized as one of the most prominent drilling problems. Drilling fluids in this case is lost either partially or completely to the formation fluid. Some of the factors which lead to this loss of circulation include naturally fractured surface, crevices, and channels. This issue of loss of circulation leads to the escalation in the expenditure and time needed for drilling to reach the requisite depth. The same issue creates loss of pressure control and problems of safety. Hence, excessive time and endeavor have been used to handle circulation loss with the aid of produced materials or muds. So, on using particles in the range from micro to macro has not proved to be of any solution to the problem. However, use of nanoparticles has shown excellent results by decreasing loss of circulation to a greater extent by enhancing carrying capacity enough to hold the cuttings

adequately and maintain the density of drilling fluid and pressure at various operational conditions (Bicerano 2008).

5.3 Pipe Sticking

The sticking of the drill pipe occurs due to the large buildup of the cutting, either by the halt in the circulation of the drilling fluid or by the loss of the filtrate in the wall of the bore well (Palaman et al. 2008). This issue has a major effect on the efficiency of the drilling and well expenditures. Many parameters are affected on the sticking of the pipe which includes drilling fluid rheology. So rheology change can cause sticking of the pipe.

To address this issue, nanofluids have been proposed to play a major concern in recovering the stuck pipe. Nanoparticles-based drilling mud has the potential to depreciate the sticking property of mud cakes by developing a thin film covering the drill pipe that lead to cutting down the pipe sticking issue (Amanullah and Al-Tahini 2009). Further, nanofluids are considered to present distinctive carrying capacity, thereby decreasing the pipe sticking by preventing the wellbore from cuttings.

5.4 Reduction Torque and Drag

The interaction between the drill string and the borehole experiences enhancement in torque and drag difficulties. Less success has been achieved by the use of micro- and macroparticles-based drilling muds on account of which torque and drag issue appears (Wasan and Nikolov 2003). However, the use of nanoparticles provides an appreciable decrease in the friction between the pipe and the borehole. So, nanofluids have the feasibility to make slightly lubricating film in the interface of the wall pipe.

5.5 Toxic Gases

The toxic and corrosive gases such as H_2S can be removed from the drilling fluids by employing nanoparticles. This hydrogen sulfide gas should be removed from the drilling fluids for reducing environmental contamination as well as to look into the matter of the health care of drilling staff and get rid of corrosion of drilling instruments (Singh et al. 2010). It has been observed that the inclusion of 14- to 25-nm ZnO particles into the drilling muds eliminates H_2S gas completely while bulk ZnO eliminates only 2.5 % and is a time-consuming process.

6 Nanomaterials as Drilling Fluid: Its Challenges

Along with the ameliorated drilling fluid performance, the less expensive characteristics of nanomaterial are an exciting feature. This leads to the low consumption of the amount of nanomaterials needed for any applications, because of the high surface area-to-mass ratio of nanoparticles, thereby enhancing their reactivity (Shah et al. 2010). Further, the utilization of nanoparticles in drilling fluids has technical and economic dominance.

Technically, nanofluids are applicable to be utilized in new oil production processes and to transcend tough drilling conditions and operations (Nasser et al. 2013). Economically, the utilization of nanoparticles has three major aspects. The prime one is the use of nanoparticles instead of expensive additives and that depreciates the price of drilling fluids. Further, the utilization of nanofluids as drilling fluids in enhanced oil recovery process by addressing the deep well challenge formations (Abdo and Haneef 2013). Also, high expenditures can be prevented by shortening the non-productive time due to the removal of hurdles.

There are some constraints for applying these conventional drilling fluids instead of the added chemicals in order to improve the drilling fluid efficiency. The important disadvantage of water-based drilling fluids is the ability of WBM to solubilize salts which may produce an unwanted increase in density. Moreover, the WBM is capable of interfering with the flow of gas and oil through porous media. Further constraints of the WBM include promotion of the delamination and dispersion of clays and its inability to drill through water-sensitive shale. Further, the corrosion of iron-based drill pipes by WBM, drill collars and drill bits is a matter of concern. Like water-based mud, use of oil-based drilling (OBD) fluids has constraints such as the cost of the OBM along various lines, as the composition of OBM is very expensive and the high cost of treatment cuttings and disposal of it. Also, OBM is not ecofriendly because of their disposal problem and pollution of the water, pollution of land, and the decimation of the coral reefs. Furthermore; dry gas reservoirs cannot use this type of fluids. Besides, WBM and OBM having limitations, GBM also likely experience a number of constraints. High-pressure production leads to the explosive nature of GBM and is the most common risk as the phase of SBM is a gas. Further, drilling string corrosion is caused by the same type. Also, the SBM cannot be used through water-bearing formations because the cuttings will flock together in these formations; therefore, it is not possible to carry out drilling with the aid of air or gas. Oil well drilling technology has evolved from vertical, horizontal to sub-sea and deep-sea wells. These specific drilling techniques require specialized drilling fluids to fix the issues (Shah et al. 2010). The traditional drilling fluids are suitable for low and medium temperature and pressure conditions.

7 Conclusion

To conclude, drilling fluids have multipurpose use in the drilling process. However, there are issues with lost circulation, pipe sticking, wellbore instability, high torque, and toxic gases, with continuous usage of these fluids with unconventional reservoirs. In the last decades of the twentieth century, the researchers discovered nanotechnology, and nowadays there is pursuit to apply this nanotechnology in the drilling process.

This chapter has elucidated the drilling fluid types, functions, and the idea of adding additives. Further, the deterioration of drilling fluids at high-temperature and high-pressure conditions has been defined. From the literature, it can be implied that nanoparticles can ameliorate drilling fluids due to their stability of the rheological properties at high-pressure and high-temperature conditions. The nano-drilling fluid can bring in great changes in oil and gas drilling industry because it can fulfill the specific needs of new drilling technologies, and it can be effective deep down the well in less time.

One of the main drawbacks in this field of research is that it has not looked into the effect of the sizes and the concentrations of nanoparticles that are generally loaded in the drilling fluids. Accordingly, each issue within the drilling well would require the use of specific sizes and concentrations of nanomaterials. Future work could be borne out in the field of property measurements to establish a better comparative study. The cost feasibility of using nanoparticles in drilling fluids can also be explored.

References

Abdo, J., & Haneef, M. D. (2013). Clay nanoparticles modified drilling fluids for drilling of deep hydrocarbon wells. *Applied Clay Science, 86*, 76–82.

Amanullah, M., & Al-Tahini, A. M. (2009). Nanotechnology—its significance in smart fluid development for oil and gas field application. In SPE Saudia Arabia Section Technical Symposium, Society of Petroleum Engineers.

Anoop, K. B., Sundararajan, T., & Das, S. K. (2009). Effect of particle size on the convective heat transfer in nanofluid in the developing region. *International Journal of Heat and Mass Transfer, 52*, 2189–2195.

Bang, I. C., & Chang, S. H. (2005). Boiling heat transfer performance and phenomena of Al_2O_3-water nano-fluids from a plain surface in a pool. *International Journal of Heat and Mass Transfer, 48*, 2407–2419.

Bicerano, J. (2008). Drilling fluid, drill-in fluid, competition fluid, and work over fluid additive compositions containing thermoset nancomposite particles; and applications for fluid loss control and wellbore strengthening. U.S. Patent Application 12/178,785.

Bönnemann, H., Botha, S. S., Bladergroen, B., & Linkov, V. M. (2005). Monodisperse copper- and silver-nanocolloids suitable for heat-conductive fluids. *Applied Organometallic Chemistry*, *19*(6), 768–773.

Chandrasekar, M., & Suresh, S. (2009). A review on the mechanisms of heat transport in nanofluids. *Heat Transfer Engineering, 30*(14), 1136–1150.

Chen, Y., & Wang, X. (2008). Novel phase-transfer preparation of monodisperse silver and gold nanoparticles at room temperature. *Materials Letters, 62*(15), 2215–2218.

Chiesa, M., & Das, S. K. (2009). Experimental investigation of the dielectric and cooling performance of colloidal suspensions in insulating media. *Colloids and Surfaces A: Physicochemical and Engineering Aspects, 335*, 88–97.

Choi, S. U. S., Zhang, Z. G., Yu, W., Lockwood, F. E., & Grulke, E. A. (2001). Anomalous thermal conductivity enhancement in nanotube suspensions. *Applied Physics Letters, 79*(14), 2252–2254.

Chon, C. H., Kihm, K. D., Lee, S. P., & Choi, S. U. S. (2005). Empirical correlation finding the role of temperature and particle size for nanofluid (Al_2O_3) thermal conductivity enhancement. *Applied Physics Letters*, *87*, 153107-1–153107-3.

Chopkar, M., Das, P. K., & Manna, I. (2006). Synthesis and characterization of nanofluid for advanced heat transfer applications. *Scripta Materialia*, *55*(6), 549–552.

Das, S. K., Choi, S. U. S., & Patel, H. (2006). Heat transfer in nanofluids: A review. *Heat Transfer Engineering*, *27*(10), 3–19.

Das, S. K., Putra, N., & Roetzel, W. (2003a). Pool boiling characterization of nano-fluids. *International Journal of Heat and Mass Transfer, 46*, 851–862.

Das, S. K., Putra, N., Thiesen, P., & Roetzel, W. (2003b). Temperature dependence of thermal conductivity enhancement for nanofluids. *Journal of Heat Transfer, 125*, 567–574.

Daungthongsuk, W., & Wongwises, S. (2007). A critical review of convective heat transfer of nanofluids. *Renewable and Sustainable Energy Reviews*, *11*(5), 797–817.

Ding, Y., Alias, H., Wen, D., & Williams, R. A. (2006). Heat transfer of aqueous suspensions of carbon nanotubes (CNT nanofluids). *International Journal of Heat and Mass Transfer*, *49*, 240–250.

Dittus, F. W., & Boelter, L. M. K. (1930). *Heat transfer in automobile radiators of the tubular type* (Vol. 2, pp. 443–461). University of California Publications in Engineering.

Duangthongsuk, W., & Wongwises, S. (2008). Heat transfer enhancement and pressure drop characteristics of TiO_2—water nanofluid in a double-tube counter flow heat exchanger. *International Journal of Heat and Mass Transfer*, *52*(7e8), 2059–2067.

Eastman, J. A., Choi, S. U. S., Li, S., Yu, W., & Thompson, L. J. (2001). Anomalously increased effective thermal conductivities of ethylene glycol-based nanofluids containing copper nanoparticles. *Applied Physics Letters*, *78*(6), 718–720.

Feng, X., Ma, H., Huang, S., et al. (2006). Aqueous-organic phase transfer of highly stable gold, silver, and platinum nanoparticles and new route for fabrication of gold nanofilms at the oil/water interface and on solid supports. *Journal of Physical Chemistry B, 110*(25), 12311–12317.

Gnielinski, V. (1976). New equations for heat and mass transfer in turbulent pipe and channel flow. *International Chemical Engineering, 16*, 359–368.

He, Y., Jin, Y., Chen, H., Ding, Y., Cang, D., & Lu, H. (2007). Heat transfer and flow behavior of aqueous suspensions of TiO2 nanoparticles (nanofluids) flowing upward through a vertical pipe. *International Journal of Heat and Mass Transfer, 50*, 2272–2281.

Henderson, K., Park, Y. G., Liu, L., & Jacobi, A. M. (2010). Flow-boiling heat transfer of R-134a-based nanofluids in a horizontal tube. *International Journal of Heat and Mass Transfer, 53*, 944–951.

Heris, S. Z., Etemad, S. G., & Esfahany, M. N. (2006). Experimental investigation of oxide nanofluids laminar flow convective heat transfer. *International Communications on Heat and Mass Transfer, 33*, 529–535.

Hong, S. W., Kang, Y. T., Kleinstreuer, C., & Koo, J. (2011). Impact analysis of natural convection on thermal conductivity measurements of nanofluids using the transient hot-wire method. *International Journal of Heat and Mass Transfer, 54*, 3448–3456.

Hong, T. K., Yang, H. S., & Choi, C. J. (2005). Study of the enhanced thermal conductivity of Fe nanofluids. *Journal of Applied Physics*, *97*(6), 064311-1–064311-4.

Kang, H. U., Kim, S. H., & Oh, J. M. (2006). Estimation of thermal conductivity of nanofluid using experimental effective particle volume. *Experimental Heat Transfer, 19*, 181–191.

Keblinski, P., Phillpot, S. R., Choi, S. U. S., & Eastman, J. A. (2002). Mechanism of heat flow in suspensions of nano-sized particles. *International Journal of Heat and Mass Transfer, 45*, 855–863.

Kostic, M., & Simham, K. C. (2009). Computerized, transient hot-wire thermal conductivity (HWTC) apparatus for nanofluid. In L. Xi (Ed.), *Proceedings of the 6th WSEAS International Conference on Heat and Mass Transfer (HMT'09)* (pp. 71–78). WSEAS Press.

Kumar, A., Joshi, H., Pasricha, R., Mandale, A. B., & Sastry, M. (2003). Phase transfer of silver nanoparticles from aqueous to organic solutions using fatty amine molecules. *Journal of Colloid and Interface Science, 264*(2), 396–401.

Lee, J. H., Lee, S. H., Choi, C. J., Jang, S. P., & Choi, S. U. S. (2010). A review of thermal conductivity data, mechanisms and models for nanofluids. *International Journal of Micro-Nano Scale Transport, 1*(4), 269–322.

Li, Q., & Xuan, Y. (2002). Convective heat transfer and flow characteristics of Cu-water nanofluid. *Science in China Series E: Technolgical Science*, *45*(4 Series E), 408–416.

Li, Y., Zhou, J., Tung, S., Schneider, E., & Xi, S. (2009). A review on development of nanofluid preparation and characterization. *Powder Technology, 196*(2), 89–101.

Liu, M., Lin, M. C., Huang, I., & Wang, C. (2005). Enhancement of thermal conductivity with carbon nanotube for nanofluids. *International Communications on Heat and Mass Transfer*, *32*, 1202–1210.

Lo, C. H., Tsung, T. T., & Chen, L. C. (2005a). Shape-controlled synthesis of Cu-based nanofluid using submerged arc nanoparticle synthesis system (SANSS). *Journal of Crystal Growth, 277* (1–4), 636–642.

Lo, C. H., Tsung, T. T., Chen, L. C., Su, C. H., & Lin, H. M. (2005b). Fabrication of copper oxide nanofluid using submerged arc nanoparticle synthesis system (SANSS). *Journal of Nanoparticle Research, 7*(2–3), 313–320.

Meibodi, M.E., Vafaie-Sefti, M., Rashidi, A. M., Amrollahi, A., Tabasi, M., & Kalal, H. S. (2010). The role of different parameters on the stability and thermal conductivity of carbon nanotube/water nanofluids. *International Communications in Heat Mass Transfer*, *37*, 319–323.

Mohammed, H. A., Al-aswadi, A. A., Shuaib, N. H., & Saidur, R. (2011). Convective heat transfer and fluid flow study over a step using nanofluids: A review. *Renewable and Sustainable Energy Reviews, 15*(6), 2921–2939.

Murshed, S. M. S., Castro, C. A. N., Lourenco, M. J. V., Lopes, M. L. M., & Santos, F. J. V. (2011). A review of boiling and convective heat transfer with nanofluids. *Renewable and Sustainable Energy Reviews, 15*(5), 2342–2354.

Murshed, S. M. S., Leong, K. C., & Yang, C. (2005). Enhanced thermal conductivity of TiO_2—water based nanofluids. *International Journal of Thermal Science*, *44*(4), 367–373.

Murshed, S. M. S., Leong, K. C., & Yang, C. (2008). Investigations of thermal conductivity and viscosity of nanofluids. *International Journal of Thermal Sciences, 47*, 560–568.

Nagasaka, Y., & Nagashima, A. (1981). Absolute measurement of the thermal conductivity of electrically conducting liquids by the transient hot-wire method. *Journal of Physics E: Scientific Instruments, 14*, 1435–1440.

Nasser, J., Jesil, A., Mohiuddin, T., Al Ruqeshi, M., Devi, G., & Mohataram, S. (2013). Experimental investigation of drilling fluid performance as nanoparticles. *World Journal of Nano Science and Engineering*.

Oakley, D. J., Morton, K., Eunson, A., Gilmour, A., Pritchard, D., & Valentine, A. (2000). Innovative drilling fluid design and rigorous pre-well planning enable success in an extreme HTHP well. In IADC/SPE Asia Pacific Drilling Technology, Society of Petroleum Engineers.

Pak, B. C., & Cho, Y. I. (1998). Hydrodynamic and heat transfer study of dispersed fluids with submicron metallic oxide particles. *Experimental Heat Transfer, 11*, 151–170.

Palaman, A., N., & Bander, D. A. A. (2008). Using nanoparlides to decrease differential pipe stricking and its feasibility in iranian oil fields. *J.Oil and Gas Business*.

Paul, G., Chopkar, M., Manna, I., & Das, P. K. (2010). Techniques for measuring the thermal conductivity of nanofluids: A review. *Renewable and Sustainable Energy Reviews*, *14*, 1913–1924.

Pioro, I. L. (1999). Experimental evaluation of constants for the Rohsenow pool boiling correlation. *International Journal of Heat and Mass Transfer, 42*, 2003–2013.

Prakash, N. G., Anoop, K. B., & Das, S. K. (2007). Mechanism of enhancement/deterioration of boiling heat transfer using stable nanoparticles suspensions over vertical tubes. *Journal of Applied Physics, 102*, 074317-1–074317-7.

Rea, U., McKrell, T., Hu, L., & Buongiorno, J. (2009). Laminar convective heat transfer and viscous pressure loss of alumina-water and zirconia-water nanofluids. *International Journal of Heat and Mass Transfer*, *52*(7–8), 2042–2048.

Rohsenow, W. M. (1952). A method of correlating heat transfer data for surface boiling of liquids. *Transactions on ASME, 74*, 969–976.

Saidur, R., Leong, K. Y., & Mohammad, H. A. (2011). A review on applications and challenges of nanofluids. *Renewable and Sustainable Energy Reviews, 15*, 1646–1668.

Salem, R. A. M., & Noah, A. (2014). Reduction of formation damage and fluid loss using nano-sized silica drilling fluids. *Petroleum Technology Development Journal, 2*, 75–88.

Sarkar, J. (2011). A critical review on convective heat transfer correlations of nanofluids. *Renewable and Sustainable Energy Reviews, 15*(6), 3271–3277.

Sergis, A., & Hardalupas, Y. (2011). Anomalous heat transfer modes of nanofluids: A review based on statistical analysis. *Nanoscale Research Letters, 6*(1), 391–427.

Shah, S. N., Shanker, N. H., & Ogugbue, C. C. (2010). Future challenges of drilling fluids and their rheological measurements. In AADE Fluids Conference and Exhibition, Houston, Texas.

Shaikh, S., Lafdi, K., & Ponnappan, R. (2007). Thermal conductivity improvement in carbon nanoparticle doped PAO oil: an experimental study. *Journal of Applied Physics, 101*(6), 4302–43027.

Shalkevich, N., Escher, W., Büurgi, T., Michel, B., Lynda, S., & Poulikakos, D. (2010). On the thermal conductivity of gold nanoparticle colloids. *Langmuir, 26*(2), 663–670.

Singh, S., Ahmed, R., & Growcock, F. (2010). Vital role of nanopolymers in drilling and stimulations fluid applications. In Paper SPE 130413 presented at the SPE Annual Technical Conference and Exhibition (pp. 19–22), Florence, Italy.

Singh, A. K., & Raykar, V. S. (2008). Microwave synthesis of silver nanofluids with polyvinylpyrrolidone (PVP) and their transport properties. *Colloid and Polymer Science, 286*(14–15), 1667–1673.

Soltani, S., Etemad, S. G., & Thibault, J. (2009). Pool boiling heat transfer performance of Newtonian nanofluids. *Heat and Mass Transfer, 45*, 1555–1560.

Sommers, A. D., & Yerkes, K. L. (2010). Experimental investigation into the convective heat transfer and system-level effects of Al_2O_3-propanol nanofluids. *Journal of Nanoparticle Research*, *12*, 1003–1014.

Suri, A., & Sharma, M. M. (2004). Strategies for sizing particles in drilling and completion fluid. *SPE Journal, 9*(01), 13–23.

Vadasz, P. (2010). Rendering the transient hot wire experimental method for thermal conductivity estimation to two-phase systems-theoretical leading order results. *Journal of Heat Transfer, 132*, 081601-1.

Vajjha, R. S., & Das, D. K. (2012). A review and analysis on influence of temperature and concentration of nanofluids on thermophysical properties, heat transfer and pumping power. *International Journal of Heat and Mass Transfer, 55*, 4063–4078.

Van Dyke, K. (1998). *Drilling fluids, mud pumps, and conditioning equipment*. University of Texas at Austin Petroleum.

Vassallo, P., Kumar, R., & Amico, S. D. (2004). Pool boiling heat transfer experiments in silicaewater nano-fluids. *International Journal of Heat and Mass Transfer, 47*, 407–411.

Wang, L., & Fan, J. (2010). Nanofluids research: Key issues. *Nanoscale Research Letters, 5*, 1241–1252.

Wang, Z. L., Tang, D. W., Liu, S., Zheng, X. H., & Araki, N. (2007). Thermal-Conductivity and thermal-diffusivity measurements of nanofluids by 3u method and mechanism analysis of heat transport. *International Journal of Thermophysics, 28*, 1255–1268.

Wang, X., Xu, X., & Choi, S. U. S. (1999). Thermal conductivity of nanoparticleefluid mixture. *Journal of Thermophysics and Heat Transfer, 13*(4), 474–480.

Wang, X., Zhu, D., & Yang, S. (2009). Investigation of pH and SDBS on enhancement of thermal conductivity in nanofluids. *Chemical Physics Letters*, *470*, 107–111.

Wasan, D. T., & Nikolov, A. D. (2003). Spreading of nanofluids on solids. *Nature, 423*(6936), 156–159.

Wawrzos, F. A., & Weintritt, D. J. (2007). Drilling fluid lubricant and method of use. U.S. Patent Application 11/957,634.

Wen, D., & Ding, Y. (2004a). Effective thermal conductivity of aqueous suspensions of carbon nanotubes (carbon nanotube nanofluids). *Journal of Thermophysics and Heat Transfer*, *18*(4), 481–485.

Wen, D., & Ding, Y. (2004b). Experimental investigation into convective heat transfer of nanofluids at the entrance region under laminar flow conditions. *International Journal of Heat and Mass Transfer, 47*, 5181–5188.

Wen, D., & Ding, Y. (2005). Experimental investigation into the pool boiling heat transfer of aqueous based alumina nanofluids. *Journal of Nanoparticle Research, 7*, 265–274.

Wen, D., & Ding, Y. (2006). Natural convective heat transfer of suspensions of titanium dioxide nanoparticles (nanofluids). *IEEE Transactions on Nanotechnology*, *5*, 220–227.

Williams, W., Buongiorno, J., & Hu, L. W. (2008). Experimental investigation of turbulent convective heat transfer and pressure loss of alumina/water and zirconia/water nanoparticle colloids (nanofluids) in horizontal tubes. *Journal of Heat Transfer, 130*, 042412–1–042412-7.

Wu, D., Zhu, H., Wang, L., & Liua, L. (2009). Critical issues in nanofluids preparation, characterization and thermal conductivity. *Current Nanoscience*, *5*, 103–112.

Xie, H., Lee, H., Youn, W., & Choi, M. (2003). Nanofluids containing multiwalled carbon nanotubes and their enhanced Thermal conductivities. *Journal of Applied Physics, 94*, 4967–4971.

Xie, H., Wang, J., Xi, T., & Ai, F. (2002). Thermal conductivity enhancement of suspensions containing nanosized alumina particles. *Journal of Applied Physics, 91*, 4568–4572.

Xuan, Y., & Li, Q. (2003). Investigation on convective heat Transfer and flow features of nanofluids. *Transactions on ASME, Journal of Heat Transfer, 125*, 151–155.

Xuan, Y., & Roetzel, W. (2000). Conceptions for heat transfer correlation of nanofluids. *International Journal of Heat and Mass Transfer, 43*, 3701–3707.

Yang, B., & Han, Z. H. (2006). Temperature-dependent thermal conductivity of nanorodbased nanofluids. *Applied Physics Letters, 89*, 083111-1–083111-3.

Yu, W., France, D. M., Routbort, J. L., & Choi, S. U. S. (2008). Review and comparison of nanofluid thermal conductivity and heat transfer enhancements. *Heat Transfer Engineering, 29* (5), 432–460.

Yu, W., France, D. M., Smith, D. S., Singh, D., Timofeeva, E. V., & Routbort, J. L. (2009). Heat transfer to a silicon carbide/water nanofluid. *International Journal of Heat and Mass Transfer, 2*, 3606–3612.

Yu, W., Xie, H., Chen, L., & Li, Y. (2010). Enhancement of thermal conductivity of kerosene-based Fe_3O_4 nanofluids prepared via phase-transfer method. *Colloids and Surfaces A, 355*(1–3), 109–113.

Yu, W., Xie, H., Wang, X., & Wang, X. (2011). Highly efficient method for preparing homogeneous and stable colloids containing graphene oxide. *Nanoscale Research Letters, 6*, 47.

Zhu, H. T., Lin, Y. S., & Yin, Y. S. (2004). A novel one-step chemical method for preparation of copper nanofluids. *Journal of Colloid and Interface Science, 277*(1), 100–103.

Zhu, H. T., Zhang, C. Y., Tang, Y. M., & Wang, J. X. (2007). Novel synthesis and thermal conductivity of CuO nanofluid. *Journal of Physical Chemistry C, 111*(4), 1646–1650.

Zuber, N. (1959). Hydrodynamic aspects of boiling heat transfer. In *Physics and mathematics*. AEC Report No. AECU-4439.

Novel Nano Copper-Tungsten-Based EDM Electrode

Ahmad Majdi Abdul Rani, Altidjani Zakaria Mahamat and Azri Hamim Ab Adzis

Abstract Using electrical discharge machining (EDM), it is possible to machine material that is difficult to machine by conventional machining technique as long as it is electrically conductive. The performance of EDM is highly dependent on the type of electrode being used, the power supply system, and the dielectric system. Copper–tungsten electrode combines the higher melting point of tungsten with the good electrical and thermal conductivity of copper, but it is difficult to manufacture due to the variation in melting point and zero miscibility of copper with tungsten. Thus, newly modified copper–tungsten–silicon (Cu–WC–Si) electrode was synthesized using ball milling method. The method was used to synthesize the new electrode material due to the possibility to overcome the problems encountered in alloying materials which have a large variation in melting temperature or low miscibility at low temperatures. Taguchi method is the main statistical tool used to design and analyse ball milling and machining processes. Material removal rate and electrode wear are the parameters used for comparing the performance between the existing copper–tungsten and new developed electrode. Milling results show a clear change in the thickness of crystalline and d-spacing of the milled powder. The performances of Cu–WC–Si electrode in machining of hardened die steel show an improvement in MRR and EW compared with that achieved by using Cu–W electrode when it is milled for less than 10 h.

Keywords EDM · New EDM electrode · Nano electrode · Copper-Tungsten · Ball milling · Surface roughness · MRR

A.M. Abdul Rani (✉) · A.Z. Mahamat
Department of Mechanical Engineering, Universiti Teknologi Petronas,
32610 Bandar Seri Iskandar, Perak Darul Ridzuan, Malaysia
e-mail: majdi@petronas.com.my

A.H. Ab Adzis
Mechanical Engineering ICOLE, Universiti Kuala Lumpur,
43650 Bandar Baru Bangi, Selangor Darul Ehsan, Malaysia

K. Viswanatha Sharma and N. Hisham B Hamid (eds.),
Engineering Applications of Nanotechnology, Topics in Mining, Metallurgy and Materials Engineering, DOI 10.1007/978-3-319-29761-3_8

1 Electrodischarge Machining

Machining process is among the most important in the manufacturing process because all the steps after the material selection need material removal process. The machining process referred to the material removal processes to produce the desired shape using cutting tool to remove material from a workpiece. Preparation of the workpiece for machining should pass through several stages such as cutting and shaping before finally machined to the desired shape. Machining process can be divided into two main categories, the conventional and non-conventional machining. In conventional machining, parts of the material are removed mechanically from the workpiece using physical machining tool to change it to final shape. The main demand in conventional machining is that the tool must be harder than the workpiece and must resist all types of mechanical stress. The machining rate and the quality of the machined surface strongly depend on the relative motion between the tool and the workpiece. Conventional machining may not be feasible when the workpiece material is harder than the tool electrode material or when low-rigidity structures with tight tolerances and fine surface quality are required. Therefore, there is an urgent need to use non-conventional machining technique to overcome these limitations.

Electrical discharge machining (EDM) is one of the most applicable non-conventional machining techniques used for die and tool manufacturing because no restriction is imposed by the mechanical properties of workpiece material such as brittleness and toughness as long as it is electrically conductive. Additionally, it has an advantage when complex shapes with sharp edges, holes and pocket are required regardless of the workpiece hardness. It is also possible to machine a very small workpiece because there is no direct contact between tool and workpiece. Proper selection of EDM variables and the optimal setting of these variables is the first step to improve the material removal rate, MRR; the electrodes wear, EW; and the surface roughness, Ra.

The main disadvantage of this technique is that it can only machine conductive material; low material removal rate, MRR; and the negative effect of electrode wears, EW, on machining process; and surface quality. The electrode manufacturing is a time-consuming process, leading to the high cost of EDM electrode. Heat concentration can affect the microstructure and may cause cracks, which is undesirable. Machining of large areas is not normally possible and in some cases, the risk of the direct contact with debris and fine powder is high.

2 EDM Electrodes

EDM electrode is the physical cutting tool. It is important to keep in mind that the shape of the produced cavity (die) is the negative of the tool electrode shape. Thus, the electrode wear reduction must be the first consideration during the design of

electrode. As EDM is a non-contact machining process, the mechanical property is not the first priority in electrode manufacturing. Since the system converts an electric energy into heat energy by a series of sparking, the electrode material must have a high electrical and thermal conductivity. The high electrical conductivity makes the discharge more easily and reduces the bulk heating. For the same heat load but at different thermal conductivities, the localized temperature will rise at different rates due to the differences in heat conduction, leading to a localized melting of the electrode material, and therefore the tool wear can be reduced with higher thermal conductivity. The material is removed by fusion and evaporation mechanism and due to this, it is important to use a high melting point material. During sparking, both the electrode and the workpiece eroded, and to reduce the volume wear and as a consequence, less tool wear and less dimensional inaccuracy. Thus, the electrode material must have high density. Ease of manufacturing and low price are other important points which should be considered in EDM electrode industry.

Currently, the commonly used materials as electrodes are copper, copper alloy, graphite, tungsten and copper–tungsten. Each of these electrodes has its advantages and drawbacks. Copper is good in electrical and thermal conductivity but very poor in wear resistance. Tungsten on the other side is the best in wear resistance but relatively low in conductivity and is very expensive. Graphite electrodes are good in wear resistance and not expensive. It has low electrical and thermal conductivity with low oxidation temperature as its main disadvantage.

Copper–tungsten (Cu–W) is one of the most used electrodes in machining of cemented tungsten carbide. Copper–tungsten electrode shows the highest thermal wear resistance. The main problems associated with this electrode are the difficulties of manufacturing due to the variation in melting temperature, zero miscibility of Cu and W and also the high cost due to the expensive nature of tungsten. This electrode shows lower material removal rate in comparison with copper due to lower conductivity. The basic demands during electrode material selection are the high melting point, good electrical and thermal conductivity, chemical stability, machinability, burr formation and low price. It is impossible to find a single material that can offer all these properties. Therefore, the development of new EDM tool electrode materials has become vital.

This research hypothesized that it is possible to use a new modified Cu–W electrode to overcome some of these problems. In newly modified electrode, the tungsten in Cu-80 %W is replaced with tungsten carbide (less than 50 %) and silicon is introduced, a suitable additive that has a good solubility with copper and tungsten. Silicon can form silicide with copper and tungsten which is an intermetallic compound that has properties which is intermediate between metal and an alloy. The expected intermetallic bonding of silicon with copper and tungsten are electrically conductive.

2.1 Fabrication Techniques

2.1.1 Powder Metallurgy (P/M) Electrodes

Powder metallurgy (P/M) is one of the main techniques used to synthesize and manufacture EDM electrode. The performance of powder metallurgy electrode on the quality of the machined component was studied by Kunieda et al. (2004). The quality of the electrode was controlled over a wide range of properties by adjusting the compaction and sintering conditions. P/M electrode performance is found to be more sensitive to the pulse current and pulse duration than that of conventional solid electrodes. Not only that, electrodes can cause negative material removal rate. The machined surface contamination caused by the eroded particles from the electrode is a function of the manufacturing parameters of P/M electrodes. Lower currents and higher frequencies are responsible for low metal removal. This is, in no small way, due to the surface structure of P/M electrodes. In contrast to the conventional solid electrodes, P/M electrodes possess more asperities on the working surface since they have more porous nature.

Various compositions of Cu–ZrB_2 and Cu–TiSi P/M EDM electrode are prepared and developed by Zaw et al. (1999) using solid-state sintering and liquid-phase sintering. The poor bonding strength between ZrB_2 and Cu particles reduces the thermal wear resistance. Prior to melting the material through spark erosion, the bond strength is easily broken down. EDM electrodes made of TiSi/Cu compound were unusable because they exhibit high wear rate, and they tend to damage the surface of the workpiece. Zaw et al. (1999) also mentioned that if bonding problems could be solved by the addition of some fluxing elements and via laser melting, then ZrB_2 may be an effective contributor to good machinability and provide increase in wear resistance.

The performance of copper powders containing resin blended with chromium powders as electrodes was investigated by Tsai and Huang (2003). The electrode material is bonded in a hot mounting machine at 20 MPa compaction pressure and 200 °C temperature. The effect of mixing ratio and compaction pressure in addition to the machining variables (such as polarity, peak current and pulse duration) was used to investigate the machining process in terms of material removal rate (MRR), electrode wear rate (EWR), surface roughness and thickness of the recast layer. The experimental results show that under positive electrode polarity, copper powders containing resin show a higher MRR than the Cu–Cr composite electrodes; but relatively the EWR is higher. The high electrode wear is responsible for the weak bonding strength of Cu–Cr composite electrodes because of low sintering pressure and temperature. Instantaneous drop of Cu and Cr particles out of the electrode leads to unstable discharge condition during the EDM process. The dropout of Cu and Cr particles in the discharge gap affects the machining process and the surface quality whenever the particles stick to the machined surfaces. Tsai and Huang (2003) suggest that using such composite electrodes as tool electrode may improve the resistance of workpiece surfaces to corrosion.

The reviewed papers about powder metallurgy EDM electrodes shows that P/M technique is a promising simple technique that can be used to develop and fabricate a new tool electrode material. The main problems with this technique are the low bonding strength of the components and the difficulties in achieving full density material.

2.1.2 Rapid Prototyping (R/P) Electrodes

The use of selective laser sintering (SLS) technique to fabricate EDM electrodes was investigated by Dürr et al. (1999). In this rapid tooling technique, a bronze–nickel electrode was built layer by layer. Moving speed and the sintering strategy show a big impact on the quality of the sintered electrodes. Slower scanning speed gives the higher particle density and lower roughness. On the other hand, a 90° direction rotation after every layer (called jitter scanning) leads to an increase in strength and a decrease in porosity compared to the alternate scanning (no rotation). The electrodes wear and material removal rate have been investigated, and the results indicate that the wear behaviour leads to an unacceptable change in the shape of the electrodes in addition to workpiece. The investigation so far conducted demonstrated that electrodes with lower porosity manifest decreased electrode wear with higher workpiece removal.

Similar research using selective laser sintering (SLS) technique was conducted by Zhao et al. (2003). The study involved manufacturing an EDM rapid prototype electrode. Infiltration was used to improve the density and the mechanical performance of selective laser sintering electrode. The results indicate that the electrode made by SLS can be used as an EDM electrode. The main disadvantages of SLS are the need for an additional treatment such as infiltration to achieve a full density due to the high porosity and the surface quality of the product parts influenced by powder particles. In addition, the scanning rate and scanning strategy are very important additional variables. The process is time consuming due to the need for heating up and cooling down process.

The use of rapid prototyping electrode for EDM was also researched by Dimla and Rothe (2004) using stereo lithography copper-coated models and copper coating of direct metal laser sintering (DMLS) models. He stated that variability of copper thickness of the rapid prototyped electrodes is clearly a big concern. Due to variations in coating thickness, the machining process was found to be unsuitable. The need for a consistent layer of copper on the SL and EDM electrodes is another reason that makes these RP electrodes unfit.

New electrical discharge machining electrode was developed and tested by Monzon et al. (2008). The electrode is manufactured using rapid prototyping followed by electroforming technologies. The electrode performance has been tested in an EDM machine, and the results were compared with conventional electrolytic copper electrodes. The results show that both the electroformed and the conventional electrodes can operate with the same parameters and conditions, except when under strong work intensity. In general, the roughness and cavities produced by

electroformed electrodes are higher than those obtained with conventional electrolytic electrodes.

Another important study about the performance of a newly manufactured die-sinking EDM electrode was done by Hsu et al. (2008). He used rapid prototyping system based on nickel electrolysis plating and copper electroforming. This method shortens the electrode manufacturability as well as the cost of electrodes. The electrode prototype using stereo lithography and the electrolysis plating was then performed. Test results indicate the critical step in pre-treatment engineering for electrolysis plating is surface roughening but no crack was found on the electrode, and that the electrical discharge machining effects are promising. The most effective factors are the electroforming current density, the ratio of depth over the width of the hole in the plating material, the concentration of the plating solution and the direction of current. It was also established that the machining time is lower at low machining current, and the electrode wear ratio seems to increase with current. The advantage of stereo lithography (SL) and electroforming technique is clear when an electrode with complex 3D geometry is needed. However, the electrode strength and cost are negatively affected.

Another rapid prototyping technique used to manufacture EDM electrode is Thermo Jet 3D printing. Ferreira and Artur Alves (2007) studied the application of indirect rapid tooling technology to manufacture EDM copper electrodes from investment casting, using prototypes of wax made by Thermo Jet 3D printing. The results show that there was parity in the machining efficiency exhibited by both the copper RT electrodes and the conventional-machined solid copper electrodes. The suitability of these electrodes leans towards roughing or semi-finishing cuts in die-sinking EDM. The present electrodes show better electrode wear ratio (EWR) compared with that of electrolytic copper.

2.1.3 Ball Milling of Electrodes

The need for new tool electrode material that can combine high electrical conductivity, thermal conductivity and high melting point for good wear resistance requires a special technique. Mechanical alloying by ball milling is one of the most practical and dependable techniques to synthesize alloy from material that are immiscible at low temperature or when the vibration of melting temperature is very high such as copper and tungsten (Li et al. 2003).

Copper–tungsten exhibits total absence of solubility in both solid and liquid states. Mechanical alloying (MA) as a solid-state, non-equilibrium process can be beneficial to the processing of such an immiscible system with the added features of refinement of the structure. Raghu et al. (2001) synthesized an ultrafine Cu–W microcomposite structure by mechanical alloying using ball milling. He affirmed that the milling behaviour depends on the composition, milling time and milling atmosphere. Metastable solid solubility in the system was also confirmed, and the crystal sizes were found in the nanocrystalline region. This result was confirmed by the lattice parameter analyses of copper and tungsten elements. They report that the

conversion of milling energy effectively to create deformed surfaces, which resulted in metastable solid solubility and nanocrystalline structure, was assisted by the oxygen available in the milling atmosphere. Li et al. (2003) used the thermo-mechanical approach to produce W–Cu composite powder by using high temperature oxidation, small amount of time, high-energy milling and reduction. The outcomes revealed that the oxygen content of W–Cu composite powder decreases with the increase in milling time, while the specific surface of final powder increases with the milling time.

3 EDM Theory

In traditional machining, the tools must be harder than the workpiece meanwhile in many non-traditional machining processes such as EDM, the electrode hardened is not one of the main required properties. The new techniques provide a technological and economic advantage over traditional methods. The thermal and electrochemical process uses thermal energy to remove material by melting or vapourizing the workpiece material. This includes electrodischarge machining (EDM), plasma beam machining, laser beam and electron beam as well as ion beam machining. In electrode discharge, machining is sometimes called electrical erosion. (Lissaman 1996; El-Hofy 2005).

Electrical discharge machining (EDM) is an electrothermal process that can erode any conductive workpiece by the formation of an electrical spark between an electrode and the workpiece. As a result, spark erosion, the shape of the electrode can be reproduced into the workpiece. The main types of EDM include diesinker EDM (electrical discharge grinding (EDG), multi-electrode and multi-lead machining), micro-hole EDM drilling and wire-cut EDM (multiple-electrode and multiple-workpiece machining). All these types are operated based on power generation, dielectric function and the tool electrode.

A typical EDM machine consists of machine tool, EDM power supply, dielectric unit, servo control and CNC control. The electrode and workpiece immersed in a tank filled with a hydrocarbon dielectric (such as oil and kerosene) can ionize in the presence of high electrical field. The frequencies of the sparks are in the range from 500 to 500,000 sparks per second, and the material removal rate is in the range of fraction of one to around 3.9 (cm^3/min). Since this is non-contact machining process, the hardness of the workpiece is no more a source of difficulty.

The main EDM electrode materials include tungsten, tungsten carbide, copper–tungsten, graphite, copper, brass and zinc alloys. The main disadvantages associated with copper electrodes are low thermal wear resistance, difficult to machine and hard to grind off burr formations. Tungsten, due to the combination of its high density and melting point, is the best choice if wear resistance is the main concern. Tungsten is seldom used as EDM electrode due to the low cutting speed, high and very low machinability. Copper–tungsten on the other hand is incomparable for its high volume and corner wear resistance. The cost of copper–tungsten electrode

depends on tungsten ration. Reducing the tungsten content would increase the corner wear, but enables smoother burning in addition to reducing the cost of the material. It is important to note that copper–tungsten typically cut only half as fast as copper does (Ostwald and Jairo 1997).

3.1 Electrodes Wear

In electrodischarge machining, tool wear does not depend on the mechanical properties such as stiffness, young modulus, hardness and yield strength. The tool wear depends on the thermal properties and also the material removal rate. Electrode wear occurs as a result of ion bombardments, where the negative electrode is bombarded by positive ions, and the positive electrode is bombarded by negative ions. The accelerated ions will lose its kinetic energy ($1/2*mv^2$) as heat when it is crashed onto the surface of the electrode. The heat generated due to this bombardment is enough to vapourize the electrode material, and a small amount of electrode material is removed.

The ion mass and volume is much bigger than the electron, but the electron velocity is much higher than that of the positive ions. Thus, the removal of material from the electrode surface depends on the electrode polarity. The main types of the electrode wear are the corner wear, end wear, side wear and volumetric wear. The number of sparks originating from a point on the electrode surface determines electrode wear. The corner of the electrode suffers more than the front because it was exposed to more attacks from the front, sides and edges, due to that more material is removed from the corner than the flat surface, leading to higher corner wear (Jameson 2001).

3.2 Material Removal Rates

The EDM process removes material by thermal energy. Once the spark is launched, the workpiece surface continuously impinged by high-energy ions or electrons, depending on the workpiece polarity. The accelerated ions and electrons have very high kinetic energy, and that kinetic energy will be converted into thermal energy leading to a high temperature on the warped piece. This high temperature on the workpiece causes a localized melting and evaporation mechanism, and we get material removal rate. When sparking electricity is turned OFF, the vapour cloud is cooled to form EDM debris. This process is repeated thousands of times every second in various points on the workpiece and therefore, the electrode gradually goes down under the servo system control. Typical removal rates range from 0.1 to 400 mm^3/min. The material removal rate depends on not only current and melting point of the workpiece, but also the other workpiece properties, the tool electrode material, pulse energy and the dielectric (Lassner 1985).

Developing a model can give better understanding about what can happen if the process parameters changed before going onto the experiment details, supposing that a single spark can create a single hemispherical crater on the workpiece. If the radius of this hemispherical is r, then the volume of this hemispherical crater is $V_{\text{hs}} = \frac{2}{3}pr^3$. The size of this crater in some manner can relate to the spark energy $E_{\text{S}} = VIt_{\text{on}}$, where t_{on} is the pulse on-time. Part of this energy that is converted to heat on the workpiece is proportional to the sparking energy and can be given as $E_{\text{w}} \propto E_{\text{s}}$. The rest of this energy dissipated in the discharge medium as heating of the dielectric medium, electromagnetic energy and sound energy, and heating of the electrode.

Thus, the working energy is $E_{\text{w}} = kE_{\text{s}}$, where k is the proportionality constant. The volume removal of material from the workpiece by a single spark is proportional to the sparking in energy. Then, we can write the material removal rate as the volume of the crater created by a singular spark divided by the total time of the spark, which is the pulse duration (Saha 2008).

$$MRR = \frac{\beta E_{\text{w}}}{[t_{\text{on}} + t_{\text{off}}]} = \frac{\beta' VIt_{\text{on}}}{[t_{\text{on}} + t_{\text{off}}]} = \frac{\beta' VI}{\left[1 + \left(\frac{t_{\text{off}}}{t_{\text{on}}}\right)\right]} \tag{1}$$

where β and β' are the proportional constants. This equation indicates that higher material removal rate, which is one of the main goals of EDM improvement, can be achieved with high current I, high potential difference V and also by increasing the pulse on-time t_{on} and decreasing the pulse off-time t_{off}.

The volumetric material removal rate in (mm^3/min) was described by El-Hofy (2005) as a function of melting point of the workpiece material and the discharge current as follows:

$$MRR = (4 \times 10^4).i.T_{\text{w}}^{1.23} \tag{2}$$

where i is the discharge current and T_{w} is the melting point of the workpiece material (°C). Another model is established by Rahman et al. (2010) to give the relations between the different EDM process parameters and the MRR using is the response surface methodology (SRM).

$$Y = C_0 + \sum_{i=1}^{n} C_i x^2 + \sum_{i=1}^{n} C_{ii} X_i^2 + \sum_{i=1}^{n-1} \sum_{j=1}^{n} C_{ij} X_{ij} \tag{3}$$

where Y is the response (MRR), n in the number of variables, x is the EDM process variables and $i\&j$ are levels of nth variables, and the terms C_0, C_i, C_{ii} and C_{ij} are the second-order regression coefficients. The application of this model shows that the material removal rate is given as follows:

$$MRR = 0.90095 + 0.86652I_P + 0.40632t_{on} - 0.07574t_{off} + 0.23562I_P^2 - 0.23825t_{on}^2 - 0.04123t_{off}^2 + 0.23298I_P t_{on} - 0.02454I_P t_{off} - 0.04957t_{on}t_{off} \quad (4)$$

where I_P is the peak current, t_{on} is the pulse on-time and t_{off} is the pulse off-time.

3.3 Surface Roughness

Let us assume that sparking the maximum surface roughness R_a is equal to the radius of the hemispherical crater. Then, the surface roughness is equal to

$$r = R_a = \left[\frac{3}{2}V_s\right]^{1/3} = \left[\frac{3}{2}bE_s\right]^{1/3} = \left[\frac{3}{2}bVIt_{on}\right]^{1/3} \quad (5)$$

This equation indicates that surface roughness does not depend on pulse off-time, t_{off}. In order to reduce surface roughness, the potential difference V, the peak current I and pulse on-time t_{on} must be decreased. By contrast, reducing any of the three terms will also reduce the material's removal rate which is undesirable. Referring to Eqs. (2) and (5), reducing the surface roughness without reducing the material removal rate can be achieved by reducing t_{on} and t_{off} simultaneously. However, there is a limit to reducing t_{off} because if it is reduced too much, then there will be unstable sparking (Saha 2008).

4 Nanocomposite Cu–WC–Si Electrodes

4.1 Synthesizing the Nanocomposite

When powders of pure metals, intermetallic or pre-alloyed powders are milled without any material transfer, then the process is called mechanical milling (MM). If material transfer occurs, then milling process is called mechanical alloying (MA). In mechanical alloying, the new crystalline structure can be different or can be the same as the base metal. This new structure can show different mechanical, chemical or physical properties. Alloying of base metal with one or more chemical element is normally required to change the bulk or the surface characteristics of the base metal to make it easier to fabricate or perform better during application. As an example, the strength of bulk material depends on plastic deformation when the slip of crystallographic planes occurs along the grains of the metal, and thus it is important to increase the resistance to slip (Wang et al. 1999). Grain refining, cold work, solid-solution hardening, hardening, and others can achieve this.

Since 1980s, mechanical alloying by ball milling is used to synthesize a variety of stable and metastable phases including supersaturated solid solutions, crystalline, quasicrystalline intermediate phases and amorphous alloys. In addition, the procedure can be used to stimulate chemical (displacement) reactions in powder mixtures at room temperature or at least at much lower temperature than normally required. Metals, ceramics, polymers and composite materials have benefited from the use of this technique (Suryanarayana 1999).

4.2 Consolidation Techniques

Figure 1 shows the main steps of synthesizing and characterization of Cu–WC–Si nanocomposite using high-energy ball mills. The first step prior to synthesizing the nanocomposite is the selection of milling variables. High-purity copper containing small amounts of silver or phosphorus melt at 1083 °C, a relatively low melting temperature. The electrical conductivity of copper at room temperature according to International Annealed Copper Standard (IACS) is 100 %, while thermal conductivity of the oxygen-free copper is 391 W/m K, which is the highest thermal conductivity among the cast copper alloys (Khan 2008). Tungsten is a metallic transition element characterized by the high melting point and relatively high thermal conductivity as compared to copper. The melting point of tungsten varies between 3387 and 3422 °C, and the thermal conductivity varies between 167 and 190 W/m K. (Lassner 1985).

Tungsten carbide is not only a hard material but also has a high melting point making it a suitable material to act as main filler for an EDM electrode. The electrical conductivity of WC is in the same range as tool steel and carbon steel, but the melting point is double. Tungsten carbide can be produced in a pure state by mixing the appropriate amounts of tungsten powder and carbon black or graphite with subsequent heating in a hydrogen atmosphere to at least 1600 °C. Its high melting point, good conductivity and ease of production can make tungsten carbide as an alternative of tungsten in Cu–W electrode when electrical conductivity is not the only main concern. The tungsten monocarbide is the only stable tungsten carbide at room temperature. It can be produced either through the reaction of tungsten trioxide with carbon in an inert atmosphere, vapour phase deposition or by electrolysis of fused salts.

Silicon is the second most abundant element after oxygen and used in glass as silicon dioxide, semiconductor, solar cells, tools, cement, grease and oil. Silicon has a relatively high melting temperature 1400 °C. Similar to water, silicon density increases with temperature such that its density in liquid state is greater than that in the solid state. The thermal conductivity of silicon is 149 W/m K, and it is used as a heat sink in semiconductors. Silicon can form silicide with tungsten and copper at temperatures lower than the melting point of the component.

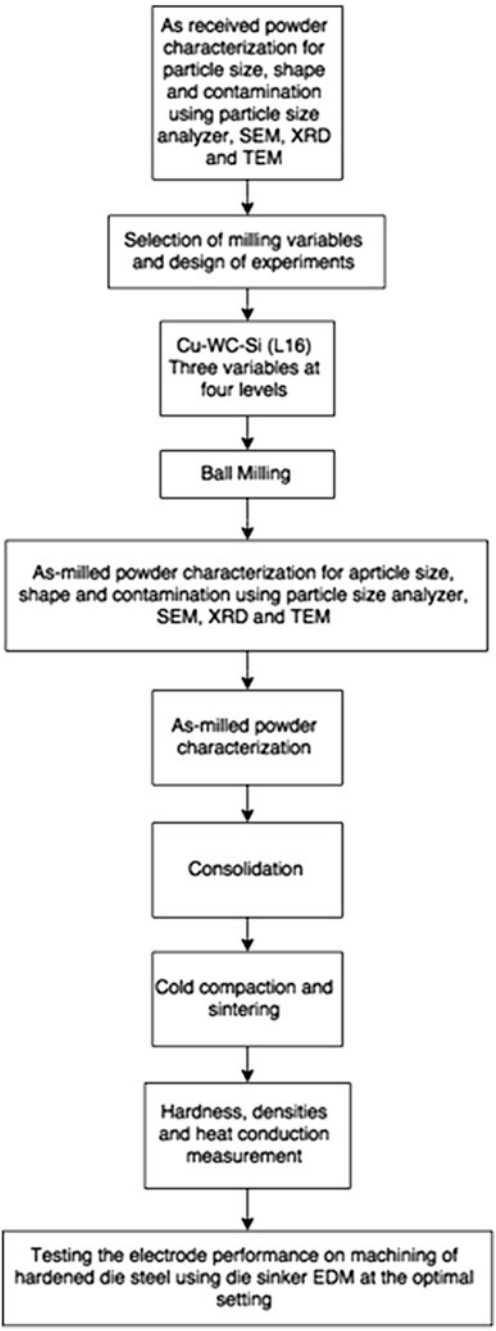

Fig. 1 Schematic diagram of the whole process including synthesizing, characterization and electrode performance

4.2.1 As-Received Powder Characterization

Copper, tungsten carbide and silicon powders (>99.5 % purity) having an average particle size of 1 μm were used for this study. The as-received powders were characterized for particle size, morphology and contamination using MALVERN MASTERSIZER 2000 particle size analyser, FESEM, XRD and TEM. The FESEM was used to observe powder morphology and particle size reduction. TEM was also used to observe the crystal structure before milling.

4.2.2 Selection of Milling Variables

Mechanical alloying and ball milling are complex processes due to the large number of variables. Using Taguchi orthogonal array, the selected milling variables are the weight per cent of WC and Si content as well as milling time while other milling process variables were kept constant.

The consolidation of milled powder by applying temperature and pressures is an important process used to fabricate the final products. Consolidation was carried out using three different techniques. The cold compaction, sintering and the hot isostatic pressing were used for Cu–WC–Si composite. Consolidation of the milled Cu–WC–Si composite was carried out using uniaxial stainless steel die pressed at 740 MP to form 13-mm-diameter cylindrical samples.

Sintering was carried out using high-temperature sintering furnace model LINN term VMK-135-S at 950 °C for 120 minimums in argon atmosphere. One of the three sintered samples from each experiment was re-sintered using HIP at 31 MPa in argon atmosphere to reveal the effect of re-sintering on final density. After compaction, the compressibility of the green compact was measured in terms of densification parameter, which is a measure of how much green density is achieved by the application of external pressure. This parameter is influenced by some factors such as hardness of powder, initial particle size and shape, interparticle friction and powder volume.

4.3 Experimental Designs

4.3.1 Taguchi Method

Taguchi design of experiments (DOE) technique is widely used to study the effect of several controlled factors on product and process improvement. Taguchi design of experiments was adopted for designing and analysing the milling experiment. Table 1 shows the milling variables and levels used for designing the milling experiments.

Table 1 The selected variables for L16 and their levels

Variables	Cu–WC–Si			
	Variable level			
	1	2.00	3.00	4.00
Time (h)	5	10.00	15.00	20.00
WC (%)	0	150.00	30.00	45.00
Si (%)	0	0.75	1.50	2.25

Table 2 Single-level L16 Taguchi orthogonal array by three variables

	Milling time (h)	Tungsten carbide (wt%)	Silicon (wt%)
Exp-1	5	0	0.00
Exp-2	5	15	0.75
Exp-3	5	30	1.50
Exp-4	5	45	2.25
Exp-5	10	0	0.75
Exp-6	10	15	0.00
Exp-7	10	30	2.25
Exp-8	10	45	1.50
Exp-9	15	0	1.50
Exp-10	15	15	2.25
Exp-11	15	30	0.00
Exp-12	15	45	0.75
Exp-13	20	0	2.25
Exp-14	20	15	1.50
Exp-15	20	30	0.75
Exp-16	20	45	0.00

The selected Taguchi orthogonal array has the following configuration. L16 Taguchi orthogonal array is shown in Table 2, representing the milling experiment configuration of Cu–WC–Si composite where all variables are set at four levels.

4.3.2 Milling Experiment

Table 3 shows the variables influencing the properties of the ball-milled powder for a given composition. Ball milling was carried out using PULVERISETTE 5 high-energy planetary ball mill. The as-received powders were weighed using a digital balance. In all experiments, the total amount of powder was 80 g, and the ball-to-powder mass ratio was fixed at 12:1. The cemented tungsten carbide ball of 10 mm diameter was loaded into a tungsten carbide bowl vial (250 ml) under a dry air atmosphere. The weighed powder was poured over the balls, and then the grinding bowl was tightly and carefully sealed with surface sealing rubber ring.

Table 3 The most important variables influencing the properties of milled powder for a given powder composition

Type of mill	High-energy planetary ball milling
Milling container	Zirconium oxide and tungsten carbide
Milling speed	300 rev/min
Milling time	5, 10, 15 and 20 h
Grinding tools	Tungsten carbide, 250-ml bowls and grinding balls (10 and 20 mm)
Ball-to-powder ratio	1:12
Extent of filling the vial	1:3
Milling atmosphere	Air
Process	Dry milling
Milling temperature	Room temperature

The grinding bowls with material and balls rotated around their own axis on a counter-rotating supporting disc. The other milling variables are kept constant as shown in a cylindrical die made of steel.

After every experiment, the bowl and balls were cleaned by milling with sand (silica) for 5 min to remove the cold-welded powder on the bowl and ball surfaces. The bowl containing the powder was then placed carefully in its position on the rotating disc and tightly closed. Pressure and temperature were kept constant for all the experiments. Milling time was divided into equal cycles of one hour separated by 15 min to cool down the milling medium.

4.3.3 As-Milled Powder Characterization

After milling, the powder was characterized again to expose the effect of milling conditions of the morphology, particle size reduction, homogenization, the formation of any metastable phase and crystalline change. Characterization was carried out using Pycnometer, XRD, FESEM and TEM methods. Pycnometer was used to analyse the effect of milling variables on tap density and SSA. The tap density and the green density were used to measure the effect of milling time on compressibility.

Scanning electron microscopy and transmission electron microscopy were employed to study the morphology and crystalline structure of as-milled powder samples. FESEM was used to observe the powder morphology, homogenization and particle size reduction. TEM techniques were used to analyse the nanosized powder morphology particle size reduction and to measure the thickness of crystallization. The X-ray analysis was conducted using Philips and Bruker 5000 X-ray systems (A Cu–Ka target of 0.154 nm) for qualitative and quantitative XRD analysis. The analysis detects the materials' chemistry, phase constitution, structure of milled powder samples and crystallite size.

The crystallite size broadening of a peak is correlated with the crystallite size through the Scherer equation (Lifshin 1999).

$$t = (k * \lambda)/B_{1/2} * \mathrm{COS}(\theta_{\mathrm{B}}) \tag{6}$$

where t is the average thickness of crystalline particles, K is a constant depending on the crystalline shape (0.89), λ is the X-ray wavelength, B is the full width at half maximum and Θ_{B} = Bragg angle. One of the main sources of error considered is the effect of internal strains on broadening.

4.3.4 Densities and Volume Measurement

The densities and specific surface area of the powder was measured according to the gas adsorption principle using Ultrapycnometer 1000 version 2.2. Measurement was carried out using helium at 19-psi pressure and room temperature. The average of the last three readings out of five was recorded with variation less than 0.008 cm^3 for volume and less than 0.16 g/cm^3 for densities. The density and volume of solid samples were measured according to the gas adsorption principle as mentioned before and confirmed using Archimedes' principle. The density and volume measured by using Archimedes' principle by measuring the following as quantities follow:

1. Weight of sample in air (A)
2. Weight of samples in the auxiliary liquid (distilled water) (B)
3. Density of the distilled water (ρ_0 = 0.997 g/cm^3), the density of air ($\rho_{a=}$ 0.0012 g/cm^3) and α is the balance correction factor (0.99985).

Then, the density and volume were calculated using the Eqs. (7) and (8), respectively.

$$\rho = \frac{A}{A-B}(\rho_0 - \rho_a) - \rho_a \tag{7}$$

$$V = \alpha \frac{A-B}{\rho_0 - \rho_a} \tag{8}$$

The effect of milling variables on compressibility and densification was calculated from the measured green density, theoretical density and the sintered densities. The compressibility and the densification measured are as follows:

$$\text{compresibility} = \frac{(\rho_{\mathrm{gr}} - \rho_{\mathrm{ta}})}{\rho_{\mathrm{ta}}} \times 100 \tag{9}$$

$$\text{Densification} = \frac{(\rho_{\mathrm{si}} - \rho_{\mathrm{gr}})}{(\rho_{\mathrm{th}} - \rho_{\mathrm{gr}})} \times 100 \tag{10}$$

where ρ_{ta} is the tap density, ρ_{gr} is the green density, ρ_{si} is the sintered density and ρ_{th} the theoretical density.

4.3.5 Heat Conduction Measurement

The transfer of heat under unsteady state condition from the surface to the centre was measured using HT17 unsteady state heat transfer. The solid cylindrical sample of 13 mm diameter and 9 mm high was stabilized at initial temperature Ti (room temperature) before dropping into stabilized heated water at 80–90 °C (T_{max}). Due to the heat transfer from the bath to the centre, the temperature of the sample increases as a function of time and distance from the surface as $T = T(r, t)$.

Assuming that the dimensionless temperature θ is defined as

$$\theta = \frac{T(r,t) - T_{\max}}{T_i - T_{\max}} \tag{11}$$

Then, the change in the dimensionless temperature with time according to Lumped model of transient heat conduction can be calculated from Eq. (13) (Cengel 2006).

$$\theta = \frac{T(r,t) - T_{\max}}{T_i - T_{\max}} = A\mathrm{e}^{-bt} \tag{12}$$

The decay constant b is the reciprocal of the time constant and given as

$$b = \frac{\alpha h A_S}{k.V} = \frac{hA_S}{\rho.V.c_p} \tag{13}$$

where k is the thermal conductivity, V is the volume of mass m, A_s is the surface area, ρ is the density and C_p is the specific heat capacity. The plot of Θ versus time t was used to study the effect of composition of electrode material and milling time on the rate of heat transfer rate (mode).

4.3.6 Settings for Performance Measurement

The electrode performance was tested on machining of hardened die steel using oil diesinker EDM machine of type Mitsubishi AE series model brn-51748. All machining experiments were conducted in a rough machining setting using TP power circuit at the following machining setting. This setting represents the optimal machining setting that can give less than 10 % error.

5 Results of Testing and Analysis

Preliminary study of EDM was conducted using conventional copper electrode on machining of cast iron and cemented tungsten carbide. The results obtained from the experiments are discussed as follows. Figure 2 is the optical image of the nital-etched grey cast iron showing flake graphite with an average of thickness equal to 3.5 μm imbedded in ferrite structure. Figure 3 is an optical micrograph of copper electrode etched using ferric chloride etchant showing different culler of copper at different orientations. The average size of the culler is around 25 ± 10 μm.

The FESEM imaged of the two workpieces of grey cast iron and cemented tungsten carbide is shown in Figs. 4 and 5. The structure of cemented tungsten

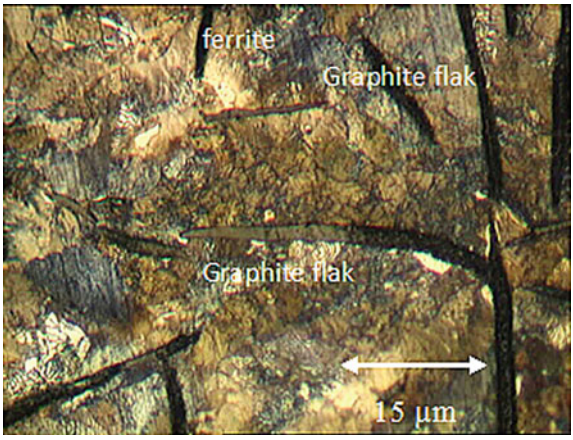

Fig. 2 Optical micrograph of a nital-etched grey cast iron showing flake graphite

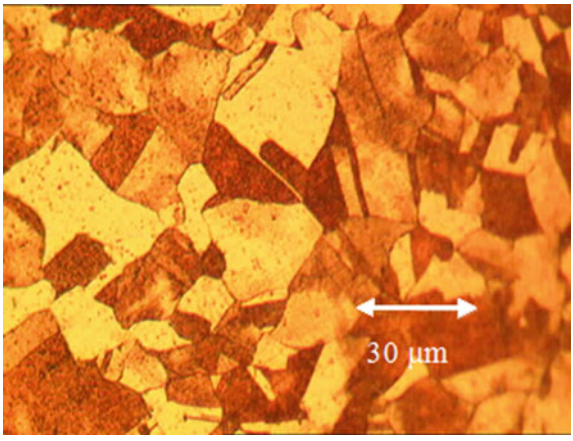

Fig. 3 Optical micrograph of copper electrode etched by ferric chloride

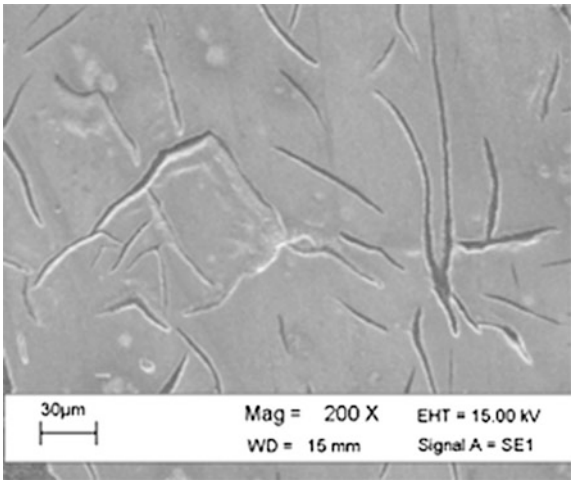

Fig. 4 SEM micrograph of grey cast iron desk break with graphite flakes embedded in pearlite

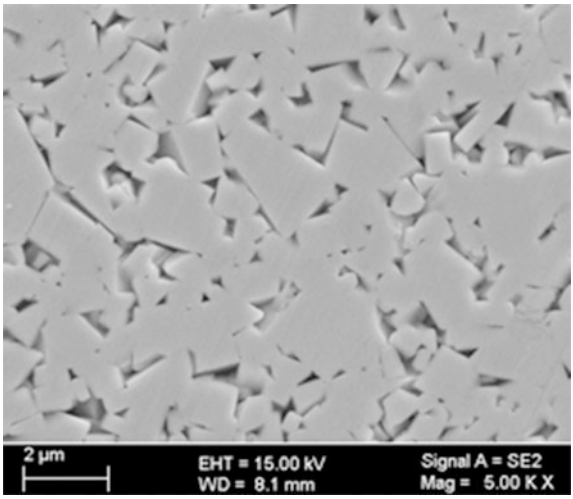

Fig. 5 SEM micrograph of cemented tungsten carbide workpiece

carbide shows the high-value tungsten content. The average particle size of tungsten particle in cemented tungsten carbide is around 2 µm.

5.1 Machining with Conventional Electrodes (Hardened Die Steel Using Cu–W Electrode)

5.1.1 Machining Set-up

Tables 4, 5 and 6 shows the machining set up for the experiments.

Table 4 The experimental layout of mixed mode L16 Taguchi orthogonal array and the observed values of MRR (mg/min), EW (mg/min), TWR and Ra (μm)

L16 Taguchi orthogonal array				Machining results			
	Peak current code (A)	Pulse on-time code (μs)	Gap voltage code (V)	MRR (mg/min)	EW (mg/min)	TWR (%)	Ra (μm)
Exp-1	1.5 (5.5)	4 (16)	0 (80)	5.80	0.46	7.93	2.61
Exp-2	1.5 (5.5)	5 (32)	0 (80)	13.60	0.74	5.44	2.04
Exp-3	1.5 (5.5)	6 (64)	1 (110)	51.10	1.29	2.52	2.24
Exp-4	1.5 (5.5)	7 (128)	1 (110)	6.20	0.11	1.77	1.61
Exp-5	2.5 (10)	4 (16)	0 (80)	101.80	7.03	6.91	3.6
Exp-6	2.5 (10)	5 (32)	0 (80)	122.00	5.66	4.64	4.06
Exp-7	2.5 (10)	6 (64)	1 (110)	110.40	4.17	3.78	4.68
Exp-8	2.5 (10)	7 (128)	1 (110)	118.80	1.56	1.31	3.4
Exp-9	3.5 (15)	4 (16)	1 (110)	172.20	11.67	6.78	4.58
Exp-10	3.5 (15)	5 (32)	1 (110)	202.10	9.04	4.47	4.96
Exp-11	3.5 (15)	6 (64)	0 (80)	195.70	6.66	3.40	4.94
Exp-12	3.5 (15)	7 (128)	0 (80)	231.00	4.56	1.97	6.01
Exp-13	4.5 (25)	4 (16)	1 (110)	300.70	19.36	6.44	5.03
Exp-14	4.5 (25)	5 (32)	1 (110)	221.90	11.13	5.02	7.69
Exp-15	4.5 (25)	6 (64)	0 (80)	369.20	12.68	3.43	4.71
Exp-16	4.5 (25)	7 (128)	0 (80)	219.30	6.82	3.11	8.36

Table 5 The mean averages of MRR (mg/min), EW (mg/min), TWR and Ra (μm)

Variables	Levels	Mean of MRR (mg/min)	Mean of EW (mg/min)	Mean of TWR (%)	Mean of Ra (μm)
Peak current	1	19.00	0.70	3.68	2.13
	2	113.00	4.60	4.07	3.94
	3	200.00	8.00	4.00	5.12
	4	278.00	12.50	4.50	6.45
Pulse on-time	1	145.00	9.60	6.62	3.96
	2	140.00	6.80	4.86	4.69
	3	182.00	7.90	4.34	4.14
	4	144.00	3.30	2.29	4.85
Gap voltage	1	315.00	11.20	3.56	9.08
	2	296.00	14.60	4.93	8.55

Table 6 The sum of square (SS) and percentage contribution (SS%) of variables

Variables	MRR (mg/min)		EW (mg/min)		Ra (μm)	
	SS	SS (%)	SS	SS (%)	SS	SS (%)
Peak current	149.20	28.30	0.30	28.23	40.42	11.42
Pulse on-time time	4.50	0.86	0.10	8.07	2.18	0.62
Gap voltage	0.37	70.84	0.70	63.71	311.39	87.97
	154.07	100.00	1.10	100.01	353.99	100.01

5.1.2 Material Removal Rate (mg/min)

The main effects plot shown in Fig. 6 indicates that the MRR (mg/min) linearly increases with peak current, but the effect of pulse on-time and gap voltage is not clear. It was observed during machining that any increase in gap voltage creates an unstable machining process with a high degree of carburization, leading to an increase in cracks enlargement as shown in Fig. 7. Due to this, a carbon particle is formed in the gap between the electrode and the workpiece, which consequently can stop the machining process. In order to continue the machine process, this particle must be removed, and the electrode tip and the workpiece must be cleaned to remove the carbon particles and the black carbon layer.

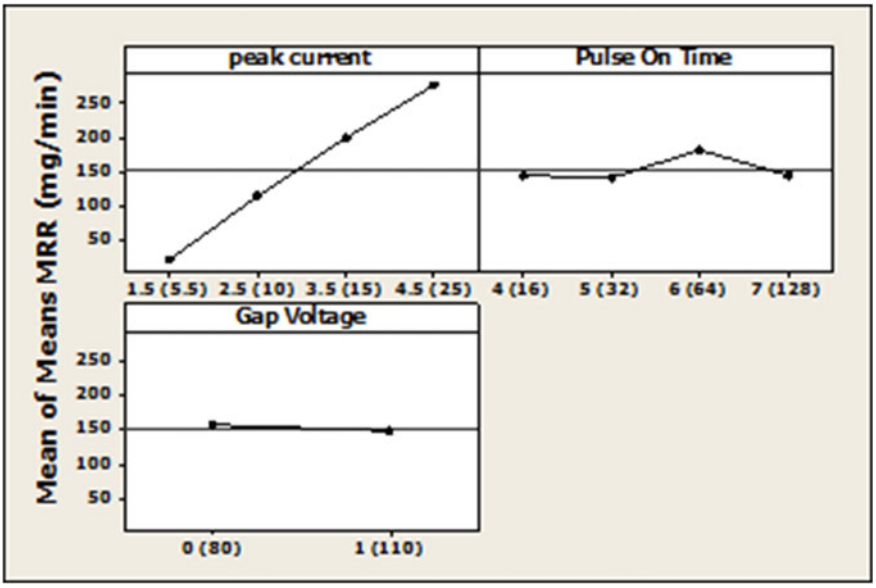

Fig. 6 The main effect plot of MRR (mg/min) for hardened die steel using Cu–W electrode

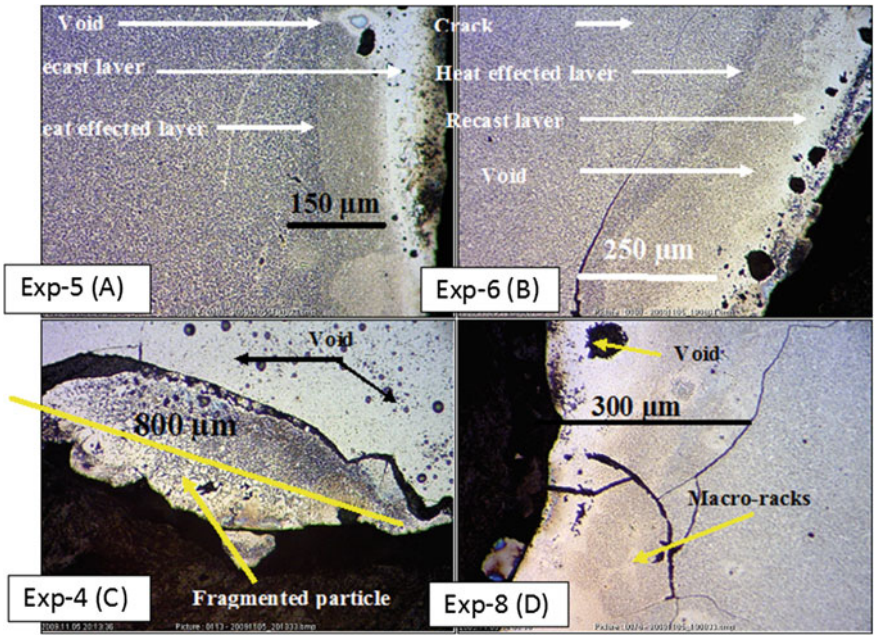

Fig. 7 Optical images show the structure of the machined surface of cemented tungsten carbide (WC-6 % Co)

5.1.3 Electrode Wear (EW)

The electrodes wear increases with peak current and gap voltage but decreases with pulse on-time. Lower electrode wear can be obtained by setting the peak current and the gap voltage at lower level at the same time, and pulse on-time should be set at higher level. This result is in agreement with the conclusion of researches conducted by Lee and Li (2001), Wang et al. (1999) and Khan (2008).

5.1.4 Tool Wear Ratio TWR (%)

The percentage of EW (mg/min) relative to the MRR (mg/min) which is called the tool wear ratio is used because it links EW with MRR. In general, as the MRR increases, the EW and surface roughness will increase. The main effect plot of TWR of Fig. 8 shows that the value of the TWR can be reduced mainly by increasing the pulse on-time and the gap voltage, but the effect of pulse on-time is more significant.

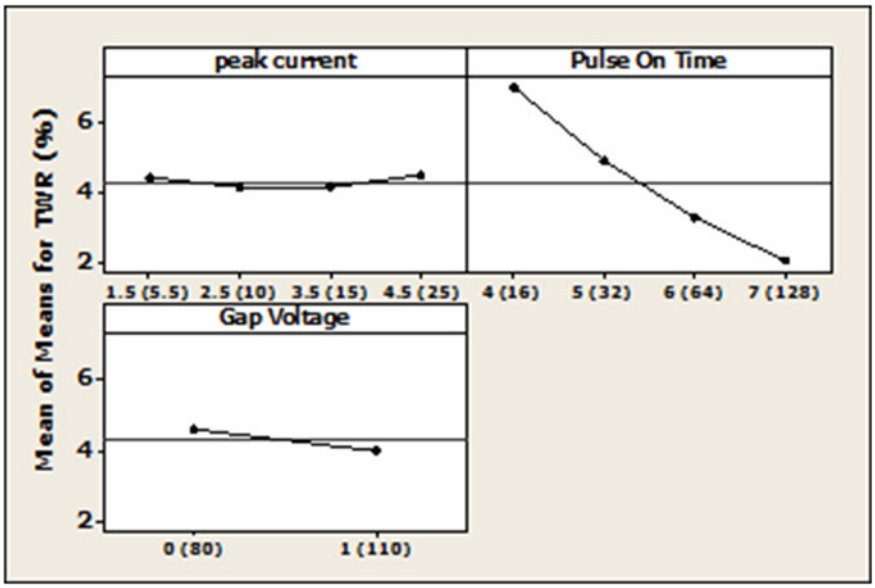

Fig. 8 The main effect plot of TWR (%) for hardened die steel using Cu–W electrode

5.1.5 Surface Roughness Ra (μm)

As expected, the value of Ra (μm) linearly increases with peak current but decreases with gap voltage. The effects of pulse on-time on surface roughness are not obvious. The negative effect of pulse on-time on Ra (μm) can be referred to the effect of longer pulse on-time on amount of material that can be melted and re-solidified from the workpiece which can create bigger crater size. The size of the crater is directly related to the discharge area; meanwhile, the shape (topography) of the crater is related to the amount of the discharge (peak current and the discharge gap). This result is in agreement with the conclusion derived by Rahman et al. (2010) and Chiang (2008).

5.1.6 Estimated Result at Optimum Condition and Confirmation Test

The analysis of the machining results shows that the maximum MRR (mg/min) can be achieved by setting the peak current at higher levels (3–4) (15–25 A), pulse on-time also at high levels 3–4 (64–128 μs) and gap voltage at level 0 (80 V). Lower EW value can be achieved by setting peak current at 1–2 (5.5–10 A), pulse on-time at 3–4 (64–128 μs) and gap voltage at level 0 (80 V). Optimal setting for lower surface roughness requires the setting of peak current and gap voltage at lower levels. It is better to use the index TWR (%) to determine the optimal setting of the machining variables because lower TWR represents the lower EW with

Table 7 Variables setting for optimal MRR (mg/min), EW (mg/min) and Ra (μm)

	Peak current code (ampere)				Pulse On-time code (μs)				Gap voltage code (volt)	
MRR (mg/min)	1.5 (5.5)	2.5 (10)	3.5 (15)	4.5 (25)	4 (16)	5 (32)	6 (64)	7 (128)	0 (80)	1 (110)
EW (mg/min)	1.5 (5.5)	2.5 (10)	3.5 (15)	4.5 (25)	4 (16)	5 (32)	6 (64)	7 (128)	0 (80)	1 (110)
RA (μm)	1.5 (5.5)	2.5 (10)	3.5 (15)	4.5 (25)	4 (16)	5 (32)	6 (64)	7 (128)	0 (80)	1 (110)

respect to the MRR. Thus, the optimal settings of parameters can be shown in Table 7.

The predicted values in of MRR (mg/min), EW (mg/min) and the Ra (μm) according to the selected variables setting were calculated using Eq. (14) Roy (1990).

$$\hat{Y}_{prd} = \bar{Y} + \sum_{i}^{n} (\hat{y}_{opt} - \bar{Y}) \tag{14}$$

where $\hat{Y}_{\text{prd}}$ is the predicted means average, $\bar{Y}$ the overall experimental means average and $\hat{y}_{\text{opt}}$ the mean averages of response at the selected setting of variables.

The predicted values tested experimentally using Cu–W electrode on hardened die steel at the same variables setting are used to calculate the predicted values. This confirmation test is important to measure the variation between the predicted values and the confirmation test and the degree of confident. The analysis carried out using one-sample *t*-test because the population standard deviation is unknown and the number of confirmation test (sample size) is limited. Table 8 shows the predicted values, the confirmation test and the one-sample *t*-test result.

The number of confirmed test (sample size) can influence the quality of the result. In manufacturing, testing many samples is not always manageable due to feasibility, time consuming and cost. The range of the derived values that contain the value of an unknown population parameter is known as confidence interval.

Table 8 The one-sample *t*-test of the predicted values and confirmation test of MRR, EW and Ra at two different current setting

Peak current 2.5 (10 A), pulse on-time 5 (32 µs) and gap voltage 0 (80 V)					One-sample *t*-test analysis			
	Test-1	Test-2	Test-3	Test-4	Mean	St. Dev.	SE mean	95 % CI
Predicted value of MRR (mg/min)	105.00	105.00	105.00	105.00	105.00	0.00	0.00	(105.00, 105.00)
Confirmation test of MRR (mg/min)	130.00	140.00	150.00	150.00	142.50	9.57	4.79	(127.27, 157.73)
Percentage of the difference (%)	18.18	27.27	36.36	36.36				
Predicted value EW (mg/min)	4.00	4.00	4.00	4.00	4.00	0.00	0.00	(4.00, 4.00)
Confirmation test of EW (mg/min)	6.40	6.20	7.50	7.70	6.95	0.76	0.38	(5.74, 8.16)
Percentage of the difference (%)	60.00	55.00	87.50	92.50				
Predicted value of Ra (µm)	4.35	4.35	4.35	4.35	4.35	0.00	0.00	(4.35, 4.35)
confirmation test of Ra (µm)	6.66	4.80	7.88	5.32	6.17	1.39	0.69	(3.96, 8.37)
Percentage of the difference (%)	54.88	11.63	83.26	23.72				

Peak current 3.5 (15 A), pulse on-time 5 (32 µs) and gap voltage 0 (80 V)			One-sample *t*-test analysis			
	Test-1	Test-2	Mean	St. Dev.	SE mean	95 % CI
Predicted value of MRR (mg/min)	192.00	192.00	192.00	0.00	0.00	(192.00, 192.00)
Confirmation test of MRR (mg/min)	200.00	190.00	195.00	7.07	5.00	(131.47, 258.53)
Percentage of the difference (%)	36.36	0.00				
Predicted value EW (mg/min)	7.33	7.33	7.33	0.00	0.00	(7.33, 7.33)
Confirmation test of EW (mg/min)	10.70	10.80	10.75	0.07	0.05	(10.15, 11.38)
Percentage of the difference (%)	87.50	92.50	73.75			
Predicted value of Ra (µm)	4.30	4.30	4.30	0.00	0.00	(4.30, 4.30)
confirmation test of Ra (µm)	7.88	5.32	6.60	1.81	1.28	(−9.66, 22.86)
Percentage of the difference (%)	83.26	23.72	43.40			

Table 8 shows the one-sample *t*-test results for confirmation test at two different peak current settings.

For MRR at high peak current setting (3.5, 5, 0), the percentage error of mean from the predicted value is 29.54 with a standard deviation (SD) equal 8.7 < 10 and confidence interval (CI) equal (12.727, 15.773). This indicates that the true population mean is greater than the predicted value (0.11) and less that mean (0.14). The values of EW and Ra, respectively, show percentage errors of 73.75, 43.4, SD equal 0.759, 1.386 > 10 and CI equal (5.742, 8.158), (3.959, 8.371).

In general, the one-sample *t*-test for MRR, EW and Ra at lower peak current setting (2.5, 5, and 0) shows higher standard deviation SD and mean of standard error SE for EW and Ra, but for MRR it is less than that calculated at higher peak current setting. The SD, which is a measure of machining stability for all machining responses, is less than 10 except for EW which is 10.75. On the other hand, the interval of conference CI (95 %) is better at higher peak current setting.

5.2 *Machining with Nanocomposite Electrode on Machining of Hardened Die Steel*

The performance of the developed EDM tool electrode is tested on machining of hardened die steel using the machining variables setting as shown in Table 9. This setting is the optimal setting, which shows low variation and better interval of confidence (IC,95 %). The machining results achieved at this setting using Cu–W electrode are MRR = 195 (mg/min), EW = 10.75 (mg/min) and TWR = 5.51 %.

Table 9 Machining setting used to test the performance of new electrode

Machining factors	Factors setting (Codes)	Factors setting (Explicit unit)
Power circuit type	TP	
Auxiliary power	0	
Polarity	+	
Peak current	3.5	15 A
Pulse on-time	5	23 µs
Pulse of time	4	16 µs
Gap voltage	0	80 V
Electric discharge stability (JS)	11	2.5 m/min
Jump-up distance	2	0.4 mm
Jump-down time	3	150 ms
Condenser selection	0	
Machining adjustment	80	
Servo voltage	0	
OP sensitivity	8	
Dielectric pressure	4	
Flushing mode	45°	

5.2.1 Performance of Cu–WC–Si Electrode on Machining of Die Steel (Cu–WC–Si)

Table 10 shows the measured MRR (mg/min) and EW (mg/min) using Cu–WC–Si composite electrode at setting as shown in Table 9. The electrode performance was characterized by measuring the material removal rate MRR (mg/min), the electrode wear EW (mg/min) and the tool wear ratio TWR (%). The results were compared with those achieved by using the conventional Cu + 80 %W electrode. The improvement measured as the percentage of the difference between the targeted value achieved by Cu–W electrode and the value achieved by the new electrode is relative to the targeted value.

Tables 11 and 12 show the mean averages, the sum of square SS and the percentage contribution SS (%) of tungsten carbide, silicon content and milling time on MRR (mg/min) of Cu–WC–Si composite electrode. The results achieved by this electrode are comparable with the conventional Cu–W electrode for milling time less than 10 h. The electrode wear on the other hand improved with milling time over 5 h.

Table 10 The machining results (MRR, EW and TWR) achieved by using Cu–WC–Si EDM electrode compared with the machining results achieved by using Cu–W electrode [MRR = 195 (mg/min), EW = 10.75 (mg/min) and TWR = 5.51 %] at the same machining condition

L16 Taguchi orthogonal array by three variables all at four levels				Machining results using Cu–WC–Si electrode			Percentage improvement in MRR, EW and TWR		
	Milling time (h)	WC (wt %)	Si (wt %)	MRR (mg/min)	EW (mg/min)	TWR (%)	MRR (+ve is better)	EW (−ve is better)	TWR (−ve is better)
Exp-1	5	0	0.00	219.00	6.80	3.11	12.31	−36.74	−43.56
Exp-2	5	15	0.75	222.00	11.10	5.00	13.85	3.26	−9.26
Exp-3	5	30	1.50	369.00	12.70	3.44	89.23	18.14	−37.57
Exp-4	5	45	2.25	301.00	19.40	6.45	54.36	80.47	17.06
Exp-5	10	0	0.75	202.00	9.00	4.46	3.59	−16.28	−19.06
Exp-6	10	15	0.00	231.00	4.60	1.99	18.46	−57.21	−63.88
Exp-7	10	30	2.25	170.00	6.40	3.76	−12.82	−40.47	−31.76
Exp-8	10	45	1.50	196.00	0.50	0.26	0.51	−95.35	−95.28
Exp-9	15	0	1.50	6.00	0.70	11.67	−96.92	−93.49	111.80
Exp-10	15	15	2.25	14.00	1.30	9.29	−92.82	−87.91	68.60
Exp-11	15	30	0.00	51.00	11.70	22.94	−73.85	8.84	316.33
Exp-12	15	45	0.75	172.00	1.60	0.93	−11.79	−85.12	−83.12
Exp-13	20	0	2.25	119.00	0.10	0.08	−38.97	−99.07	−98.55
Exp-14	20	15	1.50	6.00	4.20	70.00	−96.92	−60.93	1170.42
Exp-15	20	30	0.75	110.00	5.70	5.18	−43.59	−46.98	−5.99
Exp-16	20	45	0.00	112.00	7.00	6.25	−42.56	−34.88	13.43

Table 11 The mean averages of MRR (mg/min) and EW (mg/min) versus milling time and electrode composition

Variables	Levels	MRR (mg/min)	EW (mg/min)	TWR (%)
Milling time (h)	5	277.75	12.50	4.50
	10	199.75	5.13	2.60
	15	60.75	3.83	11.53
	20	86.75	4.25	19.80
Tungsten carbide (wt%)	5	136.50	4.15	5.14
	10	118.25	5.30	21.05
	15	175.00	9.13	8.80
	20	195.25	7.13	3.46
Silicon (wt%)	5	153.25	7.53	8.55
	10	176.50	6.85	3.88
	15	144.25	4.53	21.06
	20	151.00	6.80	4.94

Table 12 The sum of square SS and the percentage contribution SS (%) of variables on the MRR, EW and TWR achieved by using Cu–WC–Si electrode

	MRR (mg/min)		EW (mg/min)		TWR (%)	
	SS	SS (%)	SS	SS (%)	SS	SS (%)
Time (h)	122,420	87.53	200.34	79.84	774.17	29.50
WC (wt%)	15,070.25	10.77	30.005	11.95	816.72	31.12
Si (wt%)	2362.5	1.69	20.56	8.19	1033.47	39.38
Total	139,852.75	100	250.91	100	2624.35	100

5.2.2 MRR (mg/min) Achieved by Using Cu–WC–Si Electrode at Optimal Setting

The main effect plot of the MRR (mg/min) achieved by this electrode in Fig. 9 indicates that MRR decreases milling time and increases with tungsten carbide content. The effect of silicon content of the performance of Cu–WC–Si electrode in the case of MRR is insignificant.

5.2.3 EW (mg/min) Achieved by Using Cu–WC–Si Electrode at Optimal Setting

The effect of silicon content on EW is slightly more than that in MRR. The main effect plot in Fig. 10 shows that the electrode wear decreases milling time from 12 (mg/min) at 5 h milling time to 4 (mg/min) after 20-h milling time. The electrodes wear also decreases with silicon content. It decreases from 7 (mg/min) without

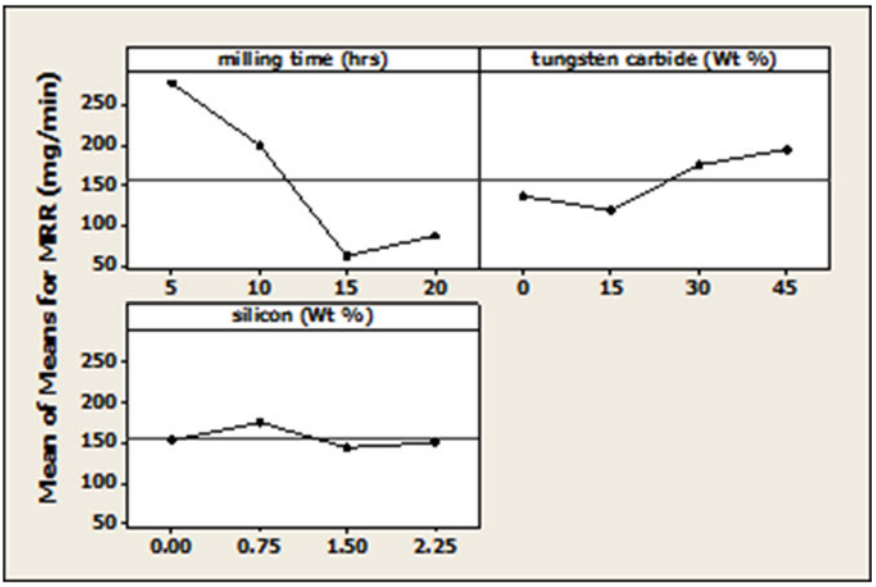

Fig. 9 The main effect plot of MRR (mg/min) of Cu–WC–Si composite electrode versus milling time (h), tungsten (wt%) and silicon (wt%)

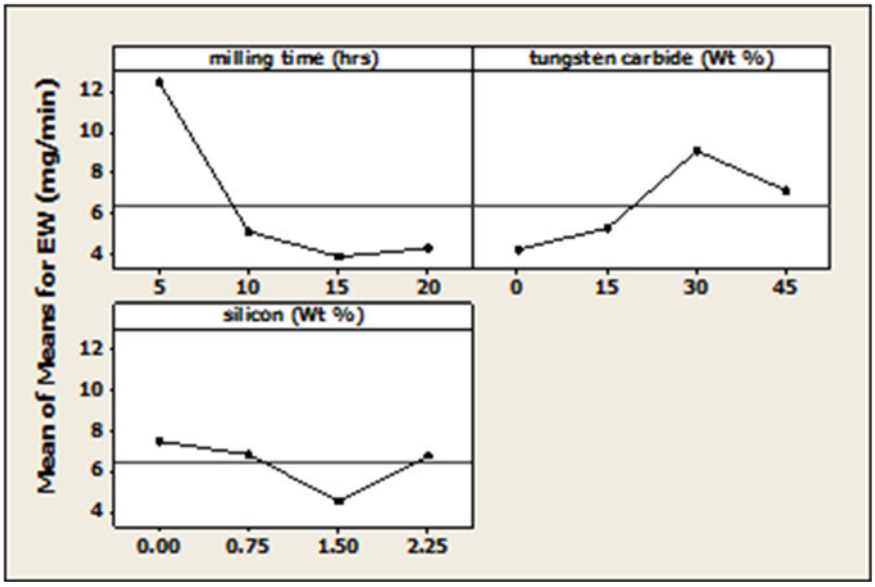

Fig. 10 The main effect plot of EW (mg/min) of Cu–WC–Si composite electrode versus milling time (h), tungsten (wt%) and silicon (wt%)

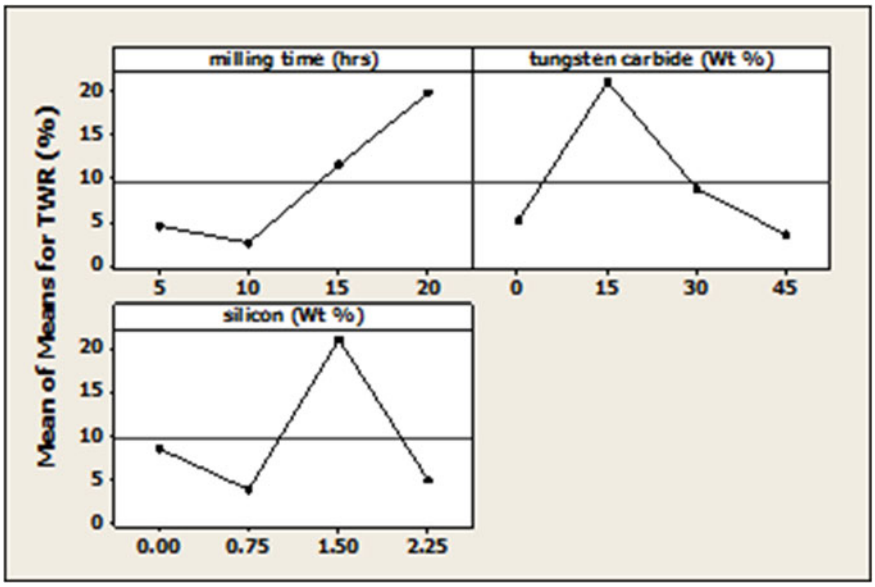

Fig. 11 The main effect plot of TWR (%) of Cu–WC–Si composite electrode versus milling time (h), tungsten (wt%) and silicon (wt%)

silicon to 4 (mg/min) with 1.5 % Si content. The electrodes wear decreases with tungsten carbide content.

5.2.4 TWR (%) of Cu–WC–Si Electrode at Optimal Setting

The main effect plot in Fig. 11 shows that the TWR (%) increases with milling time and decreases with tungsten carbide content. The minimum tool wear ratio can be achieved at 10-h milling time, 45 wt% of WC and lower silicon content.

6 Conclusion

Parametric analysis of oil die-sinker EDM process has been done using Cu and Cu–W electrodes on machining of cast iron, cemented tungsten carbide and hardened die steel. The machining experiments were designed based on Taguchi quality improvement technique. Process optimization was then carried out using analysis of variance, and the predicted values were compared with experimental values showing little or no difference. The following points are the conclusions from the analysis of the results:

1. Experimental work was carried out on the machining of grey cast iron using copper electrode. The results show that peak current, pulse on-time, working voltage and pulse off-time are the most significant factors that contributed to MRR, EW and Ra. The machining of cemented tungsten carbide revealed that the gap voltage is the main variable that controls the machining process. The gap voltage must be set to 80 V or lower to be able to machine this material. The cracks size and the fragmented particles were found to be directly linked to high gap voltage setting. The machining process of cemented tungsten carbide in the presence of fragmented particles led to the formation of layered carbon particle. Optimization of MRR and a low EW using Taguchi technique revealed that low gap voltage (80 V), higher peak current at (16 A) and mid-range pulse on-time (32 μs) are the most stable machining conditions.
2. By using high-energy ball milling of different combinations of Cu, WC and Si, and using milling time and composition as milling variables conditions, particle size of less than 50 nm was achieved, and clear change in the thickness of crystalline and d-spacing are observed using XRD. Using TEM for further investigation, a few crystalline structures randomly distributed inside the amorphous structure with the thickness of crystalline less than that of the elemental powder was discovered. The detected crystalline structure using TEM shows that the distance between any two neighbours (d-spacing) are in the range 2.5–6 Å, which varies from that of the elemental powder (around 6 Å).

The performance of the newly developed electrode on the machining of hardened die steel can be concluded as the MRR achieved by using the 5- and 10-h milling time; Cu–WC–Si composite electrode was improved by 1 to 90 % depending on the composition. These improvements in MRR are in the cost of EW. The EW improved at milling time longer than 10 h by 9–95 %, regardless the composition. The best TWR was achieved by using the 5- and 10-h milling time electrode.

References

Cengel, Y. A. (2006). *Heat and mass transfer*: *A practical approach* (3rd ed.). McGraw-Hill Education: Asia.

Chiang, K.-T. (2008). Modeling and analysis of the effects of machining parameters on the performance characteristics in the EDM process of Al_2O_3+TiC mixed ceramic. *The International Journal of Advanced Manufacturing Technology, 37*(5), 523–533.

Dimla, D. E. H. N., & Rothe, H. (2004). Investigation of complex rapid EDM electrodes for rapid tooling applications. *The International Journal of Advanced Manufacturing Technology, 23*(3), 249–255.

Dürr, H. P., Eleser, Rolf, & Saad, Nuri. (1999). Rapid tooling of EDM electrodes by means of selective laser sintering. *Computers in Industry, 39*(1), 35–45.

El-Hofy, H. (2005). *Advanced machining processes: Nontraditional and hybrid machining processes*. McGraw-Hill Professional.

Ferreira, J. M., & Artur Alves, Nuno. (2007). Rapid tooling aided by reverse engineering to manufacture EDM electrodes. *The International Journal of Advanced Manufacturing Technology, 34*(11), 1133–1143.

Hsu, C. Y., Chen, D. Y, Lai, M. Y, Tzou, G. J. (2008). EDM electrode manufacturing using RP combining electroless plating with electroforming. *The International Journal of Advanced Manufacturing Technology*, *38*(9), 915–924.

Jameson, E. C. (2001). In Elman C. Jameson (Ed.), *Electrical discharge machining*. The Society of Manufacturing Engineers.

Khan, A. (2008). Electrode wear and material removal rate during EDM of aluminum and mild steel using copper and brass electrodes. *The International Journal of Advanced Manufacturing Technology, 39*(5), 482–487.

Kunieda, M., Tsutomu, T., & Nakano, S. (2004). Improvement of dry EDM characteristics using piezoelectric actuator. *CIRP Annals—Manufacturing Technology*, *53*(1), 183–186.

Lassner, E., & Wolf-Dieter, S. (1985). *Tungsten—Properties*, *chemistry*, *technology of the element*, *alloys*, *and chemical compounds* (Vol. 477). Springer-Verlag.

Lee, S. H., & Li., X. P. (2001). Study of the effect of machining parameters on the machining characteristics in electrical discharge machining of Tungsten carbide. *Journal of Materials Processing Technology*, *115*(3), 344–358.

Li, Y. Q., Zheng, Xuanhui, Lei, Zhou Shun, Zou, Changmin, Yu, Zhiqiang, & Shu, (2003). Properties of W–Cu composite powder produced by a thermo-mechanical method. *International Journal of Refractory Metals & Hard Materials, 21*(5–6), 259–264.

Lifshin, E. (1999) *X-ray characterization of materials*. Wiley-VCH.

Lissaman, A., & Martin, S. (1996). In V. Chiles & S. C. Black (Eds.), *Principles of engineering manufacture* (3rd ed.). Elsevier Science Ltd.

Monzón, M., Benítez, A. N., Marrero, M. D., Hernández, N., Hernández, P., & Aisa, J., (2008). Validation of electrical discharge machining electrodes made with rapid tooling technologies. *Journal of Materials Processing Technology*, *196*(1–3), 109–114.

Ostwald, P. F., & Jairo, M. (1997). *Manufacturing processes and systems* (9th ed.). John Wiley & Sons.

Raghu, T. S. R., Ramakrishnan, P., & Rama Mohan, T. R. (2001). Synthesis of nanocrystalline Copper-Tungsten alloys by mechanical alloying. *Materials Science and Engineering A, 304–306*, 438–441.

Rahman, M. M., Khan, M. A. R., Kadirgama, K., Noor, M. M., & Bakar, R. A. (2010). Modeling of material removal on machining of Ti-6Al-4V through EDM using Copper Tungsten electrode and positive polarity world academy of science. *Engineering and Technology*, *71*.

Roy, R. K. (1990). *A primer on the Taguchi method* (Vol. 450). van Nostrand Reinhold.

Saha, S. K. (2008). Experimental investigation of the dry electric discharge machining (Dry EDM) process. In *Department of Mechanical Engineering* (p. 125). Indian Institute of Technology Kanpur: Kanpur.

Suryanarayana, C. (1999). *Non-equilibrium processing of materials. Pergamon Materials Series*. Pergamon.

Tsai, H. C. Y., & Huang, B. H. F. Y. (2003). EDM performance of Cr/Cu-based composite electrodes. *International Journal of Machine Tools and Manufacture, 43*(3), 245–252.

Wang, C. C., Yan, B. H., Chow, H. M., Suzuki, Y. (1999). Cutting austempered ductile iron using an EDM sinker. *Journal of Materials Processing Technology*, *88*(1–3), 83–89.

Zaw, H. M. F., Nee, J. Y. H., & Lu, A. Y. C. L. (1999). Formation of a new EDM electrode material using sintering techniques. *Journal of Materials Processing Technology, 89–90*, 182–186.

Zhao, J., Li, Y., Zhang, J. Yu, C., & Zhang, Y. (2003). Analysis of the wear characteristics of an EDM electrode made by selective laser sintering. *Journal of Materials Processing Technology*, *138*(1–3), 475–478.

Nitriding of Duplex Stainless Steel for Reduction Corrosion and Wear

Nsikan Dan, Patthi Hussain and Saeid Kakooei

Abstract Duplex stainless steel (DSS) which has a dual nature of ferrite and austenite with nearly equal ratio has found a good application in oil and gas industries because of its excellent corrosion resistance, high yield strength, good weldability, and relative low life cycle costing from reduced operating cost. Dual phases of DSS or combination of two-phase existence to be more characterize with better mechanical properties than a single-phase metal of ferrite or austenite. Nitrogen is a good strengthening alloy for DSS because it forms a solid solution of $(Fe, Cr)_2N$ which is responsible for the hardness and wear resistance in DSS. Spontaneous formation of oxide or passivated layer is responsible for shield and direct exposure of surface of stainless steel to corrosive medium though is susceptible to depletion and deterioration in high chlorine water and low pH level in production environment. Total damage of passivated region on the surface of DSS prompts initiation of localized defect such as pit which grows over a time to form crack. Oil and gas environment is characterized with high H_2S content which is a constraint in application of DSS in this environment because of its insignificant resistance to sulfide stress corrosion cracking (SSCC) and hydrogen-induced cracking (HIC).

Keywords Nitriding · Stress corrosion cracking · Pitting corrosion H_2S · CO_2

1 Introduction

Nitriding is an act of bombarding nitrogen atom into lattice or interstices of a parent material to form solid solution. Nitriding is a diffusion process that involves ionized nitrogen gas from high-concentration region to low-concentration region. It is a

N. Dan · P. Hussain (✉) · S. Kakooei
Department of Mechanical Engineering, Universiti Teknologi PETRONAS,
31750 Seri Iskandar, Tronoh, Malaysia
e-mail: patthi_hussain@petronas.com.my

K. Viswanatha Sharma and N. Hisham B Hamid (eds.),
Engineering Applications of Nanotechnology, Topics in Mining, Metallurgy
and Materials Engineering, DOI 10.1007/978-3-319-29761-3_9

thermochemical process that requires high activation energy from temperature and pressure to overcome barrier since is a nonspontaneous reaction.

Nitriding of stainless steel and other nonferrous material has found much benefit such as in improvement mechanical hardness, increase corrosion resistance, wear resistance, and yield strength. The importance of nitriding on duplex stainless steel (DSS) to increase corrosion resistance in oil and gas environment can never be overemphasized.

Duplex stainless steel is a dual-phase material which comprises approximately 50 % ratio of ferrite and austenite. Dual nature of duplex stainless steel has made it relevant in many application, especially in oil and gas environment (pipes, tubes, valves, storage tank, and Christmas tree) because its properties like yield strength, pitting resistance equivalent number (PREN), high resistance to chloride environment, good corrosion, and wear resistance and weldability. Its excellent resistance to corrosion is attributed to high chromium and molybdenum contents which are responsible for passivation layer. In oil and gas environment, molybdenum enhances resistance to localized corrosion by forming film layer MoS_2 which could prevent further dissociation of Fe on the surface of DSS. Subsequently, spontaneous formation of chromium oxide which is the most active film layer on stainless steel acts as barriers from attack on material though can be depleted by low pH level and presence of chlorine water from production system in oil and gas environment. Pitting resistance equivalent number (PREN) is a numerical guide for estimating the localized corrosion resistance of steel in chloride environment (Francis et al. 1997). In sour and CO_2 environment in the presence of chlorine water, DSS is more vulnerable to SSCC and chloride stress corrosion cracking. Other type of cracking that can occur in hydrogen sulfide environment are stress corrosion cracking (SCC), hydrogen-induced cracking (HIC), stress-oriented hydrogen-induced cracking, soft zone cracking, galvanized independent hydrogen stress cracking. Operating limits have been provided in NAEC MR1075 for corrosion resistance alloy CRA in sour environment to minimize the susceptibility of SSCC and other sulfide-related cracks.

2 Corrosion Problems in Oil and Gas Environment

Natural gas and crude oil do carry high impurity substance which are very corrosive and hence attack materials. Their inherent corrosive nature which constitutes H_2S, CO_2, and chlorine water has been the major catalyst that facilitates the degradation of steel material in oil and gas environment. For corrosion to occur, there must be an anode (corroded site), a cathode (unaffected sites), and an electrolyte (crude oil). Pipeline is used in transportation of crude from oil well to gathering site with a high-pressure-exposed steel material to resist wear and corrosive attack. Corrosion resistance alloy is oil and gas environment are still susceptible to certain corrosion such as sweet corrosion, sour corrosion, oxygen corrosion, microbiological corrosion, pitting corrosion and erosion corrosion. Destruction of passive film on stainless steel to form either localized site for corrosion propagation, corrosion is

been controlled by velocity of gas flow in the pipe, partial pressure ratio of H_2S/CO_2, chlorine content, operating temperature. When the internal surface of a pipeline is exposed to direct contact with the crude, it is then susceptible to electrochemical reaction as below:

$$Fe \rightarrow Fe^{2+} + 2e^{-} \tag{1}$$

On exposure to corrosive attack, the metals loss electron to become positively charged, these create a localized site in form pit. For corrosion to occur, there must be an anodic and cathodic reaction. In oil and gas environment, there are various possibles of cathodic reactions (Popoola et al. 2013)

$$O_2 + 4H^{+} + 4e^{-} = 2H_2O \tag{2}$$

$$2H^{+} + 2e^{-} = H_2 \tag{3}$$

$$H_2O + 2e^{-} = H_2 + 2OH^{-} \tag{4}$$

Equations 2, 3, and 4 are cathodic reactions by using different solutions either acidic or basic. The processes in Eqs. 1–4 are good promoters of corrosion, as they decrease the pH level of crude oil making material to be more susceptible to degradation and sudden failure. Hydrogen gas evolved can penetrate on degraded surface of a material causing hydrogen embrittlement.

3 Effect of Treating Temperature on Microstructure of Steel

Temperature is a relevant factor in thermochemical treatment of stainless steel. High chromium and molybdenum contents in stainless steel make it very sensitive at a temperature between 650 and 950 °C which affects the mechanical properties (Poph et al. 2006). Intermetallic phases are detrimental to the inherent good mechanical properties of steel because of their brittle nature, low corrosion resistance, low yield strength, and toughness. This effect has given restriction in application of duplex stainless steel and stainless steel in high-temperature device (Fig. 1).

Various investigators in the past had proposed a methodology to overcome inimical morphological changes that occur on the surface of stainless steel on thermochemical treatment because of the formation of chromium oxide and molybdenum oxide, nickel oxide but with little progress in establishing simultaneous improvement in hardness, wear, and corrosion resistance. J.W. Simmons in 1994 analyzed the effect of Cr_2N precipitation on austenitic stainless steel. It was observed that Cr_2N reduced the ductile strength in austenitic stainless steel (Poph et al. 2006; Simmons 1990; Uggowitzer and Harzenmoser 1989; Simmons and Atteridge 1993). The three major intermetallic phases that precipitate in stainless

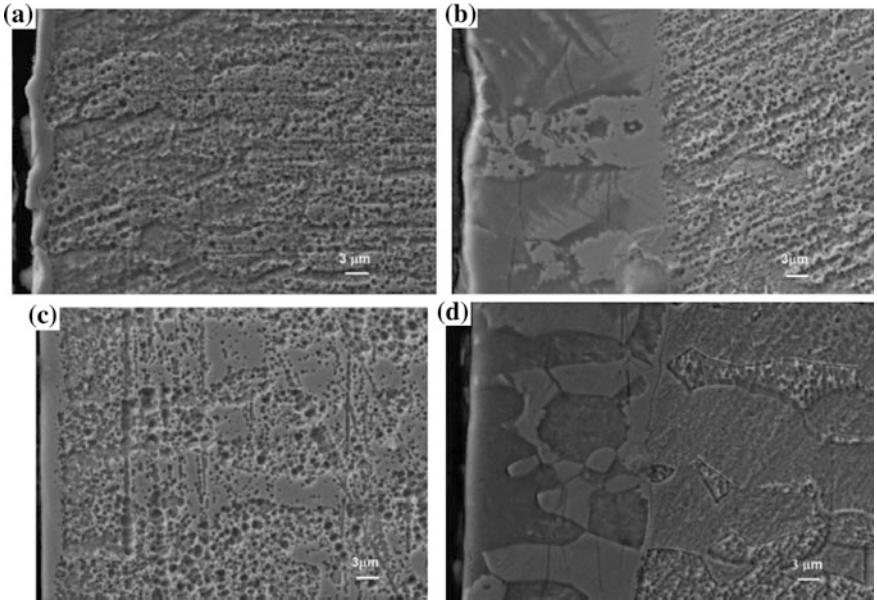

Fig. 1 Cross-sectional SEM images of duplex stainless steel, plasma nitrided at **a** 400 °C, **b** 500 °C and plasma nitrocarburized at **c** 400 °C and **d** 500 °C (Alphonsa et al. 2015)

steel during the high-temperature operation are σ-, χ-, and Laves, but the propensity of their precipitation depends on the alloy composition and temperature above 500 °C. Duplex stainless steel with high chromium composition is very susceptible to sensitization effect though most of relevant intermetallic precipitation occurs at the ferrite phase because it has a higher diffusion rate than austenite (Simmons and Atteridge 1993; Alphonsa et al. 2015). σ is associated with binary system of Fe–Cr, χ is associated with ternary system (Fe–Cr–Mo) and quaternary of Fe–Cr–Ni–Ti and Fe–Cr–Ni–Mo (Simmons 1990; Uggowitzer and Harzenmoser 1989; Simmons and Atteridge 1993). The precipitation of the phases is time and temperature dependent; the formation of nuclei in each phase can be analyzed with the aid of time–temperature–transformation (TTT) as in Fig. 2.

Intermetallic formation such as sigma phase which starts with nuclei precipitation that apparently transform to a core-like structure depending on diffusion rate and distance. This intermetallic phase is responsible for loss in toughness and ductility in DSS though increases the hardness. It is paramount to note that high-diffusion velocity gives rise to higher local supersaturating and subsequently high density precipitation. From Fig. 3, the fastest precipitation of sigma phase occurred between 720 and 800 °C. Literature has showed that the sigma affects some mechanical properties such as toughness and varies with temperature (Poph et al. 2006). There is some literature of low-temperature gas nitriding and high-temperature gas nitriding (HTGN) of stainless steel. J.H. Sung in 2007 performed HTGN of ferritic stainless steel between a temperature of 1050 and 1100

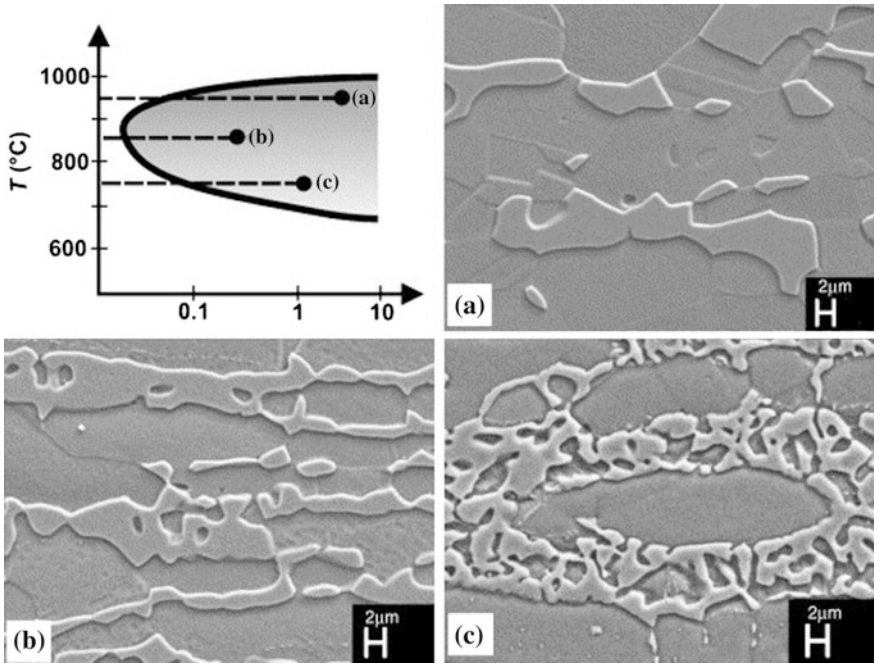

Fig. 2 Morphology of the sigma phase with respect to the isothermal annealing temperature; **a** 950 °C, **b** 850 °C, and **c** 750 °C (Poph et al. 2006)

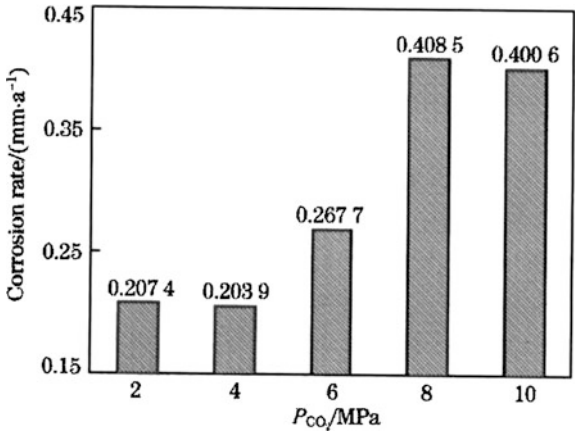

Fig. 3 Average corrosion rates of 110S tube steel under different CO_2 partial pressures (Li et al. 2012)

followed by a tempering process. An improved surface hardness after tempering was observed and improved corrosion resistance in $1NH_2SO$ (Kasper 1954). There are various methods of thermochemical treatment such as ion beam implantation, plasma nitriding, plasma immersion ion implantation, and plasma nitrocaburizing

which is a recent development that involves a single-cycle process of nitrogen and carbon. Recent development has adopted a methodology of using single-cycle process with different alloying composition of gases such as nitrogen, methane, and ammonia to achieve better surface layer with increase in hardness and wear resistance. The effect of gas ratio has been a contributing factor in determining the effective diffusion for solid solution formation and precipitation of phases. Different pretreatment processes sputtering with hydrogen have proved a great relevance because they eradicate oxide layer for better diffusion which is a barrier on the surface of a stainless steel that acts as protective shield for in-depth penetration of alloying component. Expected precipitates on treated DSS are $(Fe, Cr)_2N$, expandable austenite (responsible for wear resistance), and sigma phase, χ-, and Laves, and the characterization is done by field-emission scanning electron microscope (FESEM), X-ray diffraction XRD, and conversion electron. Characterization of DSS is peculiar to their grades also subjective on thermo-chemical treatment because variation in chemical composition by weight% (Sung et al. 2008; Hughes and Llewelyn 1959; Escriba et al. 2009; Saithala et al. 2014; Rolinski 1987) (Table 1).

4 Possible Corrosion Type on Duplex Stainless Steel in H_2S and CO_2 Environment

Duplex stainless steel has an excellent corrosion resistance to uniform corrosion, but it is susceptible to corrosion into certain operating condition and environment. In oil and gas environment, H_2S and CO_2 are the major constituents that directly affect the stability of material because of their oxidation rate on stainless steel. The combination effect of chlorine water and low pH level, in oil and gas environment, facilitates certain corrosion on DSS such as, SSCC, SCC, and HIC. In flow lines such as tubes and pipes, DSS is susceptible to erosion corrosion and cavitation. However, wellheads and valves, DSS is susceptible to crevice corrosion (Popoola et al. 2013).

Table 1 Classification of some duplex stainless steel

Grade	Cr (wt%)	Ni (wt%)	Mo (wt%)	Mn (wt%)	N (wt%)
UNS S32205/S32803	22.5	5.6	2.8	2	0.17
UNS S2304	23	4	–	–	–
UNS S32750	25	7	3.5	2	0.25
LDX 2101	21.5	1.5	0.3	5	0.22
S32760	25	7	3.5	–	0.30
S31260	25	6.5	3.0	–	0.3

5 Effect of H_2S and CO_2 Partial Pressure Ratio on Corrosion of DSS

Internal corrosion in tube and pipes is more predominate than external corrosion because of flowing pressure and velocity with the internal region of the flow line. Currently, oil field production is characterized with increasing H_2S contentment, making the most significant challenge in corrosion study. High operating velocity and pressure destabilize the oxide file DSS, making it susceptible to erosion corrosion. Available literature has showed that in oil and gas environment, the presence of H_2S can inhibit or accelerate the corrosion in carbon steel depending on H_2S/CO_2 partial pressure. The pressure ratio of H_2S and CO_2 has been of great relevance in prediction of corrosivity of stainless steel in oil and gas environment. High partial pressure of H_2S generally increases the corrosion by increase in the dissociation rate of H_2S which lowers the pH level. Z.F. Yin et al. in his consideration analyzed that increase of S^{2-} formation could result in formation of sulfides which will inhabit corrosion. From literature, K. Masamura et al. presented a critical ratio of P_{CO_2}/P_{H_2S} in identifying corrosion mechanism and susceptibility of carbon steel in H_2S/CO_2 environment. He suggested that when $P_{CO_2}/P_{H_2S} > 200$, CO_2 plays a dominating role in the environment, and he subsequently stated that $P_{CO_2}/P_{H_2S} < 200$ FeS layer will be formed on the surface on carbon steel material which will act as an inhibitor. B.F.M. Pot et al. showed that when $P_{CO_2}/P_{H_2S} > 500$ the corrosion mechanism is controlled by CO_2 while $P_{CO_2}/P_{H_2S} > 20$, the corrosion mechanism is led by H_2S (Li et al. 2012). In DSS, the surface layer is controlled basically by chromium oxide and P_{CO_2}/P_{H_2S} that favors the formation of FeS which destabilizes the adherence of chromium oxide to the base material. Figure 3 shows that increase in partial pressure of CO_2 is directly related to corrosion in carbon steel. No intensive works have been done recently on the analysis of CO_2/H_2S partial pressure ratio on DSS after heat treatment.

6 Effect of Gas Composition on Surface Morphology

The surface change of nitride stainless steel is also dependent on the composition of nitride gas which precipitates or contributes in solution formed. Untreated stainless steel characterized with this is inherent attribute of passivated layer made of oxide film as a protective shield or coat that prevents direct aggressive environmental attack. Every nitriding process is aimed at achieving a better surface layer which will improve the corrosion and wear resistance without compromising the other mechanical properties if relevant in intended application. Recent development has proved that composition of other gas such as hydrogen, ammonia, or methane gas in nitriding of stainless steel has better and improved mechanical properties than single gas nitriding. This effect is attributed to be the change in surface microstructure which advertently initiates a tribological change. Efficient nitriding

of steel can be achieved with high density of reactive nitrogen such as ions N^+ or ridicule (N). Hydrogen plays a role of removing oxide layer that might impair in-depth of nitrogen. The reactive nitrogen is enhanced by mixture with hydrogen; this due to dissociation (8.8 eV) and ionization (13.1 eV) energy of hydrogen is smaller than that of nitrogen which has 24-eV dissociation and 15.58-eV ionization energy. Increase in nitrogen composition increases the case depth, hardness, and the surface roughness of treated material (Mohammadzadeh et al. 2014).

7 Possible of Increase of Surface Roughness After Nitriding

It has been discovered that after nitriding of steel material, there is tribological change due to surface microstructural change which lead to increases in surface roughness. XRD analysis, optical microscope, and scanning electron microscope (SEM) can be used in the study of surface morphology and tribology. After gas nitriding or thermochemical treatment of steel material, there is an increase in thickness layer due to microstructural changes effected by diffusion of gas such as nitrogen. Under the same treating condition, plasma nitriding produces a higher thickness layer than the use of conventional gas nitriding because plasma nitriding completely removes passivated layer that can be an encumbrance to efficient diffusion rate. Figure 4 shows increase in surface roughness with increase in time. It also shows increase in hardness with respect to time.

Some of the possible causes of change or increase in surface roughness are the following:

- Reposition of the sputtered material on the surface,
- Sputtering that is caused collision of particles which is induced by energetic nitrogen bombardment,
- Different lattice expansion of the grains of polycrystalline material.

8 Carbide Precipitation and Its Effect

Precipitation of carbide upon thermal treatment of stainless steel is described as sensitization effect. These processes are the temperature-dependent processes which occur at a temperature between 425 and 870 °C. When a thermochemical treatment is performed within these temperatures, stainless steel is susceptible to precipitate carbide at the grain boundaries which weakens the mechanical properties of the material. The most inimical is carbide, i.e., $Cr_{23}C_6$, because of the depletion of chromium alloy which is the chief corrosion-resistant alloying element in stainless steel. Some alloying elements in stainless steel are responsible for impairing the

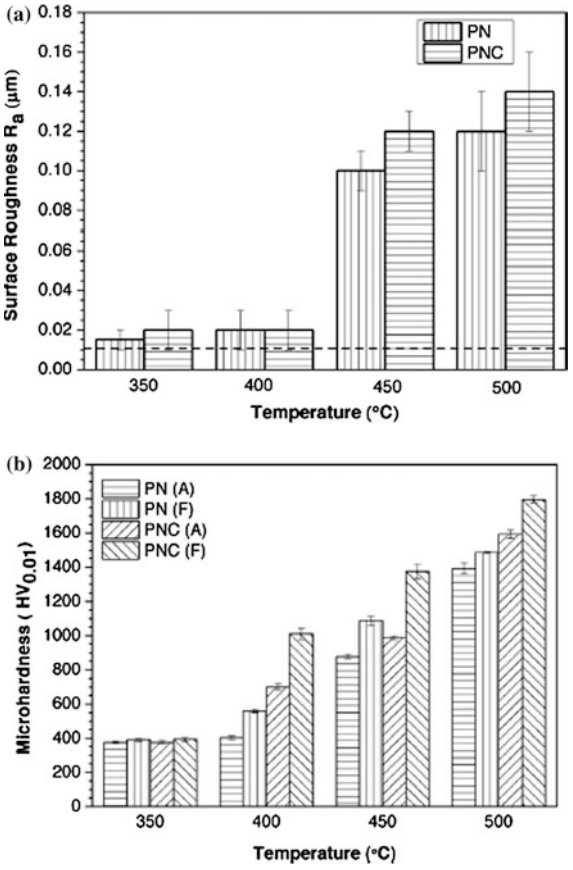

Fig. 4 **a** Surface roughness (the *dashed line* indicates that the initial surface roughness). **b** Microhardness values obtained on austenite and ferrite phases after plasma nitriding and plasma nitrocarburizing treated at different temperatures (Alphonsa et al. 2015)

sensitization effect, such as nitrogen and titanium niobium. Some of them, which have high affinity carbon, deter the precipitation of chromium and molybdenum carbide. The quantity of carbon in stainless steel has an effect on sensitization process; because of high affinity, it can diffuse very fast with the grain boundaries altering the microstructure and enhances the precipitation of carbide. Nitriding of stainless steel is also a good chemical treatment process which might form a solid solution $(CN)_2$ thereby locking up the diffusion rate of carbon at the grain boundaries.

9 Conclusion

Duplex stainless steel has played so much roles in oil and gas environment but still operates in a very close boundary between its acceptability in oil and gas environment. There is a need to further reduce the life cycle cost of DSS material used

in oil and gas environment by improving the corrosion and wear resistance of DSS which will reduce the operating cost. Nitrogen thermochemical treatment with conventional tube furnace has significant advantage over plasma nitriding which is on commercial application of pipe and tubes. Plasma nitriding is limited to size that cannot be applied on commercially. Since every engineering process ought to be sensitive to cost-effectiveness, conventional tube furnace which utilizes nitrogen from the atmosphere makes it relative cheaper than plasma nitriding. Literature has shown that nitriding of stainless steel can improve the corrosion and wear resistance by formation of thicker surface layer and expandable austenite layer within the matrix and ferrite and austenite. Nitrogen, which is an austenite former, stabilizes and enhances austenite precipitation from ferrite.

References

Alphonsa, S., Raja, V. S., & Mukherjee, S. (2015). Study of plasma nitriding and nitrocarburizing for higher corrosion resistance and hardness of 2205 duplex stainless steel. *Corrosion Science, 100*, 121–132.

Escriba, D. M., Materna-Morris, E., Plaut, R. L., & Padilha, A. F. (2009). *Chai-phase precipitation in duplex stainless steel*. *Material Characterization, 60*, 1214–1219.

Francis, F., Bryan, G., & Warburton, G. (1997). The Role of environment and metallic variable on the resistance of duplex stainless steel in sulphide SCC. Paper 12, Corrosion 97 NACE.

Hughes, H., & Llewelyn, D. T. (1959). χ phase in the Fe–Cr–Ni–Ti system. *The Journal of the Iron and Steel Institute, 192*, 170.

Kasper, J. S. (1954). The ordering of atoms in the chi phase of the iron–chromium–molybdenum system. *Acta Metallurgica, 2*, 456–461.

Li, W.-F., Xhou, Y.-J., & Xue, Y. (2012). Corrosion behavior of 100S tube steel in environment of high H_2S and CO_2 conetent. *Journal of Iron and Steel Research, International, 19*(12), 59–65.

Mohammadzadeh, R., Akbari, A., & Drouet, M. (2014). Microstructure and wear properties of AISI M2 tool steel on RF Plasma nitriding at different N_2–H_2 gas compositions. *Surface Coating Technology 258*, 566–573.

Poph, Michael, Storz, Oliver, & Glogowski, Thomas. (2006). Effect of intermetallic precipitation on the properties of duplex stainless steel. *Material Characterization, 85*(2007), 65–71.

Popoola, L. T., Grema, A. S., Latinwo, G. K., Gutti., B., & Balogun, A. S. (2013). Corrosion problem during oil and gas production and its mitigation. *International Journal of Industrial chemistry*.

Rolinski, E. (1987). Effect of plasma nitriding temperature on surface properties of austenitic 267 stainless steel. *Surface Engineering, 3*, 35–40.

Saithala, J. R., Illson, T., Thompson, I., Hilmi, A., Siddle, A., & Ramage, A. (2014). Corrosion management of duplex stainless steel gas flowlines.

Simmons, J. W. (1990). Influenence of nitride(CrN) precipitation on the plastic flow behavior of high-nitrogen austenitic stainless steel. *Scripta Metallurgicae t Materialia*, *32*(2), 265–270.

Simmons, J. W., & Atteridge, D. G. (1993). *Microstructural science* (Vol. 20, p. 3–11).

Sung, J. H., Kong, J. H., Yoo, D. K., On, H. Y., Lee, D. J., & Lee, H. W. (2008). Phase changes of the AISI 430 ferritic stainless steels after high-temperature gas nitriding and tempering heat treatment. *Materials Science and Engineering A, 489*, 38–43.

Uggowitzer, P. J., Harzenmoser, M. (1989). In J. Fact & A. Hendry (Eds.), *Proceedings of the International Conference on High Nitrogen Steels* (p. 174). London: The Institute of Metals (HNS 88, Lille, France, May 1988).

Thermal Spray Coatings for Hot Corrosion Resistance

Subhash Kamal, K.V. Sharma, P. Srinivasa Rao and Othman Mamat

Abstract Hot corrosion arises when metals are excited in the temperature range 700–900 °C in the existence of sulphate deposits, formed as a result of the reaction among sodium chloride and sulphur mixtures in the gas phase adjoining the metals. No alloy is resistant to hot corrosion occurrence indefinitely even though there are certain alloys that require a prolonged origination time at which the hot corrosion progression from the beginning stage to the circulation stage. Superalloys have been established for high-temperature applications. However, these alloys are not constantly able to meet both the high-temperature strength and high-temperature corrosion resistance simultaneously, so the need is to protect from hot corrosion. The high-temperature guarding system must meet numerous benchmarks, provide satisfactory environment resistance, be chemically and mechanically compatible with the substrate, be practically applicable, reliable and economically viable. This chapter briefly reviews the hot corrosion of some Ni- and Fe-base superalloys to recognise the occurrence. Extensive reviews on the hot corrosion of coatings have looked regularly since early 1970; the purpose of this chapter is not to repeat the published resources but relatively to emphasis on research developments and to point out some research forecasts.

Keywords Hot corrosion · Oxidation · Nano coating · Thermal spray coating

S. Kamal (✉) · P. Srinivasa Rao · O. Mamat
Department of Mechanical Engineering, Universiti Teknologi Petronas, 32610 Bandar Seri Iskandar, Perak Darul Ridzuan, Malaysia
e-mail: subhashkamal@gmail.com

K.V. Sharma
Department of Mechanical Engineering, JNTUH College of Engineering, Hyderabad 500085, Telangana State, India

K. Viswanatha Sharma and N. Hisham B Hamid (eds.),
Engineering Applications of Nanotechnology, Topics in Mining, Metallurgy and Materials Engineering, DOI 10.1007/978-3-319-29761-3_10

1 Introduction

Hot corrosion is one of the severe difficulties for high-temperature application, such as helicopter, marine, utility, industrial and land-based gas turbines; boilers; oil refinery furnace; and engines. The use of widespread collection of fuels from natural gas, kerosene, diesel oils, lingering oils and gaseous fuels together with enhanced operating temperatures cause hot corrosion (Nicholls et al. 2002). Eliaz et al. (2002) defined hot corrosion as an accelerated corrosion, resulting from the presence of salt contaminants such as Na_2SO_4, NaCl and V_2O_5 that combine to form liquefied deposits, which damage the shielding surface oxides.

Hot corrosion has been detected in boilers, aircraft, IC engines, gas turbines, fluidised bed combustion, and industrial waste incinerators since the 1940s. However, it turns out to be an issue of importance and current interest in the late 1960s when gas turbine engines of military aircrafts grieved with severe corrosion attacks when it is flying over and near sea water during the Vietnam conflict (Rapp and Mehl 2000; Rapp 2002).

Corrosion occurs when molten compounds (Na_2SO_4 melting point 884 °C) soften the shielding oxide layers, which obviously form on materials during boiler/gas turbine operation. Moreover, the vanadium compounds are excellent oxidation substances and permit oxygen and other gases in the combustion.

Atmospheric air penetrates through the metal surface and further pramotes oxidation. Once the metal is oxidised, the cyclic process starts over again resulting into greater corrosion degradation (Kamal et al. 2008; Sharma 1996).

In the present-day gas turbines, the stress is on saving energy and decreasing the amounts of contaminants emitted. This can be achieved only by creating alloys with higher melting points and the ability to retain mechanical strength at higher temperatures. The improvement of nickel-based superalloys has reached the limit, with blades exposed to critical temperatures close to melting points. Further increase in the operating temperature will result in termination of the strengthening phases and even melting.

An operation of gas turbines is usually restricted by hot corrosion, because of catastrophic failures. High temperatures have a disparate effect on the corrosion of the alloys (Maledi et al. 2006). In the beginning, gas turbines developed after the 1940s and were considered to operate at 700 °C. Developments in metallurgical methods, blade cooling performances and application of thermal spray coatings permitted for increased operating temperatures (Eliaz et al. 2002). Coatings have greater influence towards increased operating temperatures and safeguard against environmental pollutants (Stringer 1987; Gurrappa 2003).

In the power production processes, the mechanism of hot corrosion is reliant on the creation of a liquid phase that is largely Na_2SO_4 or K_2SO_4. The sulphur produced from the coal is SO_2 and SO_3 which responds to volatile alkalis to produce Na_2SO_4 vapour; further, it combines with fly ash on the boiler tubes of superheater and reheater. Such a molten phase melts the chromium oxide in the defending

coating, which permits the base metal to come in contact with sulphate ions to form sulphide ions and non-shielding oxides (Kamal et al. 2008; Rapp and Goto 1981).

Among high-temperature alloys, the promising alloys are "superalloys", namely nickel-, cobalt-, and iron-based superalloys, which show high-temperature mechanical properties and moderate resistance to hot corrosion. Investigations in the area of doping, such as magnesium oxide, cerium oxide, and calcium oxide, is already done and the reduction in the amount of hot corrosion in violent atmosphere of Na_2SO_4–60 $\%V_2O_5$ at 900 °C has been achieved. However, the major problem being faced is how to inject these inhibitors into the combustion chamber along with the fuel in actual industrial environment (Tiwari and Prakash 1998; Gitanjaly et al. 2002).

Thermal spray coatings are widely used in aqueous, wear, erosion and high-temperature applications such as diesel and gas turbine engines. Power generation with the help of coal gasification and waste incineration involves severe degradations, and therefore, coating has demonstrated to be effective (Hocking 1993). Superior understanding of the degradation behaviour and catastrophe failure devices of coatings need to be accomplished, particularly with respect to the effects of engine operating temperature and atmosphere on the coating recital (e.g. thermal cycling) (National Materials Advisory Board 1996).

Detonation-Gun is accomplished of producing the maximum pressure, velocity and density in the flow, which is higher than other spraying techniques. Therefore, the detonation-gun coatings are characterised by exceptionally high density, less oxide formation, superior bond strength, greater impact velocity and low porosity, which are suitable for applications requiring very high standards, such as aircraft engine components (Saravanan et al. 2000; Murthy and Venkataraman 2006).

2 Hot Corrosion

Simons et al. (1955) published first practical journal on hot corrosion; he described that hot corrosion is an electrochemical process in which the liquefied salt acts as an electrolyte. Seybolt (1968) ascribed Na_2SO_4 encouraged hot corrosion of Ni–Cr alloys to enhanced depletion of chromium by oxidation succeeding favoured inner fluxing of Chromium. Bornstein and DeCrescente (1969) described that during the oxidation of three different presulphidised superalloys enhanced mechanism of hot corrosion were not detected and projected a hot corrosion device proposed on the termination of protecting oxide film formed by a reaction connecting Na_2O. Goebel and Pettit (1970) prolonged this kinetics which comprises bitter dissolution, and oxide redrizzle leads disastrous oxidation due to Na_2SO_4 for alloys comprising solid acidic elements, such as vanadium or Molybdenum.

Enhanced corrosion attack is caused by other salts, viz. vanadate or sulphates–vanadate combinations and also in the presence of solid or gaseous salts such as chlorides (Bornstein et al. 1973). However, manufacturers of turbines and users of turbines conscious about hot corrosion in the 1960s, and Stringer (Stringer 1977) have conducted experimental as well as field tests to identify the nature of attack and explained its temperature dependence and the corresponding morphologies. Hot

corrosion was first associated with Na_2SO_4 in the mid-1950s (Luthra and Shores 1980). Hot corrosion became a theme of significance and most popular attention in the late 1960s when gas turbine engines of military aircraft suffered excessive corrosion attack during the Vietnam War when it is operating over sea water (Rapp and Mehl 2000). When metals are exposed to temperature range 700–900 °C, deposition of sulphates starts which leads to reaction between sodium chloride and sulphur compounds in the gas phase nearby the metals (Hancock 1987).

According to Shih et al. (1989) metals and alloys repeatedly experience an enhanced oxidation at higher temperature gas atmospheres when enclosed with a thin film of liquefied salt. This type of oxidation is generally regarded as hot corrosion. Hot corrosion is a severe damage of metals and/or an alloy due to the oxidation which is badly caused by liquid salt deposits, largely Na_2SO_4. The main source of Na_2SO_4, in aircraft engines is due to reaction between NaCl in swallowed air and sulphur in fuel as per the following reactions (Khajavi and Shariat 2004).

$$2NaCl + SO_2 + 1/2\,O_2 + H_2O \rightarrow Na_2SO_4 + 2HCl \tag{2.1}$$

$$2NaCl + SO_3 + H_2O \rightarrow Na_2SO_4 + 2HCl \tag{2.2}$$

To safe guard the turbine engines against high-temperature corrosion attack caused by impurities such as Na, S and V, thermal sprayed coatings need to be placed over the hot section parts of turbine engines and boiler tubes (Uusitalo et al. 2004).

2.1 Physical Characteristics of Hot Corrosion

High-temperature hot corrosion (Type I) is the form of hot corrosion usually arises above the melting point of sodium sulphate (884 °C), where the salt is clearly a liquid state. Goebel et al. (1973) extended the fluxing theory to explain the acidic fluxing of protective scale in Cr_2O_3 and Al_2O_3 forming alloys which contain Mo, W and V. It is observed that Al_2O_3 can be fluxed as cationic species attached to the metal surface, which is acidified by refractory metal oxides, such as MoO_3, WO_3 and V_2O_5. Further, a prolonged layer of Al_2O_3 forms on the alloy surface by using the oxygen present in the salt. This increases the sulphur activity in the salt, it increases to such an extent that the sulphides of aluminium are formed as particles in the metal substrate.

Due to the formation of sulphides of aluminium in the substrate, the key element (Al) for protecting the alloy surface gets depleted in the alloy, once sulphur is removed from the salt, the oxygen activity in the salt increases, the local basicity of salt increases to such an extent that Al_2O_3 dissolves in the basic salt at the salt/oxide interface and get reprecipitated at the gas/salt interface. This reaction continues until the sodium sulphate remains on the alloy surface and increases the rate of hot corrosion due to fluxing of shielding oxide scale. Low-temperature hot corrosion (Type II) is one of the forms of hot corrosion that occurs below melting point of Na_2SO_4, where the salt is supposed to be a solid. Higher corrosion rate during the

beginning stages were attributed to the rapid sulphation of cobalt oxide or Co (at scale/metal interface) which forms liquid eutectic melt followed by the dissolution and precipitation of cobalt oxide at the gas/salt interface by countertransport of Co^{2+}/Co^{3+} ions during the propagation stage. Thus, fluxing action of cobalt oxide prevents the formation of protective layer of Cr_2O_3, as the temperature increases, the partial pressure of SO_3 decreases, which is not sufficient to form liquid eutectic mixture. Hence, the corrosion rate at high temperature is much less than at low temperatures (Goebel et al. 1973).

2.1.1 High-Temperature Hot Corrosion (HTHC) Type I

It is beaning observed since the 1950s and it is a tremendously rapid form of oxidation attack takes place in the temperatures range between 815 and 926 °C in the existence of pure Na_2SO_4 (m.p 886 °C) (Khajavi and Shariat 2004). HTHC starts with the accumulations of bonded alkali salts (Na_2SO_4) on the component surface; the most significant source of sodium is marine, industrial atmosphere as well as fuel. During the combustion of fuels, sodium from air and sulphur from the fuel combine to form a sodium sulphate (Eliaz et al. 2002). Na_2SO_4 formation lies basically in the reaction

$$SO_2 + 2NaCl + O_2 \rightarrow Na_2SO_4 + Cl_2 \tag{2.3}$$

Hot corrosion (Type I) is analysed by a macroscopically uniform corrosion rate, which involves an internal oxidation layer which comprises internal sulphides and carbides. The exterior oxide is not shielding and is composed of the base metal oxides (nickel or cobalt); and the oxides of the other ingredients, such as chromium and aluminium (Stringer 1998).

The hot corrosion mechanism depends on temperature as shown in Fig. 1. With the increase in temperature, the attack changes from low-temperature attack (Type II) to high-temperature attack (Type I). Type I hot corrosion was first met in gas turbines of aircraft. When a gas turbine used for marine propulsion, additional type of hot corrosion was detected and it was found that it is necessary to have SO_3 present in the gas. It has been established that SO_3 should be present to cause hot corrosion attack a sum of experiments were conducted between 650 and 950 °C temperature range using oxygen–SO_2 gas mixtures. At temperatures from 650 to 750 °C, low-temperature (Type II) corrosion attack was detected when SO_3 gas pressures present in the mixture.

2.1.2 Low-Temperature Hot Corrosion (LTHC) Type II

Low-temperature hot corrosion (LTHC) was identified in the 1970s as a distinct tool of corrosion attack (Khajavi and Shariat 2004). Low-temperature hot corrosion mainly witnessed within the 650–800 °C temperature range and needs a substantial high partial pressure of SO_3, for cobalt-based superalloys. The formation of

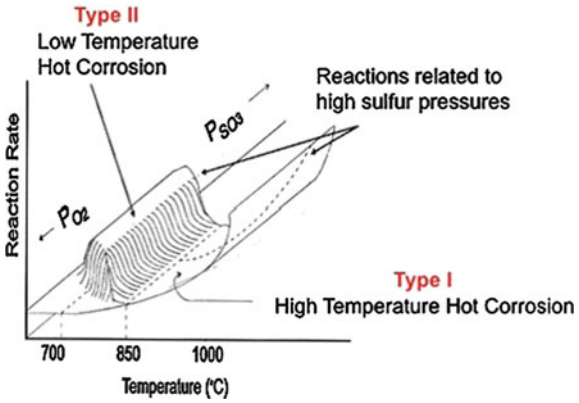

Fig. 1 Schematic to demonstrate the different hot corrosion attack as a role of temperature and SO_3 partial pressure. Various hot corrosion reaction rate surface processes are presented (Pettit 2011)

low-melting eutectic compounds occurs due to the mixture of sodium sulphate and cobalt sulphate (melting temperature of the $Na_2SO_4 \pm CoSO_4$ eutectic is 540 °C) (Eliaz et al. 2002). The formation of $Na_2SO_4 + NiSO_4$ eutectics at 671 °C has been reported for nickel-based superalloys, the morphology of attack is pitting when the LTHC takes place, low temperature corrosion characteristically shows no denuded zone, little inter-granular attack, and a layered type of corrosion scale with no subscale sulfide particles (Misra 1986). Chromium (25–40 %) and silicon are most useful in coatings for safeguarding against Type II hot corrosion. Type I or Type II hot corrosion attack mainly classified based on the morphology, and not on the temperature. Type II, or low-temperature hot corrosion is considered by a pitting attack (Stringer 1998).

2.2 *Degradation of the Superalloys*

The hot corrosion decay of superalloys typically involves two distinct phases of attack (Pettit and Meier 1985; Pettit and Giggins 1987), namely an initiation (incubation) stage and propagation stage. Such conditions are represented schematically in Fig. 2.

2.2.1 The Initiation Stage

There is no alloy developed till now which offers resistant against hot corrosion forever whereas some alloy mixtures that involve an extended beginning times before the hot corrosion attack starts from the beginning stage to the transmission stage. Hot corrosion beginning periods, degradation rate of superalloys, are similar to those in the non-existence deposits of molten salts. Different metals when oxidised movement of electrons from metallic atoms to the degradable materials propagates under the molten salts deposit. Subsequently, the oxide layer below the

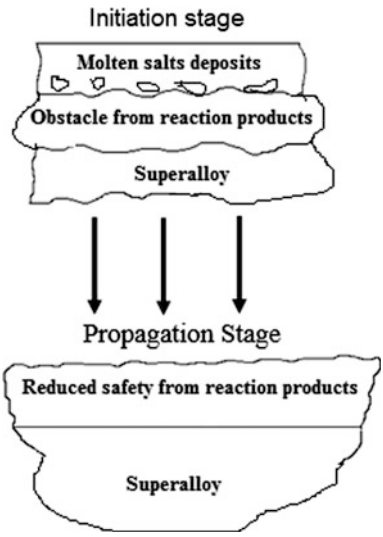

Fig. 2 Graphical diagram showing the situations that progress during the initiation and propagation of hot corrosion attack

molten salts deposit acts as a barricade on the surface of alloys (Pettit and Giggins 1987). The travel of initiation to propagation stage of hot corrosion process depends on several reasons that disturb with the time as shown in Fig. 2. In the propagation stage, the kind of corrosive species that are produced depends on the above aspects.

The above-mentioned reason accountable for multiple hot corrosion developments is detected once superalloys are left open to diverse corrosive atmospheres (Pettit and Meier 1985).

2.2.2 The Propagation Stage

Hot corrosion transmission stage of any alloy must be detached from service because it has travelled much longer corrosion time than that of initiation stage (Pettit and Meier 1985; Pettit and Giggins 1987). Superalloys contain some components that attract oxygen; we can find oxygen distribution along the deposition (Pettit and Giggins 1987).

3 Mechanisms of Hot Corrosion

From the literature review, it has been observed that there are varieties of conditions which can be considered for hot corrosion degradation of the superalloys. Researchers have proposed number of mechanisms for this type of degradation such as failure of oxide scale, sulphidation–oxidation and salt fluxing, oxide solubility, and effect of vanadium (Eliaz et al. 2002; Stringer 1987; Rapp and Goto 1981; Pettit

and Meier 1985; Goebel and Pettit 1970a, b; Beltran and Shores 1972; Otsuka and Rapp 1990).

These mechanisms can be observed in relation to each other rather than as completely different and unconnected corrosion process. The molten salt dissolution kinetics initially projected by Goebel and Petit (1970a, b). According to them, protective and safe surface oxide film vanished as a result of dissolution oxide layer under the influence of molten salt environment. This dissolution caused grouping of O^{2-} with oxides that form anions (basic fluxing) or by disintegration oxides to equivalent cations and O^{2-} (acidic fluxing) (Goebel et al. 1973).

It is has been observed that absorption of oxygen ions for dissolution is restricted by the quantity of deposition existing on the superalloy surface. As opposed to the basic dissolution, the acidic dissolution can be self-supporting (Stringer 1987; Pettit and Meier 1985). Therefore, acidic fluxing is more severe as compared to basic fluxing. In overall, the hot corrosion of the superalloys stated to arise due to basic dissolution kinetics and also because of high concentration of Al and Cr.

Hot corrosion dissolution process creates a (−)ve solubility inclination whereby the oxide on the surface of an alloy liquefied in the melted deposit at the oxide-scale/deposit interface, but precipitated out in the deposit where the solubility was lesser as an intermittent scale, as depicted in Fig. 3a. The solubility of a sum of oxides in Na_2SO_4 as a purpose of the activity of Na_2O in the Na_2SO_4 displayed that the solubilities could be streamlined via reactions with the Na_2O or SO_3 components in Na_2SO_4, Fig. 3b.

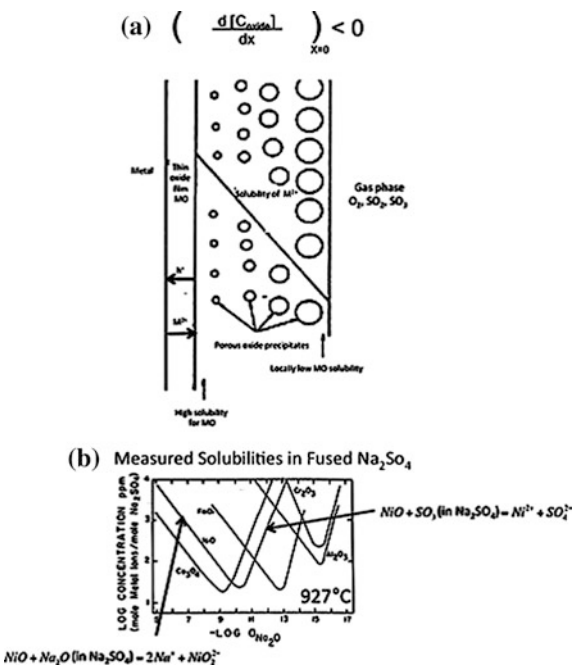

Fig. 3 **a** Sketch describing the negative solubility gradient where an oxide dissolves and reprecipitates out in the Na_2SO_4. **b** Solubilities of oxides in fused Na_2SO_4 with reactions describing the dissolution process (Pettit 2011)

With high amounts of tungsten, molybdenum and vanadium in superalloys frequently conveyed that hot corrosion follows the acidic dissolution mechanism (Eliaz et al. 2002), and these components oxidised with the existence of Na_2SO_4 and deposit on alloys causing disastrous self-supporting hot corrosion (Pettit and Meier 1985). Stott et al. (1994) suggested that sulphur-containing elements, piercing through limited paths in the oxide, which creates sulphide channels from the scale–metal border to the scale–gas border. The sulphide channels deliver easier circulation paths for the base metal ions through the oxide to the surface and finally allow more fast development of sulphide lumps above the oxide.

However, Natesan (1985) described that no passage of sulphur into the oxide, or sulphide channel development was necessary to form immense mixed iron and chromium sulphides at the oxide–gas border. Established on the experimental analysis of sulphidation–oxidation of Incoloy 800, he reported that adsorption of sulphur by the oxide scale accelerates the movement of cations such as Fe and Ni from the base metal to the scale–gas interface.

For base metal sulphidation, the partial pressure of sulphur in the gas should be more in off for the transport cations with sulphur to form sulphides as an outer scale. Hot corrosion in vanadate, sulphates and chloride atmosphere of a Ni-based superalloy is informed by Deb et al. (1996). Mass gain readings were taken in air without coated molten salts and with coated molten salts in air. Internal sulphidation of the superalloy beneath the external oxide layer is caused due to the presence of sulphur in the form of sulphates.

Rapp and Goto (1981) anticipated that shielding scales on alloy become non-shielding if negative dissolution gradients formed on the oxides in the presence of liquefied molten salts, due to possibility of continuous dissolution and reprecipitation of oxide. On the basis of oxide solubilities measurement in liquefied Na_2SO_4 as an occupation of the acidity of the molten salt, they suggested a (−)ve gradient of the solubility of the shielding oxide in the salt layer. Without any sulphide-developing reaction local deviation of sodium oxide activity and oxygen partial pressure along molten salt film was observed because of the fluxing, above-mentioned mechanism explains enhanced corrosion attack by the dissolution of the shielding oxide film (Stringer 1987).

Different research workers have examined the effect of vanadium on high-temperature hot corrosion of metals and alloys. Bornstein et al. (1973) and Goebel et al. (1973) recommended that self-supporting acidic degradation of shielding chromium and aluminium oxide scales could take place in the presence of vanadium salt layer. Zhang and Rapp (1987) further proposed that in the presence of vanadate every oxide forms an acidic solute with much higher solubility which promotes more faster attack by mixed vanadate–sulphate fluxes on oxides and further by sulphate flux.

3.1 Chemistry of Salts

3.1.1 Sulphate Chemistry

As described by Rapp and Mehl (2000) and Rapp (2002), an acid/base atmosphere is shown by oxy-anion melts of hydroxides, sulphates, etc., where in the acid constituents reflected as NO_2 (g), CO_2(g), H_2O(g) or SO_3(g), correspondingly. While the use of the Lux-Flood collection of NO_3^-, CO_3^{2-}, OH^- and SO_4^{2-} as the basic elements is collective for such fused salts, the oxide ion can otherwise be chosen as the Lewis base in common for all of these salts. For a melt of pure Na_2SO_4 (m.p 884 °C), there exists an equilibrium as given below:

$$Na_2SO_4 \rightarrow Na_2O + SO_3(g) \tag{2.4}$$

According to Rapp and Mehl (2000), chromium oxide is the best oxide for the protection of alloys from the attack by bonded sodium sulphate. Figure 4 presents the superposition of the Ellingham phase constancy plot for Cr–S–O onto the Na–S–O phase constancy diagram to examine the suitability of Cr_2O_3 in fused Na_2SO_4 at 1200 K. The chromium oxide can melt as two acidic solutes (Cr_2 $(SO_4)_3$ and CrS) and two basic solutes (Na_2CrO_4 and $NaCrO_2$) (Rapp and Mehl 2000).

3.1.2 Vanadate Chemistry

Among the transition metals, vanadium is unique; in that, it forms a low-melting oxide V_2O_5. This low melting temperature (670 °C under 1 atm of oxygen) results from the peculiar crystal structure of the compound in which vanadium is 5, coordinated with oxygen and in which there occur four different vanadium–oxygen bond lengths (Suito and Gaskell 1971).

The phase constancy diagram for the Na–V–S–O system at 900 °C has been shown in Fig. 5. The hot corrosion field is very much conscious that vanadates are most corrosive constituents in bonded salts, e.g., as a solute in bonded Na_2SO_4. The difficulty is vanadates lower the liquidus of the melt, and another problem is tendency of these strong acids to complex oxide ions, according to the following equilibria (Rapp and Mehl 2000). The dashed lines in the salt solution represent isoactivity lines of vanadate species (Hwang and Rapp 1989).

$$Na_2SO_4 \rightarrow Na_2O + SO_3 \tag{2.5}$$

$$Na_3VO_4 \rightarrow Na_2O + NaVO_3 \tag{2.6}$$

$$2NaVO_3 \rightarrow Na_2O + V_2O_5 \tag{2.7}$$

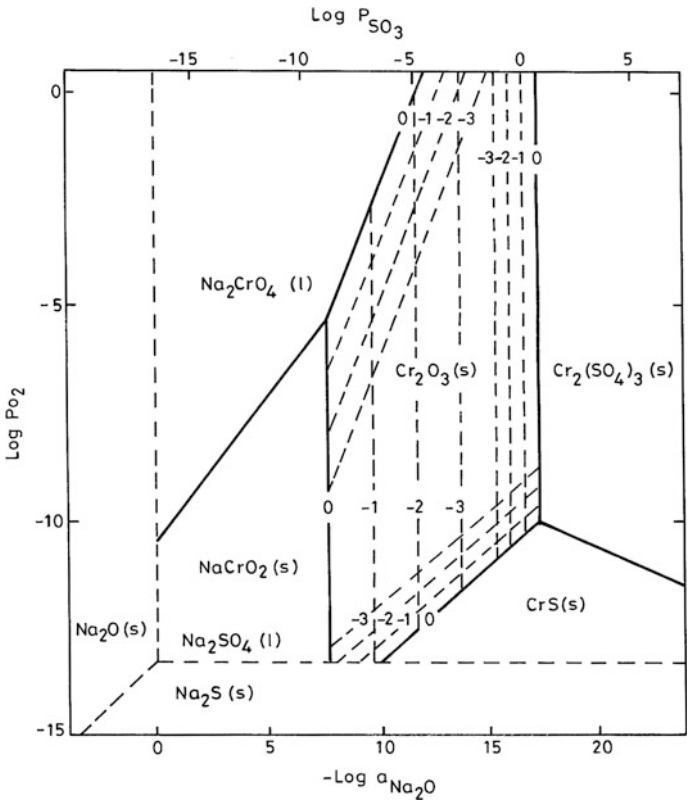

Fig. 4 Na–Cr–S–O phase constancy diagram for 1200 K (Rapp and Mehl 2000)

The stability percentage of vanadium species differs constantly with melt basicity. Na_3VO_4 is a leading compound in the melt at basicity less than 8.2, and V_2O_5 is leading at basicity larger than 16.3. For basicity between 8.2 and 16.3, $NaVO_3$ is vital vanadium solute (Hwang and Rapp 1989).

3.2 Hot Corrosion in Liquefied Salt Atmospheres

3.2.1 Liquefied Salt (Na_2SO_4–60 %V_2O_5) Atmosphere-I

Kolta et al. (1972) studied the mechanisms of reactions between Na_2SO_4 and V_2O_5. They established that reaction rate predominantly depends on temperature range between 600 and 1300 °C at molar ratios of Na_2SO_4 and V_2O_5. These researchers revealed with the reaction time increase greater than 30 min; the reaction rate goes on decreasing and finally touched zero order. The decrease in reaction time

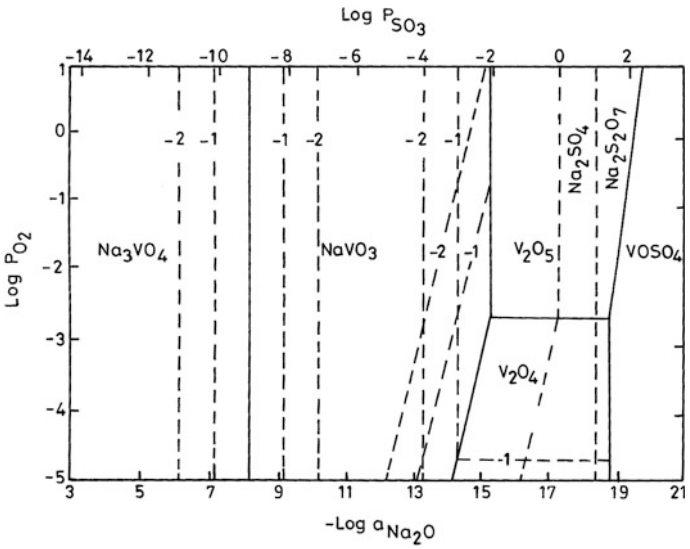

Fig. 5 Diagram showing phase stability of Na–V–S–O system at 900 °C (Rapp and Mehl 2000)

attributed with the development of vanadous sulphate mixtures such as $(NaV_3O_8)_2$. Na_2SO_4 and $(NaVO_3)_2.Na_2SO_4$, which are disintegrated at high temperatures obtaining meta- and pyrovanadates correspondingly.

The consequence of enhanced oxidation by sodium and vanadium on the nickel-base alloys is conveyed by Bornstein et al. (1975), between V_2O_5 and alloy substrate, they witnessed oxidation rate was rapid in the early stages. Inter-metallic Ni_3Al and NiAl were predominantly found to be liable to V_2O_5 corrosion. As reported by them, the composition of the melt altered by sulphidation attack and produces extra ions of oxide, i.e. $M + SO_4^- = MS + O^- + 3/2O_2$. Harshness of attack is found to be reduced by increasing early oxide ion concentration.

Hot corrosion performance of Cr_3C_2–NiCr coatings on superalloys in molten salt atmosphere at 900 °C was studied by Kamal et al. (2008). Thermogravimetry method was used by authors to know the high-temperature hot corrosion conduct of bare and Cr_3C_2–NiCr-coated superalloys in liquefied salt atmosphere (Na_2SO_4–60 % V_2O_5) at a temperature 900 °C for hundred cycles. The corrosive species were examined to disclose their compositional topographies for revealing the corrosion mechanisms. It has been observed that resistance to hot corrosion is because of development of necessary topographies such as low porosity, even fine grains and the plane splat structures.

Kofstad (1988) has anticipated that in burning, the vanadium impurities are reacted to the upper-valence vanadium oxides (V_2O_4 and V_2O_5) which react with sodium salts to form low-melting-point sodium vanadates (lowest m.p 535 °C) such as $(Na_2O)_xV_2O_4(V_2O_5)_{12-x}$, $(Na_2O)_5(V_2O_4)_x(V_2O_5)_{12-x}$, $NaVO_3$, $Na_4V_2O_7$ and Na_3VO_4. Vanadates in the oxides of metal offend and destroy eutectic temperatures

and m.p (melting point), he has established that sodium sulphate and sodium vanadates deposit as a slag on valves of diesel engines and they have melting point 400 °C. Hwang and Rapp (1989) studied the solubility of oxides in the mixed sodium sulphate–vanadate solution containing 30 mol% vanadates. They reported that the basicity of the melt, oxygen, partial pressure and proportion of V^{5+} and V^{4+} states of vanadate in the sulphate–vanadate solution decide the solubilities of oxides.

Kofstad (1988) revealed that the dissolution of oxides of metal is greater and they totally rely on the Na/V ratio. Dissolving capacity of Cr_2O_3 and Fe_2O_3 is the highest (≈50 mol%) at Na:V ratios near to 5:12. For NiO, and the dissolving capacity is about 60 mol% at Na:V = 3:2 which declines to 55 mol% at Na:V = 5:12. The presence of acidic V_2O_5 reacts with extra basic oxides to form equivalent vanadates.

3.2.2 Liquefied Salt (Na_2SO_4–25 %K_2SO_4) Atmosphere-II

Shih et al. (1989) observed the performance of K_2SO_4 + Na_2SO_4-coated aluminium diffusion coatings on a pure iron substrate with aluminium concentrations of 28–51 % at the top most surface of the coatings at 600 °C in O_2−SO_2–SO_3 gases atmosphere. Entire coating undergone submelting point hot corrosion, but the corrosion rates are lesser than pure iron, and there is a development of a liquid phase.

Wang et al. (2004) tested the hot corrosion performance of arc ion plating NiCoCrAlY (SiB) coatings sprayed on Ni-based superalloys DZ 125 and DSM 11, in liquefied 75 Na_2SO_4 + 25K_2SO_4 (wt%) at 900 °C in air for 90 h. The coating developed hot corrosion resistance of DZ125 and DSM11 superalloys. The authors established that the additions of silicon and boron can improve oxidation resistance of the coating by the formation of an unbroken oxide scale in the beginning of corrosion stage and improve the adherence of the outer scale to the coating in the succeeding hot corrosion process.

Kamal et al. (2009) assessed the cyclic hot corrosion performance of Cr_3C_2–25 %NiCr coatings on Ni- and Fe-based superalloys. The cyclic hot corrosion experiments were analysed on without coated as well as coated superalloys in the presence of different molten salts. Weight gain method is used to create the mechanism of hot corrosion of without coated and coated superalloys. It was witnessed that Cr_3C_2–NiCr-coated superalloys displayed higher hot corrosion resistance than the without coated superalloys as a result of the formation of unbroken and shielding oxides of chromium, nickel and their spinel.

A nanocrystalline NiCrAlY coating was sprayed on a Ni-based superalloy by magnetron sputtering (Ren and Wang 2006). Sputtered coating was post-aluminising for better performance. The isothermal oxidation behaviour at 1000–1100 °C and hot corrosion behaviour in the presence of 75 wt% Na_2SO_4 + 25 wt% K_2SO_4/NaCl thin layer at 900 °C of the sputtered coating with and without aluminising have been investigated. They observed that the sputtered

NiCrAlY coating obsessed outstanding oxidation resistance at 1000 °C due to the presence of huge amount of Cr and maximum percentage of Al. But the coating lost its protection at 1100 °C because of the extreme consumption of Al in the coating. Aluminised NiCrAlY coating exhibited improved resistance to hot corrosion in comparison with sputtered coating due to the development of an uninterrupted and protective Al_2O_3 scale (Ren and Wang 2006).

Zheng et al. (2006) reported that an original gloss-Al_2O_3 composite coating with a thin layer of NiCoCrAlY bond coat was deposited on K38G superalloy. They showed that this combined coating performed much better oxidation resistance at high temperature between 900 and 1000 °C and hot corrosion resistance in melted sulphate salts (75 wt% Na_2SO_4 + 25 wt% K_2SO_4) at 900 °C, much better than solo NiCoCrAlY coating and uncoated K38G. The protection kinetics of this compound coating was different from those of old metallic coatings. Further, it was reported that it has not been oxidised longer period during tests and acted as an obstacle to successfully delaying the corrosive species from penetrating into substrate.

Guo et al. (2006) studied the corrosion mechanism of the substrates coated with 0.5 mg (Na_2SO_4 + K_2SO_4 20 wt% salt mixture)/cm^2 at 900 °C. For bare DSM 11 alloy, he has observed substantial weight gain due to rapid hot corrosion attack of the alloy during the first 20 h, followed by variation due to the struggle of oxide-scale formation and spallation. After 80 h, the weight gain diminishes abruptly due to a higher amount of oxide spallation.

3.2.3 Hot Corrosion of the Nickel-Based Alloys

Bornstein et al. (1975) have observed the consequence of sodium and vanadium on the enhanced oxidation of the Ni-based superalloys. Liquid vanadium pentoxide has been observed to be a brilliant flux and cool path for oxygen penetration. They observed between V_2O_5 and Ni-based superalloys; oxidation rate is rapid during the initial stages. They determined that the sulphidation attack can be reduced if melt is prohibited from increasing concentration of oxide ion in the early stages.

Weight gain describes concurrent vanadate- and sulphate-encouraged corrosion at 650–800 °C studied by Seiersten and Kofstad (1987). Mixtures of sodium vanadate and sodium sulphate initiated corrosion by intricate kinetics. Otero et al. (1987) investigated the hot corrosion behaviour of IN657 (46.5 Cr, 1.32 Nb, bal-Ni) at 635 °C in a liquefied salt atmosphere of 60:40 V_2O_5:Na_2SO_4 (mol%). They characterised the morphology and chemical compositions of the corrosion products and found that the occurrence of oxide and sulphur promotes the development of isolated portions with outward morphology. Penetrability of these portions eased the access of oxygen; hence, protective oxide scale was lost, vanadium and its oxidised mixture with change in morphology produce various compounds which increases the protective nature of the scale as described by the author.

Otero et al. (1990) again studied the hot corrosion performance of the same alloy IN657 in same molten salt atmosphere 60 %V_2O_5–40 %Na_2SO_4. They observed that for duration less than 100 h, the corrosion rate increased with temperature

when the temperature was less than 727 °C. For temperatures greater than 727 °C, corrosion rate decreased. An increase in corrosion rate with temperature witnessed during the early stages of exposure was related to the higher volatility of the liquefied salt mixture. At temperatures greater than 727 °C, once the suitable fluidity was attained, the corrosion rate decreased due to the decrease in the oxygen solubility in the liquefied salt.

Otsuka and Rapp (1990) examined the influence of vanadate and chromate anions on hot corrosion of nickel by bonded Na_2SO_4 film in an SO_2–O_2 gas atmosphere at 900 °C. The results indicate that the standby of sulphidation may be due to the dissolution of solid Cr_2O_3 which partly seals/plugs the cracks and voids of protective oxide film. Further, they found that vanadate anions enriched the inception of the hot corrosion and sulphidation; this may be via fast degradation of protective oxide layer at cracks and voids.

The oxidation and hot corrosion studies of Ni-based superalloys in Na_2SO_4-60 $\%V_2O_5$ environment at 700 °C were carried out by Lambert et al. (1991) to investigate the effects of Si addition. On the outer surface of the alloy, they found a thin layer of NiO whereas on the Si-enriched alloy, a thin $A1_2O_3$ scale formed. They attributed that distinctly increase in oxidation rate of Ni-based superalloys due to highly corrosive condensed vanadates and sodium.

According to them, the continuous regeneration of protective oxide obstruction was significantly affected by the corrosive resistant coating, particularly in the Si-enriched alloy. They identified Ni, Cr, Al and Si complex oxides in the inner oxide layer.

Gurrappa (1999) studied the hot corrosion behaviour of Ni-based superalloy in sodium sulphate and mixture of sodium sulphate + sodium chloride. He has witnessed that the superalloy got rigorous corrosion attack in just 4 h, whereas it is entirely corroded in 70 h when examined in 90 $\%Na_2SO_4$ + 10 %NaCl. When the same alloy studied in 90 $\%Na_2SO_4$ + 5 %NaCl + 5 $\%V_2O_5$ atmosphere at 900 °C, in just 2 h superalloy lost its entire strength.

Gitanjaly and Prakash (1999) analysed the hot corrosion performance of some Ni-, Fe- and Co-based superalloys in an atmosphere of Na_2SO_4 + 60 $\%V_2O_5$ at 900 °C. In general, the author observed significant corrosion degradation in all the superalloys. However, the Ni-based superalloy Sn 75 exhibited lowermost rate of corrosion related to Superco 605. The presence of $Ni(VO_3)_2$ in the coating represented as a diffusion barricade for the oxidising corrosive species which improves corrosion resistance of Ni-based superalloy.

Tzvetkoff and Gencheva (2003) reviewed the kinetics on the development of corrosion films on Ni and Ni-based alloys in molten salts containing oxyanions. They reported that catastrophic hot corrosion failure due to rapidly induced fluxing of the protective oxide scale in the presence of acidic oxides such as those of V and Mo.

The chromate oxide layers were identified as useful for the repassivation of the surfaces which lost due to molten salt fluxing. Further, they reported that the molten sulphate mixtures are violent towards Ni-based superalloys. In such atmospheres, they additionally detected the presence of sulphides at oxide/metal boundary which

do not suggest probable protection except for a positive role of MoS_2 developed on Ni-based alloys having substantial quantity of Mo.

Author has investigated the hot corrosion behaviour of NiCoCrA1YTa coatings sprayed on the superalloys (specifically Sn 75, Sn 718 and Sf 800H) exposed to Na_2SO_4–25 $\%K_2SO_4$. Better protection attributed to the formation of thick and adherent of Cr and Al oxide scale on coating. In the subscale region, these oxides formed across the periphery of Ni-rich splat borders performed as diffusion obstacles to the internal dissemination of corrosive species which moderately minimise the mass gain. Graphics of projected oxidation mechanism of the detonation-gun-coated NiCoCrAlYTa on Sf 800H at 900 °C in Na_2SO_4–25 $\%K_2SO_4$ after 100 cycles are shown in Fig. 6.

Singh et al. (2005) studied hot corrosion behaviour of a nickel-base superalloy in molten salt atmosphere at 900 °C under repeated settings for 50 cycles of one hour each. They used thermogravimetric technique to estimate the mechanism of corrosion. They revealed that superalloy Superni 601 revealed that extreme spalling of oxide scale and the mass gain, including the spalled scale, was huge during the hot corrosion studies in the given rigorous atmosphere. They reported non-stop increase in the mass of the superalloys, but the rate of increase was more during the early period of exposure. They revealed that $NaVO_3$ formed due to the reaction of Na_2SO_4–60 $\%V_2O_5$ acts as a reagent and assists as an oxygen transporter to the metal. The chromium has great attraction for oxygen to form Cr_2O_3, which rapidly increase mass gain in the initial stages of hot corrosion.

Prakash et al. (2005) witnessed the hot corrosion performance of another Ni-based superalloy under the same conditions and at same temperature. They reported that the superalloy suffered a catastrophic hot corrosion attack which leads

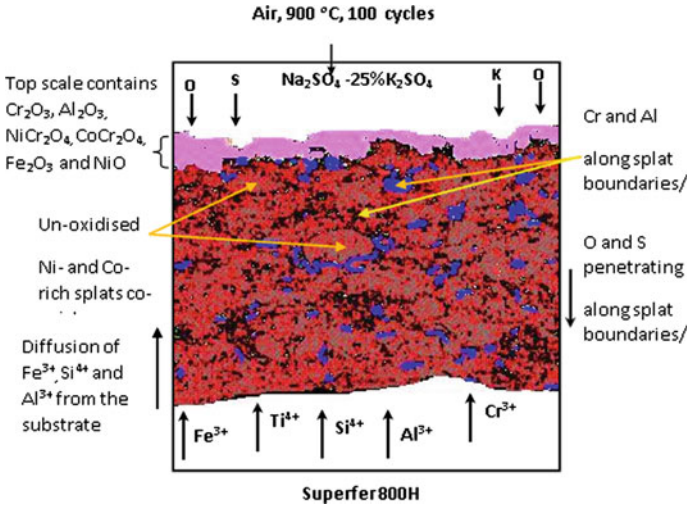

Fig. 6 Schematic of the proposed oxidation mechanism of the NiCoCrAlYTa-coated superalloy Superfer 800H at 900 °C in Na_2SO_4–25 $\%K_2SO_4$ after 100 cycles

to extreme spalling and sputtering of the scale. They concluded this behaviour with the existence of Mo in the alloy, as oxides of Mo cause an alloy-induced acidic fluxing. Ravindra et al. (2007) also reported the hot corrosion and oxidation performance of a directionally solidified Ni-based superalloy.

3.2.4 Hot Corrosion of Iron-Based Mixtures

Fairman (1962) reported severe corrosion of some metal pieces in an ash blend (V_2O_5 + 10 % Na_2SO_4) atmosphere in air. Greatest corrosion attack was established where the percentage of O_2 and V_2O_5 was higher, proposing the movement of oxygen atoms or ions on the metal surface: $2V_2O_5 \rightarrow 2V_2O_4 + 2O\downarrow$. He reported that the enhanced oxidation is a diffusion controlled process of the absorption of flaws into the oxide scale. He further suggested that the kinetic of enhanced attack could be more reasonably clarified by the catalytic action of V_2O_5 operating with the growth in the fault concentration of the scale.

Kerby and Wilson (1972) revealed that the fluxing of protective oxide layers rise the corrosion speed of metals by liquid vanadates present on the alloy surface and acted as a source of oxide ion for the corrosion reaction. The electrical conductivity enhanced with increase in temperature and with reducing oxygen pressure.

Valdes et al. (1973) studied AISI 446 stainless steel under V_2O_5 and $Na_2O.6V_2O_5$ atmosphere in the range 700–900 °C in air and established the presence of Cr_2O_3 scale with little oxides of vanadium which performed as a reasonable obstacle to corrosion. Above 850 °C in V_2O_5, a breakaway corrosion reaction occurred. No Cr_2O_3 barricade was present, but there was an uninterrupted oxide scale that consisting of Cr_2O_3, Fe_2O_3 and V_2O_5 at the metal/oxide interface from which a region of crystals grew. They suggested that the addition of Na_2O to V_2O_5 enhanced the oxide ion (O^{2-}) in the melt and made it extra destructive to acidic oxides such as Cr_2O_3.

Shi et al. (1992) studied the effect of K_2SO_4 added to a Na_2SO_4 on the low-temperature hot corrosion performance of iron aluminium alloys. He concluded that K_2SO_4 preservative increased the low-temperature hot corrosion of Fe–A1 alloys affected by Na_2SO_4 deposit in the environment containing O_2, SO_2 and SO_3, but the kinetics of corrosion remained unaffected. In the initial period, degradation/precipitation of Fe_2O_3 proceeded at a substantial rate; at a longer time, growth of a compact iron oxide conquered the enhanced hot corrosion caused by K_2SO_4 stabiliser was not ascribed to the formation of intricate sulphates. The equilibrium phase diagram for changing composition of Na_2SO_4 and K_2SO_4 is shown in Fig. 7.

Tiwari and Prakash (1996, 1997) and Tiwari (1997) have stated hot corrosion studies on high-temperature-resistant superalloys in range of 700–900 °C in the atmospheres consisting of Na_2SO_4, Na_2SO_4–15 %V_2O_5 and Na_2SO_4–60 %V_2O_5. They detected very high rates of corrosion in the atmosphere having Na_2SO_4–60 % V_2O_5. Due to the low melting point of this compound (550 °C), the corrosive environment of this mixture is huge. Tiwari and Prakash (1997) additionally

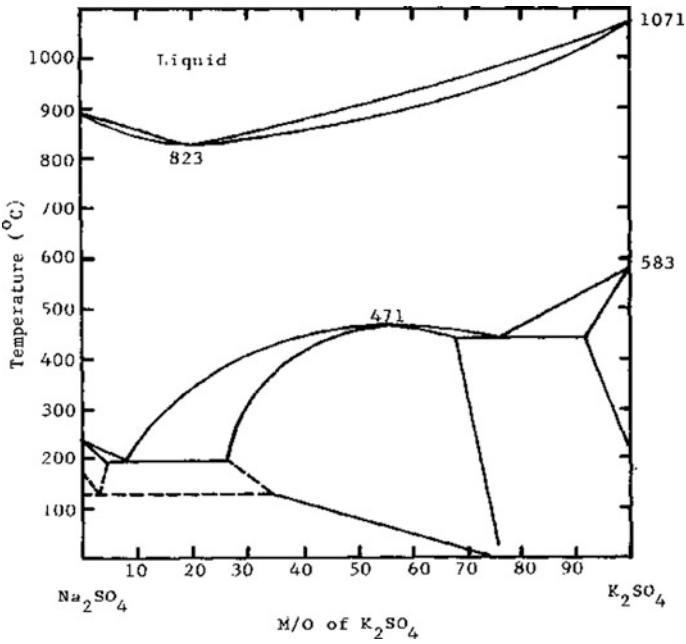

Fig. 7 Phase diagram of Na_2SO_4 and K_2SO_4 system (Shi et al. 1992)

exposed that in Na_2SO_4–60 $\%V_2O_5$ molten salt, precipitation found with the presence of cracks in the defensive scale due to degradation by the molten salt for Sf 800H and Superco 605. Greater precipitation was observed due to the presence of tungsten in the form of Na_2WO_4–WO_3 mixture. Tewari (Tiwari 1997) determined that Co-based alloy has lower corrosion protection than Ni-based superalloy in Na_2SO_4–60 $\%V_2O_5$ atmosphere at 900 °C.

Kamachi Mudali et al. (2004) reported that the stainless steels are susceptible to corrosion in the presence of violent corrosive atmosphere and also in aqueous, high temperature, axial or compressive stress and other service constraints. Under such situations, proper care is to be taken by preparing exclusively diverse surface morphology by forming corrosion-resistant thermal spray coatings.

Singh et al. (2005) investigated the hot corrosion performance of an iron-based superalloy in melt (Na_2SO_4–60 $\%V_2$–O_5) atmosphere at 900 °C under cyclic situations for 50 h and found that the superalloy underwent severe exfoliation and crackling and the mass gain was massive during the course of study.

Sidhu et al. (2006) reported that iron-base superalloy Superfer 800H underwent intense spalling, sizzling of scale along with cracking sound during cooling and detaching of the protective oxide scale in an violent atmosphere of Na_2SO_4–60 $\%V_2O_5$ at 900 °C. During the cyclic study for 50 h, the mass gained by the superalloy was enormous. It was found that the weight increased uninterruptedly, during the early period of exposure. The rate of increase in weight gain was ascribed

mainly due to the formation of $NaVO_3$ complex compound. Slower increase in mass gain after early mass gain was due to the instantaneous growth and degradation of oxide scale in the molten salt due to the following reaction. This Na_2CrO_4 vaporised as a gas

$$Cr_2O_3 + 4NaVO_3 + 3/2O_2 \rightarrow 2Na_2CrO_4 + 2V_2O_5. \quad (2.8)$$

Sidhu et al. (2006a, b) reported that the behaviour of HVOF sprayed Cr_3C_2–NiCr coatings on an iron-based superalloy in Na_2SO_4–60 $\%V_2O_5$ atmosphere at 900 °C in repeated conditions. The thermogravimetric measurements were used to study the kinetics of corrosion. The coating has effectively imparted resistance to molten salt-induced hot corrosion. The Cr_3C_2–NiCr-coated alloys offer corrosion resistance with the development of phases such as Cr_2O_3, NiO and $NiCr_2O_4$ in the protective oxide scales.

4 Some Studies on Power Plant Environments

Different researchers informed that accumulation/reduction of low-melting-point molten salts (present in the gases) on the thermal power plant tubes used for superheaters and reheaters in coal-fired boilers is an original reason for the massive damage of tube materials. At the operating temperatures of boiler tubes molten salts consisting sulphates of sodium and potassium, they simply liquefy and cause rigorous hot corrosion of boiler tubes (Rapp and Mehl 2000; Nelson et al. 1959; Backman et al. 1987; Salmenoja et al. 1996).

Boilers and other steam power plant equipment are subjected to a wide variety of failures involving one or more of several mechanisms. Overheating is described as main root cause damage in steam generators. A survey compiled by one laboratory over a period of 144 months, covering 413 inquiries, listed excess heating damage causes 201 failures or 48.7 % of those examined. Defective or improper material has been cited as the cause of most of the remaining failures (13.3 %). Although "defective material" is often blamed for a failure, this survey indicates that statistically it is one of the least likely causes of failure in power plant equipment (Handbook 1975).

Moujahid (1987) observed severe ash corrosion, mechanical deformation and cracks on the cast iron chains of moving grate used to air burning of coal. Liquid coal ash at 1300 °C is strongly acidic and dissolves spinel layers which formed on the chains at elevated temperature. The fused ash embeds coal particles and also reduces the thermal efficiency of the equipment. Drastic enhancement in ash corrosion rate has been attributed to the mechanical damages. Kamal et al. (2010) incorporated rare earth oxide (CeO_2) in NiCrAlY coating and investigated hot corrosion resistance. The coatings revealed distinctive splat spherical dendritic phases. Cerium oxide dispersed along the boundaries of splats, while Al lines scattered non-uniformly. On the coated superalloys a thick oxide film observed

which represents shielding phases such as NiO, Cr_2O_3, Al_2O_3, $NiCr_2O_4$ and Ni Al_2O_4 formed on the surface which offers resistance to hot corrosion, some of the oxides of iron and silicon moved to the top surface during initial period of exposure. Graphical drawing showing projected hot corrosion kinetics of the NiCrAlY + 0.4 wt% CeO_2-coated superalloy Superfer 800H at 900 °C in Na_2SO_4 + 60 % V_2O_5 after 100 cycles is shown in Fig. 8 (Kamal et al. 2010).

Iyer et al. (1987) witnessed the hot corrosion behaviour of Nimonic 80A under tension using combustion gases environment at 600–700 °C and reported the presence of NiO, Cr_2O_3, $Ni(VO_3)_2$ and $NiO.Cr_2O_3$ on the surface of the corroded alloy. Accelerated oxidation was observed, and the scale was reported to be spongy. They observed that the lowest melting liquid was formed even at 550 °C. They suggested that the presence of stresses enhanced the damage due to spalling, allowing fresh surface to be exposed to hot corrosion. They proposed that as vanadium content increases, some of the vanadium participates as vanadates and, therefore, increase in vanadium above certain level is not so violent. This critical level was found to be around 20 ppm vanadium.

Prakash et al. (2001) observed failure of boiler tube in the pulverised coal-fired boiler in India, a case study conducted for the period of one year. They observed total 89 failures, out of which 50 failures were caused to the hot corrosion and erosion by fly ash lumps. Under detailed investigation of five (5) samples of failed boiler tubes, they reported major cause of tube failures is overheating.

Coal is an abandoned cheep fuel available with its low price related to its worldwide obtainability and due to the forthcoming deficiency of other fossil fuel assets such as heavy oil and natural gas. But burning of coal generates very corrosive environment near the superheater boiler tubes. Hot corrosion of boiler tubes

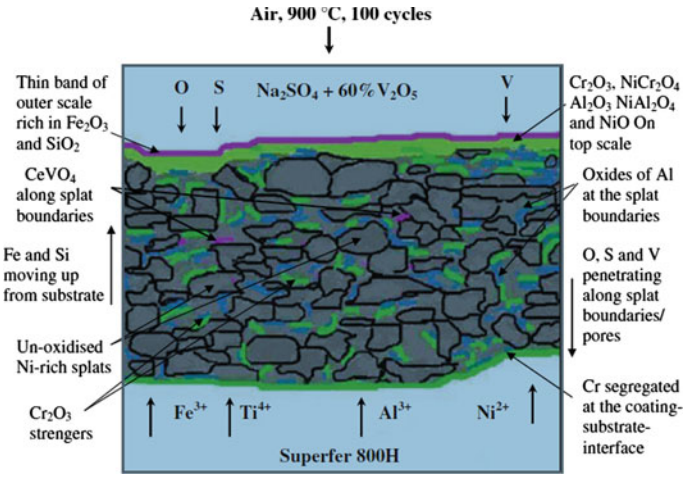

Fig. 8 Graphical drawing showing projected hot corrosion kinetics of the NiCrAlY + 0.4 wt% CeO_2-coated superalloy Superfer 800H at 900 °C in Na_2SO_4 + 60 % V_2O_5 after 100 cycles (Kamal et al. 2010)

is considered as a more demanding aspect, which results in tube wall thinning and catastrophic failure. Efforts have been made to decrease the maintenance costs of these tubes that have increased interest in protecting them with protective thermal spray coatings (Sidhu et al. 2006).

Kamal et al. (2009) and Sidhu et al. (2006c, d, e, f) carried out various tests in the laboratories and in the actual coal-fired boiler environments in order to estimate the hot corrosion damage, all the coatings deposited on Ni-based superalloy imparted better hot corrosion resistance than the uncoated one. The Stellite-6-coated superalloy did well than the NiCrBSi-coated alloy in the given environment.

5 Preventive Measures Against Hot Corrosion

The corrosion control in highly aggressive applications requires careful selection of materials. Nickel-based superalloys have better physical properties and superior corrosion resistance at higher temperatures and are used as base materials for hot section components in turbines. However, the hot corrosion is unavoidable when used at higher temperatures for longer duration of time in an extreme environment (Goebel et al. 1973).

Heath et al. (1997) proposed a number of countermeasures corresponding to the variety of corrosive environments including the following:

- Proper selection of alloy,
- Optimum design of components,
- Use of chemical additives to neutralise the corrosive components in the flue gases,
- Shielding the substrate and
- Protective coatings.

The important factors that influence hot corrosion are as follows: (a) alloy composition, (b) alloy fabrication condition, (c) deposit composition, (d) amount of deposit on superalloy, (e) gas composition and velocity, (f) temperature, (g) temperature cycles and (h) erosion (Gurrappa 1999). Eliaz et al. (2002) also, in their review of hot corrosion in gas turbine components, suggested several approaches to control the hot corrosion, which include appropriate selection of physically high-strength alloys, thermal spray coatings on hot section components, regular cleaning of hot section parts, air filtering and governing of both fuel hygiene and composition.

Hot corrosion can prevent by thermal spray coating the substrate alloy with a preventive film. This is the favoured method, even when comparatively less hot corrosion-resistant substrate alloys are used (Eliaz et al. 2002). For sufficient corrosion protection of an alloy in the given destructive atmosphere, compatible techniques and proper selection of materials are more important. Adding organic inhibitors such as pyridines, pyrimidines, quinolines is enough to diminish hot

corrosion of alloys in many corrosive atmosphere, although inhibitors have partial success due to solubility and/or thermal instability at high-temperature, intense salt solutions (Priyantha et al. 2003).

6 Role of Thermal Spray Coatings

The coatings at high temperature develop a shielding oxide film on the metal surface to limit loss of metal by oxidation. Generally, these protective oxides (e.g. $A1_2O_3$, Cr_2O_3 and SiO_2) diminish the penetration of gaseous or liquid corrosive mixture towards the substrate alloy and equally prevent substrate elements diffusion towards the external surface where they could react with the coated elements. Moreover, there should be minimum inter-diffusion phenomenon between coating and substrates as far as the quality of the coated constituent are concerned (Mevrel 1989).

Premature failure of the thermal power plant components regularly arises due to the rigorous reactions between the substrate alloy and the violent combustion atmosphere. Degradation mechanism at high temperature by distinctive molten salt film should be clearly understood, so as to reduce the tube material failure by emerging more defensive structural alloys and coatings (Li et al. 2005).

To enhance the life or enrich the performance of alloys, thermal spray coatings are contributing substantial part in today's aero- and industrial turbine engines; about 75 % of all the components in jet engines are coated (Zheng et al. 2006; Gurrappa 2000). MCrAlY-type metallic coatings regularly used in the hot segment of turbine engines, which is precisely designed and developed to meet the violent environmental operating conditions (Guo et al. 2006).

6.1 Advantages of Thermal Spray Coatings

Nearly all types of superalloys and boiler steels with enhanced strength, the requirements of defensive coatings demand have recently increased, because of high-temperature corrosion difficulties become major problems for these superalloys with growing working temperatures of current heat engines (Yoshiba 1993). Further, Porcayo-Calderon et al. (1998) have reported the use of protective coatings for the superheater/reheater parts of boiler, where the alloys rigorously undergo fireside hot corrosion. To prolong the life of alloys to work at the higher end of their performance abilities, only coatings offer a way, by permitting the mechanical properties of the substrate materials to be maintained while defending them against wear or corrosion (Sidky and Hocking 1999).

Unfortunately, it is well known in the literature that it is not always possible to develop an alloy that will be resistant to hot corrosion as well as possess good high-temperature strength by the addition of alloying elements. Some alloying

elements may help to improve the mechanical properties, while others may improve the hot corrosion resistance, but generally both properties are not improved simultaneously. Tremendous increase in mechanical properties can offer with the presence of tungsten, vanadium and molybdenum while their existence makes the alloy highly prone to hot corrosion (Gurrappa 1999).

The need for better-quality performance, higher operating temperature, prolonged component life and higher efficiency power plant places high demands on the construction materials used in a high-temperature plant. Consequently, a large number of components worked at high temperature are coated or surface treated (Nicholls 2000). According to Taylor and Evans (2001), for fossil power plants few previous efforts made on the thermal sprayed defensive coatings, however, thermal spray process is comprehensively used for gas turbine engine components.

Furthermore, improvement in the conventional steam-raising plants, substitute power supply systems, for example, combined with cycle plants, wherein a gas and steam turbine, are coupled, suggesting greater thermal efficiencies, as the inlet temperatures of gas turbine are 1200 °C and above (Nickel et al. 2002). According to them, components operated at high temperatures prone to increase oxidation rates; hence, defensive coatings with higher temperature abilities are necessary. Therefore, an alternative is to go for protective coatings for hot corrosion resistance; it is essential to cultivate appropriate coatings to enhance the operational life of the components. Although corrosion problems cannot be completely eradicated, nevertheless, 25–30 % of corrosion associated costs can be saved with the use of best corrosion anticipatory and control policies (Priyantha et al. 2003; Koch et al. 2002).

6.2 Requirement of High-Temperature Coatings

Preventive surface preparations are extensively used at low temperature, but largely limited use of these at elevated temperature applications. A huge ultimatum exists to grow and apply these coating for high-temperature applications (Stroosnijder et al. 1994). Consequently, all components working at high temperature are coated (Nicholls 2000). Superalloys have been developed for high-temperature applications; however, protective coatings are applied to improve their lifespan for use in corrosive atmospheres as they are not able to meet the requirement of high-temperature asset and high-temperature corrosion protection concurrently (Liu et al. 2001).

6.3 Coating Deposition Techniques

Nicoll (1984) reported that from manufacture point of view, chemical vapour deposition (CVD), physical vapour deposition (PVD) and thermal spray techniques (metal spraying) are used extensively. Since CVD process is a non-line-of-site

technique, appropriate covering and tool requirements is the foremost design deliberations and it is expensive. Additional limitation of the CVD process is the insertion of package particles in the coating which can lead to coating damage.

Variety of coating deposition methods are available in the market, and selecting the best coating methods depends on the useful requirements, flexibility of the coating material to the selected coating method, field of application required (size, shape of coating powder and metallurgy of the substrate), and accessibility of the powder and cost of the coating equipment such as HVOF, Detonation-gun and Plasma spray.

6.3.1 Thermal Spray Techniques

In the year nineteen hundreds, a young Swiss inventor named Dr. Max Schoop designed thermal spray method, after watching his son playing with his toy. Dr. Schoop observed that the hot lead particles were projected out of the cannon, held nearly any surface, which gave him the idea that if the molten metal projected in a spray-like manner, then a surface will be built up with that material. A variety of engineering problems have been solved using thermal spraying applications. Thermal spray technique is used across many engineering processes, from the locomotive to the space craft industry (Nicoll 1984). Thermal spraying is the most resourceful method offered for the application of coating materials used to protect parts from abrasive, adhesive, erosive wear and erosion corrosion (Marceau and Adjorlolo 1995).

Thermal spraying is a generic coating technique whereby droplets of molten or partially molten material are generated and projected at a surface to form a coating. The droplets undergo little interaction with the substrate, merely adhering to the roughened surface through physical means to form an "overlay" coating. Variety of techniques has been designed for this process, varying in the manner in which they heat the material, the operating temperature and the velocity to which the droplets are accelerated. Through the range of operating conditions generated, any material that does not undergo sublimation or degradation upon heating can be applied as a coating.

Materials ranging from polymers to metals, cermets and ceramics are regularly sprayed. In the generalised thermal spray process, the coating material in rod, wire or powder form is fed into a high-temperature heat source, where it is heated close to, or in excess of, and its melting temperature. A high-velocity accelerating gas or combustion gas stream accelerates the droplets of material to the substrate, where they impact and spread across the surface to form a "splat" (Matthews 2004). The oxidation time during thermal spray coating is short typically less than 0.01 s and can occur in either the solid or molten state. The oxidation of coatings is not always harmful, it is equally important to control and understand the different aspects of oxidation of coatings; therefore, it is important to find an optimum level for oxidation of coatings (Herman 1988; Korpiola and Vuoristo 1996; Nerz et al. 1992). Commonly, any material, which does not decay, boil, transfer or dissociate on heating, can be thermally sprayed. Subsequently, a wide range of metallic and

non-metallic materials (such as metals, alloys, ceramics, cermets and polymers) can be easily deposited by thermal spraying. Metals, carbides and cermets are the more extensively used as a coating material; also polymer deposition has been investigated (Kawase and Nakano 1996). High-temperature corrosion protection can be obtained by the deposition of metallic coating on the substrate metal with the use of thermal spray process and are listed below, summarised by Heath et al. (1997).

- Flame spraying with a powder or wire,
- Electric arc wire spraying,
- Plasma spraying,
- Spray and fuse,
- HVOF spraying and
- Detonation-Gun

  The technology continued, but expanded in the 1970s due to development of the thermal plasmas and the increasing demand of high-temperature and wear-resistant materials and coating systems (Knotek 2001).

Table 1 shows some of the significant parameters linked with these thermal spray techniques (Bhushan and Gupta 1991; Sobolev et al. 2004; Wagner et al. 1984). Speed of powder particles, flame temperature and spray environment are the main constraints which differentiate the various spraying methods. Porosity, bond strength and oxide content of the coating are the properties depended on the coating process. Also, Kuroda et al. (2008) show the grouping of numerous thermal spray processes in terms of particle temperature and velocity. Similarly, Gledhill et al. (1999) proposed the schematic diagram showing unmelted particles, splats, voids and in coming particles with unmelted.

6.4 *Nanostructured Coatings*

Nanostructured coating (Khana and Jha 1998) is the collection of crystalline/amorphous blends. It has newly attracted necessary research and engineering applications, because of the producing, a surface safety film with exceptional physiochemical properties that are frequently not achieved in the bulk coating. Nanostructured coating is a new class of manufacturing materials with superior properties and physical length between 1 and 100 nm. Broad range of engineering applications that needed resistance to abrasive wear, erosion, hot corrosion, cracking and spallation, better properties can be incorporated with nanostructured ceramic coatings produced by plasma-sprayed processes are being developed recently.

Bansal et al. (2003) compared commercial coarse-grained and the nano-Al_2O_3–13 wt% TiO_2 ceramic coatings by plasma spray on steel substrate. These nanocoatings enhanced resistance to wear and had a good bond strength which is

Table 1 Comparison of characteristics for various thermal spray processes (Bhushan and Gupta 1991; Sobolev et al. 2004; Wagner et al. 1984; Stokes and Looney 2001; Hao et al. 2005)

Deposition technique	Heat source	Material feed type	Spray gun temp. (°C)	Coating materials	Porosity level % volume
Electric arc	Arc between electrodes	Wire	6000	Ductile materials	8–15
Plasma arc spraying	Plasma arc	Powder	16,000	Metallic, ceramic, plastic and compounds	2–5
Low-pressure plasma spraying	Plasma arc	Powder	16,000	Metallic, ceramic, plastic and compounds	<5
Spray and fuse	–	Powder	–	Fusible metals	<0.5
Flame spraying	Oxyacetylene/oxy-hydrogen	Powder	3000	Metallic and ceramics	10–20
Detonation-gun spraying	Oxygen/acetylene/nitrogen gas detonation	Powder	4500	Metallic, ceramic, plastic and compounds	0.1–1
High-velocity oxy-fuel (HVOF)	Oxy-propylene/hydrogen/propane/LPG	Powder/ire	3000	Metallic and ceramic	0.1–2

twice higher than that of coarse coatings, representing "nano" coatings scientifically most usefully. Shaw et al. (2000) observed the reliance of microstructure and properties of nanostructure Al_2O_3–13 wt% TiO_2 coating by wear test. It has been observed that nanocoating performed better wear resistance than the coarse coatings. Ding et al. (2003) have conducted the wear resistance test for nanostructured zirconia coatings and coarse-grained zirconia coating by plasma-spray, coarse-grained coating shows much lesser wear resistance than their nanostructured zirconia coating. The greater properties of nanostructured coatings include improved microhardness and microstructure phases responsible for higher wear resistance.

Leblanc (2003) observed from commercial coarse-grained and nanostructured powders, he has assessed sliding wear, abrasion wear and microstructural properties of Al_2O_3–13TiO_2, Cr_2O_3–5SiO_2–3TiO_2 and TiO_2. Efficiency and features of VPS-deposited coatings are normally higher or equal to those of APS-deposited coatings. Thermal spray process for nanostructured powder coating is established to be more delicate, as compared to commercial coarse-grained powders. VPS delivers a better atmosphere for applying nanostructured coatings, as related to APS retained nanostructure in the applied coating shows the greater properties. Plasma spray produced reconstituted nanostructured alumina–titania coatings using improved processes with optimised plasma spray parameter (Jordan et al. 2001).

Kim et al. (2006) have magnificently obtained WC-Co wear-resistant nanostructured coatings by thermal spray process and the results showing substantial resistance wear when it is compared with conventional counterparts. Well-established nanostructured feedstock powder coating effectively resolved microstructural non-similarity of conventional Cr_2O_3-based solid lubricant coatings. The deposition of commercial coarse-grained and nanostructured zirconia coatings by atmospheric plasma spraying was tested for thermal shock resistance of as-sprayed coating by the water quenching method (Liang and Ding 2005). The outcomes exhibited that the nanostructured as-sprayed coating exhibited much improved thermal shock resistance than the commercial coarse-grained coating. This is due to the modification in microstructure and microstructural changes happening during thermal shock cycling. During the thermal shock cycle, the development of vertical cracks, inter-granular fracture and tetragonal monoclinic transformation on the coating surface contributed to the improved thermal shock resistance of the nanostructured zirconia coatings.

Soltani et al. (2003) have effectively deposited Y_2O_3–PSZ-nanostructured coatings. The results of wear test revealed that the nanostructured coating had a lower coefficient of friction and higher wear resistance under discontinuous testing conditions in comparison with commercial coarse-grained coatings. Lin et al. (2004) have examined that the effects of temperature between 600 °C and room temperature on the tribological properties of atmosphere plasma-sprayed nanostructured and commercial coarse-grained Al_2O_3–3 wt% TiO_2 coatings against silicon nitride ball were tested. The results revealed that wear resistance of the nanostructured coating was found better at high temperature as compared to their conventional counterpart.

7 Conclusions

1. Failure of different parts of gas turbine hot sections for ships, aircrafts, boilers, industrial waste incinerators is attributed because of high-temperature hot corrosion. For high-temperature applications, superalloys were developed, but they failed in meeting both requirements such as desired strength at high temperature and hot corrosion resistance at high temperature concurrently.
2. Thermal sprayed coatings seem to be an alternative and are extensively observed with respect to hot corrosion resistance. Hot corrosion is a serious problem and cannot be totally inhibited, but it can be identified at an initial stage to avoid disastrous failure.
3. An extensive research undertaken to assess the feasibility of various coatings in natural air environments, but additional research methods are required to test different types and combination of coating powders in more destructive corrosive atmospheres, either replicated in the laboratory or in real practical conditions.
4. While extensive perception has been collected on kinetics of hot corrosion, whereas, it has not been completely understood the reaction mechanism and further extensive analysis are required, further life of the coating has to be forecasted against hot corrosion behaviour in actual industrial environmental situations as well as by mathematical modelling which simulate the actual environment.
5. Investigators extensively tested several factors of different thermal spraying process. More ever, additional examinations need to optimise numerous coating process parameters, with distinct importance to estimate their performance of coating on hot corrosion behaviour.

References

Backman, R., Hupa, M., & Uppstu, E. (1987). Fouling and corrosion mechanisms in the recovery boiler superheater area. *Tappi Journal, 70*, 123–127.

Bansal, P., Padture, N. P., & Vasiliev, A. (2003). Improved interfacial properties of Al_2O_3–13 wt % TiO_2 plasma sprayed coatings derived from nanocrytalline powders. *Acta Materialia, 51*, 2959–2970.

Beltran, A. M., & Shores, D. A. (1972). Hot corrosion. In C. T. Sims & W. C. Hagel (Eds.), *Shores*. NY: Wiley Publ., John Wiley and Sons. (Chapter 11).

Bhushan, B., & Gupta, B. K. (1991). *Handbook of tribology: Materials, coatings and surface treatments*. New York: McGraw-Hill.

Bornstein, N. S., & DeCrescente, M. A. (1969). Relationship between compounds of sodium and sulfur and sulfidation. *Transactions of the Metallurgical Society of AIME, 245*(9), 1947.

Bornstein, N. S., DeCrescente, M. A., & Roth, H. A. (1973). The relationship between relative oxide ion content of Na_2SO_4, the presence of liquid metal oxides and sulfidation attack. *Metallurgical Transactions, 4*, 1799–1810.

Bornstein, N. S., Decrescente, M. A., & Roth, H. A. (1975). Effect of vanadium and sodium compounds on the accelerated oxidation of nickel base alloys. In: *Proceedings of the Conference on Gas Turbine Materials in the Marine Environment, MMIC-75–27* (pp. 115–160). Columbus, Ohio, USA.

Deb, D., Iyer, S. R., & Radhakrishnan, V. M. (1996). A comparative study of oxidation and hot corrosion of a cast nickel base superalloy in different corrosive environments. *Materials Letters, 29*, 19–23.

Ding, C., Chen, H., Liu, X., & Zeng, Y. (2003). Plasma sprayed nanostructure zirconia coatings for wear resistance. In C. Moreau & B. Marple (Eds.), *Thermal spray 2003: Advancing the science & applying the technology* (pp. 455–458). Materials Park, Ohio, USA: ASM International.

Eliaz, N., Shemesh, G., & Latanision, R. M. (2002). Hot corrosion in gas turbine components. *Engineering Failure Analysis, 9*, 31–43.

Fairman, L. (1962). Technical note: Mechanism of accelerated oxidation by vanadium-containing fuel ash. *Corrosion Science, 2*, 293–296.

Gitanjaly, Prakash, S., & Singh, S. (2002). Effects of MgO and CaO on hot corrosion of Fe base superalloy superfer 800H in Na_2SO_4–60 %V_2O_5 environment. *British Corrosion Journal, 37*(1), 56–62.

Gledhill, H. C., Turner, I. G., & Doyle, C. (1999). Direct morphological comparison of vacuum plasma sprayed and detonation gun sprayed hydroxyapatite coatings for orthopedic applications. *Biomaterials, 20*, 315–322.

Goebel, J. A., & Pettit, F. S. (1970a). Na_2SO_4-induced accelerated oxidation (hot corrosion) of nickel. *Metallurgical Transactions, 1*, 1943–1954.

Goebel, J. A., & Pettit, F. S. (1970b). The influence of sulphides on the oxidation behaviour of nickel-base alloys. *Metallurgical Transactions, 1*, 3421–3429.

Goebel, J. A., Pettit, F. S., & Goward, G. W. (1973). Mechanisms for the hot corrosion of nickel-base alloys. *Metallurgical Transactions, 4*, 261–275.

Guo, M. H., Wang, Q. M., Gong, J., Sun, C., Huang, R. F., & Wen, L. S. (2006). Oxidation and hot corrosion behavior of gradient NiCoCrAlYSiB coatings deposited by a combination of arc ion plating and magnetron sputtering techniques. *Corrosion Science, 48*, 2750–2764.

Gurrappa, I. (1999). Hot corrosion behavior of CM 247 LC alloy in Na_2SO_4 and NaCl environments. *Oxidation of Metals, 51*(5), 353–382.

Gurrappa, I. (2000). Hot corrosion of protective coatings. *Materials and Manufacturing Processes, 15*(5), 761–773.

Gurrappa, I. (2003). Influence of alloying elements on hot corrosion of superalloys and coatings: Necessity of smart coatings for gas turbine engines. *Journal of Materials Science and Technology, 19*(2), 178–183.

Hancock, P. (1987). Vanadic and chloride attack of superalloys. *Materials Science and Technology, 3*, 536–544.

Handbook, M. (1975). *Failure analysis and prevention* (Vol. 10). Metals Park OH, USA: ASM Publication.

Hao, D., Hua, W., Liu, J., Gong, J., Sun, C., & Wen, L. (2005). Influence of process variables on the qualities of detonation gun sprayed WC–Co coatings. *Materials Science and Engineering: A, 408*, 202–210.

Heath, G. R., Heimgartner, P., Irons, G., Miller, R., & Gustafsson, S. (1997). An assessment of thermal spray coating technologies for high temperature corrosion protection. *Materials Science Forum, 251–54*, 809–816.

Herman, H. (1988). Plasma sprayed coatings. *Scientific American, 259*(3), 78–83.

Hocking, M. G. (1993). Coatings resistant to erosive/corrosive and severe environments. *Surface and Coatings Technology, 62*, 460–466.

Hwang, Y. S., & Rapp, R. A. (1989). Thermochemistry and solubilities of oxides in sodium sulfate-vanadate solutions. *Corrosion, 45*(11), 933–937.

Iyer, S. R., Iyer, K. J. L., & Radhakrishan, V. M. (1987). High temperature corrosion of a Ni-base superalloy by Vanadium. In *Proceedings of the 10th ICMC* (Vol. IV, pp. 3665–3670) Madras, India.

Jordan, E. H., Gell, M., Sohn, Y. H., Goberman, D., Shaw, L., Jiang, S., et al. (2001). Fabrication and evaluation of plasma sprayed nanostructured alumina-titania coatings with superior properties. *Materials Science and Engineering: A, 301*, 80–89.

Kamachi Mudali, U., Bhuvaneswaran, N., Shankar, P., & Raj, Baldev. (2004). Corrosion behaviour of intermetallic aluminide coatings on nitrogen-containing austenitic stainless steels. *Corrosion Science, 46*, 2867–2892.

Kamal, S., Jayaganthan, R., & Prakash, S. (2009). Evaluation of cyclic hot corrosion behaviour of detonation gun sprayed Cr_3C_2–NiCr coating on nickel and iron based superalloys. *Surface and Coatings Technology, 203*(8), 1004–1013.

Kamal, S., Jayaganthan, R., & Prakash, S. (2010). Hot corrosion studies of detonation-gun-sprayed NiCrAlY + 0.4 wt%CeO_2 coatings on superalloys in molten salt environment. *Journal of Materials Engineering and Performance, 20*(6), 1068–1077.

Kamal, S., Jayaganthan, R., Prakash, S., & Kumar, Sanjay. (2008). Hot corrosion behavior of detonation gun sprayed Cr_3C_2–NiCr coatings on Ni and Fe-based superalloys in Na_2SO_4–60 % V_2O_5 environment at 900 °C. *Journal of Alloys and Compounds, 463*(1-2), 358–372.

Kawase, R., & Nakano, A. (1996). Production of heat and corrosion-resistant plastic coating. In *Proceedings of the 9th National Thermal Spray Conference* (pp. 257–262). Cincinnati, Ohio.

Kerby, R. C., & Wilson, J. R. (1972). Electrical conduction properties of liquid vanadates. II. The sodium. *Canadian Journal of Chemistry, 58*, 2871–2876.

Khajavi, M. R., & Shariat, M. H. (2004). Failure of first stage gas turbine blades. *Engineering Failure Analysis, 11*, 589–597.

Khana, A. S., & Jha, S. K. (1998). Degradation of materials under hot corrosion conditions. *Transactions of the Indian Institute of Metals, 51*(5), 279–290.

Kim, J.-H., Yang, H.-S., Baik, K.-H., Seong, B. G., Lee, C.-H., & Hwang, S. Y. (2006). Development and properties of nanostructured thermal spray coatings. *Current Applied Physics, 6*(6), 1002–1006.

Knotek, O. (2001). Thermal spraying and detonation spray gun processes. In R. F. Bunshah (Ed.) Handbook of hard coatings: Deposition technologies, properties and applications. Noyes Pub. Park Ridge, New Jersey, USA/William Andrew Publishing, LLC, Norwich, New York, USA (pp. 77–107) (Chapter 3).

Koch, G. H., Brongers, M. P. H., Thompson, N. G., Virmani, Y. P., & Payer, J. H. (2002). Historic congressional study: Corrosion costs and preventive strategies in the United States. Supplement to *Materials Performance*, 1–11.

Kofstad, P. (1988). *High temperature corrosion* (p. 465). London, New York: Elsevier Applied Science. (Chapter 14).

Kolta, G. A., Hewaidy, L. F., & Felix, N. S. (1972). Reactions between sodium sulphate and vanadium pentoxide. *Thermochimica Acta, 4*, 151–164.

Korpiola, K., & Vuoristo, P. (1996). Effect of HVOF gas velocity and fuel to oxygen ratio on the wear properties of tungsten carbide coating. In C. C. Bernt, (Ed.), Thermal spray: Practical solutions for engineering problems. Cincinnati, USA: ASM, October, 11–17.

Kuroda, S., Kawakita, J., Watanabe, Makoto., & Katanoda, Hiroshi. (2008). Topical review warm spraying—a novel coating process based on high-velocity impact of solid particles. *Science and Technology of Advanced Materials, 9*, 1–17.

Lambert, P., Champagne, B., & Arseneault, B. (1991). Oxidation and hot corrosion in Na_2SO_4—10 %V_2O_5 of Ni-17Cr-6Al-0.5Y and Ni-16Cr-5.7Al-0.47Y-5Si, MCrAlY Alloys at 7000 C. *Canadian Metallurgical Quarterly, 30*(2), 125–130.

Leblanc, L. (2003). Abrasion and sliding wear of nanostructured ceramic coatings. In C. Moreau & B. Marple (Eds.), *Thermal spray 2003: Advancing the science & applying the technology* (pp. 291–299). Materials Park, Ohio, USA: ASM International.

Li, Y. S., Spiegel, M., & Shimada, S. (2005). Corrosion behaviour of various model alloys With NaCl–KCl coating. *Materials Chemistry and Physics, 93*, 217–223.

Liang, Bo., & Ding, Chuanxian. (2005). Thermal shock resistances of nanostructured and conventional zirconia coatings deposited by atmospheric plasma spraying. *Surface and Coatings Technology, 197*, 185–192.

Lin, Xinhua., Zeng, Yi., Ding, Chuanxian., & Zhang, Pingyu. (2004). Effects of temperature on tribological properties of nanostructured and conventional Al_2O_3–3 wt% TiO_2 coatings. *Wear, 256*, 1018–1025.

Liu, P. S., Liang, K. M., Zhou, H. Y., Gu, S. R., Sun, X. F., Guan, H. R., et al. (2001). Cyclic oxidation behavior of aluminide coatings on the Co-base superalloy DZ40M. *Surface and Coatings Technology, 145*, 75–79.

Luthra, K. L., & Shores, D. A. (1980). Mechanism of Na_2SO_4 induced corrosion at 600–900 °C. *Journal of the Electrochemical Society, 127*(10), 2202–2210.

Maledi, N. B., Potgieter, J. H., Sephton, M., Cornish, L. A., Chown, L., & Suss, R. (2006). *Hot corrosion behaviour of Pt-alloys for application in the next generation of gas turbines*. International Platinum Conference 'Platinum Surges Ahead', the Southern African Institute of Mining and Metallurgy (pp. 81–90).

Marceau, J. A., & Adjorlolo, A. A. (1995). Commercial aircraft. In ASM, *Corrosion tests and standards*; *application and interpretation* (pp. 574–578). American Society for Testing and Material Society.

Matthews S. J. (2004). Erosion-corrosion of Cr_3C_2–NiCr high velocity thermal spray coatings (Ph. D. thesis). The University of Auckland.

Mevrel, R. (1989). State of the art on high-temperature corrosion-resistant coatings. *Materials Science and Engineering: A, 120*, 13–24.

Misra, A. K. (1986). Mechanism of Na_2SO_4-induced corrosion of molybdenum containing nickel-base superalloys at high temperatures. *Journal of the Electrochemical Society, 133*(5), 1029–1037.

Moujahid, S. E. (1987). High temperature corrosion of cast iron chains by Coal Ash. In *Proceedings of the 10th ICMC* (Vol. I, pp. 857–860). Madras, India.

Murthy, J. K. N., & Venkataraman, B. (2006). Abrasive wear behaviour of WC–CoCr and Cr_3C_2–20(NiCr) deposited by HVOF and detonation spray processes. *Surface and Coatings Technology, 200*, 2642–2652.

Natesan, K. (1985). High-temperature corrosion in coal gasification systems. *Corrosion, 41*(11), 646–655.

National Materials Advisory Board. (1996). *Coatings for high-temperature structural materials: Trends and opportunities* (pp. 1–85). Washington, DC: National Academy Press. http://www.nap.edu/openbook/0309053811/html

Nelson, H. W., Krause, H. H., Ungar, E. W., Putnam, A. A., Slunder, C. J., Miller, P. D., et al. (1959). A review of available information on, corrosion and deposits in coal- and oil-fired boilers and gas turbines. *Report of ASME research committee on corrosion and deposits from combustion gases*. New York: Pergamon Press, ASME.

Nerz, J. E., Kushner B. A., Jr., & Rotolico, A. J. (1992). Microstructural evaluation of tungsten carbide-cobalt coatings. *ASM International* (*USA*) (pp. 115–120).

Nicholls, J. R. (2000). Designing oxidation-resistant coatings. *JOM*, *52*, 28–35.

Nicholls, J. R., Simms, N. J., Chan, W. Y., & Evans, H. E. (2002). Smart overlay coatings—concept and practice. *Surface and Coatings Technology, 149*, 236–244.

Nickel, H., Quadakkers, W. J., & Singheiser, L. (2002). Analysis of corrosion layers on protective coatings and high temperature materials in simulated service environments of modern power plants using SNMS, SIMS, SEM, TEM, RBS and X-ray diffraction strudies. *Analytical and Bioanalytical Chemistry, 374*, 581–587.

Nicoll, A. R. (1984). The production and performance evaluation of high temperature coatings. In K. N. Strafford, P. K. Datta, & C. G. Googan (Eds.), *Coatings and surface treatment for corrosion and wear resistance*. Chichester: Institution of Corros. Sci. and Techol., Birmingham, Pub. Ellis Horwood Ltd. (Chapter 13).

Otero, E., Merino, M. C., Pardo, A., Biezma, M. V., & Buitrago, G. (1987). Study on corrosion products of IN657 alloy in molten salts. In *Proceedings of 10th ICMC* (Vol. IV, pp. 3583–3591). Madras, India.

Otero, E., Pardo, A., Hernaez, J., & Perez, F. J. (1990). The hot corrosion of IN-657 superalloy in Na_2SO_4–V_2O_5 melt eutectic. *Corrosion Science, 30*, 677–683.

Otsuka, N., & Rapp, R. A. (1990). Effects of chromate and vanadate anions on the hot corrosion of pre oxidized Ni by a thin fused Na_2SO_4 film at 900 °C. *Journal of the Electrochemical Society, 137*(1), 53–60.

Pettit, F. (2011). Hot corrosion of metals and alloys. *Oxidation of Metals, 76*, 1–21.

Pettit, F. S., & Giggins, C. S. (1987). Hot corrosion. In C. T. Sims, N. S. Stollof, & W. C. Hagel (Eds.), *Superalloys II*. N Y: Pub. Wiley Pub. (Chapter 12).

Pettit, F. S., & Meier, G. H. (1985). Oxidation and hot corrosion of superalloys. In M. Gell, C. S. Kartovich, R. H. Bricknel, W. B. Kent & J. F. Radovich (Eds.), *Superalloys 85* (pp. 651–687). Warrendale, Pennsylvania: Met. Soc. of AIME.

Porcayo-Calderon, J., Gonzalez-Rodriguez, J. G., & Martinez, L. (1998). Protection of carbon steel against hot corrosion using thermal spray Si- and Cr-base coatings. *Journal of Materials Engineering and Performance, 7*, 79–87.

Gitanjaly, & Prakash, S. (1999). Review on effect of additives on the hot corrosion. In *5th NACE Proceedings* (pp. 174-182). New Delhi, India, November 22–24.

Prakash, S., Puri, D., & Singh, H. (2005). Hot corrosion behaviour of plasma sprayed coating on Ni-based superalloys in Na_2SO_4–60 $\%V_2O_5$ environment. *ISIJ International, 45*(6), 886–895.

Prakash, S., Singh, S., Sidhu, B. S., & Madeshia, A. (2001). Tube failures in coal fired boilers. In *Proceedings of the National Seminar on Advances in Material and Processing* (pp. 245–253) IITR, Roorkee, India, November 9–10.

Priyantha, N., Jayaweera, P., Sanjurjo, A., Lau, K., Lu, F., & Krist, K. (2003). Corrosion-resistant metallic coatings for applications in highly aggressive environments. *Surface and Coatings Technology, 163–64*, 31–36.

Rapp, R. A. (2002). Hot corrosion of materials: A fluxing mechanism. *Corrosion Science, 44*(2), 209–221.

Rapp, R. A., & Goto, K. S. (1981). The hot corrosion of metals by Molten Salts. In J. Braunstein & J. R. Selman (Eds.), *Sympos. fused salts* (pp. 159). Pennington, NJ: The Electrochemical Society.

Rapp, R. A., & Mehl, Robert. F. (2000). Some generalities in the analyses of equilibria in lonic solutions. *Metallurgical and Materials Transactions A, 31*(9), 2105–2118.

Ravindra, T., Raghavan, S., & Kamaraj, M. (2007). Hot corrosion and oxidation behaviour of a directionally solidified nickel base superalloy. *Transactions of the Indian Institute of Metals, 60*, 385–392.

Ren, X., & Wang, F. (2006). High-temperature oxidation and hot-corrosion behavior of a sputtered NiCrAlY coating with and without aluminizing. *Surface and Coatings Technology, 201*, 30–37.

Salmenoja, K., Makela, K., Hupa, M., & Backman, R. (1996). Superheater corrosion in environments containing potassium and chlorine. *Journal of the Institute of Energy, 69*, 155–162.

Saravanan, P., Selvarajan, V., Rao, D. S., Joshi, S. V., & Sundararajan, G. (2000). Influence of process variables on the quality of detonation gun sprayed alumina coatings. *Surface and Coatings Technology, 123*, 44–54.

Seiersten, M., & Kofstad, P. (1987). The effect of SO_3 on vanadate-induced hot corrosion. *High Temperature Technology, 5*(3), 115–122.

Seybolt, A. U. (1968). Hot corrosion mechanism. *Transactions of the Metallurgical Society of AIME, 242*, 1955–1961.

Sharma, R. N. (1996). *Hot corrosion behaviour of iron- and nickel-base superalloys in salt environments at elevated temperatures* (Ph.D. thesis). Met. Mat. Engg. Deptt., University of Roorkee, Roorkee, India.

Shaw, L. L., Goberman, D., Ren, R., Gell, M., Jiang, S., Wang, Y., et al. (2000). The dependency of microstructure and properties of nanostructured coatings on plasma spray conditions. *Surface and Coatings Technology, 130*, 1–8.

Shi, L., Zhang, Y., & Shih, S. (1992). The effect of K_2SO_4 additive in Na_2SO_4 deposits on low temperature hot corrosion of iron-aluminum alloys. *Oxidation of Metals, 38*, 385–405.

Shih, S., Zhang, Y., & Li, X. (1989). Sub-melting point hot corrosion of alloys and coatings. *Materials Science and Engineering A, 120*, 277–282.

Sidhu, T. S., Prakash, S., & Agrawal, R. D. (2006a). Performance of high velocity oxy fuel—sprayed coating on an Fe-based superalloy in Na_2SO_4–60 % V_2O_5 environment at 900 °C part II: Hot corrosion behaviour of coating. *Journal of Materials Engineering and Performance, 15*, 130–138.

Sidhu, T. S., Prakash, S., & Agrawal, R. D. (2006b). Hot corrosion studies of HVOF sprayed Cr_3C_2–NiCr and Ni–20Cr coatings on nickel-based superalloy at 900 °C. *Surface and Coatings Technology, 201*(3-4), 792–800.

Sidhu, T. S., Prakash, S., & Agrawal, R. D. (2006c). Hot corrosion studies of HVOF NiCrBSi and stellite-6 coatings on a Ni-based superalloy in an actual industrial environment of a coal fired boiler. *Surface and Coatings Technology, 201*(3/4), 1602–1612.

Sidhu, T. S., Prakash, S., & Agrawal, R. D. (2006d). Characterisation of NiCr wire coatings on Ni- and Fe-based superalloys by the HVOF process. *Surface and Coatings Technology, 200*, 5542–5549.

Sidhu, T. S., Prakash, S., & Agrawal, R. D. (2006e). Studies of the metallurgical and mechanical properties of high velocity oxy-fuel sprayed stellite-6 coatings on Ni- and Fe-based superalloys. *Surface and Coatings Technology, 201*(1/2), 273–281.

Sidhu, H. S., Sidhu, B. S., & Prakash, S. (2006f). The role of HVOF coatings in improving hot corrosion resistance of ASTM-SA210 GrA1 steel in the presence of Na_2SO_4–V_2O_5 salt deposits. *Surface and Coatings Technology, 200*, 5386–5394.

Sidky, P. S., & Hocking, M. G. (1999). Review of inorganic coatings and coating processes for reducing wear and corrosion. *British Corrosion Journal, 34*(3), 171–183.

Simons, E. L., Browning, G. V., & Liebhatsky, H. A. (1955). *Corrosion, 11*, 505.

Singh, H., Puri, D., & Prakash, S. (2005a). Some studies on hot corrosion performance of plasma sprayed coatings on a Fe-based superalloy. *Surface and Coatings Technology, 192*(1), 27–38.

Singh, H., Puri, D., & Prakash, S. (2005b). Corrosion behaviour of plasma sprayed coating on Ni-based superalloys in Na_2SO_4–60%V_2O_5 environment at 900 °C. *ISIJ International, 45*(6), 886–895.

Sobolev, V.V., Guilemany, J.M., & Nutting, J. (2004). HVOF spraying. *B0655*, *Maney*, *IOM3* (pp. 5).

Soltani, R., Coyle, T. W., & Mostaghimi, J. (2003). Wear resistance of nanostructured thermal barrier coatings. In C. Moreau & B. Marple (Eds.), *Thermal spray 2003: Advancing the science & applying the technology* (pp. 1535–1540). Materials Park, Ohio, USA: ASM International.

Stokes, J., & Looney, L. (2001). HVOF system definition to maximise the thickness of formed components. *Surface and Coatings Technology, 148*, 18–24.

Stott, F. H., De Wet, D. J., & Taylor, R. (1994). The degradation resistance of thermal barrier coatings to molten deposits at very high temperatures. *Transactions of the Materials Research Society of Japan, 14A*, 135–140.

Stringer, J. (1977). Hot corrosion of high temperature alloys. *Annual Review of Materials Research, 7*, 477–509.

Stringer, J. (1987). High temperature corrosion of superalloys. *Materials Science and Technology, 3*(7), 482–493.

Stringer, J. (1998). Coatings in the electricity supply industry: past, present, and opportunities for the future. *Surface and Coatings Technology, 108–109*, 1–9.

Stroosnijder, M. F., Mevrel, R., & Bennet, M. J. (1994). The interaction of surface engineering and high temperature corrosion protection. *Materials at High Temperatures, 12*(1), 53–66.

Suito, H., & Gaskell, D. R. (1971). The thermodynamics of melts in the system VO_2–V_2O_5. *Metallurgical and Materials Transactions B, 2*, 3299–3303.

Taylor, M. P., & Evans, H. E. (2001). The influence of bond coat surface roughness and structure on the oxidation of a thermal barrier coating system. *Materials Science Forum, 369–372*, 711–717.

Tiwari, S. N. (1997). Investigations on hot corrosion of some Fe-, Ni- and Co-base superalloy in Na_2SO_4–V_2O_5 environment under cyclic conditions (Ph.D. thesis). Met. Mat. Engg. Deptt., University of Roorkee, Roorkee, India.

Tiwari, S. N., & Prakash, S. (1996). Hot corrosion behaviour of an iron-base superalloy in salt environment at elevated temperatures. In *Proceedings of the Symposium Metals and Materials Research, Indian Institute of Technology Madras* (pp. 107–117) Madras, July 4–5.

Tiwari, S. N., & Prakash, S. (1997). Studies on the hot corrosion behaviour of some superalloys in Na_2SO_4–V_2O_5. In *Proceedings of the SOLCEC*, Kalpakkam, India, January 22–24, Paper C33.

Tiwari, S. N., & Prakash, S. (1998). Literature review-magnesium oxide as inhibitor of hot oil ash corrosion. *Materials Science and Technology, 14*, 467–472.

Tzvetkoff, T., & Gencheva, P. (2003). Mechanism of formation of corrosion layers on nickel and nickel-based alloys in melts containing Ox anions—A review. *Materials Chemistry and Physics, 82*(3), 897–904.

Uusitalo, M. A., Vuoristo, P. M. J., & Mantyla, T. A. (2004). High temperature corrosion of coatings and boiler steels below chlorine-containing salt deposits. *Corrosion Science, 46*(6), 1311–1331.

Valdes, C. J., Dooley, R. B., & Wilson, J. R. (1973). *The corrosion of A.I.S.I 446 stainless steel in Molten Vanadates in the temperature range 700–900 °C* (Grant No. 7535-14). Report Defense Research Board Canada.

Wagner, N., Gnadic, K., Kreye, H., & Kronewetter, H. (1984). Particle velocity in hypersonic flame spraying of WC-Co. *Surface and Coatings Technology, 22*, 61–71.

Wang, Q. M., Wu, Y. N., Ke, P. L., Cao, H. T., Gong, J., Sun, C., et al. (2004). Hot corrosion behavior of AIP NiCoCrAlY(SiB) coatings on nickel base superalloys. *Surface and Coatings Technology, 86*, 389–397.

Yoshiba, M. (1993). Effect of hot corrosion on the mechanical performances of superalloys and coating systems. *Corrosion Science, 35*(5–8), 1115–1124.

Zhang, Y. S., & Rapp, R. A. (1987). Solubilities of CeO_2, HfO_2 and $Y2O_3$ in fused Na_2SO_4–30 mol% $NaVO_3$ and CeO_2 in pure Na_2SO_4 at 900 °C. *Corrosion, 43*(6), 348–352.

Zheng, D., Zhu, S., & Wang, F. (2006). Oxidation and hot corrosion behavior of a novel enamel-Al_2O_3 composite coating on K38G superalloy. *Surface and Coatings Technology, 200*, 5931–5936.

Application of Nanotechnology in Cancer Treatment

Biswa Mohan Biswal and Zamzida Yusoff

Abstract Cancer is one of the most common chronic diseases in man that accounts for 14 million new cancer cases and 8 million deaths per year worldwide. The current trend in the management of cancer includes established triad of surgery, radiation, and chemotherapy supplemented by biological and targeted therapy in specific cancers. Recent years saw tremendous progress in the field of biotechnology and human genomics leading to better understanding about cancer pathogenesis, discovery of cancer markers, and promising novel therapy. Despite above advances, the surgery involves loss of organ and function, radiation-induced complications, and chemotherapy-related second malignancies and drug resistance. In some cancers, both radiotherapy and chemotherapy remain ineffective. In recent years, nanotechnology shows potential promise in the management of cancer. Nanoparticles attached to cancer marker targeted antibodies could detect cancer at earlier phases of cancer development, better than existing methods. Novel designed nanomaterials could carry payload of cytotoxic drugs or lethal toxins inside cancer cells and defy host immune defence and protect normal cells, thereby could result in cancer cure with least side effects. Radiation treatment is non-specific; therefore, intratumour injection of nanomaterials could generate short-range electrons inside tumour and enhance radiation lethality to tumour and no effects to the normal tissues. Topical or parenteral injection of nanomaterials during surgical procedure could add surgeons to precisely take out tumour with useful surgical margin. Nanotechnology is a vast field of unexplored science which is unknown to medical field could possibly redefine cancer treatment. However, we do not know the long-term consequences, metabolism of nanoparticles inside body, excretion from body fluids, safety profile, and environmental effects. Despite of extensive hype in science for over a decade, there are very few nanotechnology-based drugs used in clinical practice, mostly using PEG micelle technology to avoid immune reactions and increased absorption of cancer pain medications. Lot more translational clinical

B.M. Biswal (✉) · Z. Yusoff
KPJ Ipoh Specialist Hospital, 26 Jalan Raja Dihilir, 30350 Ipoh, Perak, Malaysia
e-mail: biswal.usm@gmail.com

Z. Yusoff
e-mail: yzamzida@gmail.com

K. Viswanatha Sharma and N. Hisham B Hamid (eds.),
Engineering Applications of Nanotechnology, Topics in Mining, Metallurgy and Materials Engineering, DOI 10.1007/978-3-319-29761-3_11

research is necessary to use nanotechnology as part of oncological management in future.

Keywords Nanotechnology · Cancer · Nanoparticles · Imaging · Pathology · Surgery · Radiotherapy · Chemotherapy

Abbreviations

TSP	Thrombospondin
VEGF	Vascular endothelial growth factor
VEGFR	Vascular endothelial growth factor receptor
EGFR	Epidermoid growth factor receptor
HER-2	Human epidermal receptor-2
TKI	Tyrosine kinase inhibitor
DNA	Deoxyribonucleic acid
RNA	Ribonucleic acid
2D	Two dimensional
CT	Computer axial
MRI	Magnetic resonance imaging
PET	Positron emission tomography
AFM	Atomic force microscopy
QDs	Quantum dots
GNP	Gold nanoparticles
SPR	Surface plasma resonance
SWCNT	Single-walled carbon nanotubes
SPIONs	Superparamagnetic iron oxide nanoparticles
PEG	Polyglycolic acid
USPIO	Ultrasuperparamagnetic iron oxide
NPs	Nanoparticles
USG	Ultrasound
PAMAm	Polyamidoamine
GCC	Guanylyl cyclase C
CCD	Charge-coupled device
SLNB	Sentinel lymph node biopsy
MNP	Magnetic nanoparticle
EPR	Enhanced permeability retention
IMRT	Intensity-modulated radiotherapy
CNT	Carbon nanotube
PSA	Prostate-specific antigen
CEA	Carcinoembryonic antigen
CA 125	Cancer antigen 125
AFP	Alfa feto protein
LDH	Lactate dehydrogenase
VMA	Vanillylmandelic acid
HVA	Homovanillic acid

Tc-kit	Tyrosine protein kinase
Tg	Thyroglobulin
ALK	Anaplastic lymphoma kinase
BRAF	Murine sarcoma viral oncogene homolog B
K-ras	Kirsten rat sarcoma viral oncogene homolog
MEK	Ras–Raf–MEK–ERK pathway
NHL	Non-Hodgkin's lymphoma
GIST	Gastrointestinal stromal sarcoma
CML	Chronic myeloid leukaemia
IV	Intravenous
SC	Subcutaneous
CND	Composite nanodevice
SPARC	Second albumin-specific protein
AIDS	Acquired immune deficiency syndrome
GTN	Gestational trophoblastic neoplasm
TAM	Tumour-associated macrophage
QD	Quantum dots
OTFC	Oral transmucosal fentanyl citrate
HIF	Hypoxia-inducible factor
NSCLC	Non-small-cell lung cancer
PD-L1	Programmed death-ligand 1
p53	Tumour protein p53 (tumour suppressor)
FISH	Fluorescence in situ hybridization
IHC	Immunohistochemistry
MBC	Metastatic breast cancer
CYFRA-21-1	Cytokeratin 19 fragment
CRC	Colorectal cancer
HIV	Human immunodeficiency virus
SE	Spin echo

1 Introduction

Cancer is a generic terminology representing 100s of disease with diverse biological behaviour. Accumulation of cellular and genetic injuries could lead to cancer transformation from a single cell called clonal origin of cancer. Cancer could be caused by exposure to carcinogens, radiation, smoking, oncogenic viruses, and mechanical friction, and expression of genetic defect already exists inside the host cells. The carcinogens could be from tobacco smoking; carcinogenic chemicals are in diet, in polluted air, and from accumulation of carcinogens from chemical industries. The carcinogens in the presence of cocarcinogens transform normal cells into a malignant one through stepwise carcinogenic process. The transformed

cancer cells need many generations of growth to become a visible tumour (Fig. 1). The tumour then grows exponentially to reach its plateau. If left untreated, the large size tumour ultimately consumes most nutrition of the host leading to death of tumour-bearing patient. The above growth pattern of cancer is called Gompertzian growth (Schmidt 2004).

The tumour has six biological characteristics or capabilities acquired during multistep development of human tumour. The malignant changes represented as sustained cellular signalling defy growth suppressors, resist tumour cell death (or apoptosis), acquire replicative tumour immortality, induce angiogenesis, and encourage invasion and metastases (Hanahan and Weinberg 2011). The other characteristics of cancer are genomic instability, inflammation, reprogramming energy metabolism, and evading immune destruction. Ultimately, tumour growth could change tumour microenvironment. Recently, 4-new hallmarks of cancer are added as avoiding tumour immune destruction, tumour-promoting inflammation, genome instability, and disregulation of cellular energy. Further progress of tumour due to proliferation acquires new blood vessel supply (neoangiogenesis). The tumour neoangiogenesis is switched on and switched off by tumour factor called vascular endothelial growth factor A (VEGF-A) and thrombospondin-1 (TSP-1). The VEGF signalling via 3 receptor tyrosine kinase (VEGFR 1–3) is regulated at multiple steps. The VEGF gene expression can be upregulated by tissue hypoxia and oncogene signalling. Any new tumour acquiring a size more than 200 μ always

Fig. 1 Clinical picture of a proliferative squamous cell carcinoma cancer of cheek

has tumour neovasculature. These steps of cancer growth could be targeted using specific inhibitors for the control of cancer (Fig. 2). A tumour is a combination of many events ranging from aberrant cell formation, clonal proliferation, angiogenesis, immune response, and metastasis. Thus, cancer involves complex multiple heterotypic interactions such as stromal influence on growth, progression, and metastasis (Lorusso and Ruegg 2008; Thakor and Gambhir 2013). The above event leads to angiogenesis, inflammation, invasion, and immune response including cytokine production and maintenance of cancer stem cell. The above tumour microenvironment process has been adopted to develop chemoprevention and therapeutic strategies including incorporation of nanotechnology (Fig. 3).

Tumour neovasculature is made in haste, so they are irregular and leaky. The unique characteristics of tumour vasculature are aberrant structural dynamics, immature, tortuous, and hyperpermeable. The complex tumour vasculature is typically disorganized labyrinth of vessels with lack of conventional blood vessel hierarchy in which arterioles, capillaries, and venules are not clearly identifiable. Modern cancer treatments take advantage of such architecture to direct treatment for eradication of cancer.

Growing tumours slowly permeate through lymphatic channels and deposit cancer cells inside lymph nodes. Similarly, invasion through blood vessels leads to migration of dislodged cancer cells through bloodstream to distant host organs namely liver, lungs, brain, bone, and other sites called metastasis. Distant metastasis

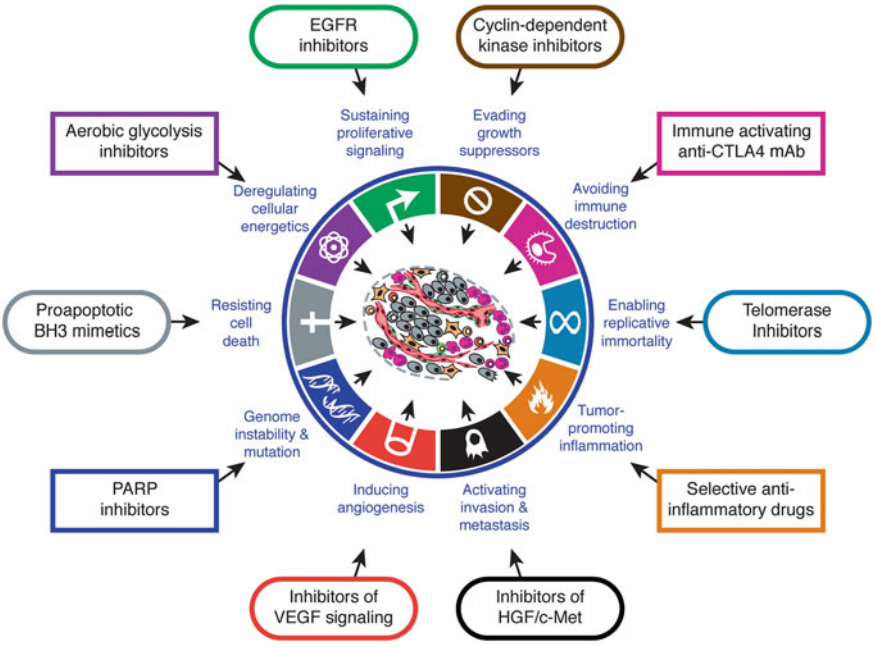

Fig. 2 Hallmarks of cancer. Reproduced with the permission from Hanahan and Weinberg (2011)

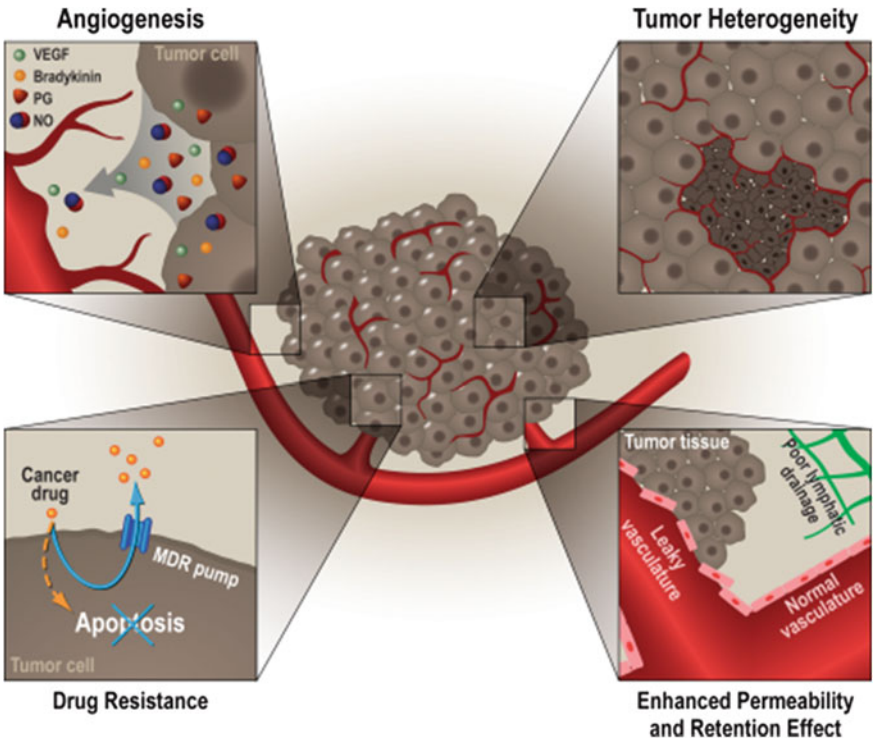

Fig. 3 Tumour host interaction, Reproduced with the permission from Thakor and Gambhir (2013)

is a multistep process which involves formation of new clone of cells with invasiveness and metastatic ability due to the accumulation of genetic aberration (Yokota 2000). The detached cancer cells get attached to proteinaceous matrix and float inside blood vessels and then travel to distant organs and arrest in capillary system. Then, the migrated cells traverse capillary wall and enter the foreign tissue. In secondary site, the tumour grows and causes cancer symptoms. Many cancers exhibit cancer-specific antigens called tumour markers. These markers are responsible for tumour proliferation, apoptosis, angiogenesis, invasiveness, and metastasis. Epidermal growth factor receptor (EGFR) is a family of tumour markers that present ubiquitously in many cancers including skin cells and epithelial lining cells. In wild state, EGFR does not cause cancer; however, in the presence of driver or sensitive mutation, the cells show enhanced proliferation, angiogenesis, aggressiveness, metastasis, and invasiveness. These mutated EGFR genes are present in 15 % of non-small-cell lung cancers in West (Boch et al. 2013). However, interestingly in Asia, these genes show sensitive mutation among almost half of non-small-cell lung cancer patients. Inhibition and/or interference of this pathway either at intracellular or at extracellular domain of EGFR could result in

arrest of tumour growth and progression. Tyrosine kinase inhibitors are routinely advocated to EGFR-mutated lung cancer patients for improvement in quality of life, local tumour control, and survival. Similarly, human epidermal receptor-2 (HER-2) genes are amplified in 20–30 % of women with breast cancer (Menard et al. 2001). Existence of HER-2 gene overexpression could predict poor prognosis and disease progression. Current anti-HER-2 treatment (Herceptin) in HER-2 overexpressed breast cancer patients improves therapy outcome among above subgroup of breast cancer patients. Besides breast cancer and lung cancer, there are numerous tumour-specific cancer markers being routinely used as diagnosis, prognostication, therapy monitoring, and tumour-directed-specific therapy. The followings are tumour-specific markers (Table 1).

Table 1 Clinically useful tumour markers for implication in cancer nanotechnology

Tumour marker	Abbreviation	Normal value	Tumour site	Remarks
Carcinoembryonic antigen	CEA	0–2.5 ng/mL	Colorectal	Non-specific, helpful for surveillance
Prostate-specific antigen	PSA	4.0 ng/mL	Prostate cancer	Diagnosis, follow-up
Cancer antigen 125	CA 125	<35 U/mL	Ovarian cancer	Surveillance
Cancer antigen 19.9	CA 19.9	0–37 U/mL	Pancreatic cancer	Useful for follow-up
Alfa feto protein	AFP	Male 0–40 ng/mL Female 10–150 ng/mL	Germ cell tumour, Hepatoma	Prognosis and monitoring
Beta HCG	β-HCG	0.8 IU/L	Germ cell tumour Gestational tumour	For prognosis and follow-up
CD 20	CD 20	2700–115,000 MESF molecules of equivalent soluble fluorochrome	B cell NHL	Useful for determination therapy
Lactate dehydrogenase	LDH	140–280 U/L	Bulky lymphoma, GCT	Useful in follow-up surveillance
Oncotype DX	OncotypeDX	21 gene assay give recurrence score from 0 to 100	Early breast cancer	Useful in early breast cancer
Mast stem cell growth factor receptor; C-KIT	c-Kit	50–90 % positive in GIST	CML/GIST	Useful as tumour marker for diagnosis
Pepsinogen	Pepsinogen	Pepsinogen I/II ratio	Cancer stomach	Useful in follow-up

(continued)

Table 1 (continued)

Tumour marker	Abbreviation	Normal value	Tumour site	Remarks
Vimentin	VMA/HVA	10–50 % positive	Neuroblastoma	For treatment response
Thyroglobulin	Tg	3–40 ng/mL	Thyroid cancer	For surveillance and monitoring
Cytokeratin fragment	CYFRA-21–1	30 % of stage I lung cancer	Lung cancer	Surveillance
Neurone-specific enolase	NSE	70 % of small cell lung cancer	Small cell lung cancer	Diagnostic
Epidermoid growth factor receptor	EGFR	10–50 % adenocarcinoma sensitizing mutation	Lung cancer (NSCLC)	Exon 19/21 driver mutation
Anaplastic lymphoma kinase	ALK	3–5 % gene rearrangement in adenocarcinoma	Lung cancer (NSCLC)	Fusion gene suggest response to crizotinib
BRAF protooncogene	BRAF V600	50 % of melanoma	Melanoma	Implication in therapy
Kirsten rat sarcoma gene	Kras	30 % of NSCLC	Lung and colorectal	Kras mutation worse prognosis in lung cancer
Programmed death receptor ligand	PD L1	5–50 % tumours	Melanoma, lungs, breast, brain tumours	Positive marker status predicts better response to immunotherapy
Mitogen-activated protein kinase	MEK	1 % of NSCLC	Lung cancer	Clinical trial no

NSCLC non-small-cell lung cancer, *CML* chronic myeloid leukaemia, *GIST* gastrointestinal stromal tumour, *GCT* germ cell tumour, *NHL* non-Hodgkin's lymphoma

1.1 Diagnosis in Cancer

The diagnosis of cancer is heavily dependent on cellular morphological feature as tissue diagnosis. The most common method of cancer diagnosis is based on microscopic tissue morphology from biopsy or tumour removed during surgery. Cells from fine-needle aspiration and other body fluids could also provide tissue diagnosis using cytological evaluation by an experienced cytopathologist. Histopathology evaluation using haematoxylin and eosin-stained histomorphology is being supplemented by immunohistochemistry and ultrastructure feature by electron microscopy. The above findings help in the decision-making for the treatment in the multidisciplinary management of cancer. Current addition of molecular, genetic, and proteomic investigations explores further dimension to cancer diagnosis. Sampling error from critical anatomical sites could pose problem for obtaining tissue for a possible tissue diagnosis. In complicated malignancies such as sarcomas and haematological malignancies, it takes a very long time to

arrive at a conclusive diagnosis. Current attempt to harvest cancer cells from circulating tumour cells from blood using liquid biopsy and next-generation gene sequencing helps in diagnosis without doing actual invasive procedure to obtain tissue (Karachaliou et al. 2015). The liquid biopsy is being slowly incorporated in the clinics for diagnosis, prognostication, and management of cancer. However, the yield of tissue and genetic fragments (DNA, RNA) are not consistent in all cancers. Therefore, sensitivity and specificity vary widely among different cancers. So far, EGFR mutation test and identification of TKI-resistant mutation in lung cancers are being clinically useful using liquid biopsy technique pending conformation of data from other cancers in future. Liquid biopsy is especially useful where obtaining tissue material using invasive technique is difficult. Current molecular and genetic tests are very time–consuming and therefore need new generation of tests for large-scale and low-cost investigation to detect plausible cancer driver mutations in cancer. Nanotechnology platforms are newer players in oncology field that could be more sensitive and cost-effective and handle large volume of patient materials in short time. Nanotechnology could take advantage of unique tumour architecture, vascularity, antigenicity, tumour biomarkers, and microenvironment for therapy and monitoring of cancer (Table 2).

Table 2 Implications of cancer characteristics for nanooncology

Characteristics	Features	Inference	Therapeutic implications
Tumour hypoxia	Low oxygen-induced HIF	More angiogenesis	Hypoxia-specific agent could be targeted
Tumour acidity	High LDH activity (Tannock 1989)	Anaerobic metabolism	Acid environment could be targeted
Leaky blood vessels	VEGFR	Defective proliferation of blood and lymphatic vessels	Nanomaterials can escape from blood vessels and concentrate inside tumour
Differential temperature	Higher metabolism in tumour	Temperature at 43° could enhance cell kill	Hyperthermia with radiation and chemotherapy enhance cell kill
Tumour-specific antigens	HER-2, CD20, EGFR, VEGFR	Specific for certain tumours (DuPage et al. 2012)	Targeting above markers could deliver payload of drugs directly to cancer cells
Concentration (EPR effect)	Nanoparticles internalize to cancer cells	More concentration of nanoparticles compared to extracellular space	Influence specific damage to cancers
Interstitial tumour fluid flow	Fluid pressure could encourage tumour invasion	Interstitial flow has promigratory effect on tumour (Muson and Scieh 2014)	Intervention at this level could prevent metastatic spread

1.2 Drawback in Current Tumour Imaging

The diagnosis and evaluation of cancer patients involve a battery of radiological investigations. Cancer imaging is based on classical 2D X-rays, ultrasound, CT scan, MRI scan, angiograms, radionuclide imaging, venograms, and PET scans. All above imaging modalities are useful for localization, estimation of extent of tumour, measurement of size, shape, and their relation to other structures, metastatic extent, and thus staging. Each modality has got its own pros and cons in terms of specificity and sensitivity. The most popular molecular imaging using CT-PET scan could not distinguish infection, inflammation, and malignant lesions. The existing imaging modalities cannot be able to detect tumours less than certain size and tumour margin. Therefore, there is a need for improvement to detect cancer before it is visible in standard imaging techniques. Existing mammograms for breast cancer, low-dose CT scan for lung cancer, and virtual endoscopy for colorectal cancer are not robust enough to detect all cancers. Nanoparticles tagged with tumour ligands as a contrast could detect cancers at earliest phases of their development, thus could assist in cancer prevention in future (Toy et al. 2014).

2 Nanotechnology

Nanotechnology is a fast growing field of science rapidly entering into medical science. Nanotechnology is defined as the application science, engineering, and technology conducted at the nanoscale using materials of size ranging from 1 to 100 nm. American physicist Dr. Richard Feynman for the first time introduced term nanoscience in his presentation on "There is plenty of room in the bottom" on December 29, 1959, at the American Physical Society conference held in California Institute of Technology (Appenzeller 1991). However, the terminology nanotechnology was introduced by Japanese physicist Prof Norio Taniguchi in 1969. Since then, the popularity of nanotechnology spreads all over the world. American scientist Dr. K. Eric Dextler further refined nanotechnology in the year 1980. When the material is miniaturized further, the physical properties of the material change considerably. Due to change in size, shape, chemical composition, surface structure, charge, aggregation, agglomeration, and solubility, the biological effects too change considerably. The improved biological effect of nanomaterial is due to their larger surface area, cellular penetrability, and vascular permeability. The above properties of nanomaterials are an advantage in medicine and biotechnology. A nanometre length is one billionth of a metre. For example, the nanoscale is so small that the thickness of a sheet of paper could measure 100,000 nm (Table 3). Using nanoscience, scientists could build atoms from scratch. The positional assembly of subatomic particles could be possible by the help of atomic force microscope (AFM). Thus, the nanomaterials are really very small.

Table 3 SI units and comparison of various length measurements in relation to nanoscale

Prefix	Length	SI unit		Value	Biological structure
Giga	100 μm	G	10^9	Human ovum	
Mega		60–120 μm	N	10^6	Human hair
Kilo		7–8 μm	K	10^3	Red blood cell
Hector	80–100 nm	h	10^2	Atom	
Meter		100 nm	m	10	HIV
Centi		30 nm	cm	10^{-2}	Picorna virus
Milli		25 nm	mm	10^{-3}	Microtubule
Micro		20 nm	micro (μ)	10^{-6}	Ribosome
Nano		7 nm	n	10^{-9}	Cell wall membrane
	6 nm				Microfilament
	2–8 nm				Quantum dots
	1–2 nm				Nanotube
	0–8 nm				Amino acid
	0.5–2 nm				DNA helix
	0.15 nm				C–C bond
	0.078 nm				Silicon atom

2.1 Nanomaterials for Cancer

An ideal nanomaterial useful for cancer treatment should be stable without alteration of pharmacological activity of given drug and also should prevent rapid degradation of drug to maintain constant blood level for an optimal duration. The drug must be released at the desired site (inside cancer cells in tumor area), thereby reducing chemotherapy-induced toxicity compared to conventional free drugs. The nanodevice should have ability for visualization by MRI scan or molecular imaging to guide chemotherapy. In cancer types where continuous drug levels are necessary for prolonged period, nanoparticles could control drug levels in blood through its unique controlled drug delivery system. The ideal nanotechnology-engineered particle should be able to survive immunological attack by the cell-mediated immunity of the patient. Due to specific delivery of drug at intended site, the normal tissue gets less exposure to drugs; thus, there could be less bone marrow suppression, alopecia (hair loss), and mucositis compared to standard free drugs. Due to low degradation of drug and low clearance by renal system, the half-life of the drug is prolonged. Further change in the property of the material could improve solubility of drug in aqueous environment. The ideal nanomaterial for cancer could use active or passive accumulation of drugs to target tumor cells and avoid exposure to normal structures.

2.1.1 Passive Tumour Targeting

This is one of the methods how anticancer drugs could concentrate inside or near cancer-bearing site in patient's body. Nanodevices are capable of increasing permeability and retention of drugs at target site. Very small size nanoparticles could easily penetrate endothelial wall of the blood vessels into the tumour tissue (Fig. 4). Leaky and defective lymphatics and blood vasculature allow accumulation of nanoparticles inside the tumor cells (Wang and Thanou 2010). Therefore, the concentration of cytotoxic drugs in tumour cells increases; however, intact vasculature of non-tumour area does not allow nanoparticles to permeate, thereby protecting normal cells.

2.1.2 Active Tumour Targeting

Nanoparticles could be carried directly to the tumour site by the help of monoclonal antibodies targeted against tumour-specific antigens expressed in excess of specific tumours. By active targeting, the nanoparticles attach to the cell surface receptor. Thereby, they bring anticancer drugs close to the cancer cells. Later, they induce cells to absorb nanoparticles. Thereby, active and passive targeting improves therapeutic ratio.

2.2 Quantum Dots

Quantum dots (QD) are nanocrystal semiconductors that are small enough to exhibit quantum mechanical properties, especially during excitation, i.e. glow to a specific colour. They emit fluorescence on excitation with light source. They show excellent optical properties with high brightness, tunable wavelength, and resistance

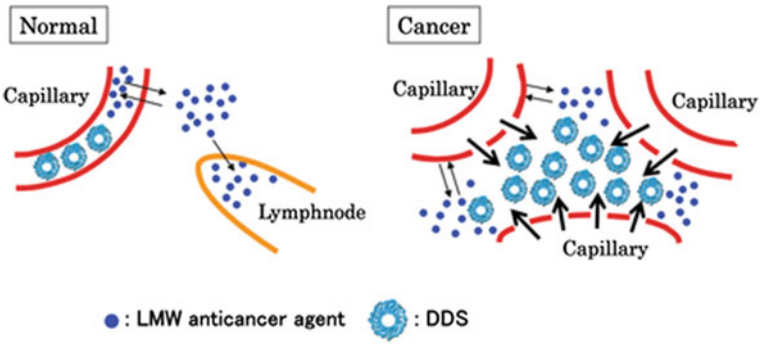

Fig. 4 Enhanced permeability and retention (EPR) effect of tumour. Reproduced with the permission from Matsumura (2014)

to photobleaching. Surface modifications of QDs lead to its application in cancer imaging. QDs in near-infrared emission could be utilized for imaging of sentinel node mapping and ultimately can be biopsied or carry out lymph node dissection. Conjugated QDs with tumour antibodies and peptides could be applicable in tumour-targeted therapy. QDs could detect metastatic cancer cells inside patients' body and thus could help in early detection of cancer and detection of minimal residual disease after treatment (Zhang et al. 2008).

2.3 Spherical Gold Nanoparticles

Colloidal gold nanoparticle (GNP) has been in use for centuries to produce vibrant coloured paintings on the glass door and windows of churches. Gold nanospheres are consisted of thin layer of gold surrounded by dielectric silica core measuring between 50 and 500 nm. The outer shell may be few nanometres thick and possesses characteristic physical properties of gold nanoparticle (GNP) with light and related to surface plasma resonance (SPR). Therefore, the surface electron of nanoshell oscillates collectively in the presence of oscillating magnetic field of light. Nowadays, optical and electronic properties of gold particles are being used in sensory probes, therapeutic agents, and drug delivery. The optical and electronic properties of gold nanoparticles could be modifiable by altering size, shape, surface, chemistry, and aggregation state. When a visible light source comes closure to colloidal gold nanoparticle, it interacts with free electrons causing a concerted oscillation of electron charge that resonates with the frequency of visible light. The resonant surface oscillation is called surface *plasmons*. A small modified gold ($\sim$30 nm) nanoparticles produce blue light of green portion of stretching light ($\sim$450 nm), while large nanoparticles produce red light. As particle size changes, the colour changes from blue to red. Thus, the colour of nanoparticle could be modified by size of monodispersion gold nanoparticles. The other uses of GNP are in photothermal ablation of cancers based on thermal ablation of tissue within tumour. The temperature could reach up to >42 °C which is biologically optimal for hyperthermia. This type of hyperthermia is very targeted unlike classical radiofrequency or extracorporeal-induced hyperthermia. In fact, GNP could be locally heated inside the tumour by near-infrared (650–950 nm) laser light without bystander effect (Zhao et al. 2015). GNP-based hyperthermia induced by non-ionizing radiation has been tried in mice, but clinical studies on human cancer have not yet been established. The main reason is being poor penetrability of non-ionizing radiation to deep-seated tissue. Thus, superficial cancer might be the optimal tumour model for GNP-induced hyperthermia. Further, GNP can scatter light and therefore can be useful in imaging cancer used as in vivo contrast agent. Use of antibody conjugation with EGFR has been used for imaging of early cervical cancer (Thekkek and Richards-Kortuno 2008).

2.4 Single-Walled Carbon Nanotube (SWCNT)

Carbon nanotubes are novel carrier system used for small- and large-sized therapeutic drugs. The surface of SWCNT could be fabricated with functional groups and thus could manipulate functional and biological properties. Their large surface area and possibility to manipulate surface and physical dimensions have been exploited for photochemical destruction of cancer cells. SWCNT is a cylindrical molecules made up of carbon atoms. They are rolled into a cylinder that could be open or close capped. Due to their large surface area, they are capable of absorbing or conjugate with wide range of molecules (Rastogi et al. 2014). Their surface area is engineered in order to enhance dispersibility in aqueous medium or provide appropriate functional group to bind to the therapeutic molecule to penetrate their target cell to treat diseases, especially cancer.

2.5 Superparamagnetic Iron Oxide Nanoparticles (SPIONs)

Nanoparticles derived from iron oxide (Fe_3O_4; magnetite) measuring <20 nm show characteristic supermagnetic properties. The SPIONs are easily modified by external magnetic field. Thus, removal of magnetic field eliminates above phenomenon. Pools of adjacent electrons are aligned in the same direction from the so-called magnetic domain. The supermagnetic materials are smaller in size, and they do not pose multiple domain like paramagnetic material. This produces paramagnetic moment used in medical imaging. The SPIONs are coated initially with PEG and then functionalized by ligand binding to cancer targets.

SPIO is also useful for cancer hyperthermia or thermal ablation of tumour. Heat can be generated by oscillating magnetic field. The magnetic field does not affect normal cells. In animal studies using SPIO, thermal treatment found useful in prostate cancer implants in peritoneum (Ferrari 2005). However, the efficiency of magnetic thermal ablation is very limited. Therefore, the thermal effect may be useful in combined modality treatment in cancer. The SPIO properties can be utilized as special contrast agent in MRI. The above SPION-enhanced MRI image could distinguish between tumour and normal tissue interface.

Ultrasmall supermagnetic iron oxide (USPIO) nanoparticles could be used in intracranial tumours (Varallyay et al. Varallyay and Nesbit 2013). USPIO is taken up by reactive phagocytic cells at the tumour margin. Therefore, nanoparticles are used as contrast material in MRI. Thus, the nanoparticle-embedded contrast shows better delineation of tumour margin well compared to MRI with conventional contrast agents. Due to decreased diffusion and phagocytosis, USPIO NP persisted longer in parenchyma so more precisely delineates the tumour margin. Nanoparticles are also used in high-resolution USG imaging. Intravenous nanoparticle contrast agents produce grey scale pulse inversion harmonic images at low acoustic power. Nanoendoscopy could be a reality similar to *PillCam*™ colon

capsule endoscopy in early detection of colorectal cancer (Jain 2012). The new innovation *Gut Bot* under development where the drug chemical release at site of abnormal areas replace endoscopy entered through anal canal.

2.6 Dendrimers

Dendrimers are highly branched polymers arranged in spherical shape. They contain multiple generations of active groups growing in branching manner. The inner core is called initiation generation zero and subsequent branching as further generations (Oerlemans et al. 2010). The dendrimers usually measure 1–15 nm. The branching generations provide large surface area to which cytotoxic drugs and ligands could bind easily by adsorption or conjugation process (Fig. 5). The cytotoxic drugs could also be stored inside hydrophobic core through hydrophobic interaction, hydrogen bond, and chemical link (Peer et al. 2007). Peptide dendrimer-based nanoparticles have potential application in nanoscale drug delivery in cancer. It acts as a vehicle for drug delivery mechanism or imaging moieties. Dendritic polymers are uniquely suitable for biomedical application in that it is a synthetic molecule that can be uniformly produced and yet has a diameter of only 5 nm. These designed multifunctional devices could have application as diagnostic agent for cancer in early stages or deliver cytotoxic drugs directly to cancer cells.

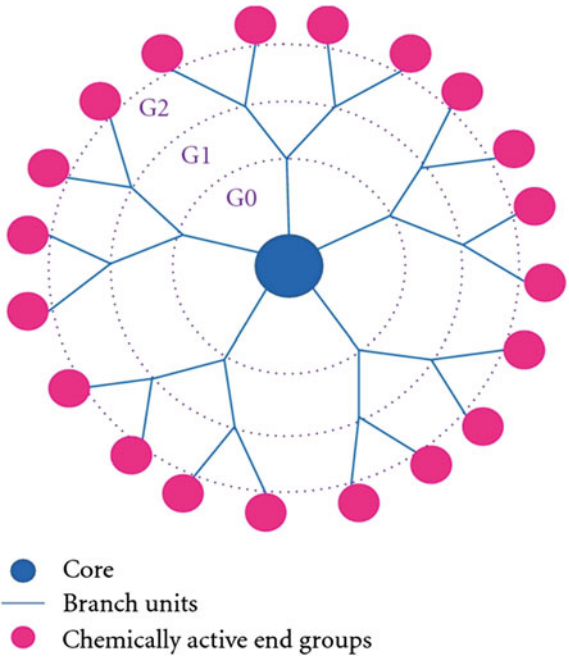

Fig. 5 Illustration of a typical dendrimer. Reproduced with the permission from Riggo et al. (2011)

Polyamidoamine (PAMAm) dendrimer is most commonly used for drug delivery due to their biodegradable properties, compatibility, and water-soluble properties. Small-sized dendrimers measuring 5 nm could be manufactured as G5 PAMAm dendrimer with more than 100 functional amines on the surface (Fukowska-Latallo et al. 2005). The nanodevice dendrimer is used to deliver methotrexate in animal studies. The dendrimer surface charge was reduced by modifying peripheral amines with acetyl group and then G5 PAMAm dendrimer conjugates with methotrexate as cytotoxic drug and folate as targeting molecule. These medicated dendrimers show good accumulation on folic acid expressing experimental tumours.

2.7 *Liposome Nanoparticles*

Liposome nanoparticles are the most commonly used nanomedicine because of its easy preparation, acceptable toxicity, and biodegradability. Liposomes are self-assembling colloidal structures composed of lipid bilayers surrounded by aqueous component which can encapsulate variety of cytotoxic drugs of either hydrophobic or hydrophilic nature (Fig. 6). The drug packing can be done by the modification of pH (pH gradient method) (Qiu et al. 2008), use of lipophilic drugs, and use of organic solvent and solvent exchange mechanism. Drug loading into liposomes can be possible by liposome formation in aqueous solution saturated with soluble drugs. These liposome nanostructures measured around 400 nm in size and thereby rapidly cleared by mononuclear phagocytic system which requires preliminary opsonization by immune system. To bypass opsonization process, PEGylation method is most commonly used. A coating of PEG chains on the surface of nanoparticle results in increased plasma half-life (Tarchilin 2005). The opsonization process of phagocytosis is masked or delayed by hydrophilic protective layer which repeals absorption of opsonin protein. The liposome nanomaterials of three generations are as follows. The first-generation liposome is called *naked liposomes* which has unmodified phospholipid surface. The second-generation liposomes are called *sleath liposomes* with a layer of hydrophilic

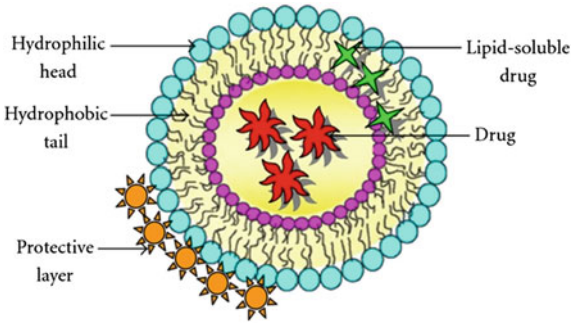

Fig. 6 Liposome nanoparticle. Reproduced with the permission from Riggo et al. (2011)

carbohydrate usually PEG. The third-generation liposomes incorporate surface ligands to improve therapeutic index by selectively or specificity and selectivity of compound.

2.8 Polymer Nanoparticles

Polymer nanoparticle devices are formed by biodegradable polymer. These include nanospheres and nanocapsule-like solid carriers measuring between 10 and 1000 nm in diameter. These are made from natural or artificial polymers and generally biodegradable. The therapeutic drug could be adsorbed, dissolved, entrapped, or encapsulated covalently by linking to polymer backbone by simple ester of amide bonds that can be hydrolyzed in vivo through change in pH. The synthetic polymers include PLA (poly(lactic acid)), PGA (poly(glycolic acid)), and PEG (polyethylene glycol), and their copolymers have been extensively used due to biocompatibility. Natural polymers such as chitosan, alginate, and gelatine have also been used. On parenteral administration, nanoparticles are more stable than liposomes but limited by poor pharmacokinetic properties, i.e. uptake of reticuloendothelial system. The surface of the nanoparticles could be coated with molecules or intercalated into their structures to increase pharmacokinetics and even targeting for delivery and imaging purpose (Bajpai et al. 2008).

2.9 Micelles

Micelles are biodegradable nanocarriers measuring 10–200 nm in diameter. They are formed by self-assembly of block polymers with hydrophilic and hydrophobic ends. Hydrophobic ends form the inner core to minimize their exposure to environment, whereby hydrophilic chains form the hydrophilic corona like shell to stabilize the core through direct contact with water.

The hydrophobic core is ideal for carrying lipophilic drugs which are solubilized and physically entrapped in the inner region with higher capacity. Normally, hydrophobic drugs come with adjuvants, i.e. ether and cremophor EL to reduce toxicity. However, addition of above drugs in micelles does not require adjuvants. Hydrophilic shell provides stability in blood and provides functional group for further modification. The drug encapsulated inside micelle can release in timely manner due to erosion of blood degradable polymer or pH changes (Oerlemans et al. 2010). The surfactant micelle modified by antibody or peptide ligands could direct drugs specifically to cancer cells, thereby reducing normal tissue toxicities.

2.10 Nanocantilevers

Cantilevers are minute micron-sized devices which are flexible beams resembling rows of diving boards built using technology called "*semiconductor lithographics*". These boards are coated with molecule capable of bindings to tumour and DNA-specific substances complimentary to specific gene sequence. Such small micron-sized device caters many nm wide cantilevers and attracts secreted products of cancer cells and selectively binds to it. The antibodies are designed to pick one or more specific molecular expression originated from cancer cells. Due to binding of molecule to antibodies, the physical properties of cantilevers change. Real-time detection of such changes provides information about the presence or absence of molecular markers and their concentration. The cantilevers serve as a diagnostic platform to detect molecular markers of cancer in vivo.

3 Application of Nanotechnology in Cancer Surgery

Surgery is the age-old treatment for solid cancers which rule over a century. Initial cancer surgery is crude, mutilating with resultant disfiguring outcome. Over the years, surgeons refined their surgery to make resection cosmetically attractive. With the progress in radiotherapy and medical oncology disciplines, the extent of surgery is decreased and is more refined. Organ and function-preserving surgeries are preferred over radical and extraradical surgery. The current progress on surgical approach is being elective planned surgery after thorough evaluation of disease extent using latest imaging studies, less or minimally invasive surgery, shorter hospital stay, and early recovery. Many surgeons resort to robotic and image-guided surgery to prevent sensitive tissue damage. Very recently, nanotechnology is being incorporated into cancer surgery (Singhal et al. 2010). The main contribution of imaging is nanoendoscopy, real-time intraoperative tumour imaging, lymphatic mapping, and use of novel nanotechnology-based instruments. Combination of modalities including radiation and effective systemic chemotherapy could improve outcome of cancer treatment in future.

Basic research on nanotechnology is evolving. There are numerous animal studies that give way to new concept in the incorporation of nanotechnology in surgery. Infrared quantum dot nanoparticles are injected into skin of breast cancer-bearing animal used for early localization by following lymphatic flow to lymph nodes. The same study is being extrapolated to other lymphatic regions. In colorectal cancer, nanotechnology is used in cancer imaging through the presence of guanylyl cyclase C (GCC) in intestinal mucosa. The interstitial receptor for bacteria diarrhoeagenic bacteria heat-stable peptide endotoxin are selectively expressed on apical membrane of intestinal mucosal cells but not on extraintestinal cells. Therefore, incorporation of ferrous oxide (FeO_2) nanoparticle to target GCC

receptor to detect and diagnose colorectal cancer using MRI imaging technique is being explored (Fortina et al. 2007).

3.1 Control of Operative Blood Loss

Nanotechnology developed at MIT and Hong Kong University uses simple liquid to control haemorrhage in open surgical wound in different rodent brain, liver, skin, spinal cord, and intestine. The liquid is composed of peptides when applied on surface, and they self-assemble into nanoscale-protective barrier gel that seals bleeding wound in less than 15 s. Following healing of wound, the gel breaks down into molecules so that cells continue to building block tissue repair (Jain 2008). Use of atomic force microscopy (AFM) could be used with nanoneedle for repair of tissue. Obataya et al. inserted nanoneedles into living cell nucleus. The cellular surgical technique could enhance outcome of surgery differently in future (Obataya et al. 2005).

3.2 Nanotechnology in Bone and Joint Surgery

Orthopedics oncosurgery involves extensive loss of tissue, thereby poor cosmetic outcome and quality of life. The nanotechnology is developed to repair bone using nano-HA/collagen/PLA composite. Bone scaffold made from nanotubes and non-biodegradable behaves like inert matrix that stimulates bone cells to grow, proliferate, and deposit new bone in damage site. Thus, the normal function of bone is recovered. The cartilage could also be regenerated using electrospun poly (1-lactide) scatter (Jain 2008).

3.3 Activated Probe and Tumour Painting

Identification of tumour and their margin localization is a very difficult problem for surgical oncologists specially at microscopic level. Application of nanoscience could assist surgeons to identify exact location of cancer in precision to excise cancerous tissue with clear margin. Organic fluorophore plus monoclonal antibodies against tumour antigens has been studied by Kaushal and coworkers to visualize colon and pancreatic experimental cancer preoperatively in experimental animals. The localization of tumour with this method has high specificity and sensitivity (Kaushal et al. 2008). In another animal model, Kobayashi and colleagues are able to demonstrate activated fluorescent imaging probe with improved signal-to-background ratio to target lung metastasis in animal models (Urano et al. 2009; Hama et al. 2007). Probes activated by photon-induced electron transfer, quencher–fluorophore interaction, and pH changes are utilized to look for tumour

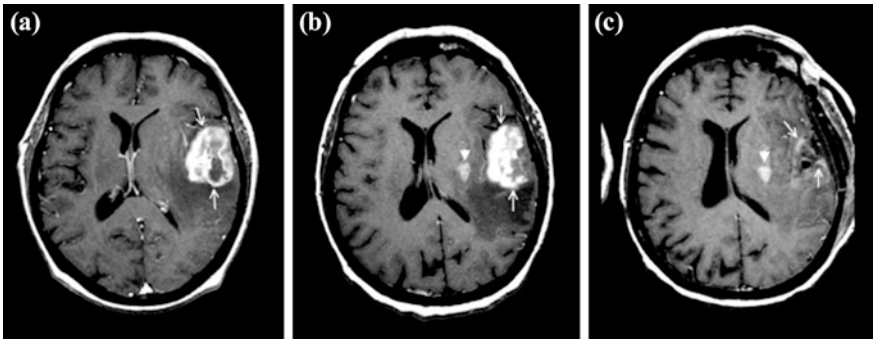

Fig. 7 A diagnosed case of glioblastoma multiforme (GBM) in fronto-temporal lobe of brain **a** showing on gadolinium-enhanced SE MRI. **b** 24 h after nanotechnology-based contrast agent ferumoxtran infusion and before surgery showed additional changes in putamen. 4 days after surgical excision **c** MRI showing residual tumour in the surgical bed. Reproduced with the permission from Neuwelt et al. (2004)

location (Urano et al. 2009). Thus, fluorescence is activated by acidic pH. By attaching Cy5.5 to a tumour-targeting peptide called chlorotoxin, Oleson and coworkers developed an imaging agent that efficiently paints tumour tissue (Veiseh et al. 2007). This tumour painting method could be used to detect metastatic foci of nanoscale measurement (200–2000 nm) which is 500 times more sensitive than MRI imaging (Fig. 7). In experimental animal brain surgery, above imaging method could light up the surrounding normal brain tissue. Using prostate cancer model, tumours as small as 200 nm width travelling inside mouse lymphatic channel could be detected. Silicon-based charge-coupled device (CCD) camera can be used for tumour visualization. Using wavelength, multiplexing capability could permit multicolour ratiometric cancer imaging during surgery and thereby possibly assist surgeons to identify tumour better. Surface-enhanced Raman spectroscopy (SERS) nanoparticles with distinct spectroscopic signature could be used for surface coating and in vivo pharmacokinetic studies.

3.4 Nanocoated Surgical Blades

Using nanocoated scalpels, surgeons could dissect tissues at cellular level. These nanoinnovations could be useful in precious neural tissues during brain surgery (Bogedal et al. 2003; Roszek et al. 2005). The hard metal could be coated with diamond on microstructured hard metal. These scalpels have low physical adhesion to materials or tissues in addition to chemical and biological inertness. Nanotechnology could enable to produce surgical blades with cutting edge diameter about 5 nm–1 μm. A diamond scalpel with a cutting edge of 3 nm has been used in neurosurgery. Crystalline and polycrystalline silicon material could be miniaturized

to 5–500-nm-scale scalpel for the use in finer ophthalmic surgery. Nanoscale diamond edge blade could be helpful in cataract surgery. Trephine with nanostructured carbon coating to obtain cutting edge of high stability is being developed for various surgery (Mali 2013).

3.5 Nanoneedles

In eye, brain, and plastic surgery, nanoscale steel needles (1–10 nm quasicrystals) are manufactured with ageing technique. The nanoneedles possess good ductility, exceptional strength, and corrosion resistance. Sillicon-based nanoneedles use atomic force microscope (AFM) which is used to penetrate cell in cellular level surgery. The nanoneedles do not indent the plasma membrane and nucleus. These nanoneedles are also useful in stem cell procedures (Mali 2013).

3.6 Nanotechnology in Sentinel Node Biopsy

Sentinel node biopsy or sampling is an established technique to sample risk groups of level-1 axillary lymph nodes in early breast cancers. It is used for proper staging work up and treatment. Axillary lymph node status is a well-known prognostic indicator of breast cancer. In standard sentinel node biopsy, a blue dye (isosulfan blue or patented blue) or radionuclide (Technetium sulphur colloid ^{99}Tc TSC) is injected into the tumour, and after a standard interval, the node is identified from its colour or radiation counts on a scintillation counter or gamma probe. The affected node is then dissected and examined for the presence of metastasis. This technique avoids morbid extensive axillary node dissection. Classical axillary lymph node dissection carries risk of lymphedema and tissue deficit. The detection rate of SLN using standard SLNB technique has been demonstrated to be 96 % sensitive and results in 7.3 % false negative as per one large meta-analysis involving 8000 patients (Wang et al. 2011).

Magnetic nanoparticles (MNPs) exhibit potential to replace standard combined technique (radionuclide plus blue dye) in SLNB due to their shared features. MNP materials for SLNB procedure can be externally detected in tissue preincision and have similar dimension as radiocolloid, and their brown black appearance acts as a visual stain (Ahmed et al. 2014). Recent studies on iron oxide such as maghemite (Gamma Fe_2O_3) and magnetite (Fe_3O_4) imaging agent coated biocompatible molecules such as dextran to form SPION below 30 nm since they exhibit superparamagnetic behaviour. Thus, ideal for SLNB as they do not agglomerate during transit from tumour to node in the presence of external magnetic field. There are advantages over standard radionuclide-based SLNB; for example, long half-life enables to transfer agent to farthest countries without fear of decay, no protection measure required and no disposal problem.

SPIO-based SLNB technique has been tried in SentiMAG trial in Guys Hospital to compare standard combined SLNB to SPIO-based SNLB (Sienna Endomagnetics, UK) using a hand-held magnetometer (Fig. 8) (Sentimag Endomagnetics, UK) (Pouw et al. 2015). Joshi et al. (2007) in the initial 19 patients detected SLNs in all 19 patients. All 19 SLNBs were also identified in subsequent trial. Sentinel lymph node detection using new technique (Fig. 9), the detection rate was 37/43(86 %) versus 14/15 (93 %) when SPION was administered.

Now, ongoing sentinel trial in UK involving SPIO has already recruited 350 patients. The mature results are expected in the near future. The recent analysis of central European SentiMag study showed equivalence of SentiMag-based SLNB with standard radionuclide-based procedure. However, the superiority of former technique is due to its simple handling, reduced preoperative preparation, and its proven efficacy (Thill et al. 2014). Besides breast cancer, SLNB technique is being used in non-small-cell lung cancer, colorectal cancer, and malignant melanoma.

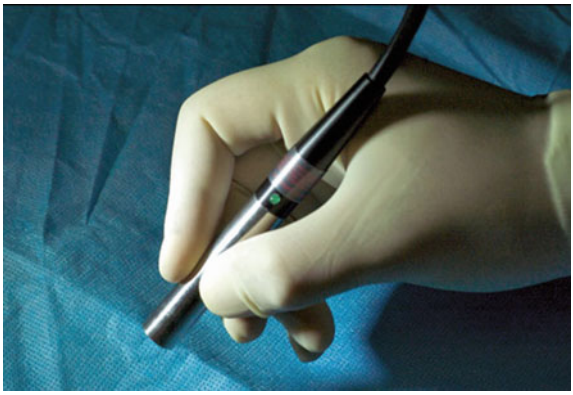

Fig. 8 SpectroPen used to effectively resect cancerous lesion with negative margin at real time. Reproduced with the permission from Parvin and Loftus 2011

Fig. 9 SentiMag system for the detection of sentinel node biopsy. Reproduced with the permission from Endomagnetics Ltd.

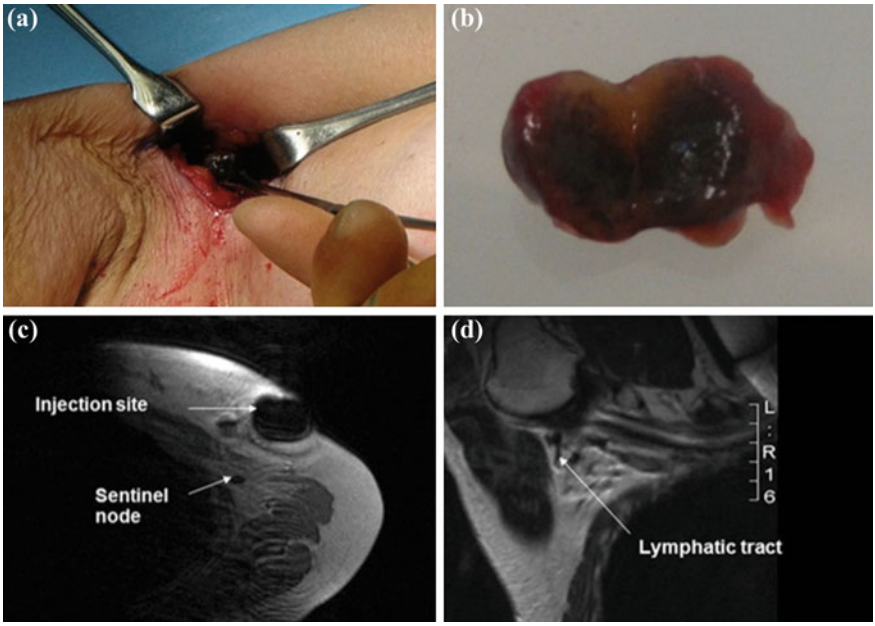

Fig. 10 Sentinel node biopsy with a subcutaneous injection of SPION (Endorem, Guerbet, France) into the breast. **a** Sentinel node identified lymph nodes in right axilla. **b** sentinel lymph node with black SPIO deposition. **c**. MRI showing the injection site and a sentinel node. **d** Two sentinel and a lymphatic tract, seen on axillary MRI. Reproduced with the permission from Douek (Thill et al. 2014)

Now, researchers use nanoscale contrast agents to delineate cancer for clear surgical resection of tumour. Devices such as tumour paint and SpectroPen are in development along with other advanced optical imaging system that allows surgeons to see the cancer cells preoperatively. Preclinical studies have proven their concept, but more applications in clinical trials are necessary for acceptance in clinical practice. Optical imaging system utilizes fluorescent dye, or proteins have obvious advantage over conventional CT/MRI or PET imaging. They are used during surgery without fear of radiation exposures. The images can also cover larger tissue areas of tumour cells than pathologists using their microscope.

Gold nanoparticles provide signal that is more than 100 times brighter than fluorescent beads used in other optical devices. Gold nanoparticles have been using Raman's spectroscopy effect, thus greatly amplifying the signal from the dye. SpectroPen combines the near-infrared laser and a detector for fluorescence, or scatter light is connected by a fibre optic cable to the spectrometer that records fluorescence Raman signal (Mohs et al. 2010). Development of biomedical imaging information system helps in diagnosis and treatment planning. Injecting nanoparticles contrast agent using albumin attach to a compound that fluorescent in response to infrared light. Using SpectroPen (Fig. 10), the tumour is precisely

delineated 10 times higher than normal tissues. Gold nanoparticles could show tumour cells at the edge of tumour, and fluorescent contrast agents reveal bulk of the tumour because of its greater penetration into solid tumours.

Zhang and coworkers developed a contrast agent called "tumour paint" that can cross blood–brain barrier in animal models. Nanoscale particles labelled with fluorescence and chlorotoxin target an enzyme overexpressed in most type of brain tumour, brain, skin, prostate, and colorectal cancers. This technique could assist neurosurgeons to excise brain tumour with accurate margin (Veiseh et al. 2007).

4 Nanotechnology in Radiotherapy

Radiotherapy is the most important modality in the multidisciplinary management of cancer. More than 60 % of cancer patients require radiotherapy during the course of their illness. For early cancers in suitable locations, radiotherapy alone could cure similar percentage of patients as radical surgery with preservation of normal anatomy. Relatively, advanced cases are treated in combination of surgery and chemotherapy for prolongation of survival. However, in advanced cancers, short course of radiation is required to control symptoms and improve quality of life. Despite of technological advancements, radiation fails to control certain group of patients due to tumour hypoxia, large volume disease, and resistance to radiation. Though combination of hyperthermia and radiotherapy potentiates cytotoxicity of radiation, existing hyperthermia techniques are not targeted or reproducible. Recently, materials in nanoscale could be incorporated into radiotherapy to improve results. The main areas of nanocollaboration are being in tumour hypoxia, targeted drug delivery, intracellular hyperthermia using nanogold spheres, and advanced cancer imaging using ferromagnetic contrast agents and nanobrachytherapy.

The nanomaterials possess special characteristics that support its incorporation in radiation oncology. These include enhanced permeability and retention (EPR) effect, characteristic of biodistribution of NPs, pharmacokinetics, and controlled release of drugs. The leaky and bizarre blood vasculature, inefficient intratumoural lymphatics, thermal effect of temperature, low pH, etc., encourage nanoparticles to preferentially accumulate in tumour and prevent their return to systemic circulation. Moreover, the intact vascular system outside tumour does not allow NPs to permeate out of the blood vessels, thus reducing occurrence of normal tissue toxicity. The nanomaterials do not excrete through usual excretion system rather eliminate via mononuclear phagocytic system and hepatic excretion, thus allowing NPs to maintain constant blood level (Longmire et al. 2008).

4.1 Nanotechnology in Tumour Imaging for Tumour Localization

Exact identification and estimation of extent of tumour growth and its draining lymphatics are of paramount importance for proper planning of radiotherapy. With the development of three- dimensional conformal radiotherapy and intensity-modulated radiotherapy, correct delineation of clinical target volume during contouring session is very important for optimal planning. Therefore, oncologists use CT/MRI/PET scan data to delineate primary tumour and draining lymphatics. Existing imaging modalities do not correctly identify small subcentimetre lymph nodes and primary tumours near bony structures. The best example is during IMRT planning for prostate cancer and breast cancer. Nanosize ferromagnetic materials as contract agents have been employed in radiology to improve accuracy of tumour imaging. The most extensively studied agent being ferumoxtran-10 is used to detect subcentimetre lymph node metastasis (Saksena et al. 2006). In a clinical trial of 88 operable prostate cancer patients, those subjected to MRI imaging with or without lymphotropic superparamagnetic nanoparticles are followed by lymphadenectomy or biopsy. The image data of both type MRIs were correlated with histological correlation. The MRI images of experimental arm had significantly higher sensitivity compared to conventional MRI (i.e. 90.5 % vs. 35.4 %) and had high specificity. Thus, these lymphotropic nanomaterials are used for lymphatic mapping in radiotherapy (Harisinghani et al. 2003) during contouring of tumour volumes. In IMRT, correct delineation of lymphatics is of utmost importance in H&N cancer, breast cancer, and anal canal cancers. Lymph node mapping generally relies on the position of lymph nodes in relation to bony landmarks on CT scanning. Using lymphotropic paramagnetic contrasted MRI, Shih et al. (2005) studied 18 prostate cancer patients with this experimental imaging and the nodes were biopsied for correlation. The authors concluded that involved lymphatics largely localized near blood vessels rather than according to bony landmarks. In breast cancer cases, MacDonald et al. (2009) used MRI nanocontrast agents in postoperative breast cancer patients for accurate delineation of malignant and benign lymph nodes. They used conventional radiotherapy fields. For nodal volume contoured in the absence of margin, in this group, 86 % of actual lymph nodes were found within the contoured volume. The authors concluded that LN-MRI is a useful tool for delineation of lymphatics. Despite of above data, the utilization of iron oxide nanoparticle-based imaging in radiotherapy is very low.

4.2 Use of Carbon Nanotubes for X-ray Generation

Carbon nanotubes have been used as electron emitter in X-ray imaging (Cao et al. 2009). In conventional X-ray, there is only one electron emitter; however, in CNT-based X-ray production, an array of CNT with each CNT is functioning as an

electron emitter. The nanobased X-ray emission produces images with high resolution. Because of ability to regenerate X-ray beam at nanometre scale, CNT has been used in the development of microbeam radiotherapy system. Nanotechnology-based diagnostics have been used in few clinical applications. The investigations could detect tumour markers at very low concentrations of femtomolar level. Thaxton et al. (2009) developed a novel bio barcode assay to detect prostate-specific antigen (PSA) by using GNPs. The above technique was applied on 18 prostate cancer patients undergoing radical prostatectomy resulting in undetectable levels of PSA on conventional laboratory units. However, in barcode assay, the PSA was detected as low as 330 fg/mL. Using new tumour marker levels on barcode assay, men with rapidly rising PSA level had worse clinical outcome. Thus, this ultrasensitive PSA barcode assay could helpful to identify patients those require postoperative radiotherapy. In another application of nanoparticles, Shao et al. developed a technique to detect circulating microvesicles that are normally secreting from glioblastoma multiforme tumour cells. Based on microvesicle detection, investigators could able to monitor and predict response to chemotherapy treatment in mouse models. Nanotechnology is also being used for the detection of circulating tumour cells in blood for real-time monitoring of tumour (Hughes et al. 2012).

4.3 Nanotechnology in Radiosensitization

Concurrent chemoradiotherapy is the most widely used technique for radiosensitization using sensitizing cytotoxic drugs, namely cisplatinum, 5 fluorouracil, gemcitabine, and paclitaxel. Another method of sensitization is increased radiation dose within tumour by using material with high atomic number (high Z) because the dose absorbed by the tissue is related to the Z^2 of that material. Maggiorella et al. (2012) studied hafnium oxide nanoparticle as radiosensitizer. This nanoparticle (NBTXR3) measured 50 mn in size is used in animal tumour xenograft models with 2 sarcoma and colorectal cancer cell lines. The hafnium oxide nanoparticle was injected directly into the tumour. The investigators found radiosensitization without increasing toxicity in mice. The above particle is being used in phase-I clinical trial on extremity soft tissue sarcoma and hypopharyngeal cancers. Similarly, gold nanoparticles are being used as a radiosensitizer. Gold being inert and biocompatible and safe material, it could be an ideal nanomaterial for radiosensitization. The gold nanoparticles have been tried in vitro and in vivo studies; however, clinical trials are lacking (Wang and Tepper 2014).

4.4 Nanomedicine for Concurrent Chemoradiotherapy

Concurrent use of chemotherapy improves local control and survival in some cancer sites. However, the normal tissue toxicities are dose limiting. Therefore, nanotechnology has been extrapolated to reduce above complications. Due to preferential accumulation of nanoparticles inside tumour, decreased vascular leak to normal tissues, and decreased elimination, the above method could reduce complications. Liposomal doxorubicin has been used concurrently with radiotherapy in non-small-cell lung cancer and head and neck cancers in clinical trials. However, the mucosal toxicities are higher despite of promising hypothesis (Koukourakis et al. 1999). Liposomal cisplatinum has been used concurrently with radical radiotherapy in head and neck cancers. Rosenthal et al. treated 20 head and neck cancer patients with liposomal cisplatinum along with conventional radiotherapy. Eleven out of 20 patients (55 %) achieved CR with 6/20 patient developed grade-3 skin and mucosal toxicity (Rosenthal et al. 2002).

4.5 Nanobrachytherapy

Nanoparticles could be manufactured to directly deliver radiation dose to the tumour like brachytherapy; thus, a technology using nanoparticles is called nanobrachytherapy (Chatterjee et al. 2013). The concept of delivering radionuclides tagged to monoclonal antibody is being a well-established technique called radioimmunotherapy. However, creating nanoscale radionuclides can gain properties such as magnetism for MR imaging. The success of nanobrachytherapy depends upon tumour-targeting specificity (i.e. EPR) and active targeting methods (using antibody and peptide binding with tumour cell receptors). Khan et al. (2008) describe a simple fabricated poly (^{198}Au) radioactive gold dendrimer composite nanodevice in distinct size (10–29 nm) for targeted radiopharmaceutical drug delivery to tumour in vivo. Irradiation of aqueous solution of ^{197}Au containing poly (amidoamine) dendrimer tetrachloroaurate salt or gold/dendrimer nanocomposite resulted in the formation of positively charged and soluble poly (^{198}Au) radioactive composite nanodevices (CNDs). In a mouse melanoma model, a single intratumoural dose of CND in PBS delivering a dose of 74microCi after 8 days causes 45 % reduction in tumour volume. No toxicity was encountered during the study.

4.6 Radiation Protection

The free radical damage from ionizing radiation can affect both cancer cells and normal cells. There are attempt to protect normal cell damage using radioprotectors, for example amifostine. Nanomaterials, for example CeO_2 nanoparticles, have been

fabricated to reduce normal tissue damage from free radicals. The cerium atom can exist in either the +3 (fully reduced) or +2 (fully oxidized) state. In its oxidized form, CeO_2 also exhibits oxygen vacancies or defects, in the lattice structure. The change in cerium valence during redox event subsequently alters the structure of the oxide lattice, possibly creating additional oxygen vacancies by lattice expansion. The electron translation within the lattice provides reduced power for free radical scavenging. Colon et al. showed that CeO_2 nanoparticles were well tolerated by study animals, and effectively protected mice from 20 Gy thoracic irradiation (Colon et al. 2009).

4.7 Radiation-Induced Drug Delivery

Delivery of nanoparticle at target site can be improved by exposure to radiation. Radiation itself can enhance vasopermeability of tumours, thus enhancing EPR effect and increasing accumulation of nanoparticles (Lammers et al. 2008). Radiotherapy can increase tumour accumulation of polymer drug conjugate such as polymer gemcitabine conjugates in rat prostate carcinoma tumour model. This phenomenon was also observed by another group (Giustini et al. 2012) using iron oxide NPs. Radiotherapy at 15 Gy significantly increases the tumour accumulation of iron oxide NPs when they use a syngeneic mouse breast cancer model. This preferential concentration effect can be further enhanced by triggered drug release such as hyperthermia-induced drug release concurrently with radiation therapy. In addition to passive drug accumulation mentioned above, active accumulation of drug is also possible by radiation-induced drug delivery. Hallahan et al. (2003) used a peptide that can bind to integrin on the irradiated tumour microvasculature. By functionalizing the surfaces of NPs with this unique peptide, they are able to preferentially deliver liposomes and albumin-based NPs to tumours. Similarly, peptides can also be used to target iron platinum NPs, nab-paclitaxel, and liposomal doxorubicin. Therefore, the radiation-enhanced tumour-targeted NP drug delivery resulted in higher therapeutic ratio.

4.8 NanoXray in Radiotherapy

NanoXray is a product of Nanobiotix using a nanoparticle crystal NBTXR3 which is a suspension of inert crystalline nanoparticle of hafnium oxide with simple coating that is formulated in distilled water. The composition of nanoparticle includes hafnium oxide core or source. When its electrons are excited by external beam radiation (usually X-ray), it causes local free radical damage to the surrounding cancer cells. The nanocrystals are not easily eliminated by usual metabolic excretion method. When they are not activated, they are inert. But on exposure to X-ray, the later are absorbed by NBTXR3 nanoparticles leading to emission of

electrons loosing electron and subsequent release of free radicals (Marill et al. 2014). X-ray energy will generate electrons with kinetic energy that will be released into the medium and will generate free radical. These nanoparticles do not react directly with blood cells or tissues. This technology has completed preclinical phase with promising findings and now planning to enter into clinical trials.

5 Nanotechnology in Medical Oncology

Cytotoxic chemotherapy is utilized in more than 50 % of cancer patients. The intension of chemotherapy ranges from cure, adjuvant, neoadjuvant, and palliative treatment. Most chemotherapy drugs are parenteral; however, some drugs are administered orally. Chemotherapy drugs act at various phases of cell cycle; thus, the drugs are classified as cell cycle-specific and cell cycle non-specific drugs. Every individual drug has their own side effects and pharmacokinetic properties. Despite of progress in cytotoxic chemotherapy, none of the chemotherapy drugs are free of side effects. In addition to cytotoxic effects on respective cancer cells, chemotherapy drugs could damage rapidly dividing cells in hair follicles, gastrointestinal mucosa, bone marrow, nail bed, and skin. The slowly dividing tissues, for example nerve tissues, could also be affected by chemotherapy drugs in addition to long-term complications and decreased fertility. Thus, existing chemotherapy drugs are not specific. Therefore, nanotechnology has been incorporated in oncology to prevent such side effects. Despite of enormous interest and technical progress, very few nanotechnology-based cytotoxic drugs are in the clinical use. Translational research using nanotechnology has been very slow. The result of animal study data are rarely duplicated on human trials. Preclinical and clinical studies (Matsumura 2014) are ongoing using micelle nanoparticles to deliver cancer chemotherapy (Fig. 11). So far, following nanotechnology-based drugs are being used in clinical practice (Table 4).

5.1 Nanoparticle Albumin-Bound Paclitaxel

The main purpose of nanotechnology in systemic therapy of cancer has increased drug delivery, reduced normal tissue complication, prolongation of drug serum level, and documentation of treatment delivery. So far, few drugs could meet FDA approval requirement. Nanoparticle albumin-bound (nab) drug method is being the first nanodrug used in clinical oncology. The nab technique levages albumin nanoparticle for the active and targeted delivery of paclitaxel to the tumour. The nab-based nanochemotherapy drugs could cross blood stromal barrier to reach cancer cells. This nanodrug is thought to be targeting a previously unrecognized tumour-activated albumin-specific biologic pathways with a nanoshell of human blood protein albumin. This nanoshuttle system activates an albumin-specific

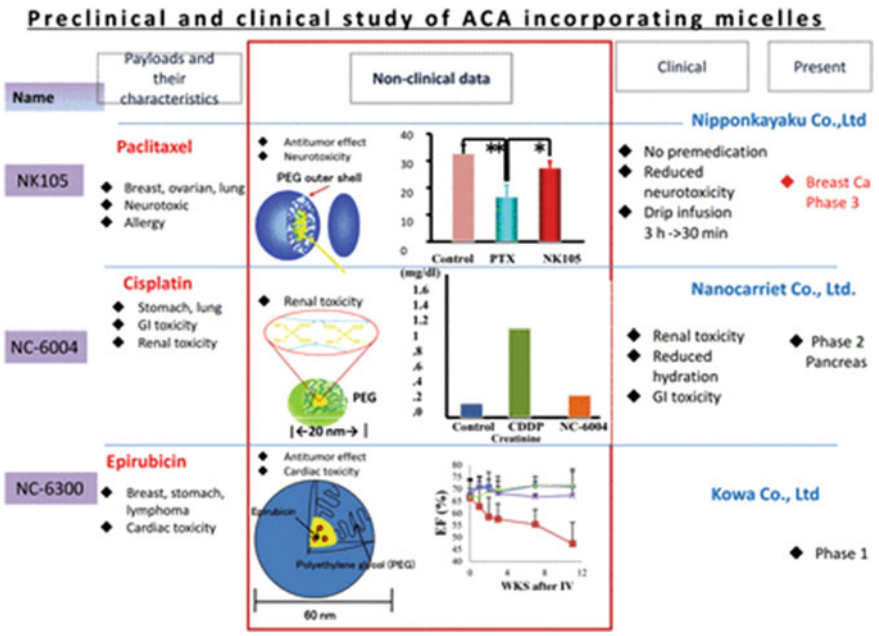

Fig. 11 Anticancer agent-incorporated micelles under clinical evaluation. NK105 is a paclitaxel (PTX) incorporating micelle. Preclinical studies indicated a higher antitumour activity and reduced neurotoxicity. A phase-I and -II trials showed that NK105 can be administered by 30-min drip infusion without any premedication and showed that NK105 reduced neurotoxicity. The phase-III trial of NK105 is now underway in patients with metastatic breast cancer. NC-6004 is a cis-dichlorodiammineplatinum (II) incorporating micelles. Preclinical studies showed that NC-6004 had no renal toxicity. A phase-I and -II trials revealed that NC-6004 can be administered with minimum hydration and the GI toxicity was reduced remarkably. NC-6300 is an epirubicin-incorporating micelles. Basic study of NC-6300 showed significant higher antitumour activity and significantly reduced cardiotoxicity of epirubicin. The phase-I trial is now underway. Reproduced with the permission from Matsumura (2014)

(Gp60) receptor-mediated transcystosis path through the cell wall of malignant cells using caveolin-1-activated caveolar transport. The stromal microenvironment and albumin-bound drug may be preferentially localized by second albumin-specific protein (SPARC), a protein secreted by the tumour cell stroma. The resulting collapse of stroma around tumour may enhance delivery of nab-chemotherapy to intracellular core of tumour.

The first nab-based drug abraxane was used in metastatic breast cancer. Abraxane has a mean particle size of approximately 130 nm. The drug contain non-toxic solvent, which enables the administration of 50 % more chemotherapy which required no premedication to prevent hypersensitivity reaction and can be

Table 4 Established nanotechnology-based drugs used in cancer treatment

Trade name	Nanoplatform	Active drug	Indication	Dose/route	Evidence
Caelyx (Janssen)	PEGylated liposome	Doxorubicin	Ovarian cancer	50 mg/m^2 q IV 4 week	Phase-III Gordon et al. (2001)
Abraxane (Celgene)	Nanoparticle albumin based	Paclitaxel	MBC	260 mg/m^2 IV weekly	Phase-III Gradishar et al. (2005)
Myocet (Cephalon)	Liposomal	Doxorubicin	MBC	75 mg/m^2 q IV 3 week	Phase-III Chan et al. (2004)
DaunoXome (Galen)	Lipid encapsulation	Daunorubicin	HIV-induced kaposi sarcoma	1000 IU/m^2 q IV 2 weeks	Phase-III Gill et al. (1996)
Oncaspar (Baxalta)	PEGylation	L-asparginase	ALL	2500 IU/m^2 IM q 2 weeks	Phase-III Patel et al. (2013)
Pagasys (Roche)	PEGylation	Interferron alfa-2b	Melanoma	450 µg/week SC	Phase-III Dummer et al. (2006)
Neulasta (Roche)	PEGylation	Filgrastim	Chemotherapy -induced Neutropenia	6 mg SC	Phase-III Vogel et al. (2005)
Actiq (Cephalon)	Nanoformulation	Fentanyl	Cancer breakthrough pain	200–1600 mcg Transmucosal	Clinical study Mystakidou et al. (2007)

MBC metastatic breast cancer, *ALL* acute lymphoblastic leukaemia

given under 30-min infusion using standard IV tubings. Subsequently, it is being in various stages of clinical development in ovarian cancer, non-small-cell lung cancer, pancreatic cancer, gastric cancer, and malignant melanoma.

In a clinical trial, metastatic breast cancer patients those failed initial lines of chemotherapies were treated with either nab-paclitaxel, or conventional paclitaxel. Grandishar et al. (2005) recruited 460 metastatic breast cancer patients those failed initial chemotherapy within 6 months with either nab-paclitaxel (260 mg/m^2 over 30 min infusion) or regular paclitaxel (175/m^2 over 3-h infusion). This pivotal clinical trial results demonstrated that abraxane had superior response rate (21.5 % vs. 11.1 % $p < 0.003$) when compared to regular paclitaxel. Bone marrow suppression was one of the doses limiting toxicity.

5.2 *Liposomal Doxorubicin (Caelyx)*

Liposomal doxorubicin is the second most popular nanotechnology-fabricated chemotherapy drug doxorubicin. The active drug doxorubicin is specially coated with 2 layers of protection using liposome. The coating allows liposomal doxorubicin to evade detection and destruction by the immune system, which increases the duration of drug in the systemic circulation. As a result, the drug has more time to reach the tumour tissue, where the medication is slowly released. Despite of full proof theoretical basis, still liposomal doxorubicin could damage normal tissue causing toxicity. The most common side effects of liposomal doxorubicin are hematotoxicity leading to depletion of 3 components of blood cells. Hand-foot syndrome is another possible side effect. In rare circumstances, liposomal doxorubicin could induce oral cancer on long-term treatment.

Caelyx is indicated in the treatment of recurrent epithelial ovarian cancer of those failed first-line platinum-based chemotherapy. AIDS-related Kaposi's sarcoma is also effectively treated with caelyx. Addition of bortezomib to caelyx could be useful in multiple myelomas after the failure of first-line chemotherapy. In ovarian carcinoma, caelyx is used at a dose of 50 mg/m^2; however, in AIDS-related Kaposi's sarcoma and recurrent multiple myelomas, 30 mg/m^2 is most commonly prescribed.

In recurrent epithelial ovarian cancers, Gordon et al. conducted a phase-III clinical trial to compare liposomal doxorubicin with topotecan on 474 patients. Liposomal doxorubicin was administered at a dose of 50 mg/m^2 (1-h infusion) every 4 weeks or topotecan 1.5 mg/m^2/day (30 min infusion) for 5 days every 3 weeks for up to 1 year. The overall response rate, progression-free survival, and overall survival were similar in both groups. In platinum sensitive group of patients, liposomal doxorubicin has significant longer median progression-free survival ($p = 0.037$) and overall survival ($p = 0.008$) compared to topotecan (Gordon et al. 2001).

5.3 Pagylated Filgrastim (Neulasta)

Neulasta is a nanomodified filgrastim which works like a natural protein to signal growth of new white blood cells. It helps to reduce the risk of infection following chemotherapy-induced neutropenia. It has shown to reduce risk of infection with fever following hematotoxic chemotherapy. In a clinical study by Vogel et al., 928 breast cancer patients were subjected to 4 cycles of AC chemotherapy and one group was subjected to 1 dose of pegfilgrastim and other group with placebo. The study result showed a 94 % reduction in febrile neutropenia, 93 % reduction number in hospitalization due to febrile neutropenia associated infection, and 80 % reduction in use of intravenous antibiotics. The infection rate drops from 17 to 1 % in treated group (Vogel et al. 2005).

5.4 Application in Gynaecological Cancers

In gynaecology, malignancies of the genital tract involve organs such as the ovaries, fallopian tubes, uterus, uterine cervix, vagina, and vulva. In developing countries, cervical cancer is the most common gynaecological cancer (Ferlay et al. 2014). For developed nations, cancers of the ovaries or the endometrial lining are more common (United Nations' Development Fund for Women (UNIFEM) 2007; Ferlay et al. 2013; Bray et al. 2013).

Chemotherapy in gynaecological malignancies is mainly used in ovarian cancers either as adjuvant treatment after debulking surgery, and/or as a neoadjuvant treatment prior to the operation. In certain patients, chemotherapy is utilized as palliative treatment to help slow down the disease progression and improve their quality of life. The management of the rare cancer of the fallopian tubes usually follows similar protocol alike ovarian cancer. Chemotherapy is also used in cervical cancer, and one of the uses is to help sensitize the affected areas to radiation therapy. For advanced stage cancers, chemotherapy is used as the first-line treatment, and there are also indications for chemotherapy in patients who could not undergo radiation therapy.

In endometrial cancer, the current accepted treatment is surgery, followed by adjuvant radiation in selected, high-risk patients (Noor Rushdan et al. 2011). However, a lot of patients at Stage 3 onwards were found to have distal recurrences (Kong et al. 2007). Researches done on these cases give rise to the new protocol of giving adjuvant chemotherapy as well as radiation in selected advanced endometrial cancer patients (Noor Rushdan et al. 2011; Kong et al. 2007; GOG 209 2012; Fleming et al. 2004; Greven et al. 2006; Zamzida et al. 2010).

Gestational trophoblastic neoplasia (GTN) is also an area where some patients will require chemotherapy. Following the primary treatment of suction and

evacuation of the molar tissues, a number of patients still have elevated human chorionic gonadotrophin (β-hCG) levels and require adjuvant treatment with chemotherapy drugs.

5.5 *Nanotechnology in Cancer of the Genital Tract*

The most need for nanotechnology will be in the choice of chemotherapy drugs for gynaecology oncology cases. Depending on the respective centres, the choice of drugs for therapy might be different, but the aim is similar. They are utilized to kill off and eradicate cancer cells, at the same time to cause no harm to normal cells (if possible) and to keep the patient cancer-free as long as they can. Unfortunately, despite years of research and the number of drugs available, the ultimate drug which fulfils these needs is still elusive (Ferrari 2005; Riggo et al. 2011).

The identified problems in chemotherapeutic drugs are as follows: (i) lack of specific distribution of drugs to the cancer area, (ii) fast redistribution of the therapeutic drug away from the intended sites, (iii) destruction of the drugs by tumour-associated macrophages (TAMs), (iv) poor penetration into cancer cells due to acidic nature of intracellular environment (as opposed to alkalinized nature of most drugs), and (v) the special properties inherent to cancer cells (Hanahan and Weinberg 2011; Allen and Cullis 2004; Niederhuber 2007; Pollard 2004; Bingle et al. 2006).

There are 2 distinct cell properties pertaining to cancer cells in a person. A small and rare population of quiescent cancer cells are known as "stem cells", and a larger population of rapidly dividing cells form the bulk of tumour mass (Hanahan and Weinberg 2011; Niederhuber 2007). Most conventional cancer drugs affect the second population of cancer cells but not the "cancer stem cells". Those cells that arise from the second type of cancer cells will die without regeneration. The first type, however, has the ability to regenerate, self-sustain itself, and invade other cells and organs and also metastasize. Because of that, despite adequate treatment and initial apparent remission, the cancer can recur after some months or years (Niederhuber 2007; Pollard 2004; Bingle et al. 2006).

The newer cancer drugs, therefore, are formulated in such ways to overcome the identified setbacks (Mamot et al. 2012; Montanari et al. 2012). The concept of nanotechnology relies on the small size of the nanoparticles (1–100 nm or up to 1000 nm depending on scientific communities or institutions) and the special properties that these particles have (NNI 2015; Mousa and Bharali 2011).

The small size allows these particles to have a larger surface area-to-volume ratio compared to other particles. This in turn facilitates their ability to enter cancer cells, at the same time enabling them to carry, bind, and absorb other molecules such as drugs, probes, and proteins. The molecules are able to bypass the acidic nature of the cell membranes without requiring conventional carriers which may cause adverse and toxic reactions to the patients. Not only the ability to reach and enter the targeted cancer cells are improved, they also stay longer in the affected areas

due to their ability to avoid the RES (reticuloendothelial system) macrophages and the P-glycoprotein pumps (Pollard 2004; Wang et al. 2008). The RES macrophages are easier to evade if the particle sizes are 200 nm or smaller. The P-glycoprotein pumps are multidrug resistance-associated protein pumps which are capable of extruding the anticancer drugs out of the cancer cells, thereby reducing their efficacies.

Besides these advantages, the nanoparticles (based on studies) may finally be able to reach the elusive "cancer stem cells" population. This breakthrough will really make a huge difference in terms of achieving a complete remission, reducing recurrence, and improving survival.

Nanoparticles can be sourced from various materials. The main criteria are only they should comply with the size in definition. They can be from biological-like materials such as lipids, phospholipids, dextran, and chitosan. Another group can be from carbon-based materials, like carbon nanotubes. Gold and iron fall into another category that is inorganic nanoparticles. Other members in this group will include metal-based compounds and semiconductor nanoparticles, e.g. quantum dots (QDs).

In general, the effects on the cancer cells can be multipronged. Firstly, they are carriers of drug particles which cause direct damage to the cancer cells. The changes occur both at intracellular and extracellular levels. The types of carriers (liposomes, micelles, polymers, dendrimers et cetera) have already been discussed elsewhere in this book. Some carriers can carry more than one drug, or carry the therapeutic agent in its prodrug form. Secondly, the nanoparticles are also capable of being used in photodynamic therapy; the theory behind it is that certain light activated chemicals can generate oxygen-based cytotoxic molecular components. The third application is thermal damage to cancer cells based on photothermal therapy.

5.6 Non-chemotherapy Applications

The main role will be imaging technology. Three main areas of usage are as follows: (1) during the initial assessment, an accurate imaging modality will allow the doctors to ascertain spread of disease and tailor the treatment accordingly. In very widespread diseases of the ovary or fallopian tubes, studies have shown that it is better to give neoadjuvant chemotherapy for 2–3 cycles prior to the debulking surgery (Bristow and Chi 2006; Bristow et al. 2007; Chan et al. 2008; Onda et al. 2008). (2) During treatment, the patients will also need imaging studies (plus tumour markers and clinical evaluation) to ensure good response and detect any chemotherapy resistance and/or disease progression. CT scans are usually carried out after the 3rd and 6th cycle of chemotherapy. (3) After therapy, imaging modalities are used in monitoring for recurrence.

For clinicians who have CT scan facilities at their disposal, heavy metals such as gold, lanthanides, and tantalum nanoparticles have been used to help enhance the imaging of solid tumours. MRI also gets improved imaging capabilities by utilizing

superparamagnetic iron oxide nanoparticle (SPRION) or ultrasmall SPRIONs which can highlight pelvic node metastases from genital tract cancers. Photoacoustic type of imaging, with the use of carbon nanoparticles, is also excellent in delineating the extent of solid tumours (Hanahan and Weinberg 2011; Allen and Cullis 2004; Mousa and Bharali 2011; Wang et al. 2008).

6 Nanotechnology in Palliative Care

Pain is the most common symptom of advanced cancer; therefore, recently, pain is included as the fifth vital sign in the medical evaluation of patients. More than 60 % of services in any palliative care facility devotes to the control of pain. The most common pain is chronic in nature and requires titrated dose of analgesics. However, breakthrough pain is a term that describes acute episode of severe pain superimposed upon background of otherwise well-controlled chronic pain caused by cancer itself, cancer treatment, or certain activities. About 65 % of patients with cancer pain suffer from breakthrough pain. Recently, novel solution using nanotechnology has been developed, including implantable drug delivery device and transdermal and transmucosal patches to facilitate opioid treatment in breakthrough pain. Tao et al. reported the use of microfabrication technology for the development of microneedle in transdermal drug delivery and implantable drug delivery devices (Mystakidou et al. 2007). A drug device with extremely microdispersion pore size thus facilitates precise diffusion rates. Such diffusion kinetics with potent opioid analgesics are accurate and predictable with controllable dosing of drug. Oral transmucosal fentanyl citrate (OTFC) is a solid formulation of fentanyl citrate, a potent analgesic (50–100-fold as potent as morphine), short-acting, rapid onset of action and lipophilic synthetic opioid. This is formulated as a solid drug matrix on a handle (lollypop) allowing rotation in the mouth for optimal absorption (Tao and Desai 2003). Remifentanil is another congener drug of fentanyl has been nano-modified as buccal mucosal patch help rapid onset of action in breakthrough pain (Sprintz et al. 2005). These nanotechnology innovative products are used for breakthrough pain among cancer patients. Thus, integration of nanotechnology into cancer therapeutics including palliative care for pain control helps in the overall management of cancer patients.

7 Nanotoxicity and Safety of Nanoparticles

There are tremendous progress and encouragement in the field of nanotechnology in medicine including oncology. As per proponents of nanoscience, nanotechnology is supposed to create revolution in the field of cancer treatment with discovery of newer medicines. Major funding agencies like NCI have allocated enormous funds to spur nanotechnology-based treatment products to benefit patients. Being a new

player in the field of oncology, use of nanotechnology in human beings is very short, so data on toxicity profile of each particle are very low. Despite of numerous promise in biotechnology, cellular, animal studies, and fabrication of novel nanoparticles, very handful of literature is available in the clinical utilization of nanomedicine in cancer. So far, nanoparticles are being used in cancer imaging for improvement in identification of tumour and nanoscale modification of existing cancer drugs in a hope to reduce side effects and maintain prolonged serum drug level and reduce resultant toxicities.

Due to lack of reporting from previous studies using nanoparticles, the data on adverse effects are non-existent. Rather, the sensitivity reaction to nab-modified paclitaxel is lower than free paclitaxel and further allows oncologists to deliver higher dose of above drugs. None of clinical trials so far reported adverse effects exclusively attributable to nanodrugs. Recently, long-term use of pegylated doxorubicin has been implicated in the development of secondary cancer in head and neck region and leukaemia (Cannon et al. 2011; Bonomi et al. 2012; Ben-David et al. 2013).

Animal studies have emphasized the importance of lung and gastrointestinal tract could be affected on the use of nanomedicine. There is also concern about use of combustion-manufactured nanoparticles (Regnic and Tinkle 2007). The fate of nanomaterials those effectively kill cancer cells is controversial. They remain inside body for long time. The reticuloendothelial system of body could not eliminate nanoparticles easily. Some authors strongly believe the used nanomaterials could react alike asbestos causing mesothelioma (Bluemann et al. 2007). Therefore, focussed research in clinical trials is warranted to document possible side effects of nanoparticles (Agarwal et al. 2013). The environmental effects of nanoparticles are of concern to environmentalists and health personnel alike. Due to lack of information to public, the suspicion on biological and environmental hazards is increasing.

8 Conclusions

The era of medical nanotechnology is challenging. Last decades have seen tremendous progress and its application in oncology. Numerous animal and human studies have been undertaken throughout the world to look for beneficial effects of nanomedicine in cancer. The major influence of nanomedicine is observed in cancer imaging using nanomodified contrast agents promising clear delineation of tumour at microscopic state. The surgery becomes more precise due to availability of nanodevices to delineate clear surgical margin on critical structures during operation. The nanoparticle-based sentinel lymph node biopsy in early breast cancer proves effective, precise, cost-effective, and without fear of radiation exposure. NanoXrays and nanobrachytherapy in their infancy need more time to prove their clinical efficacy; however, intracellular hyperthermia and photodynamic therapy are feasible techniques that could be used in conjunction with radiotherapy. The

modern multifunctional nanodevices designed for cancer detection and assessment, imaging, ablation, and drug delivery are very exciting but not proven in vivo in cancer patients. The enthusiasm of using something new must be tempered with caution. There should be clear guidelines and legislations on these new technology and associated devices. More long-term studies are also needed to monitor the well-being of patients receiving these drugs/interventions and identify any potential problems. Further progress of nanotechnology in cancer could be possible through more clinical trials and safe use of nanomaterials without affecting environment. Therefore, a collaboration between engineers, biotechnologists, and oncologists is essential to join hand in hand to achieve success in nanooncology.

References

Agarwal, M., Murugan, M. S., Sharma, A., et al. (2013). Nanoparticles and its toxic effects: A review. *International Journal of Current Microbiology and Applied Sciences, 2*(11), 76–82.

Ahmed, M., Purushotham, A. D., & Douek, M. (2014). Novel technique for sentinel lymphnode biopsy in breast cancer: A systematic review. *The Lancet Oncology, 15*(8), e351–e362.

Allen, T. M., & Cullis, P. R. (2004). Drug delivery systems: Entering the mainstream. *Science, 303*, 1818–1822.

Appenzeller, T. (1991). The man who dare to think small. *Science, 254*, 1300.

Bajpai, A. K., Shukla, S. K., Bhanus, W., & Kankane, S. (2008). Responsive polymers in controlled drug delivery. *Progress in Polymer Science, 33*(11), 1088–1118.

Ben-David, Y., Leiser, Y., Kachta, O., & El-Naaj, I. A. (2013). Does long-term treatment with Doxil predispose to oral cancer? *International Journal of Clinical Oncology, 18*(3), 554–555.

Bingle, L., et al. (2006). The role of tumour-associated macrophages in tumour progression: Implication for new anticancer therapies. *The Journal of Pathology, 196*, 254–265.

Bluemann, S. R., Cheng, K., & Ramos-Nono, M. (2007). Unique uptake of acid-prepared mesomorphous spheres by lung epithelial and mesothelial cell. *American Journal of Respiratory Cell and Molecular Biology*, *36*(3), 333–342.

Boch, C., Kollmeier, J., Roth, A., et al. (2013). The frequency of EGFR and KRAS mutations in non-small cell lung cancer (NSCLC): Routine screening data for central Europe form a cohort study. *BMJ Open, 3*, e002560.

Bogedal, M., Glieche, M., Geibert, J. C., Hoffschulz, H., Laccateli, S., Malsh, I., et al. (2003). Nanotechnology and its implications for the health of the EU citizen. www.nanoforum.org

Bonomi, M., Misiakiewicz, K., Posner, M., & Maki, R. (2012). Squamous cell carcinoma of the oral cavity in two patients previously exposed to long-term pagylated liposomal doxorubicin. *The Oncologist, 17*, 1594–1595.

Bray, F., Ren, J. S., Masuyer, E., & Ferlay, J. (2013). Estimates of global cancer prevalence for 27 sites in the adult population in 2008. *International Journal of Cancer, 132*(5), 1133–1145. doi:10.1002/ijc.27711. (Epub 2012 Jul 26).

Bristow, R. E., & Chi, D. S. (2006). Platinum based neoadjuvant therapy and interval surgical cytoreduction for advanced ovarian cancer, a meta-analysis. *Gynecologic Oncology*, *103*(3), 1070–1076 (PMID 16875720).

Bristow, R. E., Eisenhauser, E. L., Santillan, A., & Chi, D. S. (2007). Delaying the primary surgical effort for advanced ovarian cancer. A systemic review on neoadjuvant chemotherapy and interval cytoreduction. *Gynecologic Oncology, 104*(2), 480–490.

Cannon, T., Muggia, F., Hirsch, D., et al. (2011). Multiple cases of squamous cell carcinoma of the tongue and oral cavity in patients with long-term pagylated liposomal doxorubicin (PLD) for ovarian cancer. *Journal of Clinical Oncology, 29*(15 suppl), 720–726.

Cao, G., Lee, Y. Z., Peng, R., et al. (2009). A dynamic micro CT scanner based on a carbon nanotube field emission X-ray source. *Physics in Medicine and Biology, 54*(8), 2323–2340.

Chan, S., Davidson, N., Juazaite, E., et al. (2004). Phase-III trial of liposomal doxorubicin and cyclophosphamide compared with epirubicin and cyclophosphamide as firstline therapy for metastatic breast cancer. *Annals of Oncology, 15*(10), 152–1527.

Chan, Y. M., et al. (2008). Quality of life in women treated with neoadjuvant chemotherapy for advanced ovarian cancer. A prospective longitudinal study. *Gynecologic Oncology, 88*, 9–16.

Chatterjee, D. K., Wolfe, T., Lee, J., Brown, A. P., Singh, P. K., Bhattarai, S. R., et al. (2013). Convergence of nanotechnology and radiation therapy-insight and implications for clinical translation. *Translational Cancer Reserch, 2*(4), 256–268.

Colon, J., Herrera, L., Smith, J., et al. (2009). Protection from radiation induced pneumonitis using cerium oxide nanoparticles. *Nanomedicine, 5*(2), 225–231.

Dummer, R., Grobe, C., Thompson, J. A., et al. (2006). Randomized dose escalation study evaluation of peginterferron alfa-2a in patients with metastatic malignant melanoma. *Cancer, 106*(11), 2445–2451.

DuPage, M., Mazumdar, C., & Schmidt, M. (1080). Expression of tumour specific antigens underlies cancer immunoediting. *Nature, 2012*(482), 405–409. doi:10.1038/nature3

Ferlay, J., Soerjomataram, I., Ervik, M., Dikshit, R., Eser, S., Mathers, C., et al. (2014). GLOBOCAN 2012 v1.1, Cancer incidence and mortality worldwide: IARC cancer base no. 11 [internet]. Lyon, France: International Agency for Research on Cancer. Available from: http://globocan.iarc.fr. Accessed on October 16, 2015.

Ferlay, J., Steliarova-Foucher, E., Lortet-Tieulent, J., Rosso, S., Coebergh, J. W. W., Comber, H., et al. (2013). Cancer incidence and mortality patterns in Europe: Estimates for 40 countries in 2012. *European Journal of Cancer, 49*(6), 1374–1403. doi:10.1016/j.ejca.2012.12.027

Ferrari, I. (2005). Cancer nanotechnology: Opportunities and challenges. *Nature Reviews Cancer, 5*(3), 161–171.

Fleming, G. F., Brunetto, V. L., Cella, D., et al. (2004). Phase-III trial of doxorubicin plus cisplatin with or without paclitaxel plus filgrastim in advanced endometrial carcinoma: A gynecologic oncology group study. *Journal of Clinical Oncology, 22*(11), 2159–2166.

Fortina, P., Kricka, L. J., Graves, D. J., et al. (2007). Application of nanoparticles to diagnostics and therapeutics in colorectal cancer. *Trends in Biotechnology, 25*(4), 145–152.

Fukowska-Latallo, J. F., Candido, K. L., Cao, Z., et al. (2005). Nanoparticle targeting of anticancer drug improves therapeutic response in animal model of human epithelial cancer. *Cancer Research, 65*(12), 5317–5327.

Gill, P. S., Wernz, J., Scadden, D. T., et al. (1996). Randomized phase-III trial of liposomal daunorubicin versus doxorubicin, bleomycin, and vincristine in AIDS-related Kaposi sarcoma. *Journal of Clinical Oncology, 14*(8), 2353–2364.

Giustini, A. J., Petryk, A. A., & Hoopes, P. J. (2012). Ionizing radiation increases systemic nanoparticle tumour accumulation. *Nanomedicine, 8*, 818–821.

GOG 209. (2012). A randomized phase III trial of doxorubicin/cis-platin/paclitaxel and G-CSF versus carboplatin/paclitaxel in patients with stage III and IV or recurrent endometrial cancer.

Gordon, A. N., Fleagle, J. T., Guthrie, D., et al. (2001). Recurrent epithelial ovarian carcinoma: A randomized phase-III study of pegylated liposomal doxorubicin versus topotecan. *Journal of Clinical Oncology, 19*, 3312–3322.

Gradishar, W. J., Tjulandin, S., Davidson, N., et al. (2005). Phase-III trial of nanoparticle albumin-bound paclitaxel compared with polyethylated castor oil based paclitaxel in women with breast cancer. *Journal of Clinical Oncology, 23*(31), 7794–7803.

Greven, K., et al. (2006). Final analysis of RTOG 9708: Adjuvant prospective irradiation combined with cisplatin/paclitaxel chemotherapy following surgery for patients with high risk endometrial cancer. *Gynecologic Oncology, 103*(1), 155–159.

Hallahan, D., Geng, L., Qu, S., et al. (2003). Integrin mediated targeting of drug delivery to irradiated tumour blood vessels. *Cancer Cell, 3*, 63–74.

Hama, Y., Urano, Y., Koyama, Y., et al. (2007). A target cell-specific activatable fluorescence probe for in vivo molecular imaging of cancer based on a self-quenched avidin-rhodamine conjugate. *Cancer Research, 67*, 2791–2799.

Hanahan, D., & Weinberg, R. A. (2011). Hallmarks of cancer: The next generation. *Cell, 144*(5), 646–674.

Harisinghani, M. G., Barentsz, J., Hahn, P. F., et al. (2003). Noninvasive detection of clinically occult lymphnode metastases in prostate cancer. *New England Journal of Medicine, 348*, 2491–2499.

Hughes, A. D., Mattison, J., Powderly, J. D., et al. (2012). Rapid isolation of viable circulating tumor cells from patient blood samples. *Journal of Visualized Experiments, 15*(64), e4248. doi:10:3791//4248

Jain, K. K. (2008). Nanomedicine. Application of nanobiotechnology in medical practice. *Medical Principles and Practice, 17*(2), 89–101.

Jain, K. K. (2012). Nanodevices and techniques for clinical application. In K.K. Jain (Ed.), *The hand book of nanomedicine* (pp. 257–270). New York: Springer Sciences, Business media. doi:10.1007/978–1-61779-983-9_7

Joshi, T., Pankhurst, Q., Hattersley, S., et al. (2007). Magnetic nanoparticles for detecting sentinel lymph nodes. *European Journal of Surgical Oncology, 33*, 1135.

Karachaliou, N., Mayo-de-las-Casas, C., Molina-Vila, M. A., & Rossel, R. (2015). Realtime liquid biopsies become a reality in cancer treatment. *Annals of Translational Medicine, 3*(3), 36.

Kaspers, G. J., et al. (2013). Improved outcome in paediatric relapsed AML, results of a randomized trial on liposomal daunarubicin by the International BFM study group. *Journal of Clinical Oncology, 31*, 599–607.

Kaushal, S., McElroy, M. K., Luiken, G. A., et al. (2008). Fluorophore-conjugated anti-CEA antibody for the intraoperative imaging of pancreatic and colorectal cancer. *Journal of Gastrointestinal Surgery, 12*(11), 1938–1950.

Khan, M. K., Minc, L. D., Nigavekar, S. S., et al. (2008). Fabrication of (^{198}Au) radioactive composite nanodevices and their use for nano-brachytherapy. *Nanomedicine, 4*(1), 57–69.

Kong, A. et al. (2007). Adjuvant radiotherapy for Stage 1 endometrial cancer. *Cochrane Database System Review, 2*, CD 003916.

Koukourakis, M. I., Koukouraki, S., Giatromanolaki, A., et al. (1999). Liposomal doxorubicin and conventionally fractionated radiotherapy in the treatment of locally advanced non-small-cell lung cancer and head and neck cancer. *Journal of Clinical Oncology, 17*, 3512–3521.

Lammers, T., Subr, V., Peschke, P., et al. (2008). Image guided and passively tumour-targeted polymeric nanomedicines for radiochemotherapy. *British Journal of Cancer, 99*, 900–910.

Longmire, M., Choyke, P. L., Kobayashi, H. (2008). Nanomedicine (London), *3*(5), 703–774.

Lorusso, G., & Ruegg, C. (2008). The tumour microenvironment and its contribution to tumour evolution towards metastasis. *Histochemistry and Cell Biology, 130*, 1091–1103.

MacDonald, S. M., Harisinghani, M. G., Katkar A., et al. (2009). Nanoparticle-enhanced MRI to evaluate radiation delivery to the regional lymphatics for patients with breast cancer. *International Journal of Radiation Oncology Biology Physics.*

Maggiorella, L., Barouch, G., Devaux, C., et al. (2012). Nanoscale radiotherapy with hafnium oxide nanoparticles. *Future Oncology*, *8*(9), 1167–1181. doi:10:2217/fon.12.96

Mali, S. (2013). Nanotechnology for surgeons. *Indian Journal of Surgery, 75*(6), 485–492.

Mamot, C., et al. (2012). Tolerability, safety, pharmacokinetics and efficacy of doxorubicin-loaded anti-EGRF immunoliposomes in advanced solid tumours; A phase 1 dose-escalation study. *Lancet Oncology, 13*, 1234–1241.

Marill, J., Anesary, N. M., Zhang, P., et al. (2014). Hafnium oxide nanoparticles: Toward an in vitro predictive biological effect? *Radiation Oncology*, *9*(1), 150. doi:10:1186/1748-717x9-150

Matsumura, Y. (2014). The drug delivery by nanomedicine and its clinical aspects. *Japanese Journal of Clinical Oncology, 44*(6), 515–528.

Menard, S., Casalini, P., Campiglio, S., et al. (2001). HER2 overexpression in various tumour types, focussing on its relationship to the development of invasive breast cancer. *Annals of Oncology, 12*(suppl 1), S15–S19.

Mohs, A. M., Mancini, M. C., Singhal, S., et al. (2010). Hand-held spectroscopic device for in vivo and intraoperative tumor detection: contrast enhancement, detection sensitivity, and tissue penetration. *Analytical Chemistry, 82*(21), 9058–9065.

Montanari, M., et al. (2012). Phase II trial of non-pegylated liposomal doxorubicin and low-dose prednisolone in second-line chemotherapy for hormone-refractory prostate cancer. *Tumori, 98*, 701–969.

Mousa, S. A., & Bharali, D. J. (2011). Nanotechnology-based detection and targeted therapy in cancer: Nano-bio paradigms and applications. *Cancers, 3*, 2888–2903.

Muson, J. M., & Scieh, A.C. (2014). Interstitial fluid flow in cancer: Implication for disease progression on treatment. *Cancer Management and Research*, *6*, 317–328. doi:10.2147/CMAR.S65444

Mystakidou, K., Tsilika, E., & Vlahos, L. (2007). Oral transmucosal fentanyl citrate in cancer pain management: A practical application of nanotechnology. *International Journal of Nanomedicine, 2*(1), 49–54.

Neuwelt, E. A., Varallyay, P., Bago, A. G., Muldoon, L. L., Nesbit, G., & Nixon, R. (2004). Imaging of iron oxide nanoparticles by MR and light microscopy in patients with malignant brain tumours. *Neuropathology and Applied Neurobiology*, *30*(5), 456–471.

Niederhuber, J. E. (2007). Developmental biology, self-renewal and cancer. *Lancet Oncology, 8*, 456–457.

NNI. (2015). What is nanotechnology? Available online http://hww.nano.gov/nanotech-101/what/defintion. Accessed in September, 2015.

Noor Rushdan, M., Tay, E. H., Jeffrey, & L. J. H. (2011). *Handbook of gynaecologic oncology.* RA Globalcrest Sdn Bhd.

Obataya, I., Nakamura, C., Han, S., Nakamura, N., Miyake, J. (2005). Nanoscale operation of a living cell using atomic force microscope with a nanoneedle. *Nano Letters*, *5*(1), 27–30.

Oerlemans, C., Bult, M., Bos, G., et al. (2010). Polymeric micelles in anticancer therapy targeting, imaging and triggered release. *Pharmaceutical Research, 27*, 2569–2589.

Onda, T., Matsumoto, K., Shibata, T., et al. (2008). Phase III trial of upfront debulking surgery versus neoadjuvant chemotherapy for stage III/IV ovarian, tubal and peritoneal cancers; Japan clinical oncology group study (JCOG 0602). *Japanese Journal of Clinical Oncology, 38*, 74–77.

Parvin, P. P., & Loftus, M. J. (2011). What's the big idea? *16 Discoveries that could save (Or at least change) your life*. Emory Magazine, Spring 2011.

Patel, B., Kirkwood, A., Dey, A., et al. (2013). Feasibility of pegylated-asparginase (pegasp) during induction in adult with acute lymphocytic leukemia (ALL): Results from the UK phase-3 multicentre trial UKALL 14. *Blood, 122*(21), 3900.

Peer, D., Karp, J. M., Hong, S., et al. (2007). Nanocarrier is an emerging platform for cancer therapy. *Nature Nanotechnology, 2*(12), 751–760.

Pollard, J. W. (2004). Tumour-educated macrophages promote tumour progression and metastasis. *Nature Reviews Cancer, 4*, 71–78.

Pouw, J. J., Grootendorst, M. R., Bezooijen, R., et al. (2015). Preoperative sentinel lymph node localization in breast cancer with superparamagnetic iron oxide-MRI: The SentiMAG multicentre trial subprotocol. *The British Journal of Radiology.*

Qiu, L., Jing, N., & Jing, Y. (2008). Preparation and in vivo evaluation of liposomal chloroquine diphosphate loaded by a transmembrane pH gradient method. *International Journal of Pharmaceutics, 361*(1–2), 56–62.

Rastogi, V., Yadav, P., Bhattacharya, S. S. et al. (2014). Carbon nanotubes: An emerging drug carrier for targeting cancer. *Journal of Drug delivery*, Article ID 640815, p. 23. http://dx.doi.org/10.1155/2014/670815

Regnic, D. B., & Tinkle, S. S. (2007). Ethical issues in clinical trials involving nanomedicine. *Contemporary Clinical Trials, 28*(4), 433–441.

Riggo, C., Pagni, E., Raffa, V., & Caschieri, A. (2011). Nano-oncology: Clinical application for cancer therapy and future perspective. *Journal of Nanomaterials*, Article ID 164506, p. 10.

Rosenthal, D. I., Yom, S. S., Liu, L., et al. (2002). A phase I study of SPI-077 (Stealth liposomal cisplatin) concurrent with radiation therapy for locally advanced head and neck cancer. *Investigational New Drugs, 20*, 343–349.

Roszek, B., de Jong, W. H., Geertsma, R. E. (2005) Nanotechnology in medical applications: State-of-the-art in materials and devices. RIVM report. 265001001. http://rivm.openrepository.com/rivm/bitstream/10029/7265/1/265001001.pdf

Saksena, M. A., Sarkar, A., & Harisinghani, M. G. (2006). Lymphotrophic nanoparticle enhanced MR imaging(LNEMR) technique for lymph node imaging. *European Journal of Radiology, 58* (3), 367–374.

Schmidt, C. (2004). The Gompertzian view. Norton honours for the role in establishing cancer treatment application. *JNCI, 96*(20), 1492–1493.

Shih, H. A., Harisinghani, M., Zietman, A. L., et al. (2005). Mapping of nodal disease in locally advanced prostate cancer: Rethinking the clinical target volume for pelvic nodal irradiation based on vascular rather than bony anatomy. *International Journal of Radiation Oncology Biology Physics, 63*, 1262–1269.

Singhal, S., Nie, S., & Wang, M. D. (2010). Nanotechnology applications in surgical oncology. *Annual Review of Medicine*, *61*, 359–373. doi:10:1146/annurev.med.60.052907.0949.36

Sprintz, M., Beneditti, C., & Ferrari, M. (2005). Applied nanotechnology for the management of cancer pain. *Minerva Anaesthesia, 71*, 419–423.

Tannock, F. (1989). Acid pH in tumours its potential for therapeutic intervention. *Cancer Research, 49*, 4173–4184.

Tao, S. L., & Desai, T. A. (2003). Microfabricated drug delivery system: From particles to pores. *Advanced Drug Delivery Reviews, 55*, 315–328.

Tarchilin, V. P. (2005). Recent advances with liposomes as pharmaceutical carrier. *Nature Reviews Drug Discovery, 4*(2), 145–160.

Thakor, A. S., & Gambhir, S. S. (2013). Nanooncology: The future of cancer diagnosis and therapy. *CA: A Cancer Journal for Clinicians, 63*, 395–418.

Thaxton, C. S., Elghanian, R., Thomas, A. D., et al. (2009). Nanoparticle-based bio-barcode assay redefines "undetectable" PSA and biochemical recurrence after radical prostatectomy. *Proceedings of the National Academy of Sciences, 106*, 18437–18442.

Thekkek, N., & Richards-Kortuno, R. (2008). Optical imaging for cervical cancer detection: Solution for a continuing global problem. *Nature Reviews Cancer, 8*(9), 725–731.

Thill, M., Kurylcio, A., Welter, R., et al. (2014). The central European SentiMag study: Sentinel lymph node biopsy with superparamagnetic iron oxide (SPIO) vs. radioisotope. *The Breast, 23*, 175–179.

Toy, R., Bauer, L., Holmes, C., et al. (2014). Targeted nanotechnology for cancer imaging. *Advanced Drug Delivery Reviews, 76*, 79–97.

United Nations' Development Fund for Women (UNIFEM). (2007). Opportunities for Women and girls' health; Building support for cervical cancer screening. Background working paper 2.

Urano, Y., Asanuma, D., Hama, Y., et al. (2009). Selective molecular imaging of viable cancer cells with pH-activatable fluorescence probes. *Nature Medicine, 15*, 104–109.

Varallyay, C. G., Nesbit, F., Fu, R. et al. (2013). High resolution steady state cerebral blood volume maps in patients with central nervous system neoplasms using ferumoxytol, a superparamagnetic iron oxide nanoparticle. *Journal of Cerebral Blood Flow and Metabolism, 33*, 780–786. doi:10:1038/jcbfm.2013:36

Veiseh, M., Gabikian, P., Bahrami, S. B., et al. (2007). Tumor paint: A chlorotoxin: Cy5.5 bioconjugate for intraoperative visualization of cancer foci. *Cancer Reserach*, *67*(14), 6882–6888 [PubMed: 17638899].

Vogel, C. L., Wojtukiewicz, M. Z., Carroll, R. R., et al. (2005). First and subsequent use of pegfilgrastim prevents febrile neutropenia in patient in patients with breast cancer: A multicentre, double-blind, placebo controlled phase-III study. *Journal of Clinical Oncology, 23*, 1178–1184.

Wang, A. Z., & Tepper, J. E. (2014). Nanotechnology in radiation oncology. *Journal of Clinical Oncology, 32*(26), 2679–2885.

Wang, M., & Thanou, M. (2010). Targeting nanoparticles to cancer. *Pharmacological Research, 62*(2), 90–99.

Wang, Z., Wu, L. C., & Chen, J. Q. (2011). Sentinel lymph node biopsy compared with axillary lymph node dissection in early breast cancer: A meta-analysis. *Breast Cancer Research and Treatment, 129*(3), 675–689.

Wang, X., Yang, L., et al. (2008). Application of nanotechnology in cancer therapy and imaging. *CA: A Cancer Journal for Clinicians, 58*, 97–110.

Yokota, J. (2000). Tumor progression and metastasis. *Carcinogenesis, 21*(3), 497–503.

Zamzida, Y., et al. (2010). Comparison of morbidity and outcome in stage 3C endometroid uterine cancer, between patients receiving chemoradiation and those only receiving radiation, in KK Hospital Singapore. *Malaysian Journal of Obstetrics and Gynaecology* (Int OGSM Edition 2010).

Zhang, H., Yee, D., & Wang, C. (2008). Quantum dots for cancer diagnosis and therapy: Biological and clinical perspectives. *Nanomedicine (London), 3*(1), 83–91.

Zhao, J., Lee, P., Wallace, M. J., & Melancon, M. P. (2015). Gold nanoparticles in cancer therapy: Efficacy, biodistribution, and toxicity. *Current Pharmaceutical Design, 21*(29), 4240–4251.

Current Trends in the Preparation of Nanoparticles for Drug Delivery

Irshad Ul Haq Bhat, Zakia Khanam and A.H. Bhat

Abstract The efficiency of a drug depends on target specificity and its solubility. The non-specificity of the drug molecules not only needs extra doses to treat diseases but also is associated with adverse drug reactions. Thus, newly engineered nanoparticles as a vector represent an exciting example which has shifted the paradigm from conventional therapies such as surgery, chemotherapy, and radiation to the novel drug delivery system. Among the nanocarriers developed so far, silica and gold nanoparticles have emerged as potential candidates who can deliver different drug molecules at target sites in a controllable and sustainable approach. In the present era, drugs released and delivered by engineered nanoparticles have attracted enough attention because of the prospects in cancer therapy, in particular, and in the treatment of other ailments. The fundamental properties of nanoparticles in drug loading, releasing, and biochemical competency can be altered by means of suitable conjugation with appropriate coatings or external magnetic fields. Therefore, this book chapter is focused on preparation, development, and application of very recently reported silica and gold nanoparticle system as a drug delivery cargo.

Keywords Silica · Gold · Target specificity · Drug delivery cargo

I.U.H. Bhat (✉)
Faculty of Earth Science, Universiti Malaysia Kelantan, Campus Jeli,
17600 Jeli, Kelantan, Malaysia
e-mail: irshadbhat78@gmail.com

Z. Khanam
Faculty of Agro Based Industry, Universiti Malaysia Kelantan, Campus Jeli,
17600 Jeli, Kelantan, Malaysia

A.H. Bhat
Department of Fundamental and Applied Sciences,
Universiti Teknologi PETRONAS, 32610 Bandar Seri Iskander,
Perak Darul Ridzuan, Malaysia

K. Viswanatha Sharma and N. Hisham B Hamid (eds.),
Engineering Applications of Nanotechnology, Topics in Mining, Metallurgy
and Materials Engineering, DOI 10.1007/978-3-319-29761-3_12

1 Introduction

The advances of nanotechnology in medical application particularly in drug delivery have gained much impetus in recent years. Nanotechnological applications in delivering medicine have generated a pivotal field of technology that has brought great developments to combat a wide range of diseases (Ranghar et al. 2014).

The drug delivery has also provided a good chance to pharmaceutical industries to expand their profitable markets. The drug delivery with target specificity conveys optimum amount of drug to target as compared to drugs used before, which eventually reduces healthcare costs. The problems of solubility, cytotoxicity, and generic delivery of drugs have also limited their use. However, the optimistic approach of scientists toward application of nanotechnology in medicine has given new approach in diagnosing and treating medical ailments. The anticipated application in terms of drug delivery has resulted in preparation of engineered nanoparticles as a prominent tool to recognize various applications. Nanoparticles are colloidal material systems mainly composed of inorganic (silica, silver, iron, gold, copper) nanoparticles, while organic nanoparticles are lipids, proteins, nucleic acids, or polymers of 100–200 nm or less in size. These nanoparticles are also considered as protected routes for delivery of drugs which are prone to cellular metabolism or destruction before being reached to the target. Different materials with various sizes in nanometers are shown in Fig. 1.

These nanoparticles by virtue of their distinctive characteristics viz. quantum properties, ability to adsorb, and transport other compounds, etc. have earned a good place in the drug delivery process (De Jong and Borm 2008). Although, other criterias which engineered nanoparticles should address are effective binding, stability, biocompatibility, bioavailability, and target specificity (Raju et al. 2015). The photoluminescence properties of nanoparticles have played a tremendous role in imaging and have a capability to act on diseased cells, but accurate mechanism is the study of concern (Sharma et al. 2015). Nanoparticles in conjugation with other

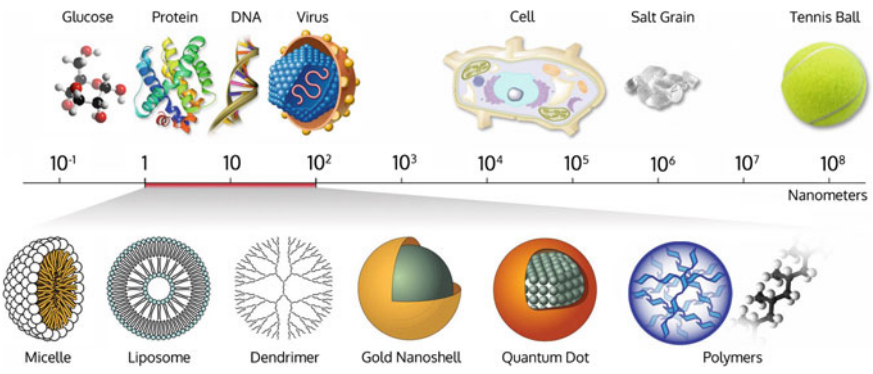

Fig. 1 Various sizes of materials in nanometers; figure adapted from Hulkoti and Taranath (2014)

therapeutic agents act as a transporter which enhances the pharmaceutical and pharmacological properties of therapeutic agents (Sun et al. 2015). Currently, nanoparticles emerged as an alternative approach to deliver drugs, alter their kinetics and distribution in the body. Thus, this book chapter is mainly focused on silica and gold nanoparticles for their exploitations as therapeutic, diagnostics, and imaging alternatives.

2 Silica Nanoparticles and Their Role in Drug Delivery

Silica nanoparticles can be classified as mesoporous nanoparticles (MSNs) or nonporous (SNPs). The pore size in MSNs ranges from 2 to 50 nm and are extensively used for the delivery of drugs by means of physical or chemical interaction. The SNPs can be associated with drugs via functional groups present. The cytotoxicity of silica NPs is characteristic of their particle size and shape, surface chemistry, stability, and selected target. The level of cytotoxicity can be altered by loading a drug of appropriate choice.

The mesoporous silica nanoparticles (MSNs) have established their role in a drug delivery process as nanocarriers owing to their greater surface area and available functional groups at the surface. The clear sign of doxorubicin loaded, newly engineered MSNs grafted with β-cyclodextrin with linker 3-carboxy-5-nitrophenylboronic acid has been established to show increased inhibition of HeLa and HepG2 cells (Chen et al. 2015). The pathway was monitored by using tracer fluorescein isothiocyanate. The study revealed that mesoporous silica nanoparticles can be exploited as a biomedical agent for treatment of cancer (Fig. 2).

The rapid metabolism of cancerous cells as compared to normal cells needs higher consumption of glucose. Niemelä et al. (2015) in a comparative study used

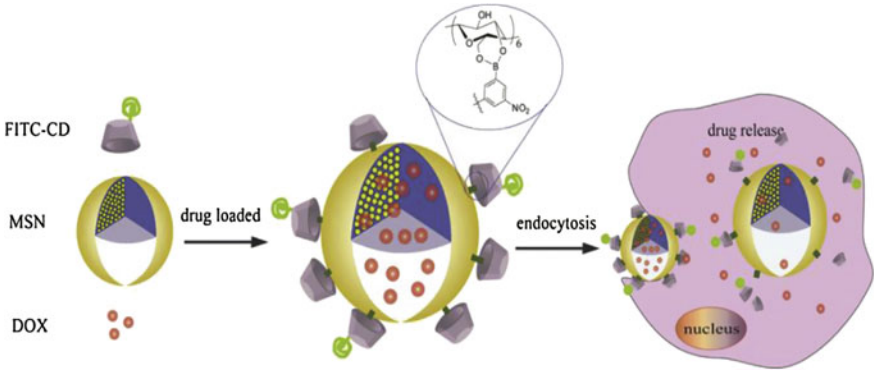

Fig. 2 Graphical illustration of DOX loading and intracellular triggered release from MSNs; figure adapted from Chen et al. (2015)

MSNs surface for adhering the glucose along with an anticancer drug celastrol for controlled delivery at target sites (Niemelä et al. 2015). Two routes were opted for this targeted drug delivery: conjugation of MSNs with sugar and by facilitation of polyethylenimine (PEI). It was concluded that apoptotic ability of celastrol was enhanced by specifically engineering the MSNs. This study ascertained the role of MSNs as a transporter for delivering a well-known anticancer agent celastrol on specific targets, HeLa and A549 cells.

The healthy cells should be escaped from becoming the target during cancer therapies. The receptor-mediated pathways of drugs can enhance the concentration of drugs at a tumor site. An et al. (2015) modified the MSNs with glycopolymer for better availability of drugs at a target site with enhanced anticancer capability (An et al. 2015). The magnetic property of newly designed nanoparticles was manipulated by application of external magnetic field. The study was able to confer that the role of glycopolymer-conjugated nanoparticles can precisely target the cancer cells via receptor-mediated endocytosis. Also, An and co-workers were able to design nanoparticles with enhanced capability to target the cancer cells along with MR imaging properties.

Hollow mesoporous silica nanoparticles (HMSNs) possess larger surface area with high degree of drug loading capacity and are considered as exceptional biocompatible nanoparticles. HMSNs are one of the most promising carriers for effective drug delivery due to their large surface area, high volume for drug loading, and excellent biocompatibility. She et al. (2015) prepared spherical HMSNs (Fig. 3) with

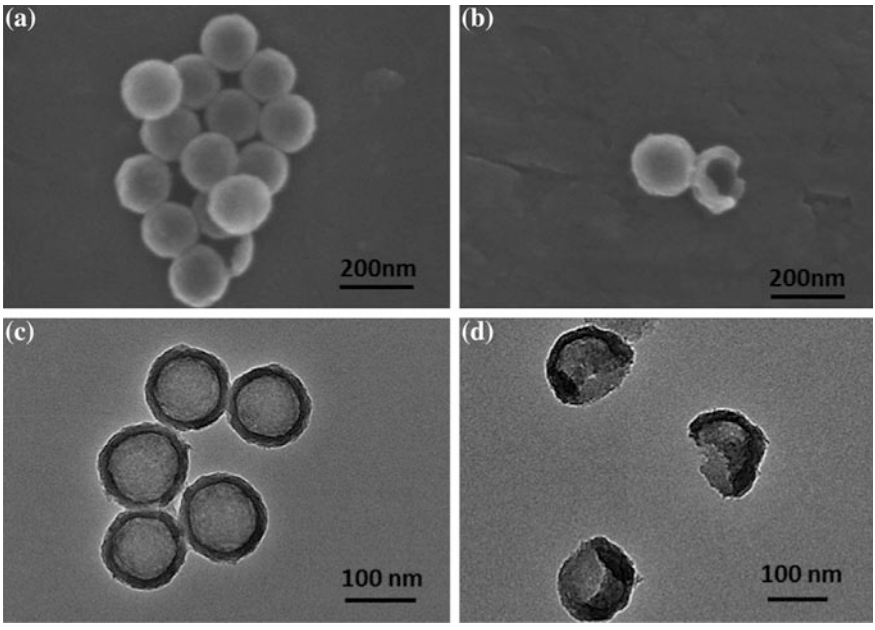

Fig. 3 SEM (**a**, **b**) and TEM images (**c**, **d**) of HMSNs; figure adapted from She et al. (2015)

bigger internal cavities by exploiting Eudragit S100 nanoparticles. The engineered nanoparticles were capable of loading high amount of drug 5-fluorouracil (5-FU) and can be projected as potential drug transporting agents for colorectal cancers (She et al. 2015). In another report, Xu et al. (2015c) revealed that HMSNs could be moieties having high drug doxorubicin hydrochloride (DOX) loading capacity, attributed to porous structures and high surface area of HMSNs, thus predicting their strong application in targeted drug delivery (Xu et al. 2015c).

The simple pH-sensitive method for preparation of mesoporous silica nanoparticles modified by polyamidoamine dendrimers was reported first time by Xu et al. (2015b). The dendrimer-modified HMSNs can provide higher number of reaction sites, thereby, retaining the drug, regulating the release, and imparting fluorescent character to drug molecule (Xu et al. 2015b). This study may offer new avenues for biomedical imaging diagnosis and cancer therapy. Ghasemnejad et al. (2015) studied for the first time the control release of betamethasone sodium phosphate loaded on MSNs (Ghasemnejad et al. 2015).

Zhang and Kong (2015) tried to enhance the selective target specificity of potential anticancer drug, DOX (Zhang and Kong 2015). The surface of silica nanoparticles was modified by DOX with the help of hydrazine linkage. They were able to deliver drug DOX loaded on silica nanoparticles to HeLa cancer lines and were monitored by using confocal laser scanning and nuclear scanning microscopy. Furthermore, the duo also reported the live tracking of nanoparticles loaded drugs in the cells.

In other report of surface modification, Tian et al. (2015) used rhodamine B (RhB) and light for better drug delivery (Tian et al. 2015). The images of live breast tumor (MCF-7) cells generated from multimodal nonlinear optical imaging microscopy revealed the effective delivery of nanoparticles. In other noticeable study, Xu et al. (2015a) modified silica nanoparticles with micelles as a gating agent, thus combined two types of drug transporters. The curcumin acted as fluorescent label and nanoparticle was loaded by DOX to evaluate the cytotoxic effects on human lung cancer (A549) cells. The presence of micelles on the surface of nanoparticles has given new opportunity to drug delivery system and hence mesoporous nanoparticles loaded with such anticancer drugs can be used both as biomedical imaging and strong anticancer agents (Xu et al. 2015a).

Cisplatin, a platinum-based complex, has long history of being used as anticancer drug, but due to certain toxic effects, e.g., neurotoxicity and nephrotoxicity, there is always a need for alternative platinum-based anticancer complexes. In this context, Ravera et al. (2015) loaded silica-based nanoparticles with Pt(IV) complexes utilizing amino groups present on external shell of nanoparticles. The fabricated silica nanoparticles were tested on human ovarian carcinoma (A2780) cells and were proved as good carriers of Pt (IV) prodrug. However, the accumulation of a drug outside the cell has affected the therapeutic ability and delivery of Pt(IV) loaded on nanoparticles to the target cells. The authors emphasized that silica nanoparticles and Pt(IV) should be chosen carefully to yield very active conjugate (Ravera et al. 2015).

Silica nanoparticles modified by polymers have been used in the process of drug delivery. Wang et al. (2015a) prepared well-characterized MSNs, modified with polymer polyethylene glycol (PEG) via disulfide bonds. In this, conjugated polymer chains acted as gatekeepers which can block drugs to be released with the pores of nanoparticles. The modification by PEG enhanced the cytotoxicity of nanoparticles due to the presence of biocompatible PEG chains (Wang et al. 2015a). Hanafi-Bojd et al. (2015) also reported that modification of silica nanoparticles by phosphate, PEG, and polyethylenimine-polyethylene glycol (PEI-PEG) groups loaded with anticancer drug, epirubicin hydrochloride (EPI), enhanced the antitumor efficacy of the drug. The modification reflects that effective nanocarriers for improvement of antitumor therapies can be generated from this combination (Hanafi-Bojd et al. 2015).

Apart from the drug delivery to cancerous targets, the engineered nanoparticles have been used to repair the damaged tissues. Ren et al. (2015) successfully delivered ascorbic acid loaded on fluorescent MSNs to human embryonic cells. The study was aimed to contribute the induction of embryonic cell differentiation toward cardiomyocytes in order to generate a new approach toward tissue engineering (Ren et al. 2015). For the demand to repair the defective bony tissues, MSNs have attracted considerable attention attributed to their biocompatibility and porous structure that can hold the drug molecules. Luo et al. (2015) loaded bone forming peptide (BFP) obtained from bone morphogenetic protein-7 (BMP-7) into MSNs. The modified MSNs by peptide provided better bioactivity and osteogenic differentiation. It was the first kind of such study where the loading of osteogenic peptide into MSNs was reported. This type of nanoparticles can be considered as a potential drug delivery bioactive material for bone repairing, bone regeneration, and bioimplant coating applications (Luo et al. 2015). Li et al. (2015) stated that silica nanoparticle-based scaffolds have great potential for bone repair and regeneration (Li et al. 2015).

The mesoporous nanoparticles in combination with organic polymers can help cell adhesion, proliferation, and biomineralization of bone cells. The MSNs surface is rich in silanol functionalities and has high tendency to react with body fluids to generate active nano-sized carbonated apatite, which can bind to natural bone. The generated bioactive bond leads to integration of implanted bone (Wang et al. 2015b). Nevertheless, the silica nanoparticles have exhibited osteoclast differentiation and enhanced osteoblast differentiation. Meddahi-Pelle et al. (2014) in their model study on rats used silica nanoparticles for fast healing of wounds in skin and liver (Meddahi-Pelle et al. 2014).

The defects in solid tissue like bone are usually fixed by autografts and allografts, but are limited due to availability, donor site morbidity, and potential disease transmission (Zhou et al. 2015). The synthetic bones from bioactive material are biocompatible, biodegradable, and osteogenic, and can be an alternative. Bioceramics, bioactive glasses, hydroxyapatite (HA), and β-tricalcium phosphate (TCP) are materials used for bone tissue regeneration (He et al. 2012, 2014 Vines et al. 2012). However, the shift toward exploitation of MSNs due to their several physiochemical advantages is considered as potential bone substitutes. Nanohydroxyapatite is an essential bone component matched with MSNs in terms of size, thus making them prominent entity for bone tissue repair. The surface of

MSNs was modified by bone morphogenetic protein-2 (BMP-2) responsible for osteoblast differentiation and stimulates bone regeneration by covalent grafting aminosilane linker. Dexamethasone (DEX) was then loaded into the pores of MSNs to construct nanoparticulate osteogenic delivery systems (DEX@MSNs-pep). The research group revealed that newly designed system had better cytocompatibility when tested with bone mesenchymal stem cells. The cellular uptake efficacy of DEX@MSNs-pep was remarkably higher than that of MSNs alone (Fig. 4).

Athinarayanan et al. (2014) reported that silica nanoparticles obtained from rice husk can be explored for bone tissue engineering. After conducting MTT assay, cell morphologies revealed the silica nanoparticles had excellent human mesenchymal stem cells (hMSC) biocompatibility, thus promoting silica nanoparticles as induction of osteogenic and chondrogenic differentiation (Athinarayanan et al. 2014). The summary of recently prepared silica nanoparticles and their role for specific target is given in Table 1.

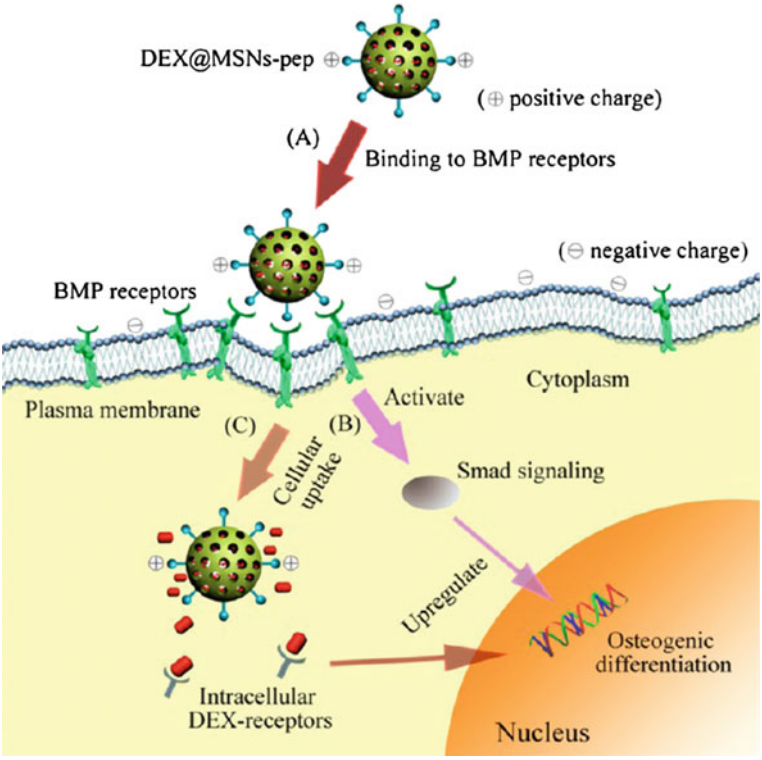

Fig. 4 Influence of DEX loaded silica nanoparticles on osteogenic differentiation. (*A*) binding to the cells surface. (*B*) Formation of complexes potentially activates the downstream osteogenic pathways. (*C*) Nanoparticles delivered into cells by endocytosis, and DEX is released into cytoplasm; figure adapted from Zhou et al. (2015)

Table 1 Role of recently modified silica nanoparticles with various loaded drugs

Drug loaded	Modifying/coating agent	Target/role	References
Chlorambucil	Folic acid and quinoline chromophore	Anticancer	Karthik et al. (2014)
DOX	Polycaprolactone and polyacrylic acid (PAA)	Neuroblastoma (SKN-BE(2))	Chen et al. (2014)
DOX hydrochloride	Bis-aminated poly(glycerol methacrylate) (BA-PGOHMAs) and cucurbit (Chen et al. 2015) uril	HeLa cell lines and fibroblast cell lines (L929)	Li et al. (2014a)
Felodipine	Cellulose acetate (CA) and PEG	Blood pressure	Wu et al. (2014)
Safranin O (S1-P) or doxorubicin (S2-P)	Peptide	Cancer treatment	de la Torre et al. (2014)
Cisplatin	Folic acid (FA) and rhodamine isothiocyanate (RITC)	Lung cancer	Mohapatra et al. (2014)
Neurotrophins	–	Sensorineural hearing loss	Wang et al. (2014)
Doxorubicin	Chitosan	Bone marrow	Hakeem et al. (2014)
Ibuprofen	Chitosan hydrogel	Titanium implants	Zhao et al. (2014a)
Mesalazine	Sodium alginate	Adenocarcinoma cell line	Popova et al. (2014)
Insulin	Chitosan, sodium alginate, or polyethylene glycol		Andreani et al. (2014b)
Doxorubicin	Cytochrome c	Cancer therapy	Zhang et al. (2014a)
Curcumin	–	Anticancer	Jambhrunkar et al. (2014)
Insulin	PEG	–	Andreani et al. (2014a)
Folic acid	Poly[(N-isopropylacrylamide)-co-(methacrylic acid)]	Laryngeal carcinoma	Liu et al. (2014)
Methylene blue and doxorubicin hydrochloride	Poly(N-isopropylacrylamide-co-acrylamide)	HELF cells and breast cancer cells (MCF-7 and HeLa)	Li et al. (2014b)

(continued)

Table 1 (continued)

Drug loaded	Modifying/coating agent	Target/role	References
DOX	Quaternary amines and PEG	Tumor accumulation and cancer therapy	Ma et al. (2014b)
Cisplatin	Carboxylic groups	Antitumor activity (A549 and MCF-7 cell lines)	Zhu et al. (2014)
Erythromycin (macrolide antibiotic)	Chitosan-PEG copolymer and (3-aminopropyl)triethoxysilane	–	Pourjavadi and Tehrani (2014)
DOX	β-cyclodextrin	Melanoma cell line (B16-F10)	Tan et al. (2014)
Antisense peptide nucleic acid (PNA)	Dye cyanine 5	HeLa cells	Ma et al. (2014a)
Curcumin	PEG	Breast adenocarcinoma cells (MCF-7)	Ma'Mani et al. (2014)
6-mercaptopurine	Methoxy polyethylene glycols	–	Zhao et al. (2014b)
Paclitaxe	–	Anticancer	Munaweera et al. (2015)
Camptothecin, CPT	Triazine or uracil uracil and adenine, respectively, linked to the bulky cyclodextrin ring	Breast cancer cells (MCF-7)	Théron et al. (2014)
DOX	Chitosan/poly (methacrylic acid) (CS-PMAA)	HeLa cells	Fang et al. (2014)
DOX	Lactobionic acid molecules coupled to heparin	HepG2 cells and tumors	Dai et al. (2014)
Sophoridine	Poly(N-isopropyl acrylamide	–	Dong et al. (2014)
DOX	Alginate/chitosan	HeLa cells	Feng et al. (2014))
Rhodamine 6G, doxorubicin	Organic alginate tyrosine-arginine-glycine-aspartic acid (K4YRGD) peptide	HepG2, liver cancer cells	Liao et al. (2014)
DOX	β-cyclodextrin	Bladder cancer therapy	Zhang et al. (2014b)
Sulfasalazine	Protein isolate	Intestine	Popat et al. (2014)

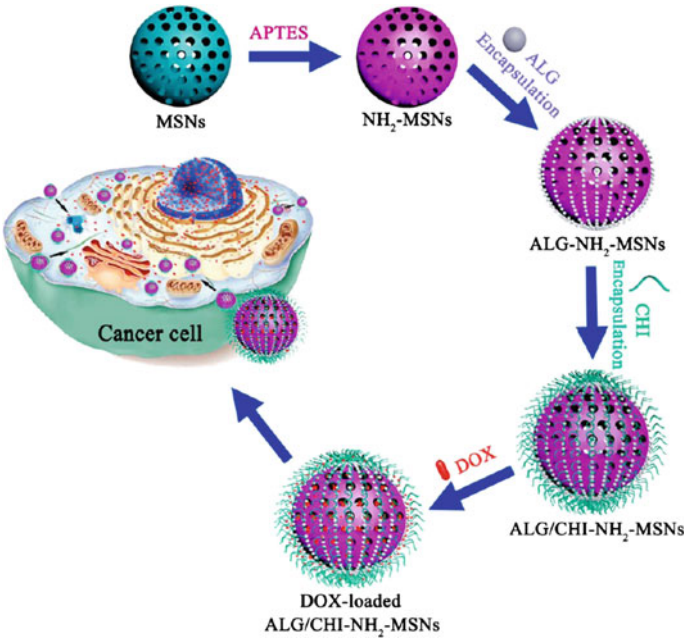

Fig. 5 Schematic depiction of pH-responsive MSN-based nanocarriers and intracellular pH-triggered DOX release; figure adapted from Feng et al. (2014)

Feng et al. (2014) revealed that fabricated pH-responsive MSN nanocarrier in combination with biocompatible polyelectrolyte multilayers of alginate/chitosan for doxorubicin for sustainable release in cancerous cells (Feng et al. 2014). The illustration is shown in Fig. 5.

3 Gold Nanoparticles and Their Role in Drug Delivery

Gold (Au) nanoparticles possess distinctive electric and magnetic properties attributed to their shape and size; therefore, a great focus in research fields such as tracking and drug delivery is the subject of interest for many researchers (Khan et al. 2015). They have been used as transporters for drug delivery also because of their biocompatibility, facile surface modification, and robust optical properties.

Seo et al. (2015) reported preparation of gold nanoparticles (AuNPs) using heavy metal-binding proteins (HMBPs) within 20 min at room temperature. The reaction rate of the proposed method is faster as compared to conventional methods commonly used for nanoparticle synthesis. The resulting nanodrug carrier AuNPs@HMBPs was loaded with DOX to evaluate the cytotoxic effects on HeLa cancer cells. The obtained nanosystem exhibited higher apoptotic effect as

compared to free DOX, indicating the better intracellular drug uptake. AuNPs are readily diffused and accumulated inside the cell nucleus without altering the cytotoxicity. The enhanced inhibition by synthesized AuNPs@HMBPs against cancerous cells provides an alternative opportunity for the treatment of cancers (Seo et al. 2015).

The green synthetic approach is best strategy followed by researchers to avoid the use of toxic reactants. AuNPs loaded with anticancer drugs resveratrol and DOX were synthesized and characterized by Tomoaia et al. (2015). The effects on HeLa and CaSki cells by these conjugates were evaluated using MTT cell viability assay for the first time. This study suggested that these AuNPs vectors can be exploited for the diagnosis of cancer (Tomoaia et al. 2015)

Phytochemicals are of tremendous importance with respect to their anticancer, antioxidant, anti-inflammatory, and antiallergic properties. Thus, Lee et al. (2015a) prepared biocompatible AuNPs attached with phytochemicals. The AuNPs prevent oxidation and act as carriers of phytochemicals or vectors; thus, this combination can increase biocompatibility and bioactivity (Lee et al. 2015a). The effect of these Phyto-AuNPs was evaluated for skin regeneration and as a healing agent. In vivo experiments revealed enhanced efficiency in overall skin growth and at the same time in generation of antioxidants. The combination of AuNPs and phytochemicals (gallic acid, protocatechuic acid, isoflavone) can be considered as potential agent for skin treatment. Similarly, Yallappa et al. (2015) prepared AuNPs by using *Mappia foetida* as bioreductant and evaluated delivery of DOX on human cancer lines. The conjugated AuNPs exhibited low toxicity toward normal epithelial cells; however, high toxicity was shown against human cancer lines (Yallappa et al. 2015). They found that optimum amount of drug was released at pH 5.3, a feasible condition for intravenous drugs. Thus, a new gold-based drug nanocarrier was developed, but extensive studies on drug delivery mechanism are yet to be explored.

Afatinib is an aniline quinazoline known for inducing apoptosis in cancer cells. Coelho et al. (2015) evaluated the afatinib delivery efficacy by pegylated thiolated polyethylene glycol gold nanoparticles (Coelho et al. 2015). They revealed that conjugated nanoparticles were capable of inhibiting cancer lines more effectively than afatinib alone. The conjugated PEG-AuNPs system with an aim to deliver drug is believed as novel candidate for drug delivery system and has to reduce toxic side effects. Figure 6 shows the illustration of drug released inside the cell as reported by Khandelia et al. (2015).

Many naturally occurring compounds, e.g., gums, glucan, and chitosan have been used in preparation of nanoparticles. Gum karaya, an exudate of plants, was used as reducing agent and stabilizer by Pooja et al. (2015) for preparation of AuNPs for drug delivery of anticancer drug gemcitabine hydrochloride (GEM) (Pooja et al. 2015). The drug in combination with nanoparticles exhibited better anticancer activity; in addition, colony formation inhibition and ROS induction were also observed as compared to GEM alone (Fig. 7). The gum karaya in association with AuNPs can be explored as possible nanocarriers for anticancer drug delivery.

Jenkins et al. (2016) utilized photosensitizer, 3-(10-hexyloxyethyl)-3-devinylpyropheophorbide-a (HPPH), along with PEG for preparation of gold

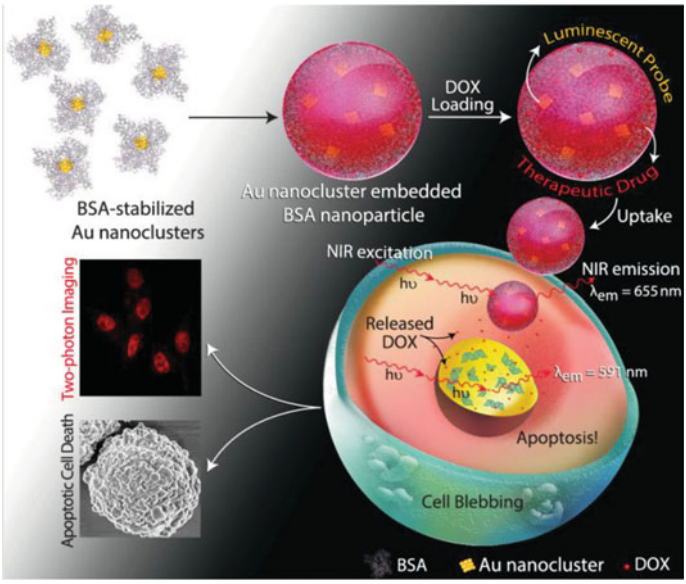

Fig. 6 Diagram depicting the formation and release of DOX from gold embedded BSA nanoparticles and their release inside HeLa cells; figure adapted from Khandelia et al. (2015)

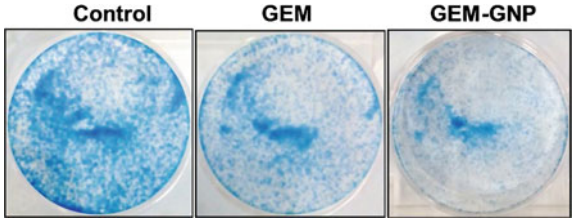

Fig. 7 Inhibition effect of gemcitabine hydrochloride loaded AuNPs stabilized by gum karaya against human lung cancer colony (A549); figure adapted from Pooja et al. (2015)

nanocages (AuNCs). By virtue of photothermal effect of AuNCs, burst release of drugs can be initiated (Jenkins et al. 2016).

McCully et al. (2015) have extensively studied that AuNPs with a low concentration of PEG functionalized with thiolated siRNA were able to induce growth inhibition of HeLa cells (McCully et al. 2015). Patra et al. (2015) stated that green synthesis is much advantageous than conventional synthesis of nanoparticles as drug delivery not only target selective, but also economical as well (Patra et al. 2015). The group synthesized nanoparticles from *Butea monosperma* (BM) leaf extract where BM leaves act as reducing as well as stabilizing agent/capping agent. They found that AuNPs were biocompatible toward cancer cells and on the basis of

drug delivery system, nanoparticles exhibited noteworthy inhibition of cancer cell proliferation (B16F10, MCF-7) as compared to anticancer drug DOX.

Lee et al. (2015b) developed pH-sensitive AuNP-drug system for the treatment of tumor. The generated nanosystem was able to deliver DOX effectively and served as an excellent alternative spectroscopic agent for detection of cancer. The controlled release of drug by gold-based nanosystem has provided new path for detection and treatment of tumors in short span of time (Lee et al. 2015b).

The AuNPs can delay the growth of tumor and its weight, attributed to their high capacity of carrying chemotherapeutic agents, and radiosensitizing capability. Park et al. (2015) reported that exploring such properties of AuNPs could benefit cancer patients, and to a larger extent can reduce resistance offered by cancer cells to different chemotherapeutic agents. The efficiency to inhibit the growth of tumor cells depends on the therapeutic performance and delivery of drugs (Park et al. 2015).

Elbialy et al. (2015), with similar context, designed AuNPs coated with iron oxide and loaded with DOX to evaluate their therapeutic effect by altering the magnetic field. Oral administration of loaded nanoparticles in the presence of external field exhibited enhanced therapeutic and lower toxic effects as compared to and lower neat DOX. Hence, this study can help in understanding the importance of better biodistribution and retention of the drug in tumor cells. The AuNPs have a tendency to absorb radiation and releases electrons (Auger electrons), which enhance its effectiveness in treating tumors (Elbialy et al. 2015).

Antosh et al. (2015) found that AuNPs in conjugation with pHLIPs (pH-low insertion peptides) increases gold uptake by cells as compared to AuNPs without pHLIP. They laid the foundation for preclinical assessment of these nanocarriers for evaluation of dose enhancement and stated that generated methodology can prove some new milestones in targeting tumors (Antosh et al. 2015).

Liu et al. (2015) reported light responsive release of drug vincristine sulfate (VCR) loaded on AuNPs conjugated into liposome with remarkable antitumor efficiency (Liu et al. 2015). The newly designed nanocarrier efficiently was able to deliver drug to HeLa cells after light exposure. This drug delivery system has provided new hope to treat lymphoblastic leukemia, cervical cancer, and breast cancers.

Similarly, Lajunen et al. (2015) investigated light-activated liposomes by loading it with nanoparticles, followed by exposure to visible and near infrared light. This study has provided new option for controlling pathological problems by releasing the drug at appropriate time and position. The functionalized and well-characterized AuNP-decorated liposomes are exceptional systems for releasing drug molecules at their targets (Lajunen et al. 2015).

Adhikari et al. (2015) stated that gastric condition facilitates the drug release due to the detachment of carboxyl-modified AuNPs from liposomes. This model study revealed that AuNP-decorated dipalmitoylphosphatidylcholine (DPPC) liposomes showed much slower drug release compared to AuNP-decorated 1,2-dimyristoyl-sn-glycero-3-phosphocholine (DMPC) liposomes. Thus, the new strategy for the controlled release of drug molecules from liposomes has been established by them (Adhikari et al. 2015). The summary of some recently fabricated AuNPs for their specific roles is given in Table 2.

Table 2 Role of modified gold nanoparticles with various loaded drugs

Drug loaded	Modifying/coating agent	Target/role	References
Paclitaxel	PEG	Liver cancer	Bao et al. (2014)
DOX	Transactivator of transcription (TAT) peptide	Brain tumor	Cheng et al. (2014)
Quinacrine dihydrochloride	Chitosan-modified gold nanoparticles (AuChi) onto the liposome surface	Bacterial infection	Thamphiwatana et al. (2014)
DOX	Cysteamine (cyst)	Breast cancer (MCF-7)	Mohammad and Yusof (2014)
Resveratrol	–	Human lung cancer cell line (A549)	Ganesh et al. (2014)
DOX		Cancerous cells (HeLa cells)	Dharmatti et al. (2014)
Cisplatin	Chitosan	Oral cancer	Goldberg et al. (2015)
Idarubicin (IDA)	Poly (lactic-co-glycolic-acid) (PLGA), maleate-polyester (MPE)	Cancer cell death	Blaudszun et al. (2014)
9-aminoacridine hydrochloride hydrate (9AA-HCl), acridine yellow (AY), acridine orange (AO), and proflavine (Pro)	Citrate	Antibacterial efficacy	Mitra et al. (2014)
DOX	Xanthan gum	Lung cancer cells	Pooja et al. (2014)
5-fluorouracil (5-Fu) and folic acid (Fa)	Pullulan	Liver cancer cell	Ganeshkumar et al. (2014)
DOX	Folic acid (FA)	Neuroblastoma	Alexander et al. (2014)
DOX	–	Breast cancer	Latorre et al. (2014)

4 Future Prospects of Engineered Nanoparticles in Drug Discovery

The fabrication of engineered nanoparticles and their approach to treat the life-threatening diseases has begun a new era of diagnostics. The novel and innovative nanoparticles have given great benefits to patients. However, there is still need of better and controlled release of drugs at the specific targets by choosing an appropriate support in conjugation with nanoparticles. The last 50 years have seen

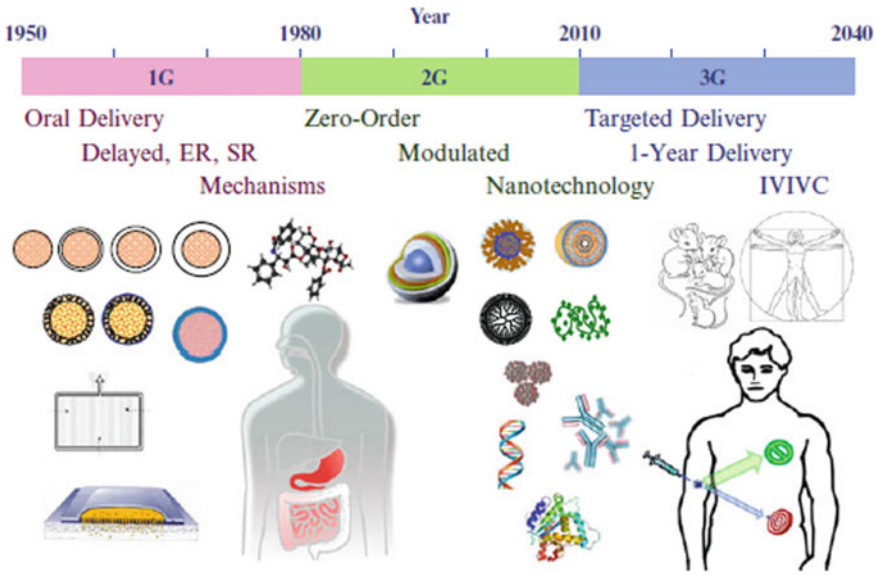

Fig. 8 Development of controlled drug delivery systems; figure adapted from Bae et al. (2013)

tremendous development in drug delivery process, although the nanotechnological drug delivery in terms of particle size was explored in early 1970s, while the first-generation (1G), second-generation (2G), and third-generation (3G) delivery process was based on the mode of administration (Fig. 8). In future, the targeted drug delivery with the help of nanoparticles or use of nanoparticles as drug itself will be improved at specific site. However, understanding of new approaches will be the thrust area of research over coming years (Bae et al. 2013).

The nanoparticle-based approach in drug delivery has demonstrated exciting efficacy against small tumors in animal models; however, the outcome at clinical stage still needs enough attention in future. The new technology, squalenoylation, nano metal oxides are generated to improve the drug loading and reduce their sudden release in the cell (Couvreur 2013). The multifunctional nanoparticles in combination with drugs acting directly on DNA by intercalation can be a thrust area for future drug delivery. The "nanotheragnostics" is also a promising mode of preparation of multifunctional nanoparticles. The integration of nanoparticle drug delivery and nano pharmacology is a major challenge to solve the problem of controlled delivery and release of drugs carried by nanoparticles. The challenge can be dealt in future by novel attitude with improved mechanism of understanding of nanomaterial behavior at cellular and molecular levels. The generation of eco-friendly and biologically compatible nanoparticle-based drug delivery systems could be a new hope to recover a large number of rejected drugs. The use of safe nanoparticle drug delivery system will add new marketable values to nano pharmaceuticals. Moghimi et al. (2011) stated that generation of biologically and

environmentally safe nanoparticulate drug delivery systems makes possible to formulate drugs in an optimal way and for personalized therapies (Moghimi et al. 2011).

5 Conclusions

The advent of engineered nanoparticles as drugs or carriers of drugs has not only opened up a new area of drug delivery process but also has overcome the problems of delivering the suspension of effective drugs. The prepared nanoparticles in combination with different drugs are best alternatives to address this problem. The presence of rich functional group surface of nanoparticles makes it prone to alteration by modifying polymers or other organic compounds. This property of nanoparticles has added extra advantage of carrying the drug to specific target. In addition, nanoparticles in combination with magnetic properties can enhance both therapeutic and imagining properties. Thus, the present book chapter has provided very recent information about the milestones achieved by different researchers in addressing the challenges faced by drugs to be delivered at specific sites and their alternate solutions.

References

Adhikari, C., Das, A., & Chakraborty, A. (2015). Controlled release of a sparingly water-soluble anticancer drug through ph-responsive functionalized gold-nanoparticle-decorated. *ChemPhysChem, 16*(4), 866–871.

Alexander, C. M., Hamner, K. L., Maye, M. M., & Dabrowiak, J. C. (2014). Multifunctional DNA-gold nanoparticles for targeted doxorubicin delivery. *Bioconjugate Chemistry, 25*(7), 1261–1271.

An, J., Zhang, X., Guo, Q., Zhao, Y., Wu, Z., & Li, C. (2015). Glycopolymer modified magnetic mesoporous silica nanoparticles for MR imaging and targeted drug delivery. *Colloids and Surfaces A: Physicochemical Engineering Aspects, 482*, 98–108.

Andreani, T., de Souza, A. L., Kiill, C. P., Lorenzón, E. N., Fangueiro, J. F., Calpena, A. C., et al. (2014a). Preparation and characterization of PEG-coated silica nanoparticles for oral insulin delivery. *International Journal of Pharmaceutics, 473*(1–2), 627–635.

Andreani, T., Kiill, C. P., Souza, A. L. R. D., Fangueiro, J. F., Fernandes, L., Doktorovová, S., et al. (2014b). Surface engineering of silica nanoparticles for oral insulin delivery: Characterization and cell toxicity studies. *Colloids and Surfaces B: Biointerfaces, 123*, 916–923.

Antosh, M. P., Wijesinghe, D. D., Shrestha, S., Lanou, R., Huang, Y. H., Hasselbacher, T., et al. (2015). Enhancement of radiation effect on cancer cells by gold-pHLIP. *Proceedings of the National Academy of Sciences of the United States of America, 112*(17), 5372–5376.

Athinarayanan, J., Periasamy, V. S., Alhazmi, M., Alatiah, K. A., & Alshatwi, A. A. (2014). Synthesis of biogenic silica nanoparticles from rice husks for biomedical applications. *Ceramics International, 41*(1), 275–281.

Bae, Y. H., Mrsny, R. J., Park, K. (2013) Dream. Chapter 26, The missing components today and the new treatments tomorrow 689. In *Cancer targeted drug delivery an elusive*. New York, Heidelberg, Dordrecht, London: Springer. doi:10.1007/978-1-4614-7876-8

Bao, Q.-Y., Zhang, N., Geng, D.-D., Xue, J.-W., Merritt, M., Zhang, C., et al. (2014). The enhanced longevity and liver targetability of paclitaxel by hybrid liposomes encapsulating paclitaxel-conjugated gold nanoparticles. *International Journal of Pharmaceutics, 477*(1–2), 408–415.

Blaudszun, A.-R., Lian, Q., Schnabel, M., Loretz, B., Steinfeld, U., Lee, H.-H., et al. (2014). Polyester-idarubicin nanoparticles and a polymer-photosensitizer complex as potential drug formulations for cell-mediated drug delivery. *International Journal of Pharmaceutics, 474*(1–2), 70–79.

Chen, X., Soeriyadi, A. H., Lu, X., Sagnell, S. M., Kavallaris, M., & Gooding, J. J. (2014). Dual bioresponsive mesoporous silica nanocarrier as an "AND" logic gate for targeted drug delivery cancer cells. *Advanced Functional Materials*, *24*(44), 6999–7006.

Chen, X., Yao, X., Wang, C., Chen, L., & Chen, X. (2015). Mesoporous silica nanoparticles capped with fluorescence-conjugated cyclodextrin for pH-activated controlled drug delivery and imaging. *Microporous and Mesoporous Materials, 217*, 46–53.

Cheng, Y., Dai, Q., Morshed, R. A., Fan, X., Wegscheid, M. L., Wainwright, D. A., et al. (2014). Blood-brain barrier permeable gold nanoparticles: An efficient delivery platform for enhanced malignant glioma therapy and imaging. *Small (Weinheim an der Bergstrasse, Germany), 10*(24), 5137–5150.

Coelho, S. C., Almeida, G. M., Pereira, M. C., Santos-Silva, F., Coelho, M. A. N. (2015). Functionalized gold nanoparticles improve afatinib delivery into cancer cells. *Expert Opinion on Drug Delivery* (Article in Press). doi:10.1517/17425247.2015.1083973

Couvreur, P. (2013). Nanoparticles in drug delivery: Past, present and future. *Advanced Drug Delivery Reviews*, *65*(1), 21–23.

Dai, L., Li, J., Zhang, B., Liu, J., Luo, Z., & Cai, K. (2014). Redox-responsive nanocarrier based on heparin end-capped mesoporous silica nanoparticles for targeted tumor therapy in vitro and in vivo. *Langmuir, 30*(26), 7867–7877.

De Jong, W. H., & Borm, P. A. (2008). Drug delivery and nanoparticle: Application and hazards. *International Journal of Nanomedicine, 3*(2), 133–149.

de la Torre, C., Mondragón, L., Coll, C., Sancenón, F., Marcos, M. D., Martínez-Máñez, R., Amorós, P., Pérez-Payá, E., Orzáez, M. (2014). Cathepsin-B induced controlled release from peptide-capped mesoporous silica nanoparticles. *Chemistry (Weinheim an der Bergstrasse, Germany)*, *20*(47), 15309–15314.

Dharmatti, R., Phadke, C., Mewada, A., Thakur, M., Pandey, S., & Sharon, M. (2014). Biogenic gold nano-triangles: Cargos for anticancer drug delivery. *Materials Science and Engineering C, 44*, 92–98.

Dong, L., Peng, H., Wang, S., Zhang, Z., Li, J., Ai, F., et al. (2014). Thermally and magnetically dual-responsive mesoporous silica nanospheres: Preparation, characterization, and properties for the controlled release of sophoridine. *Journal of Applied Polymer Science*, *131*(13), 40477.

Elbialy, N. S., Fathy, M. M., & Khalil, W. M. (2015). Doxorubicin loaded magnetic gold nanoparticles for in vivo targeted drug delivery. *International Journal of Pharmaceutics, 490*, 190–199.

Fang, W., Wang, Z., Zong, S., Chen, H., Zhu, D., Zhong, Y., et al. (2014). PH-controllable drug carrier with SERS activity for targeting cancer cells. *Biosensors and Bioelectronics*, *57*, 10–15.

Feng, W., Nie, W., He, C., Zhou, X., Chen, L., Qiu, K., et al. (2014). Effect of pH-responsive alginate/chitosan multilayers coating on delivery efficiency, cellular uptake and biodistribution of mesoporous silica nanoparticles based nanocarriers. (2014) *Applied Materials and Interfaces*, *6*(11), 8447–8460.

Ganesh, K. C., Poornachandra, Y., & Mamidyala, S. K. (2014). Green synthesis of bacterial gold nanoparticles conjugated to resveratrol as delivery vehicles. *Colloids and Surfaces B: Biointerfaces, 123*, 311–317.

Ganeshkumar, M., Ponrasu, T., Raja, M. D., Subamekala, M. K., & Suguna, L. (2014). Green synthesis of pullulan stabilized gold nanoparticles for cancer targeted drug delivery. *Spectrochimica Acta—Part A: Molecular and Biomolecular Spectroscopy, 130*, 64–71.

Ghasemnejad, M., Ahmadi, E., Mohamadnia, Z., Doustgania, A., & Hashemikia, S. (2015). Functionalized silica nanoparticles as a carrier for Betamethasone Sodium Phosphate: Drug release study and statistical optimization of drug loading by response surface method. *Materials Science and Engineering C, 56*, 223–232.

Goldberg, M., Manzi, A., Aydin, E., Singh, G., Khoshkenar, P., Birdi, A., et al. (2015). Development of a nanoparticle-embedded chitosan sponge for topical and local administration of chemotherapeutic agents. *Journal of Nanotechnology in Engineering and Medicine*, *5*(4), 041006.

Hakeem, A., Duan, R., Zahid, F., Dong, C., Wang, B., Hong, F., et al. (2014). Dual stimuli-responsive nano-vehicles for controlled drug delivery: Mesoporous silica nanoparticles end-capped with natural chitosan. *Chemical Communications, 50*(87), 13268–13271.

Hanafi-Bojd, M. Y., Jaafari, M. R., Ramezanian, N., Xue, M., Amin, M., Shahtahmasbi, N., et al. (2015). Surface functionalized mesoporous silica nanoparticles as an effective carrier for epirubicin delivery to cancer cells. *European Journal of Pharmaceutics and Biopharmaceutics, 89*, 248–258.

He, C. L., Jin, X. B., & Ma, P. X. (2014). Calcium phosphate deposition rate, structure and osteoconductivity on electrospun poly(L-lactic acid) matrix using electrodeposition or simulated body fluid incubation. *Acta Biomateriala, 10*, 419–427.

He, C. L., Zhang, F., Cao, L. J., Feng, W., Qiu, K. X., Zhang, Y. Z., et al. (2012). Rapid mineralization of porous gelatin scaffolds by electrodeposition for bone tissue engineering. *Journal of Material Chemistry, 22*, 2111–2119.

Hulkoti, N. I., & Taranath, T. C. (2014). Biosynthesis of nanoparticles using microbes-a review. *Colloids and Surfaces B: Biointerfaces, 121*(1), 474–483.

Jambhrunkar, S., Qu, Z., Popat, A., Yang, J., Noonan, O., Acauan, L., et al. (2014). Effect of surface functionality of silica nanoparticles on cellular uptake and cytotoxicity. *Molecular Pharmaceutics, 11*(10), 3642–3655.

Jenkins, S. V., Srivatsan, A., Reynolds, K. Y., Gao, F., Zhang, Y., Heyes, C. D., et al. (2016). Understanding the interactions between porphyrin-containing photosensitizers and polymer-coated nanoparticles in model biological environments. *Journal of Colloid and Interface Science, 461*, 225–231.

Karthik, S., Jana, A., Saha, B., Kalyani, B. K., Ghosh, S. K., Zhao, Y., et al. (2014). Synthesis and in vitro evaluation of charge reversal photoresponsive quinoline tethered mesoporous silica for targeted drug delivery. *Journal of Materials Chemistry B, 2*(45), 7971–7977.

Khan, A. K., Rashid, R., Murtaza, G., & Zahra, A. (2015). Gold nanoparticles: Synthesis and applications in drug delivery tropical. *Journal of Pharmaceutical Research*, *13*(7), 1169–1177.

Khandelia, R., Bhandari, S., Pan, U. N., Ghosh, S. S., & Chattopadhyay, A. (2015). Gold nanocluster embedded albumin nanoparticles for two-photon imaging of cancer cells accompanying drug delivery. *Small (Weinheim an der Bergstrasse, Germany), 11*(33), 4075–4081.

Lajunen, T., Viitala, L., Kontturi, L.-S., Laaksonen, T., Liang, H., Vuorimaa-Laukkanen, E., et al. (2015). Light induced cytosolic drug delivery from liposomes with gold nanoparticles. *Journal of Controlled Release, 203*, 85–98.

Latorre, A., Posch, C., Garcimartín, Y., Celli, A., Sanlorenzo, M., Vujic, I., et al. (2014). DNA and aptamer stabilized gold nanoparticles for targeted delivery of anticancer therapeutics. *Nanoscale*, *6*(13). 7436–7442.

Lee, J., Kim, J., Go, J., Lee, J. H., Han, D.-W., Hwang, D., et al. (2015a). Transdermal treatment of the surgical and burned wound skin via phytochemical-capped gold nanoparticles. *Colloids and Surfaces B: Biointerfaces, 135*, 166–174.

Lee, K. Y. J., Wang, Y., & Nie, S. (2015). In vitro study of a pH-sensitive multifunctional doxorubicin-gold nanoparticle system: Therapeutic effect and surface enhanced Raman scattering. *Royal Society Chemistry Advances*, *5*(81), 65651–65659.

Li, K., Sun, H., Sui, H., Zhang, Y., Liang, H., Wu, X., et al. (2015). Composite mesoporous silica nanoparticle/chitosan nanofibers for bone tissue engineering. *RSC Advanced*. doi:10.1039/C4RA15232H (In Press).

Li, Q.-L., Sun, Y., Sun, Y.-L., Wen, J., Zhou, Y., Bing, Q.-M., et al. (2014a). Mesoporous silica nanoparticles coated by layer-by-layer self-assembly using cucurbit[7]uril for in vitro and in vivo anticancer drug release. *Chemistry of Materials, 26*(22), 6418–6431.

Li, A., Zhang, J., Xu, Y., Liu, J., & Feng, S. (2014b). Thermoresponsive copolymer/SiO_2 nanoparticles with dual functions of thermally controlled drug release and simultaneous carrier decomposition. *Chemistry—A European Journal, 20*(40), 12945–12953.

Liao, Y. T., Liu, C. H., Yu, J., & Wu, K. C. W. (2014). Liver cancer cells: Targeting and prolonged-release drug carriers consisting of mesoporous silica nanoparticles and alginate microspheres. *International Journal of Nanomedicine, 9*(1), 2767–2778.

Liu, Y., He, M., Niu, M., Zhao, Y., Zhu, Y., Li, Z., et al. (2015). Delivery of vincristine sulfate-conjugated gold nanoparticles using liposomes: A light-responsive nanocarrier with enhanced antitumor efficiency. *International Journal of Nanomedicine, 10*, 3081–3095.

Liu, X., Yu, D., Jin, C., Song, X., Cheng, J., Zhao, X., et al. (2014). A dual responsive targeted drug delivery system based on smart polymer coated mesoporous silica for laryngeal carcinoma treatment. *New Journal of Chemistry, 38*(10), 4830–4836.

Luo, Z., Denga, Y., Zhang, R., Wang, M., Baid, Y., Zhaod, Q., et al. (2015). Peptide-laden mesoporous silica nanoparticles with promotedbioactivity and osteo-differentiation ability for bone tissue engineering. *Colloids and Surfaces B: Biointerfaces, 131*, 73–82.

Ma, X., Devi, G., Qu, Q., Toh, D.-F. K, Chen, G., & Zhao, Y. (2014b). Intracellular delivery of antisense peptide nucleic acid by fluorescent mesoporous silica nanoparticles *Bioconjugate Chemistry*, *25*(8), 1412–1420.

Ma, M., Zheng, S., Chen, H., Yao, M., Zhang, K., Jia, X., et al. (2014a). A combined "rAFT" and "graft From" polymerization strategy for surface modification of mesoporous silica nanoparticles: Towards enhanced tumor accumulation and cancer therapy efficacy. *Journal of Materials Chemistry B, 2*(35), 5828–5836.

Ma'Mani, L., Nikzad, S., Kheiri-Manjili, H., Al-Musawi, S., Saeedi, M., Askarlou, S., et al. (2014). Curcumin-loaded guanidine functionalized PEGylated I3ad mesoporous silica nanoparticles KIT-6: Practical strategy for the breast cancer therapy. *European Journal of Medicinal Chemistry, 83*, 646–654.

McCully, M., Hernandez, Y., Conde, J., Baptista, P. V., de la Fuente, J. M., Hursthouse, A., et al. (2015). Significance of the balance between intracellular glutathione and polyethylene glycol for successful release of small interfering RNA from gold nanoparticles. *Nano Research* (In Press). doi:10.1007/s12274-015-0828-5

Meddahi-Pelle, A., Legrand, A., Marcellan, A., Louedec, L., Letourneur, D., & Leibler, L. (2014). Organ repair, hemostasis, and in vivo bonding of medical devices by aqueous solutions of nanoparticles. *Angewandte Chemie Int Ed, 53*, 1–6.

Mitra, P., Chakraborty, P. K., Saha, P., Ray, P., & Basu, S. (2014). Antibacterial efficacy of acridine derivatives conjugated with gold nanoparticles. *International Journal of Pharmaceutics, 473*(1–2), 636–643.

Moghimi, S.M., Peer, D., & Langer, R. (2011). Reshaping the future of nanopharmaceuticals: Ad iudicium. *ACS Nano, 5*(11), 8454–8458.

Mohammad, F., & Yusof, N. A. (2014). Doxorubicin-loaded magnetic gold nanoshells for a combination therapy of hyperthermia and drug delivery. *Journal of Colloid and Interface Science, 434*, 89–97.

Mohapatra, S., Rout, S. R., Narayan, R., & Maiti, T. K. (2014). Multifunctional mesoporous hollow silica nanocapsules for targeted co-delivery of cisplatin-pemetrexed and MR imaging. *Dalton Transactions, 43*(42), 15841–15850.

Munaweera, I., Hong, J., D'Souza, A., & Balkus, K. J., Jr. (2015). Novel wrinkled periodic mesoporous organosilica nanoparticles for hydrophobic anticancer drug delivery. *Journal of Porous Materials, 22*, 1–10.

Niemelä, E., Desai, D., Nkizinkiko, Y., Eriksson, J. E., & Rosenholm, J. M. (2015). Sugar-decorated mesoporous silica nanoparticles as delivery vehicles for the poorly soluble drug celastrol enables targeted induction of apoptosis in cancer cells. *European Journal of Pharmaceutics and Biopharmaceutics, 96*, 11–21.

Park, J., Park, J., Ju, E. J., Park, S. S., Choi, J., Lee, J. H., et al. (2015). Multifunctional hollow gold nanoparticles designed for triple combination therapy and CT imaging. *Journal of Controlled Release, 207*, 77–85.

Patra, S., Mukherjee, S., Barui, A. K., Ganguly, A., Sreedhar, B., & Patra, C. R. (2015). Green synthesis, characterization of gold and silver nanoparticles and their potential application for cancer therapeutics. *Materials Science and Engineering C, 53*, 298–309.

Pooja, D., Panyaram, S., Kulhari, H., Rachamalla, S. S., & Sistla, R. (2014). Xanthan gum stabilized gold nanoparticles: Characterization, biocompatibility, stability and cytotoxicity. *Carbohydrate Polymers, 110*, 1–9.

Pooja, D., Panyaram, S., Kulhari, H., Reddy, B., Rachamalla, S. S., & Sistla, R. (2015). Natural polysaccharide functionalized gold nanoparticles as biocompatible drug delivery carrier. *International Journal of Biological Macromolecules, 80*, 48–56.

Popat, A., Jambhrunkar, S., Zhang, J., Yang, J., Zhang, H., Meka, A., et al. (2014). Programmable drug release using bioresponsive mesoporous silica nanoparticles for site-specific oral drug delivery. *Chemical Communications, 50*(42), 5547–5550.

Popova, M., Szegedi, A., Yoncheva, K., Konstantinov, S., Petrova, G. P., Aleksandrov, H. A., et al. (2014). New method for preparation of delivery systems of poorly soluble drugs on the basis of functionalized mesoporous MCM-41 nanoparticles. *Microporous and Mesoporous Materials, 198*, 247–255.

Pourjavadi, A., & Tehrani, Z. M. (2014). Mesoporous silica nanoparticles (MCM-41) coated PEGylated chitosan as a pH-responsive nanocarrier for triggered release of erythromycin. *International Journal of Polymeric Materials and Polymeric Biomaterials, 63*(13), 692–697.

Raju, G. S. R., Benton, L., Pavitra, E., & Yu, J. S. (2015). Multifunctional nanoparticles: Recent progress in cancer therapeutics. *Chemical Communications, 51*(68), 13248–13259.

Ranghar, S., Sirohi, P., Verma, P., & Agarwal, V. (2014). Nanoparticle-based drug delivery systems: Promising approaches against infections. *Brazilian Archives of Biology and Technology, 57*, 209–222.

Ravera, M., Perin, E., Gabano, E., Zanellato, I., Panzarasa, G., Sparnacci, K., et al. (2015). Functional fluorescent nonporous silica nanoparticles as carriers for Pt(IV) anticancer prodrugs. *Journal of Inorganic Biochemistry* (In Press). doi:10.1016/j.jinorgbio.2015.08.001

Ren, M., Han, Z., Li, J., Feng, G., & Ouyang, S. (2015). Ascorbic acid delivered by mesoporous silica nanoparticles induces the differentiation of human embryonic stem cells into cardiomyocytes. *Materials Science and Engineering C, 56*, 348–355.

Seo, J. M., Kim, E. B., Hyun, M. S., Kim, B. B., & Park, T. J. (2015). Self-assembly of biogenic gold nanoparticles and their use to enhance drug delivery into cells. *Colloids and Surfaces B: Biointerfaces, 135*, 27–34.

Sharma, H., Mishra, P. K., Talegaonkar, S., & Vaidya, B. (2015). Metal nanoparticles: A theranostic nanotool against cancer. *Drug Discovery Today, 20*(9), 1143–1151.

She, X., Chen, L., Velleman, L., Li, C., Zhu, H., He, C., et al. (2015). Fabrication of high specificity hollow mesoporous silica nanoparticles assisted by Eudragit for targeted drug delivery. *Journal of Colloid and Interface Science, 445*, 151–160.

Sun, L., Wu, Q., Peng, F., Liu, L., & Gong, C. (2015). Strategies of polymeric nanoparticles for enhanced internalization in cancer therapy. *Colloids and Surfaces B: Biointerfaces, 135*(1), 56–72.

Tan, S. Y., Ang, C. Y., Li, P., Yap, Q. M., & Zhao, Y. (2014). Drug encapsulation and release by mesoporous silica nanoparticles: the effect of surface functional groups. *Chemistry (Weinheim an der Bergstrasse, Germany)*, 20 (36): 11276–11282.

Thamphiwatana, S., Gao, W., Pornpattananangkul, D., Zhang, Q., Fu, V., Li, J., et al. (2014). Phospholipase A2-responsive antibiotic delivery via nanoparticle-stabilized liposomes for the treatment of bacterial infection. *Journal of Materials Chemistry B, 2*(46), 8201–8207.

Théron, C., Gallud, A., Carcel, C., Gary-Bobo, M., Maynadier, M., Garcia, M., et al. (2014). Hybrid mesoporous silica nanoparticles with pH-operated and complementary H-bonding caps as an autonomous drug-delivery system. *Chemistry–A European Journal*, *20*(30), 9372–9380.

Tian, Y., Kong, Y., Li, X., Wu, J., Ko, A. C.-T., & Xing, M. (2015). Light- and pH- activated intracellular drug release from polymeric mesoporous silica nanoparticles. *Colloids and Surfaces B: Biointerfaces, 134*, 147–155.

Tomoaia, G., Horovitz, O., Mocanu, A., Nita, A., Avram, A., Racz, C. P., et al. (2015). Effects of doxorubicin mediated by gold nanoparticles and resveratrol in two human cervical tumor cell lines. *Colloids and Surfaces B: Biointerfaces, 135*(7323), 726–734.

Vines, J. B., Lim, D.-J., Anderson, J. M., & Jun, H.-W. (2012). Hydroxyapatite nanoparticle reinforced peptide amphiphile nanomatrix enhances the osteogenic differentiation of mesenchymal stem cells by compositional ratios. *Acta Biomateriala, 8*, 4053–4063.

Wang, Y., Han, N., Zhao, Q., Bai, L., Li, J., Jiang, T., et al. (2015a). Redox-responsive mesoporous silica as carriers for controlled drug delivery: A comparative study based on silica and PEG gatekeepers. *European Journal of Pharmaceutical Sciences, 72*, 12–20.

Wang, Y., Wise, A. K., Tan, J., Maina, J. W., Shepherd, R. K., & Caruso, F. (2014). Mesoporous silica supraparticles for sustained inner-ear drug delivery. *Small*, *10*(21), 4244–4248.

Wang, Y., Zhao, Q., Han, N., Bai, L., Li, J., Liu, J., et al. (2015b). Mesoporous silica nanoparticles in drug delivery and biomedical applications. *Nanomedicine: Nanotechnology, Biology and Medicine, 11*(2), 313–327.

Wu, C., Zhao, Z., Zhao, Y., Hao, Y., Liu, Y., & Liu, C. (2014). Preparation of a push-pull osmotic pump of felodipine solubilized by mesoporous silica nanoparticles with a core-shell structure. *International Journal of Pharmaceutics, 475*(1), e298–e305.

Xu, X., Lü, S., Gao, C., Wang, X., Bai, X., Duan, H., et al. (2015a). Polymeric micelle-coated mesoporous silica nanoparticle for enhanced fluorescent imaging and pH-responsive drug delivery. *Chemical Engineering Journal, 279*, 851–860.

Xu, X., Shaoyu, L., Gao, C., Wang, X., Bai, X., Gao, N., et al. (2015b). Facile preparation of pH-sensitive and self-fluorescent mesoporous silica nanoparticles modified with PAMAM dendrimers for label-free imaging and drug delivery. *Chemical Engineering Journal, 266*, 171–178.

Xu, H., Zhang, H., Wang, D., Wu, L., Liu, X., & Jiao, Z. (2015c). A facile route for rapid synthesis of hollow mesoporous silica nanoparticles as pH-responsive delivery carrier. *Journal of Colloid and Interface Science, 451*, 101–107.

Yallappa, S., Manjanna, J., Dhananjaya, B. L., Vishwanatha, U., Ravishankar, B., & Gururaj, H. (2015). Phytosynthesis of gold nanoparticles using Mappia foetida leaves extract and their conjugation with folic acid for delivery of doxorubicin to cancer cells. *Journal of Materials Science Materials in Medicine, 26*(9), 235–247.

Zhang, P., & Kong, J. (2015). Doxorubicin-tethered fluorescent silica nanoparticles for pH-responsive anticancer drug delivery. *Talanta, 134*, 501–507.

Zhang, B., Luo, Z., Liu, J., Ding, X., Li, J., & Cai, K. (2014a). Cytochrome c end-capped mesoporous silica nanoparticles as redox-responsive drug delivery vehicles for liver tumor-targeted triplex therapy in vitro and in vivo. *Journal of Controlled Release, 192*, 192–201.

Zhang, Q., Neoh, K. G., Xu, L., Lu, S., Kang, E. T., Mahendran, R., et al. (2014). Functionalized mesoporous silica nanoparticles with mucoadhesive and sustained drug release properties for potential bladder cancer therapy. *Langmuir*, *30*(21), 6151–6161.

Zhao, P., Liu, H., Deng, H., Xiao, L., Qin, C., Du, Y., et al. (2014a). A study of chitosan hydrogel with embedded mesoporous silica nanoparticles loaded by ibuprofen as a dual stimuli-responsive drug release system for surface coating of titanium implants. *Colloids and Surfaces B: Biointerfaces, 123*, 657–663.

Zhao, Q., Wang, C., Liu, Y., Wang, J., Gao, Y., Zhang, X., et al. (2014b). PEGylated mesoporous silica as a redox-responsive drug delivery system for loading thiol-containing drugs. *International Journal of Pharmaceutics, 477*, 613–622.

Zhou, X., Feng, W., Qiu, K., Chen, L., Wang, W., Nie, W., et al. (2015). BMP-2 derived peptide and dexamethasone incorporated mesoporous silica nanoparticles for enhanced osteogenic differentiation of bone mesenchymal stem cells. *ACS Applied Materials and Interfaces, 7*(29), 15777–15789.

Zhu, X., Gu, J., Li, Y., Zhao, W., & Shi, J. (2014). Magnetic core-mesoporous shell nanocarriers with drug anchorages suspended in mesopore interior for cisplatin delivery. *Microporous and Mesoporous Materials, 196*, 115–121.